
**MULTISCALE VISCOUS AND NON-VISCOUS DEFORMATION OF BULK
& THIN FILM SYSTEMS VIA IMPROVED NANOINDENTATION
METHODOLOGY**

By

Abdul Khaliq Shah

A thesis submitted in partial fulfilment for the requirements of the degree of Doctor of
Philosophy (PhD) at the University of Central Lancashire

January 2020 examiner(s) approval

STUDENT DECLARATION FORM

Concurrent registrations

I declare that whilst registered as a candidate for the research degree, I have not been a registered candidate or enrolled student for another award of the university or other academic or professional institution.

Material submitted for other awards

I declare that no material contained in the thesis has been used in and other institution for an academic award and is solely my own work.

Signature of candidate: 

Type of award: Doctor of Philosophy

School: Jost institute for Tribotechnology, School of Engineering

Multiscale viscous and non-viscous deformation of bulk and thin film systems via improved nanoindentation methodology

ABSTRACT

By A K Shah, January 2020

Nanoindentation is a technique for studying multiscale contact deformation. Over the years, different investigators have made improvements to its methodologies. In this thesis, the current Oliver and Pharr's (1992), Fujisawa and Swain (2006) and Feng's (2002) unloading methodologies are examined, and novel robust characterisation methodologies proposed.

For any nanoindenter machine, the exact configuration including; actuator/transducer electronics and control strategies, machine calibrations etc., and the corrections associated with thermal drift, initial contact, sink-in and pile-up still limit the acquisition of consistent data. Additionally, variations in the output data are related to material characteristics and geometrical effects such as; indenter area function, surface roughness, thin film thickness, the tilt of the surface, indentation size effects etc. The main goal of the work described in the thesis was to address these factors in the characterisation methods, as for all materials, reliability and reproducibility becomes inherent, including for more challenging viscous/polymeric materials and at low load responses, where the measured properties, such as hardness and elastic modulus, can be time-dependent.

In seeking to unify the different approaches, for viscous/polymeric materials and low load testing, the well-established unloading methodologies were further developed. Previous methods treat the unloading to be fully elastic. However, a plastic correction is proposed at the point where the delayed plasticity ceases. For low load testing, a datum correction is implemented according to a parameter, the Roughness Depth Limit (RDL), which aids in splitting the deformation for determining the correct contact area. The author's DU method is demonstrated to characterise various material types at any test condition in one-cycle. Above RDL, the method compared remarkably well to tensile testing, for several material types. Results for viscous/polymeric materials, were consistent with the well-established unloading methodologies and also with hold-time methodologies. Other novel models, for thin film characterisation, were applied and found to fit precisely the DU method data, i.e. the elastic modulus as a function of depth, for substrate independent properties. With further work the method has the potential to form the basis of a formal standard for polymer characterisation which is still needed in today's industry.

Dedicated to

The honest

TABLE OF CONTENTS

STUDENT DECLARATION FORM	I
ABSTRACT	II
TABLE OF CONTENTS	IV
ACKNOWLEDGEMENTS	XVI
ACRONYMS/ABBREVIATIONS	XVII
LIST OF SYMBOLS	XIX
<hr/>	
Chapter 1.....	1
INTRODUCTION	1
1.1 Nanoindentation and its limitations	1
1.2 The rationale for studying hard thin film ceramics/compliant substrate systems.....	5
1.3 The approach towards selecting independent variables for nanoindentation studies	8
1.4 Aims and Objectives.....	10
1.5 Outline of the thesis	12
1.6 Original contributions	13
<hr/>	
Chapter 2.....	15
LITERATURE REVIEW - NANOINDENTATION OF VISCOUS/POLYMERIC MATERIALS.....	15
2.1 Introduction.....	15
2.2 Nanoindenter equipment, calibrations and corrections	15
2.2.1 Nanoindenters.....	16
2.2.2 Frame compliance and thermal drift	20
2.2.3 Indenter types and area function	22
2.2.4 Time constants.....	25
2.3 Previous nanoindentation methodologies	25
2.3.1 Nanoindentation unloading methodology	28
2.3.2 The continuous stiffness measurement technique.....	31
2.3.3 Accurate contact depth	32
2.3.4 Other factors affecting the nanoindentation response	32
2.4 Nanoindentation and associated problems of Viscous/polymeric materials	33
2.4.1 Depth-dependent properties	36
2.5 Nanoindentation hold time response	37
2.5.1 Logarithmic fits for hold time	39
2.5.2 Phenomenological Mencik’s model for hold time	39
2.6 Indentation of rough surfaces	42
2.6.1 Modelling surface roughness and adhesion within contacting bodies	43
2.6.2 Arithmetical Mean Height for 2D and 3D profiles	45
2.7 Summary	46

Chapter 3.....	47
TEST MATERIALS AND QUALITATIVE/QUANTITATIVE ASSESSMENT	47
3.1 Introduction.....	47
3.2 Viscous/polymeric materials used in this study.....	47
3.2.1 Factors affecting the mechanical properties of PET and PEN polymers	48
3.2.2 The visco-elastic-plastic regime of polymers.....	50
3.3 XRD diffraction	51
3.3.1 Variability associated with XRD testing	52
3.3.2 Methodology for monitoring the ageing	54
3.4 Coatings specifications	58
3.4.1 TiN and TiO ₂ deposition conditions	60
3.5 Qualitative/quantitative assessment all tested coatings	60
3.5.1 High Resolution Scanning Electron Microscopy (HSEM)	61
3.5.2 White Light Interferometry (WLI).....	62
3.5.3 XRD of the coatings	64
3.5.4 Topography for the coatings	66
3.5.5 Coating fracture.....	68
3.5.6 Residual stresses within coatings	68
3.6 Tensile testing	70
3.7 Summary.....	71
Chapter 4.....	73
DEVELOPED NANOINDENTATION METHODOLOGIES.....	73
4.1 Introduction.....	73
4.2 Experimentation.....	73
4.3 Nanoindentation methodologies for unloading stiffness	76
4.3.1 Viscous nature during unloading.....	79
4.3.2 Delayed elasticity	86
4.3.3 Fitting algorithm.....	88
4.3.4 Creep and Plastic correction.....	90
4.4 Plastic depth Pile-up sink-in correction.....	93
4.5 Low load correction	94
4.5.1 Determining the Roughness Depth Limit (RDL).....	100
4.5.2 Determining h_{datum}	102
4.5.3 Contact area at and above RDL.....	103
4.5.4 Spherical and Berkovich relationship for deformation above RDL	104
4.5.5 Contact area below RDL	106
4.6 Summary.....	108
Chapter 5.....	109
DEVELOPING A RELIABLE APPROACH FOR THE NANOINDENTATION TESTING OF VISCOUS AND NON-VISCOUS SYSTEMS	109
5.1 Introduction.....	109
5.2 Nanoindentation approach	110
5.2.1 Experimental details	111
5.2.2 Load-displacement behaviour	113

5.2.3	Determining the number of repetitions for each test.....	115
5.2.4	Reliability for further studies	118
5.3	Variability of PET and PEN	130
5.3.1	Variability of PET compared to PEN.....	130
5.3.2	Ageing behaviour of PET and PEN	131
5.3.3	Variation across different PET and PEN samples.....	134
5.4	Summary.....	139

Chapter 6..... 140
EXAMINATION OF DU METHODOLOGY AND VALIDATION..... 140

6.1	Introduction.....	140
6.2	Examining the DU methodology	140
6.2.1	Examining the unloading stiffness	141
6.2.2	Effect of using the displacement or load for determining stiffness	147
6.2.3	Examining the contact area	149
6.2.4	Contact depth.....	155
6.3	Validating DU methodology at High load.....	159
6.3.1	Non-viscous/non-polymeric materials	159
6.3.2	Viscous/polymeric materials	161
6.4	Validating DU methodology at different scales	164
6.5	Low load validation	169
6.5.1	Factors effecting the Roughness Depth Limit (RDL)	170
6.5.2	Effect of surface roughness on determined elastic modulus values	172
6.6	Summary.....	175

Chapter 7..... 176
NANOINDENTATION CHARACTERISATION OF COMPLIANT MATERIALS..... 176

7.1	Introduction.....	176
7.2	Viscous/polymeric material methodology	176
7.3	Viscous/polymeric material characterisation.....	178
7.3.1	Examining Logarithmic fit to hold-time data.....	178
7.3.2	Phenomenological fits	182
7.3.3	A comparison between time dependent elastic modulus determined by E_T and DU-FCSPD methods	183
7.4	Use of Neural networks in nanoindentation characterisation	186
7.4.1	Neural networks results	187
7.5	Summary.....	190

Chapter 8..... 192
DU METHODOLOGY APPLICATION TO THIN FILM CHARACTERISATION 192

8.1	Introduction.....	192
8.2	Nanoscale nanoindentation modelling of thin films systems	193
8.3	Substrate-independent coating properties.....	200
8.3.1	Discontinuous Elastic Interface Transfer Model (DEITM)	201
8.3.2	Adapted Discontinuous Elastic Interface Transfer Model (ADEITM)	205
8.3.3	Energy Dissipation Model (EM)	206
8.3.4	Five Parameter Logistic Regression Model (5PL).....	208

8.4	Comparison of depth-dependent properties data between different methods	208
8.5	The effective contact area and hardness	212
8.6	Substrate-independent coating properties using DU method	215
8.7	Summary	218
<hr/>		
Chapter 9	220
CONCLUSION AND FURTHER WORK	220
9.1	Introduction.....	220
9.2	Nanoindentation methodologies	221
9.3	Reliable indentation approach	223
9.4	Main factors and ranking	223
9.5	DU method validation.....	224
9.6	Substrate characterisation	226
9.7	Coating characterisation	227
9.8	Overall conclusion	227
REFERENCES	230
Appendix 1.	248
Appendix 2.	250
Appendix 3.	264
Appendix 4.	267
Appendix 5.	268
Appendix 6.	274
Appendix 7.	288
Appendix 8.	316

LIST OF FIGURES

Figure 1-1 Different types of contact interactions for standard testing reconstructed from Mathews et al work (2007, p.5471)	9
Figure 2-1 Schematic of Alton Paar's Ultra Nanoindentation Tester (Anton- Paar, 2019b)	16
Figure 2-2 Micro Material Nano Platform	18
Figure 2-3 Schematic of Micro Material Nano Platform showing frame compliance.....	21
Figure 2-4 Force against Time for an indentation test	22
Figure 2-5 Typical nanoindenters manufactured by micro Star technologies (Micro Star Technologies, 2019)	23
Figure 2-6 The plastic depth (h_c) and contact area $A(h_c)$ of an indentation (UK Patent 1513480.2, 2015; UK Patent 1701591.8, 2017)	24
Figure 2-7 a) Schematic of Oliver and Pharr procedure with Feng's correction for the calculation of hardness and reduced modulus, b) Typical Load- displacement graph, and c) Load-displacement of viscous/polymeric materials with "nose out"	29
Figure 2-8 Absolute value of the variation in the height of the asperities	45
Figure 3-1 Molecular structures of PET and PEN.....	48
Figure 3-2 Microstructure of biaxial PET	49
Figure 3-3 Schematic of an X-ray diffractometer	51
Figure 3-4 Effect of scan time on the intensity for PET	52
Figure 3-5 Effect of machine/environmental factors on the results for PET polymer at a scan time of 600s	53
Figure 3-6 XRD-Intensity against theta for a) PET sample b) PEN sample	56
Figure 3-7 XRD data and parameter values for determining Lateral order factor for PEN.....	58
Figure 3-8 Pulse magnetron sputtering equipment	59
Figure 3-9 XRD intensity versus 2 Theta plots using 30 mins scan time for 150nm thick coatings on PET substrate a) TiN, b) TiO ₂ and c) AZO	65
Figure 3-10 Surface profile of 200nm thick TiN coating on PET substrate determined by white light interferometry.....	66

Figure 3-11 Scatterplot of Coating thickness vs Surface roughness (Sa) for a) TiN on PET and PEN & b) TiO₂ on PET and PEN	67
Figure 3-12 Fracture mechanisms during Nanoindentation at Nano scale, adapted from (Li, Diao & Bhushan 1997)	69
Figure 3-13 Sample dimensions a) For polymers reproduced from ISO 527-1:2012, b) For metallic materials reproduced from ISO 6892-1:2016 and c) For rubbers reproduced from ISO 37:2017	71
Figure 4-1 Flow chart of the developed nanoindentation methodology by the author	74
Figure 4-2 Typical nanoindentation unloading curves a) Elastic response of SiO₂ with linear fit b) Elastic-plastic response of Aluminium with power law fit c) Low viscous response of Polystyrene with power law fit, and d) High viscous response of Acrylic with power law fit	77
Figure 4-3, a) Typical Load-displacement graph, and b) Load-displacement of viscous/polymeric materials with “nose out”	78
Figure 4-4 Contour plot for PET polymer showing experimental runs against load for factors such as a) Acceleration factor, b) Conforming factor, c) Viscofactor, and d) Creep factor. Table details experimental conditions for each run	80
Figure 4-5 Second-derivative of displacement (with respect to load) against load-60% of unloading data for (a) PET (b) Rubber (c) Nylon.....	81
Figure 4-6 Conforming factor against number of run for nanoindentation loads between 10 mN and 100 mN. Table details experimental conditions for each run.....	84
Figure 4-7 Nanoindentation unloading inverse stiffness against applied load for rubber - with a linear fit to determine FEP	87
Figure 4-8 Acquisition of test data and conditioning to determine the Full Elastic Point (FEP) and the associated stiffness (S_{FEP}).....	89
Figure 4-9 Projected contact area versus plastic depth plot using ideal spherical and 2nd order Berkovich functions a) 0-2500 nm, b) 0-50 nm and c) 0-10 nm	96
Figure 4-10 Area difference against hc(a) between the Berkovich 2nd polynomial and the ideal spherical functions (b) between the Berkovich 5th polynomial and the ideal spherical functions	97

Figure 4-11 Area difference against h_c , the area difference is between a 2nd order and a 5th order polynomial function	98
Figure 4-12 S_a against RDL for a) non-viscous materials and b) viscous materials	100
Figure 4-13 Load-displacement graph a) linear fit to the 10-70 % of data and b) showing the magnitude of the difference between the Experimental data and linear fit, intersecting with the mean difference.....	101
Figure 4-14 Contact at low loads in lateral loading for a spherical indenter	103
Figure 4-15 a) Berkovich contact area against spherical contact area, and b) Residuals plot for Berkovich contact area against spherical contact area	105
Figure 5-1 Nanoindentation actuation response of loading, hold, unloading and thermal period a) load -time response b) load rate-time response	111
Figure 5-2 Load-displacement plots for different coating on PET substrate a) TiN, b) TiO ₂ and c) AZO	114
Figure 5-3 Array of 8 x5 indentations for identifying appropriate indentation spacing	116
Figure 5-4 Standard deviation (σ) of the maximum displacement against number of indents/test	117
Figure 5-5 Stress evolution during indentation	118
Figure 5-6 Deformation of a hard coating on a compliant substrate	119
Figure 5-7 Main effects with creep correction Signal-to-noise ratio plots a) micro scale and b) nano-scale.....	125
Figure 5-8 Nanoindentation depth against time plot for TiN coating (150 nm) on PET at 10 different indentations with Load=2 mN, Load rate = 2 mN/s, Unloading rate=0.1 mN/s and Post thermal drift of 60 s.	127
Figure 5-9 Main effects with no creep correction Signal-to-noise ratio plots a) micro scale and b) nano-scale.....	129
Figure 5-10 Sample rotation relative to the X-ray beam.....	130
Figure 5-11 Effect of different sample and angle/coverage on XRD results with a scan time of 600s a) PET, b) PEN and c) Standard deviation (σ).....	131
Figure 5-12 Error bar plot of material properties as a function of time, a) Percentage Crystallinity, b) Lateral order factor and c) hardness....	133

Figure 5-13 Gauge hardness run chart by parts for a single operator a) PEN and b) PET.....	135
Figure 5-14 Gauge Modulus run chart by parts for a single operator a) PEN and b) PET.....	136
Figure 5-15 Effect of glue drops on the hardness of PEN	137
Figure 5-16 Effect of glue drops on elastic modulus of PEN, + are mean values.	138
Figure 6-1 Linear fits of E_{DU-MCP} and $E_{FIT-DU-MCP}$ with residual plots for, a) PET, b) PEN and with c) Experimental run conditions for plots.....	142
Figure 6-2 Reduced modulus against load determined by four different methods using for run 1 (see Appendix 4) for a) PEN & b) PET.....	143
Figure 6-3 Displacement (h) against stiffness (S) determined by three different methods, at maximum load and FEP using separate experiment, and by using fit coefficients at each load, for run 1 (see Appendix 4) for PET polymer.....	144
Figure 6-4 Displacement (h) against stiffness (S) determined by three different methods, at maximum load and FEP using separate experiment, and by using fit coefficients at each load, for run 1 (see Appendix 4) for PET polymer.....	145
Figure 6-5 Displacement (h) against stiffness (S) determined by three different methods, at maximum load and FEP using separate experiment, and by using fit coefficients at each load, for run 10 (see Appendix 4) for PET polymer.....	145
Figure 6-6 Stiffness (S) against load, for PET, determined by three methods using run 10 (see Appendix 4), a) No creep correction, b) Creep corrected, and c) Plastic correction	147
Figure 6-7 Elastic modulus (E) against load for, a) PET stiffness determined by displacement, b) PET stiffness determined by load, c) PEN stiffness determined by displacement, d) PEN stiffness determined by load, e) Residual plot for PET, and f) Residual plot for PEN.....	148
Figure 6-8 Reciprocal of the square root of contact area against the load, for a) PET no creep corrected, b) PET creep corrected, c) PEN no creep corrected, and d) PEN creep corrected. e) Experimental conditions for the 27 runs considered in each graph.....	149

Figure 6-9 Creep factor against reduced modulus (E_r) for a) PET no creep correction, b) PET with creep correction, c) PEN with no creep correction, and d) PEN with creep correction. e) Experimental conditions for the 27 runs considered in each graph.	151
Figure 6-10 Bar chat of elastic modulus (E) against number of cycles for a multi-loading nanoindentation test using 7 different methods, a) PET, b) PEN.....	153
Figure 6-11 Reduced modulus $E_{DU-FSPD}$ against $E_{FIT-DU-FSPD}$ plots for a) PET and b) PEN, and with residual plots.	155
Figure 6-12 a) Normalised stiffness against normalised contact depth for PET polymer using two different methods, b) Residual plot difference between elastic model data and its fit, and c) Residual plot difference between elasto perfectly plastic model data and its fit.....	157
Figure 6-13 For PET polymer, plots of Normalised Contact Depth (hc/ht) against Normalised Depth (ht) at load rates of a) 0.1 mNs^{-1}, b) 1 mNs^{-1}, c) 2 mNs^{-1}, and plots of elastic modulus (E) against Normalised Depth (ht) at load rates of d) 0.1 mNs^{-1}, e) 1 mNs^{-1}, and f) 2 mNs^{-1}.....	158
Figure 6-14 Elastic modulus (E) bar charts of non-viscous/non-polymeric materials using 10 different methods for single-cycle nanoindentation, a) SiO_2, b) Brass, c)Aluminium, d) Titanium(6AL-4V sheet G5), e) Stainless steel (316 2B grade), f) Copper and g) Mild steel	160
Figure 6-15 Elastic modulus (E) bar charts of non-viscous/non-polymeric materials using 9 different methods for single-cycle nanoindentation, a) Neoprene rubber, b) Nitrile rubber, c) Nylon (Polyamide 66), d) Polyethylene HD, e) Acrylic (Plexiglass® 8N), f) Polystyrene (STYRON™ 678E), and g) Polyethylene LD	162
Figure 6-16 Modulus and stress against percentage strain	163
Figure 6-17 Comparison of different area function plots for Berkovich and spherical indenters using DU-FP and O1-M method data	165
Figure 6-18 Elastic modulus bar charts at various load for SiO_2 using area functions determined by a) DAF file, b) calibrated by O1-M method, c) calibrated by DU-FP method and d) calibrated by DU-FP method	166

Figure 6-19	Box plots for RDL for a variety of materials a) metallic materials, b) viscous/polymeric materials, and c) high compliant materials	171
Figure 6-20	RDL against load a) PET sample, and b) PEN sample.....	171
Figure 6-21	For silicon the RDL for each indent for two different roughnesses	172
Figure 6-22	Individual plots of elastic modulus for Silicon wafer, data cleaned +/- 2 σ from mean.....	173
Figure 6-23	Histograms for the normal distribution of elastic modulus data for silicon at two different loads for smooth and rough samples.....	174
Figure 7-1	Nanoindentation displacement (h) against time, with two different logarithmic fits at Load of 150 mN with an initial Load rate of 10 mN/s a) PEN and b) PET	179
Figure 7-2	Determined fit parameters of method Log₂ (Equation 7-1) with experimental data and cubic interpolant fits, for PEN polymer.....	180
Figure 7-3	Determined fit parameters of method Log₂ (Equation 7-1) with experimental data and cubic interpolant fits, for PET polymer.....	180
Figure 7-4	Displacement against maximum load and hold time plots, using method Log₂ (Equation 7-1) terms, for PEN polymer a) All terms the total displacement, b) Second term the plastic component, and c) Third term the viscous component.	181
Figure 7-5	Nanoindentation hold time plots at Load of 90mN and initial Load rate of 5 mN/s using three different rheological methods for a) PEN and b) PET	183
Figure 7-6	Elastic modulus (E) determined using method E_T against Time and Load for a) PET and b) PEN.....	184
Figure 7-7	Elastic modulus (E) against load for different experimental runs for PET and PEN a) Experimental runs 1-9 with load rate of 0.1mN/s, b) Experimental runs 10-18 with load rate of 1mN/s , and c) Experimental runs 19-27 with load rate of 2mN/s. Refer to Appendix 4 for details on experimental runs.	185
Figure 7-8	A two-layer-feed-forward Neural network	186
Figure 7-9	Neural network results a) PET and b) PEN.....	188
Figure 7-10	Elastic modulus (E) against Load for separate neural training run a) PEN Train run 1, b) PEN Train run 2, c) PET Train run 1, d) PET Train run 2.....	189

Figure 8-1 Composite hardness (H_c) against relative indentation depth, adapted from (Korsunsky et al. 1998).....	197
Figure 8-2 Indentation stress field and associated substrate effects a)continuous, b) indentation stress field of discontinuous transfer c) components of discontinuous transfer, adapted from (Zhou et al. 2011)	200
Figure 8-3 TiN reduced modulus and hardness against normalised depth on three different substrates a) and b) on PET, c) and d) on Steel, e) and f) on Silicon. Each error bar shows one standard deviation from the mean value.....	209
Figure 8-4 TiO₂ reduced modulus and hardness against normalised depth on three different substrates a) and b) on PET, c) and d) on Steel, e) and f) on Silicon. Each error bar shows one standard deviation from the mean value.	210
Figure 8-5 AZO reduced modulus and hardness against normalised depth on two different substrates a) and b) on PET, c) and d) on Steel. Each error bar shows one standard deviation from the mean value.	210
Figure 8-6 Elastic modulus against normalized depth for 199nm TiO₂ on a) PET substrate and b) Steel substrate.	216
Figure 8-7 Elastic modulus against normalized depth fits with DEITM and ADEITM for PET and Steel substrate with coatings a) TiN, b) TiO₂ and c) AZO.....	217
Figure 8-8 Elastic modulus against normalized depth fits with 5PL for PET and Steel substrate with coatings a) TiN, b) TiO₂ and c) AZO.	218

LIST OF TABLES

Table- 2-1 Methods and different rheological components for Mencik’s work....	41
Table- 3-1 XRD data for PET and PEN.....	57
Table- 3-2 Manufacturers specifications for coating and substrate materials.....	59
Table- 3-3 Coating thickness using different techniques.....	63
Table- 4-1 Experimental details and parameter values for Experiment 4.1	75
Table- 5-1 Test conditions for Experiment 5.1 with PET substrate	113
Table- 5-2 Test conditions for Experiment 5.2.....	115
Table- 5-3 Taguchi design details for TiN coating	120
Table- 5-4 The ranking of factors for nano scale deformation	122
Table- 5-5 The ranking of factors for micro scale deformation.....	123
Table- 6-1 Method syntax with their associated methodologies	141
Table- 6-2 Nanoindentation test condition for Experiment 6.2	164
Table- 6-3 Method selection matrix for four metallics	167
Table- 6-4 Method selection matrix for four polymers	168
Table- 8-1 Coating characterisation methods.....	201
Table- 9-1 Details of load and corresponding loading and unloading rate.....	317

ACKNOWLEDGEMENTS

I would like to express my appreciation to my supervisors Professor Ian Sherrington and Dr Nathalie Renevier whose insight, guidance and support from the start of the project enabled me to develop an understanding on the subject. Their guidance in conducting research, presentation and knowledge of the industry was invaluable.

Special thanks to the Research Referee Professor Ted Smith for helping me get through the registration process. Also special thanks to Professor Bogdan J Matuszewski research tutor, Clare Altham Academic Support and the Uclan research support team for providing abundant support throughout the study.

Special thanks to my third supervisor Professor Peter Kelly and also to David Wickens, from the University of Manchester Metropolitan University, for going out of their way in providing support for the project, and to making the TiN and TiO₂ samples.

Thanks to Dr Heqing Li for providing training on the Nanoindenter platform and to Dr Zhang from Teer Coatings Ltd for providing the AZO coatings

ACRONYMS/ABBREVIATIONS

ACS	Apparent Crystal Size
ADEITM	Adapted Discontinuous Elastic Interface Transfer Model
AFM	Atomic Force microscopy
AZO	Aluminium Doped Zinc Oxide
BSE	Back Scattered Electrons
CFUBMS	Closed Field Unbalanced Magnetron Sputtering
CVD	Chemical Vapour Deposition
DC	Direct Current
DEITM	Discontinuous Elastic Interface Transfer Model
DMT	Derjaguin-Muller-Toporov
DN	Doerner and Nix Model
DOE	Design of Experiments
DSC	Differential Scanning Calorimetry
EM	Energy Dissipation method
FEA	Finite Element Analysis
FEM	Finite Element Modelling
FESEM	Field Emission Scanning Electron microscope
FEP	Full Elastic Point
HDPE	High Density Polyethylene
HIPIMS	High Power Impulse Magnetron Sputtering
HSEM	High Resolution Scanning Electron microscopy
ISE	Indentation Size Effects
ISO	International Organization for Standardization
JKR	Johnson-Kendall-Roberts
LDPE	Low Density Polyethylene
MEMS	micro Electro Mechanical Systems
MMU	Manchester Metropolitan University
NC	Non-Crystalline
OLED	Organic Light-Emitting Diode
PDF	Probability density function

PEN	Polyethylene Naphthalate
PET	Polyethylene Terephthalate
PMMA	Poly(methyl methacrylate)
PVD	Physical Vapour Deposition
RDL	Roughness Depth Limit
SD	Standard deviation
SEM	Scanning Electron microscopy
S/N	Signal to Noise Ratio
TEM	Transmission electron microscopy
TiN	Titanium Nitride
TiO ₂	Titanium Dioxide
UMAT	User Material Model Subroutine
UV	Ultraviolet
WLI	White Light Interferometry
XRD	X-Ray Diffraction
ZnO	Zinc Oxide
5PL	Five Parameters Logistic Regression or Equation

LIST OF SYMBOLS

a	Minimum Asymptote (GPa)
$A_{\text{crystalline peaks}}$	Total Area of Crystalline Peaks (a.u)
A_c	Contact area (m^2)
A_{CRDL}	Contact area at RDL (m^2)
$A(\text{hc})$	The contact area as a function of contact depth (nm^2)
a_n	Pearson 4 fitting parameters (a.u)
A_{Total}	Total Area of all Crystalline and Non-crystalline Peaks (a.u)
b	Hill's Slope (Dimensionless)
c	Inflection Point (GPa)
C_i	Creep compliance function test parameters for i Kelvin-Voigt bodies (m^2N^{-1})
C_{10}	Neo Hook material constant (Pa)
d	Inter-plane Distance (m)
dm	Maximum Asymptote (GPa)
D_l	Neo Hook material constant (Pa^{-1})
e	Asymmetry Factor (Dimensionless)
E	Elastic component of Modulus (GPa)
E_r	Reduced elastic modulus (GPa)
E_{method}	Reduced elastic modulus associated with a method (GPa)
E_t	Combined elastic modulus of Film and Substrate (GPa)
E_f	Film elastic modulus (GPa)
E_i	elastic modulus of the Indenter (GPa)
E_s	Substrate elastic modulus (GPa)
E_{ve}	viscoelastic modulus (GPa)
F	Force (mN)
FEP	Full Elastic Point (nm)
G_0	Initial Shear Modulus (GPa)
G_f	Long term Shear Modulus (GPa)
H	H (GPa)
h	displacements (nm)
hc	plastic depth (nm)

h_c (method)	plastic depth determined by the associate method (nm)
h_{cRDL}	Plastic Depth at RDL (nm)
h_{datum}	displacement due to Datum Shift (nm)
h_{FEP}	displacement at FEP (nm)
\dot{h}_h	Penetration rate at end of Hold Time (nms ⁻¹)
h_{hold}	displacement during Hold Time (nm)
h_{max}	Maximum displacement (nm)
$h_{max-fitted}$	displacement of fitted curve at maximum load (nm)
$h_{max-load}$	displacement at maximum load at end of hold period (nm)
h_n	Heights of Maxima (a.u)
h_{cn}	Normalised Contact Depth (Dimensionless)
h_o	Zero Point displacement (nm)
h_p	Penetration of Contact Element (m)
$h_{plastic}$	Plastic displacement during Delayed Elasticity (nm)
h_t	Normalised depth (nm)
h_{tip}	Tip Correction Parameter (nm)
$h_{viscous}$	Viscous displacement Rate at the end of hold (nms-1)
I_I	First invariant of the right Cauchy-Green deformation tensor
J	Creep Compliance (nm ² /mN)
J_{el}	Determinant of the Deformation Gradient
K	Bulk Modulus (GPa)
k	Load Rate (mNs-1)
K_f	Long term Bulk Modulus (GPa)
K_s	Scherrer constant (a.u)
n	Integer (Dimensionless)
$mean \frac{d^2y}{dx^2}_{range}$	Mean Acceleration (within the range of displacements)
m_n	Heights of Minima (a.u)
OF	Lateral Order Factor (a.u)
P	Load (mN)
P_c	Contact Force (N)
P_{FEP}	Load at FEP (mN)
P_{max}	Maximum Load (mN)
$P_{max displacement}$	Load at Maximum displacement (mN)
\dot{P}	Load rate (mNs-1)

R	Radius of the Plastic Zone (nm)
Ra	Arithmetical Mean Height 2D (μm)
RDL	Roughness Depth Limit (nm)
R_{eff}	Effective Radius of the Elastically Deformed Region (nm)
RF	Resolution Factor (a.u)
R_{sq}	Square of the multiple correlation coefficient (Dimensionless)
S	stiffness (mN/nm)
S_{FEP}	stiffness at FEP (mN/nm)
S_{Max}	stiffness at maximum load (mN/nm)
Sa	Arithmetical Mean Height 3D (μm)
S_u	Unloading stiffness (mN/nm)
S_n	Normalised stiffness (Dimensionless)
t	Time (s)
t_c	Coating thickness (nm)
t_R	Time to Maximum Load (s)
W	Strain Energy Density Function
λ	Wavelength (\AA)
α	Roughness parameter (Dimensionless)
β	Integral Breadth or Breadth at half maximum Intensity (Radians)
ε	Intercept Factor (Dimensionless)
$\varepsilon_{\text{datum}}$	Intercept Factor below RDL (Dimensionless)
Θ	Angles (Degrees)
σ	Standard deviation (units same as used data)
σ_f	Final Stress (GPa)
σ_o	Initial Stress (GPa)
η	Viscosity (GPa s)
ρ_j	Ramp Correction Factor (Dimensionless)
τ	Time Constant (s)
τ_i	Time Constant for i Kelvin-Voigt bodies (s)
ν	Poisson's Ratio (Dimensionless)
ϕ	Weight Factor (Dimensionless)
ϕ_f	Film Weight Factor (Dimensionless)
ϕ_s	Substrate Weight Factor (Dimensionless)
δ_{norm}	Normalised Depth (Dimensionless)
ψ	Sample tilt angle (Degrees)

Chapter 1

INTRODUCTION

1.1 Nanoindentation and its limitations

The nanoindentation technique industrialised over the years for its popularity in investigating small scale deformation mechanisms in materials has been a significant asset to the development of thin films and MEMs devices. As a characterisation technique optimisation of material composition and structure was made possible for these types of devices, unravelling the material physics from the measured deformation processes. Modelling the contact, to gain understanding, occurring in these systems is an ongoing challenge. For indentation testing, the system consists of bulk or coated material indented with a known shape and material indenter. For modelling elastic-plastic contact behaviour, an estimation of the yield strength of the material is required. One property shown to be related to yield strength of metals is the hardness (Johnson, 1987, p.157). This property has been defined in numerous ways as early as the 18th century during the industrial revolution when interests arose in indentation hardness testing for the need for classifying one material compared to another. Definitions of hardness evolved as did the technique (Broitman, 2016), definitions such as the resistance of scratching the surface, or the minimum pressure to produce a permanent set at the centre of area of contact for a spherical indenter (Hertz, 1896), or resistance to plastic or permanent deformation of the material during indentation. However, the underlying physical meaning of hardness given by Tabor (1977) for ductile materials was that it is essentially a measure of their plastic properties. In hardness testing, a rigid indenter of specific geometry is impressed into the surface of the test specimen, and the resulting impression size is related to the hardness.

These tests require the area of the residual impression to be determined optically and are applicable at macro-scale, i.e. loads higher than 2N. For the Vickers and Knoop hardness tests, loads are lower and can result in microscale deformation of 50 μm or less, and the hardness gives not an absolute but a comparative estimation of the material's resistance to penetration. Therefore, different scales exist for different hardness techniques, associated with the shape and material of the indenter, and the microstructure of the test material, making comparisons between hardness measurements a complicated procedure and should only be interpreted as an estimate (Broitman, 2016). In hardness tests, there is an assumption that the conditions are such that the plasticity beneath the indenter has reached the surface (Johnson, 1987, p.157) and the contact pressure is said to be constant. Even when this assumption is valid experimentally, the primary source of error is the strain hardening effect, shown to be insignificant with smaller indentations (Tabor, 2000, p.16). Other limitations of these techniques were due to large and varied indenter tip shapes and also different indenter setups having a low spatial resolution. Therefore, hardness data comparison between different laboratories was found to show significant variations.

Parallel to the development of hardness testing, there has been an interest in the elastic response of contacting bodies. Hertz was the first to achieve a successful analytical solution for the validation of contact between two spherical elastic bodies (Hertz, 1882). His work set a mathematical framework describing the response of a rigid cone with a homogeneous isotropic elastic half-space (Love, 1939; Sneddon, 1948). Sneddon's work subsequently was employed by the Workers at Baikov Institute of metallurgy in Moscow during the 1970s to develop a relationship between the stiffness, reduced modulus and the area of contact (Bulychev et al., 1975) whereby the indenter load-penetration diagram could be used to determine the elastic modulus. The finding was a great achievement as

the primary parameter needed for the modelling the elastic response of solid materials was the elastic modulus (E), and it could now be determined at a smaller scale by a convenient indentation test. The elastic modulus is an intrinsic property of the material and related to the material's resistance to elastic deformation under an applied load.

It was not until the early eighties that Newey et al. (1982) demonstrated an ultra-low-load penetration hardness tester with the ability to continuously record the load-penetration data and measure hardness, elasticity, adhesion and load-dependent effects. As surface coating and modification techniques became popular due to their industrial significance, a technique was needed to understand their deformation behaviours for further development. Interest of using micro/nano depth sensing indentation testing thus became widespread for investigating the hardness of surfaces (Loubet et al., 1984; Pethica, Hutchings and Oliver, 1983) and thin films (Doerner, Gardner and Nix, 1986; Jönsson and Hogmark, 1984; Stone et al., 1988). During this time Doerner & Nix (1986) presented a methodology to determine elastic modulus and hardness when indented to depth less than a micron without any optical measurements of the contact impression, which would be further improved by Oliver & Pharr (1992) and with their procedure they were able to obtain elastic modulus within 5% when compared to tensile data. It should be noted apart from nanoindentation (Oliver and Pharr, 1992) other tests are available to acquire the elastic modulus such as static (i.e. tensile, torsion, bending tests), dynamic resonant frequency methods, and wave propagation methods (i.e. the ultrasonic echo-pulse method). However, the determined values for all these tests are different even if the sample is the same since the measurements are of different physical effects and there is no set value to calibrate against. The factors affecting its value include material effects, testing conditions, and how the test data is interpreted (ASTM E111-04, 2010). All methods have their advantages and disadvantages. However, nanoindentation is classified

as a reliable characterisation technique at the small scale (Schuh, 2006; Tsui and Volinsky, 2019). The deformation behaviour can be studied statically or dynamically and applies to materials with time-dependent behaviour. This non-destructive test (in majority of the cases the functionality of the component/part is unaffected as the size of the indent is negligible compared to the component/part) has been extensively used to fulfil the industrial demands for material characterisation and now is fully standardised for both bulk and thin films (ISO 14577-1, 2002–2015; ISO 14577-2, 2002–2015; ISO 14577-3, 2002–2015).

The nanoindentation technique allows investigation of the material's physical characteristics by precision loading and measures displacements with nanometre accuracy, making it is an ideal tool to understand the deformation of materials from micro to nano scales. Not just the elastic modulus and hardness can be acquired, at different scale lengths from the load-displacement graph, but numerous other mechanical properties can also be determined such as elastic and plastic deformation work, yield stress, fracture toughness (Li, Diao and Bhushan, 1997), residual stresses in thin films (Suresh and Giannakopoulos, 1998) etc. This has been only possible due to improvements to the test equipment and the vast amount of research into the methodologies that were essential for extracting reliable materials properties.

A considerable amount of insight into the deformation of materials at various scales has been revealed using nanoindentation. This load-displacement response was found to be unique to the sample indented (Page and Hainsworth, 1993), and is due to different phenomena, material and geometrical based. Material based factors include elasticity, plasticity, fracture behaviour, phase transformation, surface adhesion, viscoelasticity etc., whereas geometrical based factors include the indenter type, indenter tip, surface roughness, thin film thickness, the tilt of the surface etc. There are also necessary

corrections for the technique which are applied for precise measurements of the displacement, i.e. frame compliance, zero-point correction and thermal drift.

While the precision of the technique has been addressed over the years, manufacturers are still investing large amounts in research and development to improve the accuracy and reliability of the test equipment. Trying to resolve the existing issues in acquiring meaningful data even for well-studied systems at certain test conditions has become a challenge (Oliver and Pharr, 2004). These current issues are not just due to the limitations of the machine, but also related to scale effects, geometrical effects (Pharr, 1998) and material characteristics involving visco-elasticity, visco-elastoplasticity (Menčík, 2006) or even phase transformation effects (Lechat et al., 2006). These issues do not just affect the accuracy of the nanoindentation data, but reliability and reproducibility become inherent, more so for viscous/polymeric materials and at low load responses. This is also applicable to thin film systems when viscous/polymeric materials are employed as substrates. At present no global nanoindentation standard exists for polymer characterisation.

1.2 The rationale for studying hard thin film ceramics/compliant substrate systems

Hard coatings on compliant substrates have been studied in several ways during the last decade due to their popularity of use within the MEMS, solar cells, optoelectronics, semiconductors and display devices. These methods include Vickers indentation testing (Mukherjee, Case and Lee, 2000), compression loading (Cotterell and Chen, 2000), fragmentation testing (Andersons, Tarasovs and Leterrier, 2007), creep experiments (Huang, Niu and Soboyejo, 2007), and simply loaded or shaft-loaded blister tests (Zhao, Zheng and Fan, 2010). All these methods have been conducted at the macro-level and ignore stress concentrations, typically observing the mechanical properties of the coating

and its failure behaviour such as adhesion, fracture, buckling and delamination etc. Also, inhomogeneity of these coatings and substrates has been ignored. It has been realised from these studies that substrate effects exist, and different factors are interrelated such as coating and substrate properties.

Although some alternative methods, e.g. the micro-cantilever-beam test (Zhang, Zhao and Qian, 2000) and the micro-bridge test (Su et al., 2000), have been used to characterise thin film on different substrates, nanoindentation using established methodology (ISO 14577-4, 2007–2016) has been the most widely used. Numerous studies considering hard and soft coatings have been conducted. The author will not attempt to cite all works but give some examples for an overview. Studies considered different elements at various scales which include; the contact problem (Chang, Hsiao and Huang, 2008), characterisation (Chawla, Jayaganthan and Chandra, 2009a; Chun et al., 2008; Magnus et al., 2011), correction factors, temperature (Beake et al., 2007), and material choice (Flores, Ania and Baltá-Calleja, 2009) and geometric phenomenon (Bulychev et al., 1975). The interpretation of experimental results typically involves contact mechanics techniques, molecular dynamic simulations or Finite Element Analysis (FEA). Overall the existing work on deformation is scattered due to the consideration of different elements of a contact problem, reflecting the different applications in which these different coating\substrate systems exist. However, the work to date in nanoindentation does not adequately describe all the different existing phenomena and the interplay between them, such as friction, real contact area, adhesion and surface roughness. Also, the thickness dependent mechanical behaviour needs further investigating, which is not fully known when substrates are compliant polymers. The exact meaning of the word compliant needs some clarity. Compliance is inversely related to the stiffness, where stiffness is an extensive property of the solid body dependent on its material property,

shape and loading conditions. It is a measure of the resistance offered by an elastic body to deformation. Thus “compliant substrates” can be referred to as those substrates in which the compliance is higher than the coating compliance. The term is typically used for polymeric substrates where the compliance of the substrate is much higher than the coating.

The main reason why the deformation behaviour for hard coating/compliant substrate systems is not fully understood is that in the past, in applications such as flat panel displays, semiconductors, photovoltaic solar cell and Micro Electro Mechanical Systems (MEMS), glass was the choice of the substrate material (Hill and Nadel, 1999). Nevertheless, attempts were made to use hard plastics such as Perspex, but the trend was to move to more compliant substrates (Chen et al., 2008; Chen and Wu, 2008; Sierros et al., 2010) in order to increase the performance/weight ratio and reduce cost. This paradigm shift is associated with many factors. One of the main factors has been a clear trend to manufacture ever smaller mechanical, optical and electronic products/devices, which has only been possible due to technological advances in measurement systems and manufacturing processes. All this has led to more insight at lower scales.

Furthermore, advances in the miniaturisation of components and devices have initiated an equal drive to produce functional film materials. In the past, functional materials such as ceramic coatings have been used to enhance the substrate’s surface properties and act as barriers to corrosion in extreme environments. These coatings, apart from edge preservation and corrosion resistance, have been used in many other applications within the semiconductor, orthopaedic, automotive, aerospace and military industries (Martin, 2009, pp.2–3, 2009; Wasa, Kanno and Kotera, 2012). These films are composed of either a single layer or multi-layers of different coatings stacked together to perform some practical function; this technology is apparent in MEM’s devices. They are also included

in flat panel displays, optoelectronic devices, electrochromic coatings, Organic Light-Emitting Diodes (OLED's), image sensors, thin film photovoltaic solar cells etc. Since 1960s many improvements have been made in manufacturing techniques within the coating industry (Makhlouf, 2011). Vapour Deposition techniques cover almost any coating requirement (ASM International, 2003). For thin films deposition, Physical Vapour Deposition (PVD) and Chemical Vapour Deposition (CVD) techniques are standard (Wasa, Kanno and Kotera, 2012). Different coatings can now be deposited on a roll to roll basis on compliant substrates, making mass production easier with reduced cost. Thus, it has become more appealing and more manageable for manufacturers to make a transition to flexible polymers, and a new generation of products containing compliant materials within the market is imminent. Unfortunately, the deformation, of different types of coatings on these substrates, is not fully resolved, and it becomes vital to study it for improved product development and efficient manufacturing. Previous nanoindentation techniques/methodologies, for both bulk and thin film systems, need to be examined to determine the mechanisms of deformation and the applicability of the associated assumptions. These coating/substrate systems behave very differently mechanically, and the mechanisms of failure may also be very different. The author will address these issues in the thesis.

1.3 The approach towards selecting independent variables for nanoindentation studies

Different independent variables become relevant depending on the study of contacting bodies. One of many factors is the scale, at each scale scientists in the past, have taken different approaches. As mechanisms are different at each scale length, different independent parameters have been used, by examining the tribological aspects of the system, to determine the effect of dependent variables measured by a particular test. For

nanoindentation, typically the independent variables can be load, load/unload rate, dwell time etc., and for the dependent variables displacement, elastic modulus, hardness etc. Consequently trying to relate one scale to another is difficult (Bhushan, 2012) and much research is still in progress on the matter. Thus, the scale has to be identified in trying to identify the independent/dependent variables. Tribological aspects are another important factor in trying to identify the independent variables. In contacting bodies, at the points of contacts, stress concentrations are present within a sub-layer, when these stresses reach a critical value, they lead to crack initiation, growth and then finally to surface or subsurface fracture. The stress concentration within this sub-layer can be influenced by material properties, surface modification and coatings, surface topography, friction, scale, adhesion, defects, material inhomogeneity and third body interactions (Goriacheva, 1998). For nanoindentation, some of these influences can vary due to load, load rate, hold time, indenter type etc. Also adding to the complexity is how these different parameters interact with each other i.e. the real contact area, surface adhesion, friction, and surface roughness are all interrelated. Another factor in trying to identify the independent variables is the different surface conditions of body-sample contact interactions, dictating which deformation study to consider. Figure 1-1 shows some of these different conditions. For each of the conditions, a suitable test can be constructed. Over the years,

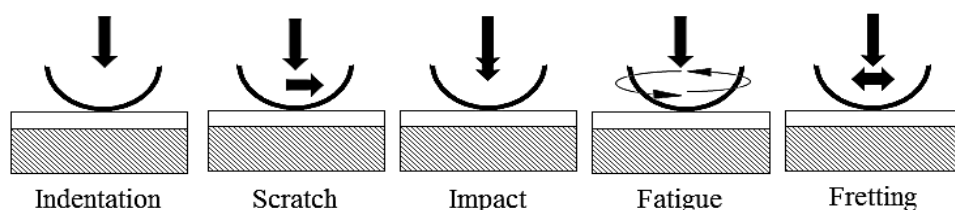


Figure 1-1 Different types of contact interactions for standard testing reconstructed from Mathews et al work (2007, p.5471)

standard tests which simulate these conditions have been developed, for the purpose of this thesis only normal loading is considered, i.e. indentation.

Accordingly, the first step, for either bulk or a selected coating/substrate system, is to set the scale, i.e. maximum load at which to conduct studies. Once established, this selection assists in identifying the independent/dependent variables according to tribological aspects. The standard tests can thus be employed to study all variables. In this thesis, studies at different scales are conducted, so the significance of different variables at each scale need to be established. The most significant variables can thus be studied further at the relevant scale. The relationships, between the input independent and output dependent variables, can be used along with contact models of the system to gain some insight to the deformation either to improve the deformation behaviour for a particular application, or for characterisation purposes to develop/select optimum materials or thin-film systems.

1.4 Aims and Objectives

The main aim of this study is to examine the accuracy/reliability of the dependent variables acquired by the unloading method, as in the nanoindentation standard (ISO 14577-1, 2002–2015), and further developed by the author, each considered with creep and sink-in/pile-up corrections. This was achieved, by comparing to standard tensile tests, for several viscous and non-viscous/non-polymeric materials, and by detailing the true deformation response due to the mechanisms/processes occurring at the various scales. The developed methodologies were reliant on a reliable approach to nanoindentation. Nanoindentation was conducted under a variety of loading conditions to examine the loading, hold and unloading periods. Accuracy of the developed methods were compared with hold-time methodologies, and also their application to thin film characterisation. These analyses involved factors such as the physical properties of the bulk material, individual material properties of substrate and coatings for thin film systems, coating

thickness, surface roughness, true contact area, stiffness, and substrate effects. The main objectives of the studies are as follows:

- Develop and combine nanoindentation unloading curve and low-load methodologies to obtain an accurate and reliable method (using MATLAB software) focussing on viscous/polymeric materials.
- Establish the characteristics of the indentation tests, by identification (at micro and nano-scale) of the relevant parameters required to characterise elastic modulus and hardness material properties. Confirm nanoindentation experimental approach for a ceramic thin film system involving viscous/polymeric material and by ranking a subset, i.e. the most significant parameters identified for further studies.
- A series of Design of Experiments (DOE's) are proposed using a variety of loading conditions to examine the loading, hold and unloading periods for viscous, non-viscous/non-polymeric materials and hard thin films on compliant systems. All tests are set up using Minitab software. The relevant tests are completed to accomplish the objectives of the DOE's.
- Validate the developed methodologies for a number of non-viscous/metallic, viscous/polymer and rubber materials at various scales by analysing/comparing results from completed DOE to standard tensile test.
- Characterise viscous/polymeric materials using adapted Logarithmic and Mencik's hold time methodologies for comparison to developed unloading methods.
- Develop a method for coating characterisation, to fit the developed unloading methodology data, and compare to previous methods.

Thus, seeking useful mathematical relationships in order to predict parameters of interest, such as plastic depth, stiffness, hardness, elastic modulus etc. These parameters can also be a function of depth or be time dependent. For thin-film systems, independent variables relationship to limits related to substrate effects and critical loads of coating failure.

1.5 Outline of the thesis

In chapter 2, a critical review of the literature on nanoindentation equipment, calibrations and corrections are given. Previous nanoindentation testing methodologies of bulk viscous and non-viscous/non-polymeric materials are reviewed. The characterisation of polymer materials using nanoindentation and problems associated are discussed. Furthermore, contact models involving surface roughness and adhesion are reviewed. In chapter 3, the test materials and the factors affecting their mechanical response are discussed, and details of additional techniques are given, for the characterisation of the elastic modulus and ageing behaviour of polymers, and the qualitative/quantitative assessment of the coatings. In chapter 4, nanoindentation methodologies developed by the author are described. In chapter 5, a reliable approach for the application of the nanoindentation methodology developed by the author is outlined. In chapter 6, the DU methodology is examined and validated for viscous and non-viscous/non-polymeric materials at various scales. In chapter 7 comparison of the hold time analysis to the DU methodology for viscous/polymeric materials is given. Also, different analytical techniques used to determine mechanical properties such as interpolating and extrapolating of the experimental data are detailed. In chapter 8, a literature review, of acquiring substrate independent coating properties, is given first followed by a methodology for characterising coatings developed by the author and compared to previous methods. In chapter 9, the conclusions are stated along with the description of further work. The study as a whole increases the understanding on how to relate the

different factors, at the various scales, to the deformation behaviour of viscous, non-viscous and hard coating/compliant substrate systems in normal loading conditions.

1.6 Original contributions

Aspects of originality found in this work are:

1. An accurate method, to characterise the elastic or viscoelastic response for viscous and non-viscous/non-polymeric materials, was established by splitting the nanoindentation unloading curve at “Full Elastic Point”. The method entails the concept of localised and non-localized contact assumptions for the contact analysis of the unloading response during nanoindentation. The Feng’s (G. Feng, 2002) method was adapted for correcting the stiffness due to the delayed plasticity instead of the creep in determining the viscoelastic modulus.
2. A novel method of determining the plastic depth at low load conditions, by determining the Roughness Depth Limit (RDL), was established. The method stipulates that the plastic depth calculated using elastic-perfectly plastic method cannot be less than the value calculated by the elastic method when a sink-in & pile-up correction is applied.
3. A developed method which reduces the costs associated with the testing by reducing the time of study and can easily be implemented by modifying the data analysis algorithm in any load/depth sensing indentation software with low costs.
4. Development of a reliable approach for the basis of nanoindentation on viscous/polymeric materials and hard coatings on compliant substrates.
5. New procedures for characterising thin films, such as the proposed 5PL model and the adapted Discontinuous Elastic Interface Transfer Model (DEITM) model, were utilised to determine thin film properties.

6. A new insight at low loads, due to the datum shift phenomenon, enhances the knowledge about the behaviour of compliant materials, and hard coatings on compliant substrates. If confirmed will narrow the gap, of understanding, between nano and microscale deformations and will imply a new explanation to the origins of friction.

Chapter 2

LITERATURE REVIEW - NANOINDENTATION OF VISCOUS/POLYMERIC MATERIALS

2.1 Introduction

The acceptance of nanoindentation and its use for viscous/polymeric material characterisation has driven manufacturers to develop the equipment for better precision. A brief review of the most popular nanoindentation machine designs is presented. As described in the introductory chapter, there are many issues in characterising viscous/polymeric materials with present standard methods. Thus, these methodologies have been reviewed, when bulk materials are tested at high and ultra-low loads, detailing the fundamentals calibrations, corrections, techniques and models for an accurate deformation response and characterisation and addressing associated issues.

2.2 Nanoindenter equipment, calibrations and corrections

Commercial nanoindenter systems and their design vary, employing a range of technologies. Load actuation devices can be electrostatic, electromagnetic or piezoelectric, and for sensing the displacement, capacitive or inductive transducers are employed (Fischer Cripps, 2007, p.215, 2011, p.203). For added precision Proportional Integral Derivative (PID) methods of control are employed in either “open loop” or “closed loop”. The “open loop” systems rely on pre-calibration of the load actuator or displacement stepper motors, whereas “closed loop” systems involve monitoring the load/displacement data and using feedback by the electronics for an accurate load/displacement output (Fischer Cripps, 2011, p.267). In “true feedback” the control

variable feedback is based on the output error determined by independent load and depth sensors, whereas for “feed-forward” mathematical models of the process and process disturbances are used for control (Haugen, 2009, pp.105–116). Some examples of popular nano-indenters have been given below.

2.2.1 Nanoindenters

The Anton Paar Ultra Nanoindentation Tester (UNHT) (Anton-Paar, 2019a) schematic is shown in Figure 2-1. It has a surface referencing dual indenter system. Where the loads on the indenter and the reference surface are obtained from the displacement produced by the springs S1 and S2 (measured with capacitive sensors C1 and C2) after a displacement

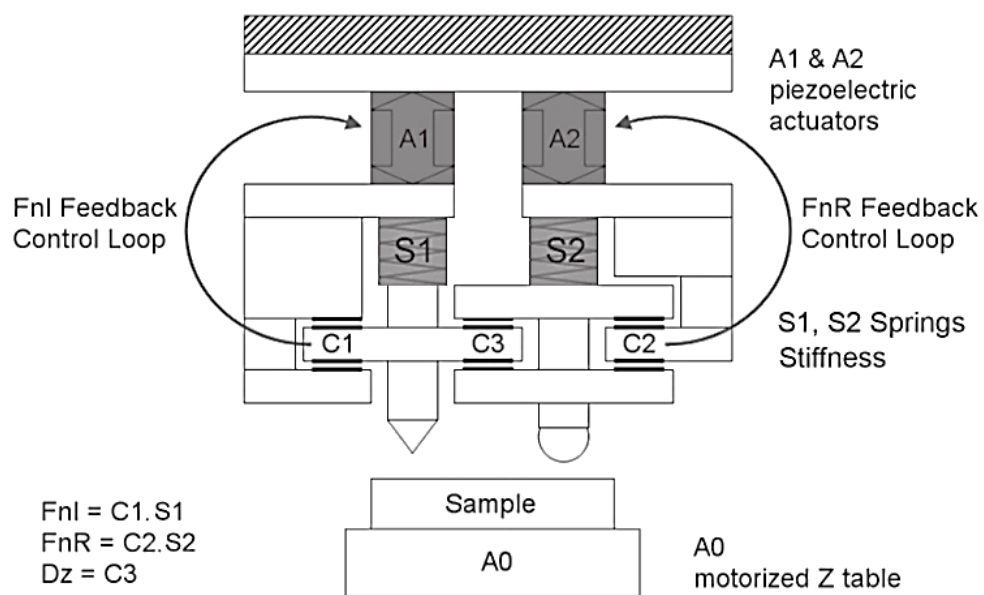


Figure 2-1 Schematic of Alton Paar’s Ultra Nanoindentation Tester (Anton-Paar, 2019b)

is applied using the piezo actuators A1 and A2. Continuous control of normal force on both the indenter and the reference is ensured by precise feedback loops aiding the load on the reference to be kept constant to ensure surface contact. The differential capacitive sensor C3 measures the relative displacement between the indenter and the reference

surface. Thus, load displacement data can be acquired with minimal thermal drift and frame compliance effects.

Another popular machine is the Hysitron's TI 950 Tribo-Indenter (Bruker, 2019) which has a three-plate capacitive transducer as both the load actuator and displacement sensor. The force is applied electrostatically while the change in capacitance simultaneously measures the displacement. The device can be load-controlled or displacement-controlled operating in "closed loop", and the feedback rate can be fast enough to track the fastest transient events.

The equipment utilised by the author is a Micro Materials Nano Platform (Micro Materials, 2019), shown in Figure 2-2. It is comprised of a pendulum, consisting of a lightweight solid ceramic cylindrical shaft, with a low friction pivot near the centre, allowing the indenter to be horizontally loaded into the adjacent material sample. The technique allows for very high strain rate indentation in addition to more conventional quasi-static indentation, allowing the study of viscous/polymeric material properties at both high and low strain rates, this is necessary for establishing the load-time dependent mechanical response fully. Also, on vertical setup, thermal drift issues are less likely to affect the displacement measurement electronics as heat transfer of any convection currents is not significant (Tiwari, 2013, p.71)

This pendulum is stiff enough to apply a maximum load of 500 mN, using ramping the current into an electromagnetic coil, i.e. the actuator thus applying a monotonically increasing and subsequently decreasing load on the pendulum and the indenter. This loading mechanism is calibrated by hanging a series of masses from a set point (the balance point) at the bottom of the pendulum while a known voltage in the coil applies a countering force, thereby establishing the correct forces applied at the diamond tip during

a measurement. This calibration for the load range, i.e. 0-200 mN, should be performed every month.

The depth measurement transducer is a capacitor consists of two parallel circular discs; an indication of the approximate position behind the indenter is shown in Figure 2-2. The

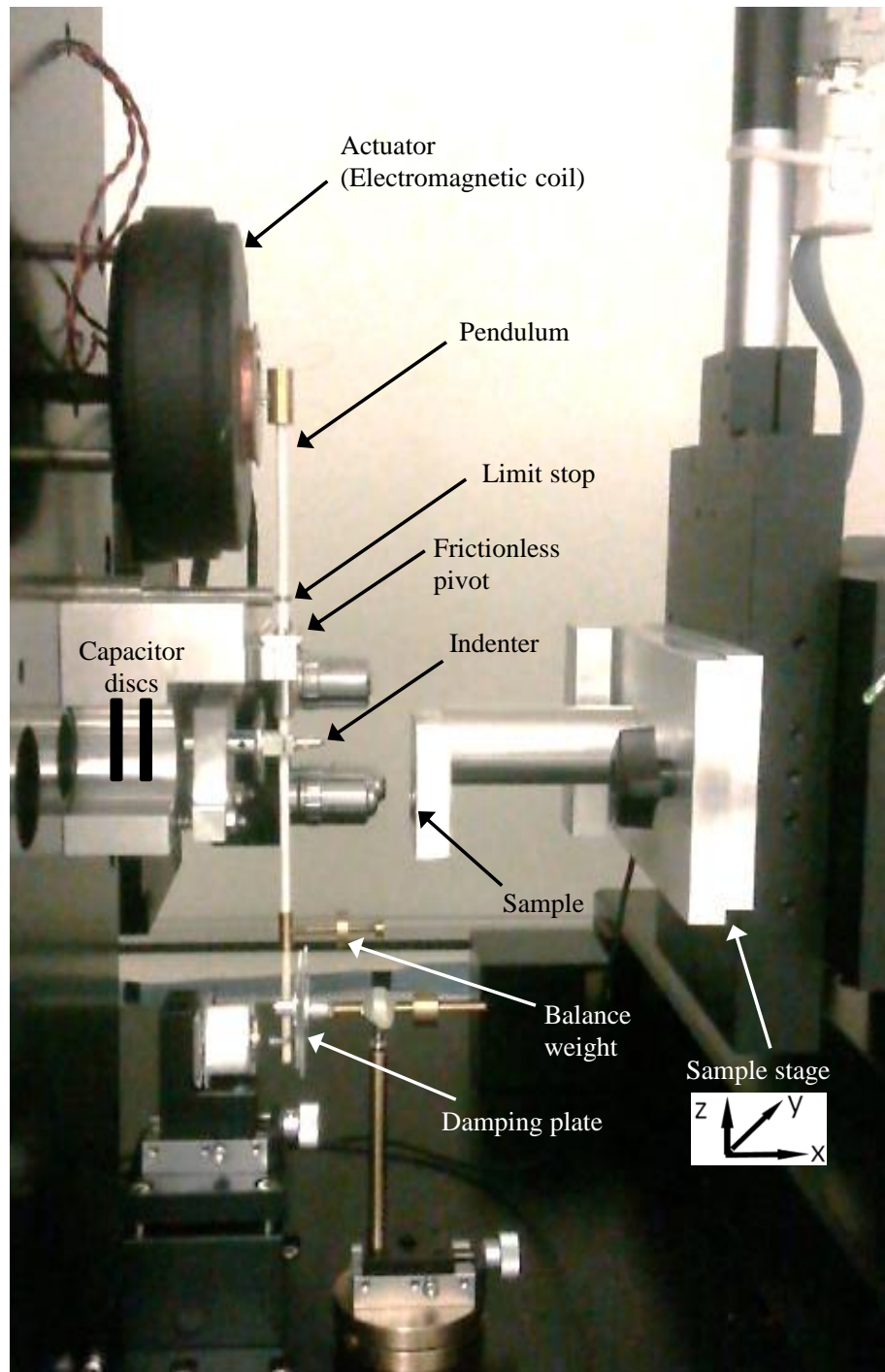


Figure 2-2 Micro Material Nano Platform

separation of these discs relates to a linear voltage range of 10 volts, equating to roughly 2 $\mu\text{m}/\text{volt}$, giving a total of 20 μm for the system. A damping plate at the bottom of the pendulum opposes the movement of the capacitor discs damping the voltage signal. Thus, during a load increment in a free pendulum test, the displacement overshoot should be eliminated, and when testing a specific specimen, the damping effect will always be higher than what is observed in a free pendulum test. The electronics controlling the voltage and separation is pre-calibrated by the manufacturer. The depth signal is also calibrated/checked automatically at the start of each test and can be performed by the user.

Precision DC motors control the samples position in the X, Y and Z planes and a separate calibration is needed for these displacements. The device operates either in load-controlled or displacement-controlled mode. Depending on which mode is used, either the displacement or load can be measured; this is due to the applied load being measured separately using the load sensor and the displacement of the indenter, as a result of the loading by the actuator, measured separately using the capacitor discs. For constant loading rate (load-controlled), proportional loading testing is used, which is an open loop system. However, in constant displacement rate test (displacement-controlled) closed loop functionality is available in newer P3 models.

For all nanoindentation testers, a “zero load” or “zero point” correction is essential. When applying the smallest possible load by the instrument, some displacement is always produced. However, for physical experiments, a datum for the dependent and independent variables is always set when calibrated. For the correction, the load-displacement data is extrapolated to zero load to determine how much initial displacement has occurred. The value of the initial penetration will depend on the type of fitting and how much data is selected (Fischer Cripps, 2011, p.80). For a spherical indentation, elastic contact is

assumed, and Hertz relationship can be used to model the load-displacement data. Alternatively, a power-law relationship can be used. For a Berkovich indenter, assuming some plasticity is occurring, a second order polynomial is preferred. Thus, whichever method is used, the determined initial displacement can be determined and added to the displacement data to set the datum.

Before an indentation test, using the Micro Materials Nano Platform, a “depth signal validation” is required to check the pendulum can move freely. The load on the pendulum is initially taken off giving a depth signal of ~ -10 volts, and then ramped up to ~ 8.9 volt referred to as the limit stop voltage. The signal between these two voltages relates to a linear change in the distance between the capacitor discs. The 10 volts range can be chosen anywhere within the linear range. In an indentation test, initial contact, i.e. a pre-contact is established at 5% (user specified) from the limit stop voltage, and a zero-point correction is performed. The load is then ramped with a known load rate, where the load, displacement and time can be measured at specific intervals. The exact procedures for the sampling rate and the zero-point calibration have been verified by the manufacturer (see Appendix 1). A sampling rate of 5×10^6 Hz with two sample point gives an effective sampling rate of 2.5×10^6 Hz, i.e. 10×10^6 sample points for a test with a maximum load of 200 mN and an unload rate of 5 mN/s. As only 4000 points are available for the hysteresis curve, the sampled points are averaged, subsequently giving 150 points for the top 10% of the unloading data.

2.2.2 Frame compliance and thermal drift

All the equipment discussed so far, are typically mounted on vibration-isolated bases to reduce the noise level in the data from the surroundings. Even with this addressed precision of the load-displacement data, two other types of corrections are essential when testing. The first source of error is the frame compliance, as the name suggested is the

increased compliance due to the frame of the machine. Figure 2-3 shows the relationship between the frame compliance and other compliances due to the sample and one measured by the indenter. Frame compliance can be determined by several methods (Fischer Cripps, 2011, pp.81–84). The most readily used method involves the analysis of the area

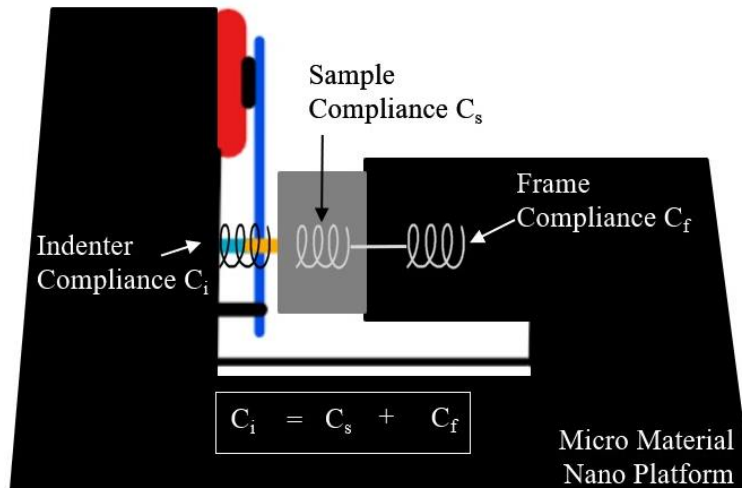


Figure 2-3 Schematic of Micro Material Nano Platform showing frame compliance

function that requires indenting on a reference material spanning the load range of the equipment. Once determined, the frame compliance can then be either subtracted from the measured stiffness to calculate the elastic modulus or alternately the displacement data can be corrected by subtracting the extra displacement due to the frame compliance.

The second sources of error in the depth measurement is due to thermal drift (Fischer Cripps, 2011, p.77). Thermal drift occurs due to the thermal expansion of the apparatus in response to environmental changes. Typically, hold periods are used to either measure the creep behaviour or thermal drift of the apparatus during the tests in order to correct for their contributions. The load schedule for a typical indentation test in Figure 2-4 shows, at the end of unloading at a load of 0.06 mN, a hold period used for the thermal correction. During a hold period, the two phenomena, i.e. creep and thermal expansions,

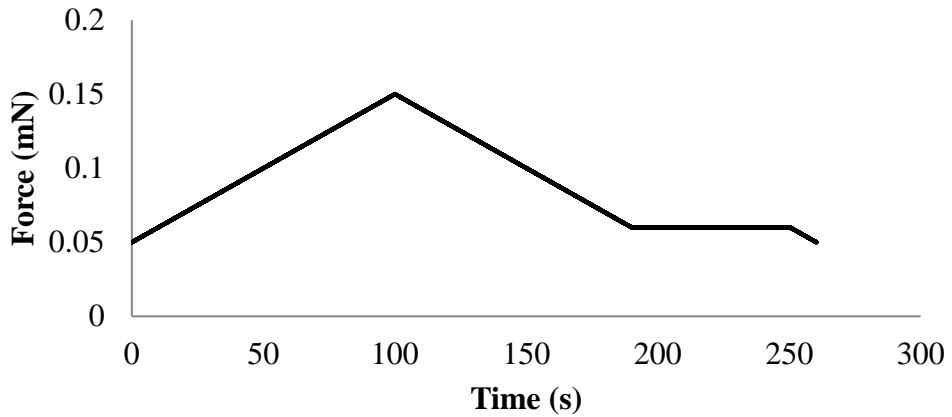


Figure 2-4 Force against Time for an indentation test

have coupled effects on the deformation and are practically indistinguishable. Thus, hold measurements for thermal drift are best carried out either at the end or the start of the indentation, applied at low loads to eliminate the effect of creep or to make it negligible. During the hold period, the load is held constant as the displacement is measured continuously with time. From this response, it is assumed that the gradient, determined by linear regression of the last 40 % of the displacement-time response, is the thermal expansion due to the combined effect of the test material and equipment.

2.2.3 Indenter types and area function

The indenter is a probe having a well-characterised shape profile and well-understood material properties, typically diamond. There are many types of indenters (Micro Star Technologies, 2019). However, they can be classified as sharp (pyramidal, conical, cubic, etc.) or blunt (spherical). The geometries can be seen in Figure 2-5. When determining hardness and elastic modulus near subsurface and of thin films, sharp indenters are preferred. These have a well-defined tip geometry and establish plasticity even at low loads. Pyramidal indenters such as the three-sided Berkovich and four-sided Vickers are commonly compared to conical indenters with equivalent half-angle that gives the same

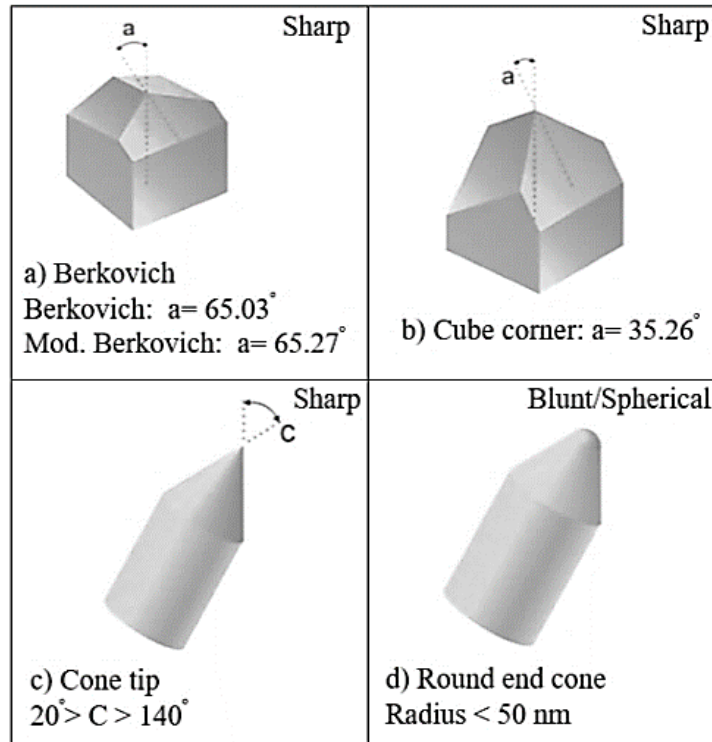


Figure 2-5 Typical nanoindenters manufactured by micro Star technologies (Micro Star Technologies, 2019)

area/ depth ratio. Blunt indenters are used, for ductile materials to determine indentation stress-strain characteristics and the yield point, as there exists a transition from elastic to plastic deformation. The main disadvantage is the geometry is not 100% spherical and precise contact area is needed for hardness and elastic modulus measurements. This is found indirectly as this method is more convenient than imaging as this small scale length (Doerner and Nix, 1986; Oliver and Pharr, 1992). Figure 2-6 shows a typical indentation profile with the circle of contact. The area function of the indenter is typically described as a function of the plastic depth (h_c) and can be presented in several forms (Fischer Cripps, 2011, p.86), a 5th polynomial to describe the area function is given as:

$$A(h_c) = a + b(h_c)^1 + c(h_c)^2 + d(h_c)^3 + e(h_c)^4 + f(h_c)^5 \quad \text{(Equation 2-1)}$$

The area of contact can be established once the h_c is known. The coefficients can be determined by several outlined techniques (Fischer Cripps, 2011, pp.84–86). Three different procedures are recommended to determine the actual contact area of the

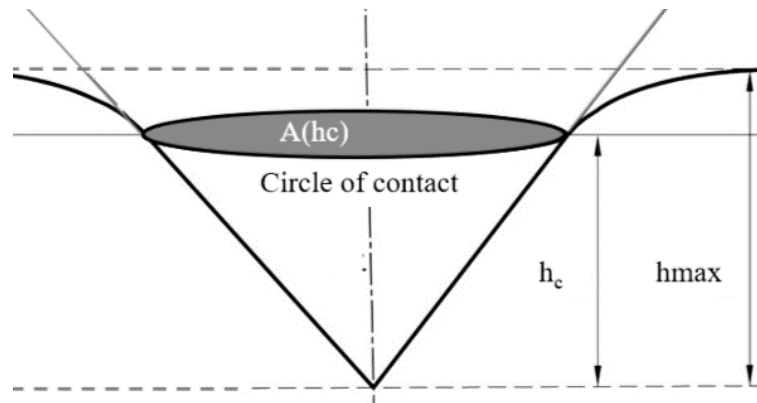


Figure 2-6 The plastic depth (h_c) and contact area $A(h_c)$ of an indentation (UK Patent 1513480.2, 2015; UK Patent 1701591.8, 2017)

indenter (Fischer Cripps, 2011, p.190). The methods involve either measuring the area directly using Atomic Force Microscopy (AFM) or Scanning Electron microscopy (SEM), or indirectly by performing tests/calibrating on the material sample with known properties. Typically, fused silica is used due to its fully isotropic elastic behaviour. An indirect approach can also be used by comparing the difference in hardness with the depth, of a known material which ought not to show any depth variation.

For sharp indenters, the same procedure applies. At ultra-low loads, sharp indenters can behave as spherical ones as some tip rounding is present, additionally with time these indenters can wear and become blunter. Thus, regular calibration for determining the precise area function of the indenter, using any of the above procedures, is critical for accurate nanoindentation results.

2.2.4 Time constants

Increments for either displacement or load-controlled tests are required for a particular schedule, earlier shown for load in Figure 2-4. A time constant (τ) is a quantity relating to how fast the response reaches a steady state when subject to a step-input/increment and how it is mathematically defined depends on the system (Weik, 2001). The τ can affect the input/output of the real-time data of the load actuator and displacement transducer, also affecting the dynamics of any feedback loops. Practically a definite increment of a physical property is not possible; an increment is always applied over infinite time (Fischer Cripps, 2011, p.142). The τ for these devices, for which the response is characteristically exponential to the step input, are typically listed by the manufacturers. These are expected to be much smaller than the time scale of experimental measurement (Sudharshan Phani and Oliver, 2017). Otherwise, the real output is not captured accurately. The measured sampling rate of 500000 Hz for the Micro Materials Nano Platform is typical giving 2 μ s between each sample point, whereas the τ for actuators and transducers selected by the manufacturer are much smaller than this value.

2.3 Previous nanoindentation methodologies

As highlighted in the introductory chapter, macro and micro-indentation techniques evolved towards what is now termed nanoindentation. The technique is used for characterisation and investigating the mechanics of material deformation at various scales. When a material is indented, the deformation processes that occur are due to different phenomena, either geometrical or materials based, affecting the appearance of the load-displacement curve. Mathematical models are then used by which this load-displacement data can be interpreted to obtain hardness, elastic modulus, and many other mechanical properties such as elastic and plastic deformation work, yield stress, fracture

toughness (Li, Diao and Bhushan, 1997), and residual stresses in thin films (Suresh and Giannakopoulos, 1998).

Many models/methods have been introduced over time to analyse the load-displacement data and will be discussed. The unloading curve shows three types of elastic recovery, depending on its severity, it can be estimated by the ratio E/Y , where E is the elastic modulus, and Y is the yield strength. For most materials which display low elastic recovery, large values of E/Y , Doerner and Nix (1986) found that the unloading curve was linear even when indented with a Berkovich indenter. When using their developed analysis of a conical indenter for this class of materials, they established the cylindrical punch method to be a good approximation for determining the h_c .

The main development in the unloading method was due to Oliver and Pharr (1992) who concluded that the initial unloading curve was not linear for the majority of materials with moderate elastic recovery. It was shown the elastic modulus results compared well to tensile tests when the unloading data was fitted using a power law. Similar to Doerner and Nix when conducting tests with a Berkovich indenter they were able to show the conical analysis was valid for all axial-symmetrical indenter types (Pharr, Oliver and Brotzen, 1992). The Oliver and Pharr (1992) method was successfully applied to characterise a vast range of materials. However, for many stiff hard materials and many inhomogeneous systems like those employed in thin hard coatings Hainsworth et al. (1996) found the unloading curve not to fit linear or power-law models when the test volume displayed considerable elastic recovery. They developed a method using the loading curve, i.e. the load-displacement squared analysis as originally proposed by (Loubet, Georges and Meille, 1985). However, in order to determine one of the two material properties, i.e. hardness or elastic modulus, one has to be known beforehand. Later for coated materials, it was shown that at higher loads elastic recovery is controlled

alone by the elastic modulus of the underlying substrate and demonstrated the effectiveness of both load–displacement and load–displacement squared plots in gaining a more complete understanding of system behaviour (Hainsworth, M.R McGurk and T.F Page, 1997).

Instead of finding the plastic depth from the slope of initial unloading curve, as in the multiple-point unload method (Doerner and Nix, 1986; Oliver and Pharr, 1992), an alternative method the single-point unload method suggested by Field & Swain (1993), determined it by uses two separate single unload-points along with the contact equation for a spherical or Berkovich indenter (Fischer Cripps, 2011, p.47,51). Both methods are successful in determining elastic modulus and hardness when elastic recovery is low to moderate however multiple-point unload method will only be discussed in this thesis due to its approval by the international standard (ISO 14577-1, 2002–2015) because of its applicability to a vast number of materials and test conditions.

Apart from these methodologies other alternative methods exist for determining the elastic modulus and hardness (Fischer Cripps, 2011, pp.68–72), the load-displacement squared analysis (Hainsworth, Chandler and Page, 1996), the stiffness ratio method (Oliver, 2001) along with the work of indentation approach (Sakai, 1993; Shorshorov, Bulychev and Alekhin, 1981) initially proposed by Stilwell & Tabor (1961). All these methods have been critically compared to the unloading method by Berasategui (2003). It was concluded that all these methods fail at low-loads due to the elastic-plastic transition and that the unloading method was the best for analysing a fully elastic response. However, analysis of sensitivity showed the error was comparable for all methods in determining the experimental parameters. Further, the stiffness ratio method was shown to have the advantage of not needing a tip calibration. However, it had the same disadvantage as the unloading method when it came to studying plastic response.

In these studies, creep, tip correction, sink-in and pile-up corrections were not considered when applying the unloading method. The advantage of the multiple-point unloading method is that there has been considerable development over the years, considering these corrections on different types of materials and low loads. These improvements will be reviewed in the following sections.

2.3.1 Nanoindentation unloading methodology

Traditionally the unloading curve is assumed to be totally elastic, and almost all nanoindenter manufacturers have adopted the procedure (ISO 14577-2, 2002–2015; ISO 14577-3, 2002–2015; ISO 14577-4, 2007–2016; Oliver and Pharr, 1992). The standard method is based on the pioneering work done by the Baikov Institute of Metallurgy in Moscow during the 1970s (Bulychev et al., 1975). The contact was modelled using an analytical model for contact between a rigid indenter with a homogeneous isotropic elastic half-space. The procedure is presented in Figure 2-7a where the data has to be initially corrected for a zero-point correction, thermal drift and load frame compliance. After these corrections the stiffness is determined from the gradient (see Figure 2-7b) of the load-displacement graph; the unloading stiffness at maximum load is then used in the calculation of plastic depth (h_c) by the following equation:

$$h_c = h_{max} - \epsilon \frac{P_{max}}{S} \quad \text{(Equation 2-2)}$$

where h_{max} and P_{max} are the maximum values of the response data, and S is the unloading stiffness at maximum load. These factors are highlighted in Figure 2-6, Figure 2-7b & c. The factor ϵ in (Equation 2-2) is due to Oliver and Pharr adapting the equation, from one describing elastic unloading of a cone, to the unloading of an indenter of a parabolic shape (Doerner and Nix, 1986). When ϵ is 1, the equation is for a cone as defined by Doerner and Nix. For a Berkovich indenter, ϵ is typically 0.75, but to account for any variations

a)

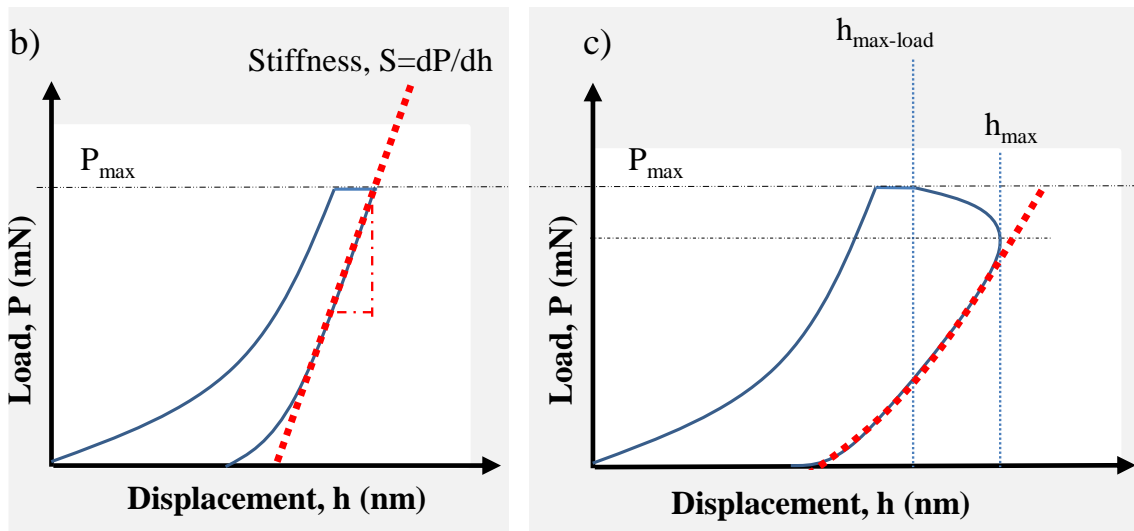
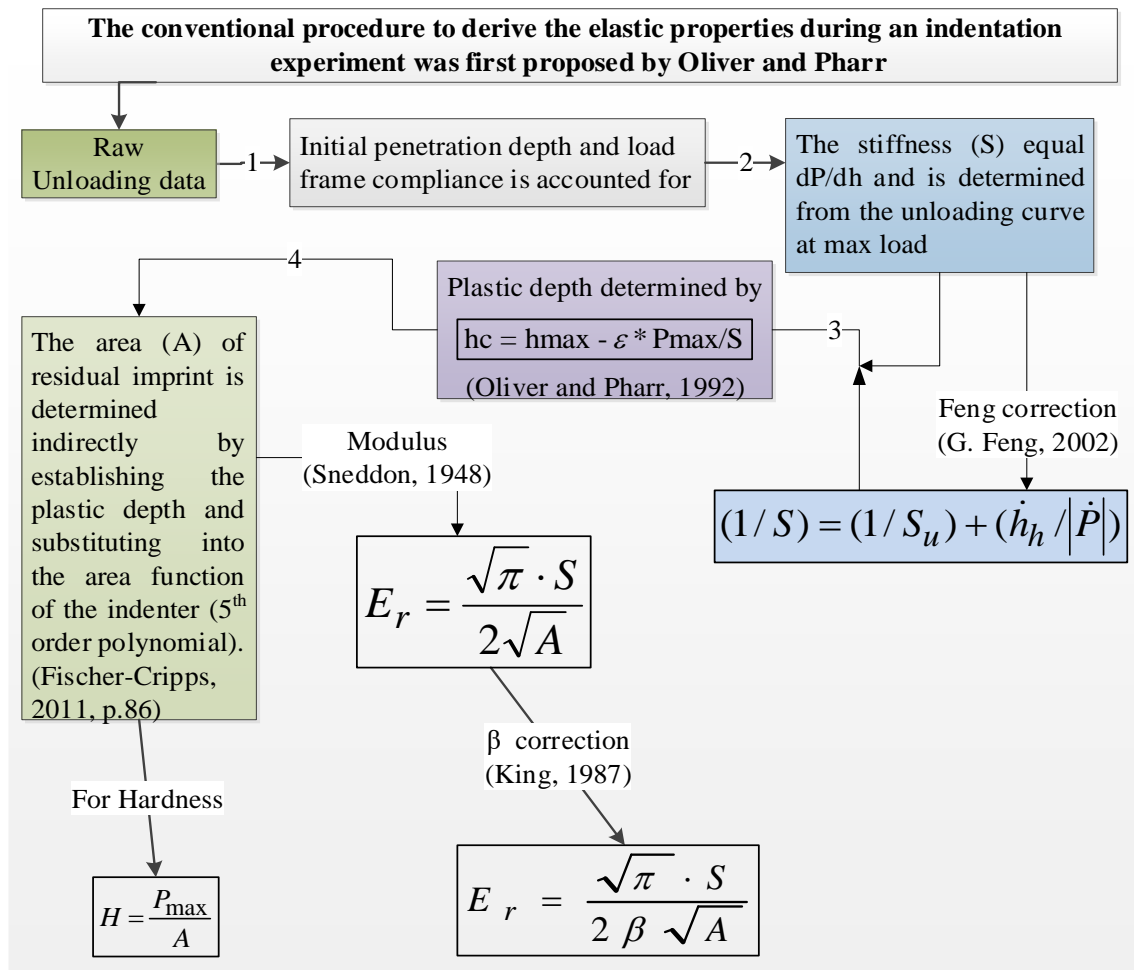


Figure 2-7 a) Schematic of Oliver and Pharr procedure with Feng’s correction for the calculation of hardness and reduced modulus, b) Typical Load-displacement graph, and c) Load-displacement of viscous/polymeric materials with “nose out”

of the tip due to wear ε can be calculated using the expression: (Pharr and Bolshakov, 2002).

$$\varepsilon = m \left[1 - \frac{2\Gamma\left(\frac{m}{2(m-1)}\right)}{\sqrt{\pi}\Gamma\left(\frac{1}{2(m-1)}\right)}(m-1) \right] \quad \text{(Equation 2-3)}$$

Where Γ is the factorial or “gamma” function and m is the exponent of the unloading curve when fitted to the power-law function of the type:

$$P = a(h - b)^m \quad \text{(Equation 2-4)}$$

Where P is the load, h is the displacement, a and b are constants determined by regression fit. In step 4 of Figure 2-7a, the contact area is determined next by (Equation 2-1). For relating the stiffness to the reduced modulus, the relationship first established by Sneddon (1948) was presented in the form:

$$S = \beta \frac{2}{\sqrt{\pi}} E_r \sqrt{A} \quad \text{(Equation 2-5)}$$

Where S is the stiffness, E_r is the reduced modulus representing the combined elastic modulus measurement of the indenter and sample, A is the contact area at P_{\max} and β is a correction factor. The basic assumption of the approach is that deformation upon unloading is purely elastic. This equation is valid for any indenter that can be described as a body of revolution of a smooth function (Pharr, Oliver and Brotzen, 1992) and for pyramidal indenters (King, 1987). Due to deviations from the assumptions used in Sneddon’s elastic derivation, a correction factor is added in (Equation 2-5). β was proposed to be unity for axisymmetric indenters, close to unity for pyramidal indenters β , 1.012 for square-based indenter, i.e. Vickers and 1.034 for a triangular punch, i.e. Berkovich (King, 1987).

For the calculation of the hardness the following equation is used:

$$H = \frac{P_{max}}{A} \quad \text{(Equation 2-6)}$$

The assumption of fully elastic unloading was due to Tabor who showed the entire unloading curve and the total amount of recovered displacement can be accurately related to the elastic modulus and the size of the contact impression, for both spherical and conical indenters, only if the indentation was loaded and unloaded a number of times (Tabor, 1948). After that, the load-displacement behaviour became perfectly reversible, i.e. elastic. A limited amount of plasticity sometimes occurs in each of the first few loadings and unloading's sequences. A multi-cycle test can be carried out to eliminate it (Oliver and Pharr, 1992). Tabor also accounted for the effects of the non-rigidity of the indenter, on the contact deformation, by defining a reduced modulus, E_r , by the following equation

$$\frac{1}{E_r} = \frac{(1 - \nu^2)}{E} + \frac{(1 - \nu_i^2)}{E_i} \quad \text{(Equation 2-7)}$$

where E and ν are the elastic moduli and Poisson's Ratios of the materials, i subscript is denoting the indenter values.

2.3.2 The continuous stiffness measurement technique

The continuous stiffness measurement technique involves applying a small oscillatory force to the indenter superimposed on the actuated force applied to penetrate the sample. It has a number of benefits (Hay, Agee and Herbert, 2010) including improved in situ surface detection, i.e. an alternate procedure for zero load correction (see section 2.2.1). The material properties can be determined as a function of depth using a single load-unload cycle and is insensitive to thermal drift (Li and Bhushan, 2002). For viscous/polymeric and soft materials, the viscoelastic properties such as the storage modulus, loss modulus and loss factors can be determined in the frequency domain using

phase-lock amplifiers. This can be done by recording the phase lag between the applied load and corresponding displacement. Although the continuous stiffness measurement technique has several benefits, it is not used in this work due to its disadvantages of intrinsically modifying the strength of the sample (Siu and Ngan, 2013). Herbert et al. (2015) found the output properties have errors associated with the test equipment itself and coupled in complex ways to the testing conditions. Apart from this, the oscillations need to be small compared to the indenter penetration else inaccurate stiffnesses can be recorded (Leitner, Maier-Kiener and Kiener, 2017). So, the alternative method to determine the viscoelastic properties employed in this thesis uses the time domain, i.e. hold time experiments. The reason being that one domain is not inherently better than the other (Herbert, Sudharshan Phani and Johanns, 2015).

2.3.3 Accurate contact depth

Determining accurate contact depth is essential in nanoindentation tests. There are two commonly used methods, the elastic case (Oliver and Pharr, 1992) and the elastic-perfectly plastic case (Bec et al., 1996). For quasi-static unloading conditions, these two models can be used to determine normalised contact depth against the normalised stiffness relationships. The crossover between these two models is used to determine which of the two is valid for the sink-in and pile-up correction (Fujisawa and Swain, 2006).

2.3.4 Other factors affecting the nanoindentation response

At different depths, the mechanical behaviour of even homogeneous isotropic solids can vary due to Indentation Size Effects (ISE) (Swadener, George and Pharr, 2002; Durst, Göken and Pharr, 2008) originally understood to be due to plasticity, i.e. geometrically necessary dislocations (Nix and Gao, 1998). ISE have also be related to many other

factors such as surface hardening (Pöhl, Huth and Theisen, 2016) or stain hardening effect due to the preparation/polishing of the sample, scale-dependent influence of grain boundaries and grain orientations (Schuessler, Wo and Zbib, 2018), tip rounding (Fu, 2006), missing tip phenomena (Hochstetter, Jimenez and Loubet, 1999a), humidity (Altaf, Ashcroft and Hague, 2011), thin oxidation layer and residual stress being present, crystal orientation and the friction between the sample (Fischer Cripps, 2011, pp.91–93). The fabrication of the sample material can cause depth related properties due to defects, varying density and porosity. Moharrami (2014) showed the reliability of mechanical properties at low tests loads is dominated by anisotropy and grain size effects but disappears at higher loads and with Finite Element Modelling (FEM) studies on porous material revealed the size, shape and location of porosity, with respect to the indenter, is critical in determining the mechanical properties. For thin film systems, ISE can also be due to gradient layers and environmental humidity causing a soft layer on the sample or oxide surface softening by chemo-chemical effects (Berasategui, 2003, pp.59–60).

In this section, the nanoindentation methodologies and associated problems were discussed. However, the characterising procedure for viscous/polymeric materials is different as there is no set nanoindentation standard; this is due to a range of issues associated with the viscoelastic behaviour and will be discussed next.

2.4 Nanoindentation and associated problems of Viscous/polymeric materials

Nanoindentation experimentation and analysis of viscous/polymeric materials are very different from that of metals or ceramics. Many studies have been conducted on polymers (Briscoe, Fiori and Pelillo, 1998; Flores and Calleja, 1998; VanLandingham et al., 2000, 2001; Wei, Shen and Lin, 2008; Yang, Zhang and Zeng, 2004) including PET (Beake et al., 2007; Beake and Leggett, 2002; Calleja, Flores and Michler, 2004). For polymers

uncertainty in the output data from errors that occurred due to the indentation unloading curve, appeared to be dependent on both the holding time at the maximum load and the unloading rate. In early nanoindentation tests, the indentation response of viscous/polymeric materials was too compliant for it to be measured accurately as the system compliance was too low, leading to the output signal to be similar to the signal noise (VanLandingham et al., 2001; VanLandingham, 2003, p.261). However, advancement in nano platform design made it possible to obtain higher precision data (Beake and Leggett, 2002). These uncertainties were related to the viscous nature, making the elastic modulus and hardness, time-dependent, or rate-dependent, and values inconsistent when measured (VanLandingham et al., 2001). Therefore, the analysis adopted by Oliver and Pharr (1992) could not be applied. VanLandingham (2001) proposed a smooth spline fitting routine to fit the unloading curves showing excellent fits to the unloading data. Furthermore, the loading/unloading characteristics of polymers change with different loading or unloading rate of the indentation (Yang, Zhang and Zeng, 2004) and there are issues in determining the initial conditions at first contact. All these factors lead to uncertainties and errors in defining the contact area for the use in the analysis of hardness and the elastic modulus. It was proposed by VanLandingham et al. (2001) that advancement of nanoindentation testing toward the quantitative characterisation of polymer properties would require material independent calibration procedures, polymer reference materials, advances in instrumentation, and new testing and analysis procedures that account for visco-elastic and visco-plastic polymer behaviour.

For stress relaxation and creep experimentation, feedback control is needed to keep either the displacement or load constant. In the open loop load actuator system of the Micro Material Nano Platform, the PID feedback is software-based correcting for any load

variation in creep experiments. However, for closed-loop system feedback, separate electronics are used to keep the relevant parameter constant.

From what was mentioned earlier, the hold time is much larger than the τ of the electronics and also the time taken between the collection of any two successive points of measurement. For viscous/polymeric materials, τ_i is much larger, caused by displacements due to creep and plasticity. The term “forward plasticity” is used to describe the occurrence of these phenomenon during loading, hold and unloading. The amount of “forward plasticity” and thus τ_i depends on the test conditions. For load-controlled, the effect is creep during loading, primary creep at start of hold and “nose out” effect during unloading (see Figure 2-7c). In comparison to displacement-controlled, it is accepted that load-controlled tests are equivalent in obtaining intrinsic material properties. However, displacement control tests do have advantages over load-controlled due to stress relaxation being four times faster than creep (Hollander and Hatton, 2004, p.250). This deduction from confined compression tests if inferred to indentation test would suggest creep and τ_i to be larger when compared with stress relaxation. Although less “forward plasticity” will be displayed under displacement control i.e. stress relaxation tests, for creep experiment the “forwards plasticity” has been accounted for using the ramp correction factor (Oyen, 2006) and for the unloading method “nose out” effect corrected by Feng (2002), a method for correcting creep effects in the reduced modulus measurement (refer to Figure 2-7a) influenced by the works of Lee and Radok (1960a), and Ting (1966). The apparent compliance measured was due to the elasticity and creep components, i.e. viscoelasticity. The solution derived, as initially proposed by Radok (1957) himself, uses the correspondence principle between elasticity and linear viscoelasticity. In Oliver and Pharr’s method (1992), a multi-loading sequence was used to eliminate any reverse plasticity; this was also applied in Feng’s (2002) method and had

to be performed at conditions when the “nose out” effect is present. In this analysis (Equation 2-8) is usually interpreted as (Equation 2-9).

$$\left. \frac{dh}{dp} \right|_u = \frac{1}{2E_r A} + \frac{\dot{h}_h}{\dot{P}} \quad (\text{Equation 2-8})$$

$$\frac{1}{S} = \frac{1}{S_u} + \frac{\dot{h}_h}{|\dot{P}|} \quad (\text{Equation 2-9})$$

where \dot{h}_h is the penetration rate at the end of the hold, \dot{P} is the load rate, E_r is the reduced modulus, A is the contact area, S_u is the unloading stiffness as measured from the unloading data and S is the creep corrected stiffness used to determine the elastic modulus.

With the correct analysis, nanoindentation can be applied to characterize a number of mechanical properties of the polymeric materials (Sinha and Briscoe, 2009, p.190). Several approaches exist to evaluate the time-dependent nature, or rate-dependent nature, of the deformation processes that occur in the polymeric materials (Beake et al., 2007; Gray and Beake, 2007; Huang, Wei and Lee, 2011; Menčík, He and Němeček, 2011; Sinha and Briscoe, 2009, p.163). It is proposed that by combining the known analytical methods that have been developed for polymeric materials, one should be able to perform a complete analysis of loading/holding/unloading data obtained from nanoindentation tests.

2.4.1 Depth-dependent properties

At surface or sub-surface regions, polymer structures are very different compared to the bulk (Sinha and Briscoe, 2009, pp.149–152), thus displaying different mechanical properties. When studying the behaviour of thin films, the scale of investigation is small, and only the near surface properties are of interest, these properties can be achieved using

nanoindentation. Depth-dependent properties can be related to possible effects such as ISE and phase transformation. Tweedie et al. (2007) showed that on indentation using images reconstructed from atomic force microscopy, the apparent stiffness of the surface of several polymers was shown to exceed that of the bulk by up to 200%, and was independent of processing scheme, macromolecular structural characteristics, and relative humidity. The enhanced apparent stiffness was said to relate to the contact stress-induced formation of a mechanically confined phase at the probe-polymer interface. The Oliver and Pharr's procedure is invalid under this circumstance because it employs a constant elastic modulus with depth assumption in the analysis to determine the area function. Work reported by Fujisawa and Swain's (2006) hypothesised that the elastic modulus of the amorphous polymer is dependent only on the unloading strain rate and is independent of the indentation depth. Their findings established this behaviour for Poly-methyl-methacrylate (PMMA) polymers. In order to single out the dependency of elastic modulus on the strain rate, the overestimation of the contact depth was eliminated by additional unloading tests to establish quasi-static test conditions, concluding no clear depth correlation based on the statistical analysis. However, it should be noted that the depth dependency cannot be disregarded as test conditions were preselected to give the required results. Thus these results cannot be valid.

2.5 Nanoindentation hold time response

The creep behaviour of the polymers materials has been characterised in a number of studies (Beake et al., 2007, 2007; Goodall and Clyne, 2006; Gray and Beake, 2007; Huang, Wei and Lee, 2011; Menčík, He and Němeček, 2011; Odegard, Gates and Herring, 2005; Wei, Shen and Lin, 2008; Yang, Zhang and Zeng, 2004). Typically, a phenomenological approach is taken in these studies where hold time data is related to

some mathematical expression and then afterwards, the parameters related to the test conditions.

Time constants are defined for these stress relaxation and creep hold-time experiments named the material time constant (τ_i). During a load increment to an elastic-plastic material the displacement response can be instantaneous (Fischer Cripps, 2011, p.142) however the τ_i of a viscoelastic solid depends on the loading conditions and the type of phenomenological model considered, and the values are shown to be much higher than the actuator/transducer. For a one spring, one dashpot and two Kelvin–Voigt phenomenological model Menčík et al. (2009) found the two τ_i to be about 20 sec and 200 sec when held at a maximum load of ~ 200 mN.

During hold time, when a constant load condition is applied, two stages are present. Indentation displacement increases with the time in the primary stage, but with a decreasing rate, the displacement rate decreases with time and approaches a constant value, which is the steady-state stage. Two different models have been proposed (Zeng, 2006) to describe the hold behaviour. The different applied stress states created by different indenter tips and the maximum indentation loads dictate the characteristic (or effective) stress, which is commonly required for use in models (Goodall and Clyne, 2006). Also due to temperature, the behaviour of the polymer can change, the simple creep equation (Chudoba and Richter, 2001) has been used by other authors to find the effect of temperature on the creep rate (Beake et al., 2007), thus proposing certain mechanisms to describe the deformation behaviour. A detailed study on the characterization of viscoelastic-plastic properties of solid polymers by instrumented indentation was conducted to successfully describe equations and procedures to obtain material parameters (Menčík, He and Němeček, 2011). The models for acquiring various parameters from the hold period are described next.

2.5.1 Logarithmic fits for hold time

The Guiu and Pratt expression is remarkably effective in representing stress relaxation curves for polymers (Ward and Sweeney, 2004, p.238). This case is for stress relaxation in tension and is derived using the Eyring equation. The change in stress varies with time, and the relation is expressed as:

$$\sigma_o - \sigma_f = \frac{1}{B} * \log\left(1 + \frac{t}{C}\right) \quad \text{(Equation 2-10)}$$

Where σ_o and σ_f are the initial and final stresses, respectively. B and C fit constants, and t is the time during the hold period. Other authors have proposed a similar version where the change in depth varies with a similar relationship (Chudoba and Richter, 2001):

$$\Delta h = A * \log(B * t + 1) \quad \text{(Equation 2-11)}$$

2.5.2 Phenomenological Mencik's model for hold time

Formulae and derivations have been presented in a previous study for a visco-elastic-plastic response to the nanoindentation hold-time, for various indenters and times of loading (Menčík, He and Němeček, 2011) and are reviewed in this section. A procedure for obtaining the parameters of the creep compliance function (J(t)), a basic material creep characteristic, from monotonic load was proposed by these authors. The formulae are based on a previous approach where elastic solutions are used, but replacing the elastic constants by a viscoelastic integral operator (Johnson, 1987; Lee and Radok, 1960b). The relationship between the indenter load F and depth h of penetration under monotonic load was expressed as:

$$\Delta h^m = K_a \varphi(F, J, t) \quad \text{(Equation 2-12)}$$

Where m and K_a were constants for the indenter geometry, and $\varphi(F, J, t)$ was a response function depending on the load (F), creep compliance (J) and time (t). For pointed

indenters such as a cone, Berkovich or Vickers the parameter “m” equals 2 and $K_a = \pi/(2 \tan \alpha)$, where α is the semi-angle of indenter tip, or an equivalent cone. For Berkovich and Vickers indenters, α is equal to 70.3 degrees.

For a spherical indenter, the parameter “m” equals 3/2 and $K_a = 3/(4\sqrt{R})$, where R is the tip radius. The general form of the response function for linearly viscoelastic materials took the form (Haddad, 2012)

$$\varphi(t) = \int_0^t J(t-u)(dF/du) du \quad \text{(Equation 2-13)}$$

Where u is a dummy variable for integration.

Mencik et al. determined two load regimes, leading to simple response functions:

1. For a constant load after a step change from 0 to F:

$$\varphi(t) = FJ(t) \quad \text{(Equation 2-14)}$$

2. After a period of load increase, the load grows by a constant rate $k = dF/dt$:

$$\varphi(t) = \int_0^{t_R} J(t-u) du \quad \text{(Equation 2-15)}$$

The load first grows by a constant rate k to the nominal value F, and then it is held constant. For this second period, (Equation 2-14) can be used, with the lower integration limit t equal to the duration of initial load increase, $t_R (= F/k)$.

J(t) was determined using the phenomenological approach. The time-dependent irreversible viscous deformation, i.e. Plastic behaviour was characterized by a slider in the rheological model, characterised by a dashpot of viscosity, η . Combining the dashpot in series with the Universal model, which consists of spring in series with one or more Kelvin-Voigt bodies (a spring in parallel with a dashpot), they were able to attain the following relationship when J(t) is inserted in (Equation 2-12).

$$h(t)^m = FK_a \left[B_0 + C_v t - \left(\sum_{i=1}^n D_i e^{-t/\tau_i} \right) \right] \quad (\text{Equation 2-16})$$

where the square bracket term equal J(t)

$$B_0 = C_0 - \frac{C_v t_R}{2} + \left[\sum_{j=1}^n C_j \right] \quad (\text{Equation 2-17})$$

$$D_i = C_j \rho_j \quad (\text{Equation 2-18})$$

$$\rho_j = \frac{t_R * \left[e^{\frac{t_R}{\tau_j}} - 1 \right]}{\tau_j} \quad (\text{Equation 2-19})$$

where ρ_j was associated with the ramp correction factor (Oyen, 2006).

Using the above equations, three particular methods are considered by the author of this thesis using different rheological components and are tabulated below:

Table- 2-1 Methods and different rheological components for Mencik's work

method	Number of Kelvin-Voigt bodies	Plasticity considered
M _{2KVP}	2	Yes
M _{2KV}	2	No
M _{1KV}	1	No

For M_{2KVP} equations are derived. However, for M_{2KV} and M_{1KV} the equation can be derived in the same way. Thus, for M_{2KVP} (Equation 2-16) becomes

$$h(t)^2 = \frac{F\pi}{2\tan\alpha} \left[-D_1 e^{-t/\tau_1} - D_2 e^{-t/\tau_2} + B_0 + C_v t \right] \quad (\text{Equation 2-20})$$

Thus, this equation can be arranged for fitting in the form

$$h(t)^2 = ae^{bt} + ce^{dt} + e + f \quad (\text{Equation 2-21})$$

Where

$$D_1 = -2a * \tan\alpha / F\pi \quad (\text{Equation 2-22})$$

$$\tau_1 = -1/b \quad (\text{Equation 2-23})$$

$$D_2 = -2c * \tan\alpha / F\pi \quad (\text{Equation 2-24})$$

$$\tau_2 = -1/d \quad (\text{Equation 2-25})$$

$$B_0 = 2e * \tan\alpha / F\pi \quad (\text{Equation 2-26})$$

$$C_V = 2f * \tan\alpha / F\pi \quad (\text{Equation 2-27})$$

Once D_i and τ_i are determined, ρ_i and C_i can be determined from (Equation 2-18) and (Equation 2-19). Also

$$J(t) = 1/E(t) \quad (\text{Equation 2-28})$$

2.6 Indentation of rough surfaces

Bowden and Tabor (1939) were the first to state the importance of surface roughness in contacting bodies. Indentation studies, conducted using spherical and Berkovich indenters, showed parameters, such as roughness parameter (α) (Johnson, 1987) and H/E^2 (Joslin and Oliver, 1990), to be significantly sensitive when surface roughness effects dominated. With analysis, by defining a critical depth, Zhang and Xu (2002) showed that surface deformation predominated when the indentation depth was below the critical, while deformed above the critical bulk deformation was predominate. Further examining the effect of indentation Kim et al. (2007) highlighted the surface roughness to be flattened. Xia et al. (2014) emphasised the contribution of the surface roughness to the ISE, detailing how roughness presents imprecision at initial contact. Recent nanoindentation studies reconfirm the surface roughness of the sample to have a severe effect on the determination of hardness and elastic modulus data (Chen et al., 2017) and

show the reliability to decrease, as the scatter of the data increases with increasing roughness.

2.6.1 Modelling surface roughness and adhesion within contacting bodies

Nanoindentation is heavily dependent on contact modelling for the interpretation of the response data. Contact problems fall within the field of contact mechanics (Bower, 2009). Many parameters have to be considered when modelling contacting bodies, as described previously in section 1.3. As the nature of the contact changes with decreasing depth, the surface roughness or adhesion may dominate, and appropriate models are needed. Thus, these models are reviewed below.

In order to model nanoindentation, i.e. normal loaded contact problems, the typical approaches used can be, a single indenter of a known geometry interacting with either a curved, half space, single asperity or multi-asperity (also known as discrete contact) surface, where each depends on the scale. Hertz (1882) was the first to solve the problem involving contact between two elastic bodies with curved surfaces; this set the foundation for contact modelling still applicable today. After the emphasis on the importance of surface roughness in contact bodies by Bowden and Tabor (1939) discrete contact became popular, in which a framework was established for the elastic deformation of multi-point asperity-contact. It has been acknowledged, for rough elastic surfaces, that the contact area is approximately proportional to the normal force (Archard, 1957). By considering the statistical nature of the surface roughness Greenwood and Williamson (1966) showed how the contact deformation depended on the topography of the surface. In this model, all surface asperities were assumed to have identical spherical curvature and Gaussian distribution height profile. Further work along this theme was presented by several authors (Archard and Onions, 1973; Pullen and Williamson, 1972; Whitehouse and Archard, 1970). In order to overcome the complexities for analysing profiles of random

surfaces to obtain the necessary parameters, an improved technique was developed by Nayak (1971). The major development of discrete contact diverged from the statistical theory of isotropic randomly rough surfaces, and modelling asperities as paraboloids with two different radii of curvature (Bush, Gibson and Thomas, 1975). Another approach proposed by Persson (2001) capable of giving an exact solution for full contact without using the asperity concept and accounted for surface roughness on all relevant length scales. This method accounted for the long-range elastic coupling between asperity contact regions, unlike the Greenwood and Williamson model (1966).

Further enhancements were made to these models by applying fractal geometry to the analysis (Bhushan and Majumdar, 1992; Persson and Tosatti, 2001). Other work that followed involved asperity interactions (Zhao and Chang, 2000), asperity interaction in adhesive contact (Sahoo and Banerjee, 2005) and asperity interaction with substrate deformation effects for rough contacting hard film/soft substrate surfaces (Yeo et al., 2010). All multi-asperity contact theories are believed to hold only for small loads and contact areas (Carbone and Bottiglione, 2008).

It is widely recognised that adhesion also affects the deformation in contacting bodies. Several authors modelled the adhesive contact proposing different theories (Johnson, Kendall and Roberts, 1971; Derjaguin, Muller and Toporov, 1975), which lead to a conflict between the two (D. Tabor, 1977). Later Maugis parameters were able to quantify which contact model, Johnson-Kendall-Roberts (JKR) considering adhesion within the contact area or Derjaguin-Muller-Toporov (DMT) considering adhesion outside the contact area, represented more accurately the adhesive contacts between specific materials (D. Maugis, 2000; Maugis, 1992). These particular studies consider only smooth surfaces in contact. However, adhesion between solids is not usually observed due to surface roughness, in which the actual contact area has the effect of breaking down

the adhesion effect (Johnson, 1987, p.126). In this thesis, the effect of adhesion is ignored due to considering the effect of surface roughness.

2.6.2 Arithmetical Mean Height for 2D and 3D profiles

The simplest definition of surface roughness for a two-dimensional profile is the Arithmetical Mean Height 2D (Ra) which is defined as (Stachowiak and Batchelor, 2005, p.467):

$$Ra = \frac{1}{L} \int_L^0 |z| dx \quad (\text{Equation 2-29})$$

Where $|z|$ is the absolute value of the variation in the height of the asperities and L is the length considered in the x-direction, as shown in Figure 2-8 below.

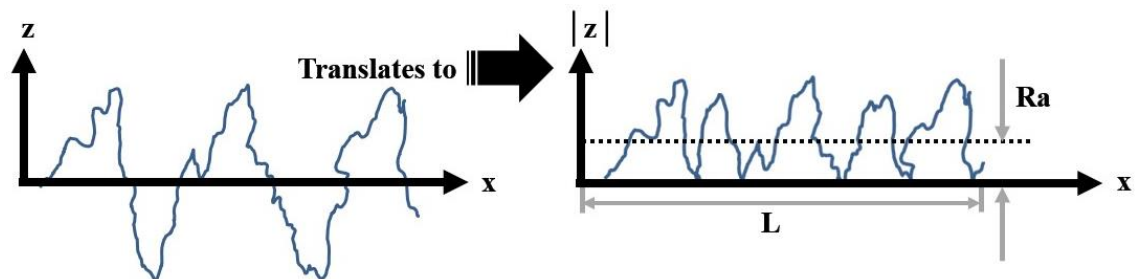


Figure 2-8 Absolute value of the variation in the height of the asperities

Similarly, for a three-dimensional profile, the Arithmetical Mean Height 3D (Sa) is defined as:

$$Sa = \frac{1}{A} \iint_A |Z(x,y)| dx dy$$

Where A is the area of the surface analysed and $|Z(x,y)|$ is the absolute value of the variation in the height of the asperities at x and y coordinates.

2.7 Summary

A detailed literature review of nanoindentation instrumentation and previous methodologies have been presented along with a review of the factors affecting the accuracy/reliability of the measured properties. The application of nanoindentation on testing viscous/polymeric materials has also been reviewed. The main focus being on the unloading and the hold time methodologies. Furthermore, the effects of surface roughness in indentations testing were described with an evaluation of the modelling techniques for, rough surface and adhesion, contact problems.

Before any experimentation, modelling or interpretation of the nanoindentation results, the materials, either bulk or coatings/substrate, need a detailed qualitative/quantitative assessment and will be addressed next.

Chapter 3

TEST MATERIALS AND QUALITATIVE/QUANTITATIVE ASSESSMENT

3.1 Introduction

In this chapter, the specifications of all the materials tested and other techniques for their qualitative/quantitative assessment are detailed, along with the assessments. For the coated samples, PET and PEN polymers were used as substrates, and thus, a review on the factors affecting their mechanical behaviour is also given. The X-ray diffraction (XRD) technique is described, and initial experiments conducted on these polymers to examine the machine/test variables are detailed. A methodology using the XRD technique to monitor the ageing of these polymers is presented.

For the qualitative/quantitative assessment of the coatings XRD, High Resolution Scanning Electron Microscopy (HSEM) and White Light Interferometry (WLI) techniques were used. The assessment included verifying coating structure and its quality. The thickness of the coatings and associated surface topography was also examined. A brief background is given for the coating materials used aimed to relate coating structural features to the mechanical properties and any implications to application. For bulk materials, the tensile technique and standards are described as it is later used to validate the nanoindentation results.

3.2 Viscous/polymeric materials used in this study

Several bulk viscous/polymeric materials were used in the thesis which included seven thermoplastics such as high-density Polyethylene (HDPE), low-density Polyethylene (LDPE), Polystyrene (STYRONTM 678E), Acrylic (Plexiglass® 8N), Nylon (Polyamide

66), Polyethylene Terephthalate (PET) and Polyethylene Naphthalate (PEN), and two Neoprene and Nitrile Rubbers (for specifications see Appendix 2). PET and PEN were also used as a substrate for thin film systems. The main difference between PEN and PET is that PEN has an extra condensed aromatic ring (see Figure 3-1) which confers higher elastic modulus and improvements in strength, chemical and hydrolytic resistance, gaseous barrier, thermal and thermo-oxidative resistance and ultraviolet (UV) light barrier resistance (Tonelli, 2002). PEN is a more recently developed material has been studied less compared to PET. Most of the studies seem to suggest that they are very similar structurally (Lechat, Bunsell and Davies, 2010; Lechat et al., 2006) i.e. the morphologies are similar. Therefore, most of the background discussed will be on PET and equally applicable to PEN.

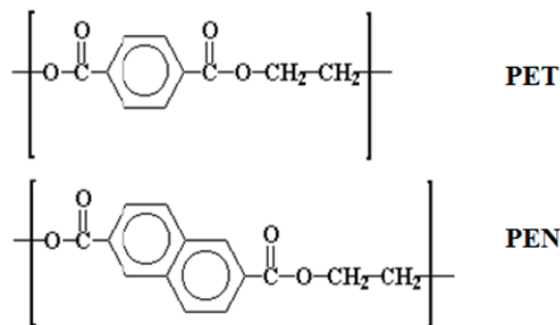


Figure 3-1 Molecular structures of PET and PEN

3.2.1 Factors affecting the mechanical properties of PET and PEN polymers

In amorphous PET primary crystallisation initially occurs where polycrystalline aggregates and grow, i.e. spherulites. Secondary crystallisation then occurs where intra-spherulitic lamellar stacks are formed, and within new crystals, nucleate and thicken (Flores, Ania and Baltá-Calleja, 2009). These spherulites contain many small crystallites when crystallized from an amorphous solid, rather than forming one large single crystal,

as shown in Figure 3-2. The degree of crystallinity can have a profound effect on the mechanical properties (Mo and Zhang, 1995), and a correlation to the elastic modulus in certain polymers has been observed (Bouaita et al., 2006). Also, for PET the hardness has shown to increase as a linear function in relation to the volume of the spherulites (Cruz et al., 1991). The different phases observed in PET such as nematic, smectic and triclinic can affect the overall hardness. An oriented mesophase has also been observed during the uniaxial deformation of PET above its glass transition temperature, i.e. hot drawing (G. E. Welsh, 2000).

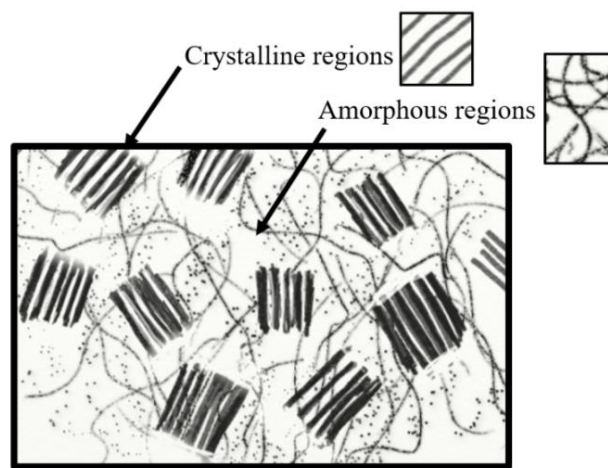


Figure 3-2 Microstructure of biaxial PET

The effect of ageing with different cooling rate from the melt on the hardness was demonstrated by Flores and Calleja (1998). It was noted after the melt was cooled roughly 100 days was needed for the hardness to level off to approximately a constant value. They used PET which was stored for three years. It is essential when devising experiment on these type of materials that this initial time elapses. It was suggested that different state of internal order developed with time and led to precursors of a final crystalline state. The smectic phase occurring due to ageing involves events towards thermodynamic equilibrium. These molecular mechanisms associated with ageing are still a matter of

debate. In their work, the visco-plastic flow of cold-drawn PET, that changes with crystal thickness, was also shown. The creep behaviour of the smectic phase lies in between that of the glassy material and the triclinic structure; the finding seems to suggest that the visco-plastic flow diminishes with increasing structural order of the material and supports the perception of the smectic-like phase being a precursor state of crystallization. It is therefore essential for experimental purposes the ageing effect is eliminated, i.e. the samples are stable.

The amount of crystallinity dictates the mechanical behaviour and can be quantified. Differential Scanning Calorimetry (DSC) a thermo-analytical technique has been used to measure % Crystallinity (Kong and Hay, 2002). However, this relates to how much phase is crystallised during a heat process and is not the state which the material exists at room temperature. As the DSC heat process itself changes the % Crystallinity, it is better calculated using XRD by separating the peaks for all the phases and comparing their amounts, giving a snapshot of the state of a material at that time, thus a way to monitor the crystallinity of each phase with time.

3.2.2 The visco-elastic-plastic regime of polymers

The glass transition temperature (T_g) of PET and PEN are 80 °C and 120 °C respectively. For these polymers, the viscous behaviour present increases with increasing temperature, and on approaching T_g they become rubbery/leathery. With further increasing the temperature only viscous behaviour remains. Below T_g it is stated, the polymers are in the glassy regime with failure modes such as brittle fracture, shear yielding and crazing (Ashby and Jones, 2006, pp.270–278). As tests in this study were conducted near room temperature, the behaviour for these types of polymers is seen to exist within the glassy regime. The material response to deformation, within this glassy regime, is visco-elastic or visco-elastic-plastic depending on the loading conditions.

3.3 XRD diffraction

XRD is widely used for the identification of unknown crystalline materials, typically minerals and inorganic compounds; however, the technique has also been used for polymer materials (Karacan, 2006). The INEL EQUINOX 2000 X-ray diffractometer was used for characterisation, of PET and PEN polymers to examine ageing, and of the coatings. The diffractometer (schematic can be seen in Figure 3-3) is equipped with nickel-filtered CuK α radiation ($\lambda = 1.540 \text{ \AA}$) which continuously records the intensities of diffracted X-rays as the detector rotates through respective scattering angles.

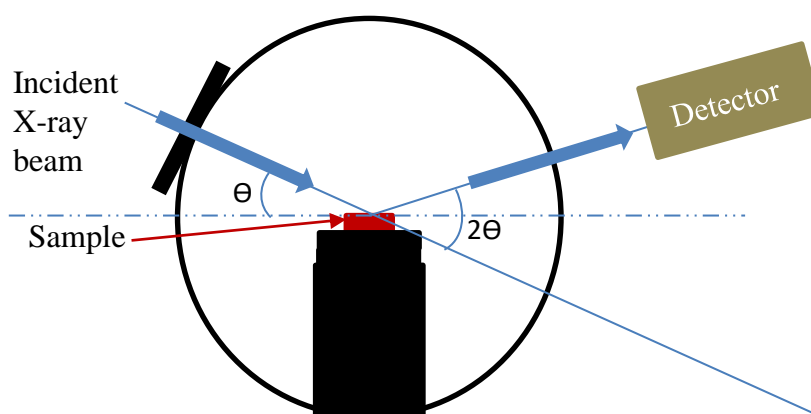


Figure 3-3 Schematic of an X-ray diffractometer

The output peaks of the x-ray diffraction pattern are directly related to the atomic distances for each phase, where the inter-plane distance d can be determined by using Bragg's law:

$$2d\sin\theta = n\lambda \quad \text{(Equation 3-1)}$$

Where λ is the wavelength of the x-ray, θ the scattering angle, and n an integer representing the order of the diffraction peak. A typical intensity plot for PET polymer can be seen in Figure 3-4.

3.3.1 Variability associated with XRD testing

The XRD testing equipment/methods employed must produce reliable results, accounting for all factors affecting the reliability. In order to assess the ageing behaviour of PET and

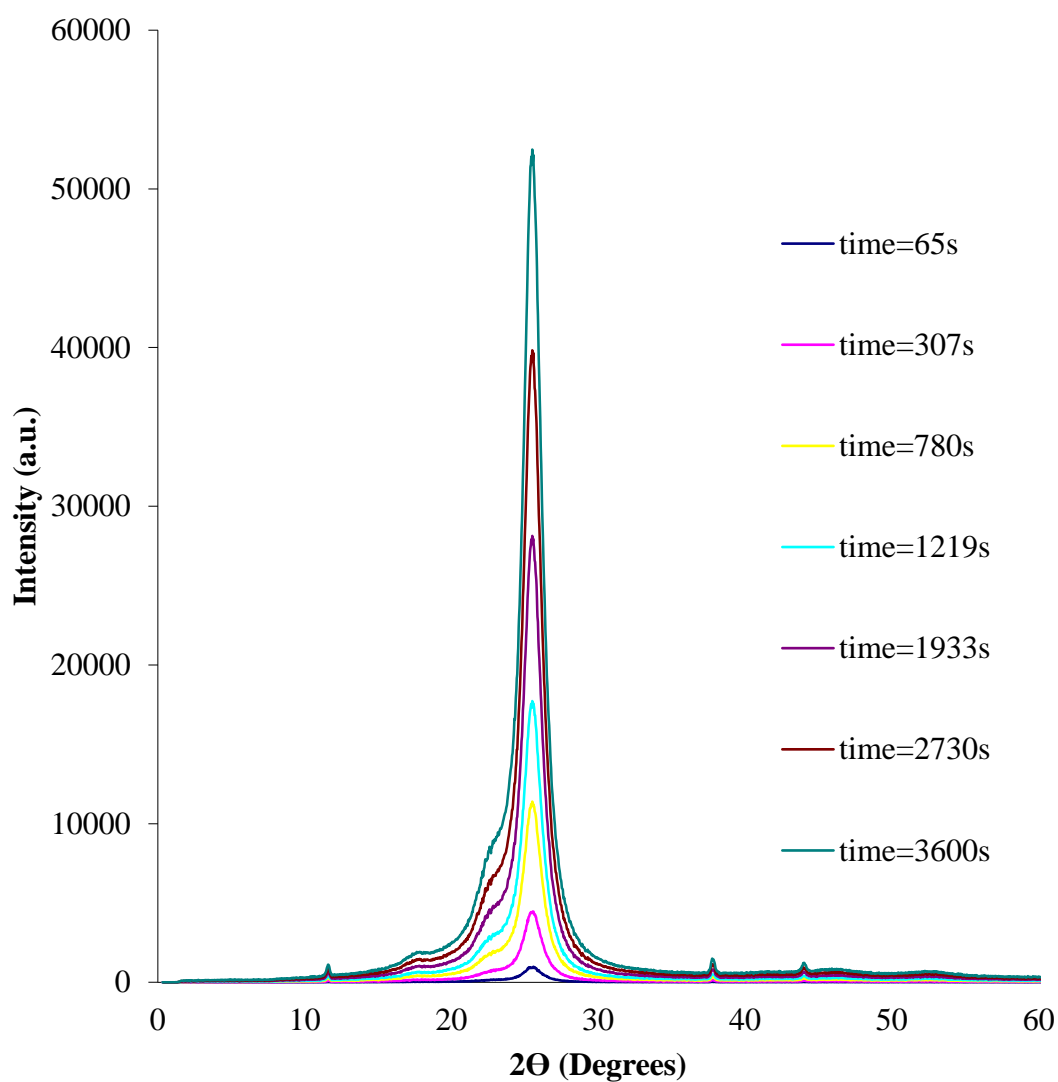


Figure 3-4 Effect of scan time on the intensity for PET

PEN accurately, initial experiments were conducted to examine the machine/test variables. Experimentation involved examining the effect of scan time (65 s to 3600 s) for PET polymer on the XRD intensities. The effect of machine/environmental factors on

the results was also examined; 3 tests were performed for PET alone at a scan time of 600 s. From Figure 3-4, it can be seen that with time, as more x-rays are deflected from the sample, the detection surges; therefore, the intensities of all the peaks increase. It can be seen that for a scan time of 600 s, all peaks are identifiable and no extra peaks further develop. The intensity is cumulative thus after 600 s any scan time should give the same percentage of crystallinity and lateral order factor. In further tests, a scan time of 600 s and above were used. Further testing was conducted to determine variation within the sample itself. This was demonstrated on three different PET samples taken from the same batch. The intensities can be seen in Figure 3-5. All three results were similar as the curves

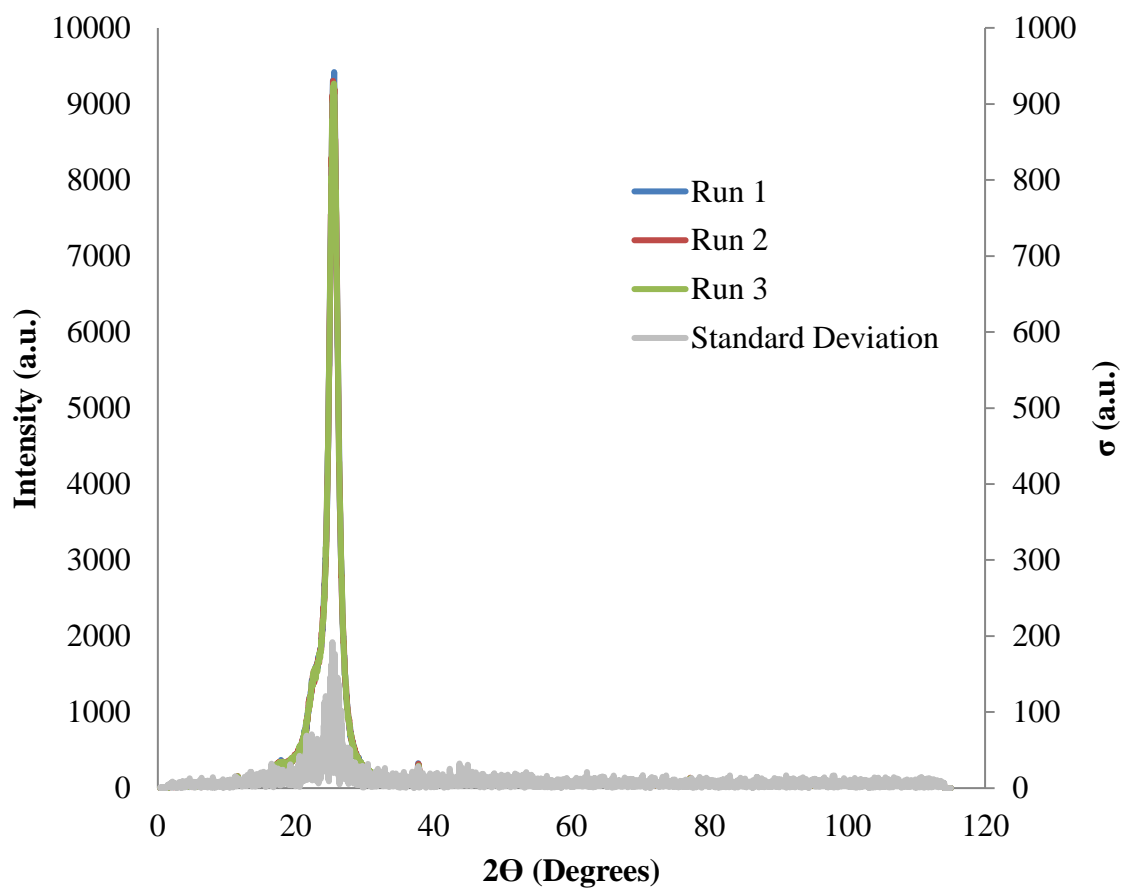


Figure 3-5 Effect of machine/environmental factors on the results for PET polymer at a scan time of 600s

overlap each other. However, by examining the σ , it is evident variation is present and exists mostly close to the peaks; which suggest the peak associated with the phase which is most abundant within the sample varies the most. The next section presents the XRD methodology for evaluating the ageing behaviour of PET and PEN polymers.

3.3.2 Methodology for monitoring the ageing

In the current study, it is necessary to establish the level of stability of PET and PEN. Many phases can be present in PET and PEN. Karacan (Karacan, 2006) identified five crystalline peaks for PEN which were considered by this author, 3 of α -phase with half-height width (which is twice the scattering angle, i.e. 2θ) of 1.26 deg, 2.06 deg and 2.10 deg, and 2 of β -phase with 2θ of 4.27 deg and 2.76 deg. Also, three crystalline peaks for PET with 2θ of 1.94 deg, 2.74 deg and 2.82 deg were considered, and a non-crystalline (NC) phase, i.e. amorphous. Information for each phase can be determined by using Peakfit software (PeakFit, 2016). The software allowed deconvolution of the XRD data to determine the individual peaks and area of all the phases by performing fits to (Equation 3-2) a Pearson 4 fitting procedure:

$$y = \frac{a_0 \left[1 + \frac{(x - \frac{a_2 a_4}{2a_3} - a_1)}{a_2^2} \right]^{-a_3} \exp \left[-a_4 \left(\tan^{-1} \left(\frac{(x - \frac{a_2 a_4}{2a_3} - a_1)}{a_2} \right) + \tan^{-1} \left(\frac{a_4}{2a_3} \right) \right) \right]}{\left[1 + \frac{a_4^2}{4a_3^2} \right]^{-a_3}} \quad \text{(Equation 3-2)}$$

Where a_0 , a_1 , a_2 , a_3 and a_4 are the fitting parameters after linear background adjustment. The mechanical properties of these polymers are affected by several factors such as chemical compositions with different amounts of additives, fillers and modifiers, along with the fabrication technique used, this can subsequently result in different material structures. When considering ageing of the samples, with same composition and fabrication method, not only crystallinity but crystal perfection, crystal size should be determined, as these two quantities can change even though the crystallinity does not

(Haji and Rahbar, 2012). Once peaks, relating to each phase, and areas are determined with the Peakfit software, the ageing related factors can be found and are presented below:

1. Using the Scherrer Equation (Patterson, 1939), the Apparent Crystal Size (ACS) can be calculated, from the 2θ of the crystalline peaks.

$$ACS = \frac{Ks * \lambda}{\beta \cos \theta} \quad \text{(Equation 3-3)}$$

where θ is the Bragg angle for the reflection concerned, λ is the wavelength of radiation (0.1542 nm), ACS is the mean length of the crystallite perpendicular to the planes (hkl), β is either the integral breadth or the breadth at half maximum intensity in radians determined for each peak relating to a particular phase, and Ks is a Scherrer constant.

2. The Lateral Order Factor (O.F.) can be related to crystallinity, perfection and size of crystallites (Bhat and Deshmukh, 2012; Manjunath, Venkataraman and Stephen, 1973) and is calculated by the equation

$$O. F. = 1 - RF \quad \text{(Equation 3-4)}$$

where RF is the resolution factor and is calculated with the equation

$$RF = \frac{m_1 + 2m_2 + m_3 \dots \dots + m_{n-1}}{h_1 + h_2 + h_3 \dots \dots + h_n} \quad \text{(Equation 3-5)}$$

where m_1, m_2, m_n are heights of minima and h_1, h_2, h_n are heights of maxima from the baseline determined from the intensity plot.

3. The % crystallinity is calculated using the equation:

$$\% \text{ Crystallinity} = \left[\frac{A_{\text{crystalline peaks}}}{A_{\text{Total}}} \right] \times 100 \quad \text{(Equation 3-6)}$$

Where $A_{\text{crystalline peaks}}$ is the total area for crystalline peaks determined for each phase and A_{Total} is the total area for all crystalline and non-crystalline peaks.

Each crystal phase is determined by deconvolution of the XRD data for each phase. The deconvoluted data with the area associated with each phase can be seen in Figure 3-6a & b for PET and PEN. It can be seen that more phases (than stated in section 3.2.1) have been identified to fully fit the data for both materials. To quantify the percentage crystallinity, the areas for these extra phases are insignificant and are eliminated from the

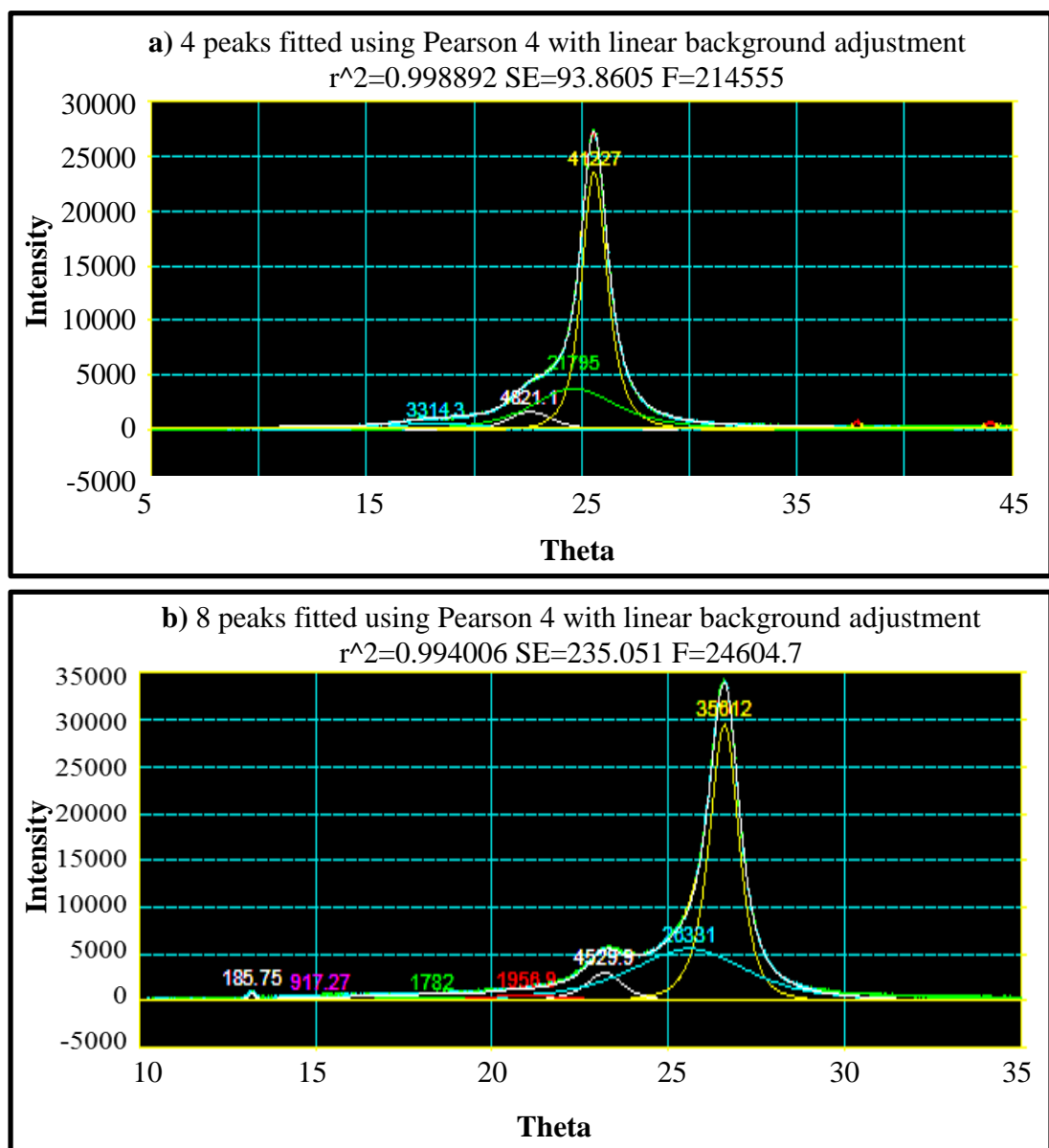


Figure 3-6 XRD-Intensity against theta for a) PET sample b) PEN sample

percentage crystallinity calculations. Apart from the percentage crystallinity, the integral breadth was used to determine the ACS. For one of the tests Table-3-1 highlights the parameters determined from the XRD data with the relevant phases for both PET and PEN. The ACS is determined from Scherrer (Equation 3-3) in which the sizes of the crystallites are related to the broadening of a peak in the diffraction pattern. The equation was established originally for metal and extended to ceramics, and valid for only small grain sizes. The peak broadening is related to other factors in various materials, such as

Table- 3-1 XRD data for PET and PEN

	Peak	Plane & Phase	Amplitude (intensity)	Center (Θ)	Area	% Crystallinity	Integral Breadth (Θ)	ACS
P E N	1	N/A	28.8	112.3	38.7	60.65	1.3	8.5
	2	(101) α	88.9	224.8	3770.5		42.4	1.1
	3	(020) β	142.1	286.1	3678.6		25.9	-0.3
	4	(110) β	272.7	401.4	2988.5		11.0	0.9
	5	(100) α	1369.9	1733.7	3780.5		2.8	3.0
	6	N/A	2344.7	4334.4	20013.0		8.5	1.7
	7	(-110) α	13999.4	13003.1	16690.6		1.2	-6.4
P E T	1	(010) ϵ	487.7	17.6	1655.8	61.47	3.4	6.3
	2	(-110) ϵ	1570.2	22.6	3527.8		2.2	-4.2
	3	N/A	3419.3	24.3	26943.5		7.9	1.5
	4	(100) ϵ	19461.7	25.5	37809.7		1.9	4.2

dislocations, stacking faults, micro-stresses, twinning, grain boundaries, sub-boundaries, coherency strain etc (Singh, 2005). Apart from this, the applicability to polymers can be questionable as the crystallites emerge from the centre outwards where the structure cannot be compared to metals and ceramics. In Table-3-1, some negative ACS values were found reflecting the limited validity of the method for polymers. For the percentage crystallinity, this study is comparative over time, and the same procedure is used; thus, the methodology is considered applicable and accurate. Another parameter used for ageing measurements was the lateral order factor.

Figure 3-7 shows the determined m and h intensities/theta values for a particular test on

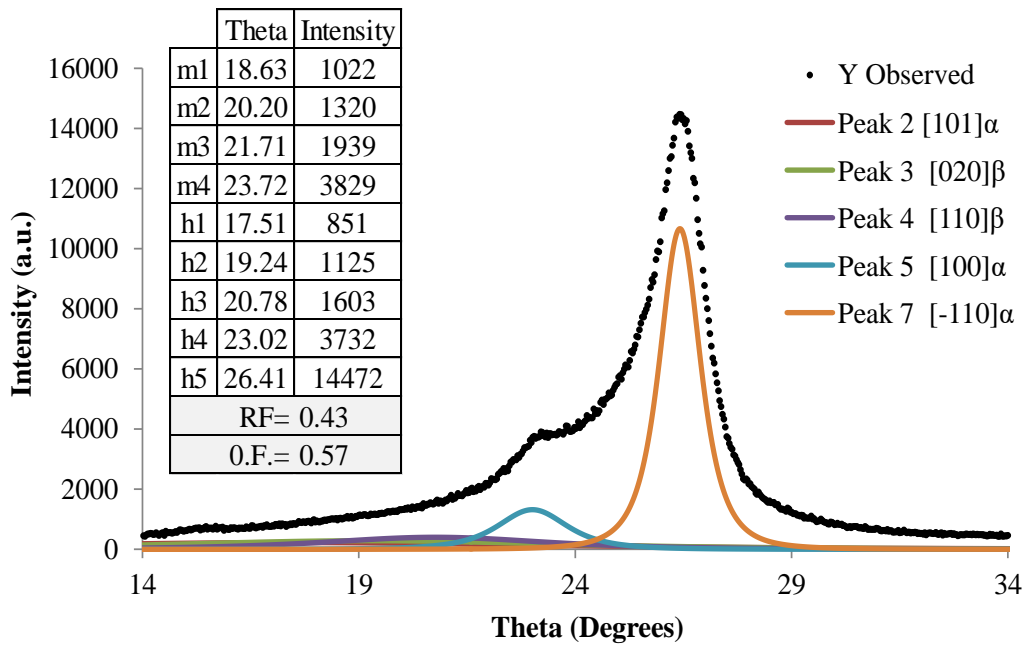


Figure 3-7 XRD data and parameter values for determining Lateral order factor for PEN

PEN. These maxima and minima were estimated qualitatively, adding variation associated with their selection, which is inherited in the OF calculations.

Thus, for these polymers, all of these above parameters can be estimated over time to give an indication of the ageing, and as the ageing process affects the mechanical properties nanoindentation hardness tests can be used to validate the results.

3.4 Coatings specifications

The coated samples were prepared by Magnetron Sputtering PVD techniques (Mattox, 2014). The TiN and TiO₂ coatings were deposited in a steel chamber using Pulsed Magnetron Sputtering shown in Figure 3-8 at the Dalton Research Institute, Manchester Metropolitan University and the AZO coatings were deposited and supplied by Teer coating Ltd. For deposition, four different substrates, namely PET, PEN, 316L grade Steel and Silicon wafer were used each with three different coatings TiN, TiO₂ and AZO.

Material specifications are highlighted in Table- 3-2. The 316L grade Steel and Silicon

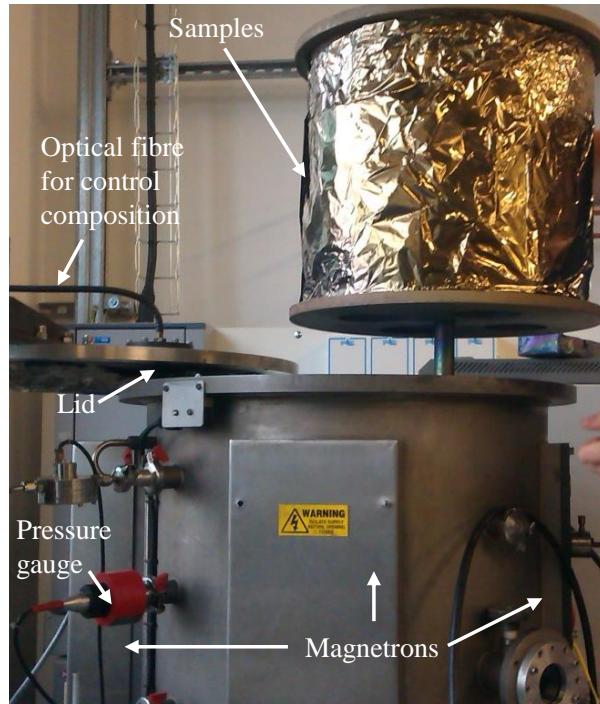


Figure 3-8 Pulse magnetron sputtering equipment

Table- 3-2 Manufacturers specifications for coating and substrate materials

	Substrates			
	Viscous		Non viscous	
	PET	PEN	316L grade Steel	Silicon wafer
Thickness (mm)	0.18	0.18	3.0	3.0
Supplier	Kolon industries Ltd	DuPontTeijinFilms	Dalton Research Institute, Manchester Metropolitan University	
Name	Astroll®	Teonex®	n/a	n/a
Code	CD105	Q65F&FA	n/a	n/a

	Coatings		
	TiN	TiO ₂	AZO
Thickness (nm)	150, 100 & 20	150, 100 & 20	150, 100 & 20
Supplier	Dalton Research Institute, Manchester Metropolitan University		Teer coating Ltd

wafers were adopted so that a contrasting comparison could be made to the highly compliant substrates.

3.4.1 TiN and TiO₂ deposition conditions

For TiN and TiO₂ no prior substrate cleaning was performed to avoid vapour formation to cause blistering during deposition. Neither the bias was initiated throughout the run so as to avoid the substrates from heating up to the point of damage. Also, the addition of Oxygen and Nitrogen were determined by monitoring the Optical emissions line and working at 20 % and 50 % for the full metal signal. Ar Pressure (from the baratron) was set at 1.00 mTorr. The MDX Pinnacle plus 500 W power supply was used with 100 kHz pulse DC and 50 % duty (5us off time). Current and voltage for TiO₂ coatings were 232 V, 2.15 A and for TiN 218 V, 2.30 A whereas current and voltage for TiN and TiO₂ on the Si wafer and glass were 370 V and 4.00 A (Power supply setpoint was 1.5 kW) respectively.

3.5 Qualitative/quantitative assessment all tested coatings

The structure/morphologies of these coating is unique to composition, the deposition technique/conditions, the arrangement taken by the atoms, i.e. stoichiometry, porosity and the surface profile (Mattox, 1998, p.585), which results in distinct mechanical properties. This can be also due to the thickness of the coating itself (Kelly et al., 2007; Ohring, 2001). Coatings usually have reduced density than in the bulk form (Ohring, 2001, p.508) which relates to the deposited structure. A less than fully-dense material will have voids and be off-stoichiometric. In this section HSEM, WLI and XRD are used for the qualitative/quantitative assessment for TiN, TiO₂ and AZO coatings.

3.5.1 High Resolution Scanning Electron Microscopy (HSEM)

The coating morphology and structure was examined using a Zeiss Supra40VP Field Emission Gun HSEM at Manchester Metropolitan University (MMU). All the coatings were examined with magnifications ranging x 15 to x 200000. Under high vacuum, the surface was scanned with high-energy beams of electrons in a raster scan pattern. Detectors collected the deflected secondary electrons, back-scattered electrons (BSE), characteristic X-rays and light (cathodoluminescence) to gain detailed information about the sample's surface topography and composition. The information was translated using software to get a detail mapping of the surface, the data from sample is then stored as images.

An appropriate size sample was needed to fit in the specimen chamber. 1 cm² samples were prepared for scanning and could be tilted to an angle of 45° within the chamber. Backscattered electrons were used for imaging, by examining atomic number contrast, for either conductive or nonconductive specimens. Whereas for secondary electron imaging, to observe morphology, the specimens had to be grounded at the surface to prevent the surge of electrostatic charge. In this mode, nonconductive samples are typically coated with either a thin film of carbon, gold or other conductive material. Thus, secondary electron imaging mode was performed after cleaning all specimens with a jet of air. TiN and TiO₂ were carbon coated for conductivity. AZO didn't need any coating as it is already conductive.

For the 0.8 μm thick TiN coating a compacted columnar structure was seen (see Appendix 3.1.1) with no cracking. This is a porous zone 1 coating. Previously for similar TiN coatings the structure, hardness and adhesion of thin coatings have been examined (Bull, 2019; Dobrzanski, Polok and Adamiak, 2005; Dobrzanski and Adamiak, 2003; Gerth and Wiklund, 2008; Gunda et al., 2005; Skoric et al., 2004). The coating morphologies in

these studies were related to the well-known structure zone model (Thornton, 1986) where coatings show a similar compacted columnar structure as the coating studied in this thesis. The surface morphology is a resultant of this columnar structure, where the columns extend out of the surface giving a unique profile.

TiO₂ typically comes in different forms, Rutile, Anatase and Brookite. Rutile is the equilibrium phase present at all temperatures. Both the metastable Anatase and Brookite phases convert to Rutile upon heating. In addition to these three phases, five high pressure forms has been reported (Hanaor and Sorrell, 2011). It is only Rutile and Anatase which play any role in the applications of TiO₂. The HSEM revealed a dense structure with no evidence of any porosity or cracking noticeable even at the highest resolution for the 1.2 µm thick TiO₂ coating (see Appendix 3.1.2). Surface pits were seen roughly 0.5 µm across; these should have a detrimental effect on the fracture behaviour of the coating since surface defects are the nucleation site for new cracks.

The dense AZO coating surface was smooth showing hardly any defects, cracking or any porosity (see Appendix 3.1.3). Many studies have previously been done to distinguish the structure of these thin films (Chang, Shen and Hon, 2003; Nomoto et al., 2011; Park, Ma and Kim, 1997). The films have been shown to be strongly oriented perpendicular to the substrate surface (c-axis orientation), i.e. the AZO (002) plane is parallel to the substrate and exhibits a polycrystalline hexagonal wurtzite structure.

3.5.2 White Light Interferometry (WLI)

WLI is a powerful technique for non-contact surface topography measurement. A beam from a short-coherent light source is divided into two paths then directed onto a sample and a reference mirror. When the beams are reflected back to the splitter, they interfere with each other leading to interference contrast fringes. The optical path difference is

varied during the measurement by changing the distance to the sample. A camera takes images at different distances, and a height profile can be calculated for the surface. The optical instrument is capable of 3D surface profilometry and surface roughness characterisation at high vertical and moderate lateral resolution. Features include wide view size with adjustable field of view and transparent film profiling, where thickness distribution of sample covered with transparent film can be measured.

In this thesis assumptions regarding the thickness of the coatings were made as set levels, i.e. 20 nm, 100 nm and 150 nm as they were needed to be specified for the DOE's. Start after the deposition of the thin-films the thicknesses were determined using a Dektak IID Veeco stylus profilometer at MMU (refer to Table- 3-3). During this deposition procedure, Kapton tape was placed on the samples, which was removed afterwards to

Table- 3-3 Coating thickness using different techniques

		Measuring techniques			
		White light interferometry			Stylus profilometer
		Mean coating height (nm)	Mean substrate height (nm)	Thickness (nm)	Approximate thickness at deposition (nm)
Coating & Levels	20nm TiN	13	-11	24	40
	100nm TiN	39	-48	87	107
	150nm TiN	82	-73	155	153
	200nm TiN	114	-111	226	200
	20nm TiO ₂	1	-12	14	40
	100nm TiO ₂			98	
	150nm TiO ₂	193	-7	199	150
	20nm AZO			24	
	100nm AZO			102	
	150nm AZO			123	

give a step height. This step height was measured for four different points on each sample and then averaged. WLI was used to confirm the results using an Omniscan microxam 5000B, 3D ADE Phase Shift interface contrast profiler. The exact coating thicknesses for TiN, TiO₂ and AZO were determined, also shown in Table- 3-3. These measurements were performed on the silicon sample assuming the deposition on all other samples were same. The thicknesses determined were used to set the levels for all the coating. However, the approximated thickness values determined initially after deposition were not similar to the ones determined by WLI. This is due to the phase differences of the substrate and coating when determining the step change with WLI, and the error can be an order of 10 nm to 30 nm. Even with this uncertainty, the levels for the coating thicknesses were set for the DOE's. Therefore, for all three coatings, three levels were chosen at 20 nm, 100 nm and 150 nm. The exact thickness values of each coating differed slightly from these set levels; in reality, this is unavoidable due to the impracticalities of depositing precise thicknesses. However, exact values were used to determine substrate independent coating properties. It should be noted that when simulating and comparing to experimental data the true thickness of the coating has an effect. When investigating thickness related effects, for each DOE, the approximated levels are just an indication of the true values.

3.5.3 XRD of the coatings

XRD (refer to section 3.3) was performed on all the coated samples. Coated PEN and PET samples were mounted in order to characterise the coatings; the scattering intensities were recorded every 0.031 ° in the range of $2\theta = 10-35^\circ$. For TiN the test run was 36 hrs, for TiO₂ 22 hrs, and for AZO 3 hrs respectively. For TiN the three different coating thickness levels were examined using XRD with a comparison to the PET substrate (see Figure 3-9a). Two particular phases are quite distinct, with (111) and (220) crystallographic planes. As the coating thickness increases the intensity of these phases

also increase as expected due to the amount of phase present. Tests were repeated for TiO₂ and AZO. TiO₂ displayed two phases, Rutile and Anatase (see Figure 3-9b). Even though Rutile is the equilibrium phase present at all temperatures Anatase is more abundant. With increasing thickness, the intensity again increases. For AZO only the 150 nm coating was examined and compared to the PET substrate. A number of Zinc Oxide (ZnO) phase were present in the coating along with the alumina phases as shown in Figure 3-9c.

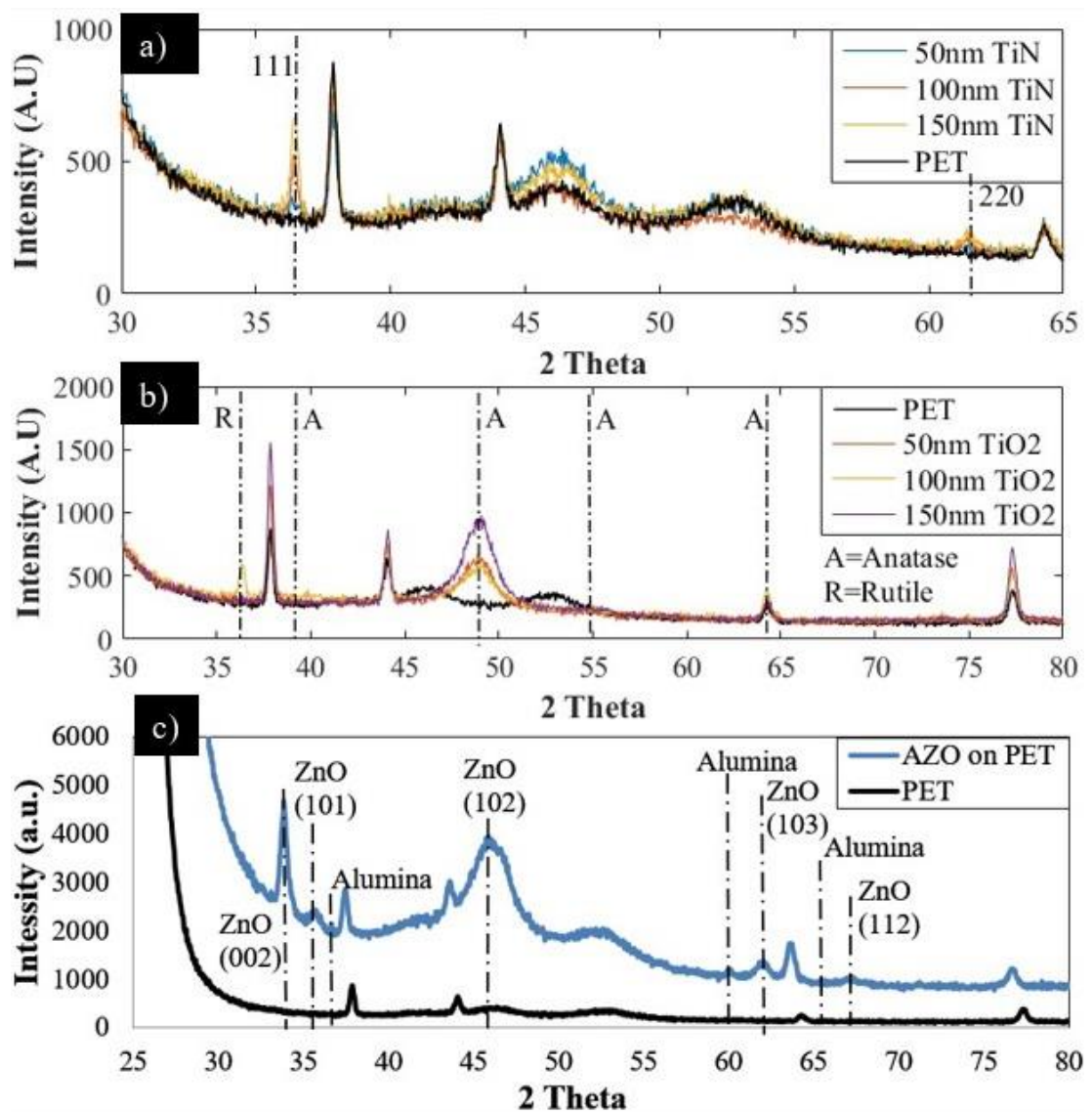


Figure 3-9 XRD intensity versus 2 Theta plots using 30 mins scan time for 150nm thick coatings on PET substrate a) TiN, b) TiO₂ and c) AZO

3.5.4 Topography for the coatings

All three coating although dense have different structures with associated phases as detected by XRD and different morphologies. Additionally, these surface morphologies can change with thickness of the coatings consequently changing the surface topography. It was assumed the three coatings would takes the profile of the substrate surface after deposition however to validate this hypothesis the profile of TiN and TiO₂ coatings at different thicknesses were determined using WLI. TiN and TiO₂ at all thicknesses of the coatings and substrates combinations were measured, i.e. two substrates and two thicknesses. From the results, a typical surface profile of 200 nm thick TiN coating is shown in Figure 3-10. Also, plots for Sa values against the coating thickness for each coating-substrate system can be seen in Figure 3-11. It is clear that the surface roughness indeed changes with the coating thickness and therefore would not retain the profile of the substrate. The hypothesis stated might be true for very thin coatings, however, from

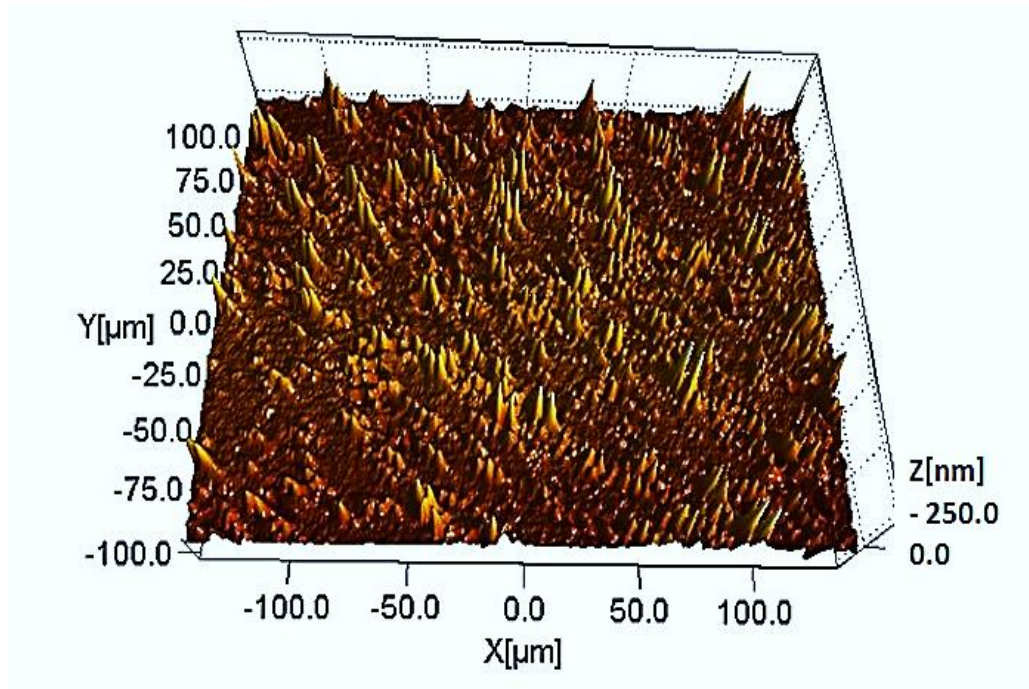


Figure 3-10 Surface profile of 200nm thick TiN coating on PET substrate determined by white light interferometry

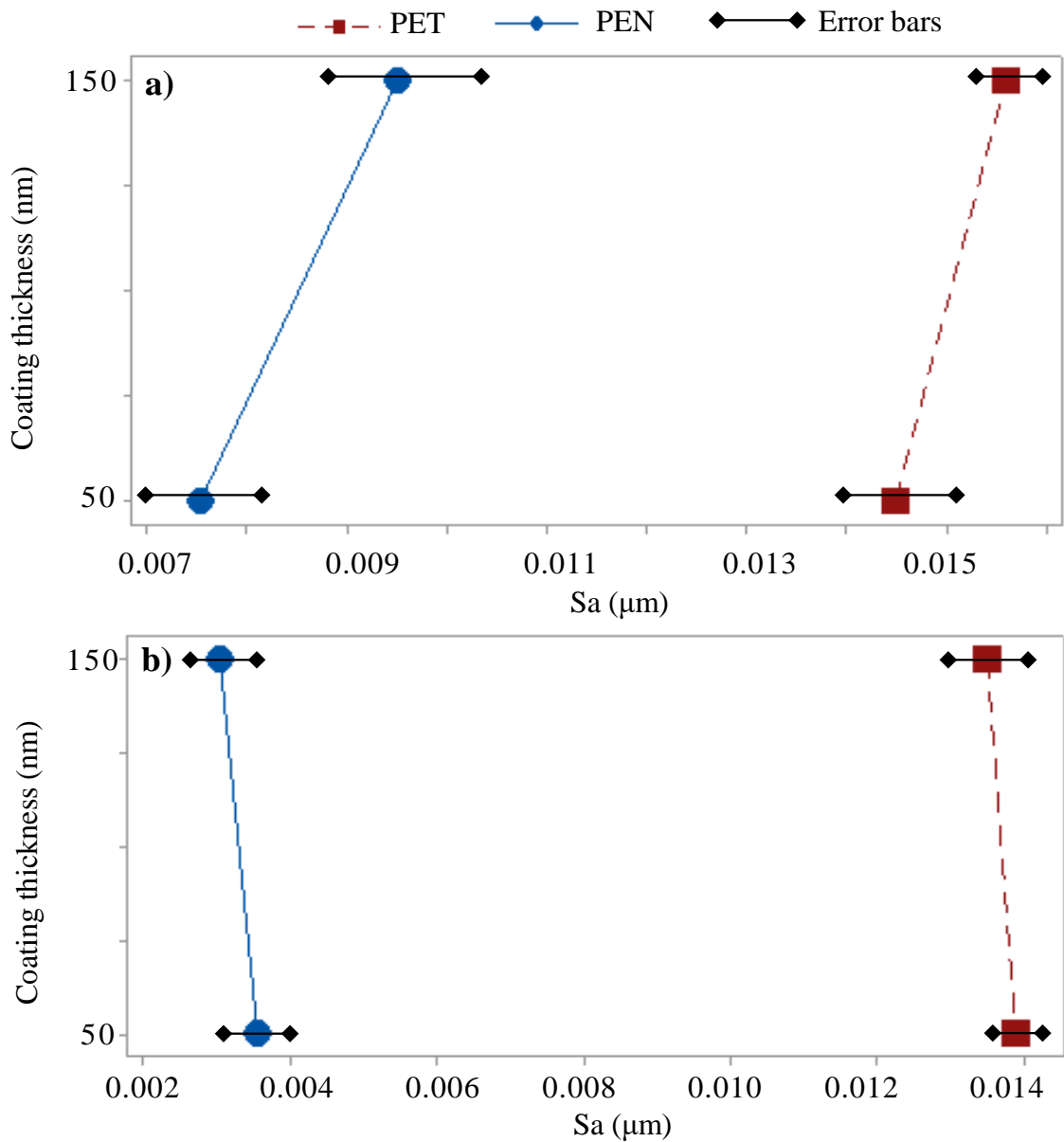


Figure 3-11 Scatterplot of Coating thickness vs Surface roughness (S_a) for a) TiN on PET and PEN & b) TiO₂ on PET and PEN

the plot, it is clear that the surface roughness increases with coating thickness for TiN and vice versa for TiO₂ on both PET & PEN substrates. Thus, when analysing the behaviour of these coating/substrate systems, the surface roughness cannot be said to be constant and surely has an implication when characterising the coating at low loads.

3.5.5 Coating fracture

All three coatings studied showed no cracking when observed at the highest magnification possible using HSEM, however cracking could still be present. To know if cracks are present magnitude of fracture events can be detected by acoustic emission methods during an indentation test (Volinsky and Gerberich, 1999). In nanoindentation the coating/substrate systems typically have three different modes of cracking. These are radial cracking, spallation caused by circumferential cracks, and channel cracking. After, radial cracking, delamination and buckling, spallation caused by circumferential cracks that describes the peeling off the coating (delamination) from around the indentation. As a result of circumferential cracking and spallation, a plateau is observed on the load-displacement curve, the load at which this occurs can be used for fracture toughness calculations. Li et al. (1997) describes this failure by a three steps fracturing process (shown in Figure 3-12). In step one high stress in the contact area causes a circumferential crack to form around the indenter, through the thickness of the coating. In step two, due to high lateral pressure delamination and buckling occurs around the contact area at the coating/substrate interface. In step three, a second circumferential crack forms through the thickness of the coating, and spallation occurs due to the high bending stresses at the edges of the buckled thin coating.

3.5.6 Residual stresses within coatings

The residual stresses are important for a complete understanding of the coating's mechanical behaviour. The stress generation during deposition within the coatings is a complex process varying with deposition techniques and growth conditions. The total internal stress established within these coatings is from the addition of extrinsic/thermal and intrinsic stresses. There are different techniques available for measuring residual

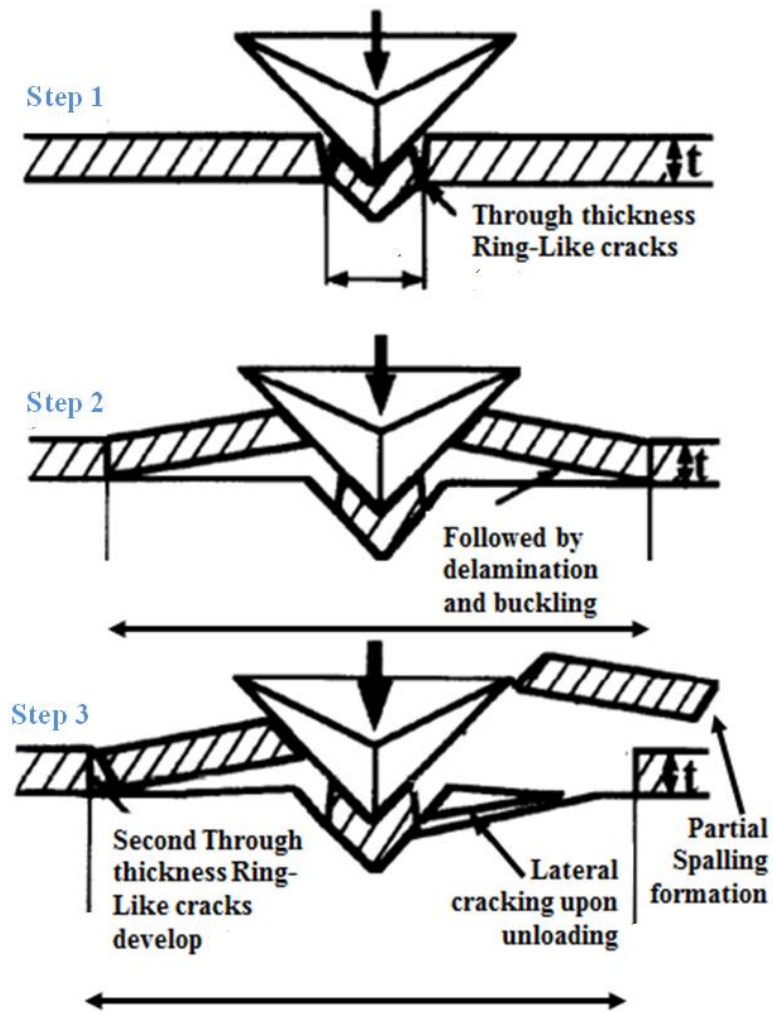


Figure 3-12 Fracture mechanisms during Nanoindentation at Nano scale, adapted from (Li, Diao & Bhushan 1997)

stresses (Chang, Shen and Hon, 2003; Michotte and Proost, 2011; Suresh and Giannakopoulos, 1998; Yin Zhang and Ya-pu Zhao, 2006) however, the most common technique is XRD utilizing the $\sin^2 \psi$ method, where the stresses are not determined directly but instead calculated using the elasticity theory. The stresses can also vary with film thickness of the coating due to the effect of intrinsic stress gradients acting over the film's thickness (Machunze and Janssen, 2008). High residual stresses can cause detachment of the coating from the substrate during deposition and also during indentation. Typical compressive stresses are favoured as they negate the induced contact

stresses and thus prolong lifetime in service (Waters, 2019). The mechanical response is not just dictated by coating microstructure but also due to these stresses.

3.6 Tensile testing

A tensile machine is a device allowing a tensile force to be applied uniaxially to a sample, ramped at a set rate, and the displacement continuously monitored. Depending on the sample material, the technique has many standards. After testing load-displacement or stress-strain plots are produced, giving a unique profile of the material tested from which material properties can be obtained such as ultimate strength, % elongation, yield strength, elastic modulus etc. For the purpose of this thesis, only the procedure to obtain the elastic modulus is discussed. The tensile standards, for polymers (BS EN ISO 527-2, 2012), for metallics (ISO 6892-1, 2016) and for rubbers (ISO 37, 2017), were adopted. Schematics of the samples are highlighted in Figure 3-13. The gauge lengths are also quantified on the figure as 80 mm, 90 mm and 33 mm for each material type respectively. It is important to only measure the extension of the gauge length otherwise the compliance of the machine and the extension near the gripping lead to errors.

The extensometers have various classifications (ASTM E28 Committee, 2016). In accordance with the rubber standard, the extensometer used was type D. However, it does not stipulate if it is to be used. The nominal rate is 500 mm/min. Any test piece breaking outside the test length (33 mm on Figure 3-13c) is discarded and a repeat test conducted on an additional test piece. The standard for plastics stipulates contact extensometers to comply with ISO 9513:1999, a class 1 type and for measurement of the tensile modulus (see ISO 527-1:2012, 3.9), the speed of testing is 1 mm/min. For metallics, the extensometer system was in accordance with ISO 9513, class 0,5 type and the test speed the same as for the plastics. For the metallics and plastics, the elastic modulus is to be computed by taking the tangent between 0.05% and 0.25% strains, however for rubbers

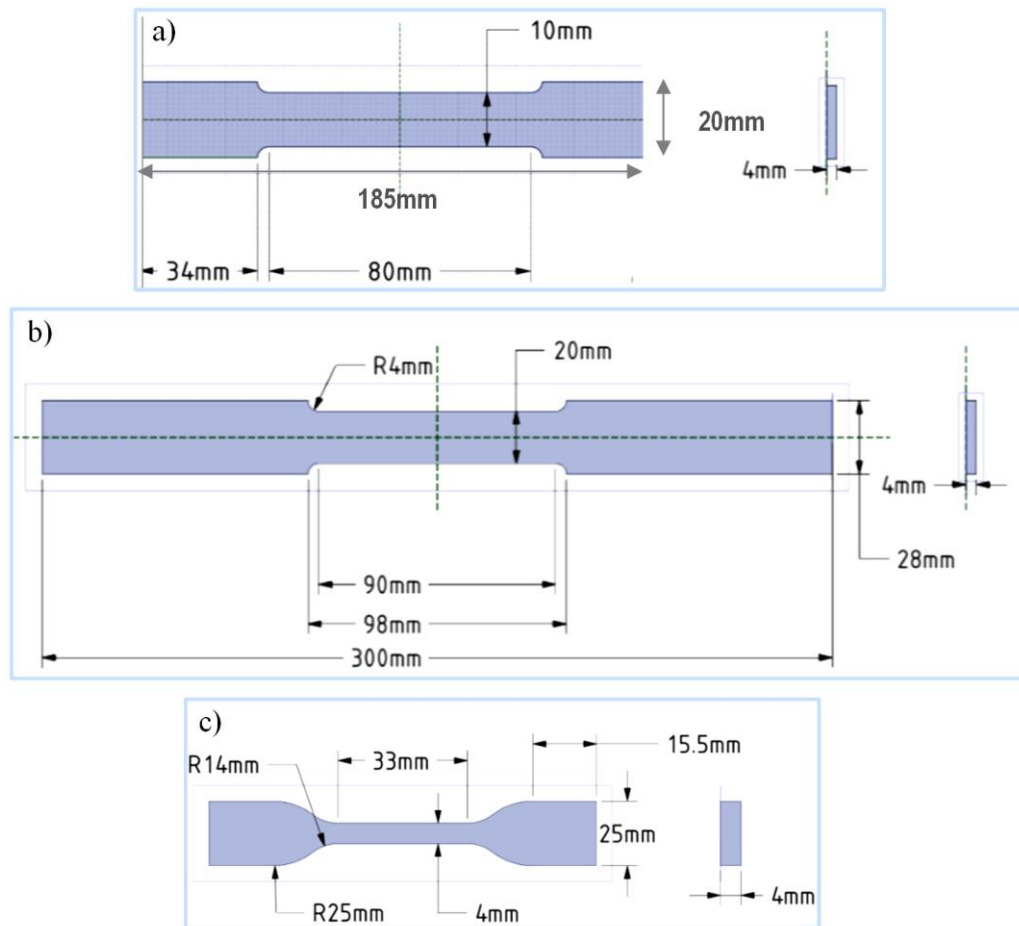


Figure 3-13 Sample dimensions a) For polymers reproduced from ISO 527-1:2012, b) For metallic materials reproduced from ISO 6892-1:2016 and c) For rubbers reproduced from ISO 37:2017

it is hard to identify an initial linear response as the tangent continually changes due to non-linear elasticity, so Secant modulus between 0% and 20% strains is considered, which is the slope of a line drawn from the origin of the stress-strain diagram and intersecting the curve at 20 % strain. The elastic modulus computed is averaged for all the samples with the standard deviation stated.

3.7 Summary

For nanoindentation characterisation, all materials and their specifications have been detailed, along with techniques used for their qualitative/quantitative assessment. For the

microstructural stability of PET and PEN, a methodology to monitor ageing was presented. The coatings were characterised, using WLI, XRD, and HSEM, determining all phases within each coating and satisfactory quality, i.e. thicknesses, surface roughness and integrity of each coating were identified. The tensile test for bulk materials was also described in order for the comparison to nanoindentation.

Previous methodologies, associated with nanoindentation characterisation, are not always accurate, especially for viscous/polymeric materials as it was described in section 2.4. This leads on to the next chapter, which details the nanoindentation methodologies developed by the author for characterising both viscous/polymeric materials, non-viscous/non-polymeric materials, which are also applicable at ultra-low loads.

Chapter 4

DEVELOPED NANOINDENTATION METHODOLOGIES

4.1 Introduction

In this chapter, nanoindentation unloading methodologies, used to derive the elastic modulus and hardness, as described in Chapter 2, have been adapted for both viscous/polymeric materials and the nanoscale. The overall methodology has several components, as shown in the flow diagram in Figure 4-1, each detailed in sequence through the chapter. However, first, the relevant experiments used to develop the methodologies are detailed. Subsequently, nanoindentation methodologies to correct the stiffness are described. As different types of materials show a spectrum of behaviour from fully elastic to viscous; the unloading curve is not understood to be fully elastic. Under this assumption, the viscous and plastic behaviours are used to determine the correct stiffness. Plastic depth corrections such as pile-up and sink-in are also considered, and a novel method to correct the plastic depth at various scales. Overall, these methodologies allow accurate calculations of the contact area (h_c) and stiffness (S) at any scale in order to determine mechanical properties such as the hardness and the elastic modulus. All these methodologies are new and have been published (UK Patent 1513480.2, 2015; UK Patent 1701591.8, 2017).

4.2 Experimentation

All experimental results/figures considered in this chapter are from two different DOE's. Experiment 4.1 considers the effect of visco-plasticity on the elastic modulus during unloading for both PET and PEN. Also, the time-dependent behaviour due to the hold

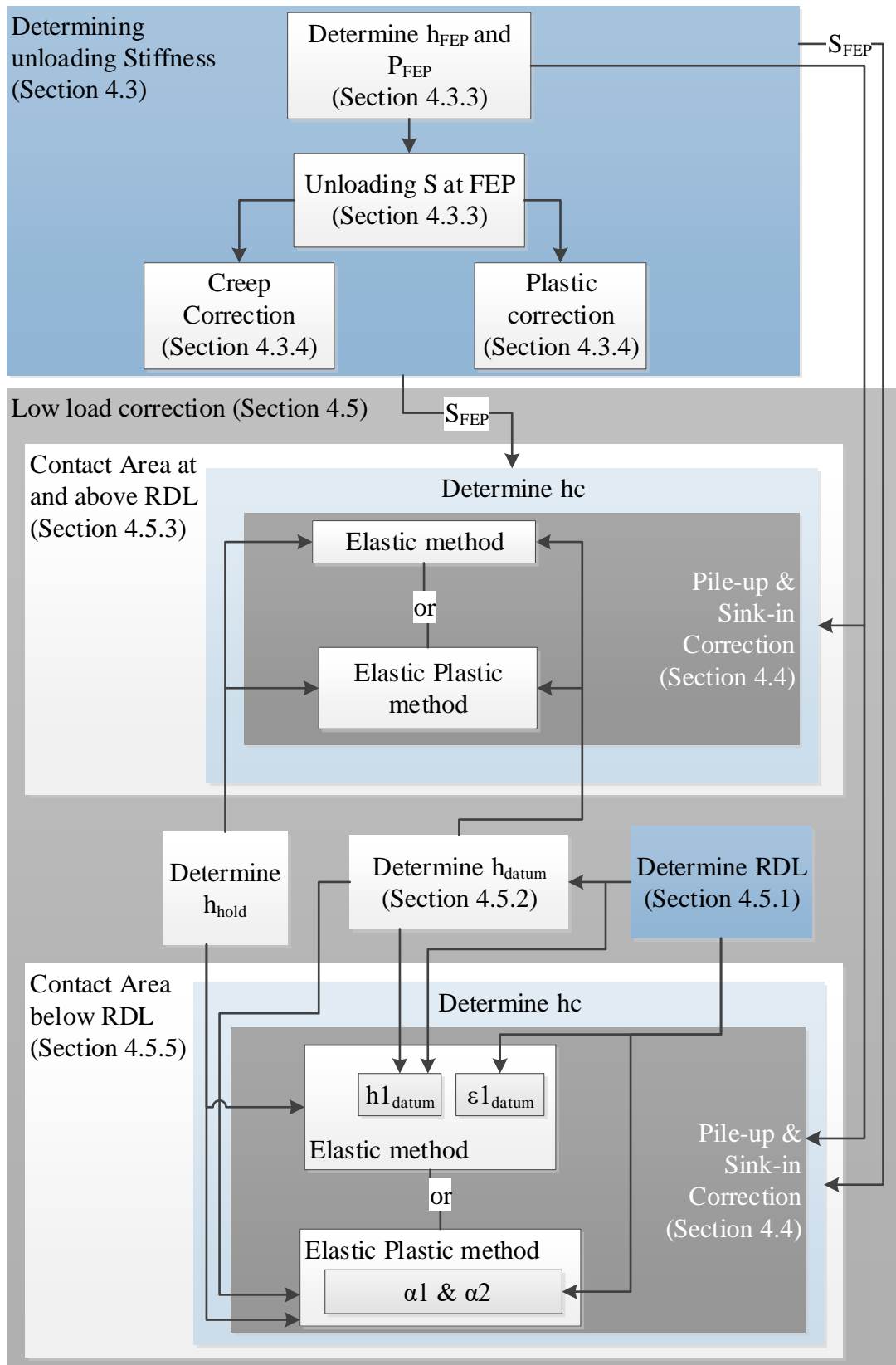


Figure 4-1 Flow chart of the developed nanoindentation methodology by the author

period was examined. A full factorial DOE was conducted for four different parameters, these were: load, load rate, unloading rate, and hold. The experimental details and values of the parameters are highlighted in Table- 4-1, and the run order can be seen in Appendix 4. Each indent for each array was repeated 10 times, and 60% of the unloading data was considered. Plastic correction and sink-in correction were applied. As displacements were above the RDL low load correction weren't needed.

Table- 4-1 Experimental details and parameter values for Experiment 4.1

Indenter	Thermal drift	Unloading rate (mN/s)	Substrate	Load (mN)	Load rate (mN/s)	Hold time (s)
Berkovich	Yes	0.1, 1, 2	PET, PEN	10, 20, 30, 40, 50, 60, 70, 80, 90,100	0.1, 1, 2	5, 20, 60

Experiment 4.2 was conducted to compare the measurement of elastic modulus and hardness using the different methodologies in determining the stiffness from the unloading curve, and also to compare different methods of calculating the plastic depth. Fourteen different materials were tested using the Micro Materials Nano Platform, the viscous polymers and rubbers have been already described in section 3.2. For the plastics, experiments were performed at a maximum load of 5 mN with a 5 s dwell period, load rate and unload rate being 0.1 mN/s. For the rubbers, experiments were performed at a maximum load of 2 mN with a 30 s dwell period, load rate and unload rate being 0.1 mN/s. For, the non-viscous materials: SiO₂, Aluminium, Brass, Copper, Stainless steel (316 2B grade), Mild steel, and Titanium (6al-4v Sheet Grade 5), the experiments were

performed at a maximum load of 200 mN with a 5 s dwell period, load rate and unload rate being 5 mN/s.

For all tests, a thermal drift correction was calculated using the post-indentation drift calibration data as described in section 2.2.2. To determine the stiffness at maximum load, 60% of the unloading data was selected. Each indent on each specimen was repeated 10 times according to the standard (ISO 14577-1, 2002–2015).

4.3 Nanoindentation methodologies for unloading stiffness

To develop the methodology, for determining material properties from the unloading data, the limitations for the Oliver and Pharr method (1992) with creep correction procedures (G. Feng, 2002) are examined. The results from these previous methods are only valid associated with the assumptions made, one particular assumption being that the initial unloading curve is fully elastic after multiple unloading cycles. However, different materials display a spectrum of viscous behaviour. This concept is utilised and the author claims that to compare results to tensile test data, the effects of actual local deformation should be eliminated because, in practice, a power law fit of the type in (Equation 2-4) for any materials may not exist, depending on the experimental conditions, at the very initial unloading. The standards (ISO 14577-1, 2002–2015) acknowledges this and 2nd order polynomial fitting is permitted to determine the stiffness and it also stipulates the fitting will not start at the top of the unloading curve. Figure 4-2 shows four different materials selected from Experiment 4.2 using monotonic loading. In Figure 4-2a a linear fit is appropriate for the elastic response of SiO₂ whereas in Figure 4-2b, the elastic-plastic response of Aluminium, at the onset of initial unloading the experimental deviate from power law fit, much more for the other two viscous materials. When it comes to examining viscous/polymeric materials, both the Oliver and Pharr method (1992) and with creep correction procedures (G. Feng, 2002), even under a multi-loading sequence,

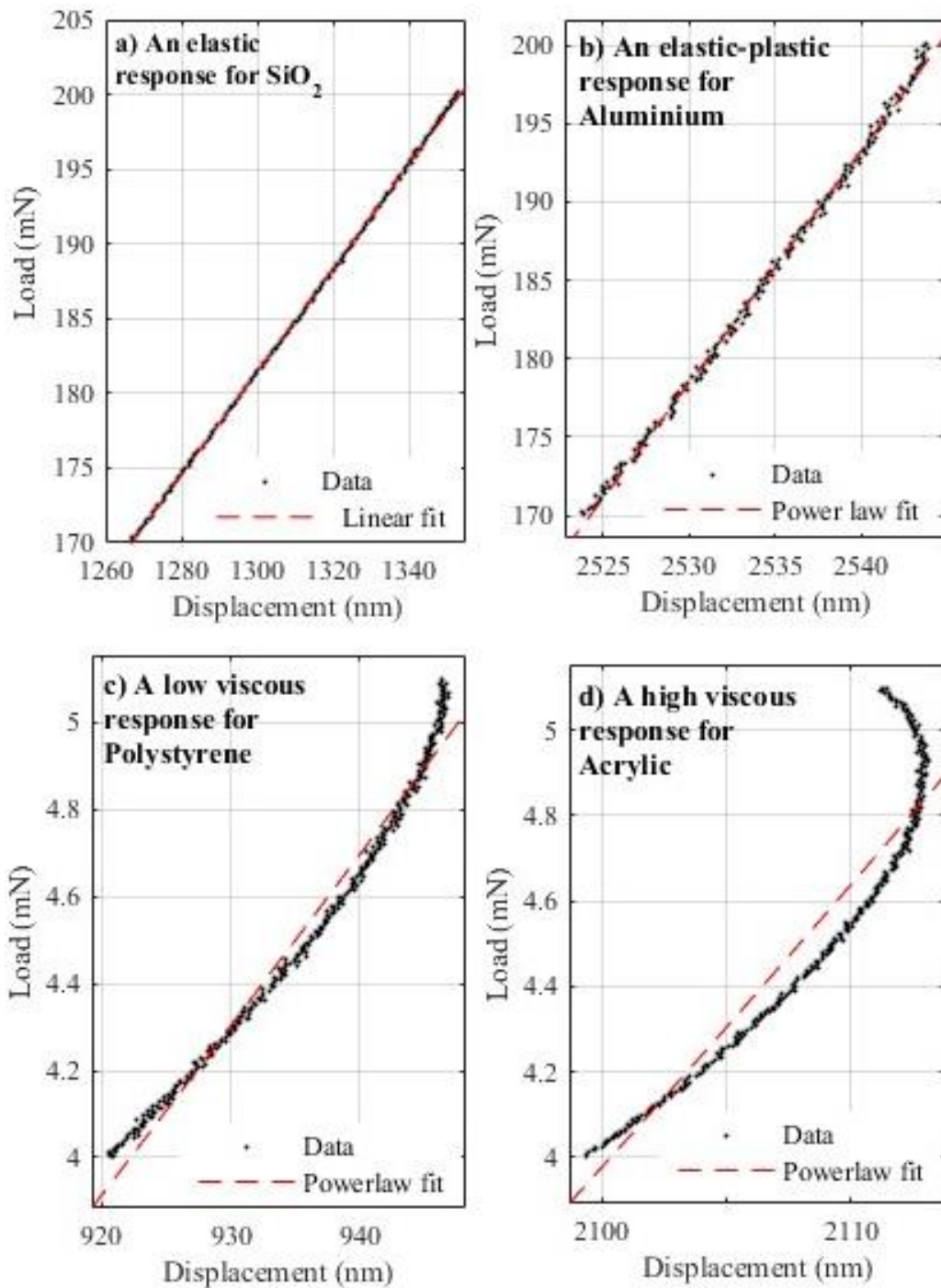


Figure 4-2 Typical nanoindentation unloading curves a) Elastic response of SiO₂ with linear fit b) Elastic-plastic response of Aluminium with power law fit c) Low viscous response of Polystyrene with power law fit, and d) High viscous response of Acrylic with power law fit

show an increase in the variability of the results if tested when a “nose out” is present. This is a direct consequence of non-equilibrium contact occurring between the sample and indenter, i.e. a changing contact area is present in the early stages of the unloading. Thus, this effect needs to be accounted for to acquire a pure elastic/viscoelastic response. By utilising a number of defined factors such as Viscofactor, Acceleration Factor and the Conforming Factor, which are descriptions of the viscous behaviour, the unloading curve is examined and the data disregarded until a “Full Elastic Point” (FEP), as shown in Figure 4-3b. The remaining data is then either a fully elastic or a viscoelastic response depending on the test sample. These two types of data can then be used to determine mechanical properties by traditional adapted means, even in a single loading-unloading

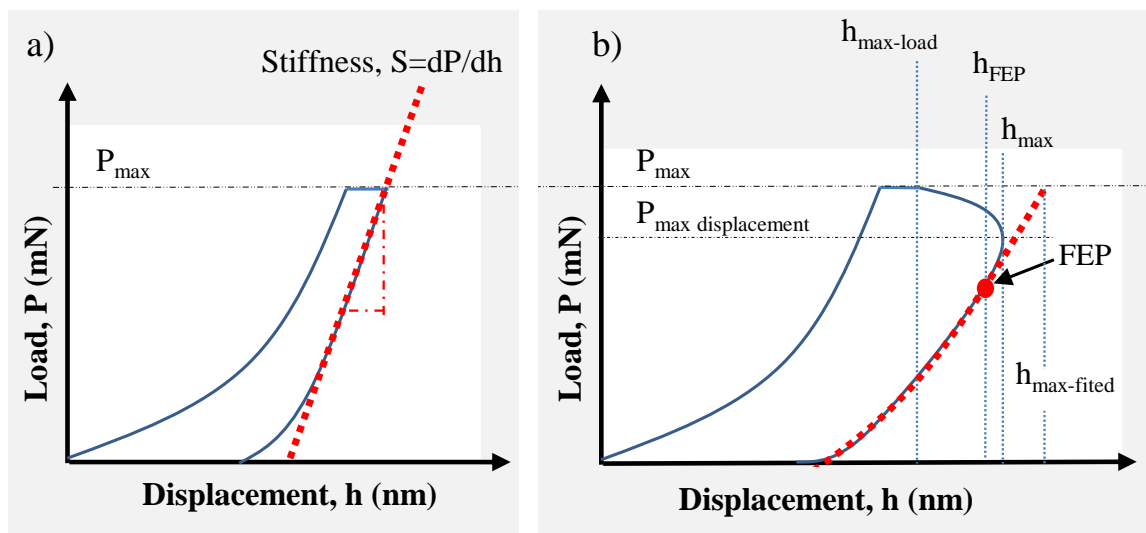


Figure 4-3, a) Typical Load-displacement graph, and b) Load-displacement of viscous/polymeric materials with “nose out”

cycle. The goodness of fit to the unloading data have been shown to have square of the multiple correlation coefficient (R_{sq}) to be above 0.99, over a wide range of experimental conditions. (UK Patent 1513480.2, 2015; UK Patent 1701591.8, 2017).

4.3.1 Viscous nature during unloading

The first step in the analysis was to separate, for the many different experimental tests, those materials which displayed a “nose out”. To better understand the viscous nature so that reliable tests could be identified later, the first factor was the Viscofactor defined as:

$$\text{Viscofactor} = \frac{1}{\left[\frac{P_{max}}{(P_{max} - P_{max \text{ displacement}})} \right]} * 100 \quad (\text{Equation 4-1})$$

These parameters are shown in Figure 4-3b. The $P_{max \text{ displacement}}$ term is the load at the tip of the “nose out” therefore when the creep is low the Viscofactor is small. This Viscofactor is a similar expression in the form as previously defined for elastic-plastic contact (Page and Hainsworth, 1993) which also resembles the creep factor (G. Feng, 2002). However, when a “nose out” is not present the Viscofactor is zero, unlike the creep factor. Thus it is more convenient for the purpose of identifying the “nose out”. This can be seen when comparing the plots in Figure 4-4, each relating to a particular factor varying at twenty different test conditions and at loads between 10 mN to 100 mN range. In these contour plots, the value outside, the outermost contour, i.e. the lowest value, is zero. Looking at the Viscofactor plot, the contours showing values greater than zero will have a prominent “nose out”. The values of viscofactor is very much unlike the creep factor, which can have a range of values over all test conditions and it is not certain which of these values will correspond to a “nose out”. However, a “nose out” be present at high enough value. Two other factors, can be seen on the plots Figure 4-4a & b, the Acceleration Factor and the Conforming Factor. The significance of these factors will be explained in reference to three materials (taken from Experiment 4.2), PET, Rubber and Nylon.

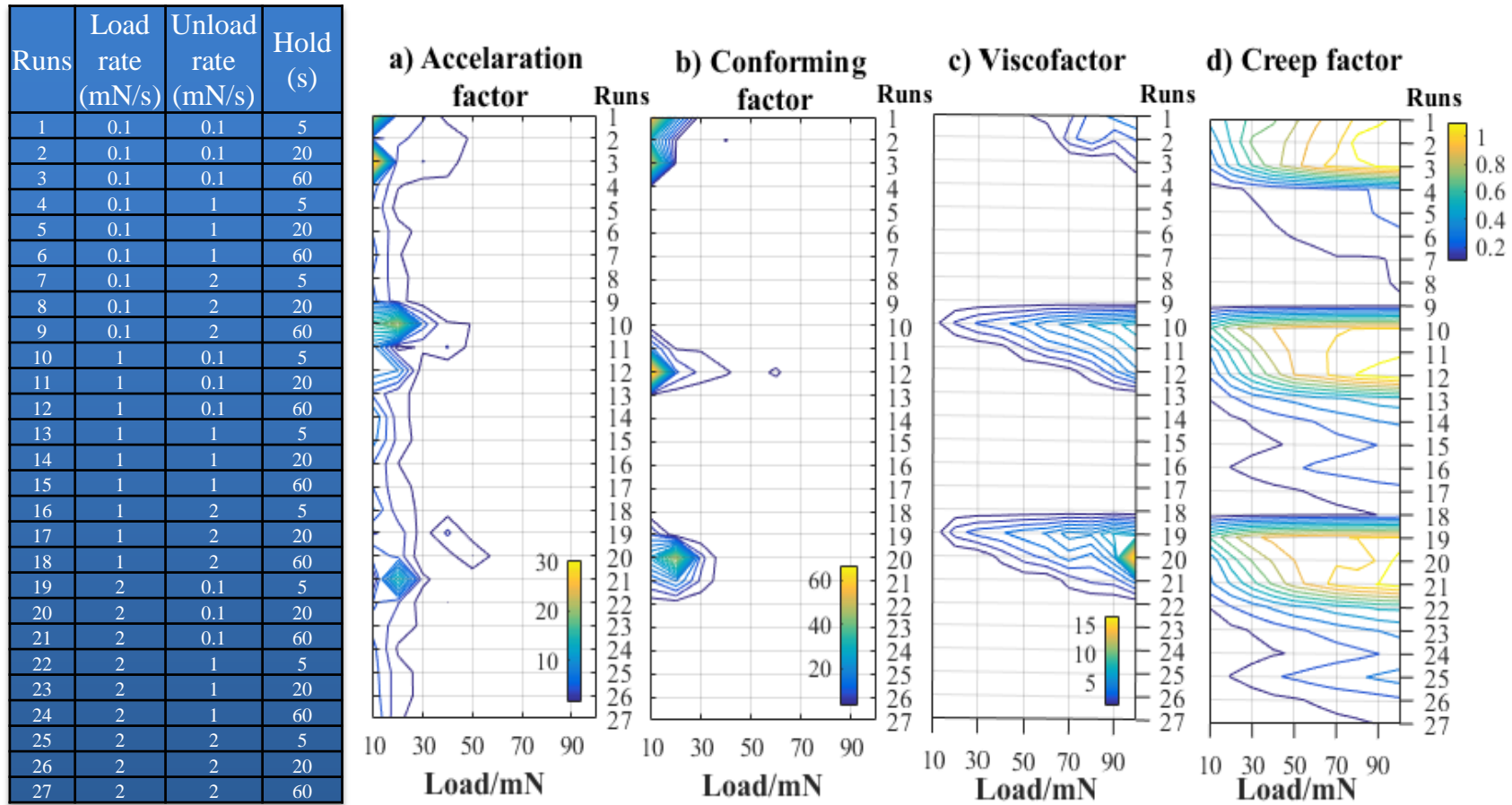


Figure 4-4 Contour plot for PET polymer showing experimental runs against load for factors such as a) Acceleration factor, b) Conforming factor, c) Viscofactor, and d) Creep factor. Table details experimental conditions for each run

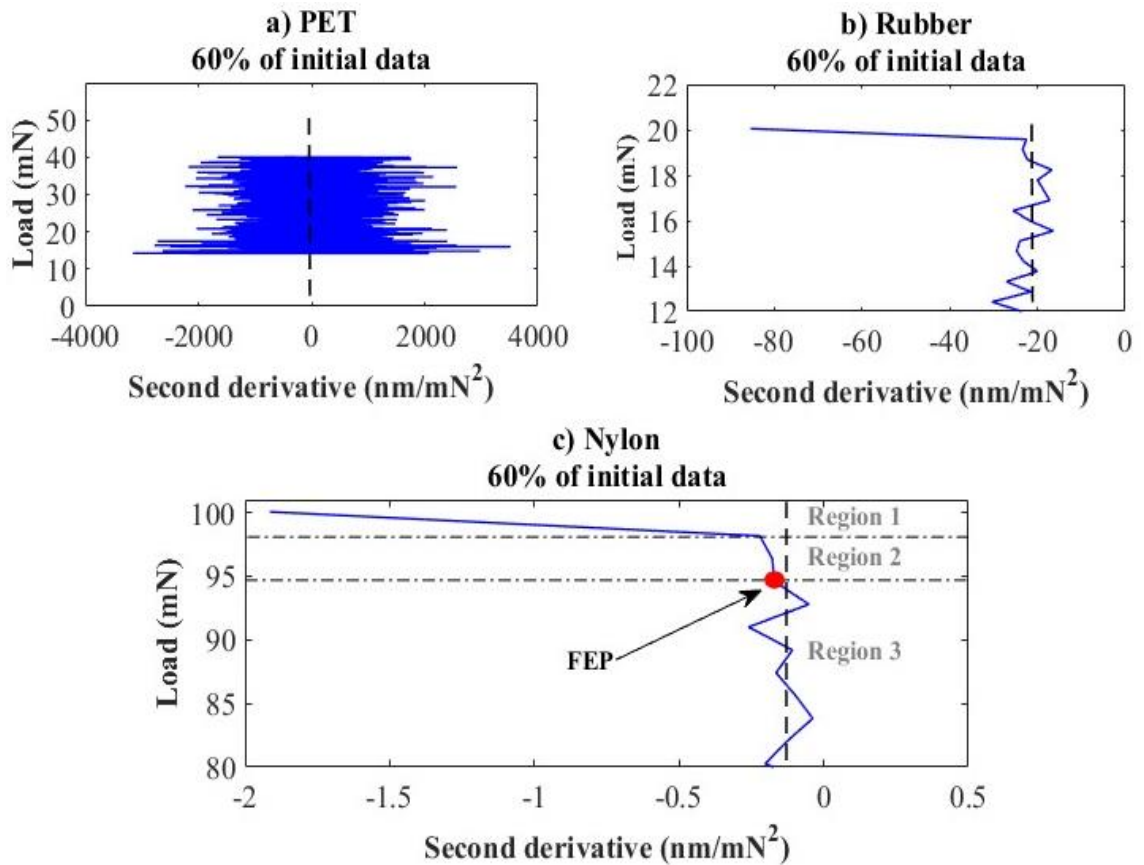


Figure 4-5 Second-derivative of displacement (with respect to load) against load-60% of unloading data for (a) PET (b) Rubber (c) Nylon

Looking at Figure 4-5a, b & c the second derivative of displacement with respect to load against load can be seen for these materials. This second derivative will also be directly proportional to the acceleration of the indenter since the unloading rate is constant. To confirm this, a graph of P against h will show

$$\frac{dh}{dP} = \frac{1}{S} = \text{reciprocal of the stiffness} \quad \text{(Equation 4-2)}$$

The velocity of the indenter can be written as:

$$velocity = \frac{dh}{dt} = \frac{dh}{dP} \cdot \frac{dP}{dt} \quad \text{(Equation 4-3)}$$

So if the load rate is constant, that is if $\frac{dP}{dt}$ is a constant then a graph of [P against $\frac{1}{S}$] or [P against $\frac{dh}{dP}$] will show identical behaviour as [P against *velocity*]. This is because the velocity is directly proportional to $\frac{dh}{dP}$. The acceleration of the indenter is a derivative of the velocity and can be written as:

$$acceleration = \frac{d(velocity)}{dt} = \frac{d(velocity)}{dP} \cdot \frac{dP}{dt} \quad \text{(Equation 4-4)}$$

Substituting for the velocity gives:

$$acceleration = \frac{d\left(\frac{dh}{dP} \cdot \frac{dP}{dt}\right)}{dP} \cdot \frac{dP}{dt} \quad \text{(Equation 4-5)}$$

If $\frac{dP}{dt}$ is a constant then

$$\begin{aligned} acceleration &= \frac{d\left(\frac{dh}{dP} \cdot \frac{dP}{dt}\right)}{dP} \cdot \frac{dP}{dt} = \frac{dP}{dt} \frac{d\left(\frac{dh}{dP}\right)}{dP} \cdot \frac{dP}{dt} \\ &= \frac{d\left(\frac{dh}{dP}\right)}{dP} \cdot \left(\frac{dP}{dt}\right)^2 = \frac{d^2h}{dP^2} \cdot \left(\frac{dP}{dt}\right)^2 \end{aligned} \quad \text{(Equation 4-6)}$$

and a graph of [P against $\frac{d^2h}{dP^2}$] will show identical behaviour as [P against *acceleration*].

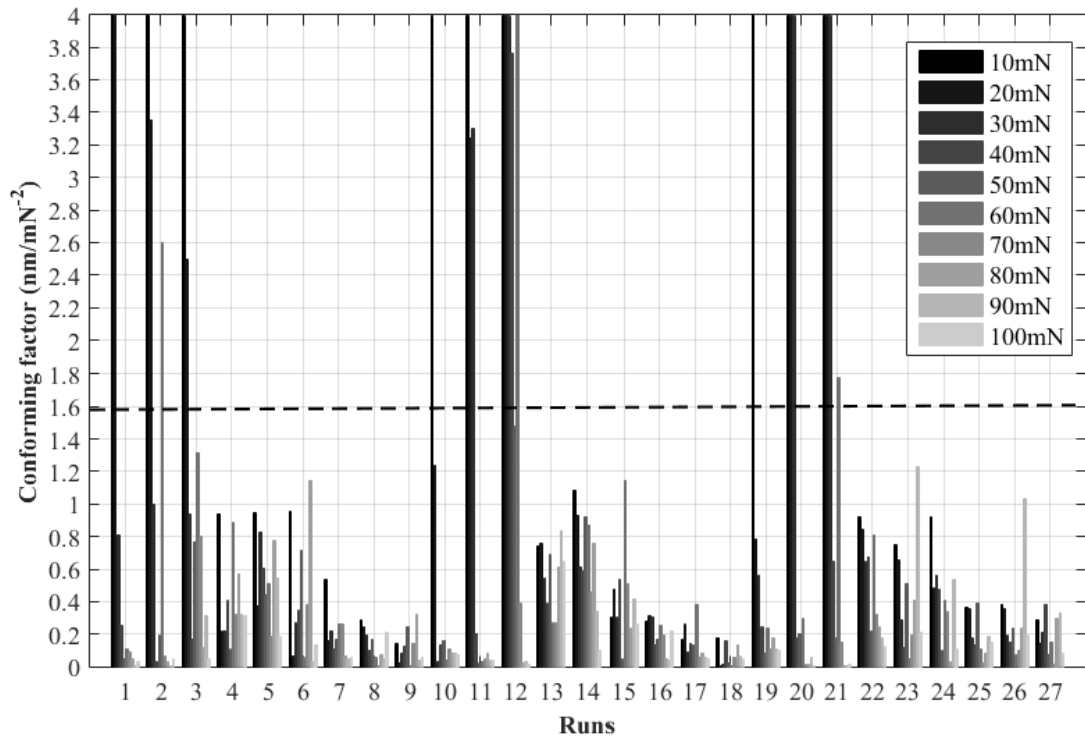
This is because the acceleration is directly proportional $\frac{d^2h}{dP^2}$. Thus, the graphs in Figure 4-5 can be seen as acceleration against load. For PET (see Figure 4-5a) there is no acceleration change thus the contact is in equilibrium. The fluctuations seen in the data are due to signal noise. It can be seen in Figure 4-5b & c that for Rubber and Nylon there is a negative acceleration in region 1, which is changing with load. If the contact is in equilibrium then there should be no acceleration. The force due to this acceleration causes non-conformity of contact, i.e. a changing contact area with time. From Figure 4-4b the non-conformity can be seen to occur at lower load and doesn't occur at higher load even

when the viscous effects are large. The definition given in this method for the Conforming factor is the difference between the second derivatives above P_{\max} displacement and below, a comparison when the contact is non-conforming (region 1 and 2) and conforming (region 3), as seen in Figure 4-5c. This factor can be written as:

$$\text{Conforming factor} = \frac{\text{absolute} \left| \left(\text{mean} \frac{d^2h}{dP^2}_{\text{upper nose}} \right) - \left(\text{mean} \frac{d^2h}{dP^2}_{\text{lower nose}} \right) \right|}{100}$$

(Equation 4-7)

This Conforming factor can be used to separate the materials in which the non-conforming contact phenomenon occurs and to determine a “conforming point” on the unloading curve. To determine the conforming point a linear fit in region 1 of Figure 4-5c can be done to establish this minimum load. This phenomenon, associated with the conforming of the contact, is present when viscous/polymeric materials are tested, and is dependent on the unloading conditions. Issues are present when determining derivatives for dataset within region 1. First, the accuracy depends on the number of data points, if averaging of the data points is considered then the real effect is less defined, this becomes more precise when spacing between the points is small. Figure 4-6 shows for all experimental conditions a value for the conforming factor were established. However, not all test conditions would produce non-conformity, due to the variability in the data in determining the second derivatives, all low values have to be excluded which can give a false account of non-conformity. Thus the dotted line in the plot was set to be the threshold value for detecting the non-conformity of a test specimen. This way only the dominate values of the Conforming factor are selected. The threshold value must be user-defined and conforming of contact can be confirmed by separate optical in-situ



Runs	1	2	3	4	5	6	7	8	9	10	11	12	13	14	15	16	17	18	19	20	21	22	23	24	25	26	27
Load rate (mN/s)	0.1	0.1	0.1	0.1	0.1	0.1	0.1	0.1	0.1	1	1	1	1	1	1	1	1	1	2	2	2	2	2	2	2	2	2
Unload rate (mN/s)	0.1	0.1	0.1	1	1	1	2	2	2	0.1	0.1	0.1	1	1	1	2	2	2	0.1	0.1	0.1	1	1	1	2	2	2
Hold (s)	5	20	60	5	20	60	5	20	60	5	20	60	5	20	60	5	20	60	5	20	60	5	20	60	5	20	60

Figure 4-6 Conforming factor against number of run for nanoindentation loads between 10 mN and 100 mN. Table details experimental conditions for each run

indentation experiments if desired. For the Conforming factor smoothing of the derivatives could have been considered, again the real effect would have been less defined. The third factor is the Acceleration factor and is defined as:

$$\text{Acceleration factor} = \text{Absolute} \left| \text{mean} \frac{d^2h}{dP^2}_{\text{lower nose}} \right| \quad (\text{Equation 4-8})$$

In the same way, as the Conforming Factor, the Acceleration Factor changes depending on the unloading conditions. At low loads relative to a high unloading rate, the acceleration has a non-zero value, even if the surfaces are conformed. Comparing the Acceleration factor with the Conforming factor, it can be seen from Figure 4-4a & b the

acceleration factor is more prominent for all experimental conditions, unlike the Conforming factor. Nevertheless, it has been realised from plots similar to those of Figure 4-5a, b & c, that at all experimental conditions, for non-viscous/non-polymeric materials the *mean* $\frac{d^2h}{dP^2}_{lower\ nose}$ is always zero. During unloading the determined values display some variation which is due to noise/fluctuations within the data. This extra acceleration is most likely due to the viscous behaviour, rubber showing the highest value which is expected. From the plots, as the load is decreased the Acceleration Factor is fairly constant, from after the FEP for the top 60 % of the data, which suggests the force due to viscous behaviour is constant on the indenter during this stage. The amount of creep occurring would depend on test condition. Though, for the sample tested the τ_i will depend on highest load during unloading and this could be larger than the total unloading time if unloading rate is high. So, the creep effect is fairly constant after FEP. However, as load decreases further the contact conditions can change, typical for these types of materials the sample pull off abruptly from the indenter.

The conforming point is always less than the FEP, thus it is not necessary to determine it. The Viscofactor is sufficient to split the unloading data for the purpose of the analysis. Even though the Acceleration factor and Conforming factors were not needed for the methodology, the main reasons to define them were to realise their effects and to confirm that the algorithm for splitting the data was adequately established.

Other factors describing the viscous behaviour, i.e. the degree of viscosity, can be the rate of penetration at the end of the hold period, $h_{max-load}$ together with h_{max} , or even the curvature of the unloading curve. Thus, other criteria could have been applied, to separate test data with a “nose out” effect from the rest of the data, such as if $h_{max-load} < h_{max}$ then viscous or otherwise non-viscous depending on the tolerances described, or if penetration

rate greater than some threshold value. Apart from the viscous nature, reverse plasticity (delayed elasticity) plays a role at initial unloading in the deformation of materials.

4.3.2 Delayed elasticity

All materials which deform plastically display delayed elasticity upon unloading (in localized deformation). This is due to plasticity (forward or reverse) or viscous plasticity during unloading, i.e. upon unloading the material is attaining equilibrium before elastically responding (Tabor, 1948). When a “nose out” effect is present plasticity is occurring alongside creep, the surface is moving inwards, resulting in a difference in the relative motion between the indenter and sample. Also, there could be some adhesion or even plunging effects. The main step in the author's analysis is to eliminate all data until delayed elasticity ceases. This is referred to as FEP in this method. This step is not needed if the response is fully elastic. In viscous/polymeric materials after contact conformity the acceleration is still changing due to delayed elastic response, this is the minimum load in the region 2 shown in Figure 4-5c, and can be determined when the first derivative of the load-displacement graph (i.e. stiffness) starts responding inversely proportional to the load as seen in Figure 4-7 (Rubber sample data are taken from Experiment 4.2). The FEP is determined when the acceleration becomes a constant, i.e. the indenter and sample move together at the same speed. At this point, the material responds in a fully elastic or viscoelastic manner without the influence of plasticity and is unique to the test conditions. The contact can be said to be in “fully conformed elastic or visco-elastic equilibrium”. At the FEP, the data relates to either elasticity or viscoelasticity depending on the material investigated. For the dataset, after FEP a second order polynomial or a power-law can be fitted to the curve. A second order polynomial is more appropriate than a power-law, and an exact match, since stiffness against load is a linear fit. At test conditions, when the time is short in reaching FEP, the accuracy of the

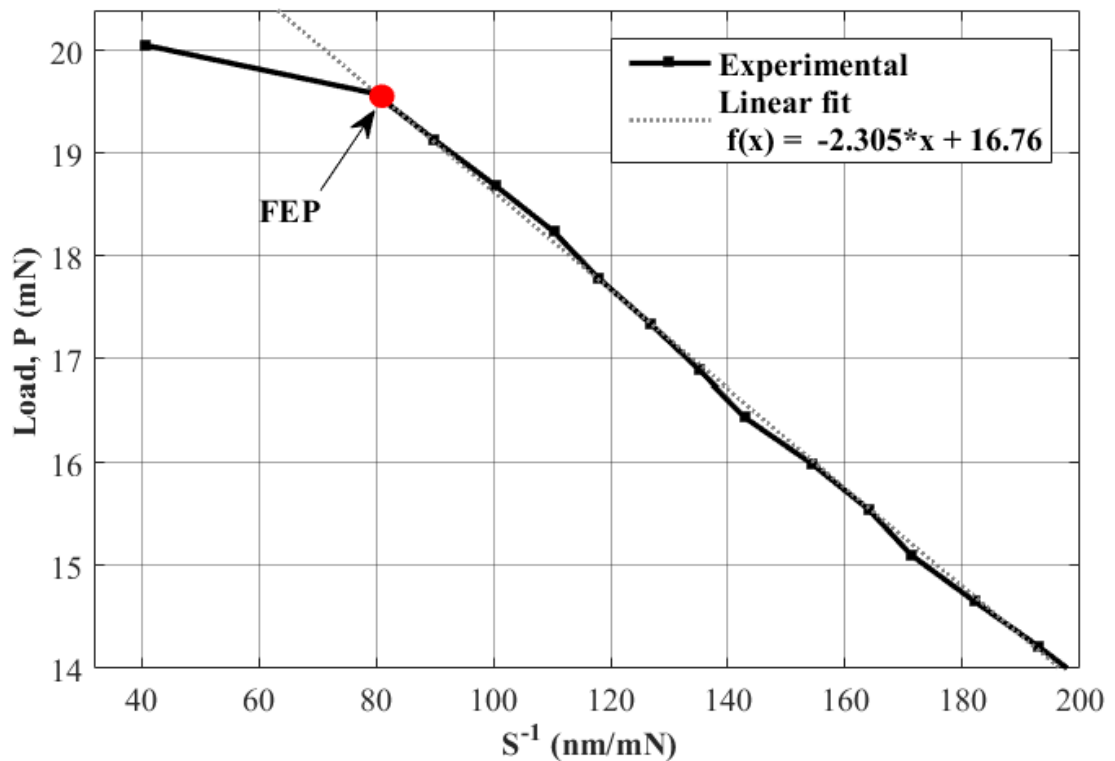


Figure 4-7 Nanoindentation unloading inverse stiffness against applied load for rubber - with a linear fit to determine FEP

method will reduce as there will be less data. Therefore, the recommended method to determine FEP uses the top 60 to 80 % of the data and splits it at h_{\max} (i.e. at nose tip). Afterwards performing a second-order polynomial fit to the data below h_{\max} , and comparing the fitted data to the experimental, the highest load at which the two data first start to differ is, in essence, the FEP. It should be noted by performing the analysis in this way the Viscofactor is not needed either. There will always be some variability in determining FEP however, by fitting the data in this manner, the error is minimised as the true curvature of the data set is used. The full fitting algorithm is detailed in the published work (UK Patent 1513480.2, 2015) and also in the next section, for both viscous and non-viscous/non-polymeric materials.

4.3.3 Fitting algorithm

An algorithm has been established for determining the FEP using the nanoindentation unloading curve; see Figure 4-8 for a flow diagram of the procedure. The process starts by first acquiring the data from the Nano-indenter machine (raw data). This data must have been corrected for frame compliance and zero-point correction and then split into load-displacement-time hysteresis data, thermal drifts data and hold-time data. This data, necessary for the analysis, is extracted by a script written for the Micro-Materials Nano Platform. However, it can be adapted for any other manufacturer depending on the layout of their data. Once machine data is extracted, second order polynomial fits to the unloading data can be used to determine FEP and S_{FEP} . Initial parameters, Viscofactor, Conforming factor and Acceleration factor, are determined by splitting load-displacement data at the “nose out”. However, these parameters are not essential for the analysis, and the data can be used later to determine test condition where reliable data can be achieved. To acquire the parameters from the unloading data, the fitting requires an additional five steps. These are shown in Appendix 5 for both viscous and non-viscous/non-polymeric materials. The reason why five steps are needed is explained. The first step is to utilize the data below the “nose out”; if data above the “nose out” is used then a higher error will be introduced during fitting. In steps two and four, the minima, for the difference between experimental data and the fit, should be zero. This is due to the experimental data being available at only measured data points. At the crossover point between these two sets of data where the minimum difference is seen zero, for both viscous and non-viscous cases, no data points are available due to the low collection rate of the data during the test. There will always be not enough data points, unless an analogue output is used, as the collection rate can't be infinity. However, for viscous/polymeric materials this effect is largely due to greater displacements with time. The minimum differences on the plot (step four)

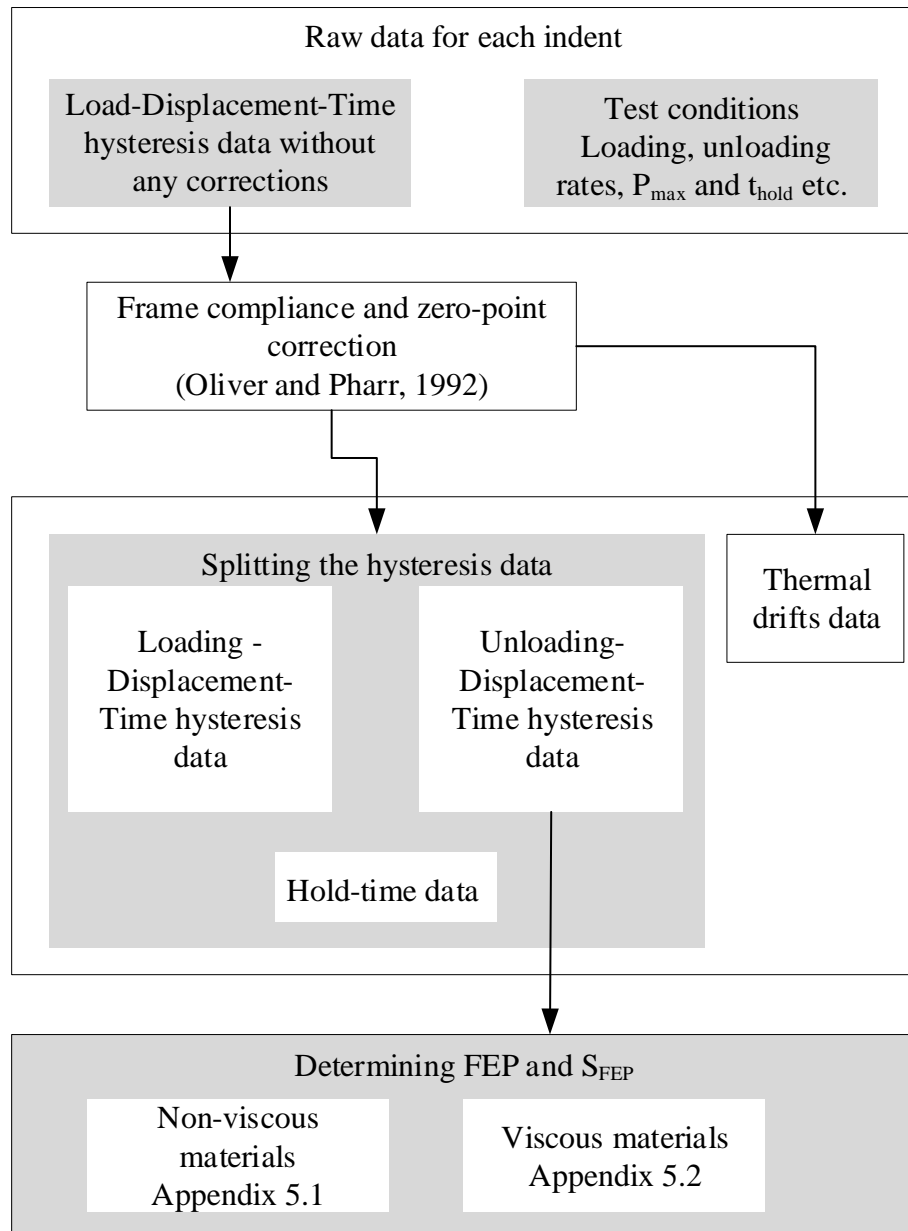


Figure 4-8 Acquisition of test data and conditioning to determine the Full Elastic Point (FEP) and the associated stiffness (S_{FEP})

aren't actually zero, but are the minimum values. If more data points were available, this value would tend to zero. Therefore, FEP should be at the last minimum. However, there is another issue, i.e. to determine precisely the last minimum because of noise in the data. For viscous/polymeric materials it is due to noise and dynamic fluctuations, these dynamic fluctuations occur about the 2nd order polynomial unloading behaviour. The

error due to noise is much less than the end delayed elasticity process, which shows a sharp rise on the plot. A more precise FEP is achieved by taking the mean difference and adding to the last minimum. This value is determined by selecting the last intersection of the difference with the mean differences (step 4 viscous). The final step splits the data at FEP and performs a second-order polynomial fit to determine the stiffness at any load, for the data set. Now that FEP and the stiffness at FEP are determined, the effect of creep and plasticity on the stiffness will be considered.

4.3.4 Creep and Plastic correction

When determining mechanical properties from the split data, the assumptions need some clarification. Under actual localised deformation, for hardness and modulus calculations compliance at FEP is used. The history of the indentation can be ignored before this point. Only at the FEP, not before or after, the stiffness equation, $S = \beta \frac{2}{\sqrt{\pi}} E_r \sqrt{A}$ (Equation 2-5), is valid. A fit cannot be extrapolated to maximum load due to non-conformity and non-elasticity.

In previous methods (G. Feng, 2002; Oliver and Pharr, 1992) the deformation was always seen as fully-elastic-localised (based on Hertzian localised deformation) in which two assumptions were made. The first assumption is that delayed elasticity at the onset of unloading is ignored. What actually happens is that local deformation causes densification/plasticity around the indenter due to diffusion and geometrical necessary dislocations, and upon unloading there is reverse plasticity (Tabor, 1948) (referred to as actual localised deformation by the author). The second assumption is that the material behaviour is fully elastic or viscoelastic. In a fully-elastic-localised deformation, the overall elasticity can also be seen as a viscous and elastic component, i.e. viscoelasticity, thus a broader term to call this and will be referred to as localised-reversible deformation.

In these previous methods, the second assumption was considered. However, for the first assumption, it was with multiple loading, the delayed elasticity was ignored. Under monotonic loading, the initial conformity and delayed elastic response can have a marked effect on the measured stiffness especially for a viscous/polymeric material, by eliminating them from the unloading data the stiffness uniquely represents the material's elastic or viscoelastic behaviour. When using a multi-loading test, differences in plasticity reduce from cycle to cycle, and the final response indicated in the past is solely due to the elasticity of the material. However, by adding another cycle more plasticity/viscous deformation is introduced into the system and temperature also increases, also affecting the measured mechanical properties. Apart from this, the material density around the indentation reaches a limit after successive cycles, and the elasticity measured would presumably be due to a composite effect of the material around the indenter and the subsurface properties. By measuring the elasticity at the first cycle, at FEP, eliminates these issues.

In previous methods, the viscous effect has always been an issue as detailed in section 2.4. The creep correction (G. Feng, 2002) corrects the stiffness for viscous effects, in the unloading method, under the assumptions of localized-reversible deformation, the apparent stiffness measured from extrapolating the data from the FEP to maximum load is taken to be due to the elasticity and creep components. S is the effective stiffness measured from the unloading curve in (Equation 2-9). When comparing (Equation 2-8) to (Equation 2-9) the elastic component related to $1/2E_rA$, thus S_u is the stiffness due to the elastic component. Whereas, the $(\frac{\dot{h}}{p})$ term relates to the viscous behaviour. Typically, the absolute value of unload rate is taken and that is why the elastic and creep components are added together. Otherwise, the creep component must be subtracted. A further note should be taken that the penetration rate at the end of hold is typically measured at steady

state, thus the hold period should be sufficient to eliminate primary creep. It should be mentioned that the creep correction (G. Feng, 2002) is applied at the turn over point, the point where hold period finishes and unloading starts for an ideal viscoelastic material. For this to be applicable for the authors developed unloading methodology (from now on his will be referred to the DU method) two assumptions are made: the first assumption is that the turn over point occurs within a range from maximum load to the load at FEP. There is no instantaneous elastic response when unloading from the maximum load. Thus it is reasonable to assume the FEP as the turn over point. The second assumption is that by determining the “true” viscoelastic response and also assuming localised-reversible deformation the penetration rate at FEP is determined. To achieve this, instead of using \dot{h}_h , the rate at which plastic deformation occurs (\dot{h}_{plastic}) is used (which is due to delayed elasticity), this will be referred to as the “Plastic correction” To calculate this plastic rate the plastic displacement can be determined using:

$$h_{\text{plastic}} = \begin{cases} \text{No Nose-out} , & h_{\text{max}} - h_{\text{max-fitted}} \\ \text{Nose-out} , & \text{Absolute} | h_{\text{max-fitted}} - h_{\text{FEP}} | - [(h_{\text{max}} - h_{\text{max-load}}) + (h_{\text{max}} - h_{\text{FEP}})] \end{cases}$$

(Equation 4-9)

For all parameters refer to Figure 4-3b for their definitions. Two cases exist, no “nose out” and the “nose out”, in both the unloading data up to the FEP is compared with a fully viscoelastic or elastic response determined by a fit to the data after the FEP. For the “nose out” case the surface initially dips in and after the “nose out” the surface dips out, these displacements are determined by the second bracketed expression for the “nose out” equation, after it is subtracted from the first bracketed expression (the displacements for ideal viscoelastic or elastic response). Once the plastic displacement is determined, the plastic rate is calculated by dividing by the time taken from the maximum load to the FEP

load. As the turn over point occurs at FEP, the plasticity has already occurred due to delayed elasticity; at this point, the stiffness does not need correcting in terms of creep. However, it is due to this occurred plastic rate that the stiffness at FEP needs to be corrected for a visco-elastic response. To obtain an elastic response, the correction can be applied by using the “true” penetration rate at FEP, which is $\dot{h}_h - \dot{h}_{\text{plastic}}$. This method also allows for hold periods where primary creep is present. A hold period is applied to stabilise the plastic deformation during the loading, and obtain \dot{h}_h from the last 20% of the hold-time data.

The creep correction method (G. Feng, 2002) has thus been adapted, as a “Plastic correction”, to determine the elastic modulus without multi-load testing and at any test conditions. The correction will assist in resolving the issues of testing viscoelastic materials since, in the past, the processes occurring during unloading were neglected in the analysis for a single load-unload cycle.

4.4 Plastic depth Pile-up sink-in correction

Apart from the “Plastic correction”, the pile-up and sink-in effects can be substantial in highly viscous/polymeric materials and must be accounted for in the measurement of the plastic depth. The expression $h_c = h_{\text{max}} - \varepsilon \frac{P_{\text{max}}}{S}$ (Equation 2-2) for the plastic depth is based on elastic unloading. However, for viscous/polymeric materials an alternative approach is widely adopted (Bec et al., 1996).

$$h_c = c_1 h_{\text{max}} - c_2 \frac{P_{\text{max}}}{S} \quad \text{(Equation 4-10)}$$

Bec et al. found both c_1 and c_2 to equal 1.2 for elastic-plastic perfectly plastic materials. Further work adapted the procedure (Fujisawa and Swain, 2006) to distinguish which method to use, either the elastic method calculated using (Equation 2-2) or the elastic-

plastic perfectly plastic method calculated using (Equation 4-10). Fujisawa and Swain described a selection procedure which is valid for tests done at one particular strain-rate test condition. For testing done at a variety of different conditions, the following logic is used.

$$h_c(S) = \begin{cases} h_{max} - \varepsilon \frac{P_{max}}{S} , & h_c(\text{elasto plastic method}) < h_c(\text{elastic method}) \\ 1.2h_{max} - 1.2 \frac{P_{max}}{S} , & h_c(\text{elasto plastic method}) > h_c(\text{elastic method}) \end{cases}$$

(Equation 4-11)

The reason for using this approach is that the contact area cannot be smaller for the elastic-plastic method compared to the elastic method. All parameters are determined at FEP.

Apart for accounting for the initial unloading curve for the purpose of characterisation, low load phenomena have more influence over the properties determined. Thus low load corrections need to be implemented for a robust methodology.

4.5 Low load correction

One of the main steps in the analysis procedure, for the calculations of elastic modulus and hardness, is to determine the contact area once the plastic depth is calculated using the stiffness at maximum load. When deformation is in the nano-regime, the contact depth determined as described in section 2.3.1, can no longer be used to determine the contact area. To understand why this is, the area function is first considered.

In this work, Micro Material's procedure, i.e. the second procedure to determine the area function coefficients using fused Silica mentioned in section 2.2.3 was used. The calibration procedure involved a series of indentation experiments and the use of load

against depth hysteresis data which covered different ranges of plastic depths. These experiments were performed in a thermal equilibrium, vibration-free environment, to find the area function coefficients of a given function which fits the projected contact area versus plastic depth plot. This was then used across a wide indentation range (0.5 mN to 200 mN) to determine the elastic modulus and hardness. The procedure gives a good account of the true contact area. However, it was realized during the analysis stage that at lower limits of loading ~ 0.5 mN, when indenting with a Berkovich indenter on ceramic thin films (film thickness ~ 30 to 150 nm) PET substrate systems, negative values of hardness and elastic modulus were obtained when using the acquired area function coefficients. Thus, some assumptions were made to establish the following procedures to avoid any negative contact areas, as detailed below.

First of all, consider a second order polynomial for the area function of the Berkovich indenter.

$$A(h_c)_{Berkovich} = a + b(h_c)^1 + c(h_c)^2 \quad \text{(Equation 4-12)}$$

When considering such a function, a negative area is obtained at very small plastic depth, comparable to the thickness of thin films, which consequently gives negative values of elastic modulus and hardness, which is not physically correct. This can be seen in Figure 4-9c which shows the projected contact area versus plastic depth plot using the function. Also included in the figure is the projected contact area calculated from a function for an ideal spherical indenter, which is:

$$A(h_c)_{Spherical} = a(h_c)^2 + b(h_c)^1 \quad \text{(Equation 4-13)}$$

For the ideal spherical function at zero plastic depth, the projected contact area is also zero. For the analysis of hardness and Modulus at low loads using a Berkovich indenter, an assumption is made that the blunting of the tip is essentially spherical. The question

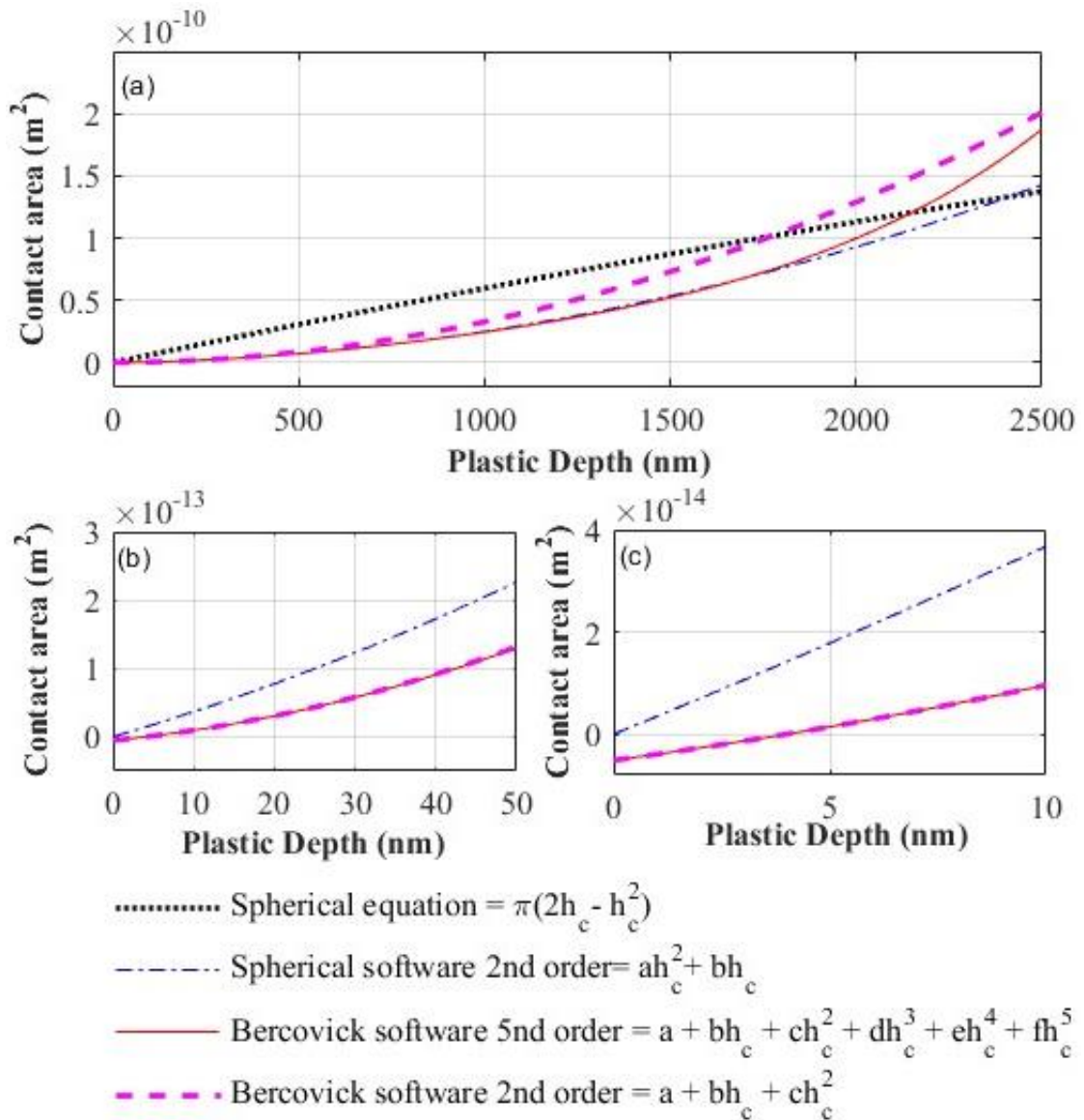


Figure 4-9 Projected contact area versus plastic depth plot using ideal spherical and 2nd order Berkovich functions a) 0-2500 nm, b) 0-50 nm and c) 0-10 nm

now becomes, at what plastic depth for the Berkovich indenter, does the 2nd polynomial and the ideal spherical functions become applicable. Looking at Figure 4-10 which shows the area difference, between the Berkovich 2nd polynomial (Equation 4-12) and the ideal

spherical functions (Equation 4-13), against the plastic depth it can be seen that the first minimum occurs at 300nm. This point can be used to classify which function to use, below it an ideal spherical is applicable whereas above it a 2nd order polynomial function

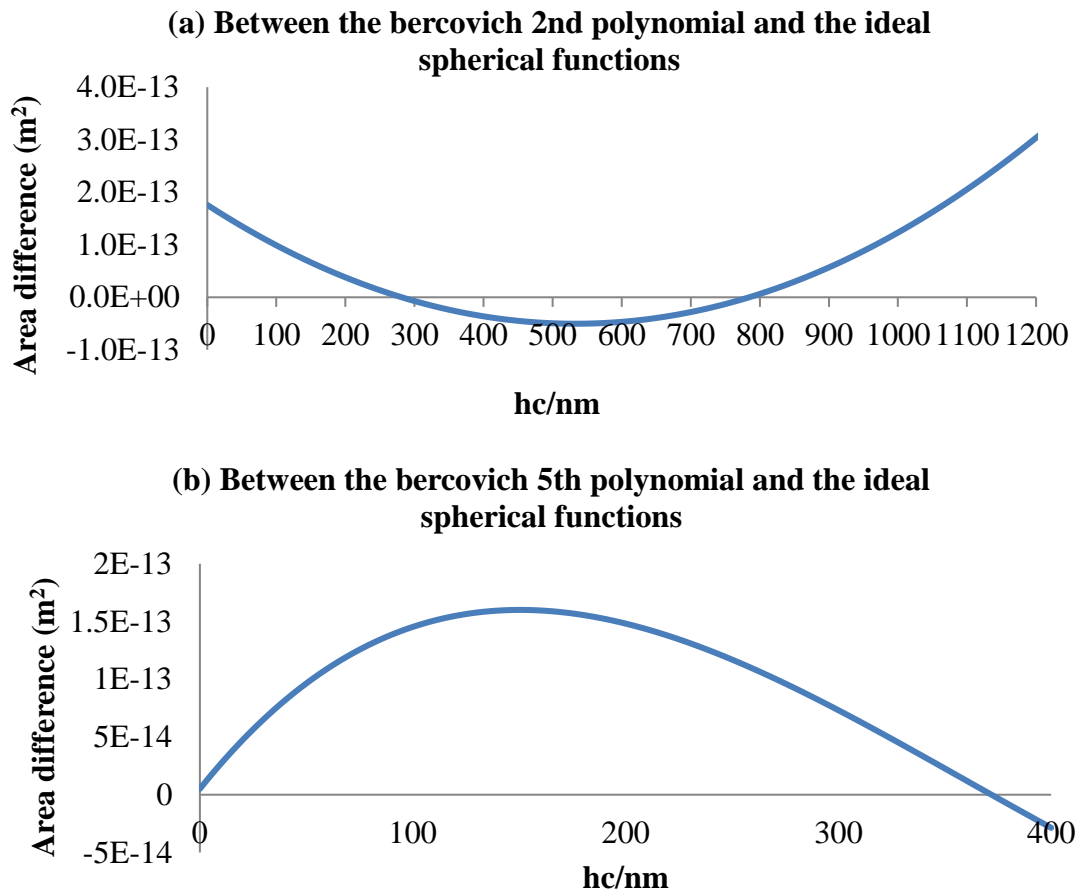


Figure 4-10 Area difference against hc(a) between the Berkovich 2nd polynomial and the ideal spherical functions (b) between the Berkovich 5th polynomial and the ideal spherical functions

is more appropriate. A more accurate and widely used area function is a fifth order polynomial (Equation 2-1) also shown in Figure 4-9. An indication of the amount of accurateness for the 5th order in relation to the 2nd order can be seen in Figure 4-11. The plot shows the area difference (calculated area difference between a 2nd order and a 5th order polynomial function) against plastic depth. It is clear from the plot that at higher loads the 5th order is more accurate, whereas approximately 2000 nm below both are

roughly the same, and either function can be used within this range. However, at low load, the fifth order area function can be only used up to 5 nm before becoming negative. As before, if spherical blunting is assumed then below ~ 370 nm, the ideal spherical

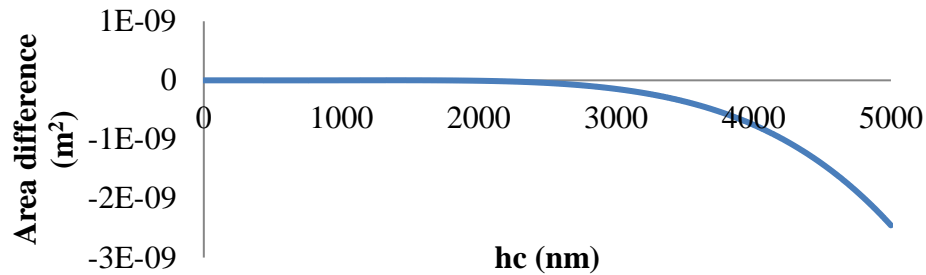


Figure 4-11 Area difference against hc , the area difference is between a 2nd order and a 5th order polynomial function

function can be used for the contact area. This value is taken from the area difference against plastic depth plot from Figure 4-10b in the similar way as for the 2nd order function. When determining mechanical properties at low load with a Berkovich indenter, even with the corrections mentioned above in this section, the contact areas are frequently negative. Previously the tip truncation length was used to form a function for the area function which allowed the determination of consistent indentation data in order to characterise a thin film sample (Chicot et al., 2014). The elastic modulus of a 2 μm to 3 μm TiHfCN coating was successfully established. This work suggests that when considering low loads, the tip blunting has a direct effect on the contact area. Hence, the ISO standard (ISO 14577-1, 2002–2015; ISO 14577-2, 2002–2015; ISO 14577-3, 2002–2015) calibrations have to be performed regularly for the correct area function.

Nevertheless, at very low loads other factors play a part in the overall displacement (see section 2.3.4) effecting the true contact area. When indented with a Berkovich indenter, as the loading in an indentation experiment increases the power law expression changes

(Bull, 2005). Accordingly, the load-depth graph goes through a number of regimes. The initial regime, where the load is approximately proportional to the displacement, is highly dependent on the indenter geometry, tilt and the roughness of the test sample. Initial contact detection, due to the random height of the asperities coming into contact with the indenter, is an issue and determining the corresponding contact area. However, this response is the same as for an elastic multi-asperity contact model proposed by Archard (1957). This linearity is said to persist only until the indenter penetration exceeds around five times the combined surface roughness. After this total elastic contact regime, the elastic-plastic regime develops. The scale length of the initial regime could be estimated from the surface roughness if this was the only parameter affecting it. However, densifications of porous material can extend the linear behaviour, and also the slope can be affected by a wet layer or oxide surface softening by the environmental humidity (Berasategui, 2003, pp.59–60). Thus, a better option to estimate the linear regime would be to establish the point where the load-displacement graphs cease to be linear.

The roughness depth limit (RDL) is defined as the displacement when the linear regime ceases. Using the RDL, the plastic depth can be determined when any factor mentioned in section 2.3.4 including the surface roughness becomes significant; this is referred to as the true plastic depth. First, the plastic depth is determined when deformation approaches RDL, where the deformation is of a conical or spherical indenter with a half space, even though using a Berkovich indenter, and h_{datum} is the plastic depth which is different from the true plastic depth as will be shown later. For implementing this method, the RDL must be determined beforehand. Once the RDL and h_{datum} are determined, the true plastic depths at, above and below the RDL can be found using adapted versions of methodologies (Oliver and Pharr, 1992; UK Patent 1513480.2, 2015; UK Patent 1701591.8, 2017).

4.5.1 Determining the Roughness Depth Limit (RDL)

RDL depends not just on the roughness, but also on the experimental conditions. It can be seen in Figure 4-12a & b that there is no correlation between the surface roughness and RDL. In these plots, a WLI was used to determine the Sa values (see Appendix 6) however, it should be noted the surface parameters at the relevant scale can be much different to the ones determined. Even though for some materials Sa is larger than RDL it will be assumed that the effect of surface roughness on the contact occurs only below RDL. The RDL is found from the load-displacement graph by the developed algorithm. Initial values are estimated by linear fits to the initial data and by using a goodness of fit

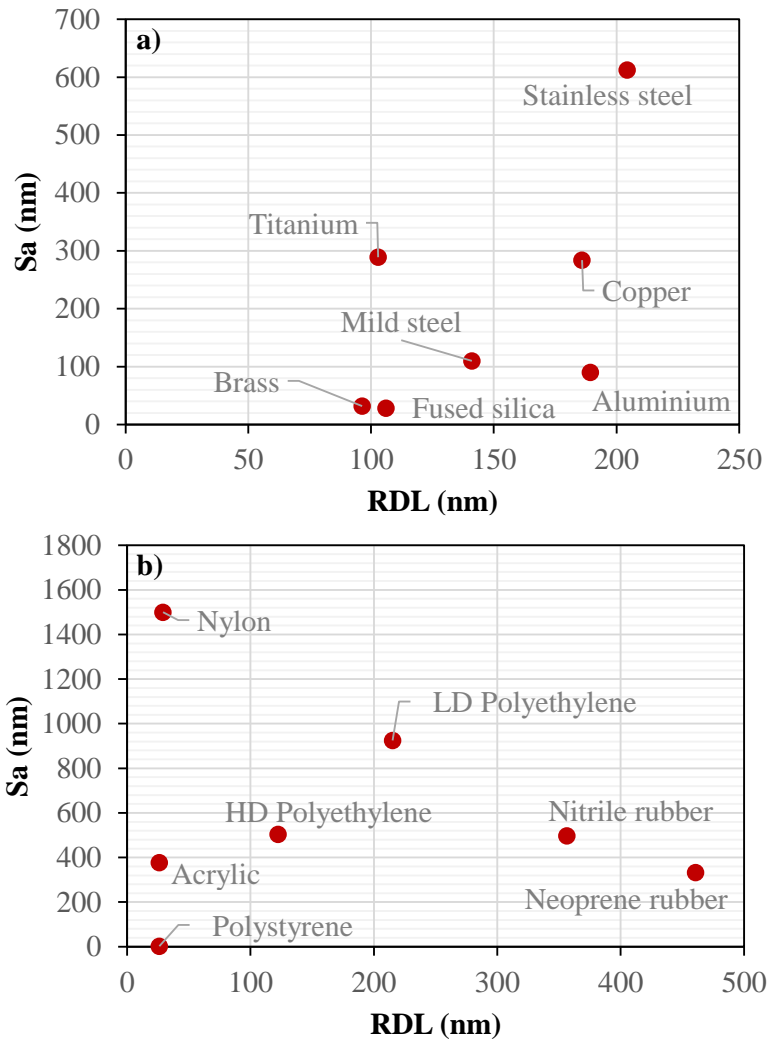


Figure 4-12 Sa against RDL for a) non-viscous materials and b) viscous materials

criteria. This is done to determine the range of displacements. Parameters such as the load rate and load, which determine the number of initial points for the fits, have to be considered. This algorithm can be modified so that an estimate for the RDL from the user can be entered, which can be roughly 10 times the surface roughness (S_a). Also, a standard test, with fixed load and loading rates, can be established for better consistency between different materials and test conditions. Further work needs to be done in this respect. Once an estimate is available the RDL is determined by first splitting the experimental data into 10 equal segments and then determining a linear fit to 10-70% of the estimated data, this is visual shown in Figure 4-13a. Next, the RDL is determined at the point of the last intersection between estimated data and 10-70% linear fit. This is achieved by taking the difference between the experimental data and linear fit and then determining the intersection to the mean of this difference, as shown in Figure 4-13b.

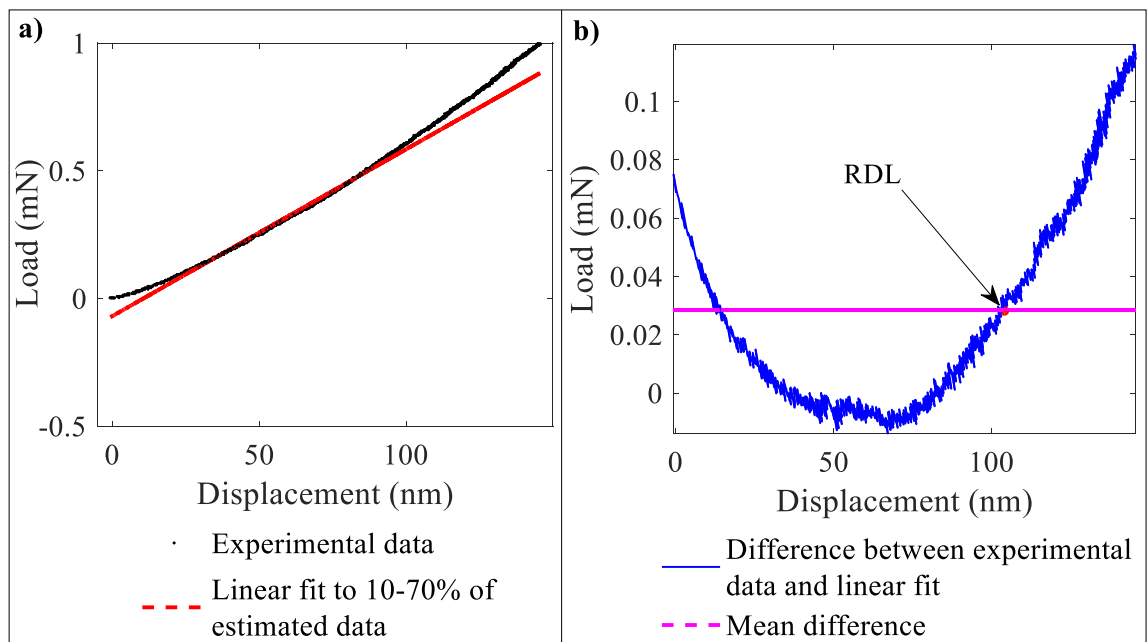


Figure 4-13 Load-displacement graph a) linear fit to the 10-70 % of data and b) showing the magnitude of the difference between the Experimental data and linear fit, intersecting with the mean difference.

4.5.2 Determining h_{datum}

Once deformation has reached the RDL, the traditional approaches (Bec et al., 1996; Fujisawa and Swain, 2006; Oliver and Pharr, 1992; UK Patent 1513480.2, 2015) which determine the plastic depth can still give negative values. This is particularly true for polymer materials. In the past, this has been associated with missing tip phenomena (Hochstetter, Jimenez and Loubet, 1999a), where a tip correction (h_{tip}) is accounted in the plastic depth equation (Bec et al., 1996) as follows

$$h_c = \alpha \left(h_{max} - \frac{P_{max}}{S} + h_{tip} \right) \quad \text{(Equation 4-14)}$$

Other authors have performed similar tip corrections adapting the standard (Oliver and Pharr, 1992) and other procedures (Doerner, Gardner and Nix, 1986). However, another explanation of this effect is proposed. It is believed that a shift in the surface occurs at initial contact which is also responsible for the linear behaviour in the regime before RDL. This shift isn't instantaneous but gradual up to RDL where it ceases. Initially, when the indenter first makes contact a small displacement is made, this is commonly corrected with the zero-point correction. It is hypothesised by the author that a shift in the zero-point datum occurs as seen in Figure 4-14 during the elastic deformation, the cause is probably reversible viscous deformation of the asperities or the upper region of the surface due to diffusion mechanisms initiated by the initial impact energy or generated flash temperatures (Smith and Arnell, 2014). The shift suggested is h_{datum} , equalling half the RDL when considering spherical contact. So, at RDL, h_{datum} can be determined in order to use previous equations to determine true plastic depth at RDL. The h_{datum} for a Berkovich indenter can also be determined. However, the associated plastic depth calculated at RDL in some instances is higher than the RDL, giving a negative h_{datum} . Thus, a good approximation is to state the indenter behaves as a spherical object at RDL, as at RDL the combination of the surface roughness and the blunting of the Berkovich

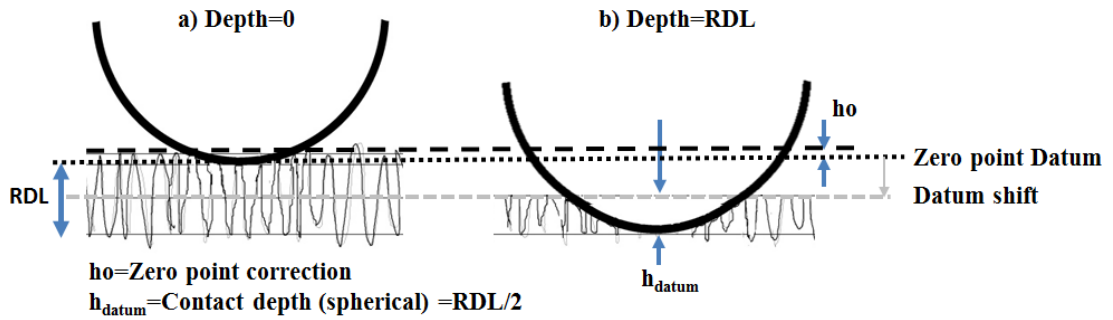


Figure 4-14 Contact at low loads in lateral loading for a spherical indenter

indenter can give an effective spherical indentation. Thus, h_{datum} is equal to the half the RDL. To determine the missing tip previously a linear relationship was assumed between the plastic depth and the stiffness at maximum load during unloading (Hochstetter, Jimenez and Loubet, 1999b). A linear relationship can be present, after RDL, on the load-displacement graph as a result of this shift. However, before RDL there is no evidence of a linear behaviour, but an extrapolation of the linear behaviour of the data above RDL.

Apart from h_{datum} , there is another component which also shifts the datum; this is the displacement that occurs during the hold period (h_{hold}), i.e. creep. Although creep is an intrinsic property, its effect during hold needs to be taken in to account for the applicability of elastic/viscoelastic contact models to find plastic depths. Accordingly it is stated that a datum shift occurs due to it. Thus, the combination of h_{datum} at RDL and h_{hold} explain the missing tip phenomena.

4.5.3 Contact area at and above RDL

To determine the true plastic depths, the two datum shifts (described in section 4.5.2) have to be considered (UK Patent 1513480.2, 2015). Thus, the equations for determining the true plastic depth (see 4.4) at and above RDL become:

$$h_c = h_{FEP} - \varepsilon \frac{P_{FEP}}{S_{FEP}} + h_{datum} + h_{hold} \quad \text{(Equation 4-15)}$$

For the elastic method, and

$$h_c = \alpha \left(h_{FEP} - \frac{P_{FEP}}{S_{FEP}} + h_{datum} + h_{hold} \right) \quad \text{(Equation 4-16)}$$

For Bec at el methods. Also, both (Equation 4-15) and (Equation 4-16) can be evaluated at FEP instead of maximum load. When considering the pile-up and sink-in correction (Equation 4-16) becomes:

$$h_c(S_{FEP}) = \begin{cases} h_{c(\text{elastic method})} = h_{FEP} - \varepsilon \frac{P_{FEP}}{S_{FEP}} + h_{datum} + h_{hold}, \\ \text{when } h_{c(\text{elastic plastic method})} < h_{c(\text{elastic method})} \\ h_{c(\text{elastic plastic method})} = \alpha \left(h_{FEP} - \frac{P_{FEP}}{S_{FEP}} + h_{datum} + h_{hold} \right), \\ \text{when } h_{c(\text{elastic plastic method})} > h_{c(\text{elastic method})} \end{cases} \quad \text{(Equation 4-17)}$$

Once the “true” plastic depth is evaluated, the contact area can be determined using (Equation 4-13) or (Equation 2-1) depending on the type of indenter used.

4.5.4 Spherical and Berkovich relationship for deformation above RDL

If indented with a spherical indenter, h_{datum} is half the RDL. If indented with a Berkovich indenter, once h_{datum} for the spherical indenter is determined at RDL, the associated h_{datum} for the Berkovich can be found by the relationship between the contact areas of a spherical indenter to a Berkovich. Such a relationship can be seen in Figure 4-15 where two

different relationships of the area of a Berkovich indenter to a spherical indenter are shown, considering depths below 300 nm. Linear and quadratic fits to the experimental data are shown on the plot, along with the fitted equations and residuals. The errors for the linear can be twice that of the quadratic. For 0-1000 nm depth ranges, a linear relationship is typically (not shown on the plot). However, at lower plastic depths a quadratic fit is more accurate. Using the quadratic function, the area for a Berkovich indenter at RDL is determined. As h_{datum} is due to the elastic deformation, once the associated plastic depth for a Berkovich indenter is found, h_{datum} for the Berkovich indenter is determined by subtracting the plastic depth from the RDL. It should be noted

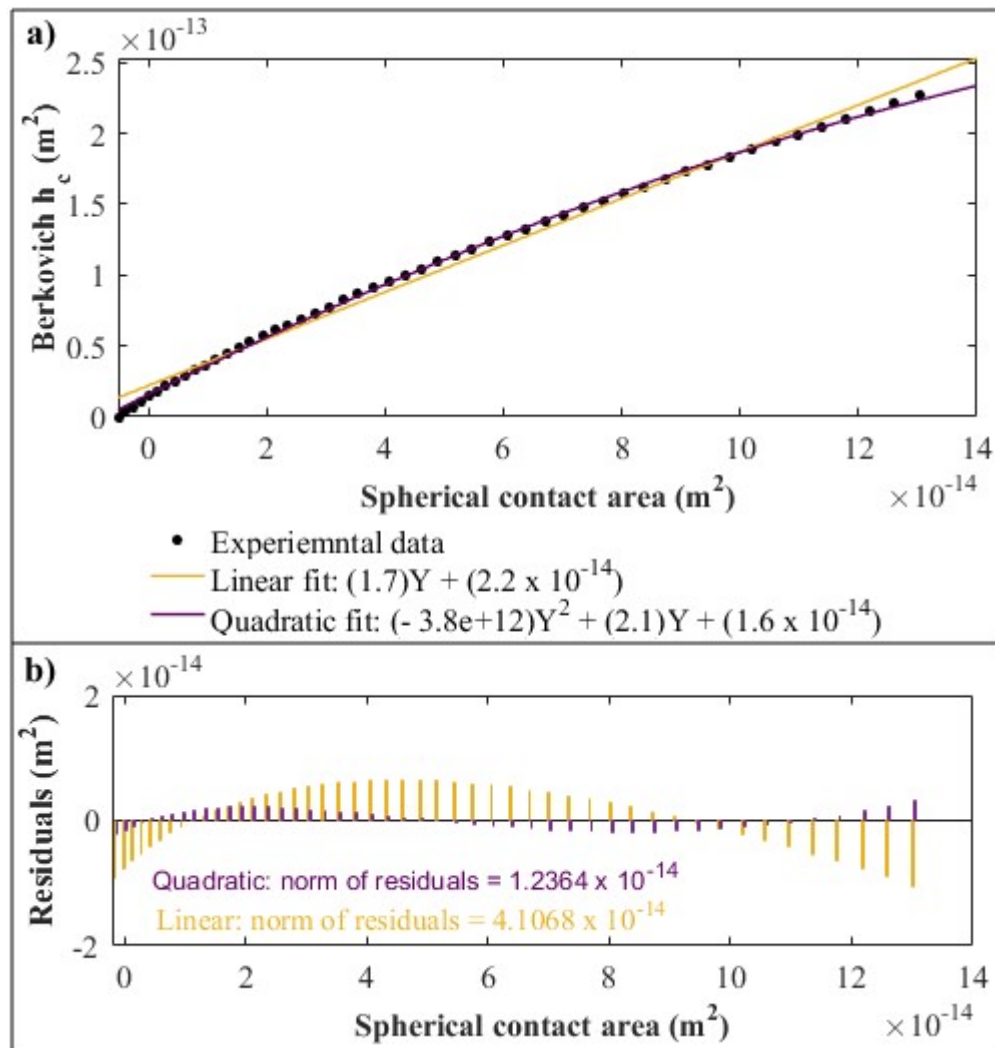


Figure 4-15 a) Berkovich contact area against spherical contact area, and b) Residuals plot for Berkovich contact area against spherical contact area

that at ultra-low depths the area function for a Berkovich indenter determined by calibration procedure can also be incorrect due to the missing tip phenomena (Hochstetter, Jimenez and Loubet, 1999b).

4.5.5 Contact area below RDL

Below the RDL the surface roughness comes into play, and the above equations for determining the plastic depth are no longer valid. If used, plastic depths still are negative. However, it has been previously deduced that for rough surfaces in contact there is a linear relationship of load with true contact area (Archard, 1957). A consensus is reached within academia for this relationship. So, in making all the terms in the plastic depth equation linear, a linear response of contact area with plastic depth can be achieved (UK Patent 1513480.2, 2015). The squared term in (Equation 4-13) is said to be negligible (Fischer Cripps, 2011, p.25) aiding in modelling this linear behaviour, so it is hypothesised:

For elastic method h_{datum} and ε also have a linear relationship, where at zero depth both equal zero. So

$$h_{1datum} = h_{datum} \times \left(\frac{h_{FEP}}{RDL} \right) \quad \text{(Equation 4-18)}$$

And

$$\varepsilon_{1datum} = \varepsilon \times \left(\frac{h_{FEP}}{RDL} \right) \quad \text{(Equation 4-19)}$$

Substituting h_{1datum} and ε_{1datum} for h_{datum} and ε in (Equation 4-15) becomes:

$$h_c = h_{FEP} - \varepsilon_{1datum} \frac{P_{FEP}}{S_{FEP}} + h_{1datum} + h_{hold} \quad \text{(Equation 4-20)}$$

This equation is compatible with (Equation 4-15) at the RDL.

For Bec at el methods, parameters α_1 and α_2 are determined and also have a linear relationship with depth, so (Equation 4-16) becomes:

$$h_c = [\alpha_1 \times h_{FEP}] - \left[\alpha_2 \times \frac{P_{FEP}}{S_{FEP}} \right] + [\alpha_2 \times h_{datum}] + [\alpha \times h_{hold}] \quad \text{(Equation 4-21)}$$

where

$$\alpha_1 = 1 + \left[(\alpha - 1) \times \left(\frac{h_{FEP}}{RDL} \right) \right] \quad \text{(Equation 4-22)}$$

$$\alpha_2 = \alpha \times \left(\frac{h_{FEP}}{RDL} \right) \quad \text{(Equation 4-23)}$$

The parameter α_1 in (Equation 4-21) makes the first bracket equal to h_{FEP} at zero displacement, so that (Equation 4-20) is compatible and also equal to it at zero depth. With depth it increases linearly. The parameter α_2 in (Equation 4-21) makes the second and third brackets equal to zero at zero displacement, similar to the elastic method. As α_2 varies linearly with displacement, it can be seen that at RDL (Equation 4-21) is compatible with (Equation 4-16). From (Equation 4-21) it can be seen that at ultra-low loads the last three brackets become negligible, with increasing depth as the deformation become more elastic their significance increases, leaving a half space deformation (elastic Hertzian localised deformation) at RDL. Again once the true plastic depth is determined the contact area can be determined as before using (Equation 4-13) or (Equation 2-1) depending on the type of indenter used.

For pile-up sink-in corrections (Equation 4-17) becomes:

$$h_c(S_{FEP}) = \left\{ \begin{array}{l} \begin{array}{l} h_c(\text{elastic method}) = \\ h_{FEP} - \epsilon_1 \frac{P_{FEP}}{S_{FEP}} + h_{1datum} + h_{hold}, \\ \text{when } h_c(\text{elastic plastic method}) < h_c(\text{elastic method}) \\ \dots\dots\dots \end{array} \\ \begin{array}{l} h_c(\text{elastic plastic method}) = \\ [\alpha_1 \times h_{FEP}] - \left[\alpha_2 \times \frac{P_{FEP}}{S_{FEP}} \right] + [\alpha_2 \times h_{datum}] + [\alpha \times h_{hold}], \\ \text{when } h_c(\text{elastic plastic method}) > h_c(\text{elastic method}) \end{array} \end{array} \right.$$

$$\text{(Equation 4-24)}$$

Once the true plastic depth is determined the contact area can be determined by (Equation 4-13) or (Equation 2-1) depending on the type of indenter used. Another method is to indent at RDL and then use (Equation 4-15) and (Equation 4-16) to determine the true plastic depth, the contact area at RDL can thus be found using (Equation 4-13) or (Equation 2-1). The contact area can be linearly extended to zero depth where its value will also equal zero. The following equation thus gives contact area as a function of the depth at FEP:

$$Ac(h_{FEP}) = Ac_{RDL} \times \left(\frac{h_{FEP}}{RDL} \right) \quad \text{(Equation 4-25)}$$

4.6 Summary

A number of different methodologies for the DU method were proposed in this chapter considering characteristics of the unloading curve, pile-up sink-in correction for the plastic depth and low load corrections. While creep correction has to be performed under certain experimental conditions using multiple loading sequences, the method is valid under all experimental conditions (associated with the limitations of the equipment) using monotonic loading.

Moreover, the overall variability associated with the testing equipment should be reduced in comparison to the standard methodology, when parameters such as the reduced modulus, hardness and viscoelastic parameters are attained from the response data. Implementation of the method can be easily done by modifying the data analysis algorithm in the software of any commercial depth-sensing indentation system at low cost.

Having fully detailed the DU methodology, an approach to reliable nanoindentation studies is essential for its application. Therefore, the next chapter details the adopted approach.

Chapter 5

DEVELOPING A RELIABLE APPROACH FOR THE NANOINDENTATION TESTING OF VISCOUS AND NON-VISCOUS SYSTEMS

5.1 Introduction

In the last chapter, methodologies were developed to characterise the mechanical properties of bulk materials, both viscous and non-viscous, and at scales where individual properties of thin films/substrate systems are needed. However, for validation and further characterisation studies, a robust framework/approach is needed for reliable results. This chapter describes such an approach, which will become the basis for all nanoindentation studies mentioned in this thesis. Also, the effect of the machine variables on the results and its variation were investigated. Nanoindentation was completed at different scales at a variety of testing conditions using a Taguchi Design of Experiments (Das and Sahoo, 2012; Minitab 18 support, 2019a; Verdi et al., 2014), to determine the most significant input parameters influencing the nanoindentation results.

In order to approve the reliability of the nanoindentation approach, it was essential that the ageing stability of the PET and PEN was confirmed. The XRD methodology was used for the ageing experiments, discussed previously in section 3.3.1, and the ageing results were compared to nanoindentation results using the developed approach. Using the optimum procedures, determined for both the equipment, the data for the ageing was acquired, parameters such as percentage crystallinity, lateral order factor and hardness were examined. The variation of the ageing results was further compared to in-sample variation. All related specifications for the materials are detailed in Chapter 3.

5.2 Nanoindentation approach

For developing the nanoindentation methodology and its applications, a number of experiments are detailed throughout the thesis. Parameters and test conditions were established/chosen from work described in sections 1.3, 2.3, 2.4 and 3.5. As a large number of input parameters were involved, to make the studies practical within the time frame and resources, DOE's approaches were used.

For viscous/polymeric materials, the material response has been historically difficult to measure with depth sensing devices because the system compliances are too low (VanLandingham et al., 2001). However, with advances in the test equipment, this has been made possible. When characterising viscous/polymeric materials, variation always exists for the measured properties and depends on a number of factors (Beake and Leggett, 2002). For indentation depths in the nano range, the factors can be surface roughness, machine effects (due to the resolution of measurement), and those linked with ISE. These factors are the main causes of reliability and reproducibility issues. Advancements in nanoindentation equipment still have not been able to resolve these issues even if other studies suggest differently (Beake and Leggett, 2002). This is due to the reliability and reproducibility of the characterised data being also related to different stages of the deformation process, which depend on the experimental conditions such as loading rate, the holding time at the maximum load and the unloading rate, and corresponds to the viscous/plastic nature of the sample material. This effect makes the elastic modulus and hardness appear time-dependent or rate-dependent, and the values are not consistent when measured (VanLandingham et al., 2001) under different arrangements. So that reliability can be addressed, the DU method (see Chapter 4) was used by the author, along with the analysis of variance statistical approach for analysing and interpreting the DOE's. The procedure, accounted for time-dependent events,

occurring during loading, hold and unloading, and distinguishes the influence of the individual input parameters, as mentioned above, on the output response.

5.2.1 Experimental details

The Micro Materials Nano Platform (see section 2.2.1) was used to examine a variety of materials, including ceramic coated compliant substrates (detailed in Chapter 3). Even though the work by Tohid and Bull (2007, p.5) highlights several issues related to open-loop feedback control. Test performed on the micromaterials nano platform, on highly viscous rubber, revealed that none of these issues were immanent for this setup. Looking at Figure 5-1 first it can be seen that peak load is the same as the pre-set target load of 2 mN, second there is no drop in the load during the hold period, and third, the rates of loading and unloading do not change. In this case, open-loop control functions correctly,

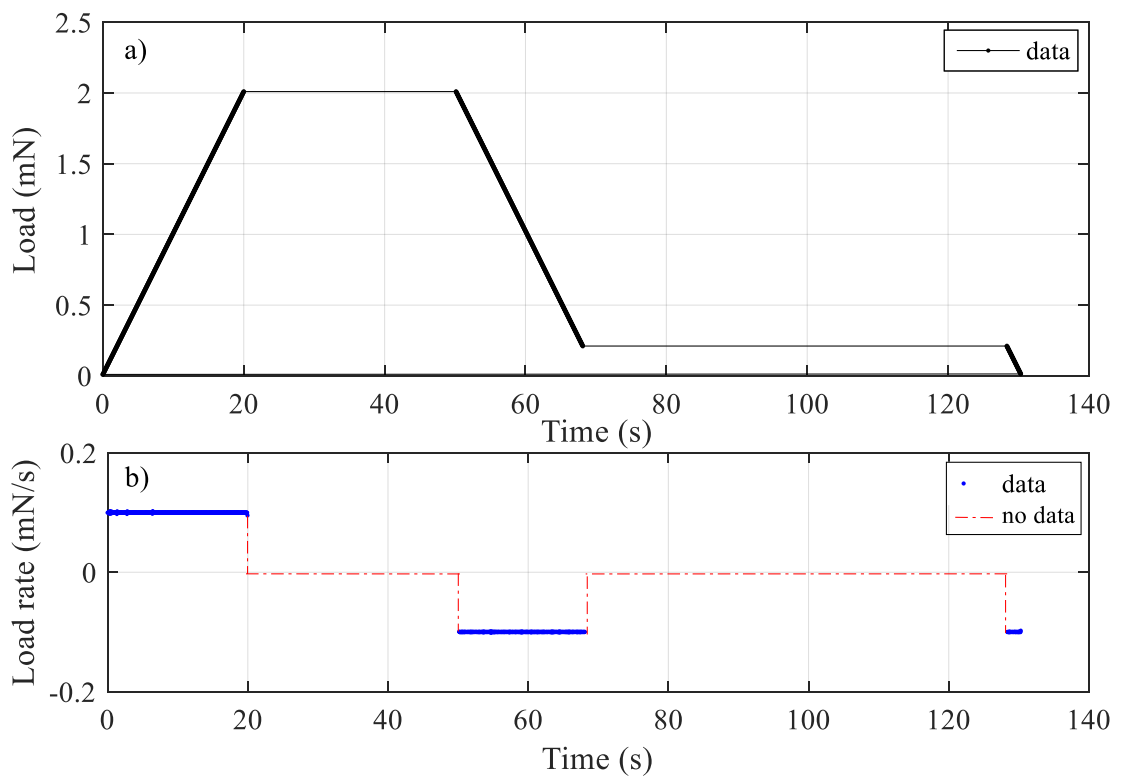


Figure 5-1 Nanoindentation actuation response of loading, hold, unloading and thermal period a) load -time response b) load rate-time response

for applying an accurate load. Also, it should be noted that during the hold periods, there are no data points for the load rate, but joined at the start and end of these periods. Thus, in this work, closed-loop is not considered or examined if more appropriate than open-loop control.

In accordance with the latest nanoindentation standard (ISO 14577-4, 2007–2016), the test samples were rinsed with ethanol before mounting to remove any intermediaries within the contact, such as fluids or dust particles. The stability of indenter tips is crucial in performing accurate tests, as with time, sharp indenters can become blunt. The manufacturers confirmed the tip geometries. The tips were also regularly cleaned by indenting on polymeric samples to pull off any contaminants. The environment was controlled/stabilised as much as possible. To minimise machine drift as much as possible, which is a consequence of the indenter coming into contact with the sample (Zhang et al., 2018), the machine was allowed to stabilise for any thermal gradients or stage vibrations, before starting the test, with the sample was mounted on stage. Tests were scheduled according to the defined study, and the temperature was recorded for each test. Even though the mounting itself can have some influence on the frame compliance, it is assumed that as long as the sample was firmly mounted, the frame compliance is as determined through the calibration method. For nanoindentation tests that included a dwell time, the load-controlled mode was used, whereas the effect with depth experiments were conducted using depth-controlled mode.

Necessary preliminary studies were conducted, allowing the most important parameters to be approved for further testing and experimentation viable within the timeframe of the study. The developed nanoindentation methodology was thus used to examine the output response of the samples using this approach. These preliminary studies involved examining loads < 2 mN defined as nano range, and > 2 mN defined as micro range, and

to establish test conditions, the ideal spacing between indentations, number of repetitions of the test, and reliability, so that significant factors could be identified. These are detailed in the next section.

5.2.2 Load-displacement behaviour

As the load-displacement behaviour is unique to a particular system, it was essential to have some idea of the displacements involved at a particular loading as well as any events that may be occurring during this process, especially for coated samples.

Initially, Experiment 5.1 was conducted on the coated samples for understanding their load-displacement behaviour and to determine the test conditions for further studies. All three coatings on PET substrates were indented with loads as shown in Table- 5-1. 10 indentations with 1s dwell at maximum load were used for each test with post thermal drift correction. A dwell period was applied so that the plastic rate at the end of dwell period can be established for the plastic correction.

Table- 5-1 Test conditions for Experiment 5.1 with PET substrate

Coatings	Load (mN)	Load and Unload rates (mN/s)
TiN	0.6	0.01
TiO₂	0.6	0.01
AZO	0.2	0.01

For the three coatings, the deformation behaviour can be seen from the load-displacement graphs, in Figure 5-2. The inflation point is defined where the gradient decreases, related to the failure of each of the coatings. It can be seen to occur at low loads and is indicated with the dotted line. The failure event happens without any abrupt/discontinuous

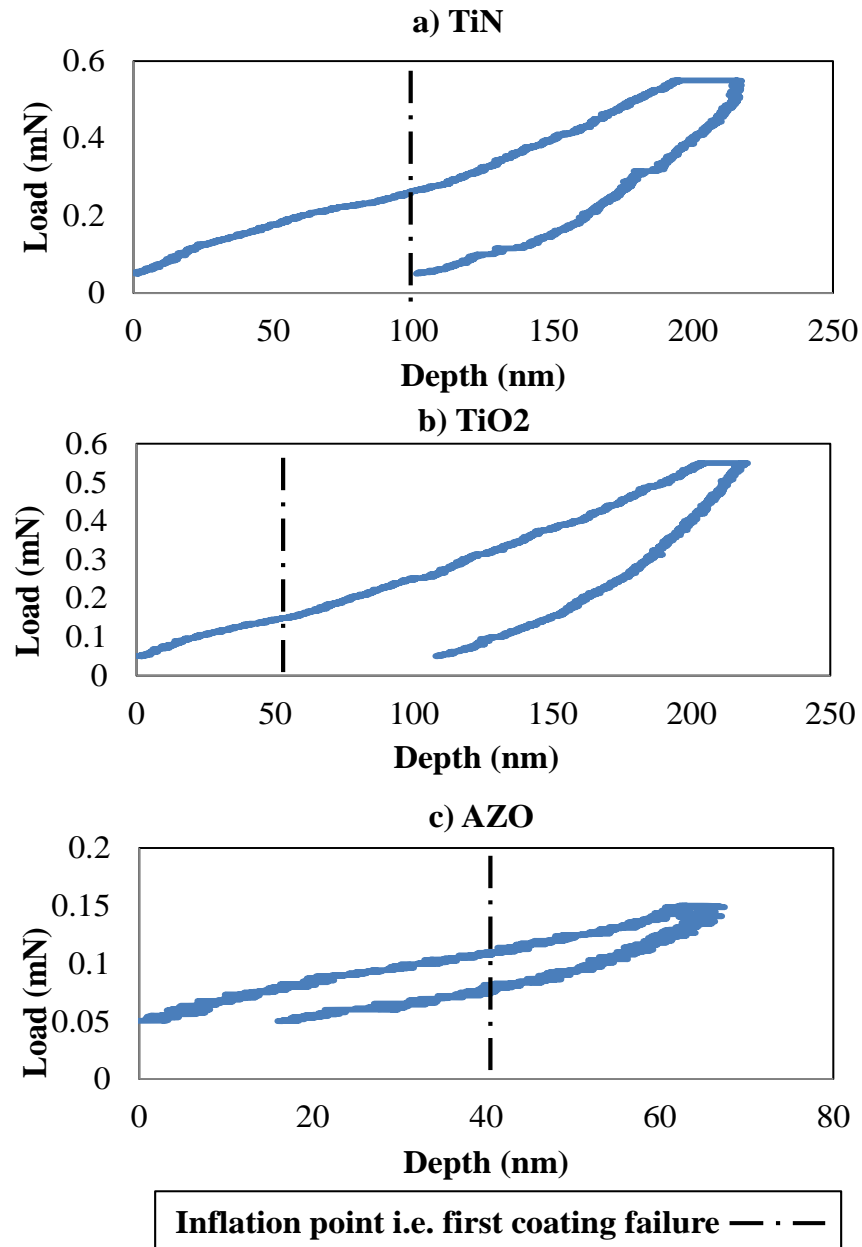


Figure 5-2 Load-displacement plots for different coating on PET substrate a) TiN, b) TiO₂ and c) AZO

displacement suggesting it is a gradual process, i.e. there was no sudden brittle fracture of the coating, i.e. sudden jumps in the displacement measurement. Instead, there seem to be either discrete brittle fractures or plasticity phenomena, too small to be distinguished. The behaviour is similar for all of the three coatings. However, in Figure 5-2a TiN shows an inflation point at twice the load compared to the other two coatings.

The behaviour for these coatings at low loads can show a high degree of variability from test to test. As the effect of the substrate is substantial, its variability is inherent within the deformation.

5.2.3 Determining the number of repetitions for each test

When studying these systems, at these loads, the variability that exists, during the analysis needs to be determined. So, the second step was to identify the number of indents, to successfully capture the true variability of the system deformation, for all further DOE's. Experiment 5.2 included five schedules with 10 indentations and was performed to determine ideal test spacing. The schedule details, i.e. the values of loads, hold time, and load/unload rates are listed in Table- 5-2. Post thermal drift correction was applied.

Table- 5-2 Test conditions for Experiment 5.2

Experiment	Load (mN) Start-End	Hold Time (s)	Load/Unload rate (mN/s)
1	30-300	0	0.033
2	30-300	0	2
3	30-300	0	40
4	30-300	20	40
5	30-300	100	40

The highest load within any study conducted in the thesis did not exceed 300 mN, so this was the upper limit of the load in this experiment. When testing, the separation of indentations should be such that previous ones do not influence further indents. The effect of small separation between the indentations can be seen in Figure 5-3. As the load

increases the indentation start to overlap. For this load, the aspect ratios for the indents, one drawn on the figure for clarity, is around 30 nm. It can be seen that a separation of about 30 nm is not enough to avoid interference by plastic deformation introduced from a previous indentation or sink-in and pile-up effects of the free surface, either it is a delayed viscous response of polymer or strain hardening effect of the plastic zone. The plastic zone can be much greater than the indentation dimension and the nanoindentation standards (ISO 14577-2, 2002–2015) stipulates the spacing should be at least 3 to 5 times

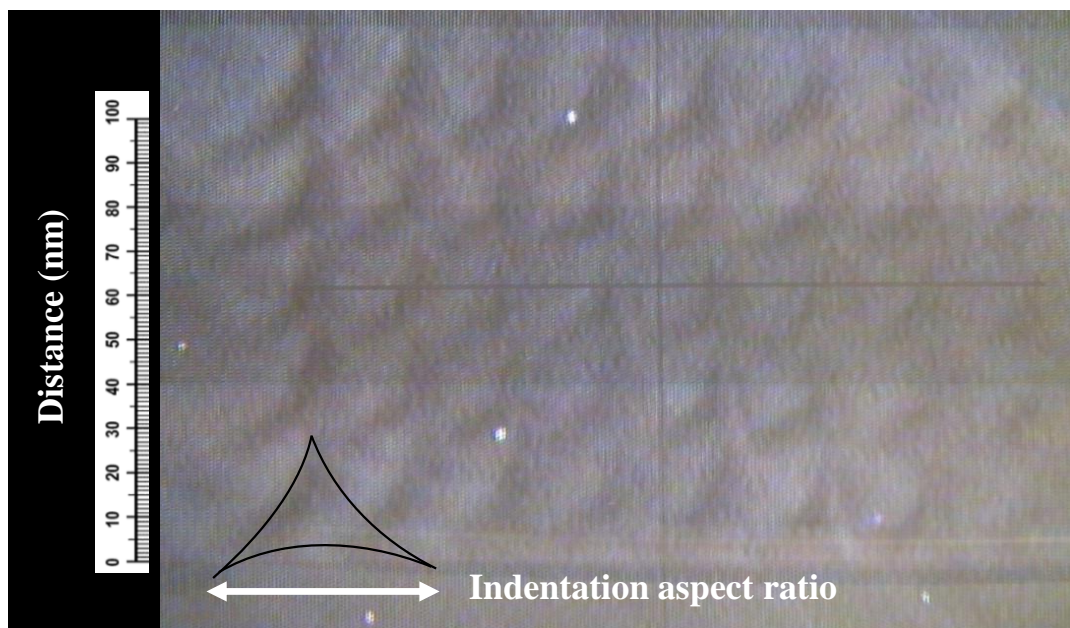


Figure 5-3 Array of 8 x5 indentations for identifying appropriate indentation spacing

of their diameter of residual impression. For a Berkovich indenter, the aspect ratio of about 7 to 1 is used for a good clearance, so that indentations of about 40 nm should be spaced at least at 8 to 10 times giving a distance of 320 to 400 nm apart as a minimum (Fischer-Cripps Laboratories, 2018). According to the standard (ISO 14577-4, 2007–2016) for a coated sample, the cracked region should not also interfere. For tests

conducted by the author, a spacing of 30 μm was set to avoid interference of the indents from any of the effects mentioned.

Experiment 5.3 included ten indentations with 1 s dwell at a maximum load of 50 mN and was performed on 150 nm TiN on PET system. The loading and unloading rates were 40 mN/s and a post thermal drift correction was applied. For this experiment, the standard deviation (σ) of the maximum displacement values for a number of indents can be seen in Figure 5-4. With more indents the σ levels off and this value is more representative of the deviation for the coating/substrate system. So, for further experimentation, 10 indents for each DOE array were selected. This was also done by considering the balance between the resources and the accuracy of the test, as reducing the experimental time was essential and other large studies were needed, 10 indents for each DOE array were appropriate and also consistent with the standards (ISO 14577-1, 2002–2015; ISO 14577-4, 2007–2016).

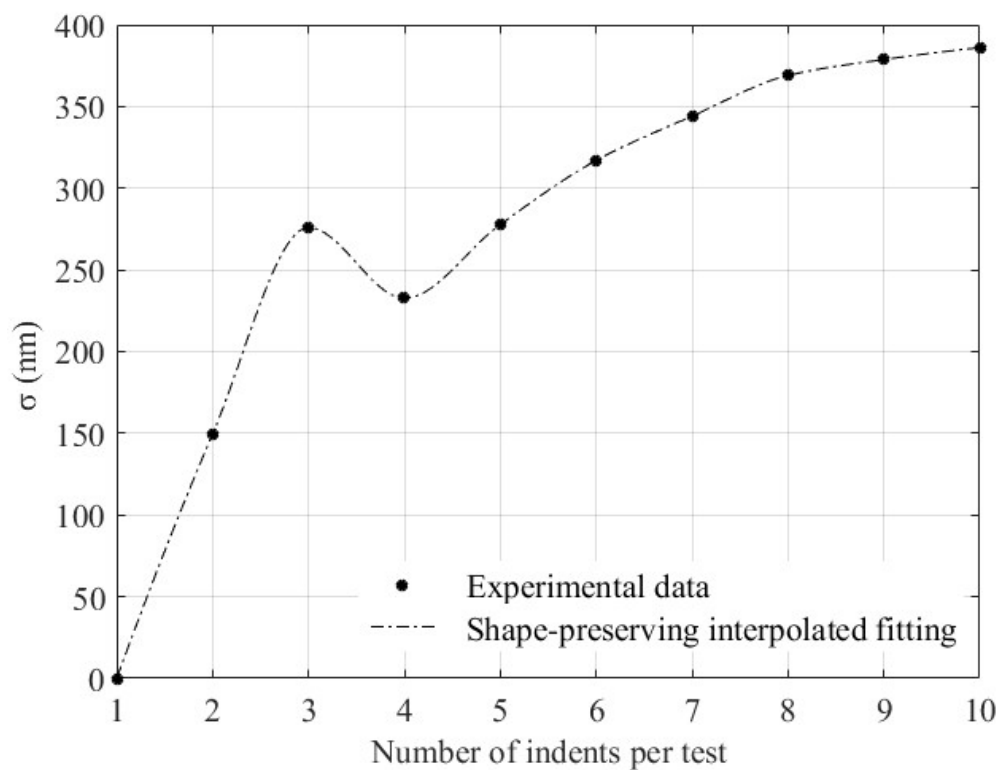


Figure 5-4 Standard deviation (σ) of the maximum displacement against number of indents/test

With additional indents further change in σ is small and this slight variation will still be captured as noise in further DOE studies.

5.2.4 Reliability for further studies

In order to start examining the deformation of a system such as thin film coating/compliant substrates using nanoindentation, the main parameters, which affect their contact deformation and the corrections associated with the methodology, were identified (see sections 1.3, 2.3, 2.4 and 3.5).

When bulk materials are indented deformation typically starts off as Hertzian i.e. elastic deformation. After Hertzian deformation, whilst the pressure underneath the indenter is increasing, at some point below the surface, plastic deformation initiates and grows; this plastic zone in sequence extends to the surface (see Figure 5-5). For a hard coating on a

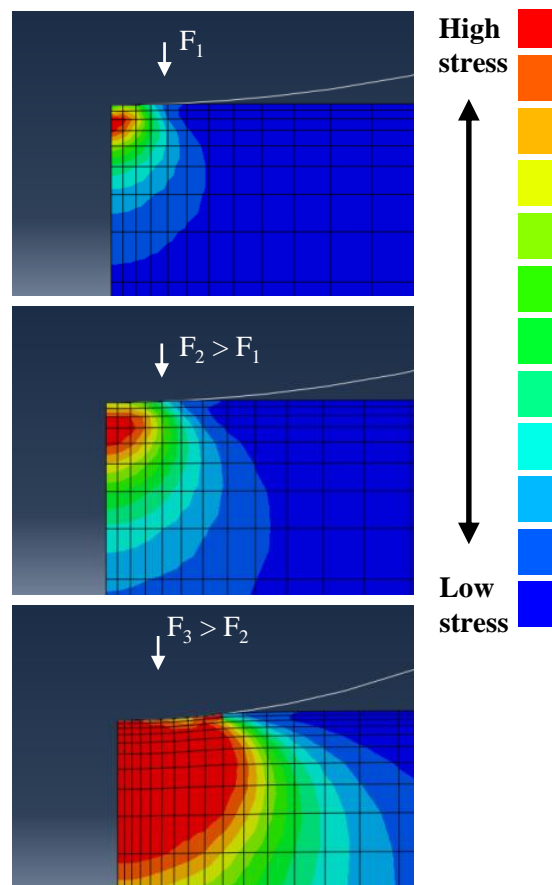


Figure 5-5 Stress evolution during indentation

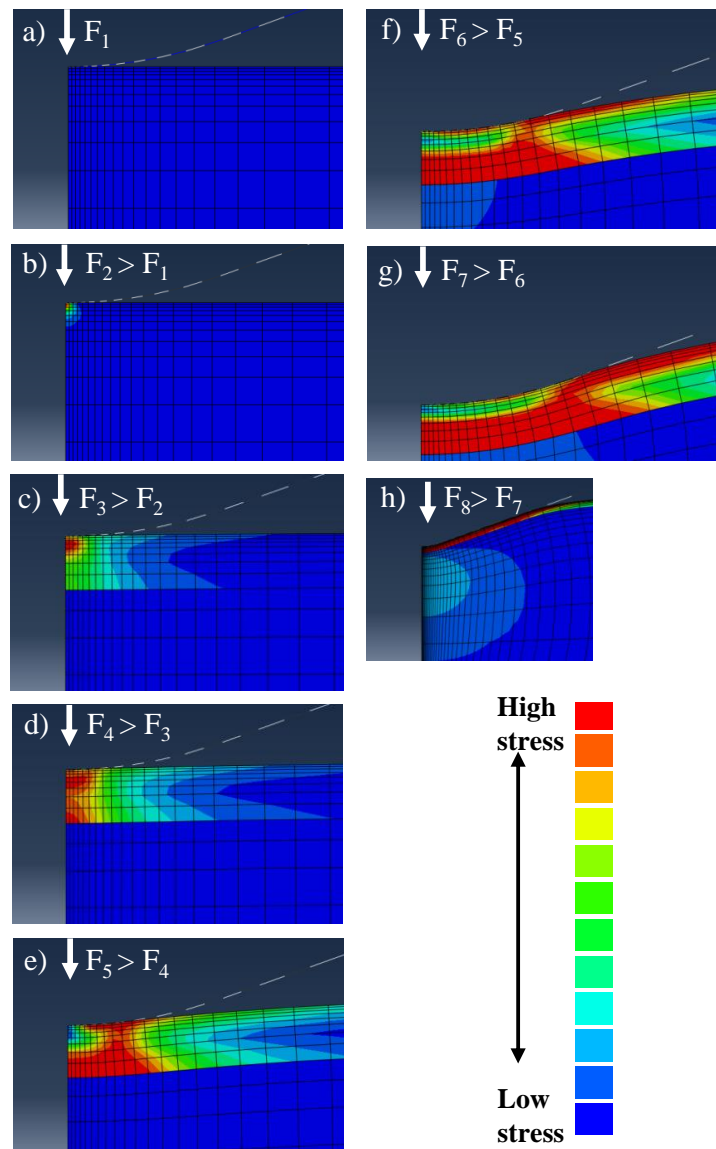


Figure 5-6 Deformation of a hard coating on a compliant substrate

compliant substrate the deformation is much more complex process. Where initial deformation exists solely within the coating in which yield first occurs (see Figure 5-6c) and as the load increases it is restricted by the interface (see Figure 5-6d). On further load increase, even though the loads can be very small ~ 0.1 mN, high stresses migrate from the interface to the surface as seen in Figure 5-6e, f & g. These high stresses would cause circumferential cracking and delamination of the coating as described in section 3.5.5. For thinner coatings the loads which cause this kind of behaviour can be even lower.

A study to identify the parameters with the most influence on the type of deformation process explained above was conducted, so time and resources of further studies were reduced. Experiment 5.4 involved ranking of nine factors using a Taguchi DOE method considering the deformation at both the nano and micro scale. The study was also done for the purpose of determining the reliability (variability from test to test) for further studies. The relationships between all nine factors and four different response factors i.e. h_{max} , h_c , H and E_r were examined. After ranking each individual response factor, ranking was done considering all four together. The experimental parameters and their associated values are highlighted in Table- 5-3. The loads highlighted dictate the scale. The developed nanoindentation method, described in Chapter 4, was used to determine the output response data. Further interactions between parameters were examined.

Table- 5-3 Taguchi design details for TiN coating

		Taguchi design details
Factors	DOE design	L36
	Factor levels	2^6 and 3^3
	Indenter	Berkovich, spherical
	Thermal drift	No, Yes
	Micro unloading rate (mN/s)	2, 40
	Nano unloading rate (mN/s)	0.1, 2
	Coating thickness (nm)	150
	Substrate	PET, PEN
	Tilt angle (degrees)	0, 5
	Nano loads (mN)	2, 10, 20
	Micro loads (mN)	50, 100, 300
	Load rate (mN/s)	0.033, 2, 40
Hold time (s)	1, 20, 100	

Initially no creep correction was performed to determine H and E. The data was also analysed again with creep correction and these results were compared with the non-creep corrected data in order to see if the creep correction had any effect on the most significant factors. For this experiment, the individual or combined ranking of the response factors were examined using the Signal to Noise Ratio (S/N), means and standard deviations (σ). In Taguchi DOE it should be noted that a high value of S/N is an indication of control factor settings that have a minimum effect on the noise factors. This is true for the ranked values for all of the control factors. Depending on a criterion i.e. minimum or maximum mean ranked factor, minimum or maximum S/N etc. favourable factors for further studies can be selected. Conventionally, for a Taguchi DOE sequence, the noise factors are designated and manipulated to force variability to occur. However, in this study, noise factors have not been deliberately chosen but are inherently present between each separate indent within a single array of the DOE. Ten indentations were considered for each array in this case. These noise factors may possibly be due to the distance of the following indentations from the first indent, time of indentation from first indent, change in temperature, or any other single unknown or combination of factors etc. The results are discussed for the ranking performed at micro and nano-scale, of the nine factors to four different responses i.e. H, h_c , h_{hold} and the E_r . These are highlighted in Table- 5-4 and Table- 5-5, along with the ranking for all four response factors considered together. By examining the data means of all the factors together, the load is apparently the most significant parameter at both the nano and micro scale when deformation is considered for a hard coating/ compliant substrate system. This is certain as, with the evolution of load, the deformation goes through a number of stages, elastic then elastic-plastic deformation within the coating or elastic deformation within the coating and combined elastic-plastic behaviour of the coating and substrate and final deformation behaviour

Table- 5-4 The ranking of factors for nano scale deformation

Response factors	S/N Ratios	Means	σ	Rank
H (GPa)	Load rate	Indenter	Indenter	1
	Load	Unload rate	Load rate	2
	Indenter	Load	Load	3
	Coating	Tilt	Hold	4
	Hold	Load rate	Unload rate	5
	Thermal drift	Hold	Coating	6
	Unload rate	Coating	Thermal drift	7
	Tilt	Thermal drift	Tilt	8
	Substrate	Substrate	Substrate	9
hc (nm)	Indenter	Load	Hold	1
	Load	Unload rate	Indenter	2
	Load rate	Tilt	Coating	3
	Hold	Coating	Tilt	4
	Coating	Thermal drift	Load	5
	Substrate	Substrate	Load rate	6
	Thermal drift	Hold	Unload rate	7
	Tilt	Indenter	Substrate	8
	Unload rate	Load rate	Thermal drift	9
h_{hold} (nm)	Load	Hold	Hold	1
	Load rate	Load	Load rate	2
	Hold	Load rate	Load	3
	Indenter	Substrate	Indenter	4
	Tilt	Tilt	Substrate	5
	Substrate	Indenter	Coating	6
	Unload rate	Unload rate	Thermal drift	7
	Thermal drift	Coating	Unload rate	8
	Coating	Thermal drift	Tilt	9
Er (GPa)	Load	Unload rate	Load	1
	Hold	Indenter	Indenter	2
	Load rate	Load	Hold	3
	Indenter	Load rate	Load rate	4
	Coating	Tilt	Unload rate	5
	Unload rate	Hold	Coating	6
	Tilt	Substrate	Thermal drift	7
	Substrate	Thermal drift	Tilt	8
	Thermal drift	Coating	Substrate	9
All Factors Together	Load	Load	Indenter	1
	Load rate	Unload rate	Hold	2
	Indenter	Indenter	Load	3
	Hold	Tilt	Load rate	4
	Coating	Hold	Coating	5
	Tilt	Load rate	Unload rate	6
	Unload rate	Substrate	Tilt	7
	Substrate	Coating	Thermal drift	8
	Thermal drift	Thermal drift	Substrate	9

Table- 5-5 The ranking of factors for micro scale deformation

Response factors	S/N Ratios	Means	σ	Rank
H (GPa)	Load rate	Load	Coating	1
	Coating	Load rate	Load rate	2
	Hold	Substrate	Hold	3
	Load	Hold	Load	4
	Thermal drift	Thermal drift	Substrate	5
	Substrate	Indenter	Unload rate	6
	Unload rate	Coating	Tilt	7
	Tilt	Unload rate	Thermal drift	8
	Indenter	Tilt	Indenter	9
hc (nm)	Load rate	Load	Load	1
	Thermal drift	Load rate	Load rate	2
	Coating	Thermal drift	Thermal drift	3
	Substrate	Hold	Hold	4
	Tilt	Indenter	Coating	5
	Load	Unload rate	Substrate	6
	Hold	Tilt	Indenter	7
	Indenter	Coating	Unload rate	8
	Unload rate	Substrate	Tilt	9
h_{hold} (nm)	Load rate	Load rate	Hold	1
	Hold	Hold	Substrate	2
	Load	Indenter	Load rate	3
	Tilt	Tilt	Coating	4
	Thermal drift	Load	Load	5
	Indenter	Thermal drift	Thermal drift	6
	Unload rate	Substrate	Indenter	7
	Substrate	Coating	Tilt	8
	Coating	Unload rate	Unload rate	9
Er (Gpa)	Coating	Load rate	Coating	1
	Thermal drift	Substrate	Substrate	2
	Substrate	Hold	Thermal drift	3
	Load rate	Load	Load	4
	Indenter	Coating	Hold	5
	Tilt	Unload rate	Indenter	6
	Unload rate	Tilt	Load rate	7
	Hold	Thermal drift	Unload rate	8
	Load	Indenter	Tilt	9
All Factors Together	Load rate	Load rate	Coating	1
	Thermal drift	Load	Hold	2
	Coating	Hold	Load	3
	Hold	Thermal drift	Load rate	4
	Substrate	Substrate	Substrate	5
	Load	Indenter	Thermal drift	6
	Tilt	Tilt	Indenter	7
	Indenter	Coating	Unload rate	8
	Unload rate	Unload rate	Tilt	9

being of the substrate, when fracture of the coating is involved, the deformation can be different.

At the nano scale the unloading rate, indenter type and the tilt are the most significant, whereas at the micro scale the load rate, hold time, and thermal drift are the most important factors. Although the two scales cannot be compared due to the study being done in two separate groups, it can be postulated that the unloading rate at the nano scale is significant due to the time-dependent mechanisms upon unloading and hold, as upon unloading the forward viscous behaviour are substantial in relation to the total unloading time, whereas this is not the case for micro scale deformation. Also, at the nano scale the loading rate is not as significant as it is at the macro-scale, this can be related to the amount of plastic deformation occurring. Undoubtedly, indenter type and the indenter tilt contribute to the response. These factors cause the stress distribution to change within the sample considerably according to the relative geometries in contact. Initial plasticity typically starts at a depth of about half the contact radius under the surface, where shear stress has a maximum value. Therefore, for spherical contact much, higher loads are required for the plasticity to reach the surface. Both indenter type and the indenter tilt are more significant at the nano scale in terms of the data mean values and have more variation associated with them as the σ is also high. At this scale the relative geometries between the indenter and sample can vary more due to the surface roughness. However, the ranking in terms of plastic depth and hold displacement shows the indenter type is not significant at all and has high S/N thus less effect of noise for either indenter compared to the rest of the factors. This also implies that plasticity is less significant cause of deformation at the nano scale. Looking at the main effect plot for the S/N (see Figure 5-7a) it can be seen that the Berkovich Indenter gives the highest S/N at the nano scale and would be more appropriate choice at this scale to reduce the effect of noise. Lower

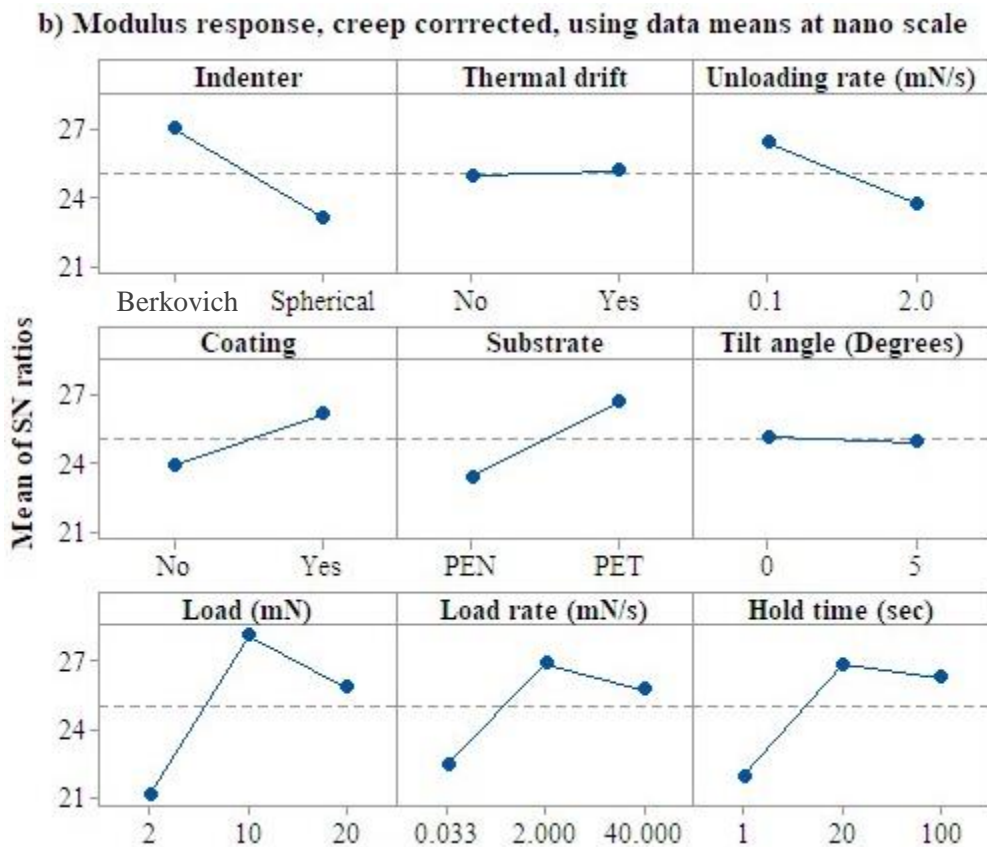
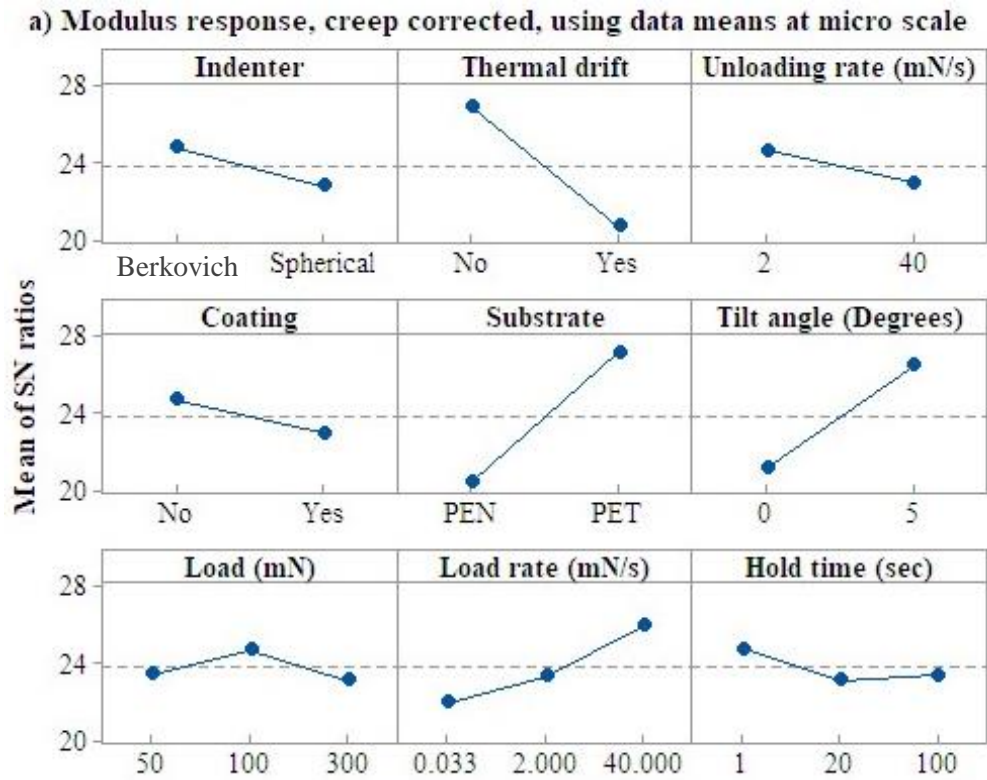


Figure 5-7 Main effects with creep correction Signal-to-noise ratio plots a) micro scale and b) nano-scale

S/N at micro scale (see Figure 5-7b) can be associated with the variation occurring due to plastic deformation since this is probably initiated by randomly heterogeneous events. This occurs much more for the Berkovich Indenter compared to the spherical indenter. Also, as the two scales cannot be compared for this study, the relative microstructural scale compared to the plastic zone size produced by the different indenters should be mentioned, their interactions will lead to different types of deformation. The explanation for the tilt being more significant at the nano scale for the data means is due to the contact geometries changing with the variation of surface profile from indent to indent, because the surface roughness and surface defects would vary with horizontal displacement of the indenter along the surface much more than at the micro scale. Thus, at lower loads, the tilt should be considered or controlled to minimise its effect. The coating at the both scales is not significant. However, the σ at microscale indicates the high variance due to the brittle fracture processes of the coating underneath the indenter. At the micro scale the load rate and hold time are noteworthy, depending on how these factors change would determine the amount of plastic deformation and creep behaviour at this scale. This also applies to nano scale even if these parameters were lower in the ranking. The load rate shows less significance at this scale implying less plasticity. Thus, overall the viscoelastic-plastic effecting parameters i.e. load, hold time, load rate and unloading rate have much more influence on the response than applying a coating. The effect of these parameters is more significant at the micro scale. Certainly, at higher loads the stresses cause the coating to fail locally with deformation occurring solely within the substrate, for this reason the substrate is higher up the ranking. In observing the substrate, although the structure of PET and PEN are very similar, at the nano scale least significance is seen in terms of S/N, means and σ . However, the substrate type has a higher S/N and σ at the micro scale. Again, it is postulated that along with the ISE, at the nano scale variability is

directly related to the noise factors i.e. the relative noise associated with the sample structure or machine accuracy is high at the nano scale compared to the micro scale. As the σ is higher at the micro scale it is more likely to be related to the visco-elastic-plastic behaviour. Thus, at both scales, factors associated with plastic deformation and creep behaviour are important and should be considered and will vary for different compliant substrates.

Previously machine stability and calibration procedures were discussed in section 2.2. In applying a thermal drift correction during the hold period, the deformation is caused by a contribution of both the creep and thermal expansion. By examining Figure 5-8, which shows ten different indents in the post hold region at low load, the depth-time relationship can be only be assumed to be linear after the initial 20 s. Thermal drift can be calculated, ignoring the initial data, where the linear behaviour is assumed only due to thermal

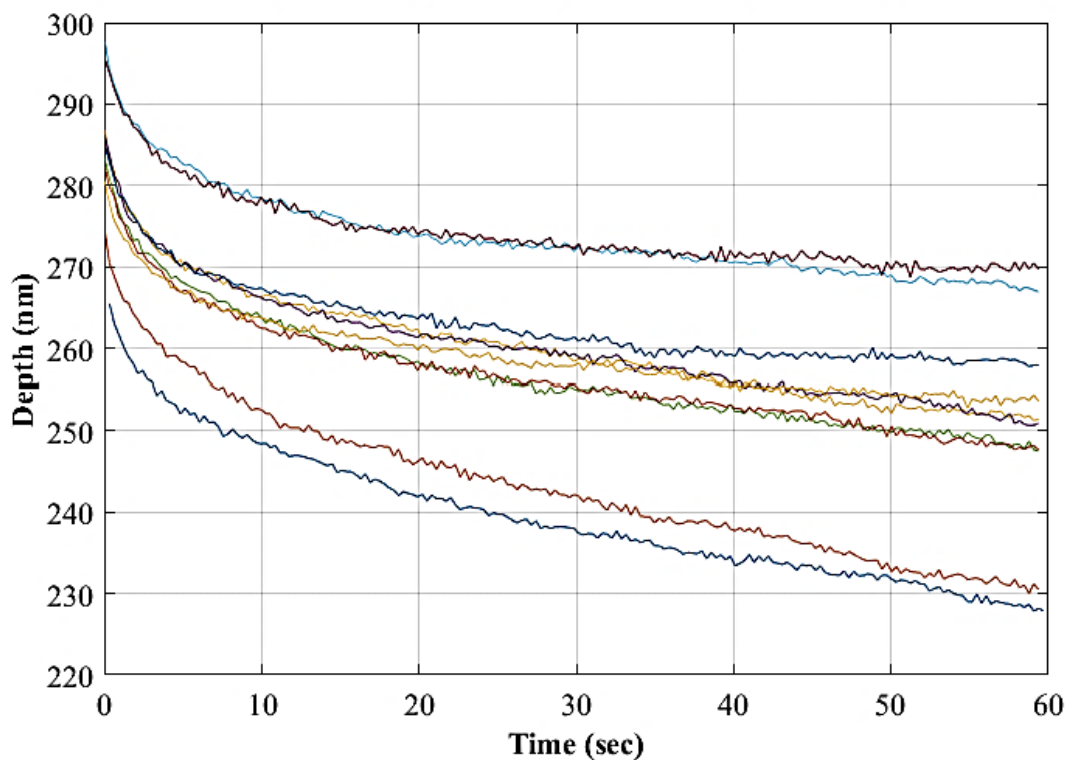
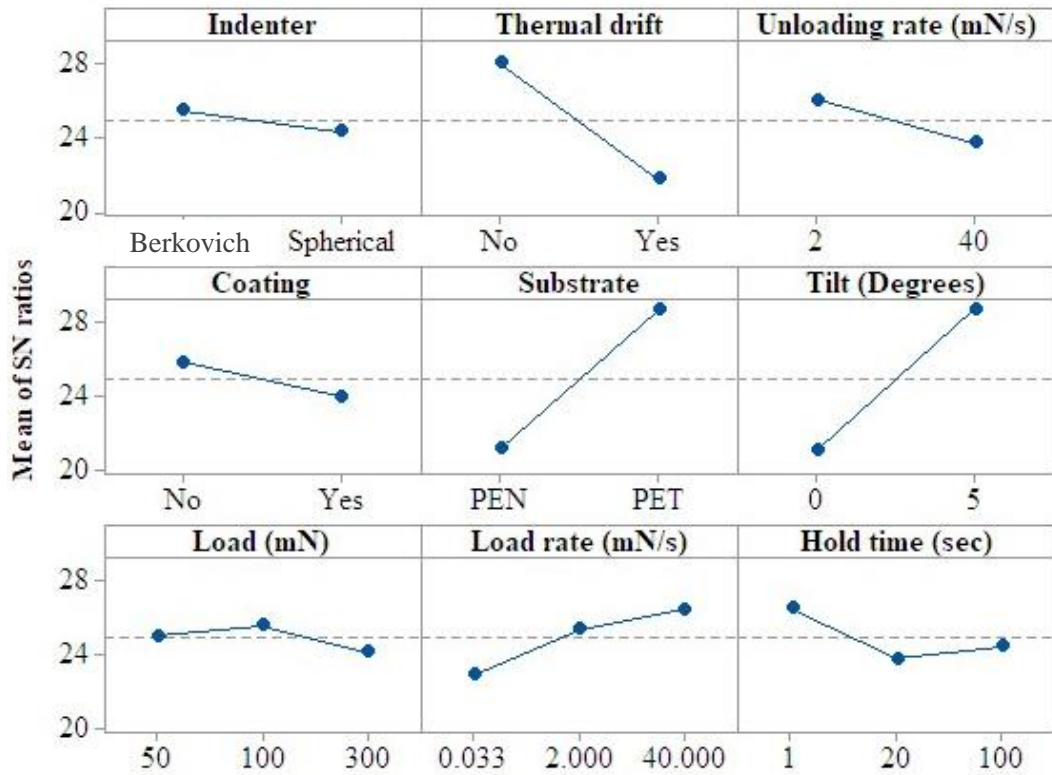


Figure 5-8 Nanoindentation depth against time plot for TiN coating (150 nm) on PET at 10 different indentations with Load=2 mN, Load rate = 2 mN/s, Unloading rate=0.1 mN/s and Post thermal drift of 60 s.

expansion. However, the gradient varies for all the indents. This leads to variation in the results. Besides this, it is also assumed that the thermal drift is constant during each test. In reality as the indenter penetrates the sample and on further occurrence of more permanent deformation the temperatures in the sample can increase as high as 100 °C, usually in the plastic zone somewhat beneath the indenter (Fischer Cripps, 2011, p.78). As plastic deformation is heterogeneous in nature the thermal gradients within the sample would vary. Upon unloading the temperature stabilizes within the sample in which the thermal gradients decrease. In the Taguchi orthogonal array adopted it was assumed the thermal gradient doesn't vary across the test. At the nano scale, the effect of applying thermal drift, depends on the loading/unloading cycle time, is insignificant as seen for the data means, but has the most variation due to the S/N ratios. Looking at Figure 5-9, the modulus response S/N ratio plots with no creep correction, in comparison to Figure 5-7 with creep correction, the only difference is that now the tilt and the thermal drift do show some significance at nano scale. It was the effect of the creep correction on the elastic modulus that showed the tilt and thermal drift to be insignificant. The reduction in significance at the nano scale for the thermal drift can be attributed to less penetration of the indenter due to the reduced time leading to less plasticity and the amount of heat generated. As the load increases the heat generated will increase as the plastic zone increases, so in contrast a larger effect in applying a thermal drift is seen in the data mean (see Figure 5-7a) at the micro scale. By applying a thermal drift correction, the variability of the response across a number of tests is reduced, where thermal drift is seen to vary from test to test. Thus, in further studies, the thermal drift correction must be applied as it has a distinct effect when creep is accounted for.

A number of factors were examined for the reliability of indentation tests. Other factors which were not considered were the different machine setups and different calibration

a) Modulus response, no creep correction, using data means at micro scale



b) Modulus response, no creep correction, using data means at nano scale

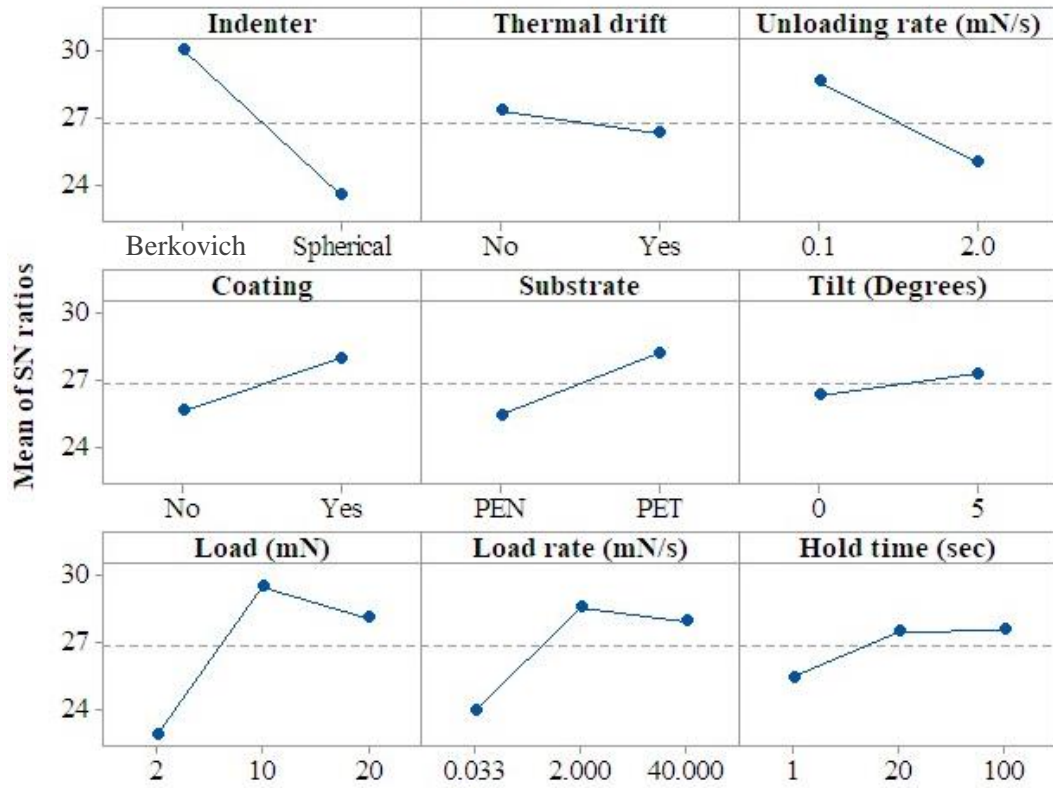


Figure 5-9 Main effects with no creep correction Signal-to-noise ratio plots a) micro scale and b) nano-scale

procedures which were outside the scope of this work. However, any test equipment, no matter how well calibrated, will have more variability at the nano scale compared to the micro. This is one limitation that cannot be avoided due to the present available technology.

5.3 Variability of PET and PEN

A detailed examination is given on the variability of PET and PEN. Nanoindentation results of coated PET and PEN systems will only be valid when the substrate is stable otherwise ageing effects and visco-plastic effects are interlaced. Also, ageing effects will present extra variability within the results. XRD (see section 3.3.2) and nanoindentation were used to examine variability and establish structural stability of these polymer substrates. If these polymers are not stable over time then the nanoindentation data cannot be compared.

5.3.1 Variability of PET compared to PEN

The XRD technique used is detailed in section 3.3 along with the determined variability associated with the test equipment. Also, a background was given in section 3.2.1 on the factors affecting the mechanical properties of polymers. Apart from the testing associated with the XRD test itself Experiment 5.5 was performed on both PET and PEN samples to determine the effect of rotating the sample on the intensities. Rotation of the sample can be seen in Figure 5-10 relative to the X-ray beam. The effect of angle/coverage on XRD results, with a scan time of 600s, can be seen in Figure 5-11 along with the standard

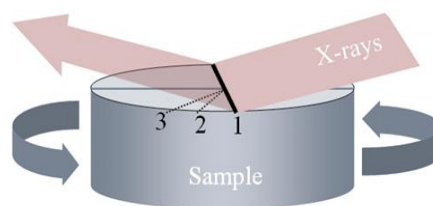


Figure 5-10 Sample rotation relative to the X-ray beam

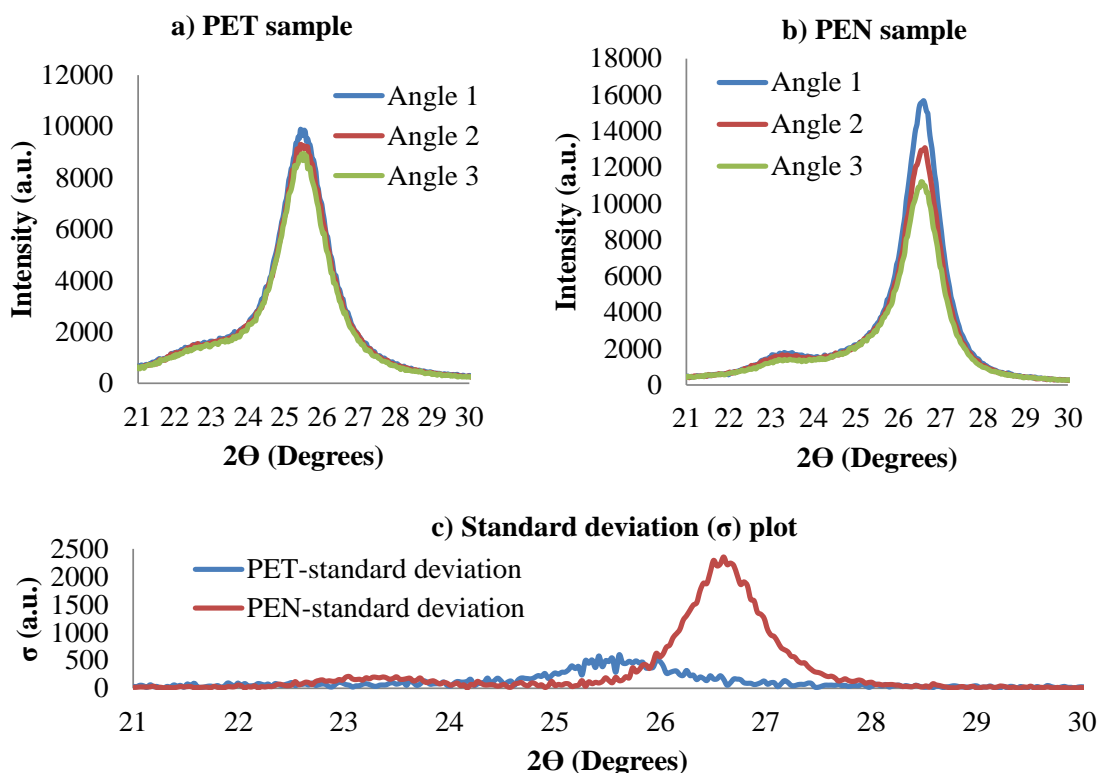


Figure 5-11 Effect of different sample and angle/coverage on XRD results with a scan time of 600s a) PET, b) PEN and c) Standard deviation (σ)

deviations (σ) for PET and PEN. It is clear that for PEN, from angle to angle, the variation is greater than that for the PET sample as shown in Figure 5-11c the standard deviations plot. This suggests that the structure of PEN is less homogeneous than for the PET sample and would manifest more variability when the mechanical properties are probed.

5.3.2 Ageing behaviour of PET and PEN

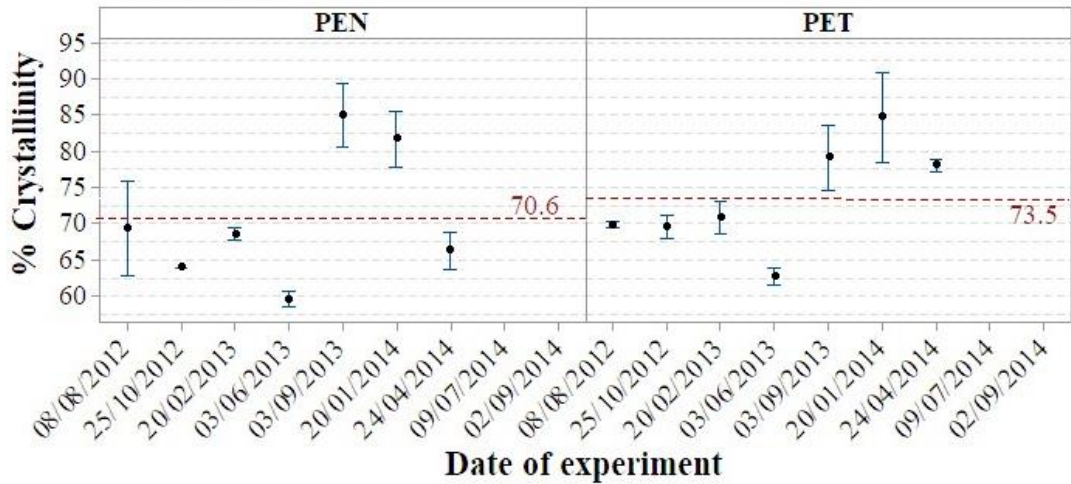
The internal structure of polymers changes with time and this in turn affects the mechanical properties (see section 3.2). When conducting deformation experimentation over a long time period, the results may not be valid due to this change in internal structure. Therefore, it becomes necessary to monitor the ageing behaviours of these compliant substrates over this study period.

For monitoring the ageing, the samples of PET and PEN were cut from a batch of A4 sample sheets, manufactured at the same time by the same fabricating processes.

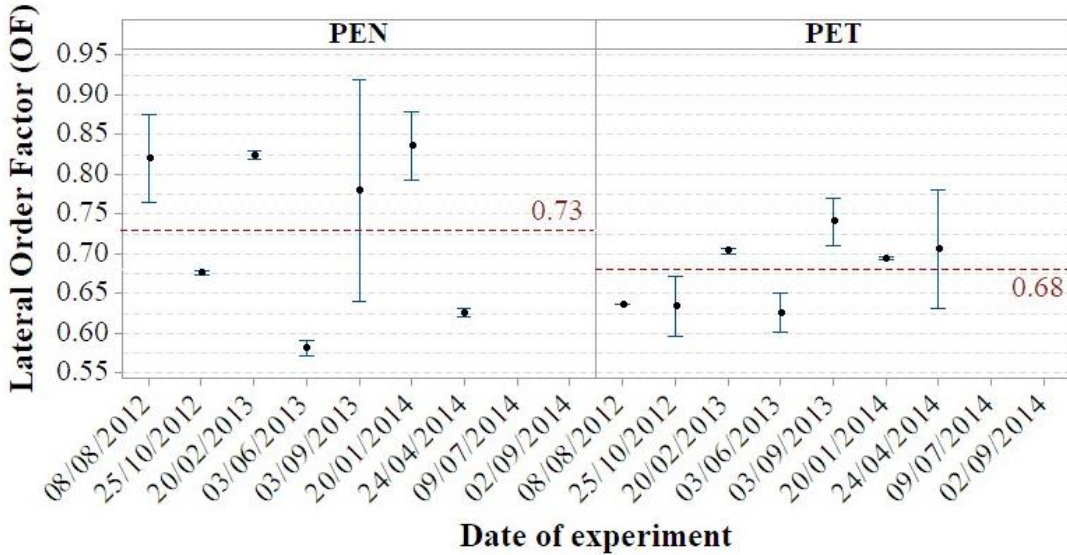
The ageing test samples were drawn, from this pool of samples, to replicate the use of samples in thin film studies, as samples for thin film deposition were taken also from that pool of samples. The aged test samples have been more prone to ageing since they were exposed to more light, temperature variations and repetitive XRD radiation. In order to distinguish the ageing effect from the in-sample variation, a separate study was conducted.

The method of monitoring the ageing using XRD is presented in section 3.3.2. Experiment 5.6 was conducted to examine ageing. Cut samples of PEN and PET sheet 125 μm were mounted in the XRD equipment described in section 3.3 and the scattering intensities were recorded every 0.031° in phase, with a range of $2\theta = 10$ to 35° for a test run of 1800 s. These tests were done every three months. Two factors, the Lateral Order Factor (OF) and the percentage crystallinity were measured over a period of two years. The error bars plots over the period are shown in Figure 5-12a and b. The error bars indicate one standard error from the mean value. These plots did not indicate if the substrates were stable, as values fluctuated over the period significantly. To determine if this was the in- sample variation or a change in structure due to ageing, the hardness was determined independently using nanoindentation over the same test period. To examine the ageing process using nanoindentation Experiment 5.7 was conducted. New samples were cut for PET and PEN and hardness tests were done every three months. These tests were done concurrent with Experiment 4.6 so the result could be compared. 10 indentations with 100 s dwell at maximum load of 50 mN. Loading and unloading rates were both 80 mN/s respectively. A post Thermal drift correction was applied. The H data for this experiment suggests both PET and PEN are stable over time (see Figure 5-12c).

a) % Crystallinity



b) Lateral Order Factor (OF)



c) Hardness (MPa)

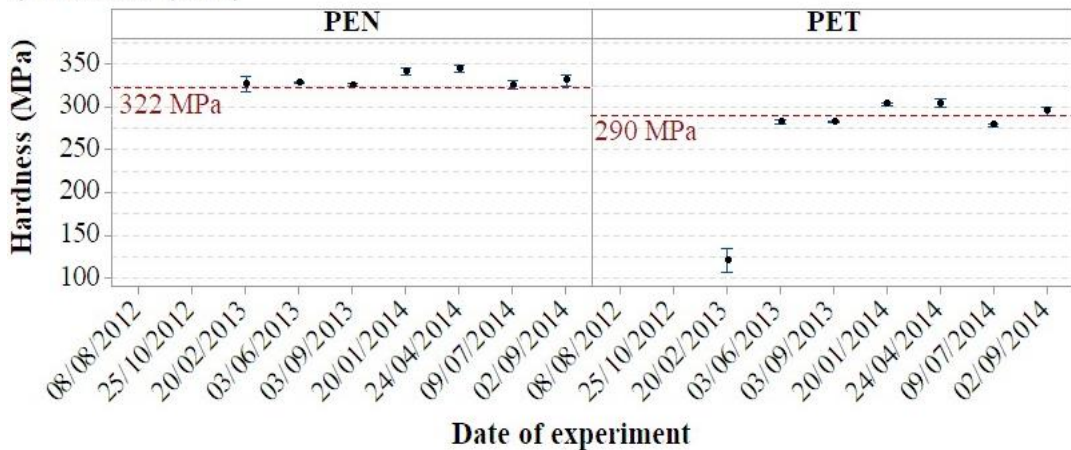


Figure 5-12 Error bar plot of material properties as a function of time, a) Percentage Crystallinity, b) Lateral order factor and c) hardness

The slight variation is mainly due to the in-sample variations or testing environment variation, despite the fact both were closely controlled. Even if there was a linear 0.5 GPa change in the H over the two years, having the time of completion of roughly two weeks for each of the DOE, within this timescale the change in substrate properties would be negligible or comparable to the in-sample variation. Thus, no ageing effects were considered when examining the results for each individual DOE. Also, as the results for each DOE are considered separately and cannot be compared, due to being in different set groups, the time period of an individual DOE needs just to be considered for the ageing, which is much less than the monitored period. This further reduces the effect of any slight ageing if any.

5.3.3 Variation across different PET and PEN samples

The percentage crystallinity and the OF showed a great amount of variation. As different samples were used each time it is necessary to determine if this was in-sample variation or associated with the method. The in-sample variation was examined separately using nanoindentation. Variation within the sample from sheet to sheet and within different position on the sheet was investigated.

For Experiment 5.8 Gauge repeatability and reproducibility (R & R) study was conducted to determine the variation on the response due to the samples. Gauge R & R studies investigate/compare statistically variability in the measurement system to the process variability. The studies allow determining how much of the overall variability is caused by different operators, between different parts and testing methods. Measurement system's variation less than 10% of process's variation is deemed to be acceptable (Minitab 18 support, 2019b). In the study, samples were compared by indentation on three different regions on an A4 sheet (P1, P2, P3), repeated on two different sheets (S1, S1), for each PEN and PET material. A maximum load of 10 mN, unloading and loading rate

at 2 mN/s and a dwell time of 10 s at maximum load was considered. Thermal drift correction was calculated using the post-indentation drift calibration data.

For both PEN and PET results from H and E measurements can be seen in Figure 5-13 and Figure 5-14. The overall variation is about 30 MPa for the H and 0.3 GPa for the E. So, variation is present within the samples itself this explains the variation of percentage crystallinity and OF. Even from Figure 5-12c the H can be seen to show this amount of

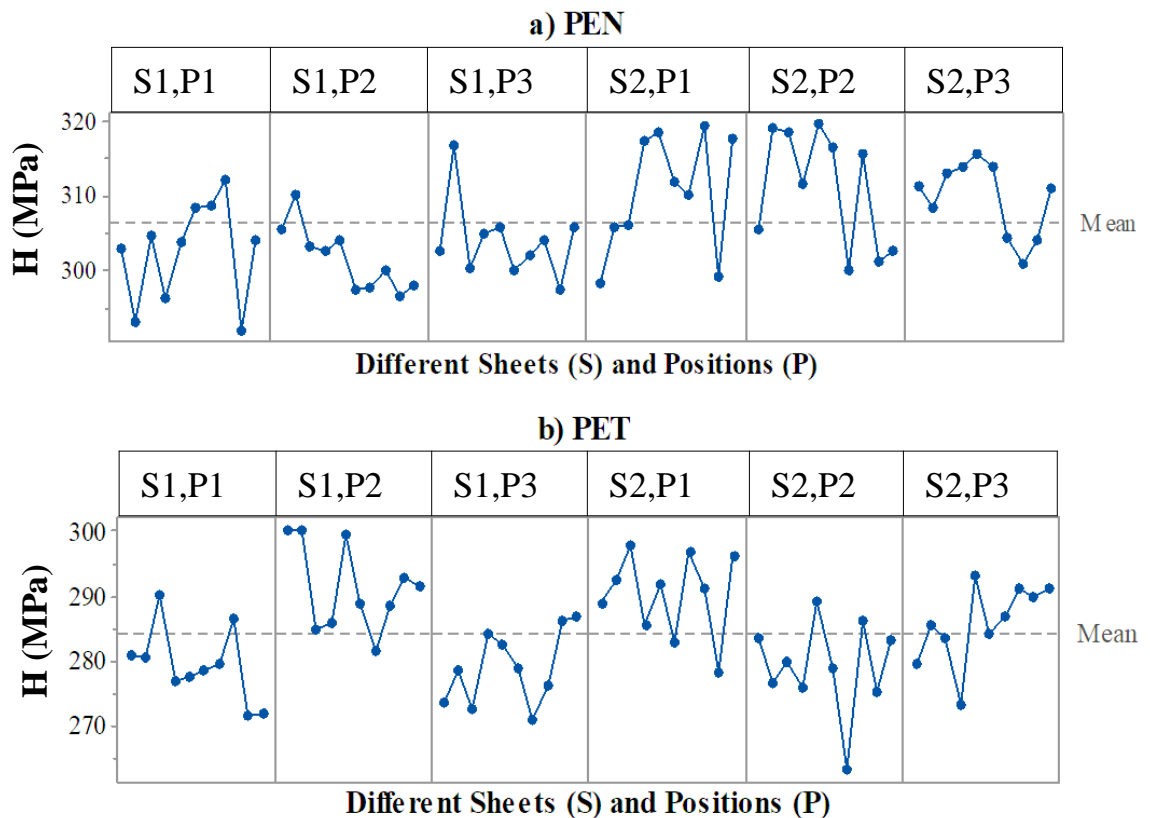


Figure 5-13 Gauge hardness run chart by parts for a single operator a) PEN and b) PET

variability which also includes the in-sample variation. However, the values do not vary as much as the percentage crystallinity and OF. One explanation is the size of area used within both tests, the XRD operates over a larger area to determine percentage crystallinity and OF, thus more variation compared to indenting on one site.

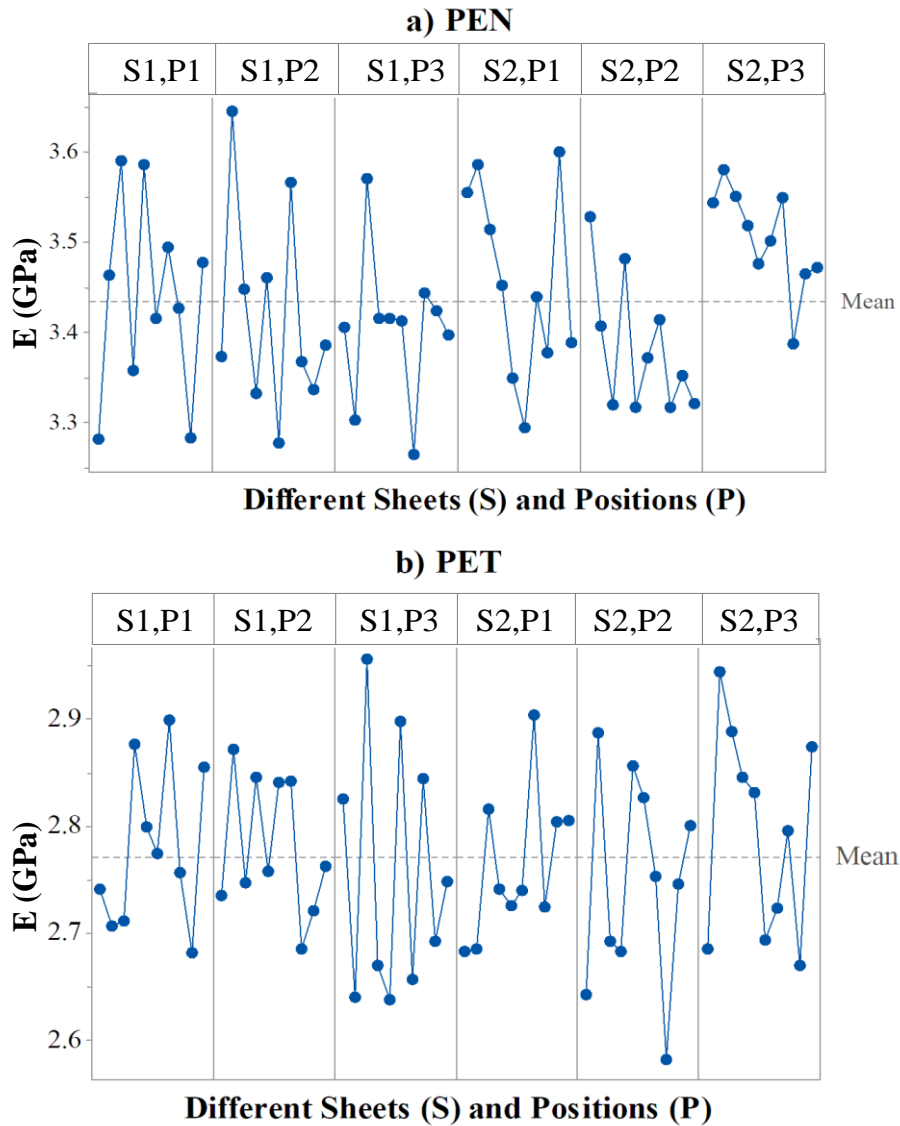


Figure 5-14 Gauge Modulus run chart by parts for a single operator a) PEN and b) PET

One of the assumptions made in the Gauge R & R study was that the variability of the one operator and mount compliance was constant from test to test i.e. the position of the sample in the machine has no effect. However, there must be variation present for the operator and the mount compliance embedded within the variation of the H and E or the variation present in H and E could be solely due to them. To examine this variation further the effect of H and E variation on the sample preparation was examined. In Experiment

5.9 three samples from the same region on a sheet of PEN were analysed to determine the variation on the response due to the effect of glueing. A maximum load of 10 mN, unloading and loading rate at 2mN/s and a dwell time of 10 s at maximum load were considered. Thermal drift correction was calculated using the post-indentation drift calibration data. The results in Figure 5-15 show H values for the three separately glued samples at each indent. The indents are independent to each other so the points on the

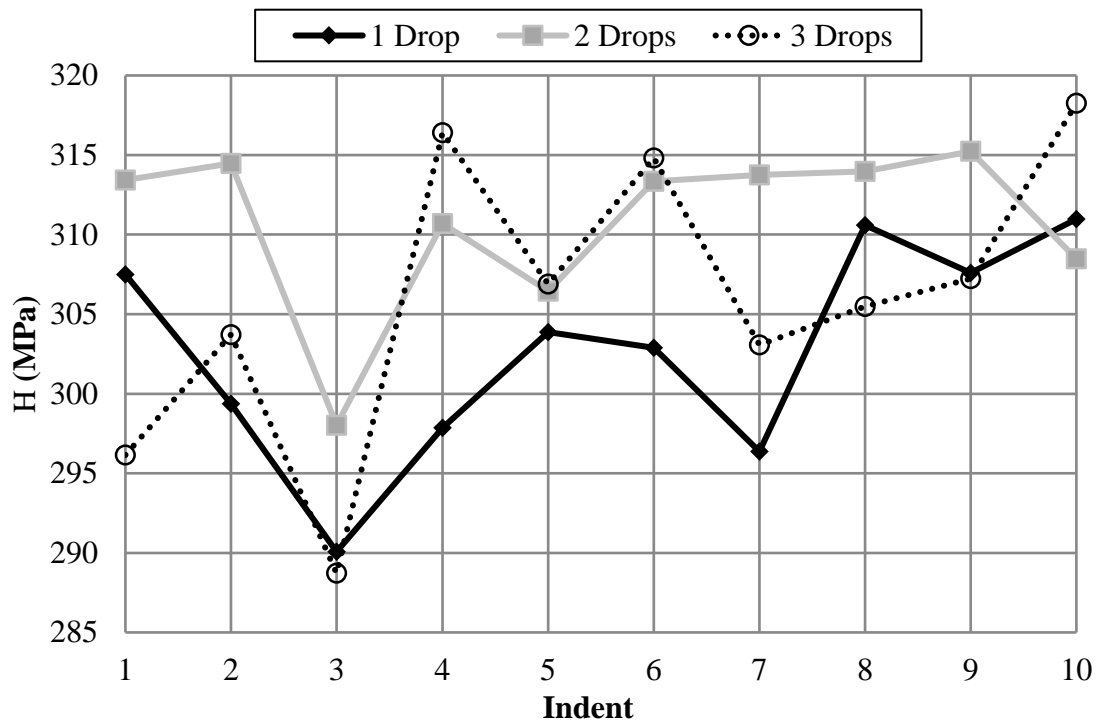


Figure 5-15 Effect of glue drops on the hardness of PEN

graph shouldn't be connected by a line. However, due to clarity the points were connected to distinguish each glued sample and how much variation occurred. It is evident that there is also variation present when glueing the sample to the sample holder and can also be linked to the variation of the operator or mounting compliance. For 3 drops it is about 30 MPa similar to the in-sample variation. As the drops decrease the variation also decreases becoming lower than the in-sample variation. Thus, becomes embedded within the in-

sample variation and this doesn't need quantifying as long as there is enough glue to stick the sample to the holder and doesn't exceed 2 drops. The results for the E values seen in Figure 5-15 are similar. The variation present when glueing the sample to the sample holder is determined by the variation of the means for the number of drops considered, and is about 0.05 GPa. Again, this variation is much lower than 0.3 GPa which was determined from Figure 5-14 thus it doesn't need quantifying due to it being embedded within the sample variance.

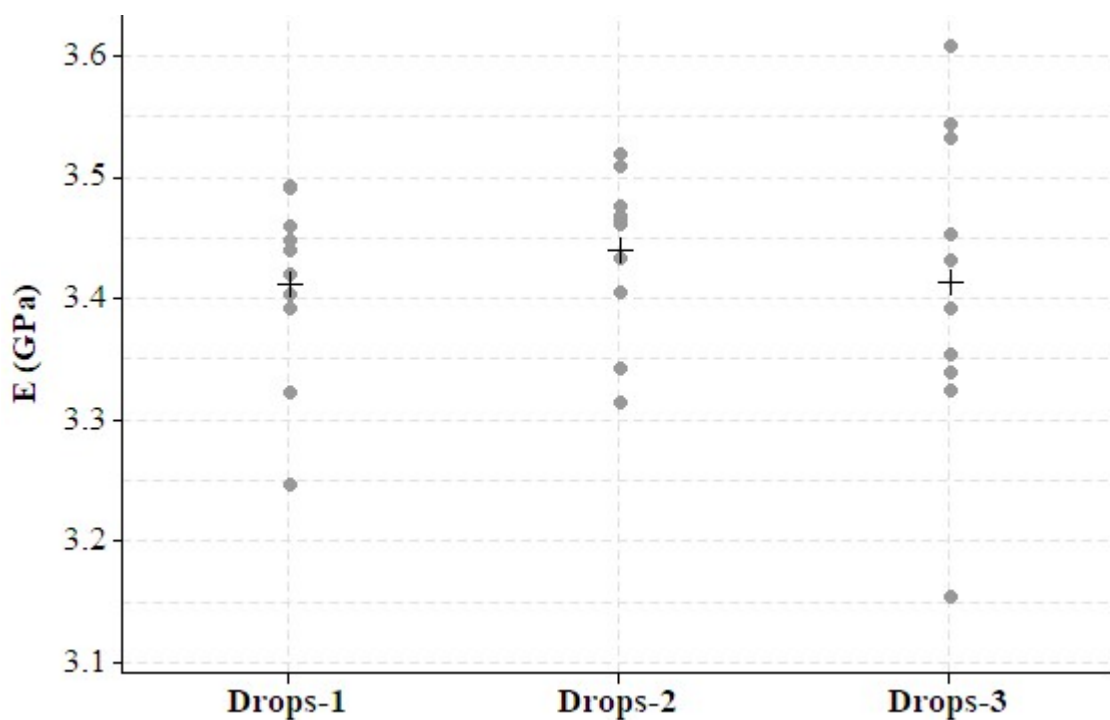


Figure 5-16 Effect of glue drops on elastic modulus of PEN, + are mean values.

In the Gauge R & R study it was not clear if the H and E values were due to the operator, mounting compliance or the in-sample variation. If assuming the effect of glueing is the same as the effect of the operator and mounting compliance then we can conclude by the above study that their variation is embedded in the variation of H and E. However, the main variability seen in the H and E values can be due to any one of these parameters.

So, minimising the glueing effect, which is intertwined with the in-sample variation, will also minimise the effects of the other factors that are embedded within the in-sample variation. It will be assumed that the Gauge R&Rs study for one operator and two drops of glue determines the in-sample variation of the sample, with the minimum effect of the operator and mounting compliance that is embedded within its variation.

5.4 Summary

An approach to reliable nanoindentation study is described consistent with the standard (ISO 14577-4, 2007–2016). By applying the approach to thin film coatings on compliant substrates the key factors were ranked and the five most important factors i.e. load, load rate, unload rate, indenter type, and hold period are selected for further studies. For the nanoindentation approach, the thermal drift correction was confirmed to be essential, however less significant for nano scale compared with the other factors. How the sample was mounted in the machine i.e. by the operator, how it was glued and tilt of the indenter with the sample can affect the deformation. Apart from the tilt and the glueing the other factors have minimum effect on the in-sample variation. It was established that the samples need to be fixed properly to the sample holder by not exceeding two drops of glue and the tilt angle needs to be controlled as much as possible by the operator. Independently the stability of the PET and PEN was established, confirming no ageing effects on their mechanical properties, so these polymers can be used for method validation.

The variations, due to machine factors, sample and in-sample, were examined, and can be useful when comparing to the variations due to the effects of different nanoindentation methodologies on the output data. In the next chapter the developed nanoindentation methodology, as used in this chapter and detailed in Chapter 4, is examined and validated using the above approach.

Chapter 6

EXAMINATION OF DU METHODOLOGY AND VALIDATION

6.1 Introduction

Using the approach in the previous chapter, different unloading methodologies, as proposed by the author, i.e. the DU methodology detailed in Chapter 4, and previous (G. Feng, 2002; Oliver and Pharr, 1992) with their associated corrections, are examined and compared. All these nanoindentation methodologies, considered at both nano and micro scales, with loads ranging between 0.1 mN to 200 mN, are rigorously validated against macroscale tensile tests. The effects on the output data when the surface roughness becomes more pronounced are discussed concerning the Roughness Depth Limit (RDL), and when testing silicon samples.

6.2 Examining the DU methodology

It is clear from Figure 2-7a that the stiffness and contact area are the main factors influencing the reduced modulus and hardness. However, methodologies by which the stiffness and contact area are determined will dictate the accuracy and reliability of elastic modulus and hardness data. The different methods examined with their associated fitting to the unloading data and corrections are tabulated in Table- 6-1, with details to the syntax used. Throughout this chapter, the methods will be referenced using the method syntax. In order to determine the reduced modulus and load relationship from the unloading data the analysis procedures for unloading stiffness and contact area are examined and discussed, starting with the unloading stiffness.

Table- 6-1 Method syntax with their associated methodologies

M1	=	DU	Developed method
		O	Oliver & Pharr
M2	=	L	Linear fit
		1	First order powerlaw fit
		3	Third order powerlaw fit
X1, X2, X3, X4, X5	=	M	Stiffness determined at maximum load
		F	Stiffness determined at FEP load
		S	Sink-in & Pile-up correction
		C	Creep correction
		P	Plastic correction
		D	Datum correction

Method syntax used

6.2.1 Examining the unloading stiffness

Initially, method DU-MCP is examined by finding the Modulus (E_{DU-MCP}) at maximum load with creep correction and sink-in correction. Experiment 4.1 highlights test materials and test conditions as in Appendix 4. The values of E_{DU-MCP} and $E_{FIT-DU-MCP}$ were compared (see Figure 6-1) for both PET and PEN polymers for all 27 different test conditions. $E_{FIT-DU-MCP}$ was calculated, using the 2nd order polynomial fit to E_{DU-MCP} against unloading load, at maximum load. Plots for both polymers show a very good match between the values computed for both methods. However, for experimental conditions at very low unload rates and small hold time, the reduced moduli calculated using the fit coefficients were different. The residuals plots show this for each indent at every test run. When these values are neglected, the reduced moduli were directly proportional to each other. Coefficients P1 and P2 were determined using linear least square fitting routine and are displayed on the figure. P1 the slope is very close to unity and P2 is very small close to zero, within these limits it is reasonable to presume that each of the two moduli have a one to one relationship. When determining E_{DU-MCP} at different testing conditions for both PET and PEN, the reduced modulus decreased with increasing

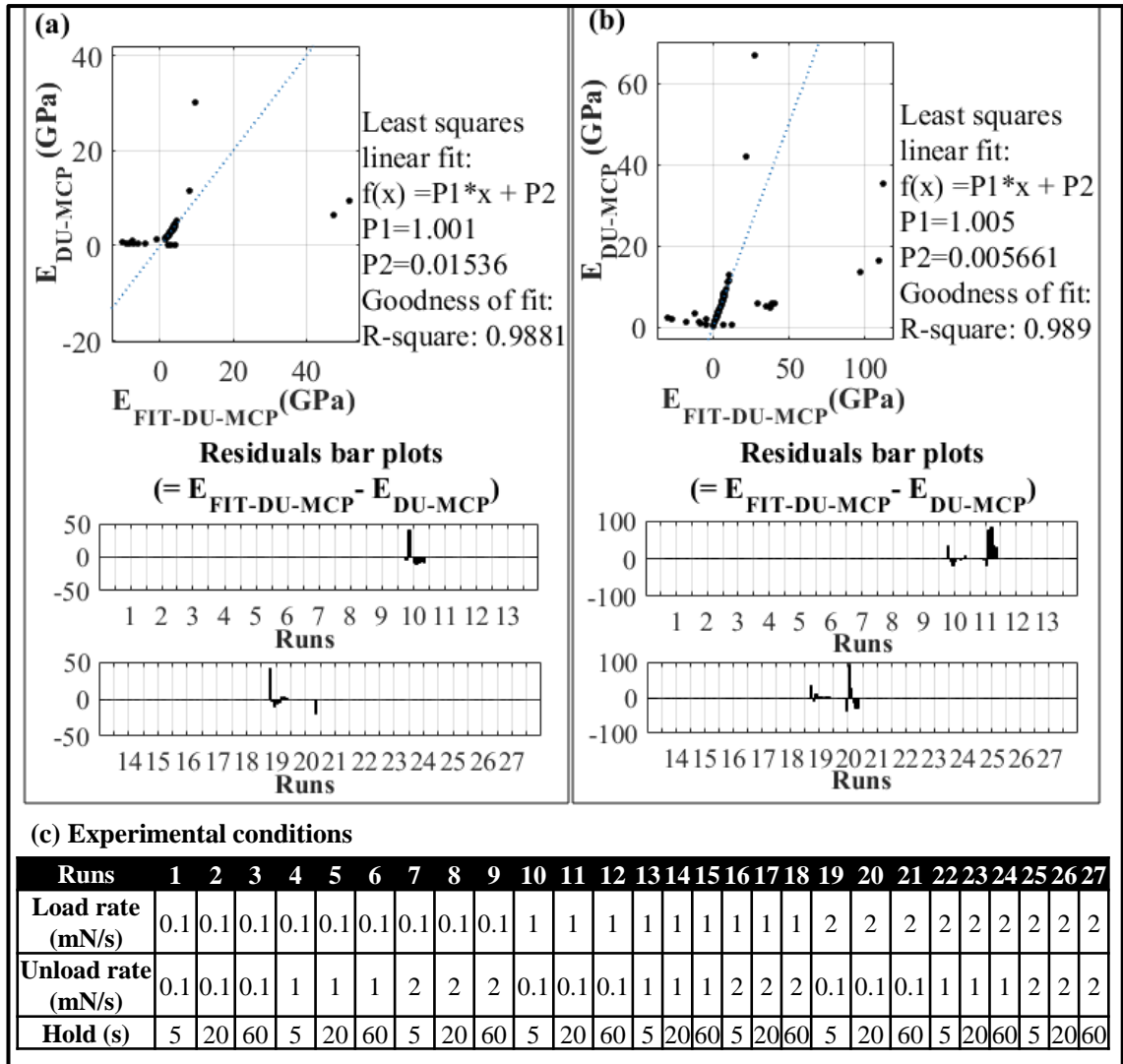


Figure 6-1 Linear fits of E_{DU-MCP} and $E_{FIT-DU-MCP}$ with residual plots for, a) PET, b) PEN and with c) Experimental run conditions for plots

load. However, $E_{FIT-DU-MCP}$, for same experimental conditions at different loads, do not show the same observed behaviour. This is shown in Figure 6-2 for the four different Reduced Modulus methods. For consistency, except for the load, all experimental conditions are the same for each. Again E_{DU-MCP} and $E_{FIT-DU-MCP}$ are presented on the plot, it can be seen that they are nearly identical (a difference of < 0.1 GPa) as expected and that they decrease with increasing load. The other two Reduced moduli were calculated by their fitted coefficients similar to $E_{FIT-DU-MCP}$, but at two different loads

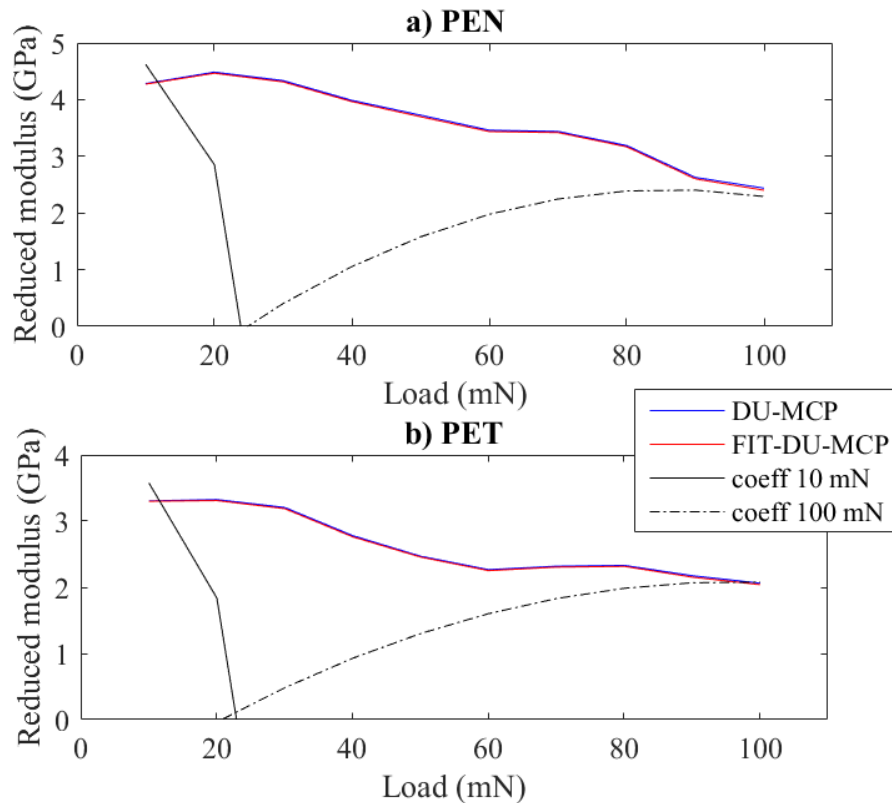


Figure 6-2 Reduced modulus against load determined by four different methods using for run 1 (see Appendix 4) for a) PEN & b) PET

10 mN and 100 mN respectively. At 10 mN the reduced modulus rapidly decreases, whereas for the 100 mN load curve the reduced modulus increases with load. The behaviour was similar for both polymers. Reduced moduli curves determined by fit coefficients show different behaviour and indicate that the reduced moduli as a function of load cannot be determined from the unloading graph. The main reason for this is that the method for determining the plastic depth has a direct influence on the contact area and consequently on the reduced modulus calculations. The results above will be explained by examining the unloading stiffness at test condition of a hold time of 5 s, load rate and unload rate of 0.1 mN/s (Run 1 in Appendix 4). Figure 6-3 shows three different stiffness's against the displacement measured during unloading. The dotted lines indicate the stiffness-load relationship calculated by the fit coefficients, determined using the DU

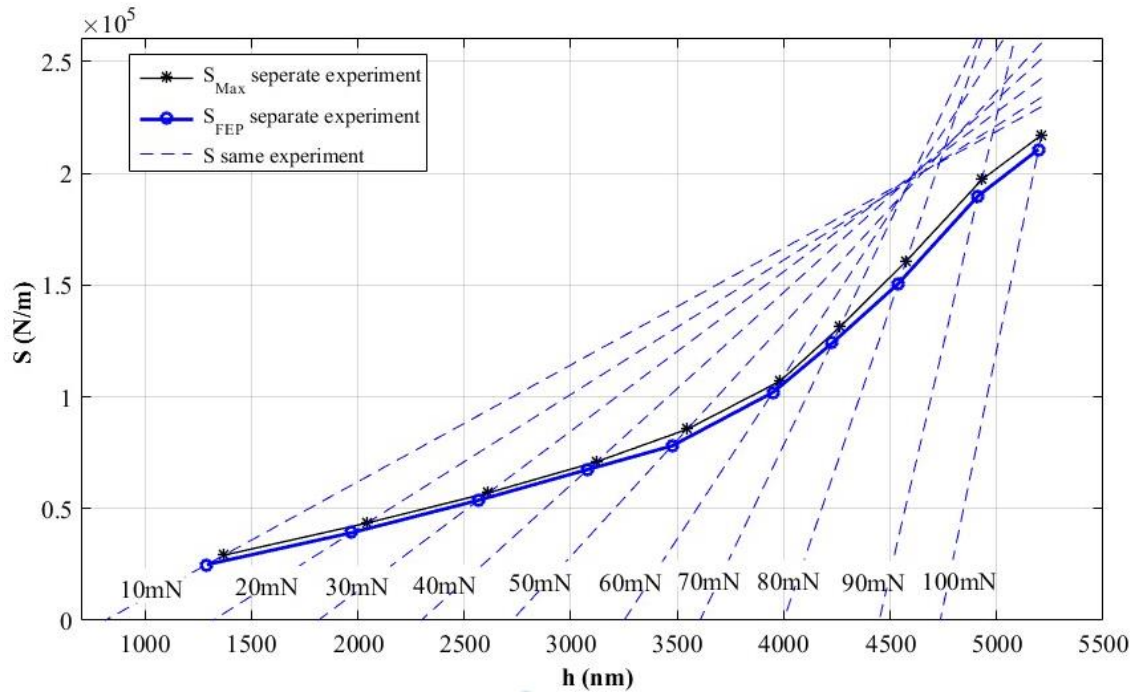


Figure 6-3 Displacement (h) against stiffness (S) determined by three different methods, at maximum load and FEP using separate experiment, and by using fit coefficients at each load, for run 1 (see Appendix 4) for PET polymer

method at a corresponding load test condition, by fitting stiffness against load using 2nd order polynomial fit. For each individual indentation the stiffness at FEP (S_{FEP}) and the stiffness at maximum load (S_{Max}) was also determined, and can be seen on the graph. The main observation is that the slope of the fitted i.e. dotted lines at a particular load does not match the slope of the S_{Max} and S_{FEP} i.e. black or blue lines, at that corresponding load. For this reason, the unloading curve stiffness cannot be used to determine the reduced modulus–load relationship. Also, along the unloading curve data both S_{Max} and S_{FEP} can be interpolated. However, between maximum load and FEP this procedure should not be valid, as explained in section 4.3.4. However, it will be shown that the variance, between interpolating S_{FEP} and S_{Max} , is around 5-10 %. Figure 6-4 (zooming in on Figure 6-3) shows interpolation of the S_{FEP} to maximum displacement and compared to the value of S_{Max} for the 90 mN load. The variance between these two values of

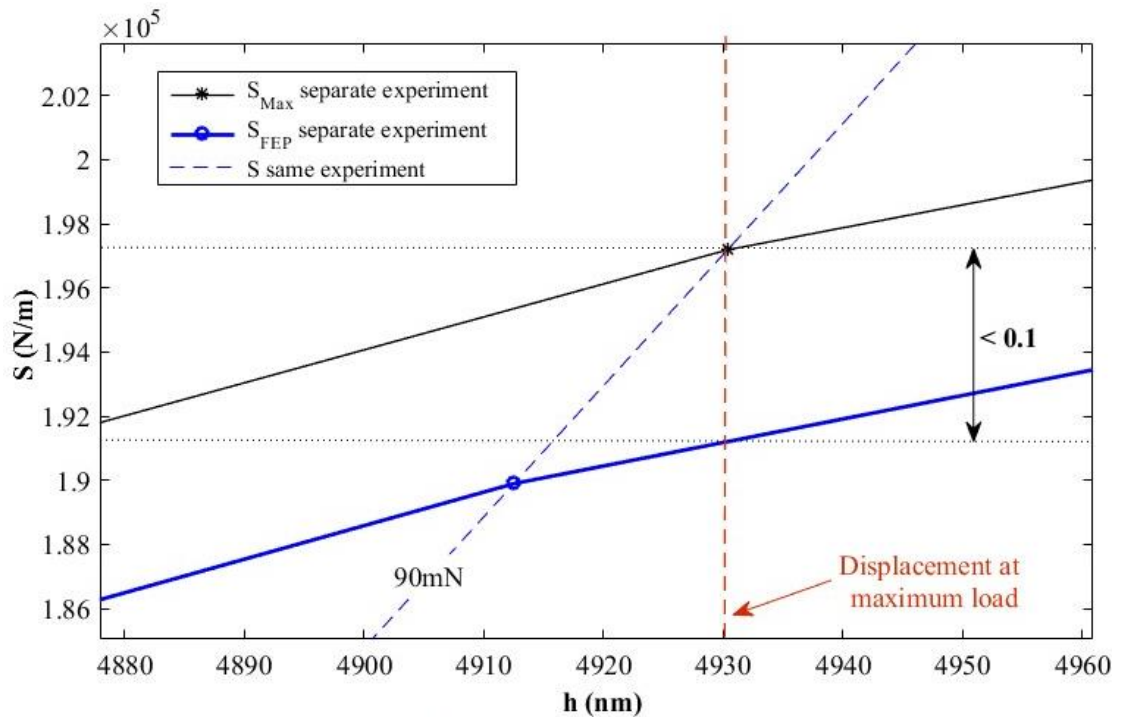


Figure 6-4 Displacement (h) against stiffness (S) determined by three different methods, at maximum load and FEP using separate experiment, and by using fit coefficients at each load, for run 1 (see Appendix 4) for PET polymer

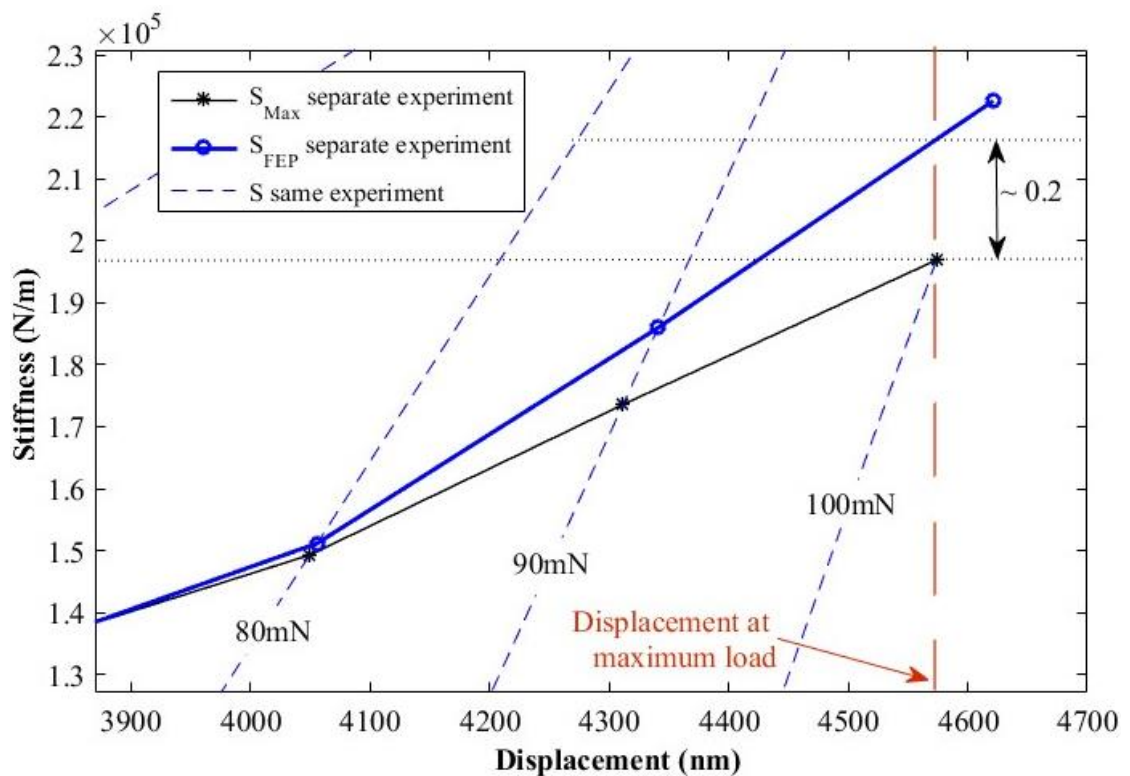


Figure 6-5 Displacement (h) against stiffness (S) determined by three different methods, at maximum load and FEP using separate experiment, and by using fit coefficients at each load, for run 10 (see Appendix 4) for PET polymer

calculating S_{Max} is roughly $\frac{\Delta S}{S} = \frac{0.1}{1.98} \approx 5\%$. Examining Figure 6-5 for which the experimental conditions are such that the nose out effect is more prominent (hold time of 5 s, load rate of 1 mN/s and unload rate of 0.1 mN/s), it shows the depth at maximum load is less than at FEP, and the S_{Max} values occurs below the S_{FEP} . The stiffness variance in this plot is around $\frac{\Delta S}{S} = \frac{0.2}{2.2} \approx 10\%$ at a load of 100 mN. Thus, as the viscous effects increase, the variance increases.

It should be emphasised that the displacement, at maximum load for each of the indents, is a combination of elastic, plastic and viscous displacements. To determine the reduced modulus the elastic stiffness is required, thus any plastic/viscous deformation had to be eliminated from the data. For a viscoelastic plastic material, during loading plastic deformation occurs, during hold there can be plasticity, and upon unloading the existence of reverse plasticity. Removing reverse plasticity effect is incredibly difficult or near impossible as it is also intertwined with viscous effects. The author presented a method to account for the plasticity (see section 4.3.4). In further examining the stiffness as a function of load, using creep and plastic corrections separately, it is reconfirmed, by examining Figure 6-6a, that the coefficients fitted stiffness's (indicated by black lines) cannot be used to determine experimental load-modulus relationship. When either creep or plastic corrected stiffness's are used, as seen in Figure 6-6b & c, the range for stiffness is reduced with the slope reducing. This will cause less variance between the values of S_{Max} and S_{FEP} . Even though the author has established the coefficients can be used to calculate the stiffness at maximum load and FEP within certain variance, dependent on the experimental conditions, to use them to calculate stiffness's during unloading and determining the reduced modulus as a function of load still needs examining further.

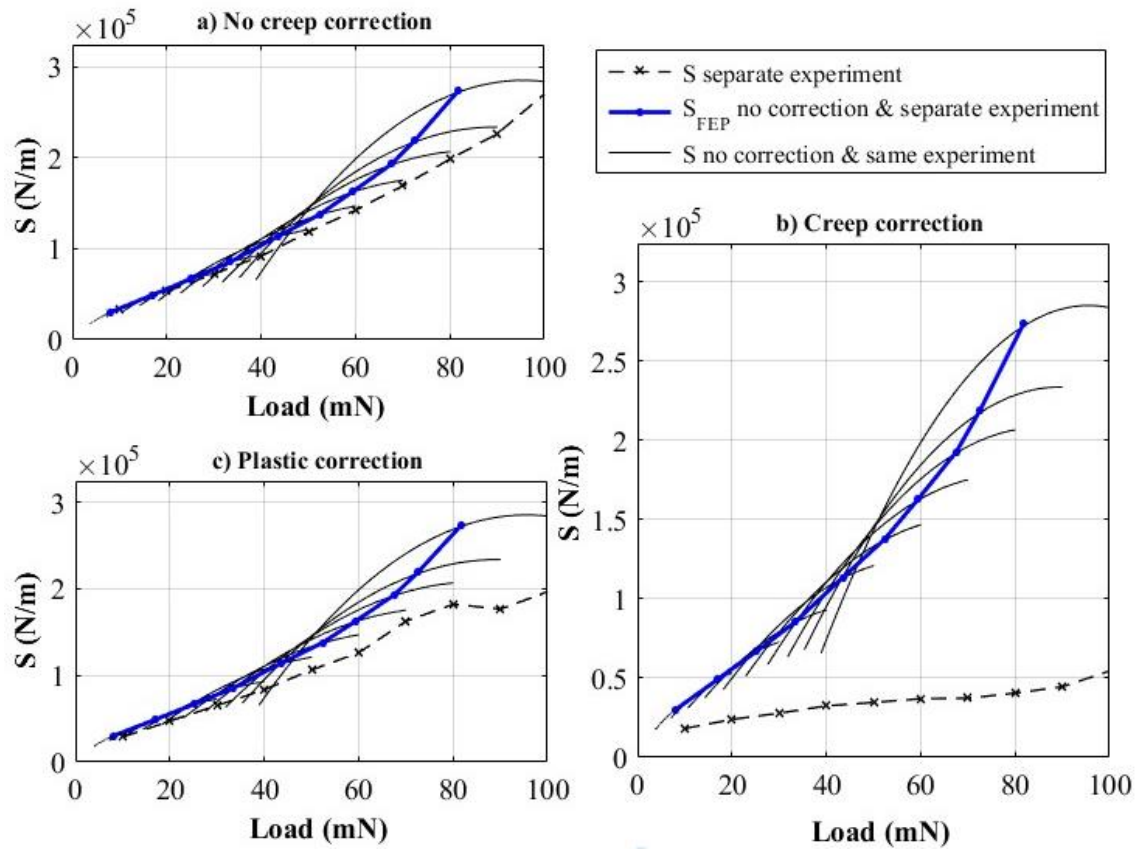


Figure 6-6 Stiffness (S) against load, for PET, determined by three methods using run 10 (see Appendix 4), a) No creep correction, b) Creep corrected, and c) Plastic correction

6.2.2 Effect of using the displacement or load for determining stiffness

When determining the S_{Max} from the unloading curve the stiffness could be either be a function of load or displacement, for function of load the equation is:

$$S = \frac{1}{bm \frac{P^m}{P}} \quad \text{(Equation 6-1)}$$

when fitting equation used is $h = a + bP^m$, where h is displacement, P is load, a, b and m are the coefficients. For function of displacement the equation is:

$$S = \frac{am(h - b)^m}{(h - b)} \quad \text{(Equation 6-2)}$$

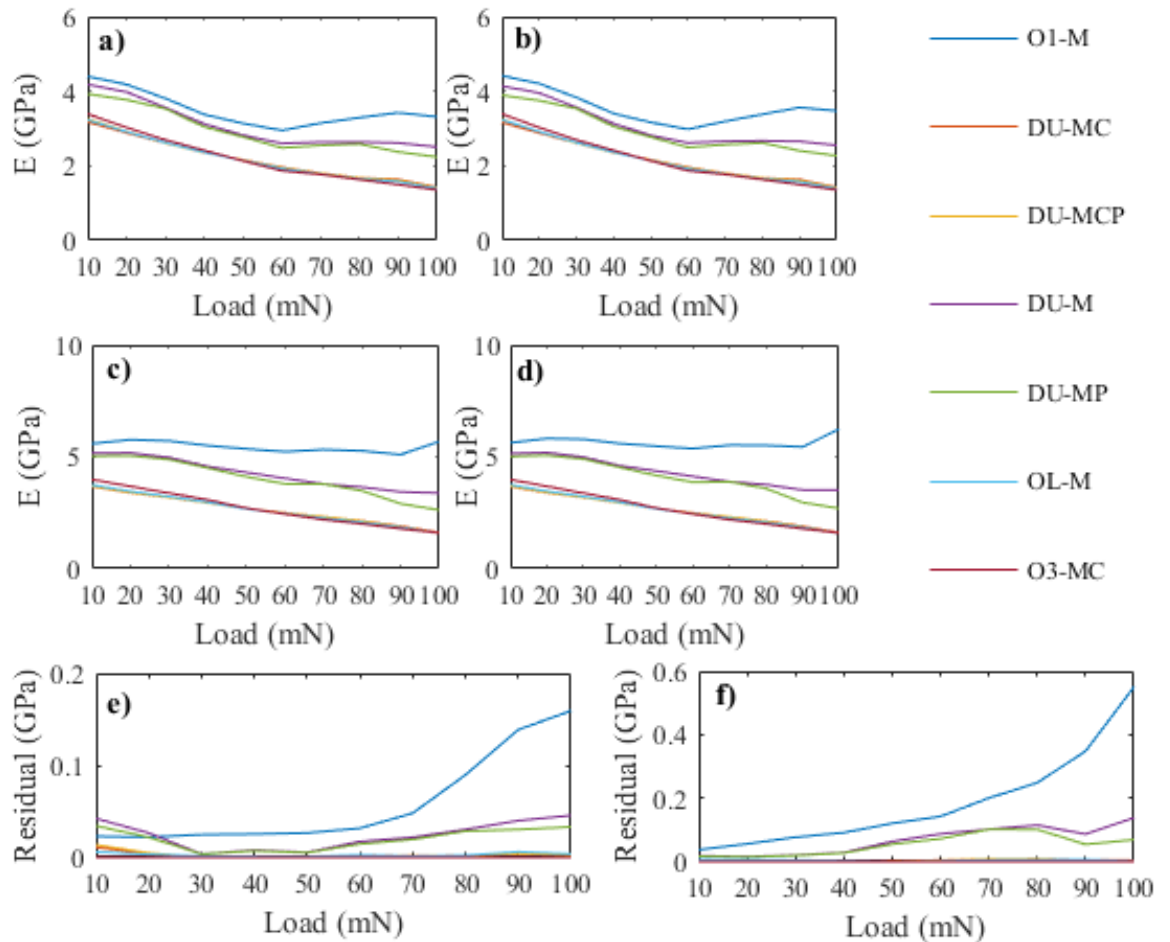
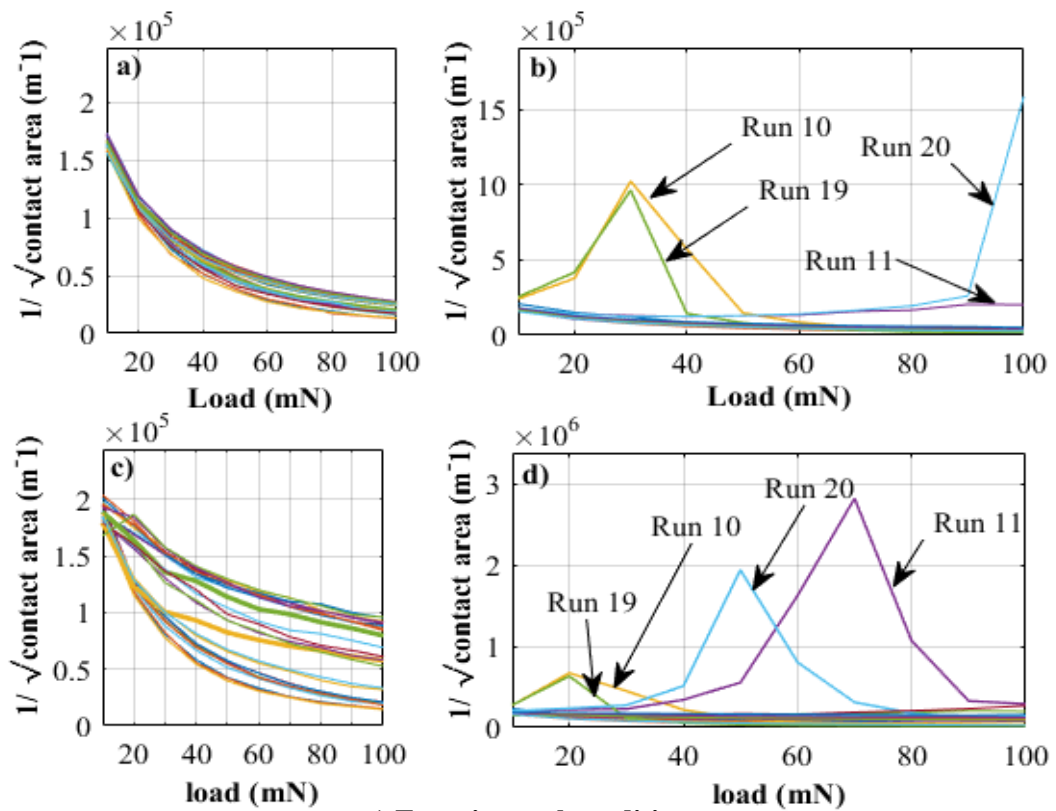


Figure 6-7 Elastic modulus (E) against load for, a) PET stiffness determined by displacement, b) PET stiffness determined by load, c) PEN stiffness determined by displacement, d) PEN stiffness determined by load, e) Residual plot for PET, and f) Residual plot for PEN

when a power law function (Equation 2-4) is used. To examine if value of the elastic modulus would depend on how the stiffness is determined, a comparison was performed for various methods, refer to table 6.1 for method syntax. The elastic modulus change, using the two equations for the stiffnesses, are plotted against the load in Figure 6-7 for both PET and PEN. Each plot was constructed using data from Run 1 (see Appendix 4). From the residual plots, Figure 6-7 e and f, that show the difference between the two results for each polymer, all methods values were less than 0.2 GPa except for O1-M showing residuals as high as 0.55 GPa. With higher loads higher residuals were found.

6.2.3 Examining the contact area

In section 6.2.1 it was shown that the stiffness increased with load. In order to examine how the reduced modulus would vary with load, the effect of the contact area needs to be known as the reduced modulus is a function of both the contact area and the stiffness. In $S = \beta \frac{2}{\sqrt{\pi}} E_r \sqrt{A}$ (Equation 2-5) the stiffness (S) is proportional to the reduced modulus (E_r), whereas the reciprocal of the square root of the contact area ($1/\sqrt{A}$) is proportional to it. In Figure 6-8a & b $1/\sqrt{A}$ is plotted against load for PEN and PET considering creep



e) Experimental conditions

Runs	1	2	3	4	5	6	7	8	9	10	11	12	13	14	15	16	17	18	19	20	21	22	23	24	25	26	27
Load rate (mN/s)	0.1	0.1	0.1	0.1	0.1	0.1	0.1	0.1	0.1	1	1	1	1	1	1	1	1	1	2	2	2	2	2	2	2	2	2
Unload rate (mN/s)	0.1	0.1	0.1	1	1	1	2	2	2	0.1	0.1	0.1	1	1	1	2	2	2	0.1	0.1	0.1	1	1	1	2	2	2
Hold (s)	5	20	60	5	20	60	5	20	60	5	20	60	5	20	60	5	20	60	5	20	60	5	20	60	5	20	60

Figure 6-8 Reciprocal of the square root of contact area against the load, for a) PET no creep corrected, b) PET creep corrected, c) PEN no creep corrected, and d) PEN creep corrected. e) Experimental conditions for the 27 runs considered in each graph.

and non-creep corrected data. In general, the effect of increasing the contact area is to apparently reduce the reduced modulus as the load increases, whereas increases in the stiffness increase the reduced modulus. From Figure 6-2, as the reduced modulus decreases with load, the effect of contact area is more influential than the effect of the stiffness in determining the reduced modulus. Apart from this, from the residual plots in Figure 6-1, runs 10, 19 and 20 for PET and 10, 11, 19 and 20 for PEN, show the most variation between the E_{DU-MCP} and $E_{FIT-DU-MCP}$ values, with residuals > 10 , also note the loads for each run (refer to Appendix 4). In Figure 6-8 b & d for these same runs, at these particular loads, $1/\sqrt{A}$ is higher indicating a possible change in mechanism i.e. assuming viscous to plastic deformation. The penetration rate at the end of hold can be directly related to the mechanism occurring. At these conditions the rates are higher and noticeable plastic deformation with high viscous effect occurring. Surely, it is the determined value of the contact area, at high viscous behaviour, that governs the quantity of fit of the reduced modulus curve. The contact area can be determined accurately at maximum load and FEP with associated assumption detailed in section 4.5. Even when the viscous effects are intermediate, i.e. runs 11 and 20 show higher $1/\sqrt{A}$ values. Creep correction below at FEP is not valid as the penetration rate is determined at the maximum load only. When assuming creep rate, at FEP, is the difference between the rates i.e. penetration rate at max load minus the plastic rate, then both plastic and creep correction can be applied. However, in using the creep correction the contact area behaviour during unloading, at high viscous behaviour, leads to complex values of the Reduced moduli 's when calculated from a polynomial fit of the second order, a different fit procedure is needed to capture the behaviour of the reduced modulus with more precision under these conditions and the residual between E_{DU-MCP} and $E_{FIT-DU-MCP}$ would become zero. Even though if a different fit is used, the reduced modulus against load curve for each indent

doesn't represent the behaviour of the system. The observation that the contact area decreases with load and below a certain value the contact area starts to increase indicates the method of determining the plastic depth in this circumstance is not correct, and exact evolution of the contact area during unloading is not revealed.

Further comparison was made between PEN and PET using creep factor against reduced modulus plots (see Figure 6-9). The creep factors were determined in the same way as Feng's work (G. Feng, 2002), for values of 0 to 1.4. It can be seen the creep correction is applied sufficiently except at the runs indicated with round shape which occur at high

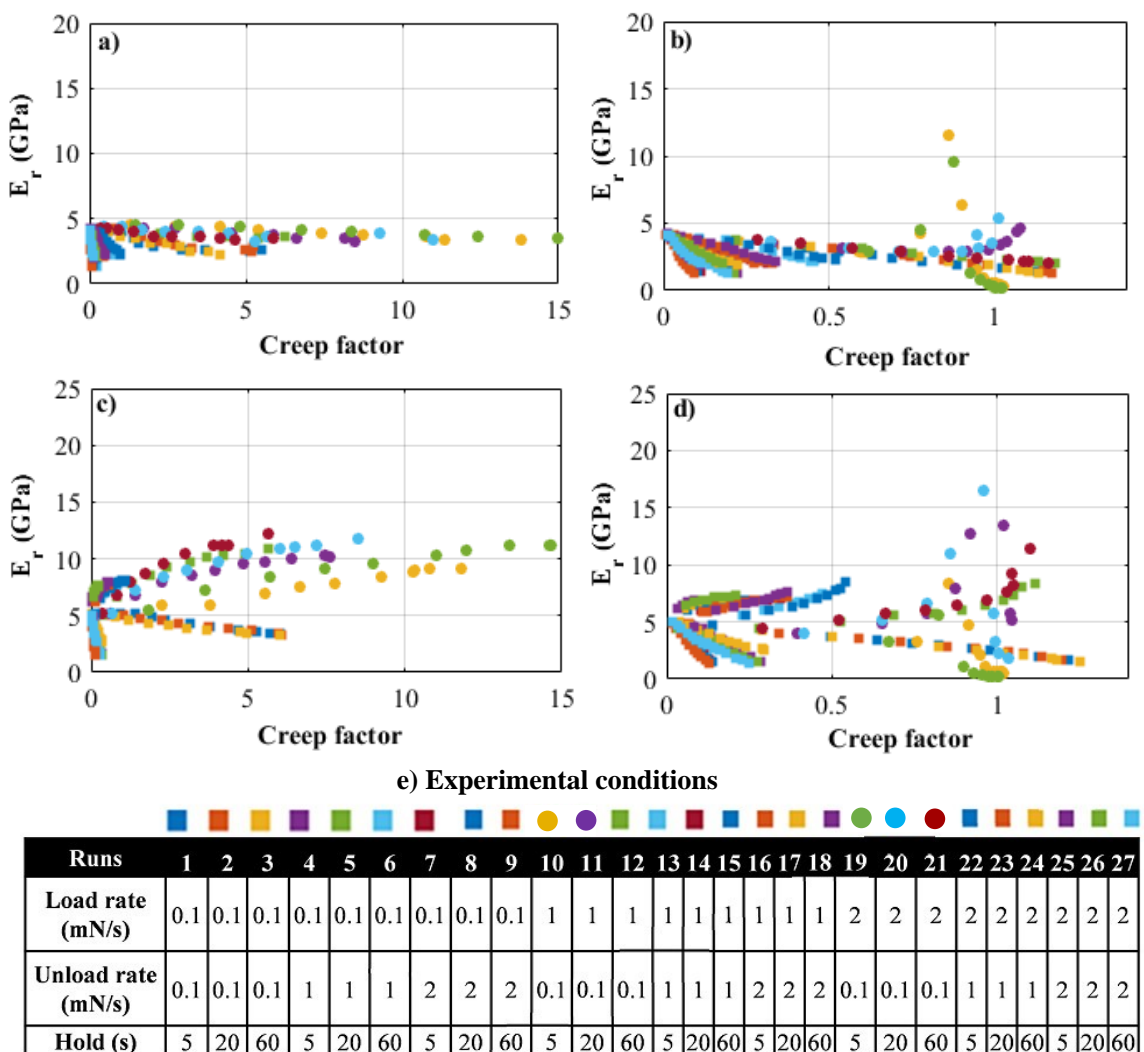


Figure 6-9 Creep factor against reduced modulus (E_r) for a) PET no creep correction, b) PET with creep correction, c) PEN with no creep correction, and d) PEN with creep correction. e) Experimental conditions for the 27 runs considered in each graph.

values of the creep factor. The results reflect the trends as above for Figure 6-8. For both PET and PEN, when using the DU method with creep correction, the calculated reduced modulus is sometimes lower and other times higher than the non-creep corrected values. This suggests changes in the mechanism for the viscous behaviour at these conditions. Also, Figure 6-1 a & b show that most of the data that doesn't fit is when the reduced modulus has either very low values or very high. These two mechanisms are visible through the creep correction data occurring in both PET and PEN at these test conditions. Realising these mechanisms and the severe effect on the reduced modulus against load curve, a separate study is conducted at these particular test conditions, using the DU method in multi cycle test configuration. Experiment 6.1 compares the different unloading methods of determining the elastic modulus of PET and PEN. Each indentation was performed at a maximum load of 100 mN and minimum load of 20 mN with 4 cycles in total, load rate 20 mN/s and unloads rate at 0.5 mN/s, and a 5 s dwell at maximum load. Thermal drift correction was calculated using the post-indentation drift calibration data. For determining the stiffness, 60% of the unloading data was selected. Each indent on each specimen was repeated 10 times.

Results of 7 different methods of determining the elastic modulus were plotted against each cycle of the multi-loading test (see Figure 6-10), unloaded 80% of the maximum load at each cycle. Each result was averaged over 10 tests showing $\pm 2\sigma$ error bars. The dotted line indicates how close the elastic modulus values of method DU-FSPD, determined at the first cycle, are in comparison to the value of method O3-MS determined at the fourth cycle. The difference in elastic modulus is roughly 0.1 GPa for PET and less than 0.4 GPa for PEN. As shown in section 5.3.3 the elastic modulus in-sample variation for both PET and PEN samples is around 0.3 GPa. Thus, the elastic modulus values determined by method DU-FSPD when compared to method O3-MS shown difference

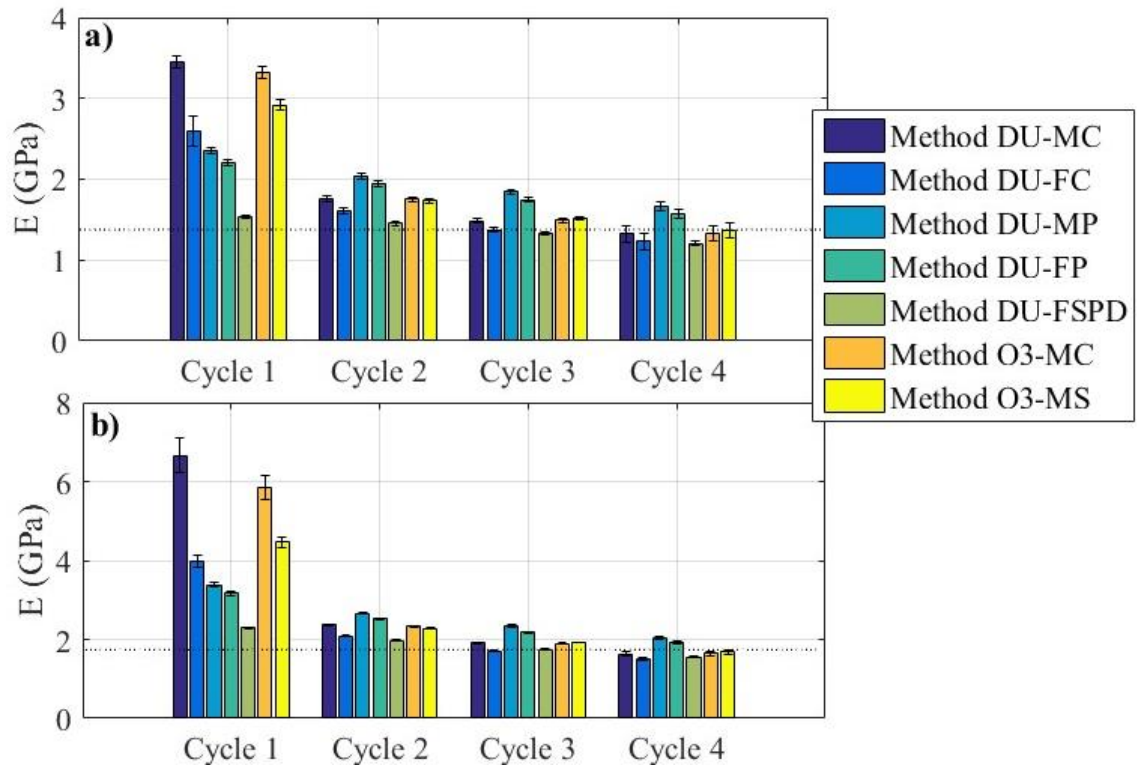


Figure 6-10 Bar chat of elastic modulus (E) against number of cycles for a multi-loading nanoindentation test using 7 different methods, a) PET, b) PEN

similar to the in-sample variation. A number of observations can be made from these plots. Methods DU-MC, DU-FC, O3-MC and O3-MS display the highest variability in the first cycle and can be related to the high viscous behaviour and plasticity at the end of hold. In comparison method DU-FSPD shows the least variability as a Plastic correction is applied i.e. elimination of reverse plasticity effect on the stiffness at end of hold, see section 4.3.4. A high variability in the first cycle definitely relates to the primary creep, and as the number of cycle's increase the variability is reduced considerably due to the transition to steady state conditions. Determining the elastic modulus from the first cycle using method DU-MC is inaccurate. For both PET and PEN, the elastic modulus determined using method DU-FSPD gives results similar to values obtained in the fourth cycle using method O3-MC. The difference can be related to the in-sample variation. The

validity of using multi-cycles is not convincing even though the reverse plasticity is eliminated. With additional cycles an increase in effective contact area would occur and also heating generated when indenter penetrates into the surface. Acquiring the elastic modulus or hardness in the first cycle would avoid these effects, even though method DU-FSPD reduces slightly in further cycles which is comparable to the in-sample variation. The elastic modulus found in the first cycle represents the true value of the response of the material.

By using method DU-FSPD the diverse effect of creep is eliminated. This was done by addressing creep within the datum correction, and determining the stiffness at FEP with correction due to the plastic rate. Reconstructing Figure 6-1 by using the reduced modulus $E_{DU-FSPD}$ and coefficient fitted reduced modulus ($E_{FIT-DU-FSPD}$) as seen in Figure 6-11, it can now be seen that both of these have an accurate one to one relationship. Referring back to Figure 6-6c the effect of the Plastic correction on the stiffness can be compared to the creep corrected data. Although the range of stiffness values for the Plastic correction isn't as low as the creep correction, the stiffnesses are a true representation at the FEP. In Figure 6-11 the reduced moduli using method DU-FSPD, which in this case are the reduced viscoelastic moduli, are determined at the different experiment's conditions. By using the plastic and datum corrections at FEP, where quasi-static conditions occur, enables the determination of the true viscoelastic behaviour related to the maximum load. However, the fitted reduced modulus against load curves, determined experimentally from each load and by the unloading data of a single test, show an opposite behaviour.

The contact area has been shown to have the most significant effect on the calculations of the reduced modulus. To calculate the contact area the contact depth must be accurately determined. Thus, the rationale behind choosing the methodology in determining the

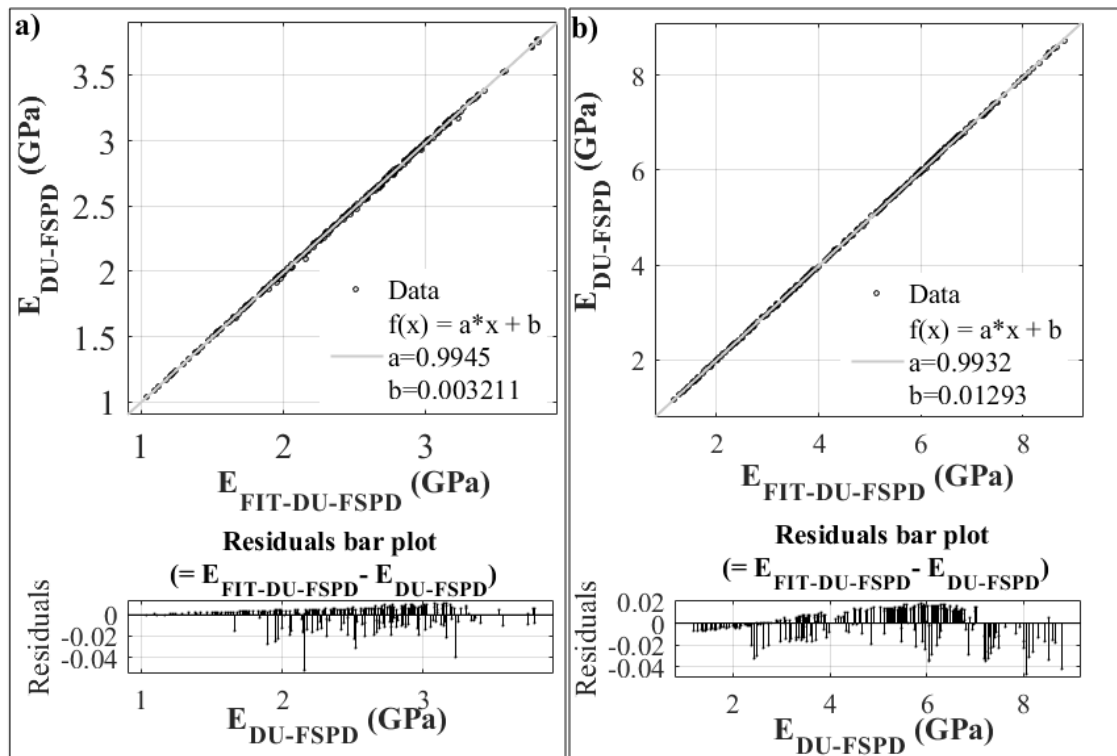


Figure 6-11 Reduced modulus $E_{DU-FSPD}$ against $E_{FIT-DU-FSPD}$ plots for a) PET and b) PEN, and with residual plots.

contact depth is detailed in the next section.

6.2.4 Contact depth

In chapter 4 all equations, from (Equation 4-14) to (Equation 4-25), used to determine the plastic depths for the DU method are valid since quasi-static behaviour occurs for even highly viscoelastic materials. However, the depth and strain rate dependency of polymers properties have been determined previously at very low loads (Fujisawa and Swain, 2006), showing the two to have a coupling effect on the elastic modulus that is impossible to separate. Experiment 4.1, conducted by the author, revealed that there is dependency of the elastic modulus with depth and also of the parameters which relate to the strain rate i.e. the test conditions. The elastic modulus affecting input parameters, depth, loading and unloading rate, and hold time were studied together and their individual effects, on the

output parameters such as the normalised contact depth and modulus, were identified statistically. For the experiment considered in section 4.2 the plastic depths and elastic modulus were accurately determined by using the method DU-FSPD.

When unloading from maximum load the non-instantaneous elastic response is due to the stored energy within the system. The release of this energy upon unloading is unique to the system. Some of this energy is due to “forwards plasticity” occurring within the material. For viscous/polymeric materials when unloading from full load, the contact depth can be overestimated, due to the “forwards plasticity” behaviour. However, when the “forwards plasticity” ceases, occurring at the FEP, the contact depth determined is solely due to the elastic or viscoelastic response, providing quasi-static conditions. Thus, the equations which were initially developed for elastic contact and quasi-static conditions become valid. One other correction for the underestimation of the contact depth due to the pile-up and sink-in was proposed by Bec et al (1996). So, both effects, the “forwards plasticity” and pile-up/sink-in, can be used to correct the contact depth. Thereby the elastic modulus of the material can be determined for a number of testing conditions, where the load rate, unload rate, hold time and the maximum load dictate the maximum displacements and the strain rates.

The plastic depth equation can be rearranged in terms of normalised contact depth (h_{cn}) and normalised stiffness (S_n), which is in the form (Fujisawa and Swain, 2006):

$$S_n = \alpha(1 - \varepsilon/h_{cn}) \quad \text{(Equation 6-3)}$$

This equation was used to fit the h_{cn} and S_n experimental data (see Figure 6-12). When performing these fits one can deduce α and ε for the range of test conditions for that particular material/indenter contact. The fits to the data are reasonable with little variation. The values of α and ε are also shown on the figure. These values can be put back into equation above and fitting iterated to give more accurate values if required. It

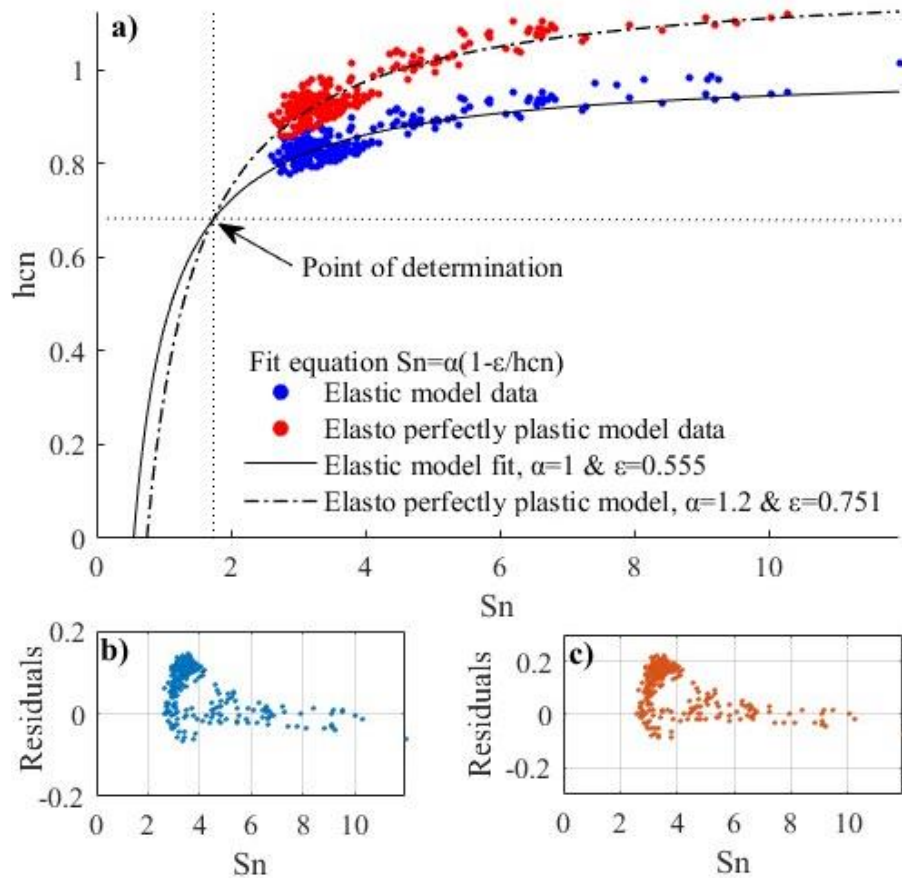


Figure 6-12 a) Normalised stiffness against normalised contact depth for PET polymer using two different methods, b) Residual plot difference between elastic model data and its fit, and c) Residual plot difference between elasto perfectly plastic model data and its fit

should be pointed out that the contact depth was determined at the FEP therefore the point of determination, as seen on the plot, is lower than the 2.25 value, as found by Fujisawa and Swain. The relationships of the normalised contact depth and the elastic modulus with the normalised depth, for different experimental parameters are shown in Figure 6-13. Plots a, b & c show undistinguishable change with increasing load rates apart from the hold period which shows the most influence on the calculated normalised contact depth at the lowest unload rate. This can be attributed to the “forwards plasticity”. Also, decreasing unload rate increases the gradient of the experimental data, for each test condition, displaying the coupling effect of the strain rate (experimental conditions) and

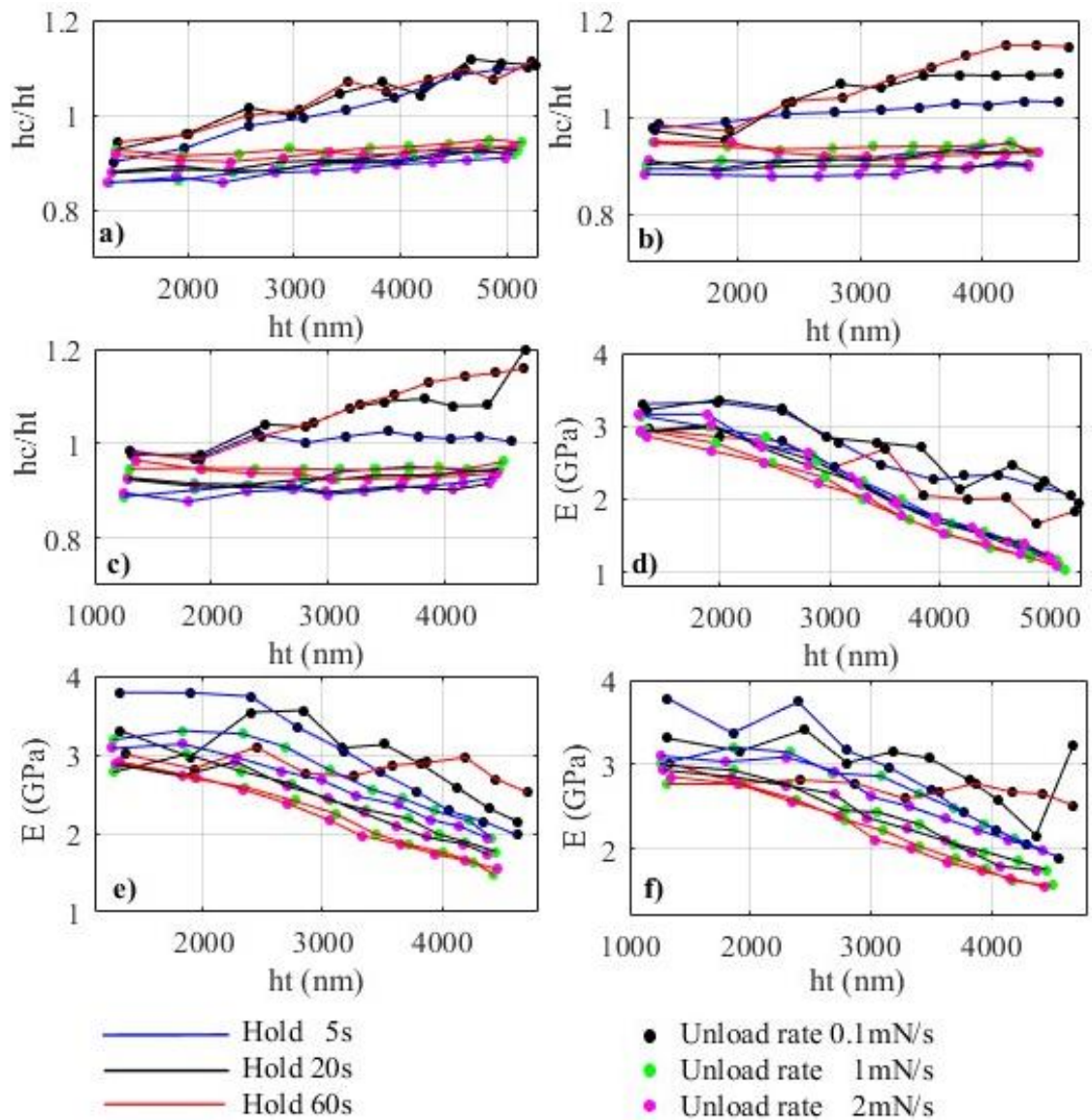


Figure 6-13 For PET polymer, plots of Normalised Contact Depth (hc/ht) against Normalised Depth (ht) at load rates of a) 0.1 mNs⁻¹, b) 1 mNs⁻¹, c) 2 mNs⁻¹, and plots of elastic modulus (E) against Normalised Depth (ht) at load rates of d) 0.1 mNs⁻¹, e) 1 mNs⁻¹, and f) 2 mNs⁻¹.

the depth related material properties of the sample. Looking at Figure 6-13d, e & f again the hold period shows the most influence on the calculated elastic modulus at the lowest unload rate. At any particular depth and unload rate, the variation of the elastic modulus values from the mean, due to the hold periods alone, is roughly equal to 0.3 GPa i.e. the in-sample variation. Thus, using plastic and pile-up/sink-in corrections the effect of

“forwards plasticity” on the elastic modulus is removed. Overall at any particular depth, the elastic moduli values determined by method DU-FSPD, which are the viscoelastic moduli, reflect the rate dependent behaviour of polymers. As for other methods accurate elastic modulus values would have not been established at these conditions. Now that the rationale behind the DU methodology is given, the method is validated at high and low loads.

6.3 Validating DU methodology at High load

The DU methodology was compared with methods both at maximum load and FEP, and with various corrections, and to the traditional Oliver and Pharr using different power law fits. Thirteen different materials used were split into two separate categories, viscous and non-viscous. All methods were validated against standard tensile tests. For tensile test procedures see section 3.6. The tensile tests were performed by Metaltech services Ltd for the metallic materials as detailed in Appendix 7.1 and by Material technology Ltd for the viscous/polymeric materials as detailed in Appendix 7.2. The tensile data will be assumed to be accurate for all the materials. For nanoindentation testing, refer to Experiment 4.2 in chapter 4 for the test conditions.

6.3.1 Non-viscous/non-polymeric materials

The analysis was initially validated at the microscale, at a load of 200 mN, refer to Figure 6-14. Ten different methods were compared. Seven different materials were chosen to display different elastic-plastic behaviours. To examine plastic, creep, sink-in and pile-up, and datum corrections, the calculated elastic moduli determined by the unloading methods are shown. Looking first at Figure 6-14a the accepted literature value for SiO₂ (Fischer Cripps, 2011, p.215), which are assumed to be accurate, fall within the machine software calculated values, concluding the analysis to be applied correctly. The difference

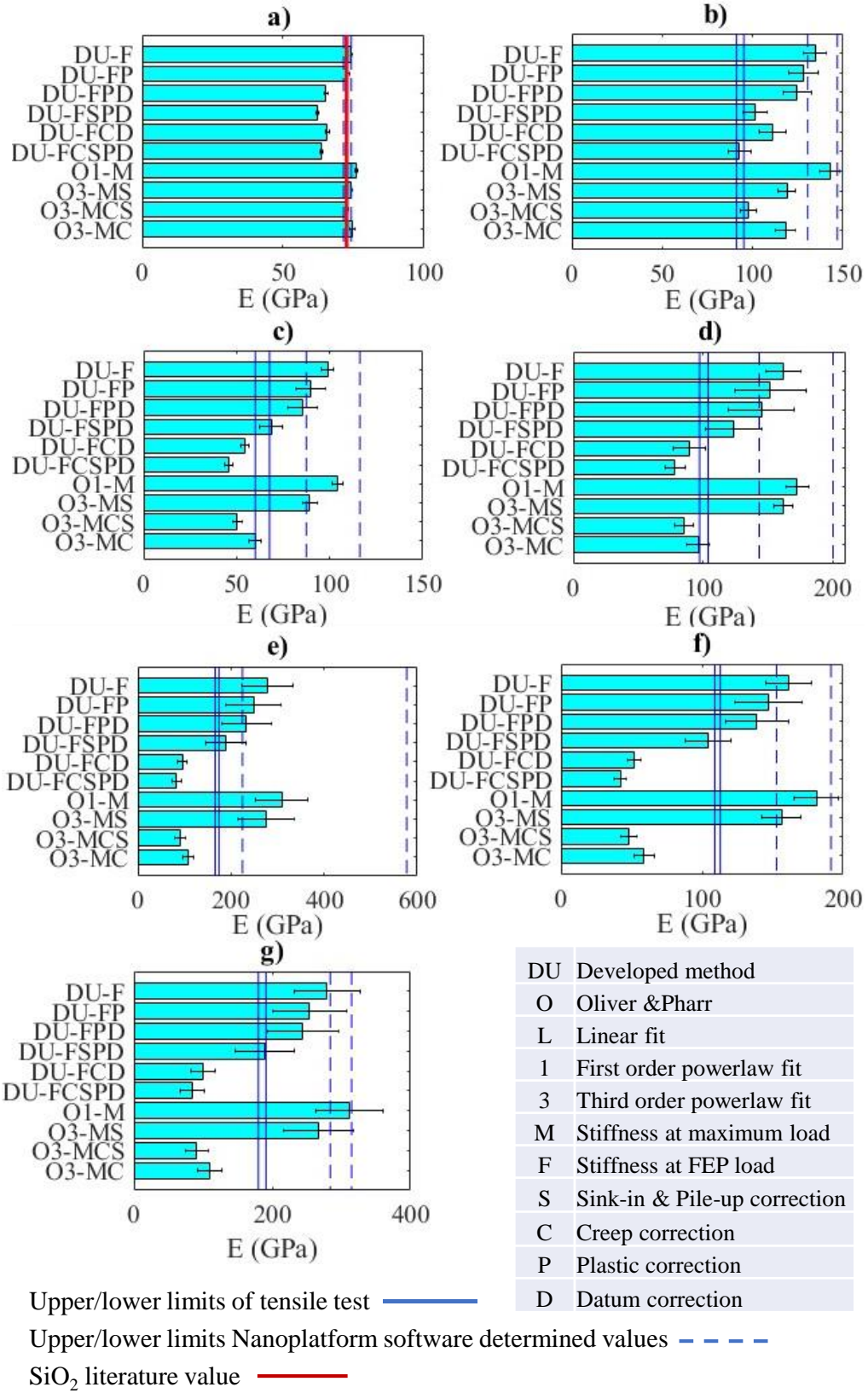
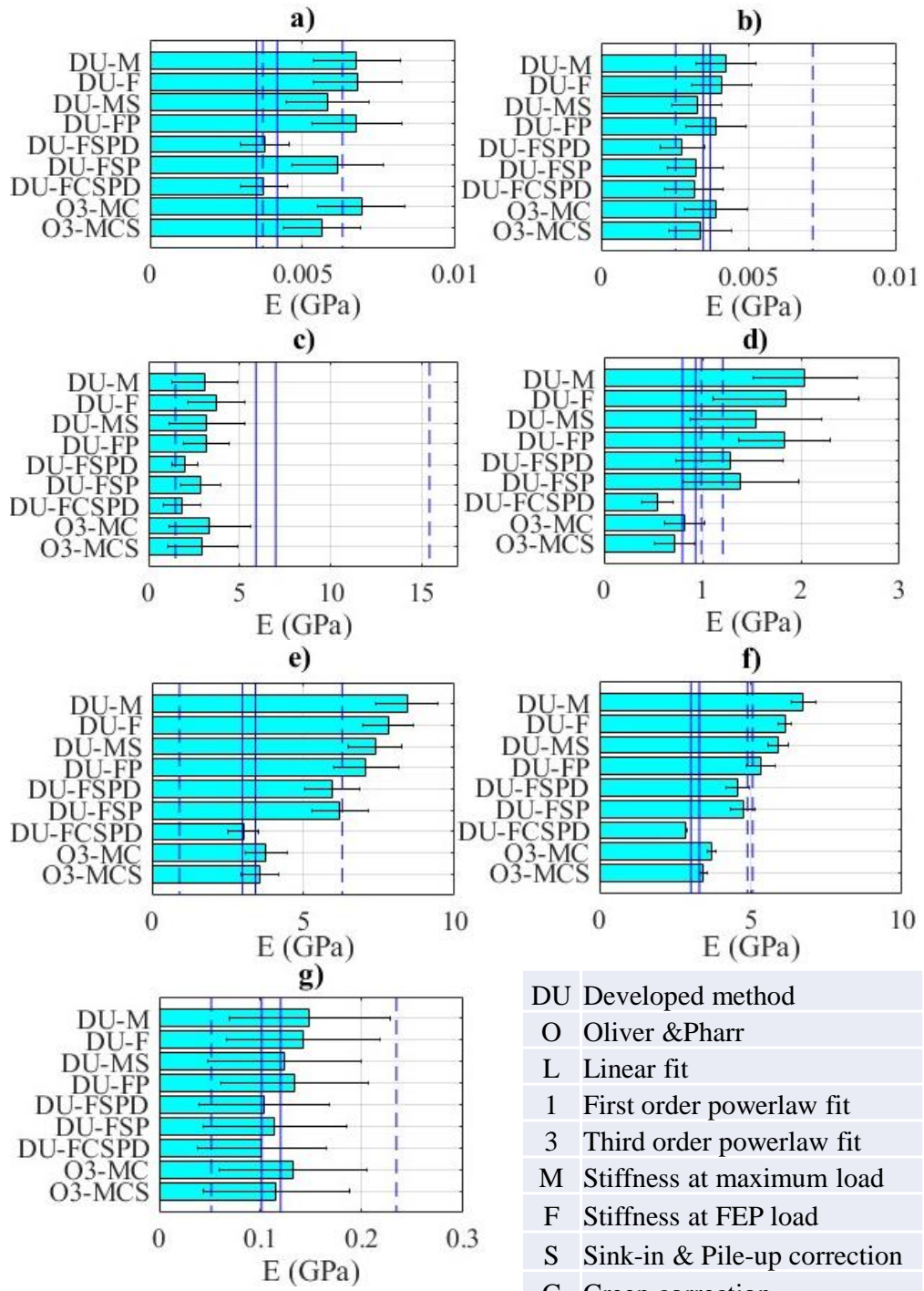


Figure 6-14 Elastic modulus (E) bar charts of non-viscous/non-polymeric materials using 10 different methods for single-cycle nanoindentation, a) SiO₂, b) Brass, c) Aluminium, d) Titanium(6AL-4V sheet G5), e) Stainless steel (316 2B grade), f) Copper and g) Mild steel

of these values in comparison with the OP-M method is mostly due to the accuracy of the fitting routines. The author has determined the OP-MCS and DU-FP to be most accurate when compared to the literature value. It should be noted that calibrating the machine with the DU-FP method would render the same results. At the experimental conditions tested, looking at the other six materials, overall method DU-FSPD is established the most accurate when compared to tensile testing. The traditional Oliver and Pharr, method O1-M is least accurate in all cases. As creep becomes significant for brass, Figure 6-14b, methods DU-FCSPD and OP-MCS are much better at determining accurate elastic modulus. Elastic modulus values in Figure 6-14c & d for Al and Ti, also show method O3-MC to be accurate when compared to tensile.

6.3.2 Viscous/polymeric materials

In examining seven different viscous/polymeric materials a number of influencing factors, the effect of applying creep, plastic and sink-in/pile-up corrections, in DU and O methods, were compared with tensile tests. The seven different materials were chosen to display different visco-elastic-plastic behaviours. The determined elastic moduli for the nine different methods are shown for all the materials. Apart from Nylon in Figure 6-15 the five remaining plots show that method DU-FCSPD accurately determines the elastic modulus. From Appendix 2.7 the value of E for Nylon as determined by the manufacturer is between 3 and 3.5 GPa indicating method O3-MC to be the most accurate. For Nylon and Polyethylene HD, shown in Figure 6-15c & d the slightly lower value of method DU-FCSPD can be attributed to the in-sample variation of polymeric materials, not determine but assumed 0.3 GPa, as found for PET.



Upper/lower limits of tensile test ———

Upper/lower limits Nanoplatform software determined values - - -

Figure 6-15 Elastic modulus (E) bar charts of non-viscous/non-polymeric materials using 9 different methods for single-cycle nanoindentation, a) Neoprene rubber, b) Nitrile rubber, c) Nylon (Polyamide 66), d) Polyethylene HD, e) Acrylic (Plexiglass® 8N), f) Polystyrene (STYRON™ 678E), and g) Polyethylene LD

For the rubbers some precaution was needed in calculating the tensile moduli. In Figure 6-16 the stress and secant modulus against the percentage strain is plotted using the force-elongation data supplied by Materials Technology Ltd. For both rubbers the secant modulus varies continuously and no linear behaviour is present. However, Materials

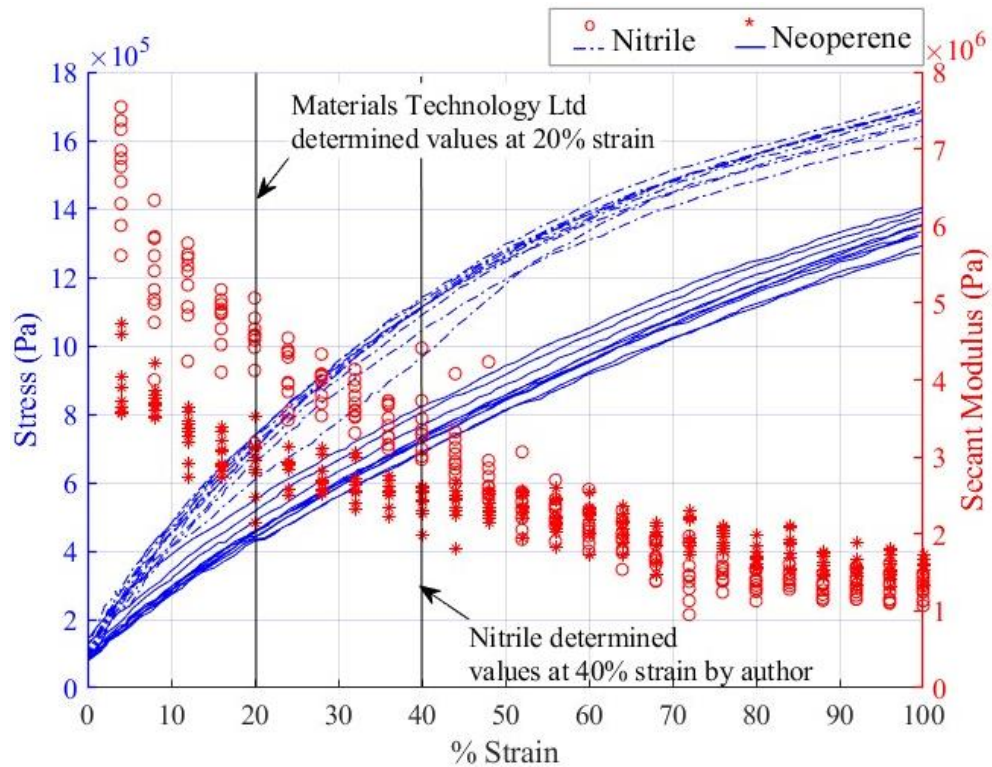


Figure 6-16 Modulus and stress against percentage strain

Technology Ltd used 0-20 % strain to determine the tangent for the secant modulus. In Figure 6-15 only Neoprene secant modulus resembled Method DU-FCSPD values. For Nitrile rubber 40 % difference in secant moduli was found comparing to the nanoindentation values. Thus, the secant modulus of Nitrile was established at 40 % strain. Other observations from Figure 6-15 is when applying a sink-in correction the elastic modulus is substantially reduced i.e. method DU-M against DU-MS, method O3-MC against O3-MCS and method DU-FP against DU-FSP. Apart from this the elastic modulus determined at maximum load is greater than the elastic modulus determined at

FEP i.e. method DU-M against DU-F. When comparing the nanoindentation to tensile tests both method DU-FCSPD and O3-MCS are as accurate. However, in section 6.2.3 method DU-FSPD was shown to eliminate the adverse effects of creep. Apart from Acrylic and Polystyrene, shown in Figure 6-15e & f, method DU-FSPD values were similar to method DU-FCSPD. So why the DU-FCSPD method is more applicable for viscous/polymeric materials will be examined further by examining also the scale dependency of the elastic modulus.

6.4 Validating DU methodology at different scales

Micro/nano scale elastic moduli are examined in Experiment 6.2 on nine of the materials from the previous section (see Table- 6.2 for corresponding loads). The elastic moduli were compared between twelve different nanoindentation methodologies and the tensile test data. For reproducibility nanoindentation tests was repeated ten times with 60 sec post thermal drift correction and 5 sec hold time. The loading/unloading rates are listed in Table- 6.2. For calibrating the indenter area function the standard (ISO 14577-2, 2002–2015) described in section 2.2.3 was used on both DU-FP and O1-M method data. The plastic depth against contact depth plots can be seen in Appendix 7.3 to have excellent

Table- 6-2 Nanoindentation test condition for Experiment 6.2

Unloading and loading rates (mNs ⁻¹)	Loads (mN)
0.050	1
0.125	2.5
0.250	5
0.500	10
1.250	25
2.500	50
3.750	75
5.000	100
7.500	150
10.000	200

fitting showing square of the multiple correlation coefficient (R_{sq}) to be above 0.99. These plots along with area function determined by the Nano platform manufacturer, using the DAF file, are replotted in Figure 6-17. When indenting on materials, more compliant than SiO_2 , error in the determined elastic modulus can occur due to the area function. In Figure 6-17 all methods, in particular the self-calibrated using DU-FP and O1-M method data, are different above 900 nm (~ 900 nm corresponding to the highest calibrated load). This difference is due to no data above 900 nm when performing fit. When indenting on compliant materials at low loads, less than calibration loads, h_c can be greater than 900 nm and the contact area is not determined correctly. Thus, the procedure adopted by the author for determining the area function assumes an ideal indenter shape for $h_c > 900$ nm. Using this procedure, SiO_2 elastic moduli for loads of 1-200 mN can be seen in Figure 6-18 c & d for methods DU-FP and O1-M. Both methods

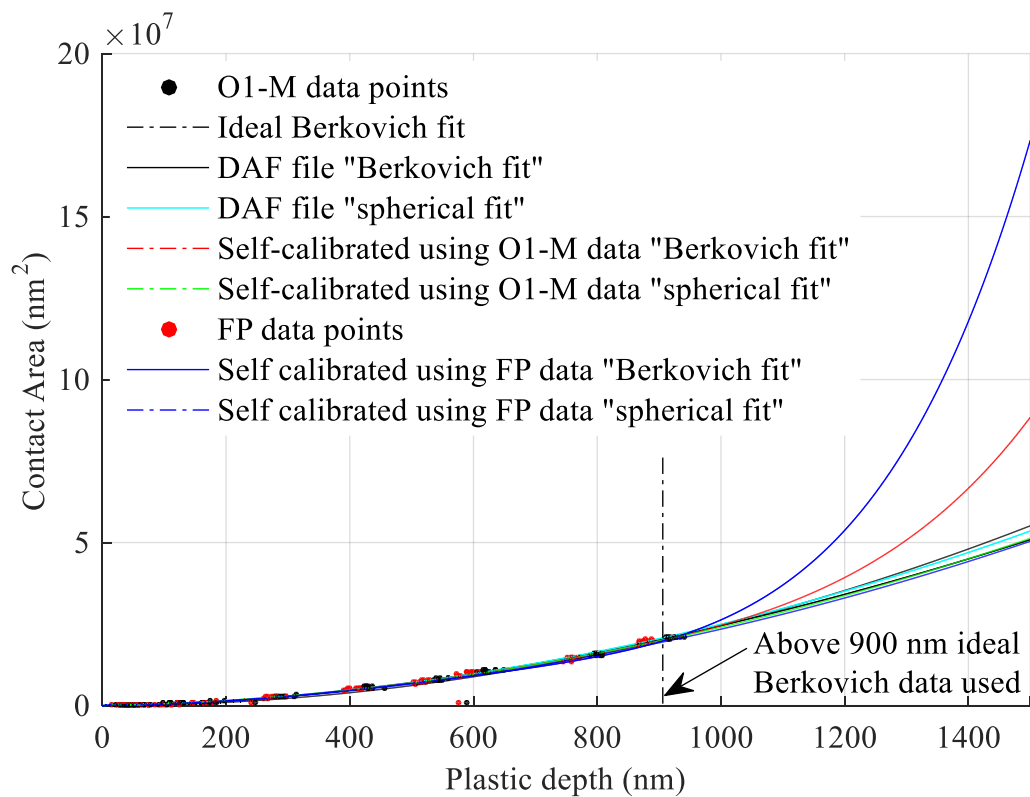


Figure 6-17 Comparison of different area function plots for Berkovich and spherical indenters using DU-FP and O1-M method data

determine accurate elastic moduli at all scales. When comparing these plots to Figure 6-18a & d, where the area functions were determined by the DAF file and calibrated using O1-M data, the adopted procedure is more accurate at lower loads when comparing the elastic moduli to the accepted literature value for SiO₂ (Fischer Cripps, 2011, p.215).

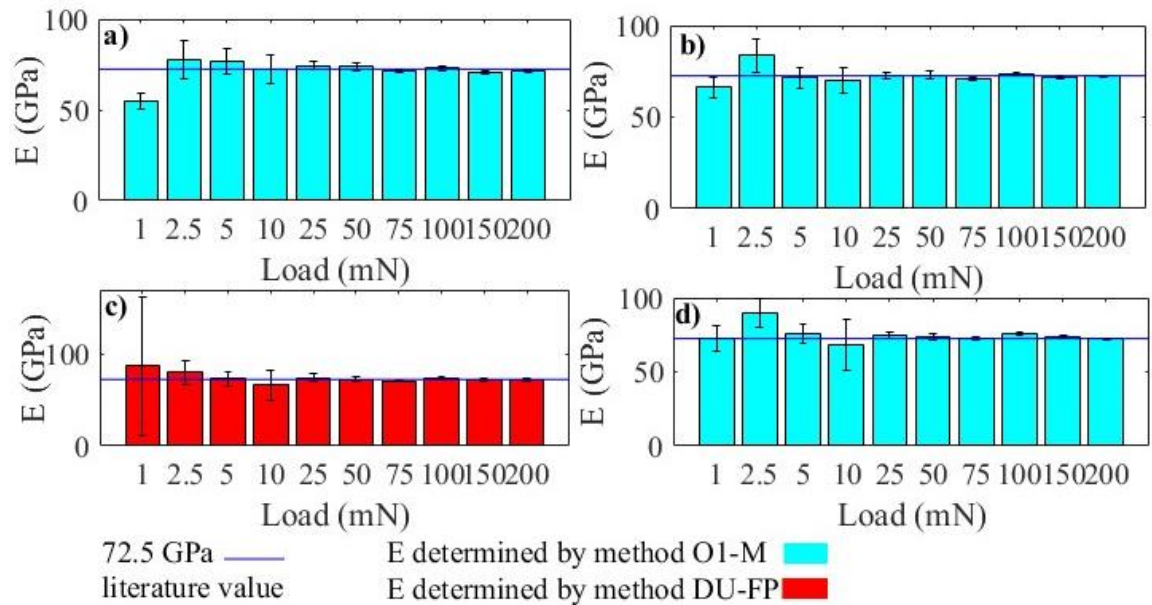


Figure 6-18 Elastic modulus bar charts at various load for SiO₂ using area functions determined by a) DAF file, b) calibrated by O1-M method, c) calibrated by DU-FP method and d) calibrated by DU-FP method

Using the adopted calibration procedure for the area function the elastic moduli for the four metallic materials, Aluminium, Brass, Copper and Mild steel are examined and compared between twelve different nanoindentation methodologies and the tensile test data. Elastic modulus bar charts for these materials for the 12 different O and DU methods are shown in Appendix 7.4. In order to distinguish which method is applicable when accurate compared to the tensile tests, for all four materials, a method selection matrix is constructed from the plots, refer to table- 6.3. At these nanoindentation test conditions only Aluminium is consistent with the results in section 6.3.1. From the selection matrix

Table- 6-3 Method selection matrix for four metallics

		Aluminium	Brass	Copper	Mild steel					
Nanoindentation analysis methods	O1-M									
	O3-MC									
	O3-MS									
	O3-MCS									
	DU-FP									
	DU-FCP									
	DU-FSP									
	DU-FCSP									
	DU-FPD									
	DU-FCPD									
	DU-FSPD									
	DU-FCSPD									
	<table border="1" style="width: 100%; border-collapse: collapse;"> <tr> <td style="width: 20%; background-color: yellow;"></td> <td>Accurate at higher loads</td> </tr> <tr> <td style="width: 20%; background-color: gray;"></td> <td>Accurate at lower loads</td> </tr> </table>							Accurate at higher loads		Accurate at lower loads
		Accurate at higher loads								
	Accurate at lower loads									

for these metallics, both O and DU (with or without datum correction) methods, are applicable and depend on sink-in/pile-up and creep behaviour. Thus, the behaviour of the material must be known in order to apply a particular method. This cannot be deduced from the tests. For example, for Aluminium the O method did not need a sink-in/pile-up or creep correction however for the DU method both corrections have to be applied. For Brass and Mild steel, the DU method with datum did not need a sink-in correction whereas did for the O method, and for Copper the O method is corrected for creep whereas not applicable for the DU method. For metallics the DU method is capable of accurate results without the datum correction this implies that minor or no shift is occurring at initial contact for these materials. One other obvious observation is that the creep correction is applicable at lower loads due to the penetration depth becoming the same order as the creep itself. It should also be noted that in majority of the cases at the lowest

scale the results were different to tensile, this is mainly due to ISE (see section 2.3.4) arising which are also dependent on the material type.

Similarly using the adopted calibration procedure for the area function the elastic moduli for the four polymeric materials, Nylon, Polyethylene HD, Polyethylene LD and Polystyrene are examined and compared between twelve different nanoindentation methodologies and the tensile test data. Elastic modulus bar charts for these materials for the 12 different O and DU methods are shown in Appendix 7.5. Again, a method selection matrix is constructed from the plots, refer to Table- 6-4. The results for Nylon appear to be inconsistent comparing to the other three polymers. The literature values of tensile modulus of Nylon can be low as 2 GPa (The Engineering Toolbox, 2019) for unfilled types thus the author believe this to be the tensile modulus of the sample tested. For the

Table- 6-4 Method selection matrix for four polymers

		Nylon	Polyethylene HD	Polyethylene LD	Polystyrene						
Nanoindentation analysis methods	O1-M										
	O3-MC										
	O3-MS										
	O3-MCS										
	DU-FP										
	DU-FCP										
	DU-FSP										
	DU-FCSP										
	DU-FPD										
	DU-FCPD										
	DU-FSPD										
	DU-FCSPD										
		<table border="1" style="width: 100%;"> <tr> <td style="background-color: #FFC107; width: 20px;"></td> <td>Accurate at higher loads</td> </tr> <tr> <td style="background-color: #9E9E9E; width: 20px;"></td> <td>Accurate at lower loads</td> </tr> <tr> <td style="background-color: #4CAF50; width: 20px;"></td> <td>Accurate</td> </tr> </table>					Accurate at higher loads		Accurate at lower loads		Accurate
	Accurate at higher loads										
	Accurate at lower loads										
	Accurate										

polymers, at these experimental test conditions, methods O3-MCS and DU-FSPD are the most accurate when compared to tensile tests. Method DU-FCSPD shows slightly lower values, however the difference is within that occurring due to the in-sample variation. From the Polyethylene LD plots in Appendix 7.5 the elastic moduli can be seen to be higher at lower load than the tensile values, however this can also be due to the in-sample variation or can be related to ISE. These results are consistent with the results in section 6.3.2 so in all cases method DU-FCSPD is considered accurate for polymers and equally valid as O3-MCS. The assumptions made for validating the nanoindentation data was that tensile data was accurate. This is not always true. Tensile tests were conducted at the macroscale but compared to data obtained at various scales. As the elastic modulus especially for polymers can be scale dependent (Chandrashekar, Alisafaei and Han, 2015; Garg, Han and Alisafaei, 2016) this can invalidate the assumption made for tensile testing.

6.5 Low load validation

At low loads of 0.1 mN to 10 mN variations in the output data from any nanoindentation method becomes more pronounced as the measurement reaches the limitation of the machine, also the noise associated with environmental factors such as vibrations is more relative to the measurements, and the effect of surface roughness becomes important. This in effect makes any fitting routine carried out by the analysis i.e. determining RDL or the unloading stiffness, less accurate. As the effects of environmental factors on variation are well known and controlled to some extent during experimentation, these will be assumed constant for the author's studies at the scale considered also refer to chapter 5.2.1. Thus, in this section the effect of test conditions on the variation of RDL, and the effect of surface roughness on the variation of the elastic modulus will be considered.

6.5.1 Factors effecting the Roughness Depth Limit (RDL)

The author shows variation in RDL values for different materials, when calculated using method in section 4.5.1, and the effect of load and load rate on values of RDL for PET and PEN polymers. RDL variation, in reference to Experiment 4.1 and 3.2 testing conditions, for 7 metallics, 4 viscous/polymeric and 2 highly compliant materials are examined, see Figure 6-19. Silver steel being a metallic was included in the viscous class of materials. Even though these tests are done using microscale conditions the determined RDL is still a low load parameter determined at low loads from the loading data. The box plots show the mean values and outliers for each material. As the viscous nature of the material increases the RDL are seen to increase. The highly compliant materials show the highest RDL values. However, all factors which effect ISE mentioned in section 2.3.4 will also dictate the RDL values.

In Figure 6-20 RDLs of PET and PEN against load for three different load rates are shown. There is a dependency of load and load rate on the RDL especially at the lower scale. For PET at loads below 40 mN at the higher load rates there is no effect. This could be due to the effect of the method itself in determining the RDL. At low loads, when the load rates are high relative to the load, the number of points for fitting the data can reduce which increases the linear range on a load-displacement graph. For lower load rates both materials still show a load rate dependency. This dependency can be related to factors responsible for ISE and also drift rates of the electronics occurring at low loads which can be due to temperature difference between the probe and the sample surface or contact vibrations (Zhang et al., 2018).

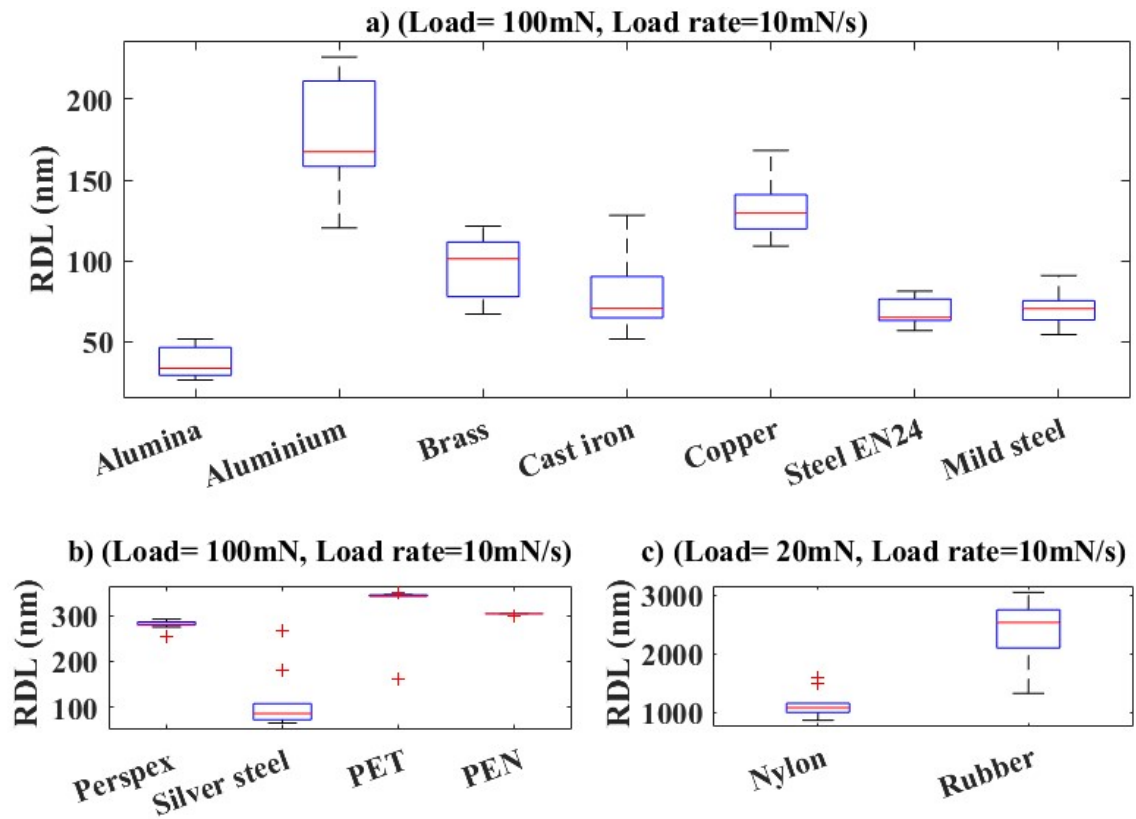


Figure 6-19 Box plots for RDL for a variety of materials a) metallic materials, b) viscous/polymeric materials, and c) high compliant materials

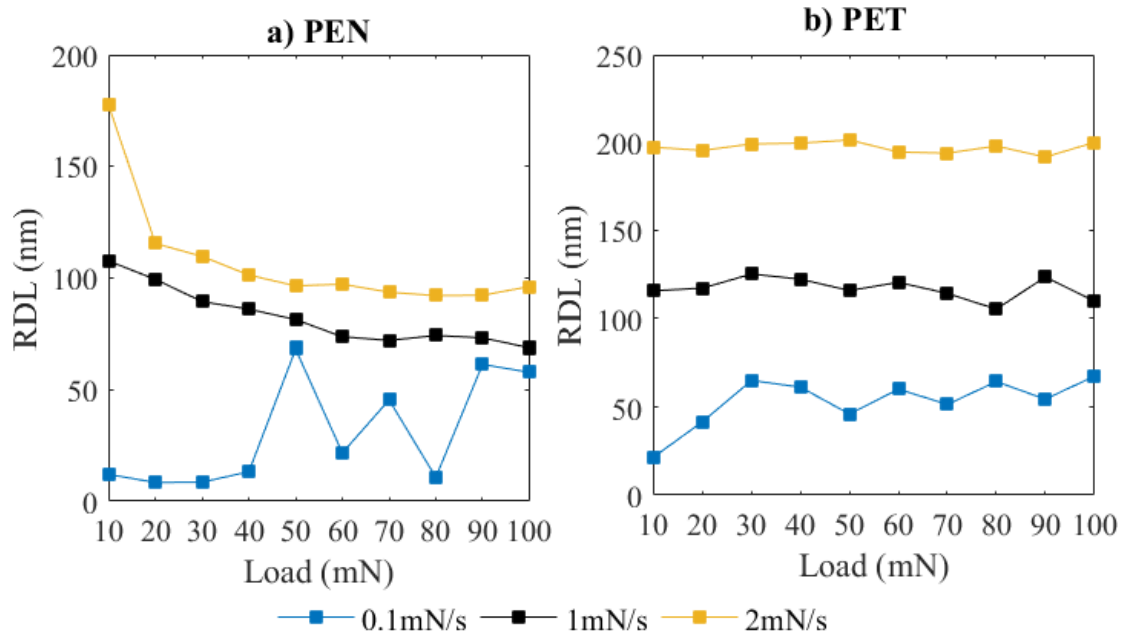


Figure 6-20 RDL against load a) PET sample, and b) PEN sample

6.5.2 Effect of surface roughness on determined elastic modulus values

In section 4.5.1 it was shown the surface roughness had no direct correlation to the RDL for all the materials considered, however the surface roughness is one of the key factors which effects the RDL and thus the hardness and elastic modulus determined by the DU method. Experiment 6.3 was used to determine the effect of roughness on the measured elastic modulus using the DU methodology. A full factorial design of experiments was conducted on two 3 mm thick silicon wafers samples, one smooth and the other sandblasted. At two loads, 0.1 mN and 10 mN, 40 indentations were taken and for the corresponding output parameter $\pm 2 \sigma$ from mean values were removed from the data. At low load the loading and unloading rates were 0.005 mN/s whereas at the high load 0.1 mN/s. The RDL for each indentation, along with the average value for each roughness can be seen in Figure 6-21. The average value of RDL for the 40 indentations was taken at the two roughness's. It can be seen the increase roughness increases the variability of each indent and also the average. For determining RDL sufficient loading data was needed i.e. RDL cannot be determined for load were displacement are below RDL. Thus,

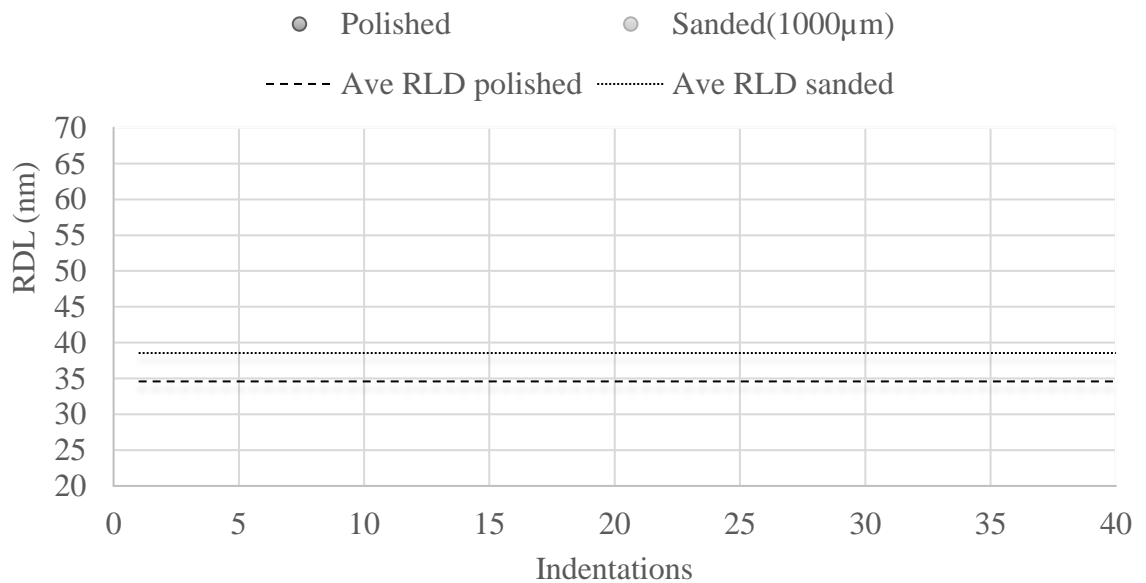


Figure 6-21 For silicon the RDL for each indent for two different roughnesses

only higher loads conditions were used to determine the RDL. Also due to low load rates, the goodness of fit (for the initial RDL guess) needed to be increased and also the increments. The individual value plot of the determined elastic modulus for the silicon samples are shown in Figure 6-22. As expected, at high load, smooth gives low variability compared with to the rough sample. However, at low load, smooth sample variability is comparable or higher than the rough sample. In the past other researchers have found the

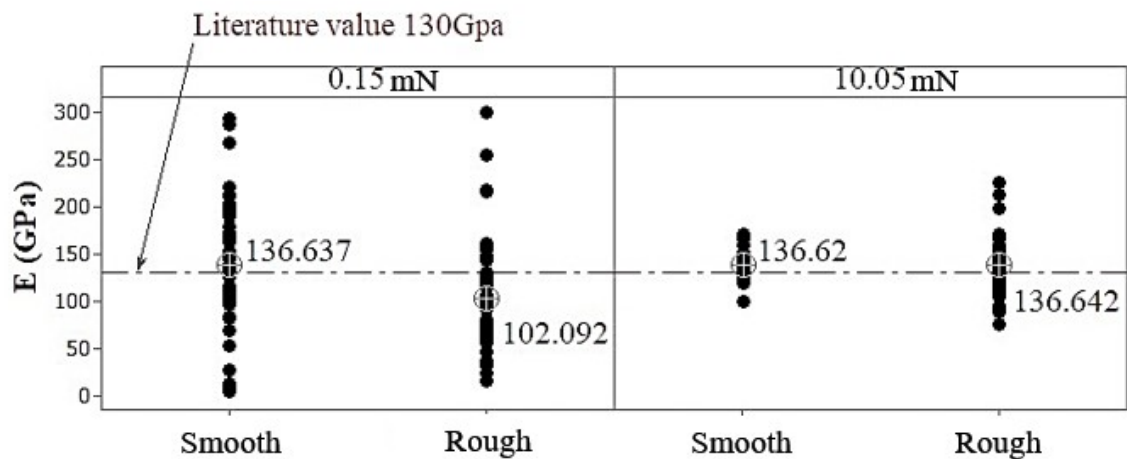


Figure 6-22 Individual plots of elastic modulus for Silicon wafer, data cleaned $\pm 2 \sigma$ from mean.

elastic modulus of silicon to vary according to the crystal orientation, structure and analysis procedures. For silicon wafer elastic modulus in 100 direction is typically 130 GPa (Hopcroft, Nix and Kenny, 2010) and 169 GPa in the 110 direction. The average elastic modulus value of polysilicon structures can differ due to the structure being dependent on the deposition conditions. At both high and low loads the values of the elastic modulus are reasonably consistent with these previous values. However, at low loads where the surface roughness comes into play the values are lower as the surface roughness increases. In Figure 6-23 histograms for the normal distribution of elastic modulus data is shown. The data is seen to resemble a normal distribution at both

roughness and loads, therefore enough data is present for accurate elastic modulus values. It is not just the surface roughness which is responsible but tilt and ISE due to geometrically necessary dislocations have also been shown to have a measured effect on mechanical properties (Laurent-Brocq, Béjanin and Champion, 2015) . All other factors contributing to ISE will also be applicable. From the Gauge (R & R) study in section 5.3.3 the tilt was shown to be significant on the in-sample variation and needed to be controlled as much as possible.

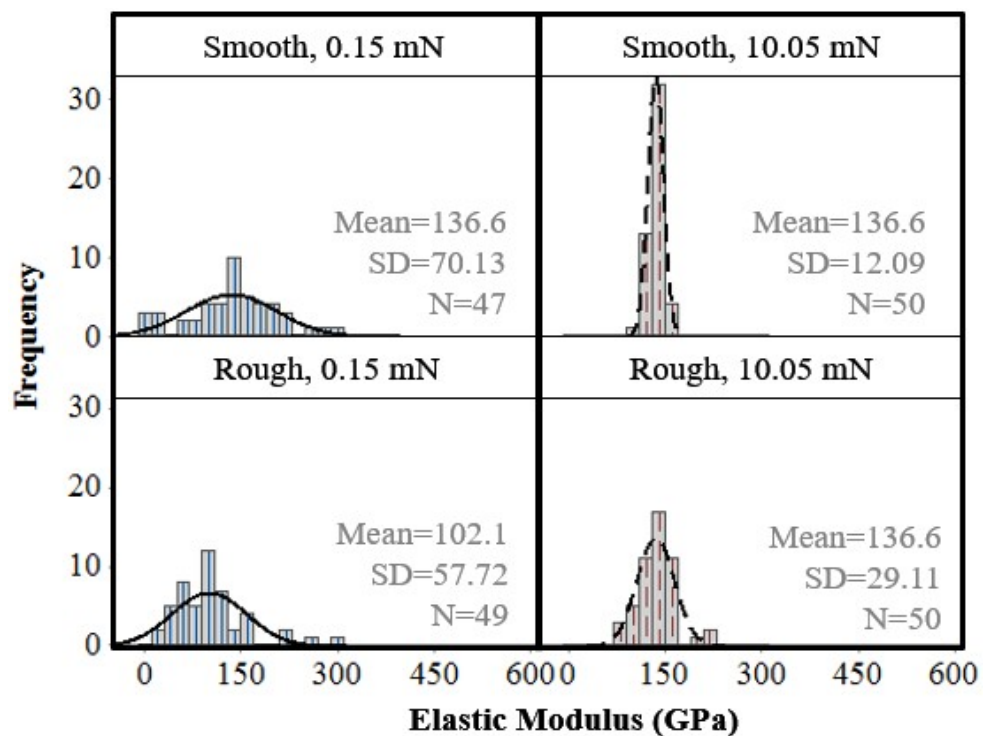


Figure 6-23 Histograms for the normal distribution of elastic modulus data for silicon at two different loads for smooth and rough samples

Additionally, the surface roughness has been shown to interaction with adhesion (Johnson, 1987, p.126) and thus with friction (McFarlane, Tabor David and Bowden Frank Philip, 1950) and as friction is correlated with load (Greenwood and Williamson, 1966) there can be interaction between all three factors with load.

6.6 Summary

For metallics the DU method is capable of determining accurate results without the datum correction, however the behaviour of the material must be known to apply a certain correction. The DU-FSPD and DU-FCSPD method has been shown to be as accurate as the most commonly used unloading method (Oliver and Pharr, 1992, 2004), with creep (G. Feng, 2002) and pile-up/sink-in corrections, for polymeric and rubber materials. At lower scale creep correction become necessary however the variation is increased in the output data. The DU methods consumes less time, by using just one cycle to determine the material properties, and are valid at all test conditions even non-quasi static. In the next chapter the viscous behaviour of polymeric materials is further examined using the hold time creep experiments and modelled to determine how well the characterisation compares to the DU method. Using characterised data from the DU method Neural network interpolation and extrapolation techniques are used to fully describe/characterise the behaviour for a polymeric material for conditions outside and in-between the test conditions. This characterised data can thus be used in FEM contact models.

Chapter 7

NANOINDENTATION CHARACTERISATION OF COMPLIANT MATERIALS

7.1 Introduction

In this chapter, mechanical properties for two compliant substrates, PET and PEN, are characterised using nanoindentation hold time analysis and the DU method. The specifications of these materials and a discussion of the factors directly affecting their mechanical properties were given in section 3.2 and Appendix 2.1 & 2.2. These will be cited throughout the chapter. Several methodologies are presented for characterisation and comparisons. After characterising these polymers at certain test conditions, a neural network technique was applied to find the characterised data within and outside the experimental test conditions. This is done due to the complex interdependency between the test parameters and the characterised data, for which a mathematical correlation could not be determined. The literature review on the different methodologies for characterisation polymers was given previously in section 2.5. First, hold time methodologies are detailed and equations defined.

7.2 Viscous/polymeric material methodology

Using the DU methodologies described in Chapter 4, it was shown that the visco-elastic response could be successfully obtained from the unloading curve for a set of input parameters, i.e. load, load rate, hold time and unloading rate etc. A single value for elastic modulus is insufficient in describing the behaviour of a polymer due to the elastic modulus being time-dependent. Thus, it is customary to use the hold time data to determine the time-dependent viscoelastic-plastic response (see section 2.4.1). The

method by (Chudoba and Richter, 2001) employing **(Equation 2-11)** will be referred to as method Log₁. Relaxing stress is needed for its application, and the relationship for the displacement is not always accurate, as the loading in the nanoindentation test is due to indentation compression. Thus, the author of this thesis proposes a method referred to as method Log₂ to express the displacement as a combination of physical effects, where the change in displacement is expressed as:

$$\Delta h = [a] + [b \times t] + [c \log((d \times t) + 1)] \quad \text{(Equation 7-1)}$$

The first term a, is a constant describing the total displacement before the hold time (displacement at hold time=0), which is dependent on the loading history. The second term is assumed to describe the irreversible plasticity during the hold time. The last term simulates the stress relaxation due to the viscous effects. All parameters a, b, c & d can be found by fitting the experimental hold-time data. These parameters are assumed to be a function of load and load rate. If a function is determined and replaced, for each parameter, then (Equation 7-1) will become a function of load, load rate and time. The advantage of this is that FEM can be conducted at any test conditions. Unfortunately, the functions for each parameter needs to be determined for a given range of test conditions and will only be applicable for these test conditions. However, outside the test conditions, these relationships can be assumed.

For the phenomenological methodology, stated in section 2.5.2, the author suggests a method E_T, by using the bracket term in (Equation 2-20) which is equal to J(t), to determine the time-dependent elastic modulus. However, this includes the effect of all physical phenomenon during the hold time.

7.3 Viscous/polymeric material characterisation

In order to understanding the deformation behaviour, of compliant materials or coating/compliant-substrate systems, with numerical methods such as FEM, the mechanical properties, for each material in the system, are needed. Although the issues of determining the properties of viscous/polymeric materials have been addressed in Chapter 6, the elastic modulus and hardness, are time-dependent, or rate-dependent and the values show some degree of variability. In this section, the different methods discussed have been used to characterise the properties of PEN and PET. All the logarithmic and rheological models discussed in section 7.3.1 and 7.3.2 are analysed using Experiment 7.1 which examines the effect of strain rate (0.033 mN/s to 40 mN/s) and load (0 to 300 N) on the creep behaviour for PET and PEN. These nanoindentation hold time experiments are conducted with a Berkovich indenter at an unloading rate of 40 mN/s and a dwell at maximum load of 100 s. The creep was examined in the constant load configuration and also a post indent thermal drift was considered.

7.3.1 Examining Logarithmic fit to hold-time data

Logarithmic fits, established with method Log_1 using the hold time data, are examined first. Although this method has been used successfully in the past for studying the creep behaviours for various polymers (Beake et al., 2007), it will be demonstrated that for both PET and PEN polymers, at experimental conditions that show high creep and plasticity, the fits are not accurate. This is visualised for a particular experimental condition along with method log_2 which accounts for the initial displacement at the start of hold. The errors in the fits, clearly seen in zoomed in area of Figure 7-1a can be linked to localised deformation, where the stresses at the tip can cause plastic deformation; this is especially true for Berkovich indenters where the viscous effect can also be high. These effects were included in the method Log_2 in order to fully fit the experimental data. (Equation 7-1)

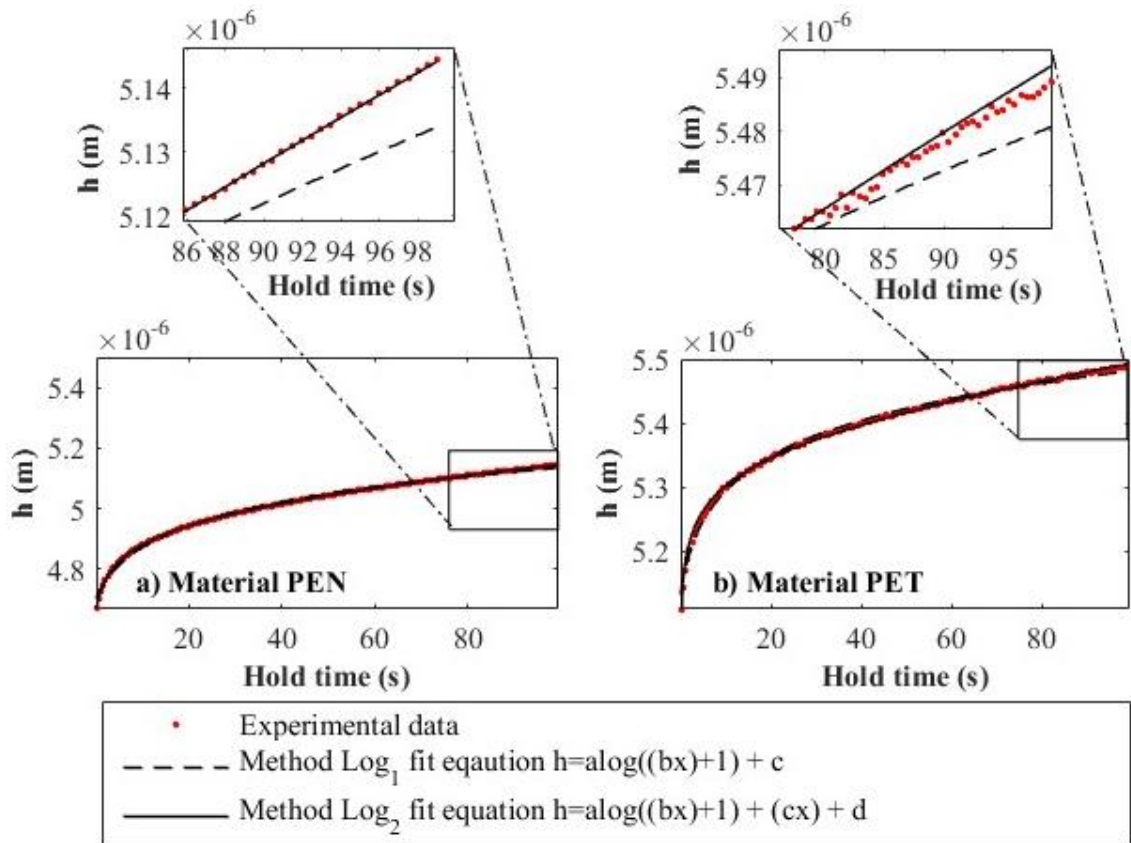


Figure 7-1 Nanoindentation displacement (h) against time, with two different logarithmic fits at Load of 150 mN with an initial Load rate of 10 mN/s a) PEN and b) PET

was thus developed such that to separate the initial loading history, the non-reversible plastic/viscous effects, and the visco-elasticity. Method Log₂ fits can be seen to be more accurate, as seen in the zoomed in part of Figure 7-1a. In order to make use of these precisely fitted parameters for FEM, an attempt was made to relate them to the experimental conditions. Each of the parameters was plotted against load and load rate. This is shown in Figure 7-2 and Figure 7-3 for PET and PEN respectively, also showing the cubic interpolant fitted data for the surface fit. Apart from the parameter “b” good fits for each parameter were hard to achieve. Each parameter showed a unique characteristic. Parameter b also gave a good polynomial fit (not shown) due to it being a constant value for all of the test conditions. For parameters a, c and d the polynomial fits were not

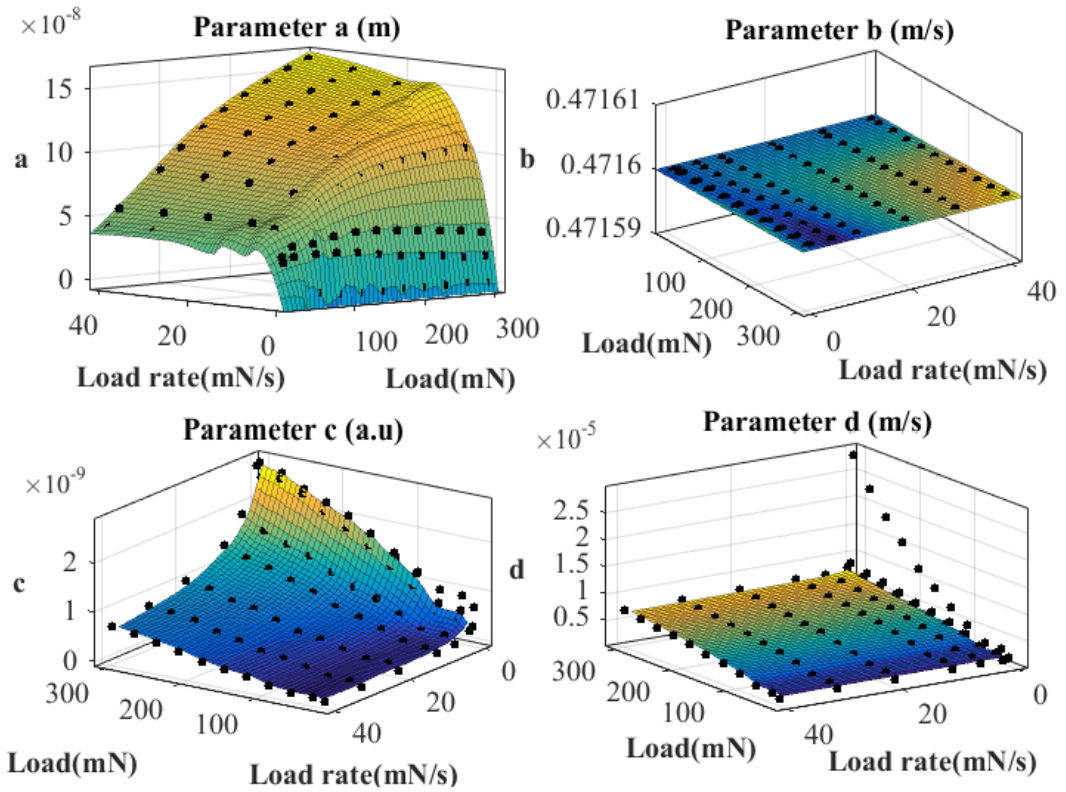


Figure 7-2 Determined fit parameters of method Log_2 (Equation 7-1) with experimental data and cubic interpolant fits, for PEN polymer.

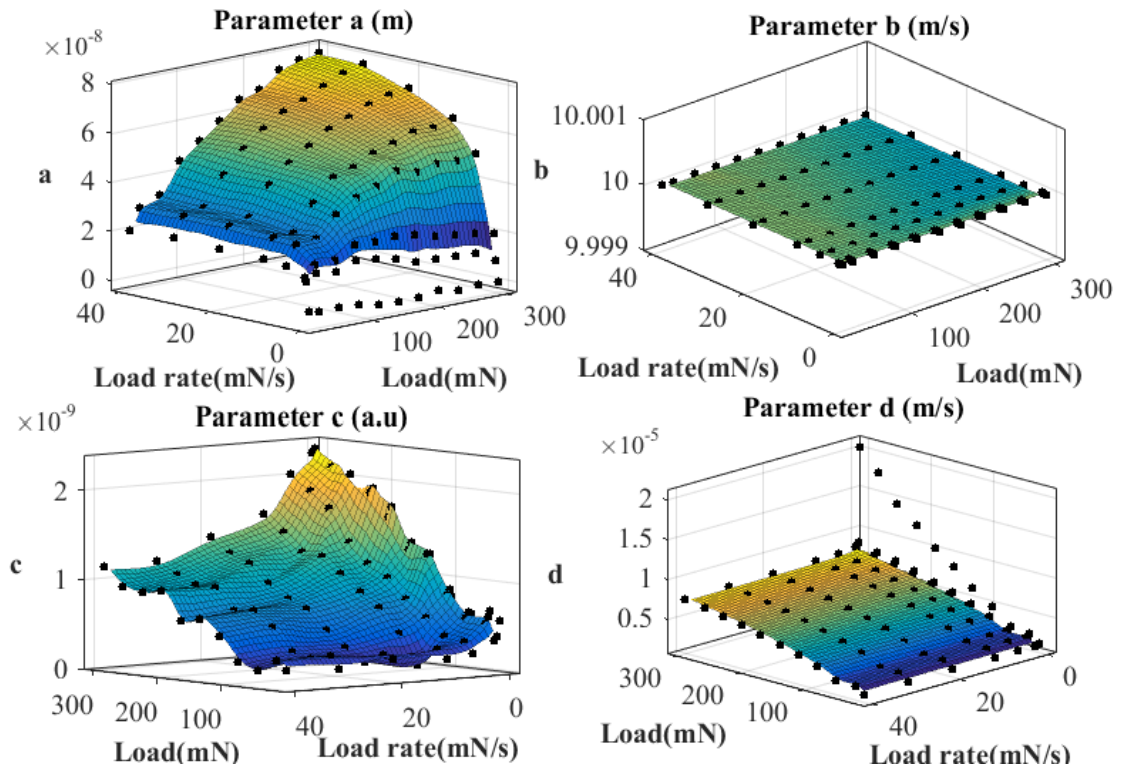


Figure 7-3 Determined fit parameters of method Log_2 (Equation 7-1) with experimental data and cubic interpolant fits, for PET polymer.

possible as these parameters change suddenly due to high load and low load rate conditions, for parameter d even a cubic spline fit was not possible. When comparing both materials, each parameter behaved similar which would suggest that the mechanisms of deformation were similar in both polymers. As these parameters have no direct relationship to the physical properties of the material and cannot be related to the test conditions, their practical use is limited.

Method Log_2 (Equation 7-1) shows that each component is additive toward the total deformation, and thus each can be considered individually. The deformation due to each component can be seen clearly in Figure 7-4. It should be pointed out that the effect of the initial loading on the hold time deformation is not considered in this model and in (Equation 7-1) there is no correlation of the displacement with the load. Therefore, it is not possible to relate it to the elastic properties of the material by comparing it to the

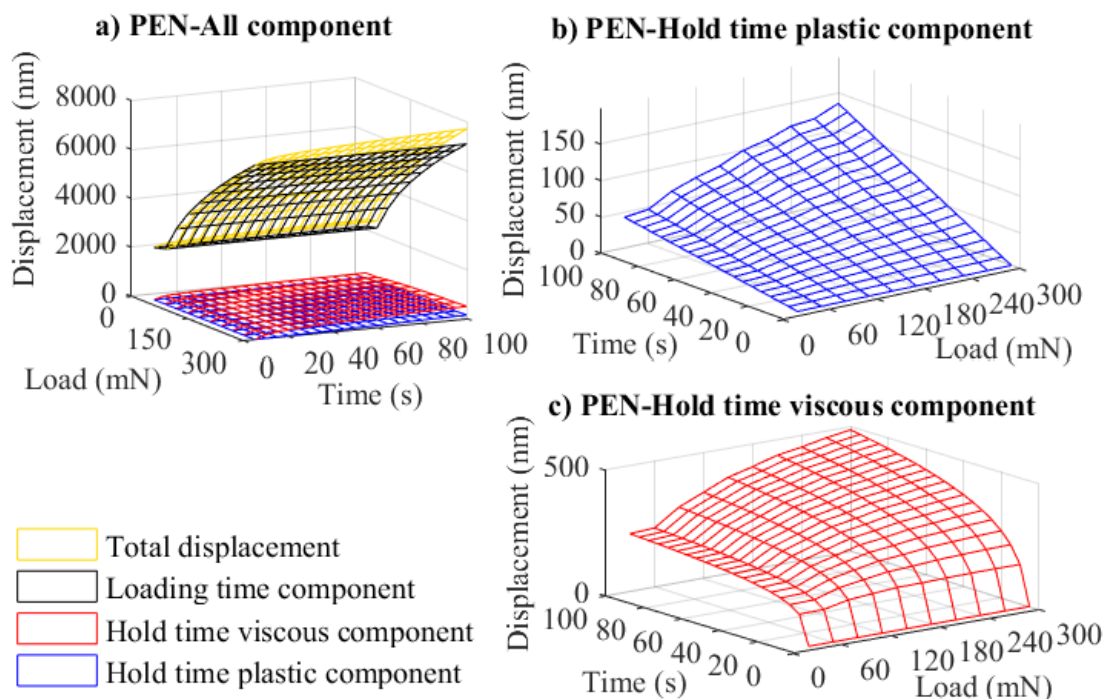


Figure 7-4 Displacement against maximum load and hold time plots, using method Log_2 (Equation 7-1) terms, for PEN polymer a) All terms the total displacement, b) Second term the plastic component, and c) Third term the viscous component.

Hertz equation (Fischer Cripps, 2011, pp.43 and 48), which is specific to the indenter type in an indentation test, and can be written in the form:

$$P = a_1 \times E_r \times h^x \quad \text{(Equation 7-2)}$$

Where P is the load, a_1 and x are constants and the values are different depending on which, spherical or Berkovich, indenter is used. E_r is the reduced modulus, and h is the penetration depth. Thus, a method is needed which account for the initial loading and allows determining the elastic modulus; this leads us to the next section.

7.3.2 Phenomenological fits

One model which accounted for the effect of initial unloading was considered in section 2.5.2 (Menčík, He and Němeček, 2011). A phenomenological route was taken to describe the physical events during hold-time, where the parameters are related to the physical properties of the polymers. Mencik et al. showed, by using their method, a plastic term and 2 Kelvin-Voigt bodies were sufficient to fit the data for a PMMA polymer. However, before fitting the data to PET and PEN, the number of Kelvin-Voigt (KV) bodies terms and if any plastic term (P) was needed were confirmed. It can be seen from Figure 7-5, for method $M_{iKV P}$ where i is an interger specifying the number of KV bodies, that a spring with 2 KV bodies and a plastic term give the best fits to the experimental data; this is also observed over a wide range of experimental conditions. In examining the fitting parameters, the deformation of each individual parameter in $h(t)^2 = ae^{bt} + ce^{dt} + e + f$ (Equation 2-21) could not be separated. This is due to the square root of all the terms not being equal to the square root of individual terms as stated below:

$$h = \sqrt{A + B + C} \neq \sqrt{A} + \sqrt{B} + \sqrt{C} \quad \text{(Equation 7-3)}$$

Thus, the moduli due to each individual component also could not be determined from Mencik's method.

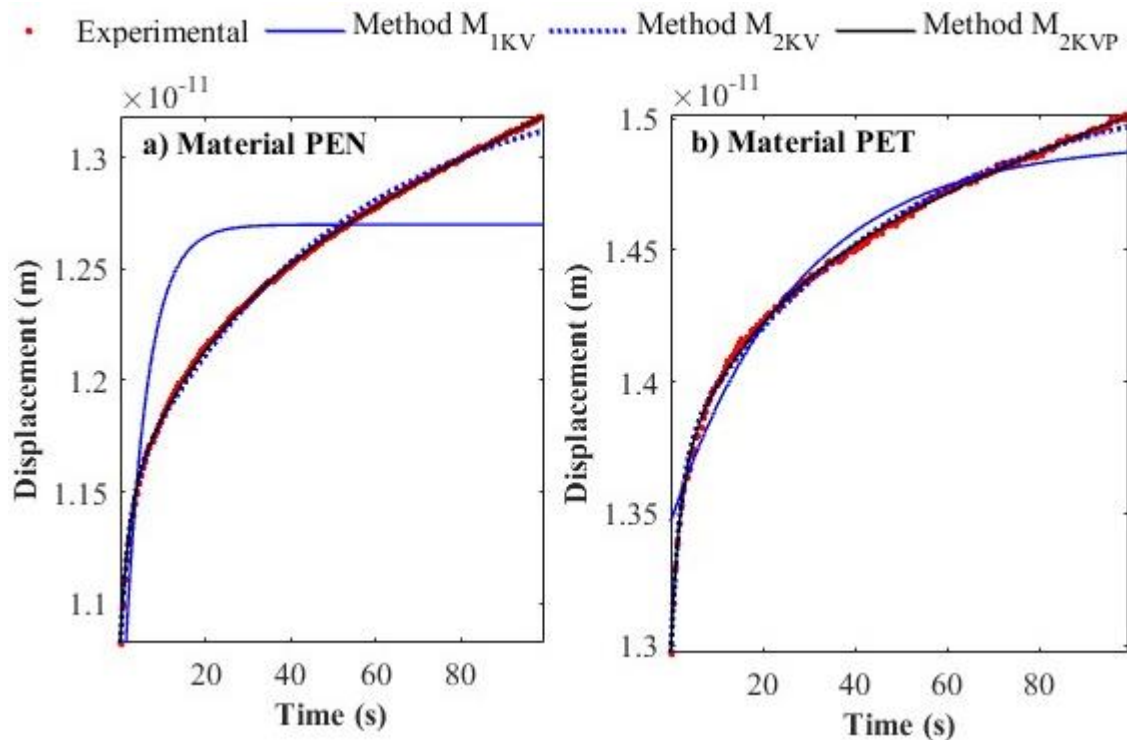


Figure 7-5 Nanoindentation hold time plots at Load of 90mN and initial Load rate of 5 mN/s using three different rheological methods for a) PEN and b) PET

7.3.3 A comparison between time dependent elastic modulus determined by E_T and DU-FCSPD methods

Using method E_T (see section 2.5.2), the elastic modulus, for both PET and PEN, is evaluated with both load and time (see Figure 7-6). The elastic modulus of PEN compared to PET is higher as expected. This elastic modulus was determined using all terms for the creep compliance, the bracketed term in (Equation 2-20), which are the instantaneous and visco-elastic-plastic effects. In order to determine how close these values were to the value obtained by the DU-FCSPD method, Experiment 4.1 was conducted and analysed (refer to Appendix 4 for test conditions). In Figure 7-7, for each of the experimental runs for PET and PEN a comparison between these two methods in determining the elastic modulus can be seen. The plots show a good match between the two curves at low loads and high load rates, confirming the exactness of the DU-FCSPD method in determining

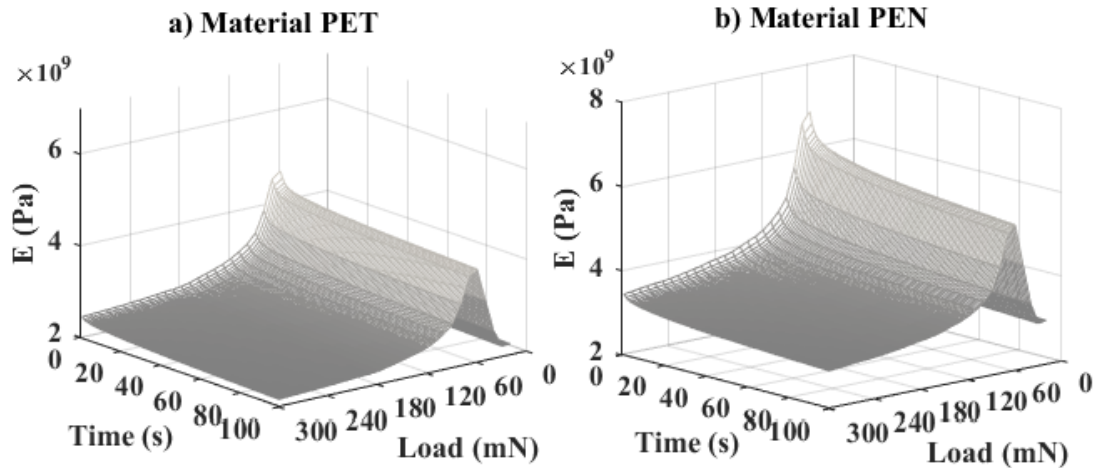


Figure 7-6 Elastic modulus (E) determined using method E_T against Time and Load for a) PET and b) PEN

the elastic modulus. The effect of plasticity on the elastic modulus values obtained by method E_T and the DU-FCSPD method can be seen more clearly, at lower load rates and high loads, and can cause a difference of ± 1.5 GPa. For PET, in particular, Figure 7-7a b & c show that the elastic modulus associated with the viscoelasticity (DU-FCSPD) is lower than the elastic modulus associated with the viscoelastic/plastic behaviour (method E_T), even though at these conditions the effect of plasticity should reduce the apparent viscoelastic modulus of the material. Thus, at lower load rates and higher loads, where the difference between the two methods is the greatest, the plasticity accounted for as in section 2.5.2 is not valid. A lower elastic modulus than the method E_T should not be possible. Thus, the assumption in the Mencik method to account for plasticity during the loading phase is only applicable at low loads and high load rates, otherwise giving higher elastic modulus than what really exists and sets a limitation on method E_T .

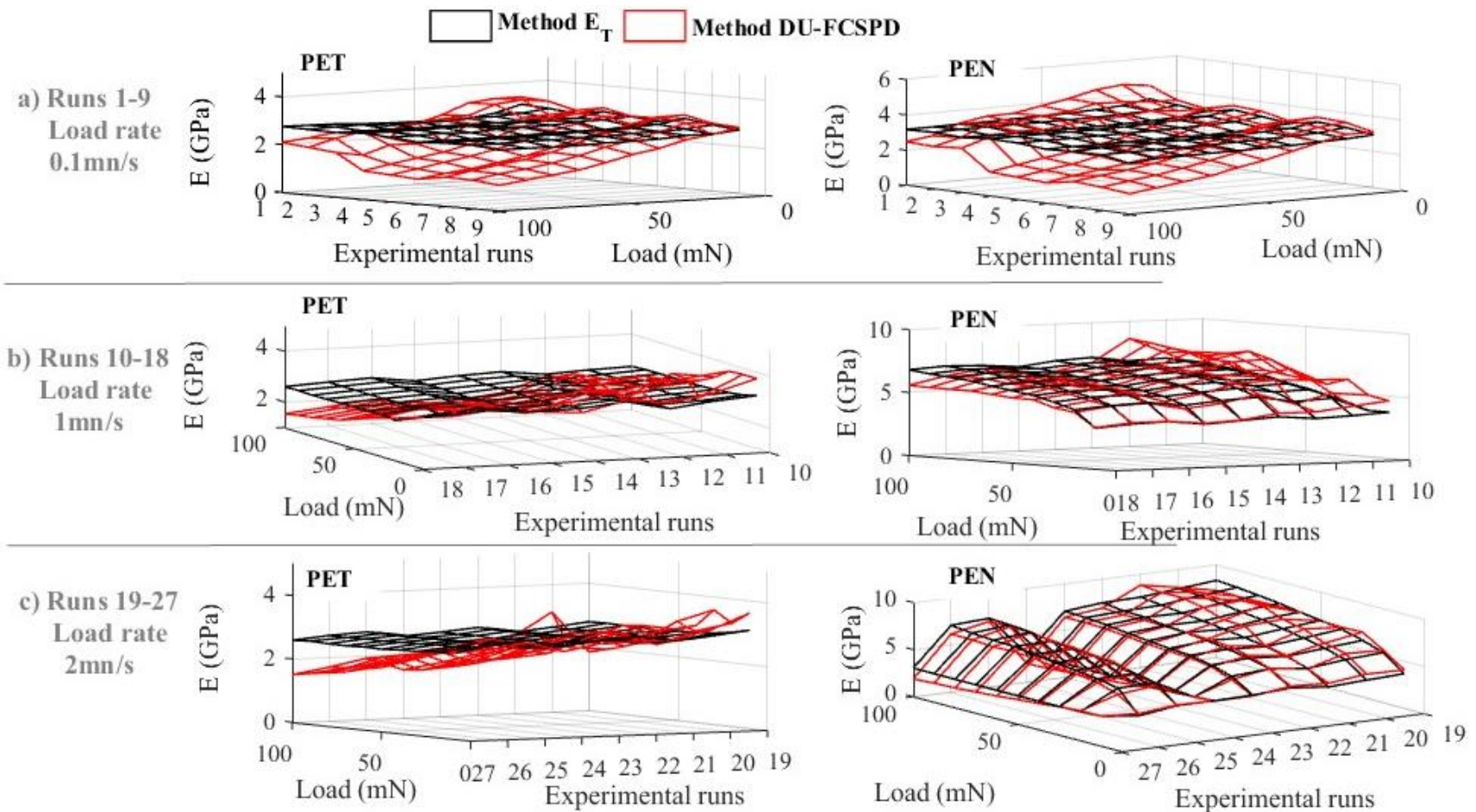


Figure 7-7 Elastic modulus (E) against load for different experimental runs for PET and PEN a) Experimental runs 1-9 with load rate of 0.1mN/s, b) Experimental runs 10-18 with load rate of 1mN/s, and c) Experimental runs 19-27 with load rate of 2mN/s. Refer to Appendix 4 for details on experimental runs.

7.4 Use of Neural networks in nanoindentation characterisation

Neural networks machine learning has been used for predictions in nanoindentation (Muliana et al., 2002; Tho et al., 2004). These types of machine learning techniques are needed when complex interdependencies between parameters exist, and no analytical relationship is possible. Using existing data determined for given variables, the Neural networks learn relationships between the variables and then can be used to predict data for different variable values. In the back-propagation fitting procedure, this is achieved by defining weights to the inputs and neurons, and also thresholds which decide on the outputs from neurons. Many neurons can be defined existing in different layers. A two-layer-feed-forward Neural network with sigmoid hidden neurons and linear output neurons is shown in Figure 7-8. These types of neural structures can fit multidimensional

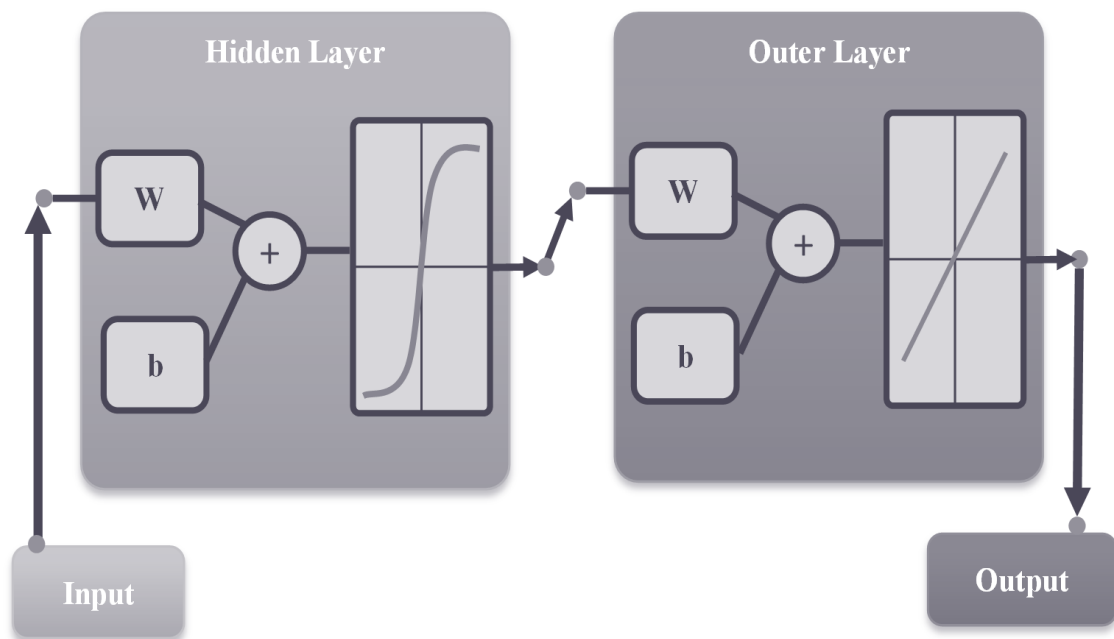


Figure 7-8 A two-layer-feed-forward Neural network

data extremely well depending on the amount of data given for learning and enough neuron in the hidden layer. Several structures were initially investigated, for the PEN sample, 10 hidden layers were sufficient, whereas 30 were needed for PET. Many

algorithms can be used for training Neural networks structures. However, within MatLab, the author utilised the Levenberg Marquardt algorithm, due to its improved performance compared to basic back-propagation and conjugate gradient algorithms (Jalali-Heravi, Asadollahi-Baboli and Shahbazikhah, 2008). Also, the mean squared error performance function is used within this algorithm to establish accurate one to one relationship between the function which would exist experimentally and the predicted function.

7.4.1 Neural networks results

It has been shown that interpolation can be applied to determine values between test conditions (see Figure 7-2 and Figure 7-3). However, when extrapolating the data, consistent values are hard to achieve due to the varying visco-elastic-plastic response. To find a way to determine values outside the test conditions, Neural network have been used. The responses of both PET and PEN were predicted using Neural networks employing the methodology as detailed in section 7.4. Data from Experiment 4.1 was used, and the experimental conditions are given in Appendix 4. The elastic modulus was predicted by splitting the experimental data into three, 60% being training data, 20% each for validation and test. Figure 7-9a & b shows the accuracy of the training, validation and test for both PEN and PEN, and it is apparent how close the values of the output and the targets are.

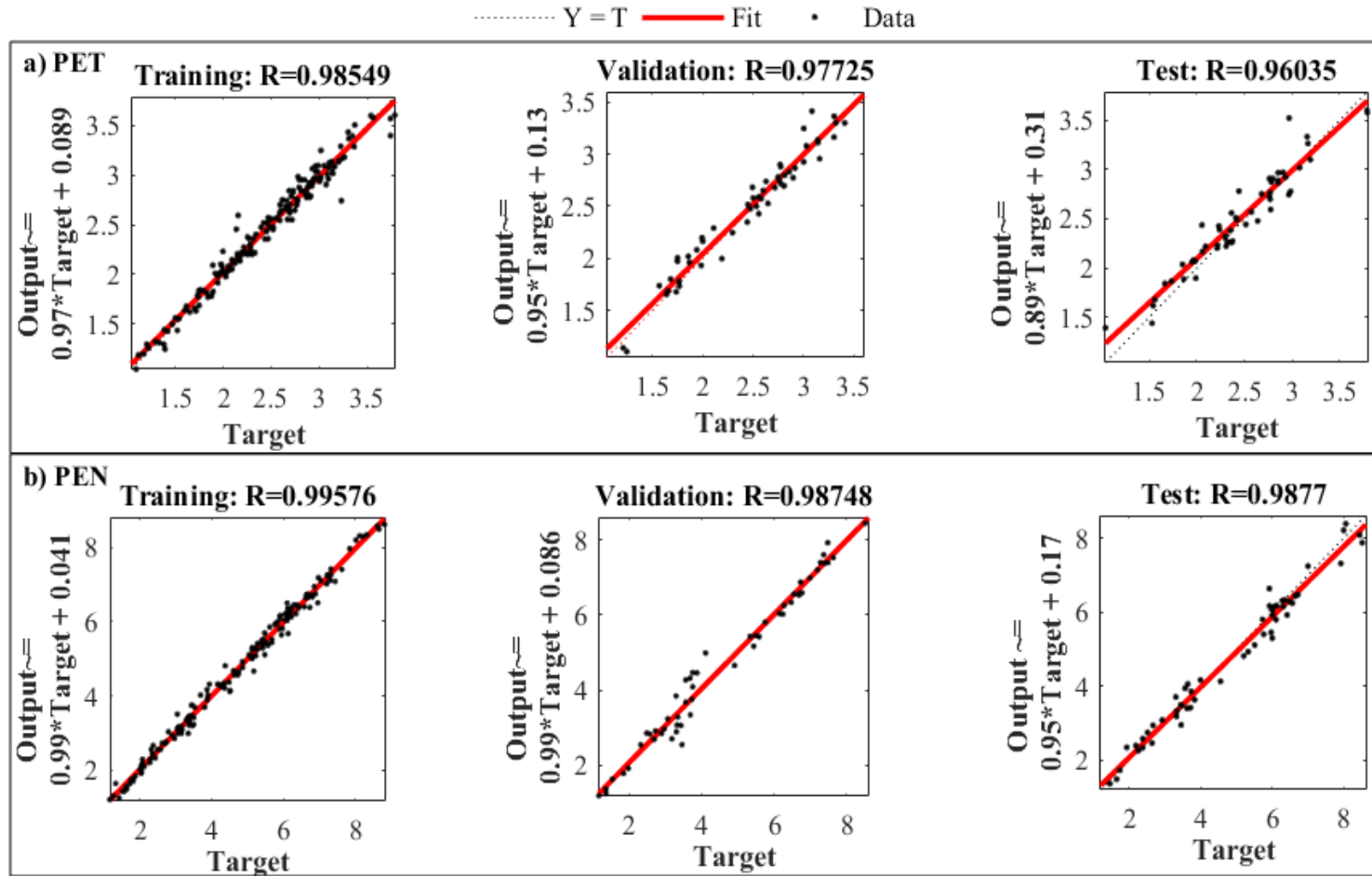


Figure 7-9 Neural network results a) PET and b) PEN

Figure 7 9a & b only show prediction within the data range. Further predictions were done at testing condition away from the original experimental test conditions. For both materials, elastic modulus against load plots can be seen in Figure 7-10. The results show reasonable values for these polymers, and confirm the PEN elastic modulus to be higher than PET. However, when the Neural networks were trained again, the results were different, sometimes showing negative values of the elastic modulus (not shown). The predicted elastic modulus against load behaviour changed from run to run. This can be seen clearly from the plots for both PET and PEN. This advocates that more data is required for the initial training for accurate results, which are reproducible every training run.

Variation for the elastic modulus was shown to exist within the sample from sheet to sheet and within different position on the sheet (see section 5.3) which is about 0.3 GPa. It can be seen when compared to Figure 7-9 that this variation is lower and when looking at

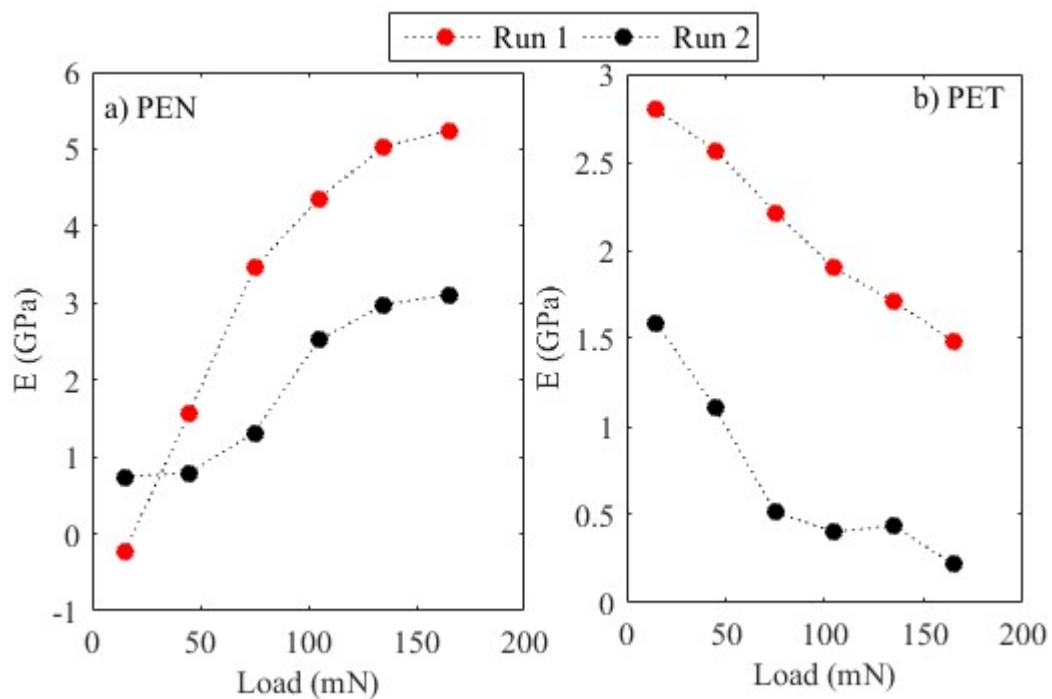


Figure 7-10 Elastic modulus (E) against Load for separate neural training run a) PEN Train run 1, b) PEN Train run 2, c) PET Train run 1, d) PET Train run 2

Figure 7-10 this variation can be as high as ~ 2 GPa for both PET and PEN. So, it is only viable to determine the elastic modulus with confidence within the range of test conditions for which the Neural network were trained.

Only at a particular load for a nanoindentation creep experiment, the material can be characterised to attain the time-dependent parameters. However, when performing indentation simulations, the parameters are needed throughout the loading cycle. In this chapter, it was noted that the values of the creep parameters and the determined mechanical properties at predefined test conditions could be found by various techniques, i.e. interpolation, extrapolation and by Neural networks. For full characterisation, parameters need to be determined at any practical test condition. However, there are issues. Interpolation can give accurate values of the parameters between the experimental, whereas when using extrapolation techniques, false values are determined, especially when the gradient change is high at the boundaries of the experimental conditions. This is more certain at low loads, sometimes giving negative values of the elastic modulus which is not valid. This can be avoided by a piecewise argument which states that below a certain load, for instance, 0.1 mN, the elastic modulus is constant whereas above, the interpolation and extrapolation techniques are used. The accuracy of this still needs further investigation. For Neural networks, it was concluded that a broad set of experiments are needed for each material to give accurate results, especially outside the test conditions, however, when trained, the Neural network can be efficient.

7.5 Summary

In this chapter, an insight into the viscous behaviour of the two polymers was given. Logarithmic and Mencik's methods were further developed by the author for the purpose of characterisation. Mencik's methods accounted for the initial loading and could be related to the elastic properties of the material, whereas the Logarithmic method could

not. Using Mencik's methods, it was shown that the individual components of the elasticity could not be separated. Thus, all components were used, for the creep compliance, to determine the elastic modulus. Method E_T compared well with the DU method except for test conditions which showed high viscous behaviour, confirming the elastic modulus determined by the DU method to be correct for non-quasi static conditions.

Moreover, interpolation was successfully applied to determine values between test conditions. However, when extrapolating outside the test conditions, the trained Neural network did not determine accurate parameters. It was concluded that interpolation and other extrapolation techniques be employed to determine parameters for FEM. The next chapter is dedicated to reviewing characterisation of hard coatings/compliant substrates systems using nanoindentation and details the application of the DU methodology to thin film characterisation.

Chapter 8

DU METHODOLOGY APPLICATION TO THIN FILM CHARACTERISATION

8.1 Introduction

When a coated system is used in a particular application, the mechanical performance of that system is critical (Bull, 2005). As the performance depends on the whole system, not just individually for the coating and substrate, once the coating layers and substrate are characterised, modelling and simulation can lead to better design decisions, for improved products and efficient manufacturing. However, one of the challenges encountered by nanoindentation studies is determining the mechanical properties of just the thin film itself without the influence of the underlying substrate.

For a quantitative analysis of the coating's mechanical properties, such as hardness and elastic modulus, determined via depth sensing techniques, the values can vary due to the different analytical methods linked with their assumptions, as shown in Chapter 6. Therefore, using the most accurate determined methods, i.e. O3-MCS, DU-FSPD AND DU-FCSPD unloading methods (refer to table 6.1 for method syntax), the plastic hardness and elastic modulus values, for TiN, TiO₂ and AZO coated systems, were determined as a function of depth, and compared. This data was thus used to characterise each coating using different models. The Adapted Discontinuous Elastic Interface Transfer Model (ADEITM) showed better fitting than the Discontinuous Elastic Interface Transfer Model (DEITM). However, the Five Parameter Logistic Regression Model (5PL) was the most accurate fit to the data.

This chapter includes a detailed literature review on earlier models for characterising thin films. The models mentioned above and the Energy Dissipation Model (EM) were

detailed further and used to determine the elastic modulus of the coating without the knowledge of the individual Poisson's Ratio of the coating and substrate and were compared to each other.

8.2 Nanoscale nanoindentation modelling of thin films systems

After the recognition of the technique through the work of Oliver & Pharr (1992), low load testing of thin films became increasingly popular (Hainsworth, Bartlett and Page, 1993a; Whitehead and Page, 1992). Nanoindentation test data was found to be unique, i.e. signifying a true mechanical “fingerprint” of the sample tested (Page and Hainsworth, 1993). In section 5.2.2, for the TiN, TiO₂ and AZO coatings, the unique load-displacement curves were plotted, also displaying information regarding the failure of the coatings. The typical deformation of these types of coated systems was also described in section 5.2.4. When trying to probe mechanical properties, the substrate contributes to the total deformation, and its effect needs to be eliminated in order to achieve only the coating properties. Nanoindentation measurement of the elastic modulus of thin films is strongly affected by the substrate due to the elastic field not being confined to the film itself; stresses exist as a long-range field that extend into the substrate even when the applied load is low. Thus, the determined stiffness, affected by the substrate, invalids the use of the standard Oliver and Pharr method (1992) for predicting the coatings elastic modulus correctly. The hardness of the coating is much harder to quantify due to the complex interactions of the plastic zone with the substrate. To completely avoid substrate effects when indented, typically 1/10 rule is applied (H. Bückle, 1961; Manika and Maniks, 2008). However, when the substrates become more compliant it is no longer valid (Hainsworth, Bartlett and Page, 1993a; Hay, O'Hern and Oliver, 1998; Page and Knight, 1989; Saha and Nix, 2002). It has been shown that the coating properties can be determined through modelling the contact of thin film systems.

The earliest models were based on the area law-of-mixtures concept. Buckle proposed an empirical equation for the hardness of a thin film given by linear interpolation of the coating and substrate hardness with a single weight factor (Westbrook, Conrad and Metals, 1973, pp.453–491). Jönsson and Hogmark (1984) later proposed the area fraction model where the individual area contribution of the substrate and the coating was determined by the geometry of the indent to find the overall hardness. Further improvements considering ISE (De Maria et al., 2001) and factors such as constraints by the surrounding coating and friction of the indenter (Poisl, Fabes and Oliver, 1993) have been proposed to the area fraction model.

The changing contributions of the substrate and film to the compliance, as measured by the indenter, to the overall combined young modulus were accounted for by Doerner and Nix (1986). Good agreement between empirical data was achieved for tungsten film on silicon. However, the constants used to describe the changing contribution had to be determined empirically, and the method was only applicable for particular films on given substrate types. This model was further developed by King (1987). It should be noted that these analyses considered a flat-ended cylindrical, quadrilateral, and triangular punches indenting a layered isotropic elastic half-space. These obtained mathematical expressions were further developed by considering a Berkovich indenter (Saha and Nix, 2002).

Other authors (Bhattacharya and Nix, 1988) developed equations using FEM to determine the hardness and modulus for a perfectly sharp tip indenting a hard/soft thin film on a hard/soft substrates for different coating thicknesses. Moreover, the deformation was examined for a harder stiffer layer, with variable thicknesses, compared to the substrate and by using FEM (Komvopoulos, 1989). The highest stress was found to occur below the surface, and the yielding always initiated below the interface in the substrate and grew

within the substrate. Also, the thickness of the coating played a critical role in the size and location of the plastic zone.

The volume fraction model (Bull and Rickerby, 1990; Burnett and Rickerby, 1987) as originally proposed by Sargent (1979) was used to compare experimental results. These models consider the various stages of deformation, which comprise of stage 1 when the plastic zone is just in the coating, stage 2 where the plastic zone of the coating and substrate interact and stage 3 where the plastic zone advances into the substrate. It was found that the Bhattacharya equation (Bhattacharya and Nix, 1988) did not fit the experimental data due to not correctly predicting the yield stresses, for the different coating thicknesses. This was because the initial analysis was developed using a perfect cone indenter. Therefore, a precise area function was needed to obtain the correct response. To obtain a more accurate equation, the FEM data would have to be recalculated using a precise area function. The volume fraction model was better in determining the hardness. Therefore, it was suggested that the increase in hardness for the thin film was due to the interaction of the plastic zone of the film and substrate, and not due to the change in structure and intrinsic properties of the coating. Extending the work of Bhattacharya and Nix (1988) experimental data were fitted using the volume fraction model for titanium coating on a sapphire substrate (Fabes et al., 1992). The model used a cone shape for the deforming volume, which differed from the hemispherical shape. Chechenin et al. (1995) showed that none of the models were successful in determining the composite hardness for hard films on soft substrates and proposed spheroidal shape for the plastic zone.

A successful alternative model to determine the elastic modulus was given by Gao et al. (1992). An expression for the combined modulus was established using a moduli-perturbation method. Many other similar empirical relations have been proposed using

weighting factors in combination with experimental or finite element modelling. The formulae were further used to study various coating (Swain and Weppelmann, 1993).

For hard coating on compliant substrates, the “1/10” rule of Buckle is not valid since the coating flexes as the foundation, i.e. the substrate beneath, gives way (Page and Knight, 1989). The deformation is a combination of bending and stretching within the coating. Apart from the plastic deformation, the viscous behaviour in polymeric substrates is also responsible for the failure of the foundation (Hainsworth, Bartlett and Page, 1993b). A plate resting on an inelastic foundation has been used to model this type of behaviour (Ramsey, Chandler and Page, 1991, pp.504–509). Extending this work, incorporating fracture of the coating, McGurk et al. (1994) were able to demonstrate the model on several coated systems. Sun et al. (1995) also studied the nanoindentation process of a hard coating on a softer substrate. An equation to describe the critical ratios of coating thickness to indentation depth at which the substrate effect was less than 2% of the deformation was derived, showing a polynomial function of the ratio of yield strength of the coating and substrate.

Empirical expressions were further developed by Mencík et al. (1997). They compared and tested several weighting functions, and recommended the expression by Gao et al. (1992). Korsunsky et al. (1998) reviewed previous models for coating/substrate deformation and developed an energy-based model to investigate the deformation at various scale lengths. It was stated that the volume fraction model predicted deformation more precisely but was more complex to apply. A number of PVD arc-evaporated coatings were investigated including TiN, where the composite hardness was determined with the depth of indentation. They also proposed various stages of deformation, as seen in Figure 8-1 which also shows the change in composite hardness. Stage 1a is only elastic response within the coating, stage 1b is elastic-plastic deformation of the coating, stage

2a can be of fracture of the coating or coating-substrate mixed transition, stage 2b is substrate dominated mixed deformation, and lastly, stage 3 only consists of the substrate deformation. The model worked remarkably well, giving excellent results and was said to apply to a wide range of coatings and thicknesses manufactured by different techniques.

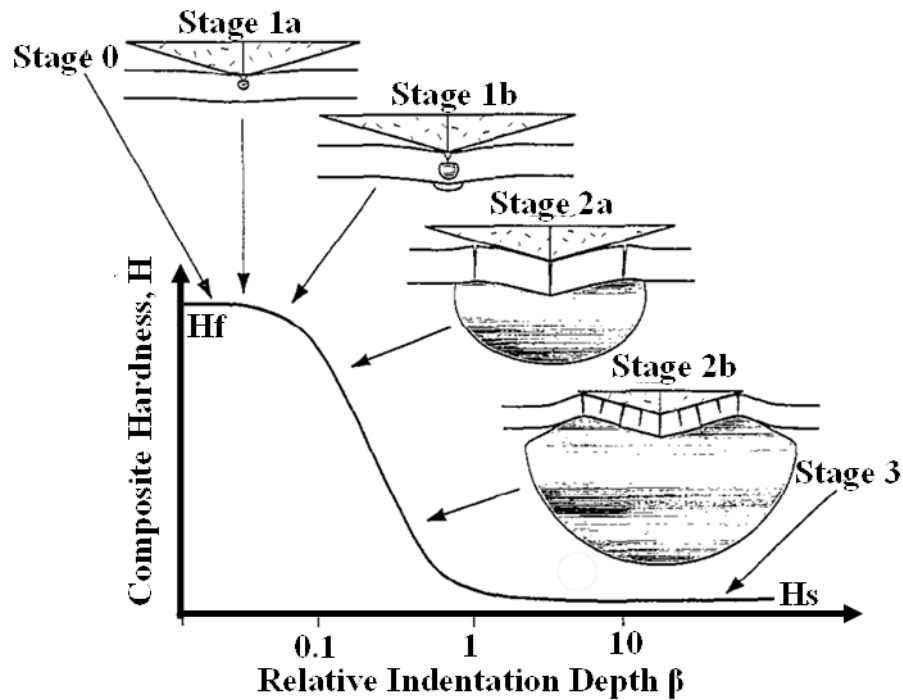


Figure 8-1 Composite hardness (H_c) against relative indentation depth, adapted from (Korsunsky et al. 1998)

For a hard coating on a soft substrate the principal driving force for coating failure and crack formation during indentation was confirmed to be due to the plastic deformation of the underlying substrate (Thomsen, Fischer-Cripps and Swain, 1998). A mathematical approach which solves the problem of Hertzian stress distribution in a coated half-space was given by Schwarzer et al. (1999) to determine the elastic modulus of thin film and extended further considering plastic deformation (Chudoba, Schwarzer and Richter, 2000).

In reviewing previous models, the energy-based predictive model for determining the effect of plastic depth (indentation depth) on the hardness and modulus of a coated system has been extended by Bull, Berasetegui and Page (2004). When the effects of fracture of the coating were introduced, the solution was found to be more accurate. In all previous work as described above, it should be noted that the materials were considered homogeneous with no residual stresses.

Other authors applied a numerical analysis of spherical indentation response of thin hard films on soft substrates (Vanimisetti and Narasimhan, 2006). It was found that the plastic zone attains a self-similar shape comparable to the expanding cavity model proposed by Johnson (1970). Beyond a certain stage when indented, the film was said to experience bending and behaved similarly to the model proposed by McGurk et al (1994), showing a transition from Hertz-type behaviour to a dominated flexure of the film. Also, the film–substrate system was shown to become more compliant with reduction in substrate yield strength or by occurrence of compressive residual stresses in the film. Overall understanding how the stresses evolved during each stage, including the effect of the interface, explains the deformation. The evolution of plastic zone from the coating to the substrate and contact radius were said to be important factors.

Similarly, studies were conducted investigating the effect of a conical indenter on soft film/hard substrate and hard film/soft substrate systems and with FEM simulations, to configure different mechanical parameters, such as elastic modulus, Poisson's ratio and initial yield stress, in such a way that the piling-up and sink-in phenomena could be observed (Pelegri and Huang, 2008). It was found that when the elastic modulus of a coating was larger than its substrate, the calculated value of the combined modulus decreased with the maximum indentation displacement and vice versa if it was smaller than its substrate. The calculated elastic modulus of thin films corresponded more to the

mechanical properties of substrates than did the calculated hardness. The sink-in of the hard film on soft substrate was more severe than that just indented on the substrate.

Huang and Chang (2010) studied AZO films on different substrates revealing different characteristics during the nanoindentation test. It was found the higher the hardness and elastic modulus of the hard coatings compared to the soft substrates, the earlier the substrate effect occurred under a smaller indentation depth, and that the “1/10” rule, where indentation depth less than 1/10 of the coating thickness are also considered valid (H. Bückle, 1961), was not applicable in this case. A modification of the fitting model (Bhattacharya and Nix, 1988) was made to evaluate the effective values of H. Also a calibration was performed on the King model to determine the effect of the parameter α , which is an important factor for determining the substrate effect (King, 1987).

More recently, Zhou et al. (2011) developed a universal method to accurately and reliably extract the elastic modulus of a thin film on a substrate. Whereas previous models by Doerner and Nix (1986) and Gao et al. (1992) assumed continuous transfer of the internal stress within the coating/substrate system a discontinuous elastic interface transfer model was proposed by Zhou and colleagues. This discontinuity in stress at the interface can be seen in Figure 8-2. This method worked well for 25 different combinations of 5 films on 5 substrates that encompassed a wide range of compliant films on stiff substrates to stiff films on compliant substrates. Other work, considering compliant films on stiff substrates and stiff films on compliant substrates, showed an accurate prediction of the composite response for E_f/E_s values between 0.1 and 10 (Hay and Crawford, 2011).

In this section, a detailed review was given on how coating properties are determined through modelling the contact response of thin film systems. The next section further details previous DEITM and EM models, and also the ADEITM and 5PL model proposed by the author, for analysis of the studied coatings.

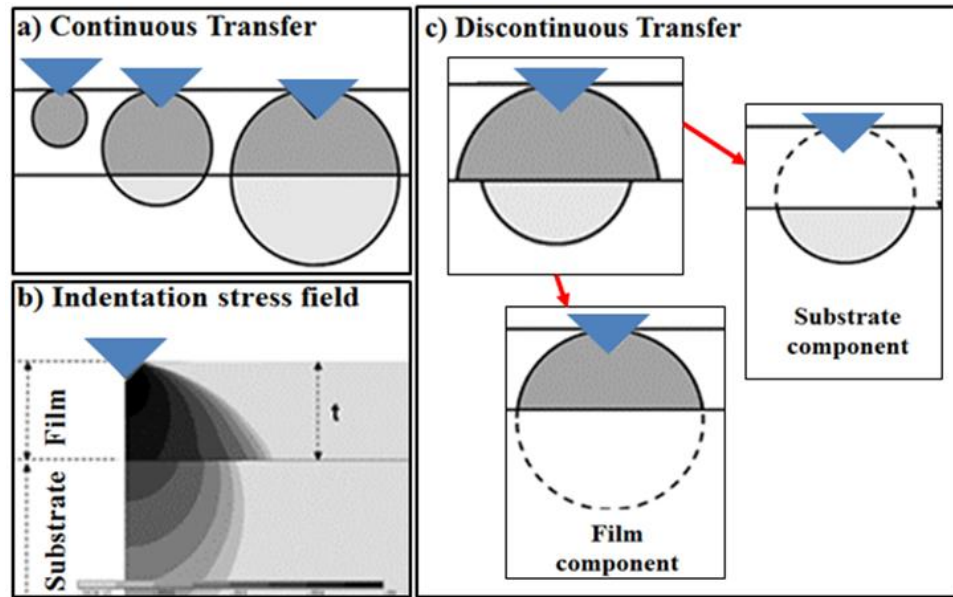


Figure 8-2 Indentation stress field and associated substrate effects a)continuous, b) indentation stress field of discontinuous transfer c) components of discontinuous transfer, adapted from (Zhou et al. 2011)

8.3 Substrate-independent coating properties

Using the O3-MCS, DU-FSPD and DU-FCSPD unloading methods, the elastic modulus with indentation depth was established for all the coatings. Typically one-tenth of the coating thickness is used to obtain the coating elastic modulus (Manika and Maniks, 2008). However, for hard coatings on compliant substrates, this value is much smaller. As previously discussed in section 8.2 there have been numerous authors who have considered forming the relationship of the elastic modulus and hardness with the depth, normalized depth or normalized contact area through the consideration of different phenomena's. The methodologies adopted in this work are listed in Table- 8-1. An adaptation of DEITM and the work of Gao et al. (1992) is referred to as ADEITM Model, and the Five Parameter Logistic Regression Model (5PL) are both proposed by the author. The DEITM method was used since it can successfully determine elastic modulus and hardness for many film-substrate combinations, encompassing a wide range of compliant

Table- 8-1 Coating characterisation methods

Models	Reference
DN	(Doerner and Nix, 1986)
DEITM	(Zhou and Prorok, 2010a)
ADEITM	The author
EM	(Bull, Berasetegui and Page, 2004)
5PL	The author

films on stiff substrates to stiff films on compliant substrates. It is shown that models used previously for determining coating properties can also be used when data is acquired by the DU method. Thus, all the models are compared when data is acquired by the DU method (see section 4.5). First the formulation for each model is detailed.

8.3.1 Discontinuous Elastic Interface Transfer Model (DEITM)

The empirical function of the Combined Modulus of the coating/substrate system is shown by Doerner and Nix (1986) to be

$$1/Et = (1 - \phi)/Ef + \phi/Es \quad \text{(Equation 8-1)}$$

Where Ef and Es are related to the film elastic modulus (E_{film}) and substrate elastic modulus ($E_{substrate}$) by the following two equations

$$Ef = \frac{E_{film}}{-\nu^2 + 1} \quad \text{(Equation 8-2)}$$

And

$$Es = \frac{E_{substrate}}{-\nu^2 + 1} \quad \text{(Equation 8-3)}$$

and ϕ is the weight factor and can be expressed in the form

$$\phi = \exp\left(-\alpha_d\left(\frac{t_c}{h}\right)\right) \quad \text{(Equation 8-4)}$$

h is the penetration depth, t_c is the thickness of the coating and α_d a constant. Initially the effective depth was used in their work, but later the normalized depth was introduced by Saha and Nix (2002).

On the other hand, in the discontinuous elastic interface transfer model, the weighted factors are associated separately for the coating and substrate by Zhou and Prorok (2010a) due to the fact the elastic strain field is discontinuous across the coating/substrate interface. These factors are expressed as:

$$\phi_f = \exp\left(-\alpha_f\left(\frac{t_c}{h}\right)\right) \quad \text{(Equation 8-5)}$$

$$\phi_s = \exp\left(-\alpha_s\left(\frac{t_c}{h}\right)\right) \quad \text{(Equation 8-6)}$$

Where the apparent value of the elastic modulus is related to the elastic modulus of the coating and substrate by the expression similar to (Equation 8-1)

$$\frac{1}{Et} = \frac{1 - \phi_s}{Ef} + \frac{\phi_f}{Es} \quad \text{(Equation 8-7)}$$

Substituting (Equation 8-5) and (Equation 8-6) into (Equation 8-7) the elastic modulus becomes:

$$\frac{1}{Et} = \frac{1 - \exp\left(\alpha_s\left(\frac{t_c}{h}\right)\right)}{Ef} + \frac{\exp\left(\alpha_f\left(\frac{t_c}{h}\right)\right)}{Es} \quad \text{(Equation 8-8)}$$

A regression fit can be performed to determine Ef by fitting $\frac{1}{Et}$ with $\frac{t_c}{h}$ with known value of Es . For determining the true film elastic modulus (Zhou and Prorok, 2010b)

$$\frac{1}{Et} = \left[(1 - \phi_s) \left(\frac{(Ef)^{0.1}}{Es} \right) \right] + \left[\frac{\phi_f}{Es} \right] \quad \text{(Equation 8-9)}$$

Substituting (Equation 8-5) and (Equation 8-6) into (Equation 8-9) the true film elastic modulus becomes:

$$\frac{1}{Et} = \left[\left(1 - \exp\left(\alpha_s \left(\frac{t_c}{h}\right)\right) \right) \left(\frac{(Ef)^{0.1}}{Es} \right) \right] + \left[\frac{\exp\left(\alpha_f \left(\frac{t_c}{h}\right)\right)}{Es} \right] \quad \text{(Equation 8-10)}$$

The above analysis excludes the effect of the indenter. However, if the Combined Modulus of the coating/substrate system becomes comparable to the diamond indenter then the reduced modulus must be related to the Combined Modulus of the coating/substrate system by

$$1/Er = 1/Et + 1/Ei \quad \text{(Equation 8-11)}$$

This is based on springs in series, where E_i is the elastic modulus of the indenter. Rearranging (Equation 8-11) becomes:

$$Et = (Ei)(Er)/(Ei - Er) \quad \text{(Equation 8-12)}$$

The combined coating/substrate system data can be corrected and then fitted to the above equations, or even better, Et can be substituted from (Equation 8-12) into (Equation 8-8) and (Equation 8-10). The resulting expression is (Equation 8-13) and the film elastic modulus is given by (Equation 8-14). When using both these equations to fit the raw experimental data, the effect of the Poisson's Ratio of the coating and substrate is included in the analysis.

(Equation 8-13)

$$Er = Ef \times Es \times \left[\frac{Ei}{\left(\exp\left(-\alpha_f \times \frac{t_c}{h}\right) \times Ef \times Ei\right) - \left(\exp\left(-\alpha_s \times \frac{t_c}{h}\right) \times Ei \times Es\right) + (Ef \times Es) + (Ei \times Es)} \right]$$

204

(Equation 8-14)

$$Er = Ef \times Es \times \left[\frac{Ei}{-\left(Ei \times Es \times \exp\left(-\alpha_s \times \frac{t_c}{h}\right) \left(\frac{Ef}{Es}\right)^{0.1}\right) + \left(\exp\left(-\alpha_f \times \frac{t_c}{h}\right) \times Ef \times Ei\right) + \left(Ei \times Es \times \left(\frac{Ef}{Es}\right)^{0.1}\right) + (Ef \times Es)} \right]$$

8.3.2 Adapted Discontinuous Elastic Interface Transfer Model (ADEITM)

Nearly all the work on the characterisation of thin films is associated with applying weights to the coating and substrate, with successive publications revising the equations and giving different physical explanations (see section 8.2), while still managing to get accurate fits to the nanoindentation data. The author gives one such approach where the weighted factors have been associated separately for the coating and substrate, as in the DEITM model (Zhou and Prorok, 2010a), and the apparent value of the elastic modulus is related to the elastic modulus of the coating and substrate by the expression similar to Goa et al. (Gao, Cheng-Hsin and Jin, 1992)

$$E_t = [E_s \times \phi_f] + [(1 - \phi_s)E_f] \quad \text{(Equation 8-15)}$$

E_f and E_s are related to the film elastic modulus and substrate elastic modulus by the Equations (Equation 8-2) and (Equation 8-3). Substituting for E_t from (Equation 8-12) into (Equation 8-15) gives:

$$E_r = E_i \times \left[\frac{(\phi_f \times E_s) - (\phi_s \times E_f) + E_f}{(\phi_f \times E_s) - (\phi_s \times E_f) + E_f + E_i} \right] \quad \text{(Equation 8-16)}$$

Substituting (Equation 8-6) and (Equation 8-5) into (Equation 8-16) the elastic modulus becomes:

$$E_r = E_i \left[\frac{\exp\left(-\phi_f \times \frac{t_c}{h}\right) E_s - \exp\left(-\phi_s \times \frac{t_c}{h}\right) E_f + E_f}{\exp\left(-\phi_f \times \frac{t_c}{h}\right) E_s - \exp\left(-\phi_s \times \frac{t_c}{h}\right) E_f + E_f + E_i} \right] \quad \text{(Equation 8-17)}$$

A regression fit can be performed to determine E_f by fitting E_r with $\frac{t_c}{h}$ with known value of E_s .

8.3.3 Energy Dissipation Model (EM)

The method relates to the stored energies in each layer and substrate (Bull, Berasetegui and Page, 2004). For the relative effective radius of the elastically deformed region (R_{eff}) to the thickness of the coating (t), two piece-wise expressions for the elastic modulus (E) are determined.

For $R_{eff} \leq t$

$$E = Ef \quad \text{(Equation 8-18)}$$

For $R_{eff} > t$

$$E = \left[\left(3 \left(\frac{t_c}{2R_{eff}} \right) - \frac{t_c^3}{2R_{eff}^3} \right) Ef \right] + \left[\left(1 - \left(3 \left(\frac{t_c}{2R_{eff}} \right) \right) + \frac{t_c^3}{2R_{eff}^3} \right) Es \right] \quad \text{(Equation 8-19)}$$

Where t_c is the thickness of the coating; Bull (2004) used the radius of the plastic zone to get an indication of the value of R_{eff} . This was previously defined by Johnson

$$R = k_2 \times \delta \times \left(\frac{E}{H} \right)^{\frac{1}{2}} \times \cot(\psi)^{\frac{1}{3}} \quad \text{(Equation 8-20)}$$

where k_2 is 3.64 for a Berkovich indenter, $\psi=0.71$, δ is the indentation depth, E and H are the materials elastic modulus and hardness. The effective radius is some order magnitude of the plastic zone radius and is defined as:

$$R_{eff} = \alpha \times R \quad \text{(Equation 8-21)}$$

Substituting k_2 , ψ and into (Equation 8-20) and then substituting R into (Equation 8-21) gives:

$$R_{eff} := 4.14 \times \alpha \times \delta \times \sqrt{\left(\frac{E}{H}\right)} \quad \text{(Equation 8-22)}$$

Also, letting the normalised depth (δ_{norm}) be defined as

$$\delta_{norm} = \delta/t_c \quad \text{(Equation 8-23)}$$

Thus

$$\delta = \delta_{norm} \times t_c \quad \text{(Equation 8-24)}$$

Also defining

$$U = E/H \quad \text{(Equation 8-25)}$$

Substituting (Equation 8-22), (Equation 8-24) and (Equation 8-25) into (Equation 8-19) gives (Equation 8-26). This equation can be used to perform a regression fit to determine Ef by fitting the surface response of H , δ_{norm} and U with the known value of Es .

$$H = \frac{1}{\left(\left(\frac{5}{U^2}\right) \times \alpha^3 \times \delta_{norm}^3\right)} \left[\begin{aligned} & (0.36Ef \times \alpha^2 \times \delta_{norm}^2 \times U) \\ & - \left((0.7 \times 10^{-2})Ef\right) \\ & + \left(Es \times \alpha^3 \times \delta_{norm}^3 \times U^{\frac{3}{2}}\right) \\ & - \left(0.36Es \times \alpha^2 \times \delta_{norm}^2 \times U\right) \\ & + \left((0.7 \times 10^{-2})Es\right) \end{aligned} \right] \quad \text{(Equation 8-26)}$$

8.3.4 Five Parameter Logistic Regression Model (5PL)

It will be shown that apart from when the Energy method, previous methods are generally poor at fitting the nanoindentation data with the datum correction. Thus, to determine coating and substrate elastic modulus from the determined reduced modulus with normalised depth data, the 5PL Model is used. The related expression is described as:

$$f(x) = dm + \frac{a - dm}{\left(1 + \left(\frac{x}{c}\right)^b\right)^e} \quad \text{(Equation 8-27)}$$

where x is the normalised depth, a is the Minimum asymptote and can be set to the coating or substrate depending which is lower, b is Hill's slope, c is the inflection point (and is defined as the point on the curve where the curvature changes direction or signs), dm is the maximum asymptote and again can be set to the coating or substrate depending which has the higher value, and lastly e is asymmetry factor. When e is set to one a symmetrical curve around the inflection point can be fitted and the equation also equals a four-parameter logistic equation. For the DEITM Model (Zhou and Prorok, 2010a) all parameters, except the coating/substrate reduced modulus and normalised depth, are related to the Poisson's Ratio of the coating and substrate. Thus, for this model parameters b , c & e are also related to those parameters and dimensional analysis could be used to determine an equation in terms of the Poisson's ratio, however (Equation 8-27) can still be used as it fits experimental data accurately.

8.4 Comparison of depth-dependent properties data between different methods

Experiments 8.1 details the several DOE's conducted on various coating/substrate systems using nanoindentation (for details refer to Appendix 8.1). Multi-indent tests were attempted using the micromaterial's nanoindenters. However, for depth-controlled mode,

sometimes depth target was achieved and sometimes load target, for load-controlled mode, the thermal drift for all ten indents had to be considered together, which was substantial over the time of the test. Thus, for each DOE, single indent tests were used with either depth-controlled or load-controlled modes. The O3-MCS, DU-FSPD and DU-FCSPD unloading methods were used to determine the reduced modulus data at various depths. These results are discussed below by examining Figure 8-3, Figure 8-4 and Figure 8-5, which show all indents at each depth of all the film-substrate combinations. The data in these plots was corrected by eliminating data $\pm 2\sigma$. Also, the normalised RDL can be seen on the plot for an indication of the data to be above or below RDL. The values of reduced modulus and hardness can be compared to previous works. Chawla et al. (2009b) found E between 100-300 GPa and H between 10-25 GPa for various thickness of nanocrystalline TiN films on glass substrate deposited using magnetron sputtered. Wu et al. (2006) found, for 550 ± 30 nm thick TiO_2 deposited using magnetron sputtered, E to

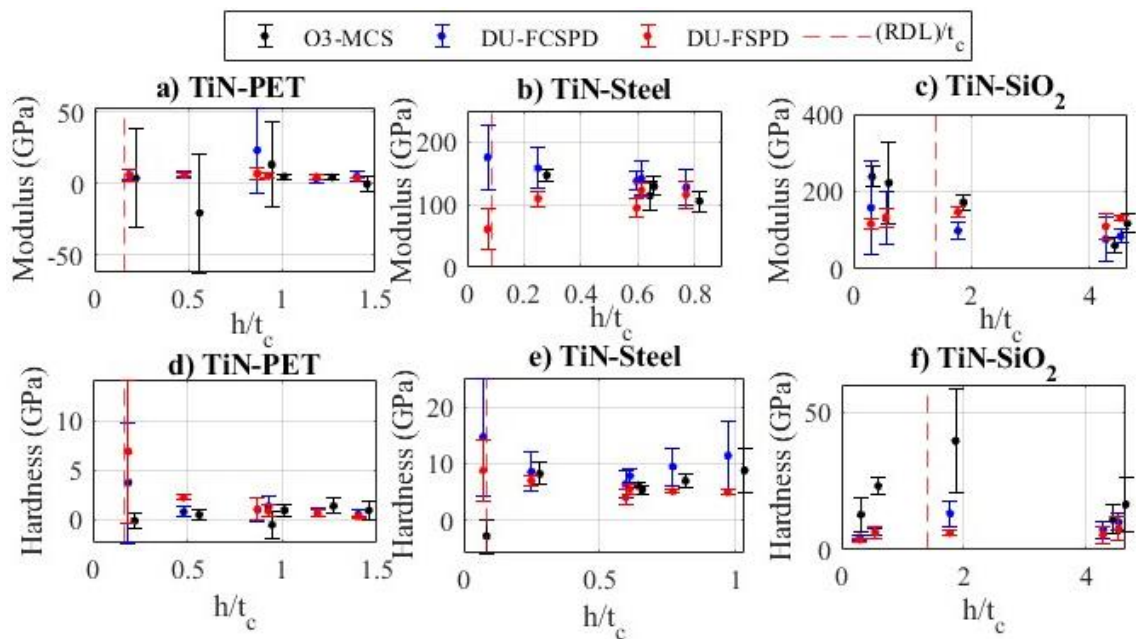


Figure 8-3 TiN reduced modulus and hardness against normalised depth on three different substrates a) and b) on PET, c) and d) on Steel, e) and f) on Silicon. Each error bar shows one standard deviation from the mean value.

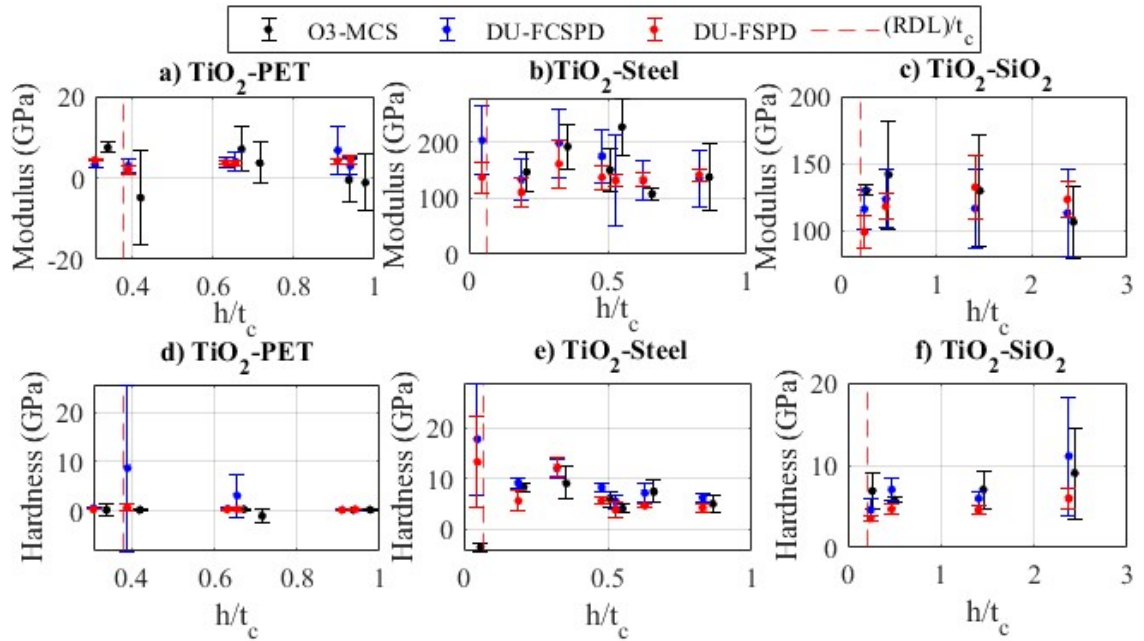


Figure 8-4 TiO₂ reduced modulus and hardness against normalised depth on three different substrates a) and b) on PET, c) and d) on Steel, e) and f) on Silicon. Each error bar shows one standard deviation from the mean value.

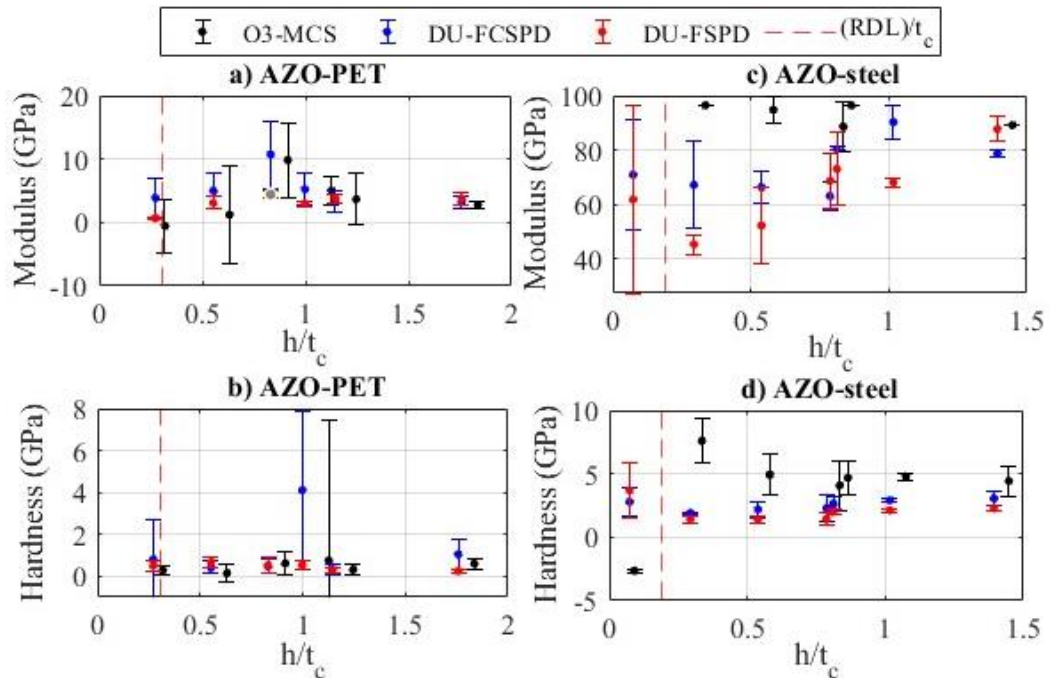


Figure 8-5 AZO reduced modulus and hardness against normalised depth on two different substrates a) and b) on PET, c) and d) on Steel. Each error bar shows one standard deviation from the mean value.

be ~133 GPa and H to be ~13 GPa. For AZO, H has been reported to be 13.7 GPa (Huang and Chang, 2010), and 7-11 GPa (Chang, Hsiao and Huang, 2008), and the E reported as 17-20 GPa (Chang, Li and Lin, 2012) and 110-120 GPa (Chang, Hsiao and Huang, 2008). These reported values are consistent with the values found in Figure 8-3, Figure 8-4 and Figure 8-5, and can only be used as an indicator, however, the figures show the reduced modulus being the combined effect of the coating-substrate. These coating are also different, the deposition conditions along with the thickness of coating dictate the mechanical properties. Overall, for all coatings, it can be seen that all methods have similar normalised depth against hardness and reduced modulus relationships. However, there are some differences, at these low loads, for PET substrate systems, the reduced modulus values computed using the O3-MCS method are in the majority of cases negative. These results are not valid as reduced modulus cannot be negative. The same applies to some of the hardness values. In this case, the contact area determined using elastic assumptions is not valid. For PET samples at low normalised depths, there is hardly any effect of the coating. However, there is a significant change in hardness and reduced modulus of some of the data, which is due to the combined effect of the coating and substrate, where the coating has not cracked. Apart from some of the data for AZO on steel, method DU-FSPD shows the least amount of variation. For the creep corrected methods, the variation is high, especially below RDL. As the effect of creep can be significant at low loads, due to it being the same order of magnitude as the displacement, the creep correction should be used. Using the DU-FCSPD method, which shows less variation than O3-MCS, better fitting prediction can be deduced.

In the next section further insight is given on the effective contact area and hardness, determined by DU method, for the interpretation of the hardness data for thin film systems.

8.5 The effective contact area and hardness

The loading curve and unloading curves show different power-law exponents, this relates to the fact that the unloading geometry is effected by the plastic zone (Fischer Cripps, 2011, p.63), it is further noted that the contact angle changes with depth (Fischer Cripps, 2011, p.51). Also it has been stated that FEM has revealed an elastic zone is beneath the indenter which depend of the value E/Y (Fischer Cripps, 2011, p.57). This indicates that there is strong evidence that the plasticity is the cause. Johnson expanding cavity model is based on a hemispherical hydrostatic core of a radius equal to the contact circle; this is far the most popular model when the plasticity has reached the surface. This is a representation of the event at maximum load in a nanoindentation test with a conical indenter. There is evidence that at low loads plasticity can be present even when the contact is believed to be elastic (Fischer Cripps, Karvanková and Vepřek, 2006). It is noted that plasticity caused during loading produces geometrical necessary dislocation around the indenter at the early loading (Fischer Cripps, 2011, p.92). As the density of geometrical necessary dislocation increase with decreasing depth (Fischer Cripps, 2011, p.92) the plasticity changes. This clearly hardens/densifies the material around the indenter, and is hypothesised that the effective geometry changes i.e. a combination of the indenter geometry and the hardened/dense material around the indenter tip. At higher loads as in Oliver and Pharr's method (Oliver and Pharr, 1992) a parabolic indenter is modelled to represent the unloading curve even though indented with a Berkovich indenter. Their concept of effective indenter shape is only related to the shape of the residual impression during unloading (Oliver and Pharr, 2004), the power law exponent of the shape profile of the residual impression is compared to the power law exponent of the loading curve. It should be noted these two aspects are separate but indicated that plasticity is as important as well as the geometries of the indenter and residual impression.

Thus, modelling parabolic and spherical shapes better represent the shape of the indenter when comparing experimental data as the effective indenter geometry can be either depending on the study sample. Thus, at higher loads as the plasticity develops beneath the indenter a second phenomenon is also believed to occur, its effect is also hypothesised to change the effective geometry due to plasticity, leading to the shape profile of the surface impression as mentioned in Oliver and Pharr's work. This also aids in the pileup process. During unloading these two phenomena are reversed. The initial delayed elasticity is due to reversing of the plasticity beneath the indenter whereas the hardened/dense material around the indenter tip reverses at lower loads. At these loads the plasticity due to ISE is accounted for in method DU-FCSPD, using the plastic correction. This is why at certain test conditions, as in previous section 8.4, there are substantial differences between methods DU-FCSPD and O3-MCS.

In section 8.4 evolution of the hardness with displacement was seen for each coating, where the substrate plays an important role. The plastic zone would interact with the interface and further extend into the substrate at higher loads. However, the meaning of hardness for each method needs to be clarified. Traditionally the hardness is determined by first finding the contact area at max load i.e. at conditions of a fully developed plastic zone which has reached the surface (Fischer Cripps, 2011, pp.24, 62), once the area is found the hardness can be determined by (Equation 2-6). The determined hardness using residual impression which include the reverse effects during unloading i.e. reverse plasticity and elasticity, are termed the true hardness (in hardness tests at micro scale the contact area is typically determined by the optically inspecting the residual impression in which reverse effects are included). When determining the hardness using nanoindentation by establishing the contact area by indirect method then only for an ideal rigid plastic material the hardness equals the true hardness. The apparent hardness, which is the

hardness determined using the Oliver and Pharr method, do not account for the reversal effects during unloading. However, when using the previous unloading methods at non-quasi static test conditions, the contact area determined isn't correct when there is substantial delayed elasticity, and it is only at FEP the contact area can be determined. Determining the hardness using the contact area at FEP, results in a contact area accounting for the initial reverse plasticity. However it has been stated that the residual impression doesn't change much upon unloading for elastic-plastic material i.e. only the depth recovers (Tabor, 1948), it can thus be assumed that the reversal effect due to elasticity during unloading has negligible effect on the contact area. Thus, in accordance with the DU method, the hardness found at FEP using the contact area and load at FEP is equivalent to the true hardness. At lower loads when the plastic zone has not reached the surface, then the hardness may be referred to partial hardness, which can be either true or apparent.

In the next section the DN model (Doerner and Nix, 1986), DEITM, ADEITM, EM and 5PL models are fitted to the data acquired by the DU-FCSPD to examine if coating properties can be determined.

8.6 Substrate-independent coating properties using DU method

To further acquire substrate independent coating properties, the relationship between elastic modulus with normalised depth was established using the above methodologies by a fit to the data. The fitting was performed using the reduced modulus data attained from method DU-FCSPD. The data on the PET substrate was not sufficient for an initial guess for the coating properties, as there was insufficient data, so the steel substrate samples were used. Fits for all coating substrate combinations were achieved (see Appendix 8.2) using all the models but with different levels of reliability. However, when sufficient data were not available (coating on PET substrates), due to the limitations of the Nanoindenter at low loads, apart from the EM model the techniques were still capable of fitting the data when an estimate of the coating elastic modulus was available. For the EM model, the data for the reduced modulus was first corrected, where the combined modulus of the coating/substrate system was used by subtracting the effect of the indenter. In the DN and ADEITM models, the combined effect of the indenter, and the coating and substrate, is accounted for in the analysis of the fitting procedure and can be fitted directly to the reduced modulus. The EM technique did not need the Poisson's Ratio of the coating and substrate. For the other methods, the used Poisson's Ratios were 0.25 for TiN (Vijgen and Dautzenberg, 1995), 0.27 for TiO₂ (CRM, 2014), and 0.3 for AZO (Chang, Hsiao and Huang, 2008; Huang and Chang, 2010), and are assumed to be constant within the coating and substrate. This leads to some degree of uncertainty for these techniques as the value of the Poisson's ratio may not be accurate for the system under study.

To examine the difference between the techniques, first the DN, DEITM were compared, this can be seen for a TiO₂ sample in Figure 8-6. For this sample an elastic modulus of 165 GPa was predicted by EM model. It can be seen that both models are capable of fitting the data, but for the PET substrate the accuracy depends on the amount of data

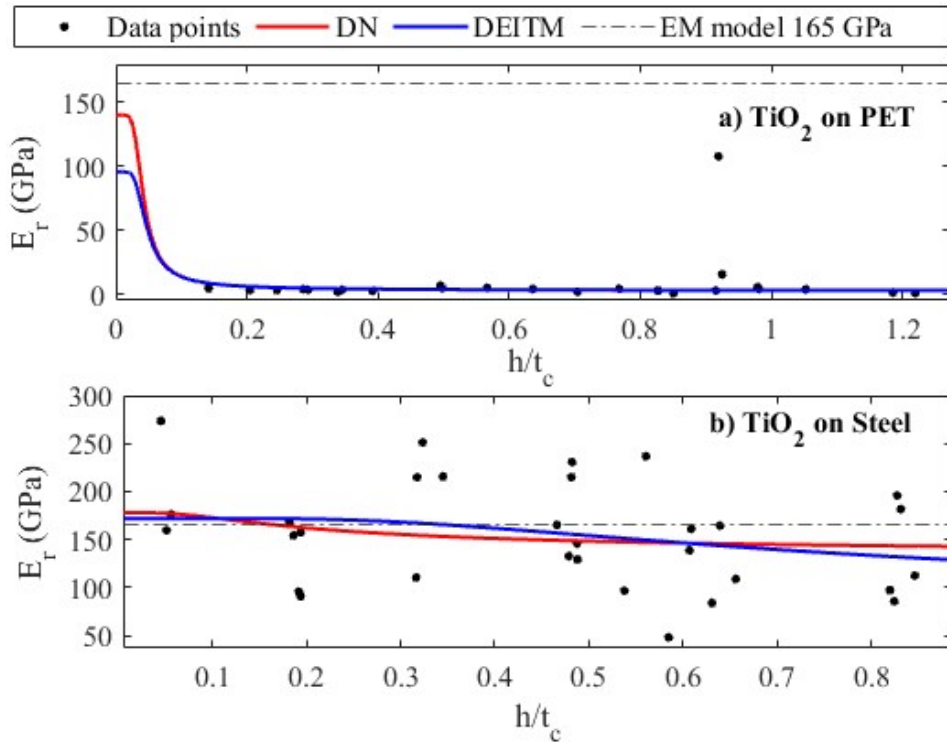


Figure 8-6 Elastic modulus against normalized depth for 199nm TiO₂ on a) PET substrate and b) Steel substrate.

where the coating shows a greater influence on the deformation. Due to the extra parameter in the DEITM model, better fits were expected compared to DN Model. Further, the DEITM was compared to the ADEITM model, from Figure 8-7 it can be seen that both models are very similar in fitting the data. However, the ADEITM model is capable of higher accuracy when data resolution is low. Even though the DEITM model accounts for the substrate effects (Zhou and Prorok, 2010b) the extrapolation of the curve to zero depth did not give the elastic modulus of the coating, this is due to the fact the adjusted equations in the technique were not developed using the data from the DU method. Thus, further investigations of similar nature on a combination of coating and substrates need to be performed for both DEITM and ADEITM models. Previous models and the ADEITM model explain the deformation behaviour by phenomenological modelling, considering springs in parallel, in series or even a combination, to fit the

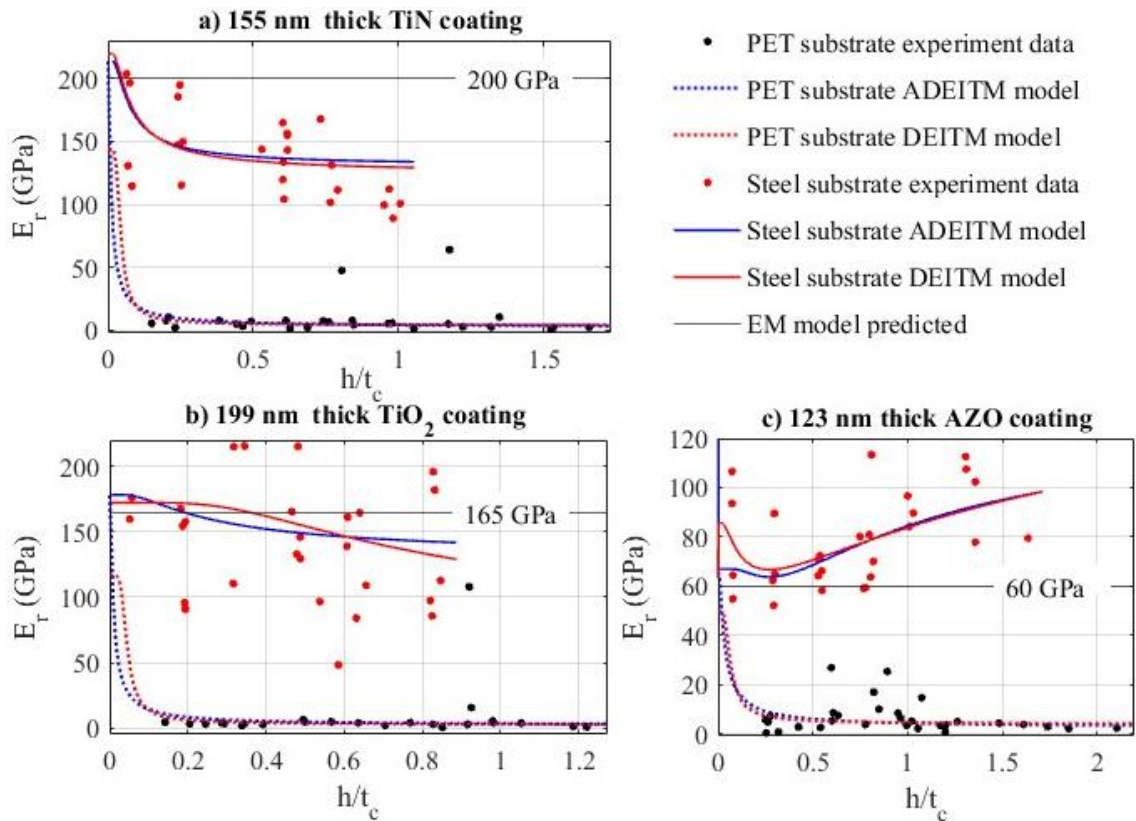


Figure 8-7 Elastic modulus against normalized depth fits with DEITM and ADEITM for PET and Steel substrate with coatings a) TiN, b) TiO_2 and c) AZO.

reduce modulus data with normalised depth fits. Unfortunately, the true physical explanation is not still apparent. Using the extracted DU method data, the 5PL model was as reliable as any of the other models, as evidenced in Appendix 8.2. The author found it to be one of the most reliable and fast techniques. The 5PL model is used for prediction of the probability of occurrence of an event, in this case, the deformation and also that the normalised depth can be seen as concentration, it can be said that as the depth increases the concentration of the substrate effect increase. So, it is the substrate effect that determines the overall deformation and thus the reduced modulus. This explanation has only been possible due to the fact the correct data for the reduce modulus was determined at the associated depths. In examining Figure 8-8, it is seen the EM Model values overlap

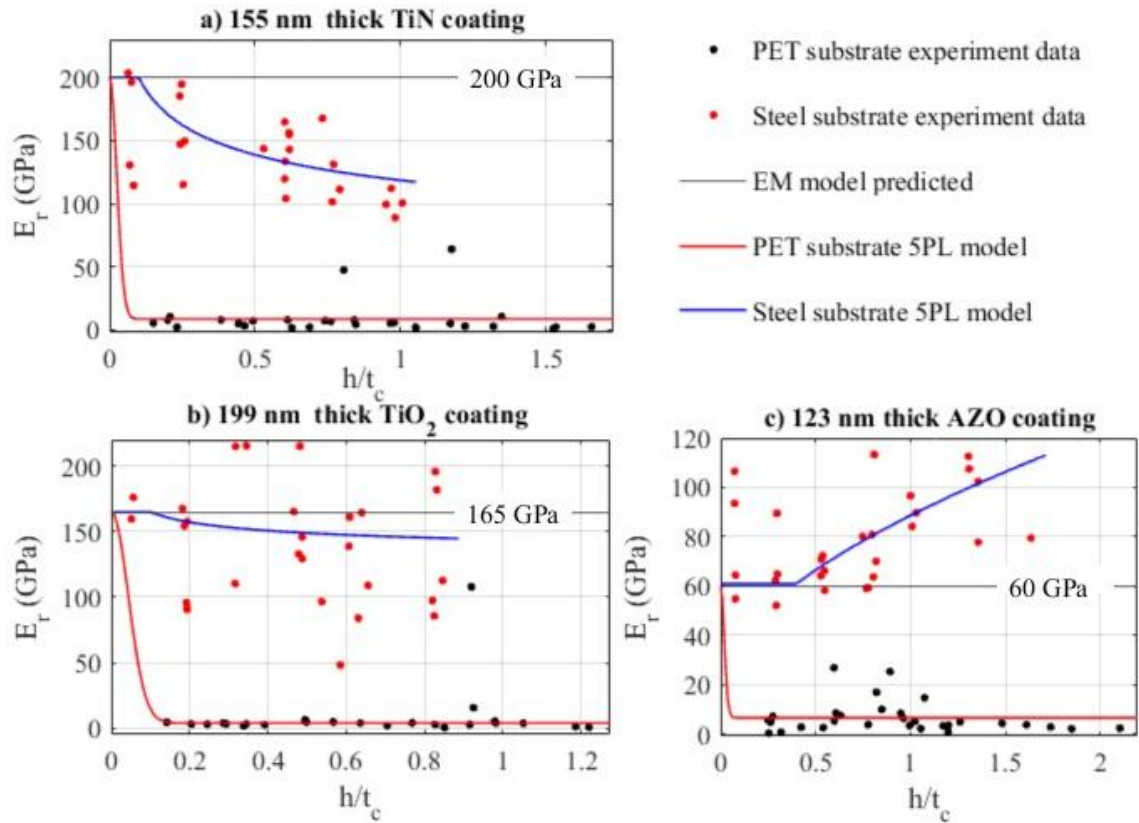


Figure 8-8 Elastic modulus against normalized depth fits with 5PL for PET and Steel substrate with coatings a) TiN, b) TiO₂ and c) AZO.

at a minimum of the 5PL Model. As the initial guess for coating elastic modulus, for fitting the 5PL Model, the EM predicted value was used, and that this overlapping is occurring, it suggests the coating properties are accurately determined using this model. As expected, the determined elastic modulus for TiN was the highest of all the coatings. The elastic modulus value of TiO₂ was higher than ~133 GPa, i.e. the highest value reported in the literature (2006). Otherwise, the coatings show realistic properties values.

8.7 Summary

A detailed literature review of nanoindentation application to thin film compliant systems has been presented along with modelling of nanoindentation processes. The DU method acquired data showed a similar relationship with normalised depth when compared to the

previous unloading methods, suggesting previous coating characterisation models could be used to fit the data. However, due to insufficient data acquired for the coating substrate combinations, it was not possible to conclude which model was the best, all models are capable of fitting the data. However, the ADEITM model and SPL models were less time consuming, and practically more efficient for determining fits to establish exact thin film properties.

The next chapter, comprehensively concludes all developed methodologies, their validation and applications, as detailed in the thesis.

Chapter 9

CONCLUSION AND FURTHER WORK

9.1 Introduction

The well-established nanoindentation unloading methodologies were further developed to address the different factors which cause unreliability in the characterised data. Thus, a critical analysis is given in this thesis on the issues in getting accurate reliable data via nanoindentation. In seeking to unify the different approaches, many novel contributions were made so that different material types, could be successfully tested, at any test condition, in one-cycle, especially for more challenging viscous/polymeric materials and low load testing. A viable approach consistent with the nanoindentation standards was also required. Previous methods assumed the unloading to be fully elastic. However, a plastic correction was proposed at the point during unloading where the delayed plasticity cease. A procedure, associated with sink-in and pile-up, was essential in determining the contact depth. At low load, implementation of a datum correction was needed, which aided in splitting the deformation for determining the correct contact area. The parameter defined for splitting the displacement was named RDL. Above RDL, the method was worked remarkably well when compared to the tensile test for several material types. For viscous/polymeric materials, results showed consistency with the well-established unloading methodologies, and also with hold-time methodologies. These hold time methodologies were also developed by the author. Other novel models, for thin film characterisation, were applied to fit precisely the DU method data, i.e. the elastic modulus as a function of depth, for substrate independent properties. All the conclusions and further work are detailed next.

9.2 Nanoindentation methodologies

For load/depth sensing indentation, a unified method has been developed named the “DU method” which is capable of determining reliable elastic moduli and hardness data, as previous methods, at any test condition, for both viscous and non-viscous/non-polymeric materials. It is proposed that determining the elastic moduli and hardness in this way potentially will give less variability from machine to machine and differing analysis procedures. The method reduces the costs associated with the testing by reducing the time of study by 75% and can be easily be implemented by modifying the data analysis algorithm in any load/depth sensing indentation software with low costs.

Using the DU method, the nanoindentation test data obtained in this project was successfully used to extract the stiffness and contact area for the determination of mechanical properties of a range of materials, even at non-quasi-static loading conditions, with only one unloading cycle. In these experiments, the effect of the contact area is more influential than the effect of the stiffness in determining the elastic modulus.

In developing the DU methodology, for the unloading stiffness, the delayed elasticity was eliminated successfully without the use of the Viscofactor, Conforming Factor, Acceleration Factor or any other creep factor. This was achieved by fitting a second-order polynomial fit to the unloading data and then determining the FEP for acquiring the stiffness. However, the initial penetration rate within the sample needed to be accounted for, due to its effect on the apparent stiffness. The creep correction below maximum load is not valid because the penetration rate is determined at the maximum load only. Thus, a Plastic correction was performed.

The pile-up and sink-in effects can be substantial in highly viscous/polymeric materials and must be accounted for. The work by Fujisawa and Swain (2006) was extended using the simple logic that the contact area cannot be smaller for the elastic-perfectly plastic

method than the elastic method. However, the point at which this correction must be applied concerning a “purely” elastic case is not known. Further work needs to be done in this respect so that the correction can be applied to any material without the user deciding if sink-in or pile-up is present. As E/H and the strain hardening exponent are the main contributors to this phenomenon, examining them along with AFM profile of the indent, for a number of materials, could reveal how much of the correction is needed.

RDL's can be successfully distinguished for determining contact areas. Apart from experimental limitations and associated noise, variations in RDL are shown to be dependent on load and load rate. It was also shown that there was no correlation of RDL with the surface roughness parameter (Sa). It was concluded that all factors which affect ISE mentioned in section 2.3.4 would dictate the value of RDL and also drift rates of the electronics. So, the RDL should be determined for each condition for a nanoindentation test. If the data is such that the maximum displacement is less than the RDL, then the RDL cannot be determined due to insufficient data, and a separate test is needed. For tests where the test conditions are set the average values of the RDL should be considered.

The DU methodology suggested a method to establish the true contact area considering the datum shift mechanism. In which the area function was calibrated using the DU-FP method. For this method, the datum correction is valid for viscous /polymeric materials and does not seem to be applicable for non-viscous metallics. The true contact area along with the unloading stiffness can be used to determine the elastic modulus with the correction factor β equal to one in the Sneddon expression, and by using the maximum load, the hardness (if applicable, i.e. if plastic deformation has reached the surface) can be determined. Further work for the β value used need to be confirmed by both phenomenological and mechanistic approaches, to determine which factors are related to it.

Also, further work is needed to determine if the datum shift mechanism occurring at low load affects static friction values. The author has been unable to identify work considering such phenomena concerning friction and wear. To resolve the datum shift mechanism as a root cause of friction, further deformation studies should be carried out at low loads with a tangential aspect on different contact systems.

9.3 Reliable indentation approach

Apart from a robust methodology presented, a reliable approach was also needed for nanoindentation testing. This work developed an approach in line with the ISO standards. The thermal drift correction was confirmed to be essential. Also, it was found that there can be a marked effect on the deformation by how the sample was mounted in the machine, i.e. by the operator, how it was glued and tilt of the indenter with the sample. It was established that the samples need to be adequately fixed to the sample holder by not exceeding two drops of glue and the tilt angle needed to be controlled as much as possible by the operator, or by sensors attached to the platform. Additionally, for the micromaterial's nano tester ten indents for each array in a DOE was sufficient for representing the test variation. If different equipment is used, then the number of indents should be confirmed.

9.4 Main factors and ranking

In order to study a subset of the main factors, first the main factors for indentation testing were identified/confirmed to be: load, load rate, unload rate, indenter type, coating, hold period, thermal drift correction, the tilt of the sample surface about the indenter and the sample. Then these parameters were investigated to establish the rank of their influence on the response. The main variability in the response data, which leads to non-reproducible data, are the factors most affected by noise factors. At the nanoscale, these

are thermal drift, substrate and the unload rate, whereas for the macro scale it is the stress developing factors within the sample being load, tilt, indenter, and the unload rate. This variability is unavoidable and thus was quantified in each of the conducted studies. At the nanoscale, the Berkovich indenter is seen as more appropriate in order to reduce the effect of noise. Whereas at the microscale the variation can be associated with the time-dependent mechanisms occurring in the material under the Berkovich indenter, in which the fracture of the coating can directly be associated with the noise. So out of the initial nine factors, five were identified to be significant for coating/complaint system deformation study. These being: the load, substrate, load rate, unload rate and hold period. The Berkovich indenter was selected so that deformation within the coating could be achieved before fracture. Even though in these studies, the effects on the response due to the operator, sample mounting, and the tilt factors, were ignored, and these factors controlled as much as possible to minimise their effects, further work should be conducted to investigate their effects on the deformation.

9.5 DU method validation

The methodology was validated for non-viscous and viscous/polymeric materials using single cycle tests. For metallics, the DU method is capable of determining accurate results without the datum correction. However, the behaviour of the material must be known in order to apply the appropriate corrections. For both polymeric and rubber materials, the DU-FSPD and DU-FCSPD methods are as accurate as the most commonly used unloading method (Oliver and Pharr, 1992, 2004), with creep (G. Feng, 2002) and pile-up/sink-in corrections. Also, when compared to hold time methodology, the method produced similar results except for test conditions which showed high viscous behaviour, confirming the elastic modulus determined by the DU method to be correct for non-quasi-static conditions.

A multi-cycle study showed the DU method determined results, which were almost identical values to the fourth cycle determined by Feng's method. The DU method eliminated the effects due to primary creep. The validity of the reasoning, behind why the preference of using multi-cycles over a single test, is not clear even though the reverse plasticity is eliminated. Realising the effect of plasticity on the geometry of the indenter and additional heating during each cycle, where both effects have a direct influence on the mechanical properties, favours acquiring the elastic modulus or hardness in the first cycle.

Using the DU method, the elastic modulus-load curves, determined from the fitted unloading data, still showed an opposite behaviour to that measured experimentally from different tests at varying loads. The response is mostly due to the effective contact area changing at different rates during unloading. The area after FEP is likely to be more than in the elastic case, and this effect varies relative to the decreasing load, as at lower loads, the density of geometrical necessary dislocations increases. Further work along these lines, to resolve the plasticity during loading and reverse plasticity upon unloading, is needed for a better understanding of the mechanisms of scale-dependent plasticity.

The DU method is fully capable of determining accurate and reliable mechanical properties above deformations $> RDL$. However, at ultra-low loads, it is not just the surface roughness, but tilt and ISE related factors lead to a high degree of variation of the output nanomechanical properties. Tests on Silicon showed that for higher roughness, the elastic modulus decreased. However, it could not be established which factors attributed to it.

9.6 Substrate characterisation

The author showed that the visco-elastic response could be successfully obtained from the unloading curve for a set of input parameters, i.e. load, load rate, hold time and unloading rate. The logarithmic fits to the experimental data have shown to be successful in capturing the deformation behaviour of PET during the hold. However, it is not clear how the determined parameters relate to the load and load rate. All parameters, for both PET and PEN, behaved similarly with load and load rate, which indicated the mechanisms of deformation to be similar for both. Also, these parameters have no direct relationship to the physical properties of the material and cannot be related to the test conditions, so their practical use is limited. For both logarithmic and phenomenological methods, for all the test conditions studied, no single expression was identified in terms of time, load and load rate. This is unfortunate as an expression in terms of these variables is essential to simulate the deformation of different systems, which include polymer materials. Consequently, these parameters and their associated expressions for time-dependent material properties, have to be determined for each experimental condition. Therefore, the use of Neural networks method has been adopted by the author to establish these parameters. It is possible to perform several tests, at different experimental conditions, using nanoindentation in order to first characterise a particular polymer and then use Neural networks to find material properties at various experimental conditions. However, the tests need repeating several times to validate the process successfully.

Interpolation was successfully applied to determine values between test conditions. However, when extrapolating outside the test conditions, the trained Neural network did not accurately determine parameters. Thus, overall interpolation and other extrapolation techniques could be employed to determine parameters for FEM.

For the PET and PEN, the overall in-sample variation was shown to be around 0.3 GPa. This value is higher than the variation of test sample variation found using the DU method, where the glueing of the sample also affects. Furthermore, this is greater than the variation when finding the material properties using Neural networks with interpolation. Thus, it is concluded that the elastic modulus can be acquired with confidence using these methods.

9.7 Coating characterisation

When comparing the data from the DU method to the standard methodology, a similar relationship with normalised depth was found suggesting previous coating characterisation models could be used to fit the DU method data. The methods developed by the author, i.e. the 5PL and ADEITM were as good as the pervious studied methods for establishing exact thin film properties, however practically more efficient.

In considering the number of data points, for substrate-independent coating properties, good fitting was achieved, to the elastic modulus against normalised depth data. Further work is needed, taking more data points at smaller depth increments to increase the accuracy of the fits. The determined elastic modulus for the coatings needs further confirmation, as being the minimum of the fit curve, for the five parameters logistic regression method. Other methods can be used for this validation. If substrate effects are to blame then by performing further tests on different substrates the effect of substrate on the minimum value can be determined as done by Zhou and Prorok (2010b), also different coating/substrate systems can be considered.

9.8 Overall conclusion

The convenient nanoindentation test, employing the DU methodology, can replace expensive industrial tensile tests, as similar mechanical properties can be achieved for

depths $>$ RDL, for a range of materials, even at non-quasi-static loading conditions, with only one unloading cycle, aiding, miniaturisation and manufacturer of devices with the precise characterisation of mechanical properties, at the scale need, for optimum design choices. Also, the method compared well with previous unloading methodologies, and more physically justified, without any crude assumption related to the deformation. The method compared well with hold time methodologies and was successfully applied for coating characterisation. Further research is also required, as the methodologies presented have the potential to form the basis of a formal standard for polymer characterisation which is still needed in today's industry.

Proposed further work includes analysis of the DU methodology, using FEM contact deformation studies and comparison to load-displacement data, for confirming the existence of the “Datum shift” mechanism at low loads. This will aid in further understanding of contact between materials and clarify results below RDL. As variation in the output data at these depths is high, to investigate the high variation, advance equipment would become essential for precise acquisition of the data, with less machine drift. The highly sensitive force-displacement transducer developed by Zhang et al. could be used for this purpose (Zhang et al., 2018). Also, the machine dynamics and effects of closed-loop feedback, should be examined, to see the effect on the determined RDL.

Further the response should be related to the different influencing ISE factors, as these can be due to contact geometry, material behaviour and structure, machine factors, and environment-related factors. At this scale, the effects, of the collective contributions of these factors, should be separated/isolated for each factor if possible. Alternative methods can also be compared, one being that of the author, in which the RDL is determined beforehand with an initial test and the contact area determined using equation 4.25. If the ISE's can be isolated than relationships, to the measured elastic modulus and hardness on

various material and coating/substrate systems, should be established. The choice of material systems and their surface profiles will surely affect the RDL, identifying lower RDL will reduce the variability in the output data. The variability of the output data is always going to be inherent at such low load conditions, primarily due to surface roughness, where the contact detection is an issue. As thermal drift and tilt shows some significance at this scale, advance technique to eliminate them should be applied, this could be an extra indenter in the vicinity of contact like in the Anton Paar Ultra Nanoindentation Tester (UNHT) (Anton-Paar, 2019a), or laser (Keysight, 2019) and in-situ (Huang et al., 2012) techniques. The work should also demonstrate compatibility across the different test instrumentation, and can only be possible through controlled experimentation, and quantified with accurate analysis methods, involving sound, statistical analysis.

REFERENCES

Altaf, K., Ashcroft, I.A. and Hague, R. (2011) 'Investigation of the effect of relative humidity on polymers by depth sensing indentation', *Journal of Materials Science*, 46(23), p. 7551.

Andersons, J., Tarasovs, S. and Leterrier, Y. (2007) 'Analysis of Thin Film Cracking and Buckling on Compliant Substrate by Fragmentation Test', *Key Engineering Materials*, 348–349, pp. 329–332.

Anton-Paar (2019a) *Ultra Nanoindentation Tester (UNHT³)* :: Anton-Paar.com., Anton Paar Available at: <https://www.anton-paar.com/uk-en/products/details/ultra-nanoindentation-tester-unht3/> (Accessed: 23 July 2018).

Anton-Paar (2019b) *The Ultra Nanoindentation Tester: New generation of thermal drift free indentation* :: Anton-Paar.com., Anton Paar Available at: <https://www.anton-paar.com/us-en/products/applications/the-ultra-nanoindentation-tester-new-generation-of-thermal-drift-free-indentation/> (Accessed: 30 May 2019).

Archard, J.F. (1957) 'Elastic Deformation and the Laws of Friction', *Proceedings of the Royal Society of London. Series A, Mathematical and Physical Sciences*, 243(1233), pp. 190–205.

Archard, J.F. and Onions, R.A. (1973) 'The contact of surfaces having a random structure', *Journal of Physics, Series D*, 6, pp. 289–304.

Ashby, M.F. and Jones, D.R.H. (2006) *Engineering materials 2: an introduction to microstructures, processing and design*. Butterworth-Heinemann.

ASM International (2003) 'CVD and PVD Coatings', in Cramer, S. D. and Covino, B. S. (eds.) *Corrosion: Fundamentals, Testing, and Protection*. , pp. 759–762. Available at: 10.31399/asm.hb.v13a.a0003685 (Accessed: 27 May 2019).

ASTM E28 Committee (2016) *Practice for Verification and Classification of Extensometer Systems*. ASTM International. Available at: 10.1520/E0083-16 (Accessed: 2 June 2019).

ASTM E111-04 (2010) *ASTM E111-04*. Available at: [about:reader?url=https%3A%2F%2Fwww.astm.org%2Fstandards%2FE111.htm](https://www.astm.org/standards/E111.htm) (Accessed: 30 December 2016).

Beake, B.D., Bell, G.A., Brostow, W. and Chonkaew, W. (2007) 'Nanoindentation creep and glass transition temperatures in polymers', *Polymer International*, 56(6), pp. 773–778.

Beake, B.D. and Leggett, G.J. (2002) 'Nanoindentation and nanoscratch testing of uniaxially and biaxially drawn poly(ethylene terephthalate) film', *Polymer*, 43(2), pp. 319–327.

- Bec, S., Tonck, A., Georges, J.-M., Georges, E. and Loubet, J.-L. (1996) ‘Improvements in the indentation method with a surface force apparatus’, *Philosophical Magazine A*, 74(5), pp. 1061–1072.
- Berasategui, G. (2003) *Determining the properties of thin-coated systems by nanoindentation*. Ph.D. University of Newcastle upon Tyne. Available at: <http://ethos.bl.uk/OrderDetails.do?did=1&uin=uk.bl.ethos.399329> (Accessed: 10 June 2018).
- Bhat, N., V. and Deshmukh, R., R. (2012) *NISCAIR ONLINE PERIODICALS REPOSITORY (NOPR): X-ray crystallographic studies of polymeric materials*. Available at: <http://nopr.niscair.res.in/handle/123456789/26172> (Accessed: 1 June 2019).
- Bhattacharya, A.K. and Nix, W.D. (1988) ‘Analysis of elastic and plastic deformation associated with indentation testing of thin films on substrates’, *International Journal of Solids and Structures*, 24(12), pp. 1287–1298.
- Bhushan, B. (2012) *Fundamentals of Tribology and Bridging the Gap Between the Macro- and Micro/Nanoscales*. Springer Science & Business Media.
- Bhushan, B. and Majumdar, A. (1992) ‘Elastic-plastic contact model for bifractal surfaces’, *Wear*, 153(1), pp. 53–64.
- Bouaita, N., Bull, S.J., Palacio, J.F. and White, J.R. (2006) ‘Dynamic nanoindentation of some polyolefins’, *Polymer Engineering & Science*, 46(9), pp. 1160–1172.
- Bowden, F.P. and Tabor, D. (1939) ‘The Area of Contact between Stationary and between Moving Surfaces’, *Proceedings of the Royal Society of London. Series A, Mathematical and Physical Sciences*, 169(938), pp. 391--413.
- Bower, A.F. (2009) *Applied Mechanics of Solids*. CRC Press.
- Briscoe, B.J., Fiori, L. and Pelillo, E. (1998) ‘Nano-indentation of polymeric surfaces’, *Journal of Physics D: Applied Physics*, 31, pp. 2395–2405.
- Broitman, E. (2016) ‘Indentation Hardness Measurements at Macro-, Micro-, and Nanoscale: A Critical Overview’, *Tribology Letters*, 65(1), p. 23.
- Bruker (2019) *Hysitron TI 950 TriboIndenter | Nanoindenter Overview.*, *Bruker.com* Available at: <https://www.bruker.com/products/surface-and-dimensional-analysis/nanomechanical-test-instruments/standalone-nanomechanical-test-instruments/ti-950-triboindenter/overview.html> (Accessed: 23 July 2018).
- BS EN ISO 527-2 (2012) *Plastics. Determination of tensile properties. Test conditions for moulding and extrusion plastics*. Available at: <https://shop.bsigroup.com/ProductDetail/?pid=000000000030216860> (Accessed: 29 December 2018).
- Bull, S.J. (2019) ‘Microstructure and indentation response of TiN coatings: The effect of measurement method’, *Thin Solid Films*, 688, p. 137452.

- Bull, S.J. (2005) 'Nanoindentation of coatings', *Journal of Physics D: Applied Physics*, 38, pp. R393–R413.
- Bull, S.J., Berasetegui, E.G. and Page, T.F. (2004) 'Modelling of the indentation response of coatings and surface treatments', *Wear*, 256(9–10), pp. 857–866.
- Bull, S.J. and Rickerby, D.S. (1990) 'New developments in the modelling of the hardness and scratch adhesion of thin films', *Surface and Coatings Technology*, 42(2), pp. 149–164.
- Bulychev, S.I., Alekhin, V.P., Shorshorov, M.K., Ternovskii, A.P. and Shnyrev, G.D. (1975) 'Determining Young's modulus from the indenter penetration diagram', *Zavodskaya Laboratoriya*, 41(9), pp. 1137–1140.
- Burnett, P.J. and Rickerby, D.S. (1987) 'The mechanical properties of wear-resistant coatings: I: Modelling of hardness behaviour', *Thin Solid Films*, 148(1), pp. 41–50.
- Bush, A.W., Gibson, R.D. and Thomas, T.R. (1975) 'The elastic contact of a rough surface', *Wear*, 35(1), pp. 87–111.
- Calleja, F.J.B., Flores, A. and Michler, G.H. (2004) 'Microindentation studies at the near surface of glassy polymers: Influence of molecular weight.', *Journal of Applied Polymer Science*, 93(4), p. 1951.
- Carbone, G. and Bottiglione, F. (2008) 'Asperity contact theories: Do they predict linearity between contact area and load?', *Journal of the Mechanics and Physics of Solids*, 56(8), pp. 2555–2572.
- Chandrashekar, G., Alisafaei, F. and Han, C.-S. (2015) 'Length scale dependent deformation in natural rubber', *Journal of Applied Polymer Science*, 132(43) Available at: 10.1002/app.42683 (Accessed: 24 May 2019).
- Chang, J.F., Shen, C.C. and Hon, M.H. (2003) 'Growth characteristics and residual stress of RF magnetron sputtered ZnO:Al films', *Ceramics International*, 29(3), pp. 245–250.
- Chang, R.C., Li, T.C. and Lin, C.W. (2012) 'Influence of various thickness metallic interlayers on opto-electric and mechanical properties of AZO thin films on PET substrates', *Applied Surface Science*, 258(8), pp. 3732–3737.
- Chang, S.-Y., Hsiao, Y.-C. and Huang, Y.-C. (2008) 'Preparation and mechanical properties of aluminum-doped zinc oxide transparent conducting films', *Surface and Coatings Technology*, 202(22–23), pp. 5416–5420.
- Chawla, V., Jayaganthan, R. and Chandra, R. (2009a) 'Microstructural characteristics and mechanical properties of magnetron sputtered nanocrystalline TiN films on glass substrate', *Bulletin of Materials Science*, 32(2), pp. 117–123.
- Chawla, V., Jayaganthan, R. and Chandra, R. (2009b) 'Microstructural characteristics and mechanical properties of magnetron sputtered nanocrystalline TiN films on glass substrate', *Bulletin of Materials Science*, 32(2), pp. 117–123.

Chechenin, N.G., Böttiger, J. and Krog, J.P. (1995) 'Nanoindentation of amorphous aluminum oxide films I. The influence of the substrate on the plastic properties', *Thin Solid Films*, 261(1), pp. 219–227.

Chen, L., Ahadi, A., Zhou, J. and Ståhl, J.-E. (2017) 'Quantitative study of roughness effect in nanoindentation on AISI316L based on simulation and experiment', *Proceedings of the Institution of Mechanical Engineers, Part C: Journal of Mechanical Engineering Science*, 231(21), pp. 4067–4075.

Chen, Z. and Wu, L.Y.L. (2008) 'Chapter 14. Scratch resistance of protective sol-gel coatings on polymeric substrates', in *Tribology of Polymeric Nanocomposites*. Elsevier, pp. 325–353. Available at: <http://www.sciencedirect.com/science/article/pii/S1572336408550142> (Accessed: 2 August 2011).

Chen, Z., Wu, L.Y.L., Chwa, E. and Tham, O. (2008) 'Scratch resistance of brittle thin films on compliant substrates', *Materials Science and Engineering: A*, 493(1–2), pp. 292–298.

Chicot, D., Yetna N'Jock, M., Puchi-Cabrera, E.S., Iost, A., Staia, M.H., Louis, G., Bouscarrat, G. and Aumaitre, R. (2014) 'A contact area function for Berkovich nanoindentation: Application to hardness determination of a TiHfCN thin film', *Thin Solid Films*, 558, pp. 259–266.

Chudoba, T. and Richter, F. (2001) 'Investigation of creep behaviour under load during indentation experiments and its influence on hardness and modulus results', *Surface and Coatings Technology*, 148(2–3), pp. 191–198.

Chudoba, T., Schwarzer, N. and Richter, F. (2000) 'Determination of elastic properties of thin films by indentation measurements with a spherical indenter', *Surface and Coatings Technology*, 127(1), pp. 9–17.

Chun, D.M., Kim, M.H., Lee, J.C. and Ahn, S.H. (2008) 'TiO₂ coating on metal and polymer substrates by nano-particle deposition system (NPDS)', *CIRP Annals - Manufacturing Technology*, 57(1), pp. 551–554.

Cotterell, B. and Chen, Z. (2000) 'Buckling and cracking of thin films on compliant substrates under compression', *International Journal of Fracture*, 104(2), pp. 169–179.

CRM (2014) *TiO₂ target, Titanium Dioxide sputtering target, TiO₂ sputtering target, evaporation material, Titanium dioxide powder, titanium dioxide nanometer powder*. Available at: http://www.china-raremetal.com/product/Titanium_Dioxide_TiO2.htm (Accessed: 20 September 2014).

Cruz, C.S., Calleja, F.J.B., Zachmann, H.G., Stribeck, N. and Asano, T. (1991) 'Relating microhardness of poly(ethylene terephthalate) to microstructure', *Journal of Polymer Science Part B: Polymer Physics*, 29(7), pp. 819–824.

D. Maugis (2000) 'Contact, Adhesion and Rupture of Elastic Solids', *Springer-Verlag, Solid-State Sciences, Berlin 2000*

D. Tabor (1977) 'The hardness of solids', *J. Colloid Interface Sci.*, 58, pp. 145–179.

- Das, S.K. and Sahoo, P. (2012) ‘Influence of Process Parameters on Microhardness of Electroless Ni-B Coatings’, *Advances in Mechanical Engineering*, 4, p. 703168.
- De Maria, G., Ferro, D., D’Alessio, L., Teghil, R. and Barinov, S.M. (2001) ‘Hardness of titanium carbide films deposited on silicon by pulsed laser ablation’, *Journal of Materials Science*, 36(4), pp. 929–935.
- Derjaguin, B.V., Muller, V.M. and Toporov, Y.P. (1975) ‘Effect of contact deformations on the adhesion of particles’, *J. Colloid Interface Sci.*, 53, pp. 314–325.
- Dobrzanski, L.A. and Adamiak, M. (2003) ‘Structure and properties of the TiN and Ti(C,N) coatings deposited in the PVD process on high-speed steels’, *Journal of Materials Processing Technology*, 133(1–2), pp. 50–62.
- Dobrzanski, L.A., Polok, M. and Adamiak, M. (2005) ‘Structure and properties of wear resistance PVD coatings deposited onto X37CrMoV5-1 type hot work steel’, *Journal of Materials Processing Technology*, 164–165, pp. 843–849.
- Doerner, M.F., Gardner, D.S. and Nix, W.D. (1986) ‘Plastic Properties of Thin Films on Substrates as Measured by Submicron Indentation Hardness and Substrate Curvature Techniques’, *Journal of Materials Research*, 1(06), pp. 845–851.
- Doerner, M.F. and Nix, W.D. (1986) ‘A Method for Interpreting the Data from Depth-Sensing Indentation Instruments’, *Journal of Materials Research*, 1(04), pp. 601–609.
- Durst, K., Göken, M. and Pharr, G.M. (2008) ‘Indentation size effect in spherical and pyramidal indentations’, *Journal of Physics D: Applied Physics*, 41(7), p. 074005.
- Fabes, B.D., Oliver, W.C., McKee, R.A. and Walker, F.J. (1992) ‘The Determination of Film Hardness from the Composite Response of Film and Substrate to Nanometer Scale Indentations’, *Journal of Materials Research*, 7(11), pp. 3056–3064.
- Field, J.S. and Swain, M.V. (1993) ‘A Simple Predictive Model for Spherical Indentation’, *Journal of Materials Research*, 8(02), pp. 297–306.
- Fischer Cripps, A.C. (2007) *Introduction to Contact Mechanics*. 2nd ed. Springer.
- Fischer Cripps, A.C. (2011) *Nanoindentation*. 3rd Edition. Springer.
- Fischer Cripps, A.C., Karvánková, P. and Vepřek, S. (2006) ‘On the measurement of hardness of super-hard coatings’, *Surface and Coatings Technology*, 200(18–19), pp. 5645–5654.
- Fischer-Cripps Laboratories (2018) *Nanoindentation – Important Factors to Remember When Performing a Nanoindentation Test by Fischer-Cripps Laboratories - Lesson 6.*, AZoM.com Available at: <https://www.azom.com/article.aspx?ArticleID=5423> (Accessed: 8 August 2018).
- Flores, A., Ania, F. and Baltá-Calleja, F.J. (2009) ‘From the glassy state to ordered polymer structures: A microhardness study’, *Polymer*, 50(3), pp. 729–746.

- Flores, A. and Calleja, F.J.B. (1998) 'Mechanical properties of poly(ethylene terephthalate) at the near surface from depth-sensing experiments.', *Philosophical Magazine A*, 78(6), pp. 1283–1297.
- Fu, G. (2006) 'Effects of tip rounding on the fundamental relations used in the analysis of nanoindentation data', *Materials Letters*, 60(29), pp. 3855–3856.
- Fujisawa, N. and Swain, M.V. (2006) 'Effect of unloading strain rate on the elastic modulus of a viscoelastic solid determined by nanoindentation', *Journal of Materials Research*, 21(03), pp. 708–714.
- G. E. Welsh, D.J.B. (2000) 'A transient mesophase on drawing polymers based on polyethylene terephthalate (PET) and polyethylene naphthoate (PEN)', *Journal of Materials Science*, 35(20), pp. 5225–5240.
- G. Feng, A.H.W.N. (2002) 'Effects of Creep and Thermal Drift on Modulus Measurement Using Depth-sensing Indentation', *Journal of Materials Research*, 17(03), pp. 660–668.
- Gao, H., Cheng-Hsin, C. and Jin, L. (1992) 'Elastic contact versus indentation modeling of multi-layered materials', *International Journal of Solids and Structures*, 29(20), pp. 2471–2492.
- Garg, N., Han, C.-S. and Alisafaei, F. (2016) 'Length scale dependence in elastomers – comparison of indentation experiments with numerical simulations', *Polymer*, 98, pp. 201–209.
- Gerth, J. and Wiklund, U. (2008) 'The influence of metallic interlayers on the adhesion of PVD TiN coatings on high-speed steel', *Wear*, 264(9–10), pp. 885–892.
- Goodall, R. and Clyne, T.W. (2006) 'A critical appraisal of the extraction of creep parameters from nanoindentation data obtained at room temperature', *Acta Materialia*, 54(20), pp. 5489–5499.
- Goriacheva, I.G. (1998) *Contact mechanics in tribology*. Springer.
- Gray, A. and Beake, B.D. (2007) 'Elevated Temperature Nanoindentation and Viscoelastic Behaviour of Thin Poly(ethylene terephthalate) Films', *Journal of Nanoscience and Nanotechnology*, 7(7), pp. 2530–2533.
- Greenwood, J.A. and Williamson, J.B.P. (1966) 'Contact of Nominally Flat Surfaces', *Proceedings of the Royal Society of London. Series A. Mathematical and Physical Sciences*, 295(1442), pp. 300–319.
- Gunda, R., Biswas, S.K., Bhowmick, S. and Jayaram, V. (2005) 'Mechanical properties of rough TiN coating deposited on steel by cathodic arc evaporation technique', *Journal of the American Ceramic Society*, 88(7), pp. 1831–1837.
- H. Bückle (1961) *VDI-Berichte*, 41, pp. 14–20.
- Haddad, Y.M. (2012) *Viscoelasticity of Engineering Materials*. Springer.

- Hainsworth, M.R McGurk and T.F Page (1997) ‘The effect of coating cracking on the indentation response of thin hard-coated systems’, *Surface & Coatings Technology*, 102, pp. 97–107.
- Hainsworth, S.V., Bartlett, T. and Page, T.F. (1993a) ‘The nanoindentation response of systems with thin hard carbon coatings’, *Thin Solid Films*, 236(1), pp. 214–218.
- Hainsworth, S.V., Bartlett, T. and Page, T.F. (1993b) ‘The nanoindentation response of systems with thin hard carbon coatings’, *Thin Solid Films*, 236(1–2), pp. 214–218.
- Hainsworth, S.V., Chandler, H.W. and Page, T.F. (1996) ‘Analysis of nanoindentation load-displacement loading curves’, *Journal of Materials Research*, 11(8), pp. 1987–1995.
- Haji, A. and Rahbar, R.S. (2012) ‘Structure evolution and mechanical behaviour of poly (ethylene terephthalate) fibers drawn at different number of drawing stages’, *Chemical Industry & Chemical Engineering Quarterly*, 18(2), pp. 233–243.
- Hanaor, D.A.H. and Sorrell, C.C. (2011) ‘Review of the anatase to rutile phase transformation’, *Journal of Materials Science*, 46(4), pp. 855–874.
- Haugen, F. (2009) *Basic Dynamics and Control*.
- Hay, J., Agee, P. and Herbert, E. (2010) ‘Continuous Stiffness Measurement During Instrumented Indentation Testing’, *Experimental Techniques*, 34(3), pp. 86–94.
- Hay, J. and Crawford, B. (2011) ‘Measuring substrate-independent modulus of thin films’, *Journal of Materials Research*, 26(06), pp. 727–738.
- Hay, J.L., O’Hern, M.E. and Oliver, W.C. (1998) ‘The Importance of Contact Radius for Substrate-Independent Property Measurement of Thin Films’, *MRS Online Proceedings Library Archive*, 522 Available at: 10.1557/PROC-522-27 (Accessed: 14 August 2018).
- Herbert, E.G., Sudharshan Phani, P. and Johanns, K.E. (2015) ‘Nanoindentation of viscoelastic solids: A critical assessment of experimental methods’, *Current Opinion in Solid State and Materials Science*, 19(6), pp. 334–339.
- Hertz, H. (1896) ‘On hardness’, *Verh. Ver. Beforderung Gewerbe Fleisses 61, 1882 p 410. Translated and reprinted in English in Hertz’s Miscellaneous Papers, Macmillan & Co, London, (Ch 6)*
- Hertz, H.R. (1882) ‘Ueber die Beruehrung elastischer Koerper (On Contact Between Elastic Bodies)’, *Gesammelte Werke (Collected Works)*, 1
- Hill, R.J. and Nadel, S.J. (1999) *Coated Glass Applications and Markets*. Temescal Books.
- Hochstetter, G., Jimenez, A. and Loubet, J.L. (1999a) ‘Strain-rate effects on hardness of glassy polymers in the nanoscale range. Comparison between quasi-static and continuous stiffness measurements’, *Journal of Macromolecular Science, Part B*, 38(5–6), pp. 681–692.

- Hochstetter, G., Jimenez, A. and Loubet, J.L. (1999b) ‘Strain-rate effects on hardness of glassy polymers in the nanoscale range. Comparison between quasi-static and continuous stiffness measurements’, *Journal of Macromolecular Science, Part B*, 38(5–6), pp. 681–692.
- Hollander, A.P. and Hatton, P.V. (2004) *Biopolymer Methods in Tissue Engineering*. Springer Science & Business Media.
- Hopcroft, M.A., Nix, W.D. and Kenny, T.W. (2010) ‘What is the Young’s Modulus of Silicon?’, *Journal of Microelectromechanical Systems*, 19(2), pp. 229–238.
- Huang, C.-C., Wei, M.-K. and Lee, S. (2011) ‘Transient and steady-state nanoindentation creep of polymeric materials’, *International Journal of Plasticity*, 27(7), pp. 1093–1102.
- Huang, H., Zhao, H., Mi, J., Yang, J., Wan, S., Xu, L. and Ma, Z. (2012) ‘A novel and compact nanoindentation device for in situ nanoindentation tests inside the scanning electron microscope’, *AIP Advances*, 2(1), p. 012104.
- Huang, M., Niu, X. and Soboyejo, W.O. (2007) ‘Creep induced rate effects on radial cracks in multilayered structures’, *Journal of Materials Science: Materials in Medicine*, 18(1), pp. 65–69.
- Huang, Y.-C. and Chang, S.-Y. (2010) ‘Substrate effect on mechanical characterizations of aluminum-doped zinc oxide transparent conducting films’, *Surface and Coatings Technology*, 204(20), pp. 3147–3153.
- ISO 37 (2017) *Rubber, vulcanized or thermoplastic -- Determination of tensile stress-strain properties*. Available at: <https://www.iso.org/standard/68116.html> (Accessed: 1 August 2018).
- ISO 6892-1 (2016) *Metallic materials — Tensile testing — Part 1: Method of test at room temperature*. Available at: <https://www.iso.org/obp/ui/#iso:std:iso:6892:-1:ed-2:v1:en> (Accessed: 1 August 2018).
- ISO 14577-1 (2002–2015) *Metallic materials -- Instrumented indentation test for hardness and materials parameters -- Part 1: Test method.*, ISO Available at: <http://www.iso.org/cms/render/live/en/sites/isoorg/contents/data/standard/05/66/56626.html> (Accessed: 29 May 2019).
- ISO 14577-2 (2002–2015) *Metallic materials -- Instrumented indentation test for hardness and materials parameters -- Part 2: Verification and calibration of testing machines.*, ISO Available at: http://www.iso.org/iso/home/store/catalogue_tc/catalogue_detail.htm?csnumber=56628 (Accessed: 4 February 2017).
- ISO 14577-3 (2002–2015) *Metallic materials -- Instrumented indentation test for hardness and materials parameters -- Part 3: Calibration of reference blocks.*, ISO Available at: http://www.iso.org/iso/home/store/catalogue_tc/catalogue_detail.htm?csnumber=56627 (Accessed: 4 February 2017).

ISO 14577-4 (2007–2016) *Metallic materials -- Instrumented indentation test for hardness and materials parameters -- Part 4: Test method for metallic and non-metallic coatings.*, ISO Available at: http://www.iso.org/iso/home/store/catalogue_tc/catalogue_detail.htm?csnumber=61823 (Accessed: 4 February 2017).

Jalali-Heravi, M., Asadollahi-Baboli, M. and Shahbazikhah, P. (2008) ‘QSAR study of heparanase inhibitors activity using artificial neural networks and Levenberg–Marquardt algorithm’, *European Journal of Medicinal Chemistry*, 43(3), pp. 548–556.

Johnson, K.L. (1987) *Contact Mechanics*. Reprint. Cambridge University Press.

Johnson, K.L. (1970) ‘The correlation of indentation experiments’, *Journal of the Mechanics and Physics of Solids*, 18(2), pp. 115–126.

Johnson, K.L., Kendall, K. and Roberts, A.D. (1971) ‘Surface Energy and the Contact of Elastic Solids’, *Proceedings of the Royal Society of London. A. Mathematical and Physical Sciences*, 324(1558), pp. 301–313.

Jönsson, B. and Hogmark, S. (1984) ‘Hardness measurements of thin films’, *Thin Solid Films*, 114(3), pp. 257–269.

Joslin, D.L. and Oliver, W.C. (1990) ‘A new method for analyzing data from continuous depth-sensing microindentation tests’, *Journal of Materials Research*, 5(1), pp. 123–126.

Karacan, I. (2006) ‘A comparative study of structure-property relationships in highly oriented thermoplastic and thermotropic polyesters with different chemical structures’, *Journal of Applied Polymer Science*, 100(1), pp. 142–160.

Kelly, P.J., vom Braucke, T., Liu, Z., Arnell, R.D. and Doyle, E.D. (2007) ‘Pulsed DC titanium nitride coatings for improved tribological performance and tool life’, *Surface and Coatings Technology*, 202(4–7), pp. 774–780.

Keysight (2019) *High Temperature Nanoindentation - The State-of-the-art Laser Heating Technique - Keysight Technical Backgrounder*. Available at: <https://about.keysight.com/en/newsroom/backgrounders/G200/#3> (Accessed: 14 June 2019).

Kim, J.-Y., Kang, S.-K., Lee, J.-J., Jang, J., Lee, Y. and Kwon, D. (2007) ‘Influence of surface-roughness on indentation size effect’, *Acta Materialia*, 55, pp. 3555–3562.

King, R.B. (1987) ‘Elastic analysis of some punch problems for a layered medium’, *International Journal of Solids and Structures*, 23(12), pp. 1657–1664.

Komvopoulos, K. (1989) ‘Elastic-Plastic Finite Element Analysis of Indented Layered Media’, *Journal of Tribology*, 111(3), pp. 430–439.

Kong, Y. and Hay, J.N. (2002) ‘The measurement of the crystallinity of polymers by DSC’, *Polymer*, 43(14), pp. 3873–3878.

Korsunsky, A.M., McGurk, M.R., Bull, S.J. and Page, T.F. (1998) ‘On the hardness of coated systems’, *Surface and Coatings Technology*, 99(1–2), pp. 171–183.

- Laurent-Brocq, M., Béjanin, E. and Champion, Y. (2015) ‘Influence of roughness and tilt on nanoindentation measurements: A quantitative model’, *Scanning*, 37(5), pp. 350–360.
- Lechat, C., Bunsell, A.R. and Davies, P. (2010) ‘Tensile and creep behaviour of polyethylene terephthalate and polyethylene naphthalate fibres’, *Journal of Materials Science*, 46(2), pp. 528–533.
- Lechat, C., Bunsell, A.R., Davies, P. and Piant, A. (2006) ‘Mechanical behaviour of polyethylene terephthalate & polyethylene naphthalate fibres under cyclic loading’, *Journal of Materials Science*, 41(6), pp. 1745–1756.
- Lee, E.H. and Radok, J.R.M. (1960a) ‘The Contact Problem for Viscoelastic Bodies’, *Journal of Applied Mechanics*, 27(3), pp. 438–444.
- Lee, E.H. and Radok, J.R.M. (1960b) ‘The Contact Problem for Viscoelastic Bodies’, *Journal of Applied Mechanics*, 27(3), p. 438.
- Leitner, A., Maier-Kiener, V. and Kiener, D. (2017) ‘Dynamic nanoindentation testing: is there an influence on a material’s hardness?’, *Materials Research Letters*, 5(7), pp. 486–493.
- Li, X. and Bhushan, B. (2002) ‘A review of nanoindentation continuous stiffness measurement technique and its applications’, *Materials Characterization*, 48(1), pp. 11–36.
- Li, X., Diao, D. and Bhushan, B. (1997) ‘Fracture mechanisms of thin amorphous carbon films in nanoindentation’, *Acta Materialia*, 45(11), pp. 4453–4461.
- Loubet, J.L., Georges, J.M., Marchesini, O. and Meille, G. (1984) ‘Vickers Indentation Curves of Magnesium Oxide (MgO)’, *Journal of Tribology*, 106(1), pp. 43–48.
- Loubet, J.L., Georges, J.M. and Meille, G. (1985) ‘Vickers Indentation Curves of Elastoplastic Materials’, *Microindentation Techniques in Materials Science and Engineering* Available at: 10.1520/STP32952S (Accessed: 25 June 2018).
- Love, A.E.H. (1939) ‘BOUSSINESQ’S PROBLEM FOR A RIGID CONE’, *The Quarterly Journal of Mathematics*, os-10(1), pp. 161–175.
- Machunze, R. and Janssen, G.C.A.M. (2008) ‘Stress gradients in titanium nitride thin films’, *Surface and Coatings Technology*, 203(5–7), pp. 550–553.
- Magnus, F., Ingason, A.S., Sveinsson, O.B., Olafsson, S. and Gudmundsson, J.T. (2011) ‘Morphology of TiN thin films grown on SiO₂ by reactive high power impulse magnetron sputtering’, *Thin Solid Films*, (0) Available at: 10.1016/j.tsf.2011.07.041 (Accessed: 22 November 2011).
- Makhlouf, A.S.H. (2011) ‘1 - Current and advanced coating technologies for industrial applications’, in Makhlouf, A. S. H. and Tiginyanu, I. (eds.) *Nanocoatings and Ultra-Thin Films*. Woodhead Publishing Series in Metals and Surface Engineering. Woodhead Publishing, pp. 3–23. Available at: 10.1533/9780857094902.1.3 (Accessed: 27 May 2019).

Manika, I. and Maniks, J. (2008) ‘Effect of substrate hardness and film structure on indentation depth criteria for film hardness testing’, *Journal of Physics D: Applied Physics*, 41(7), p. 074010.

Manjunath, B.R., Venkataraman, A. and Stephen, T. (1973) ‘The effect of moisture present in polymers on their X-ray diffraction patterns’, *Journal of Applied Polymer Science*, 17 Available at: 10.1002/app.1973.070170407 (Accessed: 8 March 2016).

Martin, P.M. (2009) *Handbook of Deposition Technologies for Films and Coatings: Science, Applications and Technology*. William Andrew.

Mattox, D. (1998) *Handbook of Physical Vapor Deposition (PVD) Processing - 1st Edition*. Available at: <https://www.elsevier.com/books/handbook-of-physical-vapor-deposition-pvd-processing/9780815514220> (Accessed: 5 August 2018).

Mattox, D.M. (2014) *Handbook of Physical Vapor Deposition (PVD) Processing*. Cambridge University Press.

Maugis, D. (1992) ‘Adhesion of spheres: The JKR-DMT transition using a dugdale model’, *Journal of Colloid and Interface Science*, 150(1), pp. 243–269.

McFarlane, J.S., Tabor David and Bowden Frank Philip (1950) ‘Relation between friction and adhesion’, *Proceedings of the Royal Society of London. Series A. Mathematical and Physical Sciences*, 202(1069), pp. 244–253.

McGurk, M.R., Chandler, H.W., Twigg, P.C. and Page, T.F. (1994) ‘Modelling the hardness response of coated systems: the plate bending approach’, *Surface and Coatings Technology*, 68–69, pp. 576–581.

Menčík, J. (2006) ‘Determination of mechanical properties by instrumented indentation’, *Meccanica*, 42(1), pp. 19–29.

Menčík, J., He, L.H. and Němeček, J. (2011) ‘Characterization of viscoelastic-plastic properties of solid polymers by instrumented indentation’, *Polymer Testing*, 30(1), pp. 101–109.

Menčík, J., He, L.H. and Swain, M.V. (2009) ‘Determination of viscoelastic–plastic material parameters of biomaterials by instrumented indentation’, *Journal of the Mechanical Behavior of Biomedical Materials*, 2(4), pp. 318–325.

Menčík, J., Munz, D., Quandt, E., Weppelmann, E.R. and Swain, M.V. (1997) ‘Determination of elastic modulus of thin layers using nanoindentation’, *Journal of Materials Research*, 12(9), pp. 2475–2484.

Michotte, S. and Proost, J. (2011) ‘In situ measurement of the internal stress evolution during sputter deposition of ZnO:Al’, *Solar Energy Materials and Solar Cells*, (0) Available at: 10.1016/j.solmat.2011.11.013 (Accessed: 17 December 2011).

Micro Materials (2019) *Nanoindenter | Nanoindentation | Micro Materials | Products.*, *Micro Materials* Available at: <http://www.micromaterials.co.uk/core-nanoindentation/> (Accessed: 23 July 2018).

Micro Star Technologies (2019) *Micro Star Tech.* Available at: <http://www.microstartech.com/> (Accessed: 2 August 2018).

Minitab 18 support (2019a) *Taguchi designs.* Available at: <https://support.minitab.com/en-us/minitab/18/help-and-how-to/modeling-statistics/doe/supporting-topics/taguchi-designs/taguchi-designs/> (Accessed: 1 June 2019).

Minitab 18 support (2019b) *What is a gage R&R (repeatability and reproducibility) study?.* Available at: <https://support.minitab.com/en-us/minitab/18/help-and-how-to/quality-and-process-improvement/measurement-system-analysis/supporting-topics/gage-r-r-analyses/what-is-a-gage-r-r-study/> (Accessed: 1 June 2019).

Mo, Z. and Zhang, H. (1995) 'The Degree of Crystallinity in Polymers by Wide-Angle X-Ray Diffraction (Waxd)', *Journal of Macromolecular Science, Part C*, 35(4), pp. 555–580.

Moharrami, N. (2014) *Extracting reliable mechanical properties using the nanoindentation technique.* Ph.D. University of Newcastle upon Tyne. Available at: <http://hdl.handle.net/10443/2738> (Accessed: 10 June 2018).

Mukherjee, C., Case, E.D. and Lee, A. (2000) 'Silica coatings on bismaleimide (BMI) polymeric substrates', *Journal of Materials Science*, 35(6), pp. 1389–1396.

Muliana, A., Haj-Ali, R.M., Steward, R. and Saxena, A. (2002) 'Artificial neural network and finite element modeling of nanoindentation tests', *Metallurgical and Materials Transactions A*, 33(7), pp. 1939–1947.

Nayak, P.R. (1971) 'Random Process Model of Rough Surfaces', *Journal of Lubrication Technology*, 93(3), pp. 398–407.

Newey, D., Wilkins, M.A. and Pollock, H.M. (1982) 'An ultra-low-load penetration hardness tester', *Journal of Physics E: Scientific Instruments*, 15(1), p. 119.

Nix, W.D. and Gao, H. (1998) 'Indentation size effects in crystalline materials: A law for strain gradient plasticity', *Journal of the Mechanics and Physics of Solids*, 46(3), pp. 411–425.

Nomoto, J., Hirano, T., Miyata, T. and Minami, T. (2011) 'Preparation of Al-doped ZnO transparent electrodes suitable for thin-film solar cell applications by various types of magnetron sputtering depositions', *Thin Solid Films*, 520(5), pp. 1400–1406.

Odegard, G.M., Gates, T.S. and Herring, H.M. (2005) 'Characterization of viscoelastic properties of polymeric materials through nanoindentation', *Experimental Mechanics*, 45, pp. 130–136.

Ohring, M. (2001) *Materials Science of Thin Films: Deposition and Structure.* 2nd edn. Academic Press.

Oliver, W.C. (2001) 'Alternative technique for analyzing instrumented indentation data', *Journal of Materials Research*, 16(11), pp. 3202–3206.

Oliver, W.C. and Pharr, G.M. (1992) 'An Improved Technique for Determining Hardness and Elastic Modulus Using Load and Displacement Sensing Indentation Experiments', *Journal of Materials Research*, 7(06), pp. 1564–1583.

Oliver, W.C. and Pharr, G.M. (2004) 'Measurement of Hardness and Elastic Modulus by Instrumented Indentation: Advances in Understanding and Refinements to Methodology', *Journal of Materials Research*, 19(01), pp. 3–20.

Oyen, M.L. (2006) 'Analytical techniques for indentation of viscoelastic materials', *Philosophical Magazine*, 86(33–35), pp. 5625–5641.

Page, T.F. and Hainsworth, S.V. (1993) 'Using nanoindentation techniques for the characterization of coated systems: a critique', *Surface and Coatings Technology*, 61(1), pp. 201–208.

Page, T.F. and Knight, J.C. (1989) 'Factors affecting the tribological behaviour of thin hard TiN and TiC coatings', *Surface and Coatings Technology*, 39–40, pp. 339–354.

Park, K.C., Ma, D.Y. and Kim, K.H. (1997) 'The physical properties of Al-doped zinc oxide films prepared by RF magnetron sputtering', *Thin Solid Films*, 305(1–2), pp. 201–209.

Patterson, A. (1939) 'The Scherrer Formula for X-Ray Particle Size Determination', *Physical Review*, 56(10), pp. 978–982.

PeakFit (2016) *PeakFit - The Automatic Choice for Spectroscopy, Chromatography and Electrophoresis*. Available at: <http://www.sigmaplot.co.uk/products/peakfit/peakfit.php> (Accessed: 8 March 2016).

Pelegri, A.A. and Huang, X. (2008) 'Nanoindentation on soft film/hard substrate and hard film/soft substrate material systems with finite element analysis', *Composites Science and Technology*, 68(1), pp. 147–155.

Persson, B.N.J. (2001) 'Theory of rubber friction and contact mechanics', *The Journal of Chemical Physics*, 115(8), pp. 3840–3861.

Persson, B.N.J. and Tosatti, E. (2001) 'The effect of surface roughness on the adhesion of elastic solids', *The Journal of Chemical Physics*, 115(12), pp. 5597–5610.

Pethica, J.B., Hutchings, R. and Oliver, W.C. (1983) 'Hardness measurement at penetration depths as small as 20 nm', *Philosophical Magazine A*, 48(4), pp. 593–606.

Pharr, G. m., Oliver, W. c. and Brotzen, F. r. (1992) 'On the generality of the relationship among contact stiffness, contact area, and elastic modulus during indentation', *Journal of Materials Research*, 7(03), pp. 613–617.

Pharr, G.M. (1998) 'Measurement of mechanical properties by ultra-low load indentation', *Materials Science and Engineering A*, 253(1–2), pp. 151–159.

Pharr, G.M. and Bolshakov, A. (2002) 'Understanding Nanoindentation Unloading Curves', *Journal of Materials Research*, 17(10), pp. 2660–2671.

- Pöhl, F., Huth, S. and Theisen, W. (2016) 'Detection of the indentation-size-effect (ISE) and surface hardening by analysis of the loading curvature C ', *International Journal of Solids and Structures*, 84, pp. 160–166.
- Poisl, W.H., Fabes, B.D. and Oliver, W.C. (1993) 'A Quantitative Model for Interpreting Nanometer Scale Hardness Measurements of Thin Films', *MRS Online Proceedings Library Archive*, 308 Available at: 10.1557/PROC-308-201 (Accessed: 20 August 2018).
- Pullen, J. and Williamson, J.B.P. (1972) 'On the Plastic Contact of Rough Surfaces', *Proceedings of the Royal Society of London. Series A, Mathematical and Physical Sciences*, 327(1569), pp. 159–173.
- Radok, J.R.M. (1957) 'Visco-elastic stress analysis', *Quarterly of Applied Mathematics*, 15(2), pp. 198–202.
- Ramsey, P.M., Chandler, H.W. and Page, T.F. (1991) 'Modelling the contact response of coated systems', in McGUIRE, G. E., McINTYRE, D. C. and Hofmann, S. (eds.) *Metallurgical Coatings and Thin Films 1991*. Oxford: Elsevier, pp. 504–509. Available at: 10.1016/B978-0-444-89455-7.50094-0 (Accessed: 20 August 2018).
- Saha, R. and Nix, W.D. (2002) 'Effects of the substrate on the determination of thin film mechanical properties by nanoindentation', *Acta Materialia*, 50(1), pp. 23–38.
- Sahoo, P. and Banerjee, A. (2005) 'Asperity interaction in adhesive contact of metallic rough surfaces', *Journal of Physics D: Applied Physics*, 38(22), p. 4096.
- Sakai, M. (1993) 'Energy principle of the indentation-induced inelastic surface deformation and hardness of brittle materials', *Acta Metallurgica et Materialia*, 41(6), pp. 1751–1758.
- Sargent, P.M. (1979) *Factors affecting the microhardness of solids*. Thesis. University of Cambridge. Available at: 10.17863/CAM.22438 (Accessed: 20 August 2018).
- Schuessler, B.J., Wo, P.C. and Zbib, H.M. (2018) 'The influence of grain boundaries and grain orientations on the stochastic responses to low load nanoindentation in Cu', *Materials Science and Engineering: A*, 715, pp. 226–235.
- Schuh, C.A. (2006) 'Nanoindentation studies of materials', *Materials Today*, 9(5), pp. 32–40.
- Schwarzer, N., Richter, F. and Hecht, G. (1999) 'The elastic field in a coated half-space under Hertzian pressure distribution', *Surface and Coatings Technology*, 114(2–3), pp. 292–303.
- Shorshorov, M.K., Bulychev, S.I. and Alekhin, V.P. (1981) 'Work of plastic and elastic deformation during indenter indentation', *Soviet Physics Doklady*, 26
- Sierros, K.A., Banerjee, D.A., Morris, N.J., Cairns, D.R., Kortidis, I. and Kiriakidis, G. (2010) 'Mechanical properties of ZnO thin films deposited on polyester substrates used in flexible device applications', *Thin Solid Films*, 519(1), pp. 325–330.

Singh, A.K. (2005) *Advanced X-ray Techniques in Research and Industry*. Amsterdam ; Washington, D.C: IOSPress.

Sinha, S.K. and Briscoe, B.J. (2009) *Polymer Tribology*. Imperial College Press.

Siu, K.W. and Ngan, A.H.W. (2013) 'The continuous stiffness measurement technique in nanoindentation intrinsically modifies the strength of the sample', *Philosophical Magazine*, 93(5), pp. 449–467.

Skoric, B., Kakas, D., Rakita, M., Bibic, N. and Peruskob, D. (2004) 'Structure, hardness and adhesion of thin coatings deposited by PVD, IBAD on nitrided steels', *Vacuum*, 76(2–3), pp. 169–172.

Smith, E.H. and Arnell, R.D. (2014) 'The Prediction of Frictional Temperature Increases in Dry, Sliding Contacts Between Different Materials', *Tribology Letters*, 55(2), pp. 315–328.

Sneddon, I.N. (1948) 'Boussinesq's problem for a rigid cone', *Mathematical Proceedings of the Cambridge Philosophical Society*, 44(04), pp. 492–507.

Stachowiak, G. and Batchelor, A.W. (2005) *Engineering Tribology*. 3rd edn. A Butterworth-Heinemann Title.

Stilwell, N.A. and Tabor, D. (1961) 'Elastic Recovery of Conical Indentations', *Proceedings of the Physical Society*, 78(2), p. 169.

Stone, D., LaFontaine, W.R., Alexopoulos, P., Wu, T.-W. and Li, C.-Y. (1988) 'An investigation of hardness and adhesion of sputter-deposited aluminum on silicon by utilizing a continuous indentation test', *Journal of Materials Research*, 3(1), pp. 141–147.

Su, Y.-J., Qian, C.-F., Zhao, M.-H. and Zhang, T.-Y. (2000) 'Microbridge testing of silicon oxide/silicon nitride bilayer films deposited on silicon wafers', *Acta Materialia*, 48(20), pp. 4901–4915.

Sudharshan Phani, P. and Oliver, W.C. (2017) 'Ultra High Strain Rate Nanoindentation Testing', *Materials*, 10(6) Available at: 10.3390/ma10060663 (Accessed: 23 July 2018).

Sun, Y., Bell, T. and Zheng, S. (1995) 'Finite element analysis of the critical ratio of coating thickness to indentation depth for coating property measurements by nanoindentation', *Thin Solid Films*, 258(1–2), pp. 198–204.

Suresh, S. and Giannakopoulos, A.E. (1998) 'A new method for estimating residual stresses by instrumented sharp indentation', *Acta Materialia*, 46(16), pp. 5755–5767.

Swadener, J.G., George, E.P. and Pharr, G.M. (2002) 'The correlation of the indentation size effect measured with indenters of various shapes', *Journal of the Mechanics and Physics of Solids*, 50(4), pp. 681–694.

Swain, M.V. and Weppelmann, E.R. (1993) 'A Simple Method for Determination of the Elastic Modulus of Thin Films on a Substrate', *MRS Online Proceedings Library*, 308, p. null.

Tabor, D. (2000) *The Hardness of Metals*. OUP Oxford.

Tabor, D. (1948) 'A Simple Theory of Static and Dynamic Hardness', *Proceedings of the Royal Society of London. Series A. Mathematical and Physical Sciences*, 192(1029), pp. 247–274.

The Engineering Toolbox (2019) *Engineering Materials*. Available at: https://www.engineeringtoolbox.com/engineering-materials-properties-d_1225.html (Accessed: 21 May 2019).

Tho, K.K., Swaddiwudhipong, S., Liu, Z.S. and Hua, J. (2004) 'Artificial neural network model for material characterization by indentation', *Modelling and Simulation in Materials Science and Engineering*, 12(5), p. 1055.

Thomsen, N.B., Fischer-Cripps, A.C. and Swain, M.V. (1998) 'Crack formation mechanisms during micro and macro indentation of diamond-like carbon coatings on elastic–plastic substrates', *Thin Solid Films*, 332(1–2), pp. 180–184.

Thornton, J.A. (1986) 'The microstructure of sputter-deposited coatings', *Journal of Vacuum Science & Technology A*, 4(6), pp. 3059–3065.

Ting, T.C.T. (1966) 'The Contact Stresses Between a Rigid Indenter and a Viscoelastic Half-Space', *Journal of Applied Mechanics*, 33(4), pp. 845–854.

Tiwari, A. (2013) *Nanomechanical Analysis of High Performance Materials*. Springer Science & Business Media.

Tohid, R.R. and Bull, S.J. (2007) 'Getting accurate nanoindentation data from time-dependent and microstructural effects of zinc', *International Journal of Materials Research*, 98(5), pp. 353–359.

Tonelli, A.E. (2002) 'PET versus PEN: what difference can a ring make?', *Polymer*, 43(2), pp. 637–642.

Tsui, T. and Volinsky, A.A. (2019) 'Editorial for the Special Issue on Small-Scale Deformation using Advanced Nanoindentation Techniques', *Micromachines*, 10(4), p. 269.

Tweedie, C.A., Constantinides, G., Lehman, K.E., Brill, D.J., Blackman, G.S. and Van Vliet, K.J. (2007) 'Enhanced Stiffness of Amorphous Polymer Surfaces under Confinement of Localized Contact Loads', *Advanced Materials*, 19(18), pp. 2540–2546.

UK Patent 1513480.2 (2015) *Method for measuring mechanical properties of materials using depth sensing indentation*, UK patent application number 1513480.2.

UK Patent 1701591.8 (2017) *Determination of mechanical properties using nanoindentation at high and low loads*, UK patent application number 2540821.

Vanimisetti, S.K. and Narasimhan, R. (2006) 'A numerical analysis of spherical indentation response of thin hard films on soft substrates', *International Journal of Solids and Structures*, 43(20), pp. 6180–6193.

VanLandingham, M.R. (2003) *Review of Instrumented Indentation*. DIANE Publishing.

VanLandingham, Villarrubia, J. S., Guthrie, W. F. and Meyers, G. F. (2001) 'Nanoindentation of Polymers: An Overview', *Macromolecular Symposia*, 167, pp. 15–44.

VanLandingham, Villarrubia, J. S., Meyers, G. F. and Dineen, M. (2000) 'Advancing Nanoscale Indentation Measurements Toward Quantitative Characterization of Polymer Properties', *Microscopy and Microanalysis*, 6(No. Suppl. 2:Proceedings), pp. 1108–1109.

Verdi, D., Garrido, M.A., Múnez, C.J. and Poza, P. (2014) 'Mechanical properties of Inconel 625 laser cladded coatings: Depth sensing indentation analysis', *Materials Science and Engineering: A*, 598, pp. 15–21.

Vijgen, R.O.E. and Dautzenberg, J.H. (1995) 'Mechanical measurement of the residual stress in thin PVD films', *Thin Solid Films*, 270(1–2), pp. 264–269.

Volinsky, A.A. and Gerberich, W.W. (1999) 'Acoustic Emission Analysis of Fracture Events in Cu Films with W Overlayers', *MRS Online Proceedings Library Archive*, 563 Available at: 10.1557/PROC-563-275 (Accessed: 2 June 2019).

Ward, I.M. and Sweeney, J. (2004) *An Introduction to the Mechanical Properties of Solid Polymers, 2nd Edition*. 2nd Edition. Wiley-Blackwell.

Wasa, K., Kanno, I. and Kotera, H. (2012) *Handbook of Sputter Deposition Technology: Fundamentals and Applications for Functional Thin Films, Nano-materials and MEMS*. William Andrew.

Waters, P. (2019) '*Stress analysis and mechanical characterization of thin films for microelectronics and MEMS applications*'

Wei, P.J., Shen, W.X. and Lin, J.F. (2008) 'Analysis and modeling for time-dependent behavior of polymers exhibited in nanoindentation tests', *Journal of Non-Crystalline Solids*, 354(33), pp. 3911–3918.

Weik, M.H. (2001) 'time constant', in Weik, M. H. (ed.) *Computer Science and Communications Dictionary*. Boston, MA: Springer US, pp. 1786–1786. Available at: 10.1007/1-4020-0613-6_19616 (Accessed: 19 October 2019).

Westbrook, ed.), J.H. (Jack Hall), Conrad, ed.), Hans and Metals, A.S. for (1973) *The Science of hardness testing and its research applications*. Metals Park, Ohio : American Society for Metals. Available at: <https://trove.nla.gov.au/version/45462669> (Accessed: 15 August 2018).

Whitehead, A.J. and Page, T.F. (1992) 'Nanoindentation studies of thin film coated systems', *Thin Solid Films*, 220(1), pp. 277–283.

Whitehouse, D.J. and Archard, J.F. (1970) 'The Properties of Random Surfaces of Significance in their Contact', *Proceedings of the Royal Society of London. A. Mathematical and Physical Sciences*, 316(1524), pp. 97–121.

- Wu, K.-R., Ting, C.-H., Wang, J.-J., Liu, W.-C. and Lin, C.-H. (2006) 'Characteristics of graded TiO₂ and TiO₂/ITO films prepared by twin DC magnetron sputtering technique', *Surface and Coatings Technology*, 200(20–21), pp. 6030–6036.
- Xia, Y., Bigerelle, M., Marteau, J., Mazeran, P.-E., Bouvier, S. and Alain, I. (2014) 'Effect of Surface Roughness in the Determination of the Mechanical Properties of Material Using Nanoindentation Test', *Scanning*, 36
- Yang, S., Zhang, Y.-W. and Zeng, K. (2004) 'Analysis of nanoindentation creep for polymeric materials', *JOURNAL OF APPLIED PHYSICS*, 95, pp. 3655–3666.
- Yeo, C.-D., Katta, R.R., Lee, J. and Polycarpou, A.A. (2010) 'Effect of asperity interactions on rough surface elastic contact behavior: Hard film on soft substrate', *Tribology International*, 43(8), pp. 1438–1448.
- Yin Zhang and Ya-pu Zhao (2006) 'Applicability range of Stoney's formula and modified formulas for a film/substrate bilayer', *Journal of Applied Physics*, 99(5), pp. 53513-1–7.
- Zeng, K.Y. (2006) in *Handbook of Theoretical and Computational Nanotechnology*, M. Rieth and W. Schommers Eds., American Scientific Publisher, 4, p. 387.
- Zhang, T.-Y. and Xu, W.-H. (2002) 'Surface Effects on Nanoindentation', *Journal of Materials Research*, 17(7), pp. 1715–1720.
- Zhang, T.-Y., Zhao, M.-H. and Qian, C.-F. (2000) 'Effect of Substrate Deformation on the Microcantilever Beam-Bending Test', *Journal of Materials Research*, 15(09), pp. 1868–1871.
- Zhang, Y., Oh, Y., Stauffer, D. and Polycarpou, A. (2018) 'A microelectromechanical systems (MEMS) force-displacement transducer for sub-5 nm nanoindentation and adhesion measurements', *Review of Scientific Instruments*, 89, p. 045109.
- Zhao, M., Zheng, W. and Fan, C. (2010) 'Mechanics of shaft-loaded blister test for thin film suspended on compliant substrate', *International Journal of Solids and Structures*, 47(18–19), pp. 2525–2532.
- Zhao, Y. and Chang, L. (2000) 'A Model of Asperity Interactions in Elastic-Plastic Contact of Rough Surfaces', *Journal of Tribology*, 123(4), pp. 857–864.
- Zhou, B. and Prorok, B.C. (2010a) 'A Discontinuous Elastic Interface Transfer Model of Thin Film Nanoindentation', *Experimental Mechanics*, 50(6), pp. 793–801.
- Zhou, B. and Prorok, B.C. (2010b) 'A new paradigm In thin film Indentation', *Journal of Materials Research*, 25(9), pp. 1671–1678.
- Zhou, B., Schwieker, K., Frye, B. and Prorok, B.C. (2011) 'Advances in Thin Film Indentation', in Proulx, T. (ed.) *MEMS and Nanotechnology, Volume 4*. New York, NY: Springer New York, pp. 75–81. Available at: <http://www.springerlink.com/content/x363111050622t26/> (Accessed: 3 August 2011).

Appendix 1.

1.1 Confirmation email from micromaterials on method

From: Stephen Goodes <steveg@micromaterials.co.uk>
Sent: Thursday, 28 June 2018 11:39
To: abdul786.shah@gmail.com
Cc: jacques@micromaterials.co.uk
Subject: RE: zero point

Dear Abdul,

My college Jacques has asked me to reply to your email regarding the indentation depth offsets etc.

The “zero load calibration or “zero-point load calibration” enables the system to establish the relationship between the coil current and the “free” displacement of the pendulum. Therefore, once the calibration has been performed the system can move the pendulum into any position by applying a coil current calculated from the calibration. This calibration is used during the contact procedures to place the indenter onto the sample surface with, ideally, zero load applied to the surface. In practice the sample will feel a small load (L_o) made up from any error in the zero-point calibration (L_c) and any “initial load” (L_i) selected by the user (that is to say $L_o = L_c + L_i$). The “raw” hysteresis curves produced by the scheduler assume that the load starts from L_i and the depth starts from zero and so the analysis procedures try to adjust the load values by an estimate of L_c and correct the corresponding depth values with an estimate of the depth H_o that would be produced by the load L_o . The estimate of L_c can be determined during the analysis of each curve using three different user selected methods...

- 1) A power law, $P = A*(H-H_o)^m$ where $P = \text{Load}$, $H = \text{Depth}$ and A , H_o and m are fitted constants
- 2) A linear fit, $P = H_o + A*H$
- 3) Manual fit, here the user simply enters a value for the depth offset

The depth offset H_o is then added to the depth data before the user selected indentation analysis is performed. The values of H_o for each indentation curve are saved into a data file and this allows the data to be correctly re-analysed in future as follows...

Option “Use Original Corrections” will analyse the data with any H_o values already present in the data

Option “Remove Any Corrections” will subtract any H_o values from the depth data before analysing and saving the data

Option “Calculate New Corrections” will subtract any existing H_o values from the depth data and then calculate new values using one of the fitting options above before analysing and saving the data

Therefore...

<<Also, in order to export the Hysteresis data with a “zero-point correction” + “thermal drift correction” +” frame compliance correction”, I am right to say the options in the pyramidal analysis would be the “Calculate New Corrections” and thermal drift “yes” selected. If so can this also be confirmed.>>

You are correct in this statement but also if the data has already been corrected then you could select the “Use Original Corrections” and thermal drift “yes” selected.

The maximum number of points that can be saved for a hysteresis curve in your system is 4000 and the system endeavours to implement the data acquisition in such a way as to evenly distribute the points collected throughout the curve. In addition, each point plotted and saved is actually the mean value of a number of samples taken at a defined sampling rate (this is a standard noise reduction method). Both the number of samples acquired for the mean calculation and the data rate at which they are acquired can be set by the user. Setting fewer samples with a high data rate will give more data points in the curve but may increase the noise. The sample parameters are accessed from the main menu as follows...

System>>Non-Protected Settings>>Control Unit>>Filters and Rates. The panel entries “Indentation Depth” and “(aux) Indentation Depth” are those used by the system when acquiring indentation data. The default values have been found to give a good compromise between noise and data density.

I hope all that makes sense

Very Best Regards,

Stephen G.

Dr S. R. Goodes
Director of Instrument Development
micro Materials Ltd
Willow House, Yale Business Village
Ellice Way, Wrexham LL13 7YL, UK
Tel: +44 (0)1978 261615


Registered in England & Wales no. 2332065 at the above address

The information in this e-mail is confidential and may also be legally privileged. It is intended for the addressee only. Access to this e-mail by anyone else is unauthorised. It is not to be relied upon by any person other than the addressee except with our prior written approval. If no such approval is given, we will not accept any liability (in negligence or otherwise) arising from any third party acting, or refraining from acting, on such information. Unauthorised recipients are required to maintain confidentiality. If you have received this e-mail in error, please notify us immediately, destroy any copies and delete it from your computer system.

Copyright in this e-mail and any document created by us will be and remain vested in us and will not be transferred to you.

Appendix 2.

2.1 PEN data sheet

Product Information				
 DuPont Teijin Films Teonex® PEN film				
Technical Datasheet - Teonex® Q65F & FA				
Product Description				
<p>Teonex® Q65F is a highly transparent, biaxially oriented polyethylene naphthalate (PEN) film suitable for optical and optoelectronic applications. The film is treated on one side to provide enhanced adhesion, winding and handling properties. Teonex® Q65FA is the same film which has been further processed to deliver reduced thermal shrinkage levels to maintain dimensional stability and reproducibility through high temperature processing steps. Both films are available in thicknesses of 100, 125, and 200 microns.</p>				
TABLE 1 - Typical Values for Major Properties (100 microns)				
General		Value	Units	Method
Density		1.36	g/cm ³	JIS C-2151
Area Yield	100 μm	7.35	m ² /kg	Calculated
	125 μm	5.88		
	200 μm	3.68		
Mechanical		Value	Units	Method
Young Modulus	MD	5060	MPa	ASTM D882-67 (Modified to TDF**)
	TD	6240		
Tensile Strength	MD	226	MPa	JIS C-2318 (Modified to TDF)
	TD	237		
Elongation to break	MD	110	%	JIS C-2318 (Modified to TDF)
	TD	90		

2.1.1 PEN specifications

Thermal		Value		Units	Method
Melting Point		269		°C	DSC
Glass Transition Temperature		121		°C	DSC
		Q65F	Q65FA		
Thermal Shrinkage (150°C, 30min.)	MD	0.5	0.02	%	JIS C-2318 (Modified to TDF)
	TD	0.4	0.02		
Thermal Shrinkage (200°C, 10min)	MD	0.9	0.2		
	TD	0.8	0.1		
Coefficient of Thermal Expansion		MD	.17	10 ⁻⁶ /K	TDF Method
Coefficient of Hydrolytic Expansion		MD	11	10 ⁻⁶ /%RH	TDF Method
Chemical		Value		Units	Method
Moisture Absorption		0.4		%	TDF Method
Moisture Permeability		2		g/m ² /day	JIS-Z0208
Optical		Value		Units	Method
Refractive Index	n _x	1.744			TDF Method
	n _y	1.763			
	n _z	1.498			
Total Luminous Transmission		87		%	JIS K6714
Haze		0.6		%	JIS K6714
Surface		Value		Units	Method
Surface Roughness (R _a)	Inside	0.6		nm	TDF Method
	Outside	2			

* Typical values represent measurements on defined samples and are for illustration purposes only.

**TDF = Teijin DuPont Films Japan Ltd.

DuPont Teijin Films Contacts	
Continental Europe DuPont Teijin Films (Luxembourg) SA BP-1681 L-1016 Luxembourg Telephone +352 2616 4004 Fax +352 2616 5000 http://www.dupontteijinfilms.com	United Kingdom DuPont Teijin Films (UK) Ltd PO Box 2002 Middlesbrough England TS90 8JF Telephone +44 (0) 1642 572000 Fax +44 (0) 1642 572075 e-mail: europa_films@gb.dupont.com e-mail: packaging_films@gb.dupont.com

This information corresponds to our current knowledge on the subject. It is offered solely to provide possible suggestions for your own experimentations. It is not intended, however, to substitute for any testing you may need to conduct to determine for yourself the suitability of our products for your particular purposes. This information may be subject to revision as new knowledge and experience becomes available. Since we cannot anticipate all variations in actual end-use conditions, DuPont Teijin Films makes no warranties and assumes no liability in connection with any use of this information. Nothing in this publication is to be considered as a license to operate under or a recommendation to infringe any patent right.

'Caution: Do not use in medical applications involving permanent implantation in the human body. For other medical applications, see "DuPont Teijin Films Medical Caution Statement", H-50102-I-DTF.'

Melinex®, and Mylar®, are registered trademarks of DuPont Teijin Films U.S. Limited Partnership. Teijin® and Tetoron® are registered trademarks of Teijin Limited and are licensed to DuPont Teijin Films U.S. Limited Partnership. Teonex® is a registered trademark of Teijin DuPont Films Japan Limited and is licensed to DuPont Teijin Films U.S. Limited Partnership.

The goods represented above are only examples of possible applications. DuPont Teijin Films does not imply that any DuPont Teijin Films products have been used in the manufacture of such goods. All third party trademarks and brand names are recognised.

©2007. DuPont Teijin Films. All rights reserved



2.2 PET order sheet

abdul

From: Mike Wood <mikewooddcp@btconnect.com>
Sent: 14 December 2011 11:06
To: abdul
Subject: Re: DATA SHEET
Attachments: img098.jpg

Dear Abdul,

Having checked with Lloyd Paton the product you purchased was our WOF 175. The Crystal Clear 180 Polyester Film you referred to is Llod Patons product reference.

However with WOF 175 this is what we call a write on film and is plain polyester. In other words we do not put a coating on this product and the only added value we give it is the conversion from master reels to A4 size sheets.

Therefore bearing in mind your reason for wanting a technical data sheet I think the best I can do in these circumstances is to furnish you with a copy of the data sheet from our Korean suppliers who reference the product CD105.

I trust the above is clear and the technical data sheet is of some help to you.

Kind regards

Mike
Direct Coated Products Ltd.

----- Original Message -----

From: [abdul](#)
To: mikewooddcp@btconnect.com
Sent: Tuesday, December 06, 2011 3:45 PM
Subject: DATA SHEET

Dear Mike Wood

Relating to the conversation we had over the telephone, the A4 Size Crystal Clear 180 Mic Polyester were bought from LLOYD Paton Limited, ref no. DF180/A4/100. It would be most appreciated if you could please send me the data sheet for the product.

Regards

Abdul Shah

2.2.1 PET specifications

ASTROLL®

PRODUCT INFORMATION

2011-04-01

CD101-105

**For solvent based
Coating & Printing**

Description

ASTROLL CD101-105 clear polyester films are chemically primed to provide enhanced adhesion for solvent based coating and printing. CD-series possess optical clarity and low balanced shrinkage for improved flatness after thermal processing.

ASTROLL CD101-105 are classified on side of chemically treated.

CODE	Inside	Outside
CD101	-	Chemical
CD102	Corona	Chemical
CD103	Chemical	-
CD104	Chemical	Corona
CD105	Chemical	Chemical

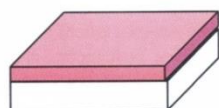
Performance

ASTROLL CD101-105 are designed for excellent adhesion to numerous solvent-based coating systems, so that it can be widely used in the field of food packaging, graphic arts, and other industrial usages.

Application

- ☞ Gravure and flexographic printing
- ☞ Graphic arts
- ☞ Membrane switch
- ☞ Label

Schematic of ASTROLL® CD101-105



Primer for adhesion

PET (12~300um, 48~1200G)

ASTROLL is the registered trademark for Kolon Industries' biaxially oriented PET film.

KOLON INDUSTRIES, INC.

PI-1

2.2.2 PET specifications

ASTROLL®
POLYESTER FILM

INSPECTION DATA

2011-11-11

Customer	Type	Dimension	Condition
DCP	CD105	175 Mic × 1,565 mm × 1,000 m	23±3°C
		700 G × 61.61 Inch × 3,280 Ft	50±10% R.H.

Properties		Unit	Standard	Measured	Test Method
Average Thickness		μm	175.0±2.7	174.1	KOLON Method
Tensile Strength	MD	Kg/mm ²	18.0±4.0	16.6	ASTM D-882
	TD		18.0±4.0	19.7	
Elongation at Break	MD	%	240.0±40.0	242.5	ASTM D-882
	TD		190.0±40.0	156.2	
F-5 Value	MD	Kg/mm ²	11.5±1.0	11.4	ASTM D-882
	TD		11.0±1.0	12.0	
Heat Shrinkage	MD	%	1.00±0.50	1.00	ASTM D-2305 (150°C, 30min.)
	TD		0.50±0.50	0.50	
Friction Coefficient	μS	-	0.70↓	0.34	ASTM D-1894
	μK		0.70↓	0.27	
Haze		%	2.50±0.50	2.61	ASTM D-1003
Wetting Tension		dynes/cm	38±4	36	ASTM D-2578

KOLON INDUSTRIES, INC.
PRESIDENT



KOLON INDUSTRIES, INC.
FILM PC QA Team Manager

2.3 Acrylic data sheet

Plexiglas® 8N

Polymethyl Methacrylate Acrylic
Evonik Industries AG

PROSPECTOR®

www.ulprospector.com

Technical Data

Product Description

Product Profile:

PLEXIGLAS® 8N is an amorphous thermoplastic molding compound (PMMA).

Typical properties of PLEXIGLAS® molding compounds are:

- good flow
- high mechanical strength, surface hardness and abrasion resistance
- high light transmission
- very good weather resistance
- free colorability due to crystal clarity

Special properties of PLEXIGLAS® 8N are:

- optimum mechanical properties
- maximum heat deflection temperature
- good flow / melt viscosity
- AMECA listing.

Application:

Used for injection molding optical and technical items.

Examples:

optical waveguides, luminaire covers, automotive lighting, instrument cluster covers, optical lenses, displays, etc.

General

Material Status	• Commercial: Active		
Literature ¹	• Processing - Injection (English) • Technical Datasheet (English)		
UL Yellow Card ²	• E65495-100849262		
Search for UL Yellow Card	• Evonik Industries AG • Plexiglas®		
Availability	• Europe		
Features	• Amorphous • Good Abrasion Resistance • Good Colorability	• Good Flow • Good Weather Resistance • High Hardness	• High Strength
Uses	• Automotive Applications • Automotive Backlights	• Displays • Lenses	• Optical Applications • Protective Coverings
Forms	• Pellets		
Processing Method	• Injection Molding		
Multi-Point Data	• Creep Modulus vs. Time (ISO 11403-1) • Isochronous Stress vs. Strain (ISO 11403-1) • Isothermal Stress vs. Strain (ISO 11403-1)	• Secant Modulus vs. Strain (ISO 11403-1) • Shear Modulus vs. Temperature (ISO 11403-1) • Specific Volume vs. Temperature (ISO 11403-2)	• Viscosity vs. Shear Rate (ISO 11403-2)

Physical	Nominal Value (English)	Nominal Value (SI)	Test Method
Density	1.19 g/cm ³	1.19 g/cm ³	ISO 1183
Melt Volume-Flow Rate (MVR) (230°C/3.8 kg)	0.183 in ³ /10min	3.00 cm ³ /10min	ISO 1133
Mechanical	Nominal Value (English)	Nominal Value (SI)	Test Method
Tensile Modulus	479000 psi	3300 MPa	ISO 527-2/1
Tensile Stress (Break)	11200 psi	77.0 MPa	ISO 527-2/5
Tensile Strain (Break)	5.5 %	5.5 %	ISO 527-2/5
Impact	Nominal Value (English)	Nominal Value (SI)	Test Method
Charpy Unnotched Impact Strength 73°F (23°C)	9.5 ft-lb/in ²	20 kJ/m ²	ISO 179/1eU

1 of 3



UL and the UL logo are trademarks of UL LLC © 2015. All Rights Reserved.
UL Prospector | 800-788-4668 or 307-742-9227 | www.ulprospector.com.

Form No. TDS-33101-en
Document Created: Thursday, October 01, 2015
Added to Prospector: November, 2000
Last Updated: 3/19/2014

The information presented on this datasheet was acquired by UL Prospector from the producer of the material. UL Prospector makes substantial efforts to assure the accuracy of this data. However, UL Prospector assumes no responsibility for the data values and strongly encourages that upon final material selection, data points are validated with the material supplier.

Thermal	Nominal Value (English)	Nominal Value (SI)	Test Method
Heat Deflection Temperature			
66 psi (0.45 MPa), Unannealed	217 °F	103 °C	ISO 75-2/B
264 psi (1.8 MPa), Unannealed	208 °F	98.0 °C	ISO 75-2/A
Glass Transition Temperature	243 °F	117 °C	ISO 11357-2
Vicat Softening Temperature	226 °F	108 °C	ISO 306/B50
CLTE - Flow (32 to 122°F (0 to 50°C))	4.4E-5 in/in/°F	8.0E-5 cm/cm/°C	ISO 11359-2
Flammability	Nominal Value (English)	Nominal Value (SI)	Test Method
Flame Rating (0.0630 in (1.60 mm))	HB	HB	UL 94
Fire Rating	B2	B2	DIN 4102
Optical	Nominal Value (English)	Nominal Value (SI)	Test Method
Refractive Index	1.490	1.490	ISO 489
Transmittance ⁴	92.0 %	92.0 %	ISO 13468-2
Haze	< 0.50 %	< 0.50 %	ASTM D1003
Injection	Nominal Value (English)	Nominal Value (SI)	
Drying Temperature	< 208 °F	< 98.0 °C	
Drying Time	2.0 to 3.0 hr	2.0 to 3.0 hr	
Processing (Melt) Temp	428 to 500 °F	220 to 260 °C	
Mold Temperature	140 to 194 °F	60.0 to 90.0 °C	

Notes

¹ These links provide you with access to supplier literature. We work hard to keep them up to date; however you may find the most current literature from the supplier.

² A UL Yellow Card contains UL-verified flammability and electrical characteristics. UL Prospector continually works to link Yellow Cards to individual plastic materials in Prospector, however this list may not include all of the appropriate links. It is important that you verify the association between these Yellow Cards and the plastic material found in Prospector. For a complete listing of Yellow Cards, visit the UL Yellow Card Search.

³ Typical properties: these are not to be construed as specifications.

⁴ D65



Plexiglas® 8N
Polymethyl Methacrylate Acrylic
Evonik Industries AG

PROSPECTOR®
www.ulprospector.com

Where to Buy

Supplier

Evonik Industries AG
Essen, Germany
Telephone: +49-201-177-01
Web: <http://corporate.evonik.com/en/Pages/default.aspx>

Distributor

GUZMAN GLOBAL S.L
Telephone: +34-963-992-400
Web: <http://www.grupoguzman.com/>
Availability: Portugal, Spain

Plastribution
Telephone: +44-845-345-4560
Web: <http://www.plastribution.co.uk/>
Availability: United Kingdom

TER HELL PLASTIC GMBH
TER HELL PLASTIC is a Pan European distribution company. Contact TER HELL PLASTIC for availability of individual products by country.
Telephone: +49-232-3941-0
Web: <http://www.terhell.de/>
Availability: Germany

Ultrapolymers
Ultrapolymers is a Pan European distribution company. Contact Ultrapolymers for availability of individual products by country.
Telephone: +32-11-57-95-57
Web: <http://www.ultrapolymers.com/>
Availability: France, Romania

3 of 3



UL and the UL logo are trademarks of UL LLC © 2015. All Rights Reserved.
UL Prospector | 800-788-4668 or 307-742-9227 | www.ulprospector.com.

The information presented on this datasheet was acquired by UL Prospector from the producer of the material. UL Prospector makes substantial efforts to assure the accuracy of this data. However, UL Prospector assumes no responsibility for the data values and strongly encourages that upon final material selection, data points are validated with the material supplier.

Form No. TDS-33101-en
Document Created: Thursday, October 01, 2015
Added to Prospector: November, 2000
Last Updated: 3/19/2014

2.4 High density polyethylene data sheet

Product Datasheet

ExxonMobil

ExxonMobil™ HDPE HMA 016 High Density Polyethylene Resin

Product Description

HMA 016 is a HDPE grade, characterized by fast cycling and good impact strength. It has high gloss and high dimensional stability.

General

Availability ¹	• Africa & Middle East	• Asia Pacific	• Europe
Additive	• Thermal Stabilizer: Yes		
Applications	• Closures	• Housewares	
	• Food Packaging Containers	• Toys	
Revision Date	• 03/01/2013		

Resin Properties	Typical Value (English)	Typical Value (SI)	Test Based On
Density	0.956 g/cm ³	0.956 g/cm ³	ExxonMobil Method
Melt Index (190°C/2.16 kg)	20 g/10 min	20 g/10 min	ASTM D1238

Thermal	Typical Value (English)	Typical Value (SI)	Test Based On
Heat Deflection Temperature (0.45 MPa)	147 °F	64 °C	ISO 75-2/B
Peak Melting Temperature	271 °F	133 °C	ASTM D3418

Molded Properties	Typical Value (English)	Typical Value (SI)	Test Based On
Tensile Stress at Yield	3300 psi	23 MPa	ISO 527-2/1A/50
Tensile Strain at Yield	10 %	10 %	ISO 527-2/1A/50
Tensile Strain at Break	> 100 %	> 100 %	ISO 527-2/1A/50
Flexural Modulus	140000 psi	970 MPa	ISO 178
Environmental Stress-Crack Resistance 122°F (50°C), 10% Igepal	2 hr	2 hr	ASTM D1693

Impact	Typical Value (English)	Typical Value (SI)	Test Based On
Notched Izod Impact Strength	1.9 ft-lb/in ²	4.0 kJ/m ²	ISO 180/1A

Additional Information

The molded properties were measured on 4 mm (157.5 mil) thick injection molded specimen based on ISO 294-1.

Heat Deflection temperature sample preparation, injection based on ISO1872. Tested flatwise position with specimen size of 80mm x 10mm x 4mm.

ESCR was measured on 2 mm (78.7 mil) thick compression molded plate (F50, 10 % Igepal, 50°C, 122°F)

Legal Statement

Contact your ExxonMobil Chemical Customer Service Representative for potential food contact application compliance (e.g. FDA, EU, HPFB).

This product is not intended for use in medical applications and should not be used in any such applications.

Notes

Typical properties: these are not to be construed as specifications.

¹ Product may not be available in one or more countries in the identified Availability regions. Please contact your Sales Representative for complete Country Availability.

2.5 Low density polyethylene data sheet



LDPE Low Density Polyethylene

Description	
A semi crystalline material with milky white base colour and waxy feel. Excellent impact resistance, semi flexible soft material chemical resistance and electrical insulation are excellent.	
Typical Applications	
Caps, lids, containers, pipe couplings, fenders flexible lids	
Types of grade available	
Injection moulding	
Extrusion	
Blow moulding	
General Processing	
Drying Time	N/A
Drying Temperature	N/A
Type of Drier	N/A
Purging	DYNAPURGE M / K OR F
Moisture Absorption	<0.2%
Other Considerations	Organic dies should not be used for colouring due to leaching
Processing Injection Moulding	
Barrel Settings	150C to 250C
Injection speed	Fast for mouldings with high surface gloss
Injection Pressure	High
Back Pressure	Low
Screw Speed	Medium
Tool Temperature	30C
Melt Temperature	180C to 280C
Processing Stability	Residence time should not exceed 5 to 6 minutes
Gate Considerations	All types of gate are used
Sprue & Runner Considerations	No special requirements
Processing Extrusion	
Barrel Settings	170C to 200C
Screw Speed	50 – 80 rpm
Screen Packs	80 mesh
Haul-off / Cooling	Water bath chilled 10c

Calibration	Suitable for use with a vacuum calibrator or sizing plates.
Mechanical Properties	
Shrinkages	2% to 3%
Flexural Modulus	.125 -.759 GPa
Tensile strength at Yield	7 -24 MPa
Physical Properties	
Density	0.917
Cold Bend	
Cold Flex	
Elongation at Break	500%
Tensile Modulus	.140 -.350 GPa
General Impact Strength	Good
Material Finish	Mat and wax like
Thermal Properties	
Vicat Softening Temperature	85C
Heat Deflection Temperature	50c
Flammability	
Flammability Rating	Not flame retardant
Weatherability	
Suitability for outdoor use	LDPE has poor UV stability unless modified with Carbon black and UV stabiliser
Fillers & Additives	Carbon Black, graphite
Chemical Resistance	
Resistant to	Dilute and concentrated acids, alcohols & esters
Not resistant to	Aliphatic and aromatic hydrocarbons
Food Contact Status	Suitable for food contact
Colouring	As the natural colour is off-white then a wide colour range is possible; this does not include transparent colours. Can be coloured by techniques such as masterbatch, dry colouring and liquid colouring. When dry colouring, adhesion promoters such as paraffin can be used
WEEE & ROHS Compliance	Contains no hazardous substances
Bonding	The material may not be joined to itself using solvents as

2.6 Polystyrene data sheet

STYRON™ 678E General Purpose Polystyrene Resin Trinseo

PROSPECTOR®
www.ulprospector.com

Technical Data

Product Description

STYRON™ 678E is a general purpose polystyrene with high flow and good toughness. It is designed for injection molding cap coating and for use either pure or in a mixture with other easy flowing high impact polymers in injection molding applications.

Applications:

- Thin-walled containers
- Coextrusion cap coating

Complies with:

- Europe EU-Directive 2002/72/EC by Europe REGULATION (EC) 10/2011
- U.S. FDA 21 CFR 177.1640
- Consult the regulations for complete details.

General

Material Status	• Commercial: Active		
Literature ¹	• Technical Datasheet		
UL Yellow Card ²	• E162447-238291		
Search for UL Yellow Card	• Trinseo • STYRON™		
Availability	• Europe		
Features	• Good Toughness	• High Flow	• High Impact Resistance
Uses	• Containers	• General Purpose	• Thin-walled Parts
Agency Ratings	• EU 2002/72/EC	• EU No 10/2011	• FDA 21 CFR 177.1640
Appearance	• Clear/Transparent		
Forms	• Pellets		
Processing Method	• Blow Molding • Extrusion	• Injection Molding • Sheet Extrusion	• Thermoforming

Physical	Nominal Value (English)	Nominal Value (SI)	Test Method
Density			
--	1.05 g/cm ³	1.05 g/cm ³	ISO 1183
--	0.0379 lb/in ³	1050 kg/m ³	ISO 1183 ⁴
Apparent Density	0.60 g/cm ³	0.60 g/cm ³	ISO 60
Melt Mass-Flow Rate (MFR) (200°C/5.0 kg)	11 g/10 min	11 g/10 min	ISO 1133
Melt volume-flow rate (200°C/5.0 kg)	0.671 in ³ /10min	11.0 cm ³ /10min	ISO 1133 ⁴
Water Absorption			ISO 62 ⁴
Saturation	0.0 %	0.0 %	
Equilibrium	0.0 %	0.0 %	
Viscosity number	91.0 cm ³ /g	91.0 cm ³ /g	ISO 307, 1157, 1628 ⁴
Mechanical	Nominal Value (English)	Nominal Value (SI)	Test Method
Tensile modulus	479000 psi	3300 MPa	ISO 527-2 ⁴
Tensile Stress			
Yield	6240 psi	43.0 MPa	ISO 527-2/5
Yield	6090 psi	42.0 MPa	ISO 527-2 ⁴
Tensile Strain			
Yield	2.0 %	2.0 %	ISO 527-2 ⁴
Break	2.0 %	2.0 %	ISO 527-2/5
Nominal strain at break	2.0 %	2.0 %	ISO 527-2 ⁴
Flexural Modulus	508000 psi	3500 MPa	ISO 178
Flexural Stress	11600 psi	80.0 MPa	ISO 178

1 of 3



UL and the UL logo are trademarks of UL LLC © 2015. All Rights Reserved.
UL Prospector | 800-788-4688 or 307-742-9227 | www.ulprospector.com.

The information presented on this datasheet was acquired by UL Prospector from the producer of the material. UL Prospector makes substantial efforts to assure the accuracy of this data. However, UL Prospector assumes no responsibility for the data values and strongly encourages that upon final material selection, data points are validated with the material supplier.

Form No. TDS-31937-en
Document Created: Thursday, October 01, 2015
Added to Prospector: November, 2000
Last Updated: 11/19/2014

STYRON™ 678E
General Purpose Polystyrene Resin
Trinseo

PROSPECTOR®
www.ulprospector.com

Hardness	Nominal Value (English)	Nominal Value (SI)	Test Method
Rockwell Hardness (R-Scale)	105	105	ISO 2039-2
Ball Indentation Hardness	21800 psi	150 MPa	ISO 2039-1
Thermal	Nominal Value (English)	Nominal Value (SI)	Test Method
Heat Deflection Temperature			
66 psi (0.45 MPa), Annealed	187 °F	86.0 °C	ISO 75-2/B
66 psi (0.45 MPa)	180 °F	82.0 °C	ISO 75-2 ⁴
264 psi (1.8 MPa), Annealed	180 °F	82.0 °C	ISO 75-2/A
264 psi (1.8 MPa)	160 °F	71.0 °C	ISO 75-2 ⁴
Vicat Softening Temperature			
--	199 °F	93.0 °C	ISO 306/A120
--	187 °F	86.0 °C	ISO 306/B50
50°C/h, B (50N)	187 °F	86.0 °C	ISO 306 ⁴
CLTE			ISO 11359-2 ⁴
Flow	4.4E-5 in/in/°F	8.0E-5 cm/cm/°C	
Transverse	4.4E-5 in/in/°F	8.0E-5 cm/cm/°C	
Electrical	Nominal Value (English)	Nominal Value (SI)	Test Method
Surface resistivity	1.0E+13 ohms	1.0E+13 ohms	IEC 60093 ⁴
Volume resistivity	> 3.9E+16 ohms-in	> 1.0E+15 ohms-m	IEC 60093 ⁴
Electric strength	3400 V/mil	140 kV/mm	IEC 60243-1 ⁴
Relative Permittivity			IEC 60250 ⁴
100 Hz	2.50	2.50	
1 MHz	2.50	2.50	
Dissipation Factor			
1 MHz	6.0E-5	6.0E-5	ASTM D150 IEC 60250 ⁴
100 Hz	9.0E-5	9.0E-5	IEC 60250 ⁴
Flammability	Nominal Value (English)	Nominal Value (SI)	Test Method
Flame Rating ⁵ (0.0630 in (1.60 mm))	HB	HB	UL 94
Burning Behav. at 1.6mm nom. thickn. 0.06 in (1.60 mm), UL	HB	HB	ISO 1210 ⁴

Notes

¹ These links provide you with access to supplier literature. We work hard to keep them up to date; however you may find the most current literature from the supplier.

² A UL Yellow Card contains UL-verified flammability and electrical characteristics. UL Prospector continually works to link Yellow Cards to individual plastic materials in Prospector, however this list may not include all of the appropriate links. It is important that you verify the association between these Yellow Cards and the plastic material found in Prospector. For a complete listing of Yellow Cards, visit the UL Yellow Card Search.

³ Typical properties: these are not to be construed as specifications.

⁴ Tested in accordance with ISO 10350. 23°C/50%r.h. unless otherwise noted.

⁵ This rating not intended to reflect hazards presented by this or any other material under actual fire conditions.

2 of 3



UL and the UL logo are trademarks of UL LLC © 2015. All Rights Reserved.
UL Prospector | 800-788-4668 or 307-742-9227 | www.ulprospector.com.

Form No. TDS-31937-en
Document Created: Thursday, October 01, 2015
Added to Prospector: November, 2000
Last Updated: 11/19/2014

The information presented on this datasheet was acquired by UL Prospector from the producer of the material. UL Prospector makes substantial efforts to assure the accuracy of this data. However, UL Prospector assumes no responsibility for the data values and strongly encourages that upon final material selection, data points are validated with the material supplier.

2.7 Nylon data sheet



EPLAMID 66 NATURAL

Polyamide 66

TEKNİK BİLGİ / DATA SHEET

Malzeme Bilgisi / Material Information

: Bu ürün Eplamid 66 Naturel katkısız malzemedir ve enjeksiyon kalıplama için uygundur.

: Eplamid 66 Natural is an unreinforced polyamide 66 and is suitable for injection moulding.

	TEST METHOD	DEĞERLER/VALUES
FİZİKSEL TESTLER / PHYSICAL TESTS		
YOĞUNLUK / DENSITY (23°C)	ISO 1183	1,12-1,14 g/cm ³
KATKI ORANI / ASH CONTENT	ISO 3451	... %
R. VİSKOZİTE / R. VISCOSITY (%96 H ₂ SO ₄)	ISO 307	2,4-2,7
AKIŞKANLIK İNDİSİ / MELT FLOW RATE MVR (260°C/5.0 Kg)	ISO 1133	... cm ³ /10min.
NEM ALMA / MAX. MOISTURE	ISO 62	0,20%
KALIP ÇEKME / MOLD SHRINKAGE - PARALEL/NORMAL (3 mm)	ISO 294-4	1,4 / 1,6 %

SERTLİK TESTİ / HARDNESS TEST		
SERTLİK / HARDNESS (SHORE D - 23°C)	ISO 868	75-80 D

MEKANİK TESTLER / MECHANICAL TESTS		
ÇEKME ESNEKLİK MODÜLÜ / TENSILE MODULUS (23°C)	ISO 527-2	3000-3500 N/mm ²
KOPMA MUKAVEMETİ / TENSILE STRESS AT BREAK (23°C)	ISO 527-2	70-80 N/mm ²
KOPMADAKİ UZAMA / TENSILE STRAIN AT BREAK (23°C)	ISO 527-2	5-10 %
BASMA ESNEKLİK MODÜLÜ / FLEXURAL MOD. (23°C)	ISO 178	2900-3300 N/mm ²
BASMA BÜKÜLME DAYANIM / FLEXURAL STRENGTH (23°C)	ISO 178	80-100 N/mm ²
İZOD DARBE (ÇENTİKLİ) / İZOD IMPACT (NOTCHED / 23°C)	ISO 180/1A	6-8 kJ/m ²
CHARPY DARBE / CHARPY IMPACT (NOTCHED / 23°C)	ISO 179/1eA	6-8 kJ/m ²

İSİ TESTLERİ / THERMAL TESTS		
ERİME NOKTASI / MELTING POINT	ISO 3146	240-260 °C

YANMA VE ELEKTRİKSEL TESTLERİ / FLAMMABILITY AND ELECTRICAL PROPERTIES		
YANMA TESTİ / FLAME RETARDENCY (1,6 mm)	UL-94	V2
KIZGIN TEL TESTİ / GLOW WIRE - GWFI (1,6 mm)	TS EN 60695-2-12	750 °C
KIZGIN TEL TESTİ / GLOW WIRE - GWIT (1,6 mm)	TS EN 60695-2-13	... °C
CTI (SOLUTION A)	IEC 60112	... V

TEST KOŞULLARI / TEST CONDITIONS		
Laboratuvar koşulları 23 ±2°C, 45-55 % RH dir. Bu ortamda kuru olarak (DAM olarak) yapılmıştır.		
Laboratuvar conditions are 23 ±2°C and 45-55 % RH. Also tests are made dry as molded (DAM).		

ÇALIŞMA KOŞULLARI / PROCESSING CONDITIONS		
Malzeme enjeksiyon çalışma sıcaklığı 260°C' dir. Hammaddenin kurutma sıcaklığı 80°C olup ortalama kurutma süresi 2-4 saattir.		
Recommended injection moulding temperature is 260°C. Drying temperature of raw material is 80°C and average drying time is 2-4 hours.		

ONAY / APPROVAL
Ufuk YILMAZ

Bu Teknik Bülteinde belirtilen bilgiler güvenli bir şekilde test edilerek verilmiştir fakat EPSAN Plastik farklı şartlar altında elde edilebilecek değerlerden sorumlu tutulamaz. Ürünümüzün kullanımında ve sizin tarafınızdan üretilen ürünler bizim kontrolümüz dışında olduğu için sorumluluk tamamen size aittir. Eplamid ve Eplon Epsan Plastik Ltd. Şti' nin patentli ürünüdür. Elektronik ortamda hazırlanan raporlarda imza gerektirmez.

The information in this datasheet is given in good faith but without warranty. These data do not release you from the obligation to test our products as to their suitability for the intended processes and uses. The application, use and processing of our products and the products manufactured by you are beyond our control and, therefore, entirely your own responsibility. Eplamid and Eplon are registered name of Epsan Plastik Ltd. Şti.

KK-004/R07

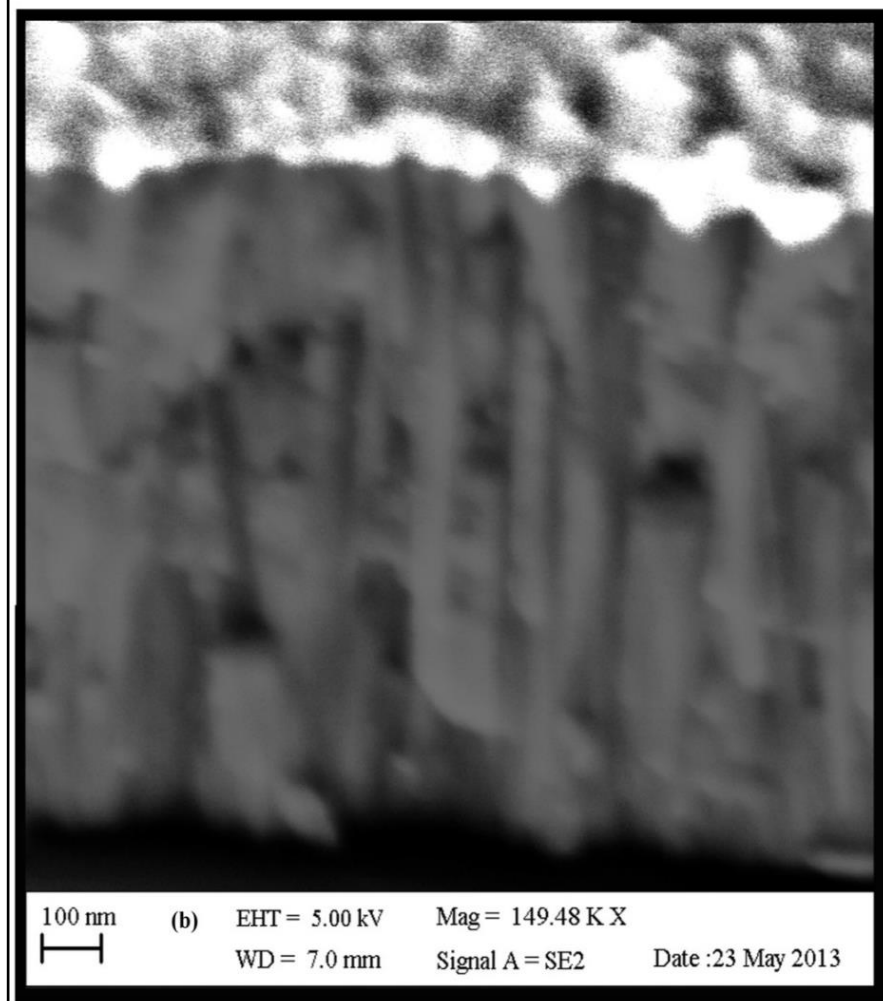
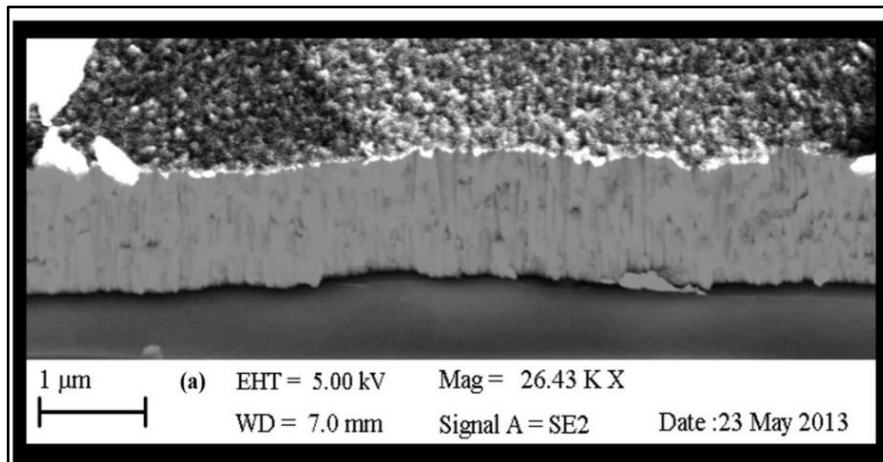
HAZ.TAR.:20.08.2003

REV.TAR.:27.01.2010

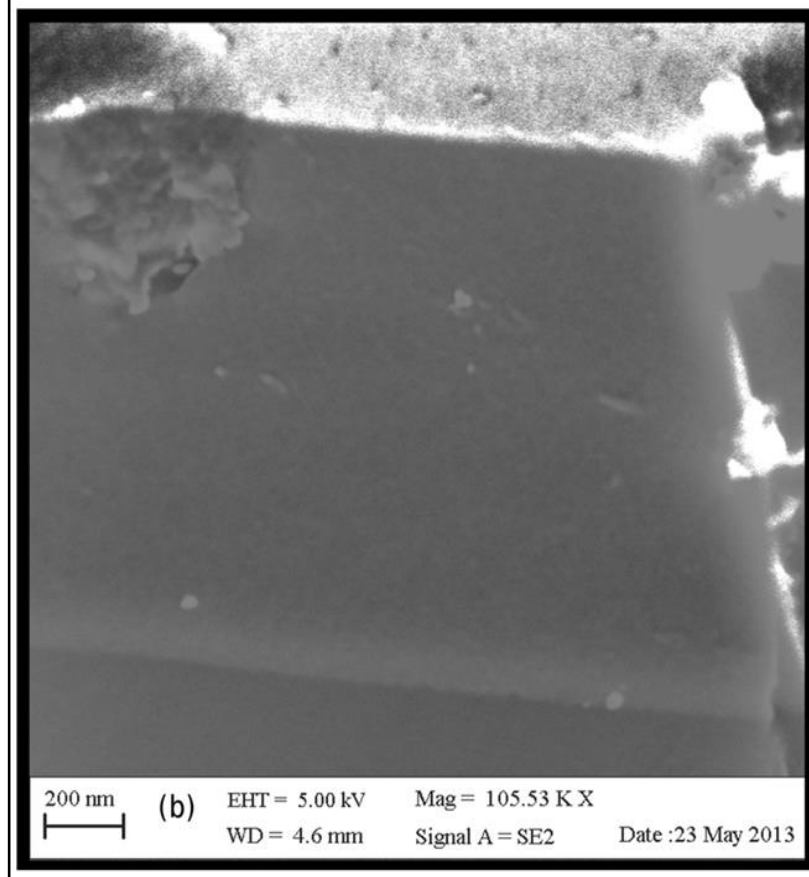
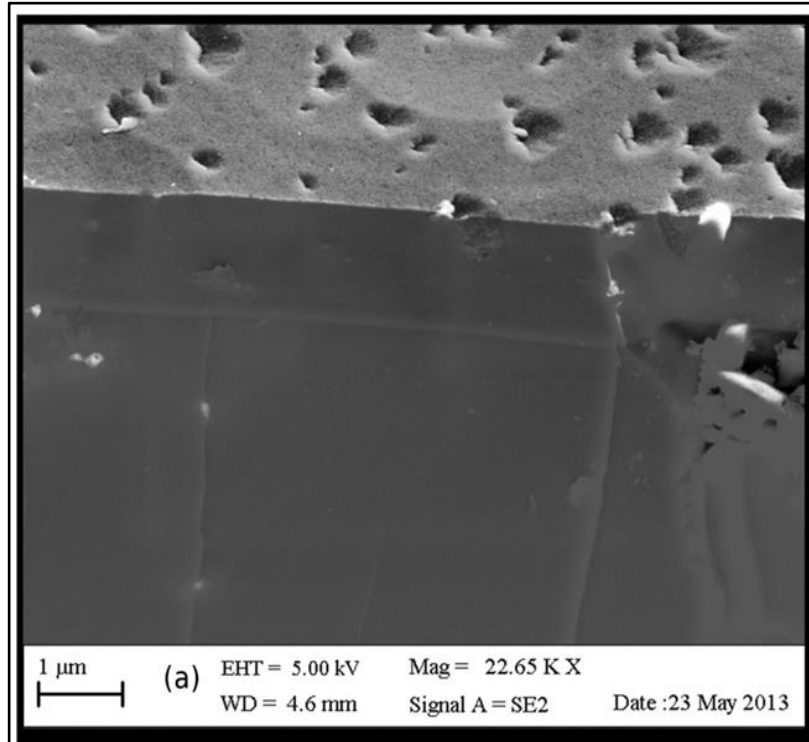
Appendix 3.

3.1 HSEM results

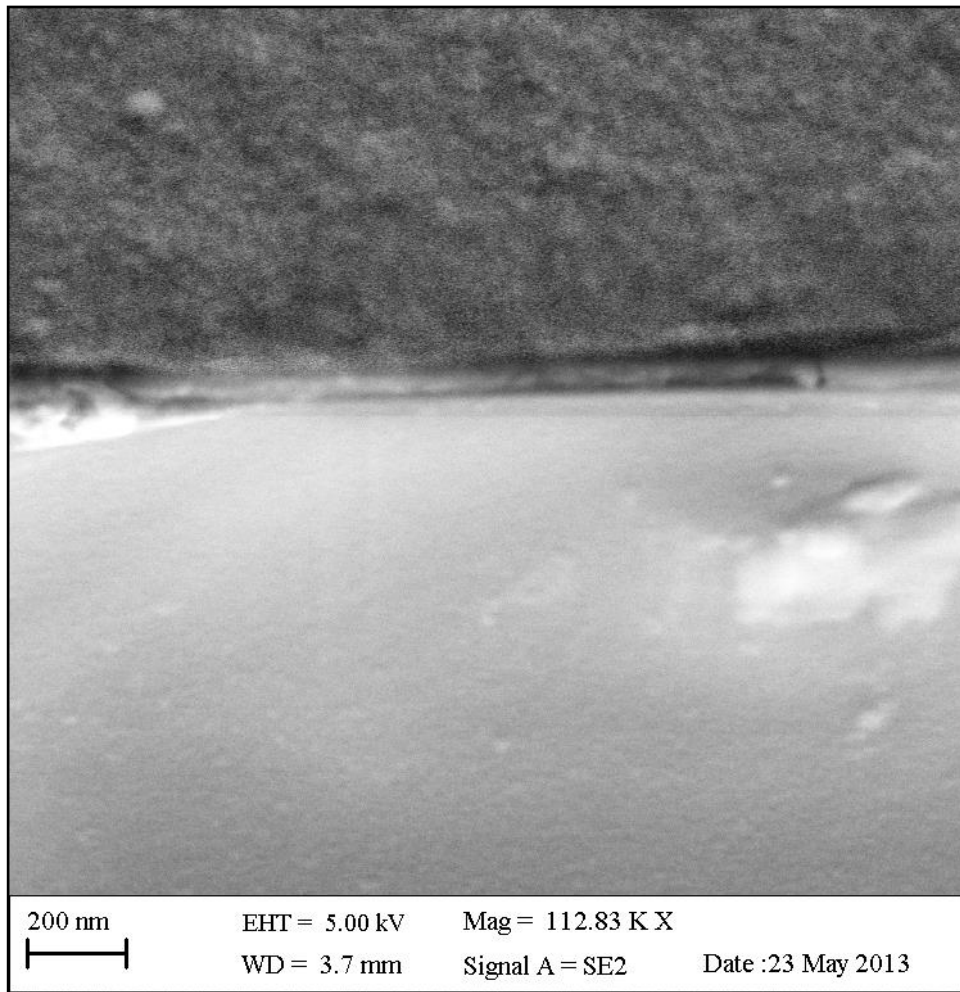
3.1.1 HSEM for 800nm thick TiN coating on PET a) 26.46 magnification & b) 149.48 magnification



3.1.2 HSEM for 1.2 μm thick TiO_2 coating on PET a) 22.65 magnification & b) 105.53 magnification



3.1.3 HSEM for 123nm thick coating on PET substrate at 22.65 magnification



Appendix 4.

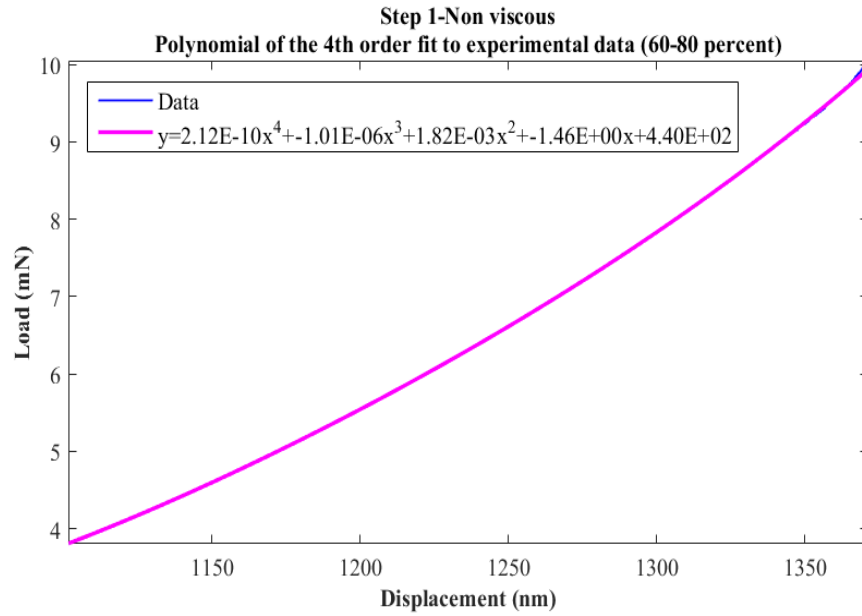
4.1 Run Order for Experiment 4.1

RUN	LOAD	LOAD RATE	UNLOADING RATE	HOLD TIME
1	10,20,30,40,50,60,70,80,90,100	0.1	0.1	5
2	10,20,30,40,50,60,70,80,90,100	0.1	0.1	20
3	10,20,30,40,50,60,70,80,90,100	0.1	0.1	60
4	10,20,30,40,50,60,70,80,90,100	0.1	1	5
5	10,20,30,40,50,60,70,80,90,100	0.1	1	20
6	10,20,30,40,50,60,70,80,90,100	0.1	1	60
7	10,20,30,40,50,60,70,80,90,100	0.1	2	5
8	10,20,30,40,50,60,70,80,90,100	0.1	2	20
9	10,20,30,40,50,60,70,80,90,100	0.1	2	60
10	10,20,30,40,50,60,70,80,90,100	1	0.1	5
11	10,20,30,40,50,60,70,80,90,100	1	0.1	20
12	10,20,30,40,50,60,70,80,90,100	1	0.1	60
13	10,20,30,40,50,60,70,80,90,100	1	1	5
14	10,20,30,40,50,60,70,80,90,100	1	1	20
15	10,20,30,40,50,60,70,80,90,100	1	1	60
16	10,20,30,40,50,60,70,80,90,100	1	2	5
17	10,20,30,40,50,60,70,80,90,100	1	2	20
18	10,20,30,40,50,60,70,80,90,100	1	2	60
19	10,20,30,40,50,60,70,80,90,100	2	0.1	5
20	10,20,30,40,50,60,70,80,90,100	2	0.1	20
21	10,20,30,40,50,60,70,80,90,100	2	0.1	60
22	10,20,30,40,50,60,70,80,90,100	2	1	5
23	10,20,30,40,50,60,70,80,90,100	2	1	20
24	10,20,30,40,50,60,70,80,90,100	2	1	60
25	10,20,30,40,50,60,70,80,90,100	2	2	5
26	10,20,30,40,50,60,70,80,90,100	2	2	20
27	10,20,30,40,50,60,70,80,90,100	2	2	60

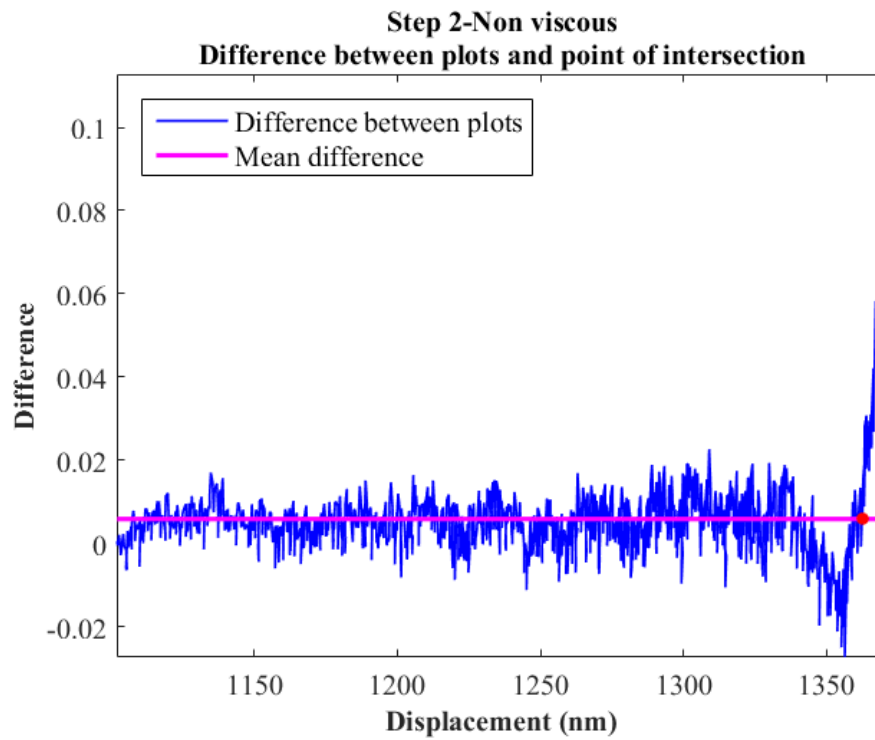
Appendix 5.

5.1 Non-viscous

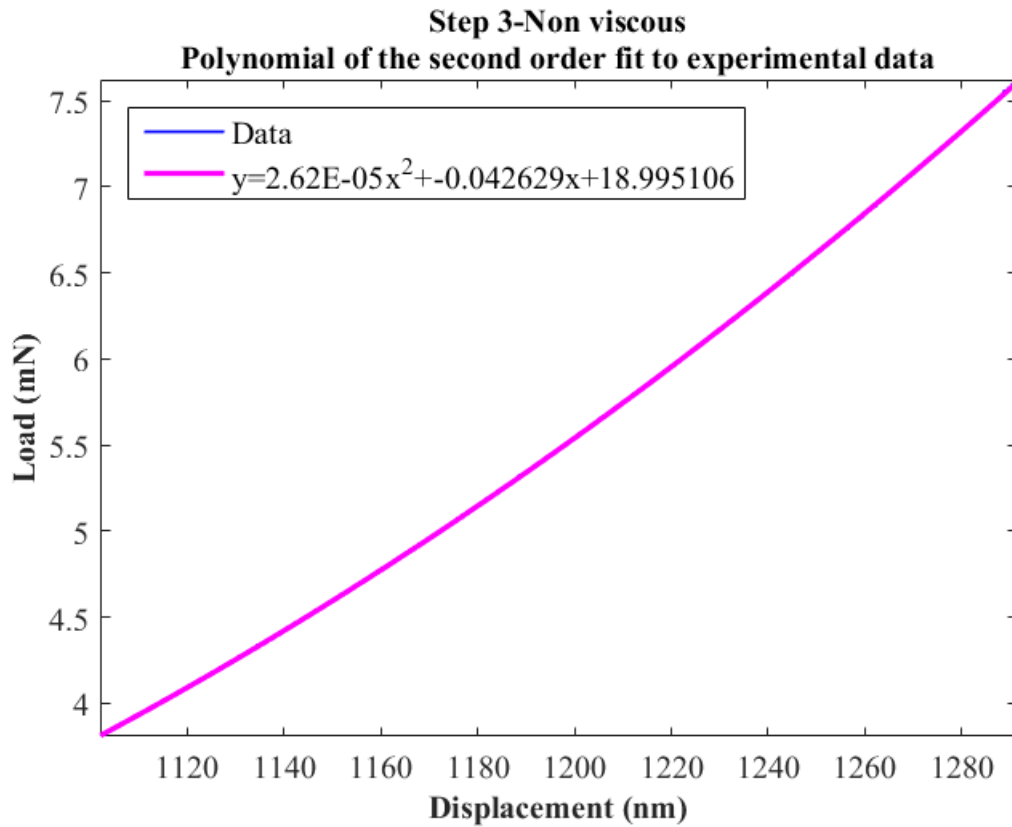
5.1.1 Poly4 fit to eliminate initial nose out data



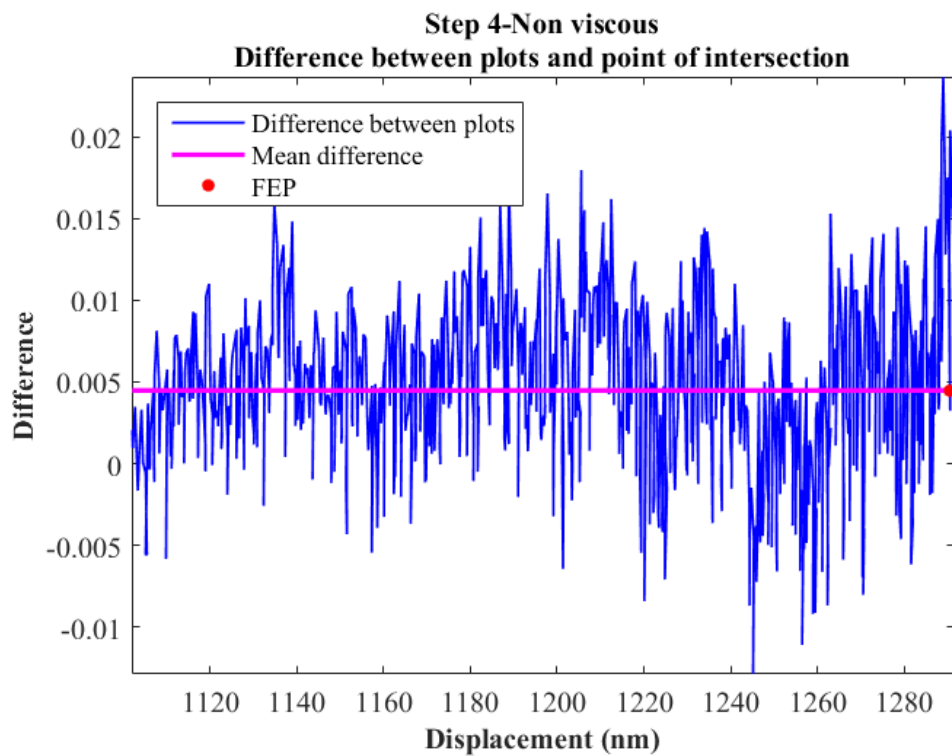
5.1.2 Determining the minimum of the difference between fit and experimental at the highest load



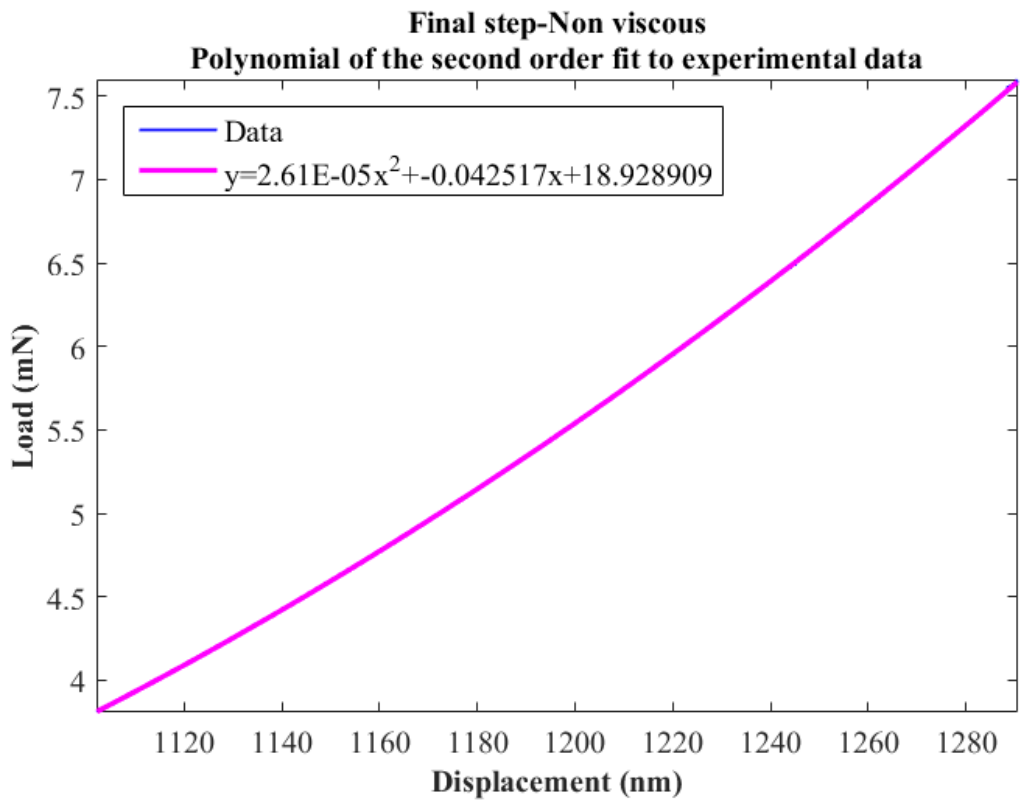
5.1.3 Poly2 fit to extracted data



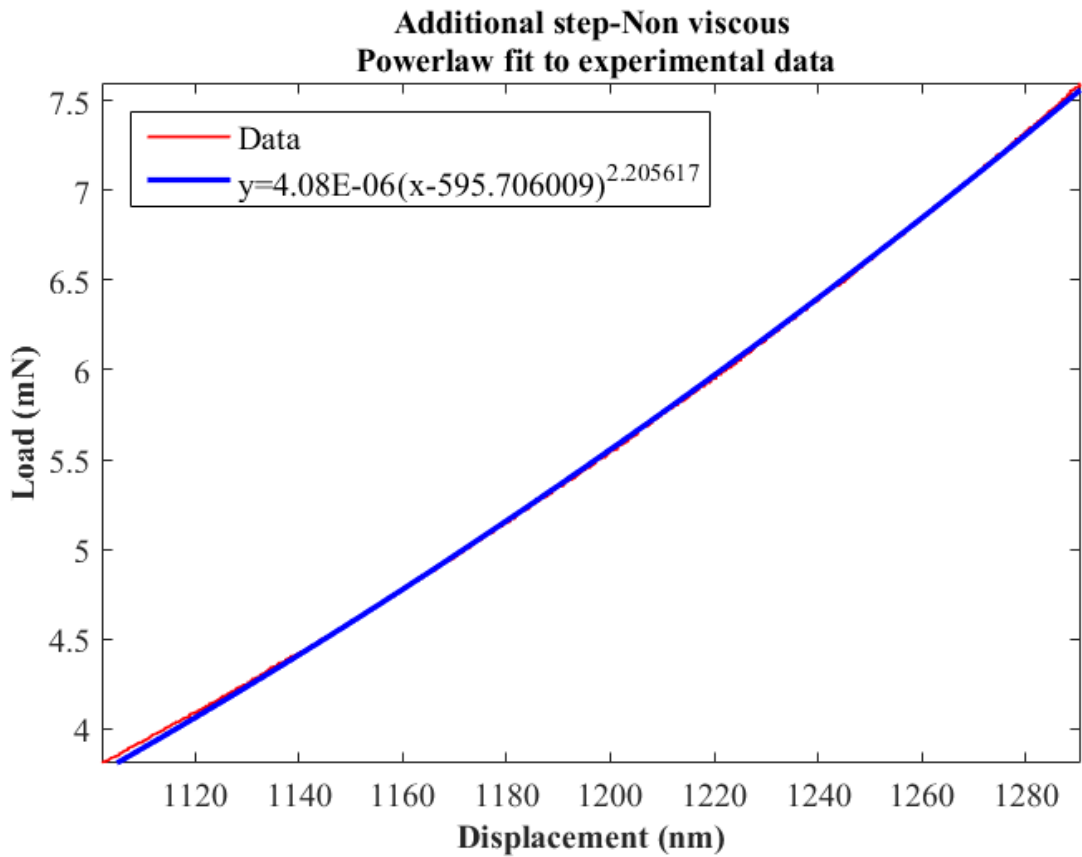
5.1.4 Determining the minimum of the difference between fit and experimental at the highest load



5.1.5 Final poly2

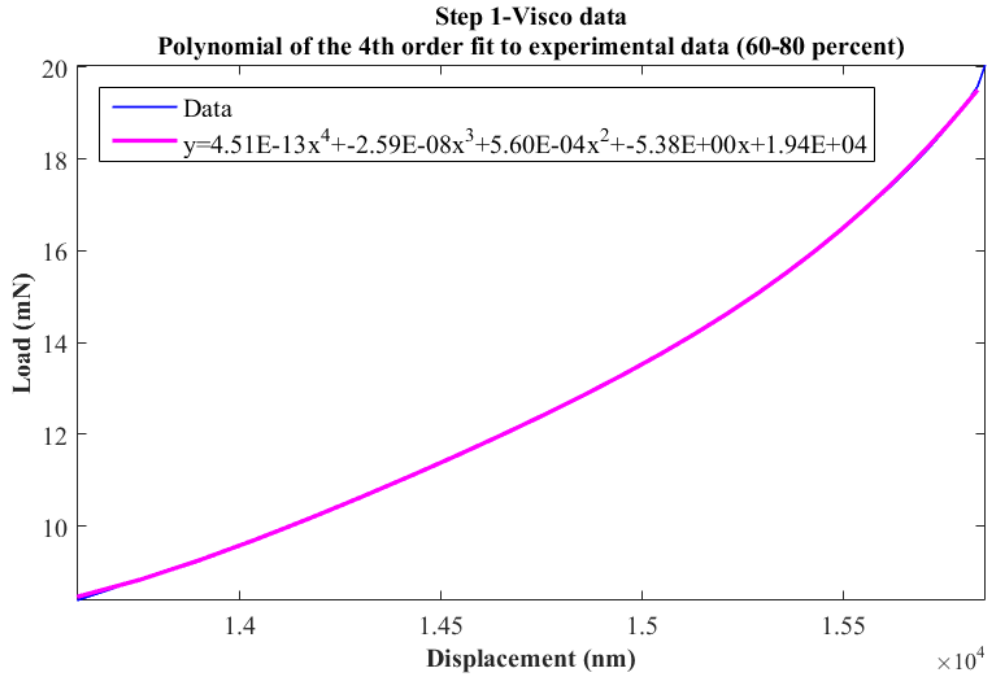


5.1.6 Power law fit

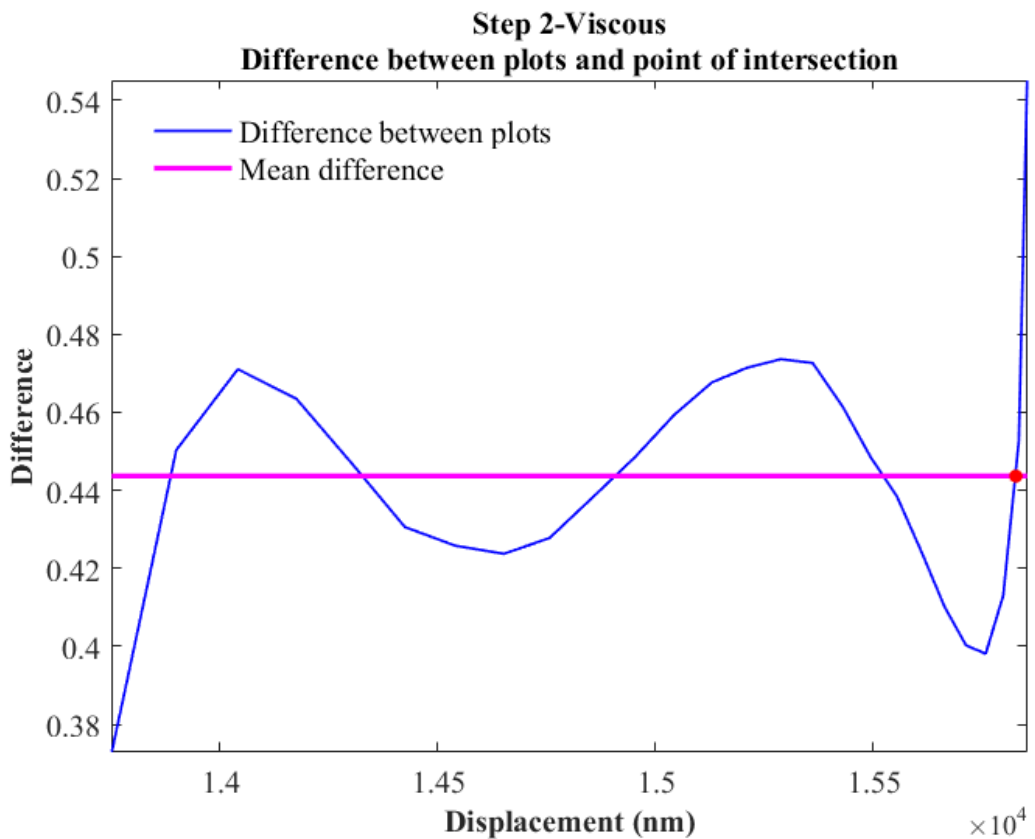


5.2 Viscous-Rubber

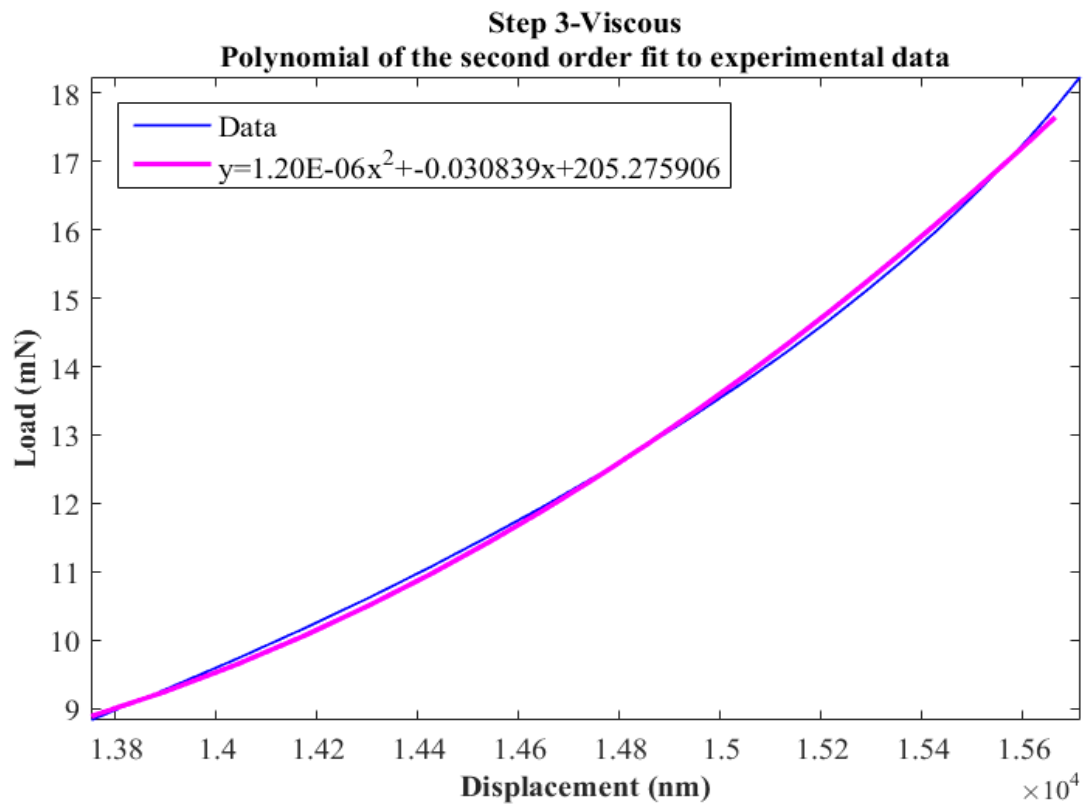
5.2.1 Poly4 to eliminated initial nose out data



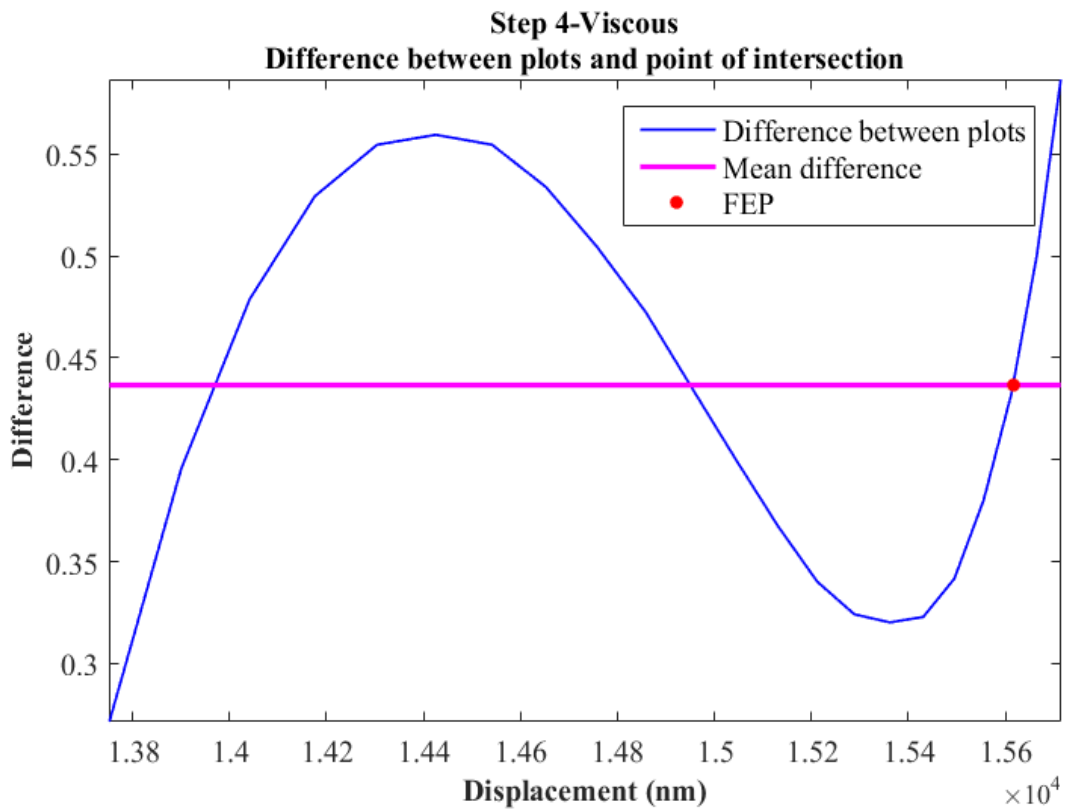
5.2.2 Determining the minimum of the difference between fit and experimental at the highest load



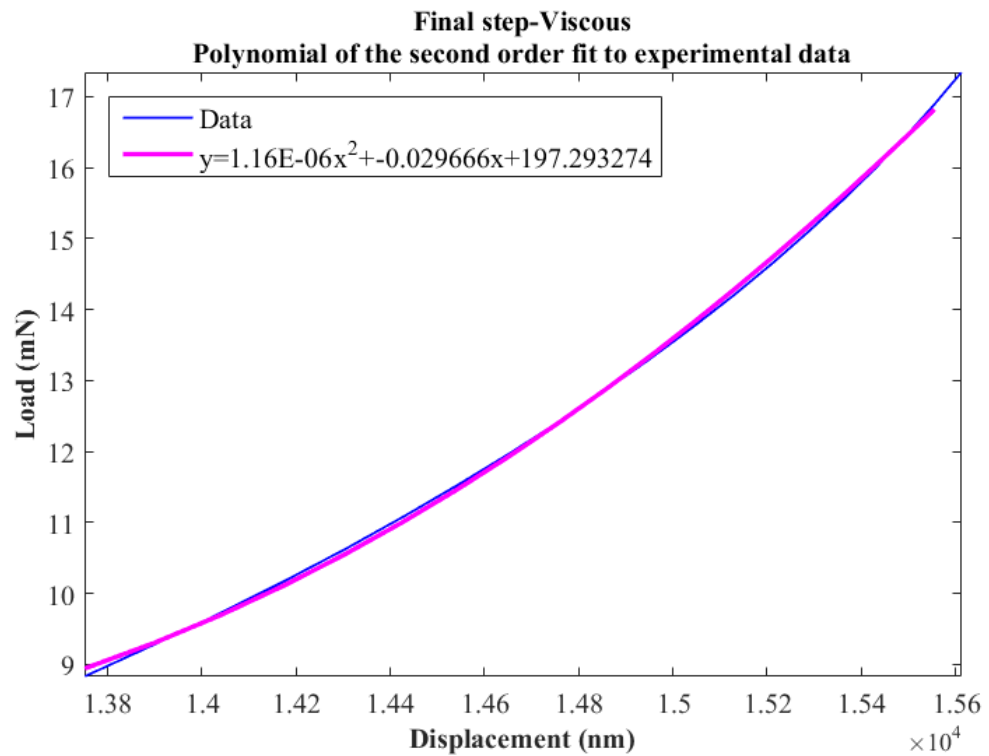
5.2.3 Poly2 to extracted data



5.2.4 Determining the minimum of the difference between fit and experimental at the highest load

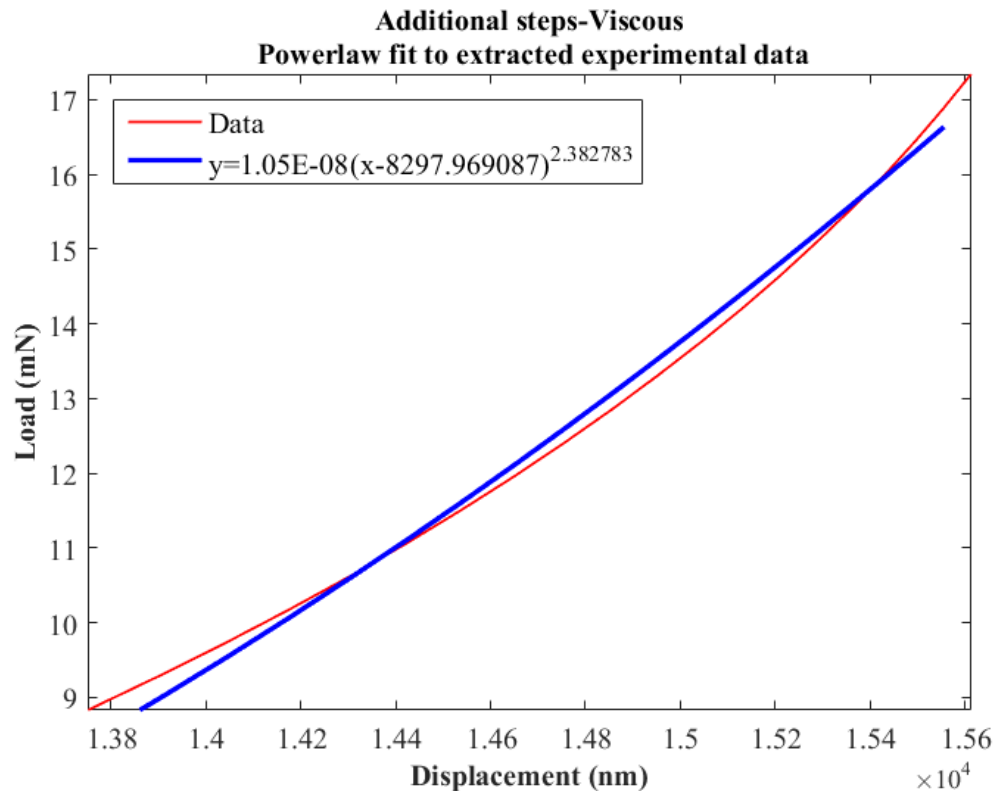


5.2.5 Final poly2



5.2.6 Power law fit

The power law fit is not possible on a positive gradient, thus is not performed and the ϵ value at a default of 0.75 is used. Even if it is performed using the data after the “nose out” the fit are not good as shown in the figure below.

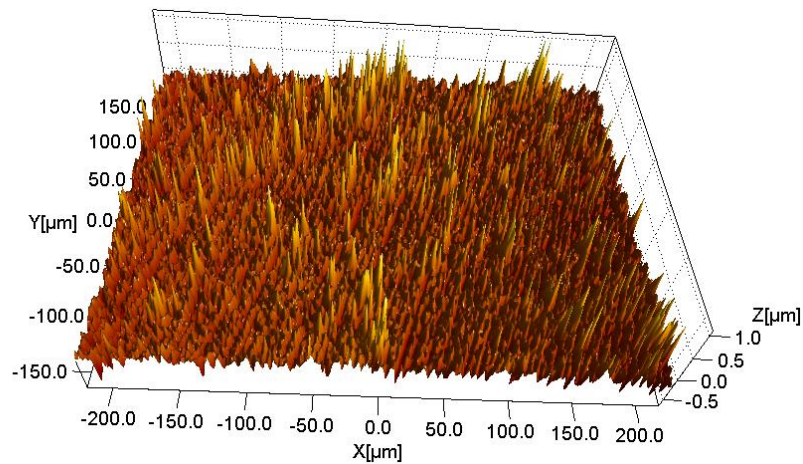


Appendix 6.

6.1 WLI results for fourteen tested materials

6.1.1 WLI results for Aluminium a) 3D surface profile, and b) corresponding table of surface parameter

a)

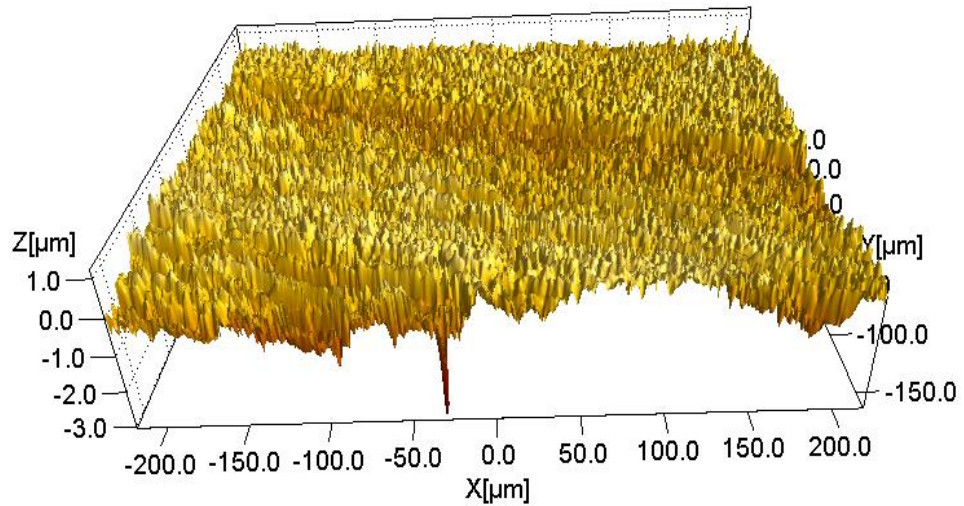


b)

Parameters	Values	Parameters	Values
Sa	0.0899 μm	Svi	0.115
Sq	0.126 μm	Spk	0.26 μm
Ssk	0.931	Sk	0.251 μm
Sku	7.88	Svk	0.132 μm
Sy	1.77 μm	Std	28 deg
Sz	1.66 μm	Stdi	0.704
Sds	0.0354 1/μm ²	Srw	438 μm
Ssc	0.00169 1/μm	Srwi	0.139
Smin	-0.666 μm	Shw	8.58 μm
Smax	1.1 μm	Sfd	2.84
Smean	2.01E-08 μm	Sc120	3.5 μm
Sti	0.566	Str20	0.252
Sdq	94.8 1/μm	Sc137	2.33 μm
Sdr	0.447 %	Str37	0.168
S2A	1.41E+05 μm ²	Sdc0_5	0.909 μm
S3A	1.42E+05 μm ²	Sdc5_10	0.0637 μm
Sbi	0.665	Sdc10_50	0.131 μm
Sci	1.47	Sdc50_95	0.188 μm

6.1.2 WLI results for Copper a) 3D surface profile, and b) corresponding table of surface parameter

a)

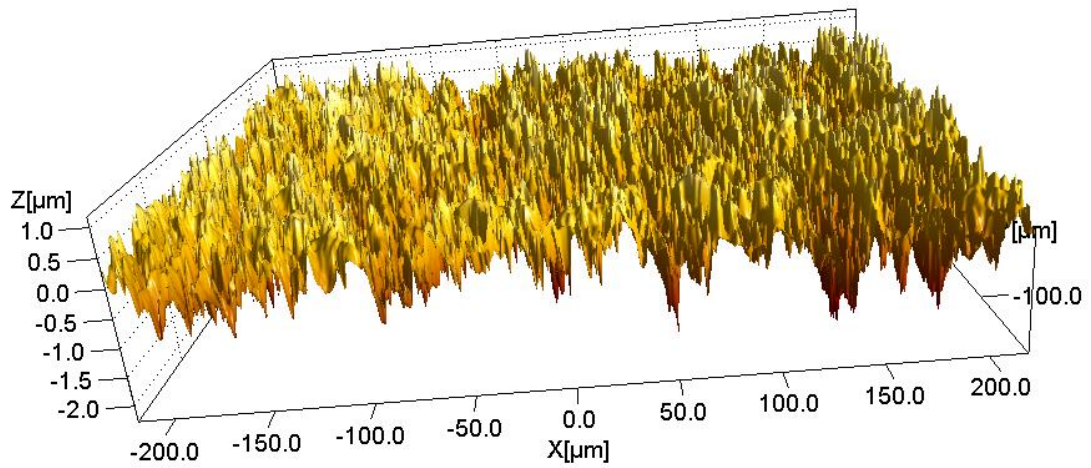


b)

Parameters	Values	Parameters	Values
Sa	0.284 μm	Svi	0.148
Sq	0.35 μm	Spk	0.229 μm
Ssk	-0.676	Sk	0.752 μm
Sku	3.21	Svk	0.494 μm
Sy	4.27 μm	Std	67.5 deg
Sz	3.55 μm	Stdi	0.518
Sds	0.0563 1/μm ²	Srw	438 μm
Ssc	0.00337 1/μm	Srwi	0.102
Smin	-3.04 μm	Shw	8.58 μm
Smax	1.22 μm	Sfd	2.74
Smean	6.35E-08 μm	Sc120	36 μm
Sti	0.374	Str20	0.204
Sdq	191 1/μm	Sc137	17.3 μm
Sdr	1.78 %	Str37	0.0981
S2A	1.41E+05 μm ²	Sdc0_5	0.752 μm
S3A	1.44E+05 μm ²	Sdc5_10	0.0855 μm
Sbi	0.743	Sdc10_50	0.325 μm
Sci	1.24	Sdc50_95	0.718 μm

6.1.3 WLI results for Titanium a) 3D surface profile, and b) corresponding table of surface parameter

a)

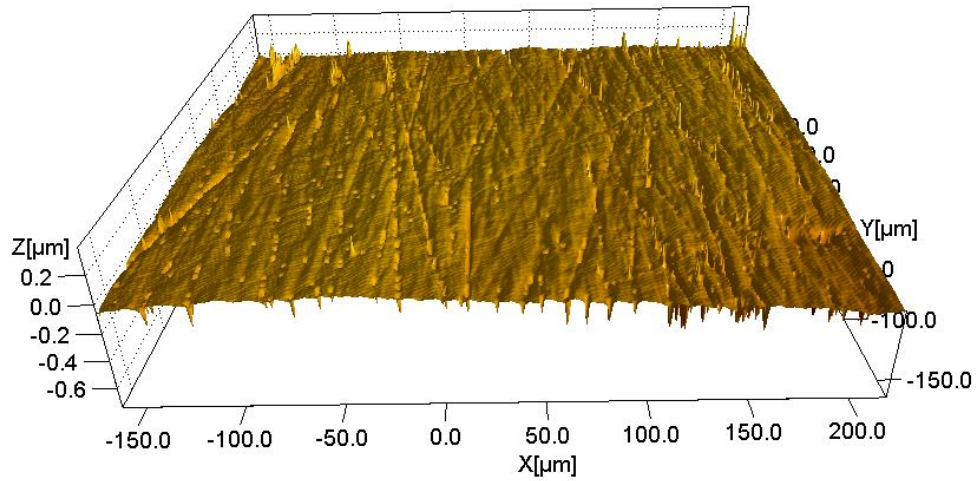


b)

Parameters	Values	Parameters	Values
Sa	0.289 μm	Svi	0.136
Sq	0.361 μm	Spk	0.254 μm
Ssk	-0.476	Sk	0.939 μm
Sku	3.29	Svk	0.425 μm
Sy	3.45 μm	Std	0 deg
Sz	2.95 μm	Stdi	0.632
Sds	0.0383 1/μm ²	Srw	249 μm
Ssc	0.00184 1/μm	Srwi	0.153
Smin	-2.28 μm	Shw	8.93 μm
Smax	1.17 μm	Sfd	2.76
Smean	-1.33E-08 μm	Sc120	8.93 μm
Sti	0.334	Str20	0.256
Sdq	211 1/μm	Sc137	5.24 μm
Sdr	2.18 %	Str37	0.151
S2A	1.41E+05 μm ²	Sdc0_5	0.642 μm
S3A	1.44E+05 μm ²	Sdc5_10	0.0898 μm
Sbi	0.685	Sdc10_50	0.414 μm
Sci	1.36	Sdc50_95	0.649 μm

6.1.4 WLI results for Brass a) 3D surface profile, and b) corresponding table of surface parameter

a)

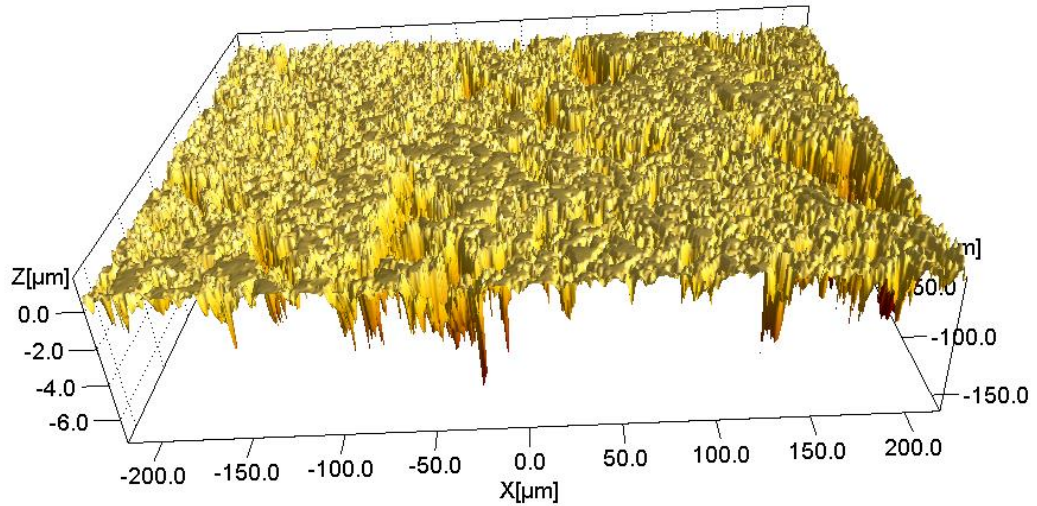


b)

Parameters	Values	Parameters	Values
Sa	0.0319 μm	Svi	0.203
Sq	0.0477 μm	Spk	0.0483 μm
Ssk	-2.8	Sk	0.0808 μm
Sku	18.5	Svk	0.0961 μm
Sy	1.13 μm	Std	176 deg
Sz	0.787 μm	Stdi	0.472
Sds	0.0898 $1/\mu\text{m}^2$	Srw	438 μm
Ssc	0.000417 $1/\mu\text{m}$	Srwi	0.0776
Smin	-0.751 μm	Shw	7.29 μm
Smax	0.382 μm	Sfd	2.64
Smean	1.18E-07 μm	Scl20	76.7 μm
Sti	0.269	Str20	0.491
Sdq	36.2 $1/\mu\text{m}$	Scl37	39 μm
Sdr	0.0649 %	Str37	0.249
S2A	1.41E+05 μm^2	Sdc0_5	0.334 μm
S3A	1.42E+05 μm^2	Sdc5_10	0.0068 μm
Sbi	0.994	Sdc10_50	0.034 μm
Sci	0.87	Sdc50_95	0.0863 μm

6.1.5 WLI results for Stainless steel a) 3D surface profile, and b) corresponding table of surface parameter

a)

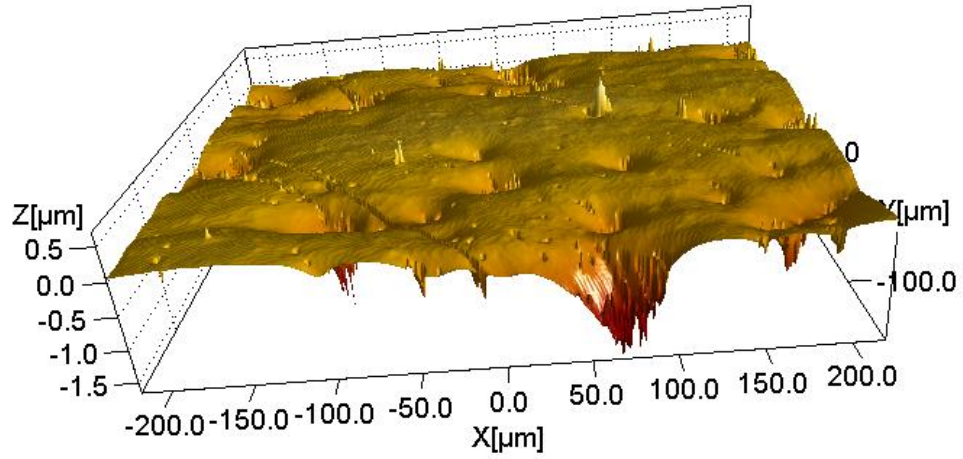


b)

Parameters	Values	Parameters	Values
Sa	0.612 μm	Svi	0.267
Sq	0.898 μm	Spk	0.291 μm
Ssk	-2.5	Sk	0.472 μm
Sku	10.2	Svk	2.05 μm
Sy	9.12 μm	Std	0 deg
Sz	8.25 μm	Stdi	0.838
Sds	0.0524 1/μm ²	Srw	233 μm
Ssc	0.00816 1/μm	Srwi	0.147
Smin	-7.39 μm	Shw	9.73 μm
Smax	1.73 μm	Sfd	2.75
Smean	-1.30E-08 μm	Sc120	17.5 μm
Sti	0.742	Str20	0.326
Sdq	453 1/μm	Sc137	11.4 μm
Sdr	8.92 %	Str37	0.212
S2A	1.37E+05 μm ²	Sdc0_5	1.11 μm
S3A	1.49E+05 μm ²	Sdc5_10	0.0548 μm
Sbi	1.47	Sdc10_50	0.201 μm
Sci	0.439	Sdc50_95	2.36 μm

6.1.6 WLI results for Mild steel a) 3D surface profile, and b) corresponding table of surface parameter

a)

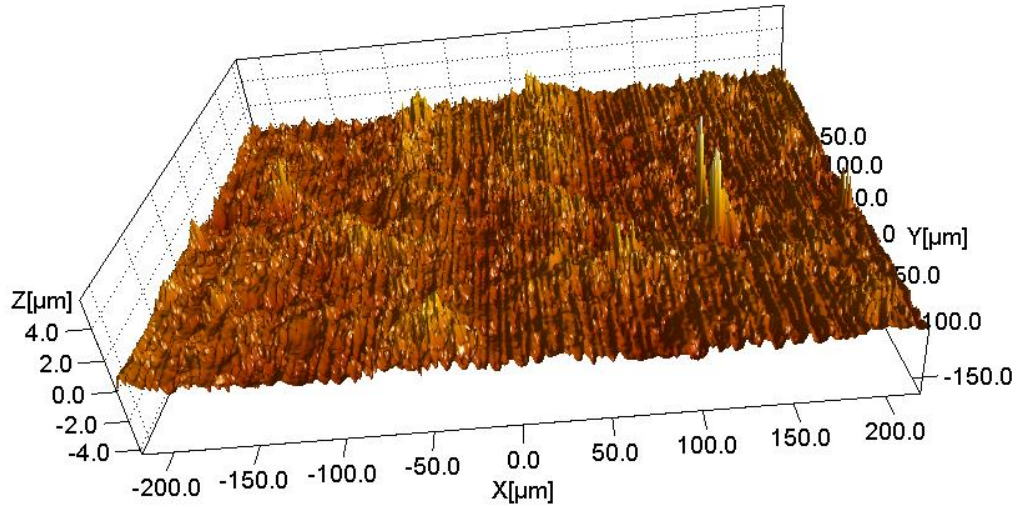


b)

Parameters	Values	Parameters	Values
Sa	0.11 μm	Svi	0.202
Sq	0.159 μm	Spk	0.0762 μm
Ssk	-2.55	Sk	0.219 μm
Sku	13.9	Svk	0.297 μm
Sy	2.35 μm	Std	89.6 deg
Sz	1.94 μm	Stdi	0.519
Sds	0.03 1/μm ²	Srw	438 μm
Ssc	0.00125 1/μm	Srwi	0.0784
Smin	-1.66 μm	Shw	12.9 μm
Smax	0.696 μm	Sfd	2.84
Smean	-1.79E-08 μm	Sc120	46.8 μm
Sti	0.724	Str20	0.674
Sdq	38.8 1/μm	Sc137	29.2 μm
Sdr	0.0743 %	Str37	0.421
S2A	1.41E+05 μm ²	Sdc0_5	0.538 μm
S3A	1.42E+05 μm ²	Sdc5_10	0.0236 μm
Sbi	1.01	Sdc10_50	0.0944 μm
Sci	0.821	Sdc50_95	0.33 μm

6.1.7 WLI results for Neoprene a) 3D surface profile, and b) corresponding table of surface parameter

a)

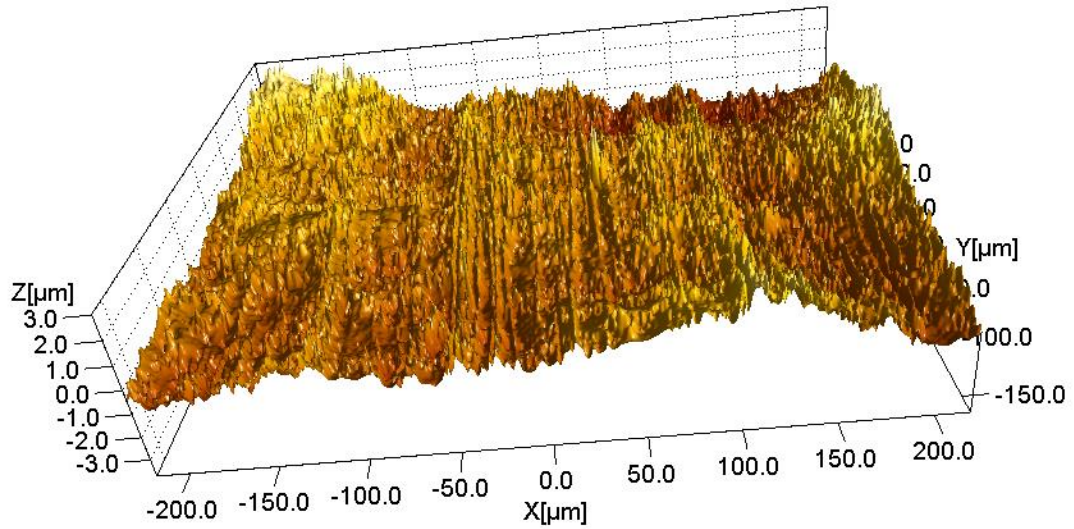


b)

Parameters	Values	Parameters	Values
Sa	0.333 μm	Svi	0.1
Sq	0.442 μm	Spk	0.816 μm
Ssk	0.881	Sk	0.969 μm
Sku	8.21	Svk	0.405 μm
Sy	10.1 μm	Std	1.22 deg
Sz	7.52 μm	Stdi	0.614
Sds	0.0393 1/μm ²	Srw	438 μm
Ssc	0.0119 1/μm	Srwi	0.118
Smin	-4.34 μm	Shw	9.51 μm
Smax	5.74 μm	Sfd	2.77
Smean	4.31E-08 μm	Scl20	28.1 μm
Sti	0.533	Str20	0.242
Sdq	224 1/μm	Scl37	16.2 μm
Sdr	2.34 %	Str37	0.14
S2A	1.41E+05 μm ²	Sdc0_5	4.97 μm
S3A	1.45E+05 μm ²	Sdc5_10	0.243 μm
Sbi	0.573	Sdc10_50	0.586 μm
Sci	1.74	Sdc50_95	0.566 μm

6.1.8 WLI results for Nitrile a) 3D surface profile, and b) corresponding table of surface parameter

a)

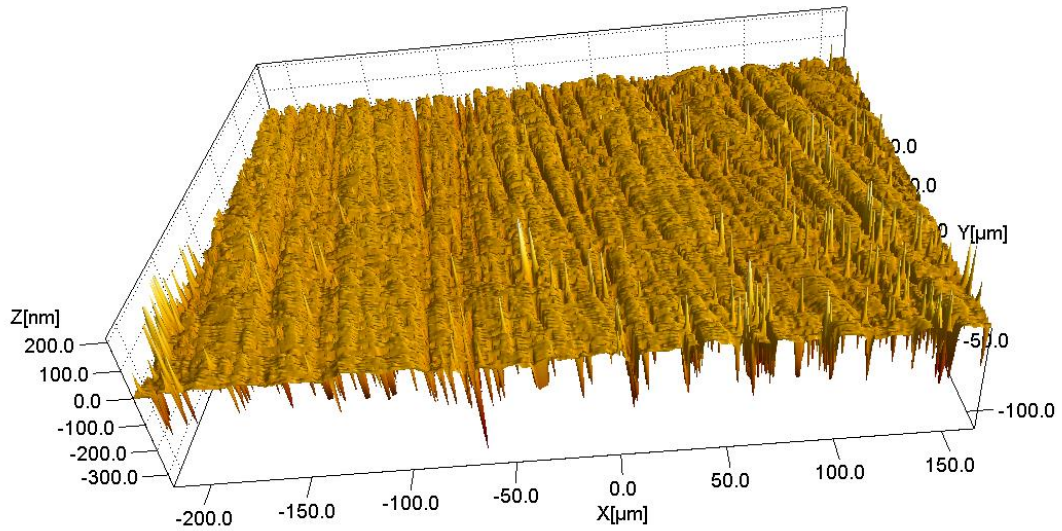


b)

Parameters	Values	Parameters	Values
Sa	0.497 μm	Svi	0.103
Sq	0.639 μm	Spk	0.943 μm
Ssk	0.41	Sk	1.55 μm
Sku	3.77	Svk	0.609 μm
Sy	6.76 μm	Std	0 deg
Sz	5.84 μm	Stdi	0.544
Sds	0.0422 1/μm ²	Srw	438 μm
Ssc	0.0014 1/μm	Srwi	0.0773
Smin	-3.74 μm	Shw	10.7 μm
Smax	3.02 μm	Sfd	2.8
Smean	-5.48E-08 μm	Sc120	49.6 μm
Sti	0.539	Str20	0.687
Sdq	197 1/μm	Sc137	34.9 μm
Sdr	1.89 %	Str37	0.483
S2A	1.41E+05 μm ²	Sdc0_5	1.91 μm
S3A	1.44E+05 μm ²	Sdc5_10	0.325 μm
Sbi	0.574	Sdc10_50	0.84 μm
Sci	1.7	Sdc50_95	0.894 μm

6.1.9 WLI results for SiO₂ a) 3D surface profile, and b) corresponding table of surface parameter

a)

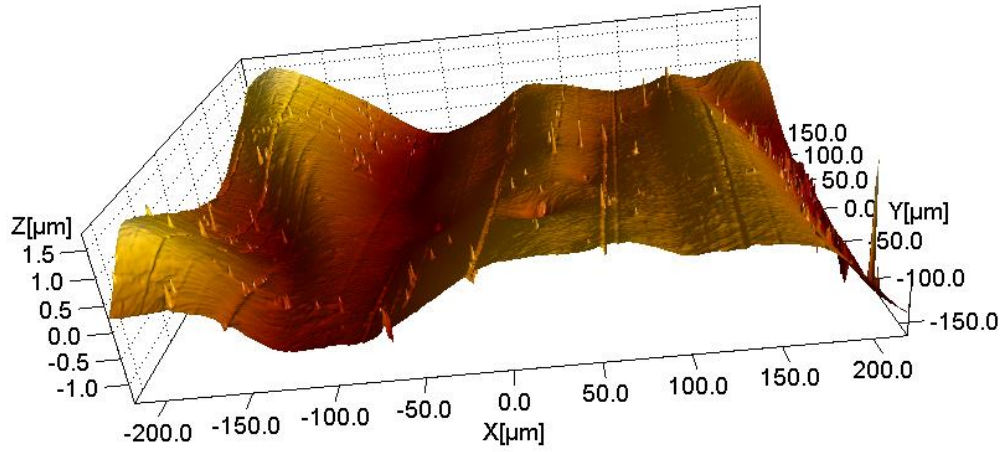


b)

Parameters	Values	Parameters	Values
Sa	0.0281 μm	Svi	0.269
Sq	0.0431 μm	Spk	0.0355 μm
Ssk	-2.29	Sk	0.038 μm
Sku	10.4	Svk	0.108 μm
Sy	0.595 μm	Std	8.3 deg
Sz	0.578 μm	Stdi	0.59
Sds	0.082 1/μm ²	Srw	438 μm
Ssc	0.000854 1/μm	Srwi	0.199
Smin	-0.351 μm	Shw	5.76 μm
Smax	0.243 μm	Sfd	2.52
Smean	-5.97E-08 μm	Sc120	1.97 μm
Sti	0.953	Str20	0.0595
Sdq	54.3 1/μm	Sc137	1.17 μm
Sdr	0.147 %	Str37	0.0352
S2A	1.41E+05 μm ²	Sdc0_5	0.211 μm
S3A	1.42E+05 μm ²	Sdc5_10	0.0036 μm
Sbi	1.34	Sdc10_50	0.0167 μm
Sci	0.523	Sdc50_95	0.106 μm

6.1.10 WLI results for Acrylic a) 3D surface profile, and b) corresponding table of surface parameter

a)

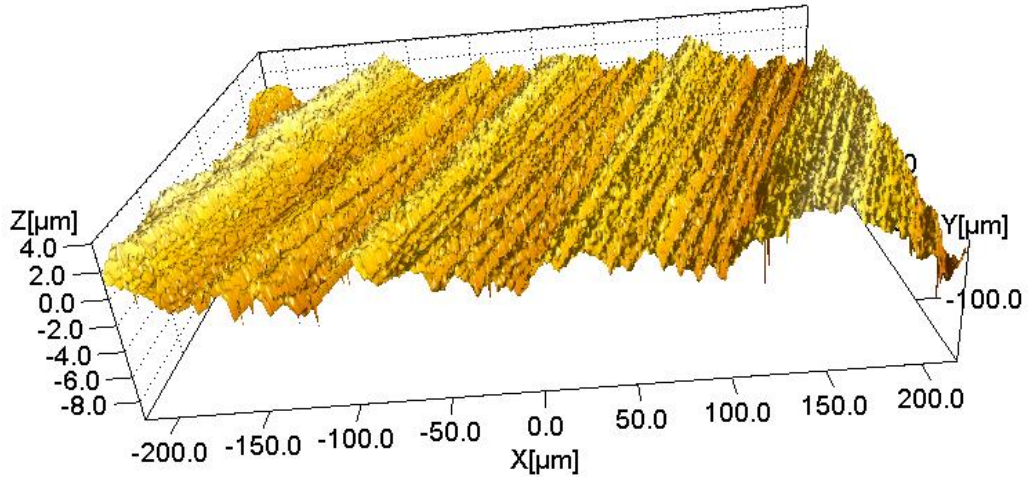


b)

Parameters	Values	Parameters	Values
Sa	0.377 μm	Svi	0.0881
Sq	0.46 μm	Spk	0.595 μm
Ssk	-0.0275	Sk	1.15 μm
Sku	2.75	Svk	0.331 μm
Sy	3.16 μm	Std	0 deg
Sz	2.59 μm	Stdi	0.221
Sds	0.013 $1/\mu\text{m}^2$	Srw	438 μm
Ssc	0.000941 $1/\mu\text{m}$	Srwi	0.0425
Smin	-1.37 μm	Shw	18.2 μm
Smax	1.78 μm	Sfd	2.83
Smean	1.81E-07 μm	Sc120	43.7 μm
Sti	0.442	Str20	0.2
Sdq	32 $1/\mu\text{m}$	Sc137	33.7 μm
Sdr	0.0495 %	Str37	0.154
S2A	1.41E+05 μm^2	Sdc0_5	1.1 μm
S3A	1.42E+05 μm^2	Sdc5_10	0.171 μm
Sbi	0.673	Sdc10_50	0.475 μm
Sci	1.44	Sdc50_95	0.778 μm

6.1.11 WLI results for LD Polyethylene a) 3D surface profile, and b) corresponding table of surface parameter

a)

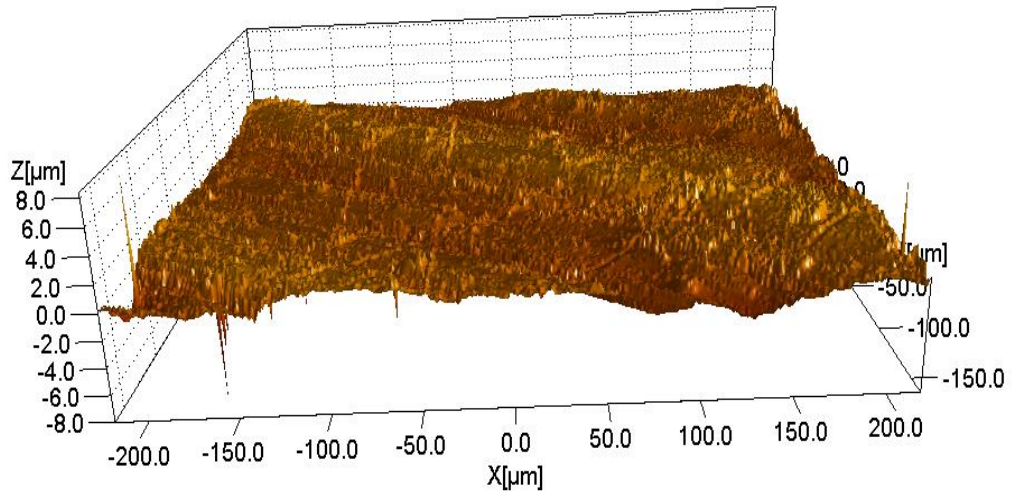


b)

Parameters	Values	Parameters	Values
Sa	0.925 μm	Svi	0.097
Sq	1.13 μm	Spk	1.25 μm
Ssk	0.267	Sk	2.95 μm
Sku	2.71	Svk	0.849 μm
Sy	13.6 μm	Std	164 deg
Sz	11.6 μm	Stdi	0.441
Sds	0.0608 1/μm ²	Srw	438 μm
Ssc	0.00565 1/μm	Srwi	0.094
Smin	-9.47 μm	Shw	9.12 μm
Smax	4.11 μm	Sfd	2.67
Smean	-7.18E-08 μm	Sc120	21.1 μm
Sti	0.335	Str20	0.0969
Sdq	369 1/μm	Sc137	15 μm
Sdr	6.06 %	Str37	0.0689
S2A	1.41E+05 μm ²	Sdc0_5	2.07 μm
S3A	1.50E+05 μm ²	Sdc5_10	0.436 μm
Sbi	0.555	Sdc10_50	1.74 μm
Sci	1.75	Sdc50_95	1.58 μm

6.1.12 WLI results for HD Polyethylene a) 3D surface profile, and b) corresponding table of surface parameter

a)

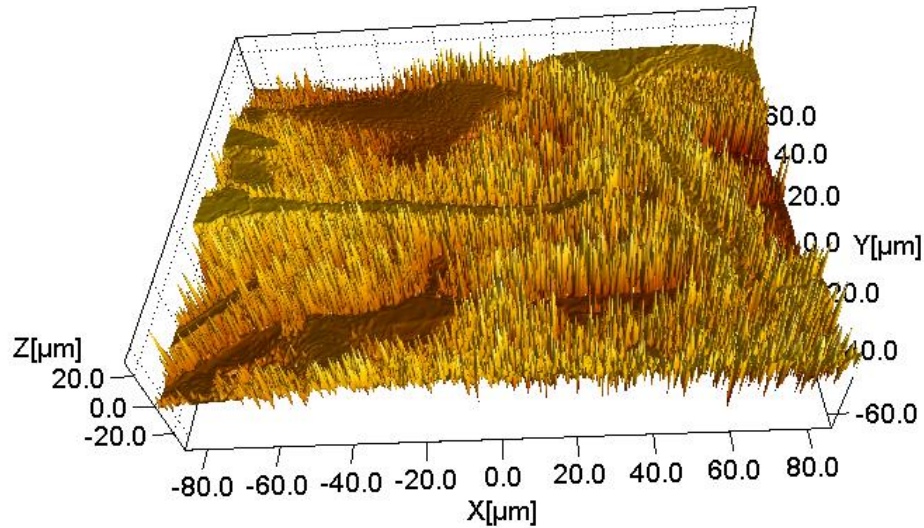


b)

Parameters	Values	Parameters	Values
Sa	0.504 μm	Svi	0.118
Sq	0.623 μm	Spk	0.823 μm
Ssk	-0.00266	Sk	1.63 μm
Sku	2.95	Svk	0.646 μm
Sy	16.4 μm	Std	52.2 deg
Sz	9.36 μm	Stdi	0.538
Sds	0.0559 1/μm ²	Srw	438 μm
Ssc	0.00937 1/μm	Srwi	0.0992
Smin	-8.03 μm	Shw	9.31 μm
Smax	8.35 μm	Sfd	2.73
Smean	-6.11E-07 μm	Sc120	40.3 μm
Sti	0.758	Str20	0.145
Sdq	211 1/μm	Sc137	29.1 μm
Sdr	2.09 %	Str37	0.105
S2A	1.41E+05 μm ²	Sdc0_5	7.35 μm
S3A	1.44E+05 μm ²	Sdc5_10	0.164 μm
Sbi	0.627	Sdc10_50	0.886 μm
Sci	1.56	Sdc50_95	0.952 μm

6.1.13 WLI results for Nylon 66 a) 3D surface profile, and b) corresponding table of surface parameter

a)

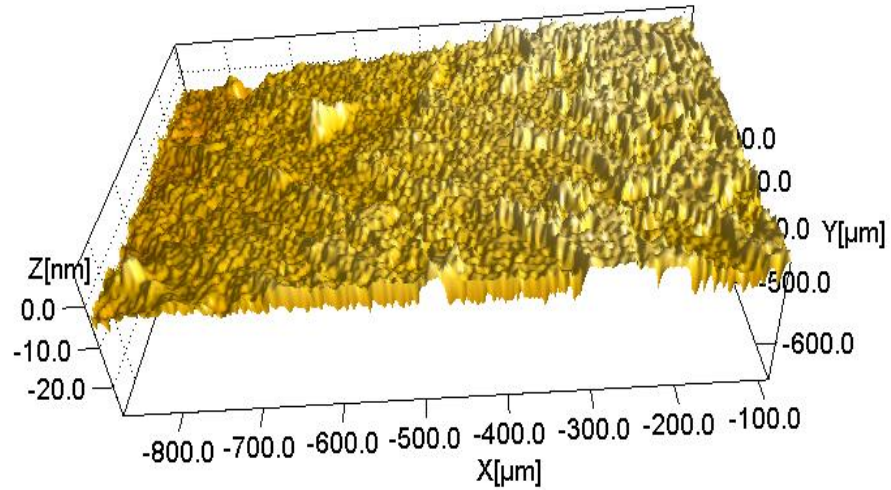


b)

Parameters	Values	Parameters	Values
Sa	6.01 μm	Svi	0.121
Sq	7.51 μm	Spk	5.86 μm
Ssk	-0.308	Sk	18.2 μm
Sku	3.52	Svk	8.87 μm
Sy	61.1 μm	Std	0.826 deg
Sz	59 μm	Stdi	0.801
Sds	0.409 1/μm ²	Srw	109 μm
Ssc	0.727 1/μm	Srwi	0.137
Smin	-32.6 μm	Shw	2.74 μm
Smax	28.5 μm	Sfd	2.69
Smean	-4.72E-07 μm	Sc120	12.4 μm
Sti	0.713	Str20	0.634
Sdq	16584 1/μm	Sc137	7.23 μm
Sdr	8773 %	Str37	0.369
S2A	2.20E+04 μm ²	Sdc0_5	16.9 μm
S3A	1.95E+06 μm ²	Sdc5_10	2.08 μm
Sbi	0.649	Sdc10_50	10 μm
Sci	1.45	Sdc50_95	11.6 μm

6.1.14 WLI results for Polystyrene a) 3D surface profile, and b) corresponding table of surface parameter

a)



b)

Parameters	Values	Parameters	Values
Sa	0.00242 μm	Svi	0.165
Sq	0.0031 μm	Spk	0.0033 μm
Ssk	-0.479	Sk	0.0071 μm
Sku	7.07	Svk	0.0042 μm
Sy	0.0875 μm	Std	0 deg
Sz	0.0474 μm	Stdi	0.687
Sds	0.0045 1/μm ²	Srw	1751 μm
Ssc	1.30E-06 1/μm	Srwi	0.0799
Smin	-0.076 μm	Shw	34.3 μm
Smax	0.0115 μm	Sfd	2.66
Smean	-8.52E-10 μm	Sc120	276 μm
Sti	0.769	Str20	0.301
Sdq	0.339 1/μm	Sc137	209 μm
Sdr	6.01E-06 %	Str37	0.228
S2A	1.62E+06 μm ²	Sdc0_5	0.0065 μm
S3A	1.62E+06 μm ²	Sdc5_10	0.0014 μm
Sbi	0.616	Sdc10_50	0.0035 μm
Sci	1.57	Sdc50_95	0.0056 μm

Appendix 7.

7.1 Metallic materials tensile results

Metaltech Services Limited
 Station Approach
 Team Valley Industrial Estate
 Gateshead, NE11 0ZF
 T: +44 (0) 191 3726942
 E: info@msl-ltd.com
 W: www.msl-ltd.com

Date Received: 06.09.2018
 Date Tested: 12.10.2018
 Date Issued: 15.10.2018
 Issue No: 1
 Page: 1 of 3
 Doc No: MSD-47 Rev 2

MSL

TEST CERTIFICATE: MSL 3904

Order Details	
Customer	University of Central Lancashire, School of Engineering, C&T Hub, Room CM235, Computing & Technology Building, Preston, Lancashire, PR1 2HE
Order Number	3351068
Description	Machined Tensile Specimens

Tensile Test to BS EN ISO 6892-1:2016									
Material		Mild Steel							
Specimen ID	Specimen Size (mm)	XS Area (mm ²)	Elastic Modulus (GPa)	R _{eH} (MPa)	R _{eL} (MPa)	R _{p0.2} (MPa)	Tensile Strength (MPa)	% Elongation (GL:80 mm)	% Reduction of Area
1	20.29 x 4.94	100.23	180	256	253	253	330	43	76
2	20.25 x 4.95	100.24	186	234	233	233	317	40	76
3	20.27 x 4.97	100.74	191	226	225	225	328	37	75
4	20.23 x 4.95	100.14	181	238	235	235	329	38.5	75
5	20.26 x 4.96	100.49	186	236	234	234	329	37.5	74

Tensile Test to BS EN ISO 6892-1:2016							
Material		Stainless Steel					
Specimen ID	Specimen Size (mm)	XS Area (mm ²)	Elastic Modulus (GPa)	R _{p0.2} (MPa)	Tensile Strength (MPa)	% Elongation (GL:80 mm)	% Reduction of Area
6	20.32 x 4.97	100.99	174	307	598	50.5	77
7	20.35 x 4.98	101.34	166	308	598	50.5	82
8	20.34 x 4.98	101.29	168	310	600	51	81
9	20.24 x 4.96	100.39	170	307	601	51	81
10	20.33 x 4.98	101.24	173	309	599	50.5	83

For MSL:

Prepared by:



Reviewed by:



Name: Joseph Smith
 Title: Testing Engineer

Name: Lovlesh Beharry
 Title: Engineering Manager



7858

The above results relate only to the properties of the items tested. Any offsets are retained for a maximum of 60 days.
 Metaltech Services Limited. Registered in England and Wales No.01803148. VAT Registration No.569339004.

Metaltech Services Limited
 Station Approach
 Team Valley Industrial Estate
 Gateshead, NE11 0ZF
 T: +44 (0) 191 3726942
 E: info@msl-ltd.com
 W: www.msl-ltd.com

Date Received: 06.09.2018
 Date Tested: 12.10.2018
 Date Issued: 15.10.2018
 Issue No: 1
 Page: 2 of 3
 Doc No: MSD-47 Rev 2

MSL

TEST CERTIFICATE: MSL 3904

Tensile Test to BS EN ISO 6892-1:2016							
Material	Aluminium Alloy						
Specimen ID	Specimen Size (mm)	XS Area (mm ²)	Elastic Modulus (GPa)	R _{p0.2} (MPa)	Tensile Strength (MPa)	% Elongation (GL:80 mm)	% Reduction of Area
11	20.27 x 4.00	81.08	67.5	278	338	16.5	29
12	20.29 x 4.00	81.16	67.5	278	338	16.5	27
13	20.27 x 4.00	81.08	67.6	279	339	17.5	30
14	20.28 x 3.99	80.92	67.7	280	340	16.5	31
15	20.32 x 4.00	81.28	66.0	279	339	17.5	32

Tensile Test to BS EN ISO 6892-1:2016							
Material	Copper						
Specimen ID	Specimen Size (mm)	XS Area (mm ²)	Elastic Modulus (GPa)	R _{p0.2} (MPa)	Tensile Strength (MPa)	% Elongation (GL:80 mm)	% Reduction of Area
16	20.26 x 3.02	61.19	111	214	248	43	75
17	20.26 x 3.02	61.19	109	214	247	42.5	76
18	20.22 x 3.02	61.06	112	214	248	41.5	74
19	20.26 x 3.02	61.19	111	214	248	43	76
20	20.29 x 3.02	61.28	113	214	248	44	76

Tensile Test to BS EN ISO 6892-1:2016							
Material	Brass						
Specimen ID	Specimen Size (mm)	XS Area (mm ²)	Elastic Modulus (GPa)	R _{p0.2} (MPa)	Tensile Strength (MPa)	% Elongation (GL:80 mm)	% Reduction of Area
21	20.28 x 3.02	61.25	93.8	245	362	41	52
22	20.24 x 3.03	61.39	95.1	243	363	45.5	54
23	20.26 x 3.03	61.39	91.5	244	363	47	57
24	20.23 x 3.03	61.30	95.1	243	362	43.5	55
25	20.25 x 3.03	61.36	91.1	244	362	46	53

For MSL:

Prepared by:



Name: Joseph Smith
 Title: Testing Engineer

Reviewed by:



Name: Lovlesh Beharry
 Title: Engineering Manager



7858

The above results relate only to the properties of the items tested. Any offcuts are retained for a maximum of 60 days.
 Metaltech Services Limited. Registered in England and Wales No.01803148. VAT Registration No.569339004.

Metaltech Services Limited
 Station Approach
 Team Valley Industrial Estate
 Gateshead, NE11 0ZF
 T: +44 (0) 191 3726942
 E: info@msl-ltd.com
 W: www.msl-ltd.com

Date Received: 06.09.2018
 Date Tested: 12.10.2018
 Date Issued: 15.10.2018
 Issue No: 1
 Page: 3 of 3
 Doc No: MSD-47 Rev 2

MSL

TEST CERTIFICATE: MSL 3904

Tensile Test to BS EN ISO 6892-1:2016							
Material Titanium Alloy							
Specimen ID	Specimen Size (mm)	XS Area (mm ²)	Elastic Modulus (GPa)	R _{p0.2} (MPa)	Tensile Strength (MPa)	% Elongation (GL:80 mm)	% Reduction of Area
26	20.32 x 3.92	79.65	100	314	491	24.5	43
27	18.86 x 3.97	74.87	99.7	318	495	24	43
28	18.86 x 3.94	74.31	103	585	704	21.5	45
29	19.05 x 3.92	74.68	104	581	701	22	44
30	19.86 x 4.00	79.44	97.4	296	466	23	45

*** End of Report ***

For MSL:

Prepared by:



Name: Joseph Smith
 Title: Testing Engineer

Reviewed by:





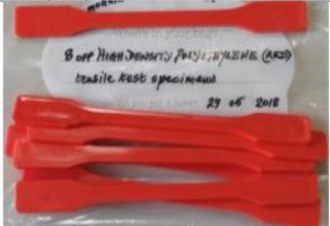

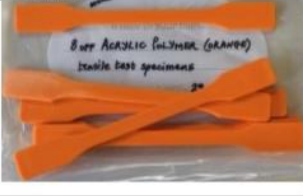
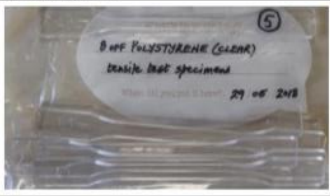


Name: Lovlesh Beharry
 Title: Engineering Manager



7858

The above results relate only to the properties of the items tested. Any offcuts are retained for a maximum of 60 days.
 Metaltech Services Limited. Registered in England and Wales No.01803148. VAT Registration No.569339004.

7.2 Viscous/polymeric materials tensile results

	Materials Technology Ltd. 5 Rushington Court, Rushington Business Park, Chapel Lane, Southampton SO40 9NA Tel: +44 (0) 2380 580240 e-mail: info@mtechltd.co.uk Web: www.mtechltd.co.uk	
Tensile Tests on Plastic & Rubber Samples		
Client: Mr. A. Shah University of Central Lancashire Fylde Rd Preston PR1 2HE	Date: 14 th August 2018	Mat Tech Job No: 15495
Request Details: Perform tensile testing on a range of plastic and rubber dumbbell samples supplied by UCLAN. It was requested that stress-strain data along with the calculation of the Young's Modulus and statistics according to the standards were included. Post testing all samples were marked and returned to UCLAN for their own analysis.		
Sample List: The samples supplied are detailed in the table below:		
Plastic Samples 7 off of each type tested in accordance with BS EN ISO 527-2 (note bags state 8 off, however only 7 were supplied in each case).		
1. Nylon 66 	2. Polyethylene HD 	3. Polyethylene LD 
4. Acrylic 	5. Polystyrene 	
Rubber Samples 10 off of each type tested in accordance with BS EN ISO 37.		
6. Neoprene Rubber 	7. Nitrile Rubber 	

Test Parameters:

Test parameters are summarised in the table below:

	Test standard	Dumbbell Type	Test speed	No of Samples Tested
Plastic samples 1, 4 & 5	BS EN ISO 527-2	Injection moulded dimensions generally in accordance with a type 1A dumbbell, excepting they were 185mm long exceeding the standard type 1A dumbbell length of 170mm.	1mm/minute	7 of each type, with the exception of 2* (see further comments below)
Plastic samples 2 & 3	BS EN ISO 527-2 performed up to 0.5% strain to obtain modulus figures. Testing then completed at 100mm/minute to obtain yield & tensile strength etc.		1mm/minute up to 0.5% strain then 100mm/minute	
Rubber samples 7 & 8	BS EN ISO 37	Die cut Type 1 dumbbells	500mm/minute	10 of each type.

* For sample 2 (HDPE) the samples necked outside the extensometer, and tests had to be performed using crosshead separation rather than using an extensometer. Due to this results were obtained for 5 samples only.

Results:

Results are summarised below, full results are appended to the report:

	Stress @ Peak (MPa)	Strain @ Peak %	Stress @ Break (MPa)	Strain @ Break %	Modulus (MPa)
1. Nylon 66	92.511	3.204	90.682	4.424	6477.279
2. Polyethylene HD	24.348	21.529	6.649	98.921	844.028
3. Polyethylene LD	8.646	86.509	8.646	86.509	111.021
4. Acrylic	49.319	2.198	7.935	122.685	3160.502
5. Polystyrene	34.542	1.086	34.474	1.101	3171.911
6. Neoprene Rubber	3.692	214.639	3.640	216.581	3.167
7. Nitrile Rubber	4.339	222.307	4.296	223.388	4.787



J. Bates (Director)

Test Parameters	Test Machine	Extensometer Type	Range over which Young's Modulus measured
Plastic samples 1, 4 & 5	Testometric M350CT	Epsilon extensometer with a resolution of 0.0001mm. Note for polyethylene samples 2 & 3, final break was performed by cross head measurement following Young's Modulus determination.	Tangent in the strain interval from 0.05 % to 0.25 %
Plastic samples 2 & 3			
Rubber samples 7 & 8		Long travel Testometric extensometer with a resolution of 0.01mm	Secant in the strain interval from 0% to 20 %

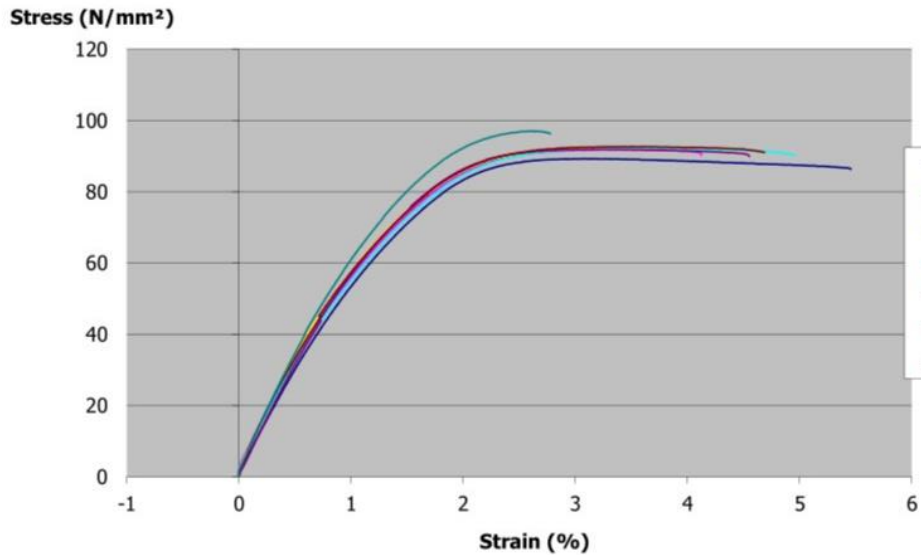
Customer : UCLAN I5495
 Material Type : 1 Nylon 66
 Condition :
 Operator : J Bates

Test Name : 24. ISO 527-2 Rigid Plastics
 Test Type : Tensile
 Test Date : 06/08/2018 15:28
 Test Speed : 1.000 mm/min

Comments :

Test No	Width (mm)	Thickness (mm)	Stress @ Peak (N/mm ²)	Strain @ Peak (%)	Force @ Break (N)	Stress @ Break (N/mm ²)	Elong. @ Break (mm)
1	9.840	3.900	89.327	3.170	3314.000	86.356	1.364
2	9.800	3.900	91.915	3.248	3449.000	90.241	1.031
3	9.780	3.890	92.498	3.326	3450.000	90.684	1.102
4	9.780	3.900	92.156	3.485	3439.000	90.163	1.241
5	9.800	3.900	91.915	3.190	3436.000	89.901	1.138
6	9.770	3.900	92.696	3.402	3471.000	91.095	1.172
7	9.800	3.900	97.070	2.607	3682.000	96.337	0.695
Mean	9.796	3.899	92.511	3.204	3463.000	90.682	1.106
S.D.	0.023	0.004	2.302	0.287	109.465	2.942	0.210

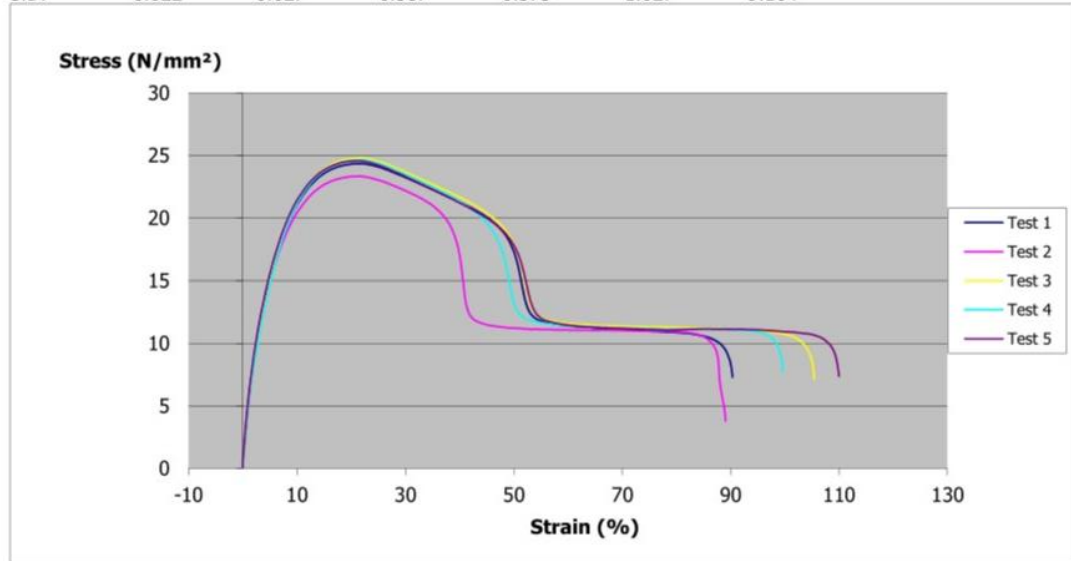
Test No	Strain @ Break (%)	Youngs Modulus (N/mm ²)
1	5.456	5895.286
2	4.122	6279.958
3	4.406	6449.342
4	4.962	6398.131
5	4.552	6473.705
6	4.687	6983.921
7	2.780	6860.610
Mean	4.424	6477.279
S.D.	0.840	362.477



Customer : UCLAN I5495
Material Type : 2 HDPE
Age :
Coating :
Operator : Justin
 Comments :

Test Name : 12.3 General plastics method
Test Type : Tensile
Test Date : 09/08/2018 10:00
Test Speed : 100.000 mm/min
Pretension : 2.000 N

Test No	Width (mm)	Thickness (mm)	Stress @ Peak (N/mm ²)	Strain @ Peak (%)	Stress @ Break (N/mm ²)	Strain @ Break (%)
1	9.770	3.950	24.353	22.095	7.271	90.370
2	9.750	3.900	23.340	21.350	3.771	89.104
3	9.750	3.900	24.805	21.684	7.093	105.484
4	9.750	3.950	24.662	21.398	7.753	99.647
5	9.800	3.900	24.581	21.120	7.357	110.003
Mean	9.764	3.920	24.348	21.529	6.649	98.921
S.D.	0.022	0.027	0.587	0.375	1.627	9.164

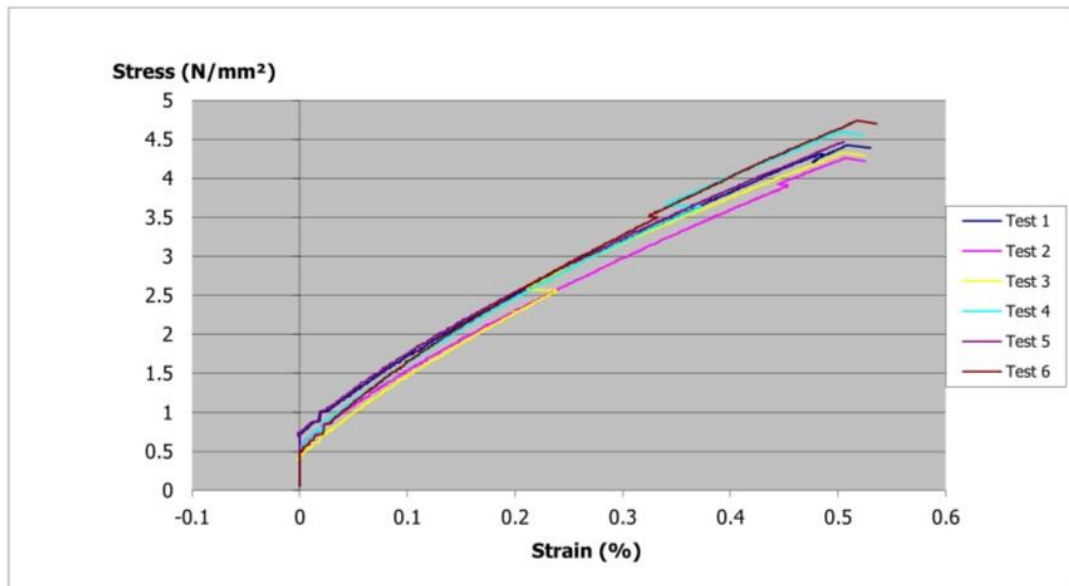


Customer : UCLAN I5495
Material Type : 2 HDPE
Condition : Modulus check only
Operator : J Bates

Test Name : 24. ISO 527-2 Rigid Plastics
Test Type : Tensile
Test Date : 09/08/2018 08:44
Test Speed : 1.000 mm/min

Comments :

Test No	Youngs Modulus (N/mm ²)
1	797.659
2	787.950
3	930.904
4	842.250
5	809.073
6	896.332
Mean	844.028
S.D.	57.971

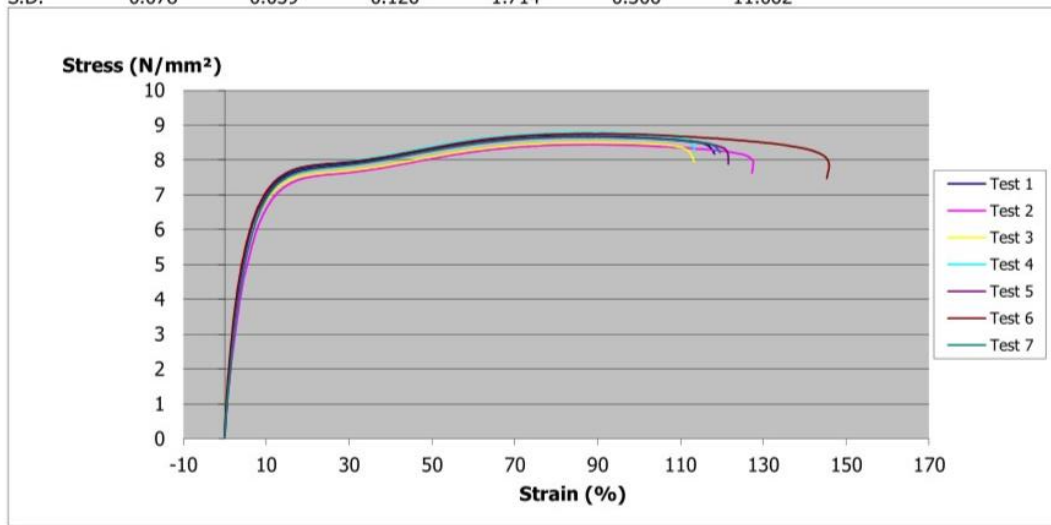


Customer : UCLAN 5495
Material Type : 3 LDPE
Age :
Coating :
Operator : Justin

Test Name : 12. General plastics method
Test Type : Tensile
Test Date : 09/08/2018 09:11
Test Speed : 100.000 mm/min
Pretension : 2.000 N

Comments :

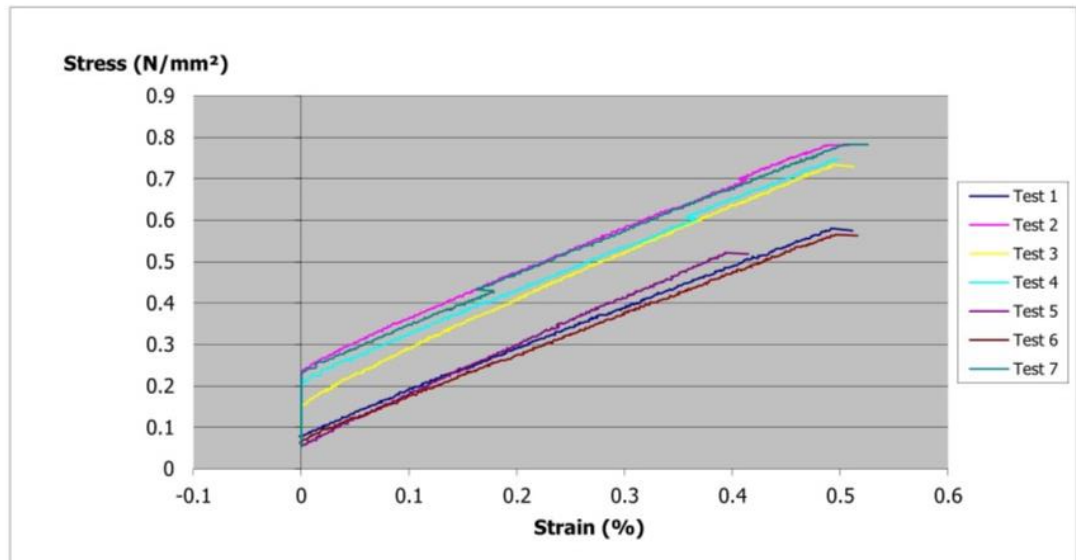
Test No	Width (mm)	Thickness (mm)	Stress @ Peak (N/mm ²)	Strain @ Peak (%)	Stress @ Break (N/mm ²)	Strain @ Break (%)
1	9.700	3.800	8.695	84.880	8.169	118.240
2	9.750	3.900	8.447	86.760	7.619	127.200
3	9.850	3.850	8.504	86.680	7.945	113.320
4	9.680	3.800	8.786	85.800	8.264	113.560
5	9.640	3.800	8.675	84.680	7.881	121.560
6	9.630	3.800	8.758	86.960	7.463	145.320
7	9.650	3.850	8.656	89.800	8.204	119.600
Mean	9.700	3.829	8.646	86.509	7.935	122.685
S.D.	0.078	0.039	0.126	1.714	0.306	11.062



Customer : UCLAN I5495
Material Type : 3 LDPE
Condition : Modulus check only
Operator : J Bates
Comments :

Test Name : 24. ISO 527-2 Rigid Plastics
Test Type : Tensile
Test Date : 09/08/2018 08:22
Test Speed : 1.000 mm/min

Test No	Youngs Modulus (N/mm ²)
1	102.188
2	111.769
3	119.777
4	105.571
5	118.749
6	101.109
7	117.982
Mean	111.021
S.D.	8.076

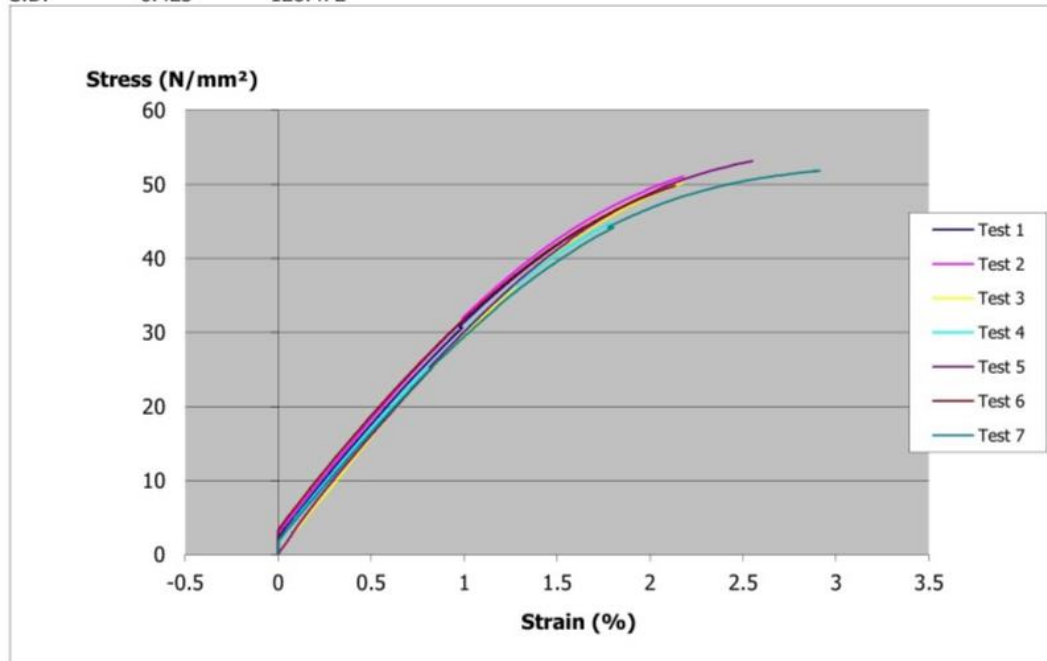


Customer : UCLAN I5495
 Material Type : 4 Acrylic
 Condition :
 Operator : J Bates

Test Name : 24. ISO 527-2 Rigid Plastics
 Test Type : Tensile
 Test Date : 07/08/2018 09:15
 Test Speed : 1.000 mm/min

Test No	Width (mm)	Thickness (mm)	Stress @ Peak (N/mm ²)	Strain @ Peak (%)	Force @ Break (N)	Stress @ Break (N/mm ²)	Elong. @ Break (mm)
1	9.880	3.850	44.193	1.644	1681.000	44.193	0.411
2	9.870	3.860	51.079	2.180	1946.000	51.079	0.545
3	9.870	3.840	50.289	2.179	1906.000	50.289	0.545
4	10.020	3.980	44.835	1.786	1788.000	44.835	0.447
5	9.870	3.980	53.153	2.550	2088.000	53.153	0.638
6	9.880	3.980	49.844	2.135	1960.000	49.844	0.534
7	9.860	3.860	51.840	2.908	1973.000	51.840	0.720
Mean	9.893	3.907	49.319	2.198	1906.000	49.319	0.549
S.D.	0.056	0.068	3.458	0.430	133.340	3.458	0.106

Test No	Strain @ Break (%)	Youngs Modulus (N/mm ²)
1	1.644	3126.084
2	2.180	3137.069
3	2.182	3124.761
4	1.789	3168.788
5	2.551	3418.703
6	2.135	3158.717
7	2.882	2989.390
Mean	2.195	3160.502
S.D.	0.423	128.472

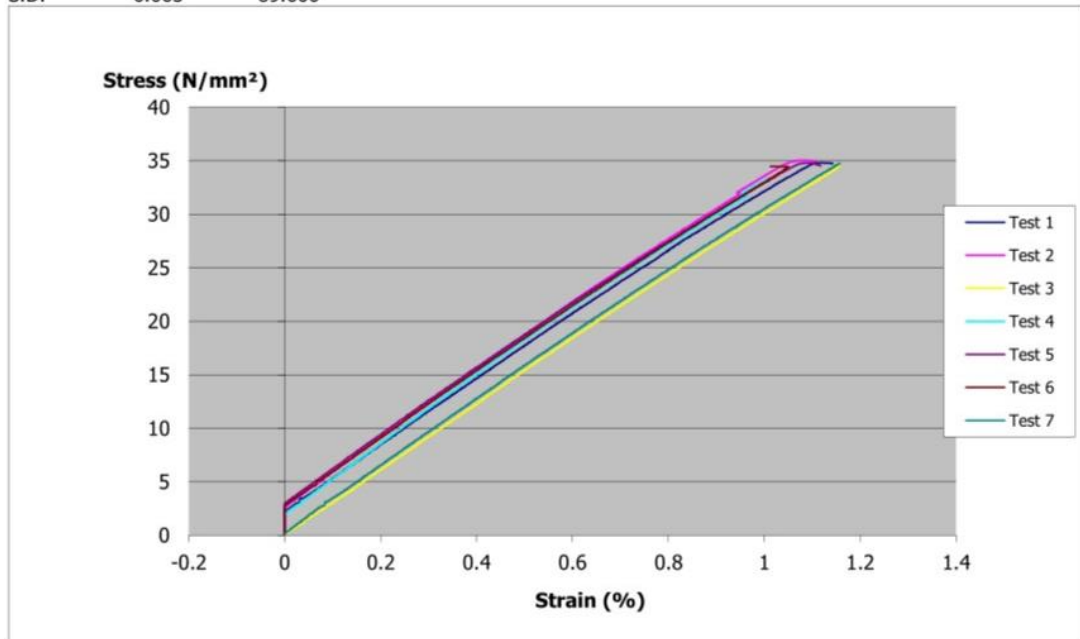


Customer : UCLAN I5495
 Material Type : 5 Polystyrene
 Condition :
 Operator : J Bates
 Comments :

Test Name : 24. ISO 527-2 Rigid Plastics
 Test Type : Tensile
 Test Date : 07/08/2018 08:44
 Test Speed : 1.000 mm/min

Test No	Width (mm)	Thickness (mm)	Stress @ Peak (N/mm ²)	Strain @ Peak (%)	Force @ Break (N)	Stress @ Break (N/mm ²)	Elong. @ Break (mm)
1	9.850	3.900	34.830	1.117	1335.000	34.752	0.286
2	9.860	3.820	35.046	1.072	1315.000	34.913	0.277
3	9.860	3.850	34.562	1.156	1312.000	34.562	0.290
4	9.850	3.850	33.305	1.006	1263.000	33.305	0.252
5	9.850	3.850	34.808	1.080	1310.000	34.544	0.280
6	9.860	3.820	34.488	1.012	1299.000	34.488	0.253
7	9.860	3.820	34.754	1.157	1309.000	34.754	0.290
Mean	9.856	3.844	34.542	1.086	1306.143	34.474	0.275
S.D.	0.005	0.029	0.575	0.062	21.912	0.537	0.016

Test No	Strain @ Break (%)	Youngs Modulus (N/mm ²)
1	1.143	3130.288
2	1.109	3215.335
3	1.158	3023.830
4	1.008	3301.470
5	1.118	3209.177
6	1.012	3207.668
7	1.158	3115.608
Mean	1.101	3171.911
S.D.	0.065	89.600



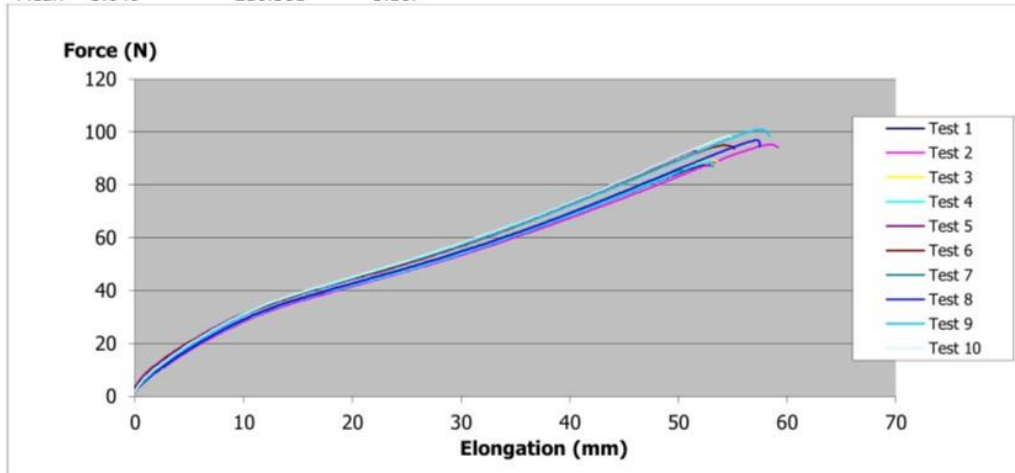
Customer : UCLAN
Job : I5495
Material : 6 Neoprene 1
Age :
Operator : J. Bates

Test Name : 30. Rubber Method to ISO 37
Test Type : Tensile
Test Date : 07/08/2018 15:25
Test Speed : 500.000 mm/min
Pretension : 2.000 N

Comments :

Test No	Width (mm)	Thickness (mm)	Force @ Peak (N)	Stress @ Peak (N/mm ²)	Strain @ Peak (%)	Stress @ Yield (N/mm ²)	Strain @ Yield (%)
1	6.150	4.120	87.500	3.453	206.994	3.453	206.994
2	6.180	4.100	95.300	3.761	228.527	3.761	228.527
3	6.100	4.110	89.500	3.570	209.097	3.570	209.097
4	6.080	4.080	89.200	3.596	208.950	3.596	208.950
5	6.120	4.100	92.900	3.702	205.960	3.702	205.960
6	6.100	4.110	95.200	3.797	216.680	3.797	216.680
7	6.060	4.090	85.800	3.462	198.664	3.462	198.664
8	6.030	4.130	96.900	3.891	225.490	3.891	225.490
9	6.290	4.140	101.000	3.879	227.039	3.879	227.039
10	6.270	4.130	98.700	3.812	218.987	3.812	218.987
Mean	6.138	4.111	93.200	3.692	214.639	3.692	214.639
S.D.	0.086	0.019	5.058	0.163	10.217	0.163	10.217

Test No	Stress @ Break (N/mm ²)	Strain @ Break (%)	Youngs Modulus (N/mm ²)
1	3.438	208.841	3.037
2	3.714	231.301	2.989
3	3.546	211.542	3.173
4	3.499	209.622	3.113
5	3.678	206.800	3.263
6	3.737	220.760	3.338
7	3.433	199.415	3.175
8	3.791	227.230	3.126
9	3.775	230.950	3.223
10	3.792	219.347	3.236
Mean	3.640	216.581	3.167

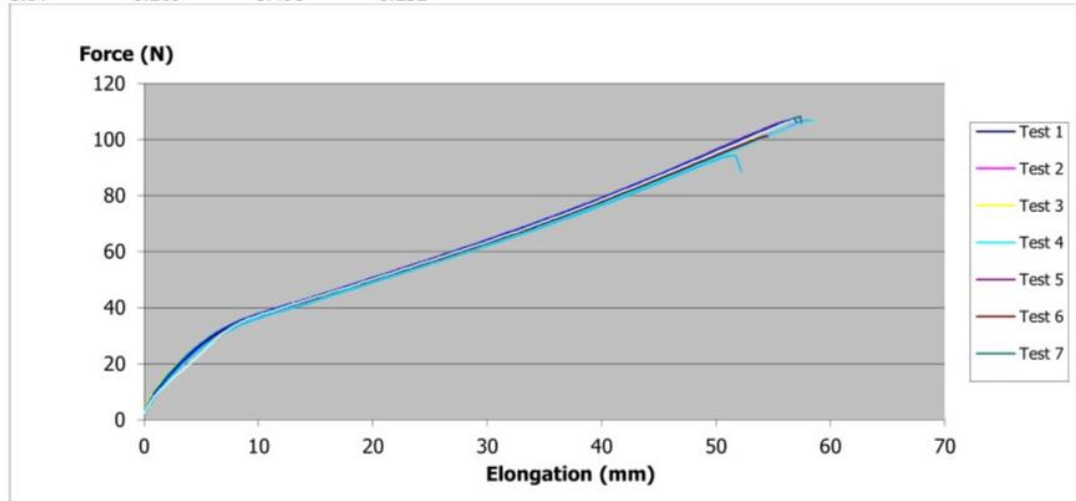


Customer : UCLAN
 Job : I5495
 Material : 7 Nitrile Rubber
 Age :
 Operator : J. Bates
 Comments :

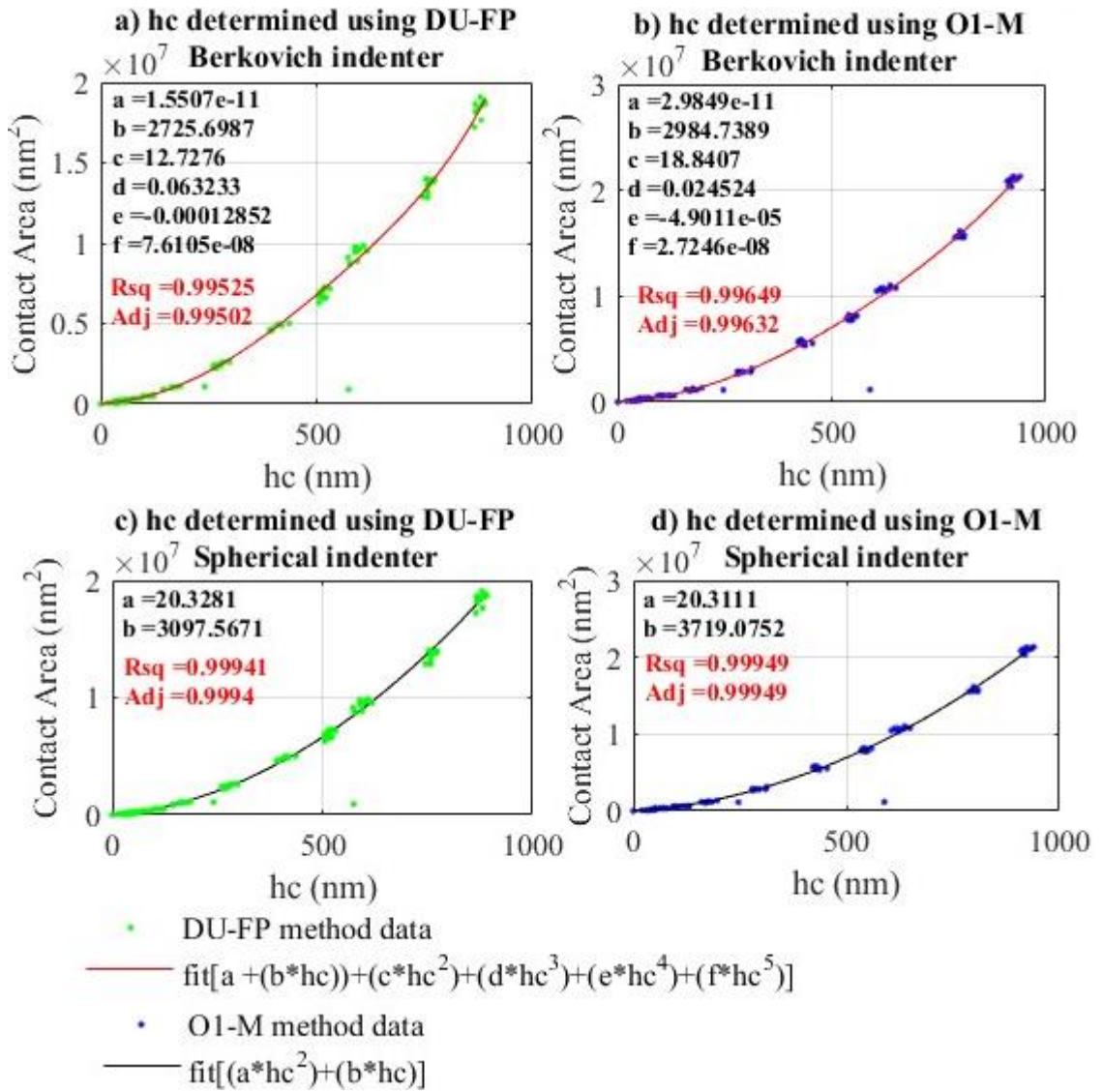
Test Name : 30. Rubber Method to ISO 37
 Test Type : Tensile
 Test Date : 07/08/2018 16:08
 Test Speed : 500.000 mm/min
 Pretension : 2.000 N

Test No	Width (mm)	Thickness (mm)	Force @ Peak (N)	Stress @ Peak (N/mm ²)	Strain @ Peak (%)	Stress @ Yield (N/mm ²)	Strain @ Yield (%)
1	6.050	3.990	106.300	4.404	224.267	4.404	224.267
2	5.900	3.990	106.900	4.541	230.779	4.541	230.779
3	6.080	4.050	100.400	4.077	213.080	4.077	213.080
4	5.960	4.000	106.800	4.480	230.997	4.480	230.997
5	5.970	3.980	106.400	4.478	222.548	4.478	222.548
6	5.960	4.000	101.200	4.245	215.537	4.245	215.537
7	6.030	4.000	108.200	4.486	229.520	4.486	229.520
8	6.050	3.980	106.900	4.440	226.338	4.440	226.338
9	6.100	4.000	94.300	3.865	203.391	3.865	203.391
10	6.100	4.000	106.800	4.377	226.608	4.377	226.608
Mean	6.020	3.999	104.420	4.339	222.307	4.339	222.307

Test No	Stress @ Break (N/mm ²)	Strain @ Break (%)	Youngs Modulus (N/mm ²)
1	4.395	224.905	4.837
2	4.537	231.732	4.869
3	4.061	214.320	4.628
4	4.459	232.185	4.918
5	4.461	223.064	5.055
6	4.241	216.132	4.887
7	4.395	229.840	4.886
8	4.415	228.138	4.905
9	3.631	206.434	4.746
10	4.361	227.127	4.144
Mean	4.296	223.388	4.787
S.D.	0.269	8.498	0.252

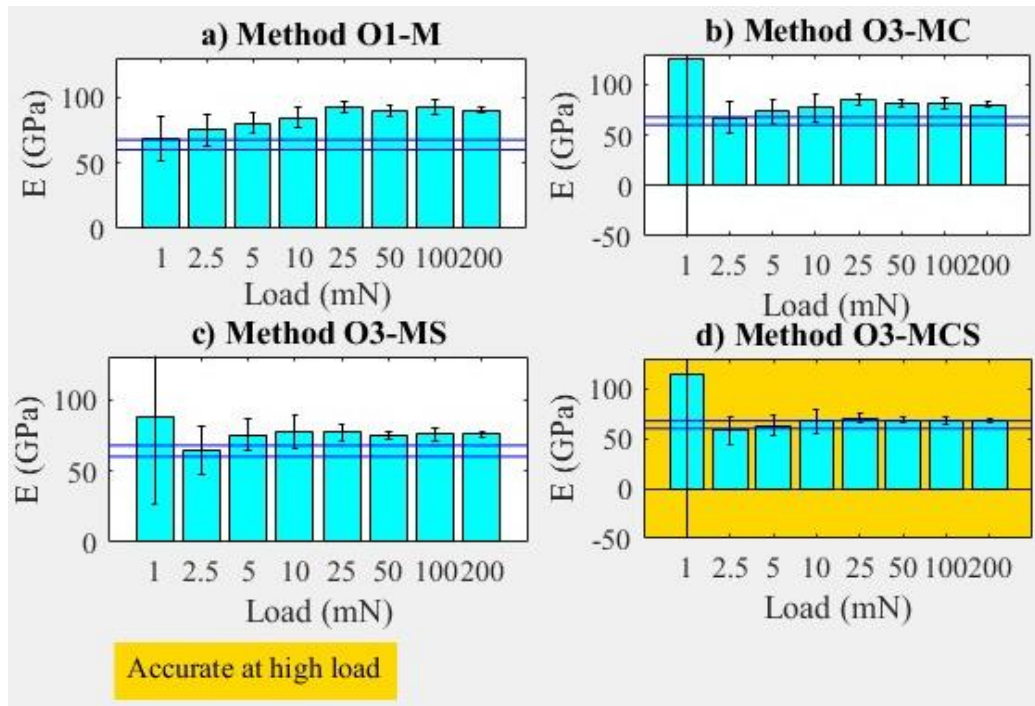


7.3 Area function plots

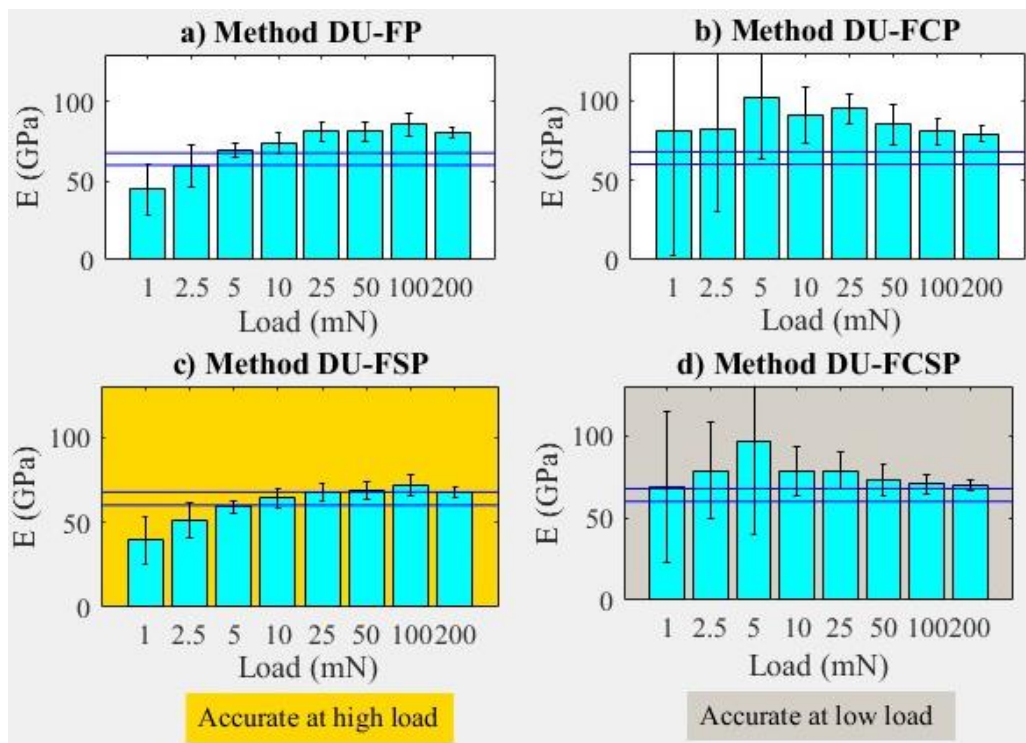


7.4 Elastic moduli against load plots for metallic materials

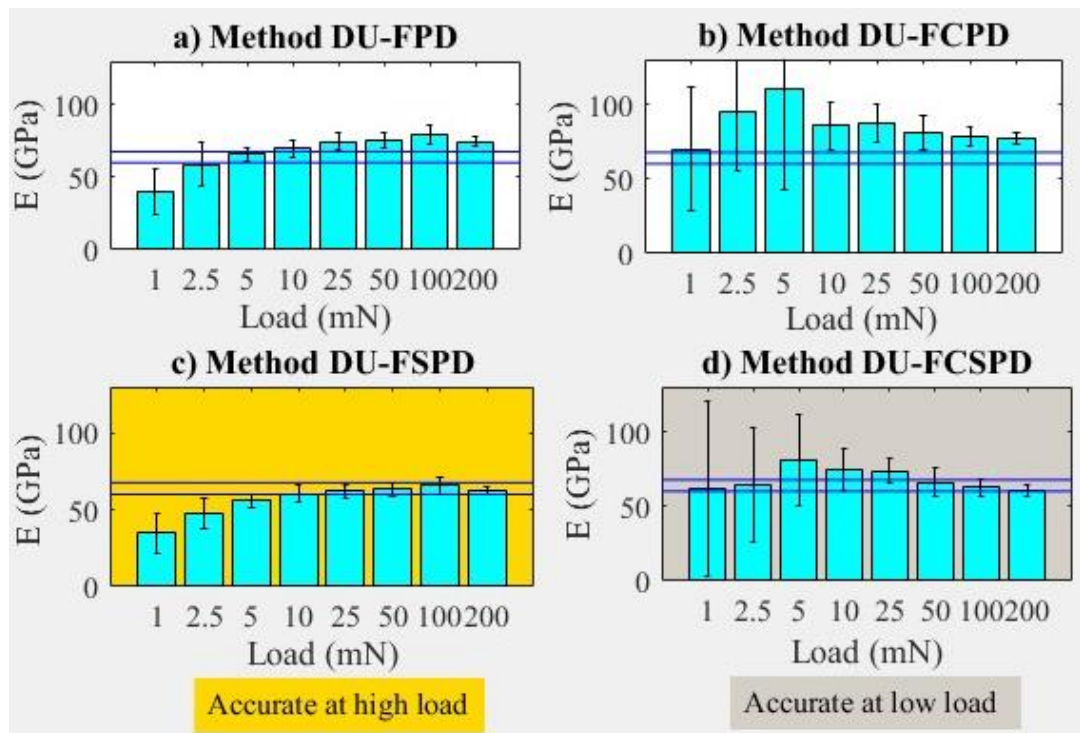
7.4.1 Aluminium elastic moduli (O methods) against load plots



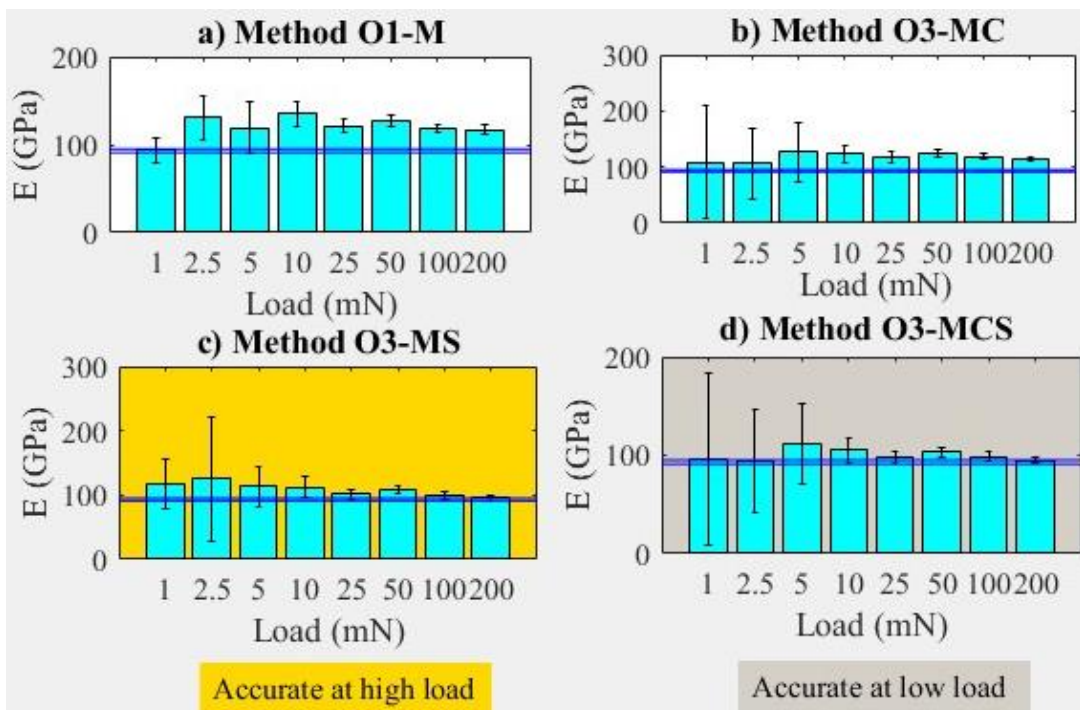
7.4.2 Aluminium elastic moduli (DU methods without datum) against load plots



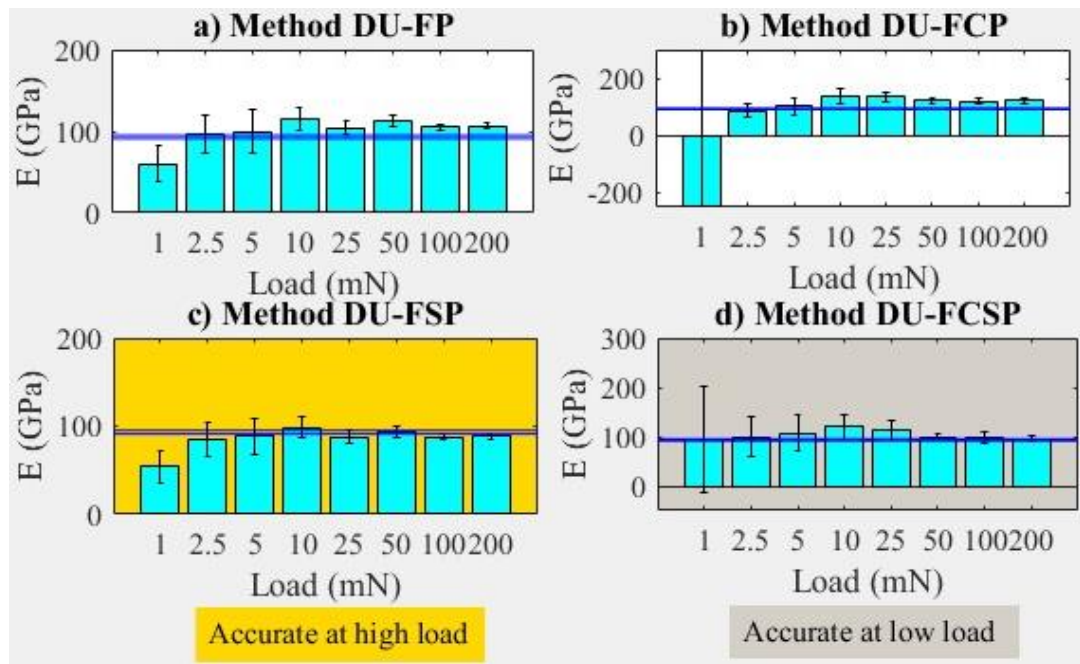
7.4.3 Aluminium elastic moduli (DU methods with datum) against load plots



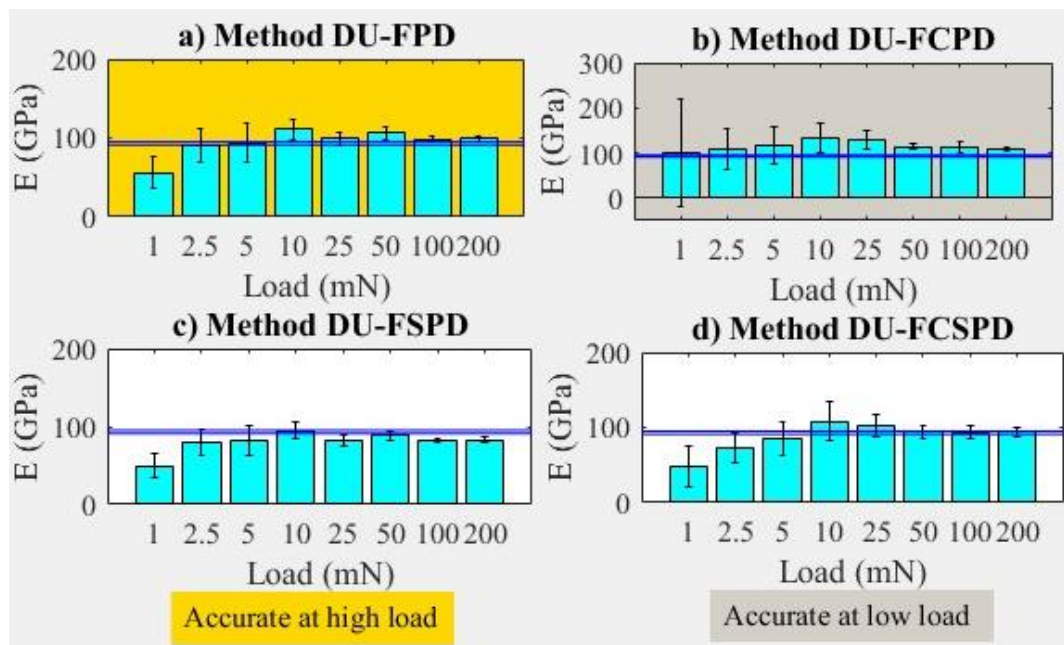
7.4.4 Brass elastic moduli (O methods) against load plots



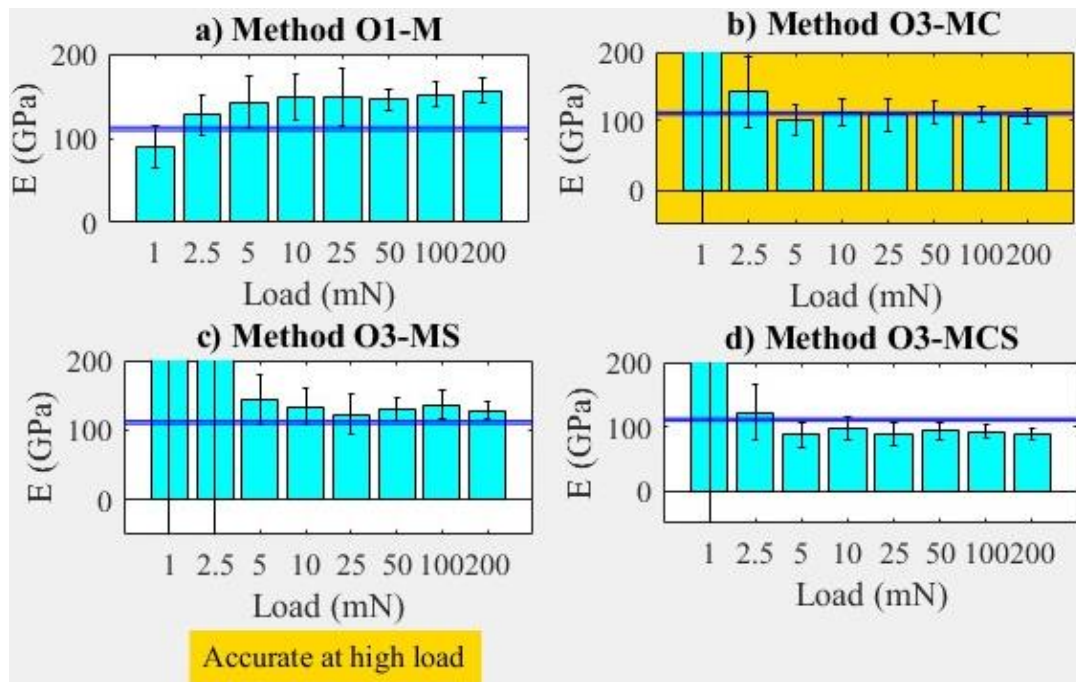
7.4.5 Brass elastic moduli (DU methods without datum) against load plots



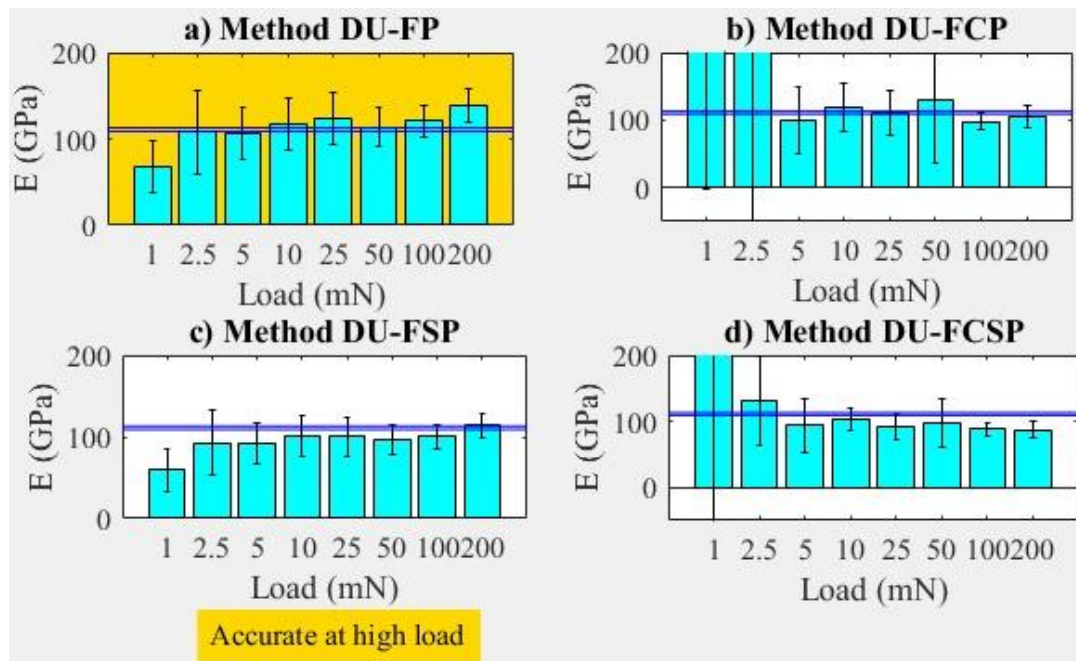
7.4.6 Brass elastic moduli (DU methods with datum) against load plots



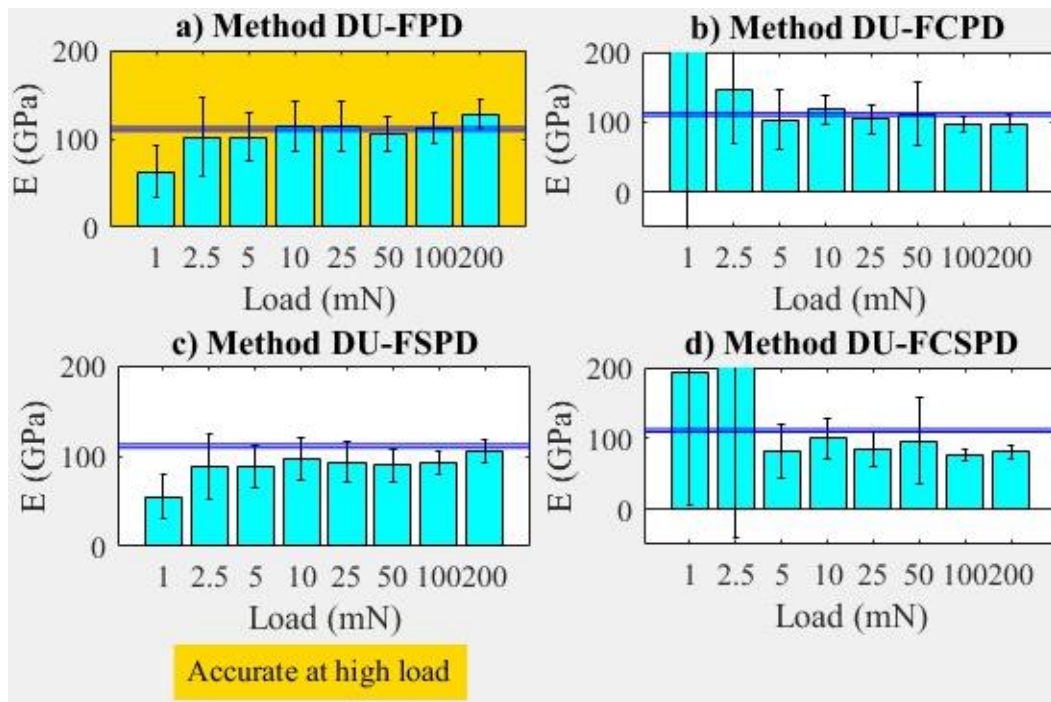
7.4.7 Copper elastic moduli (O methods) against load plots



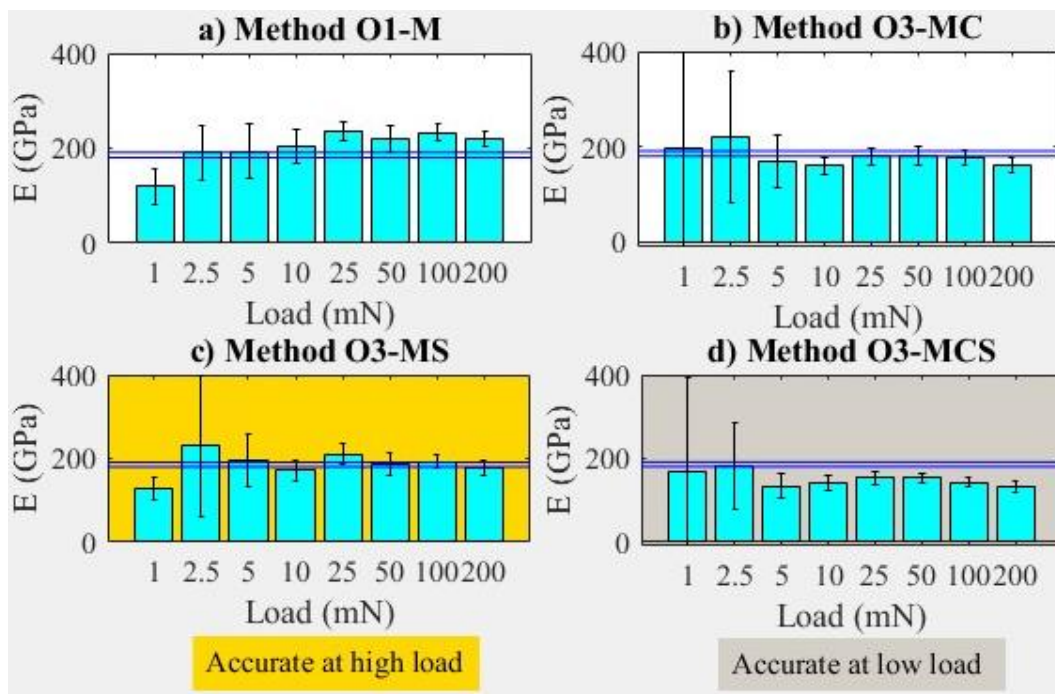
7.4.8 Copper elastic moduli (DU methods without datum) against load plots



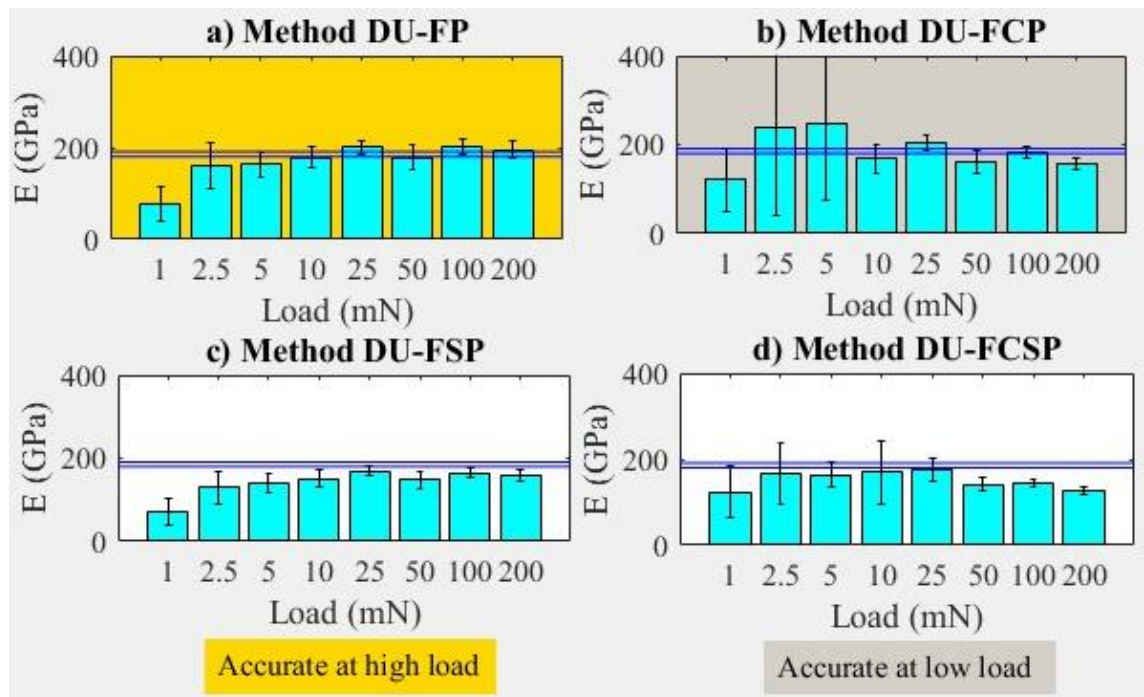
7.4.9 Copper elastic moduli (DU methods with datum) against load plots



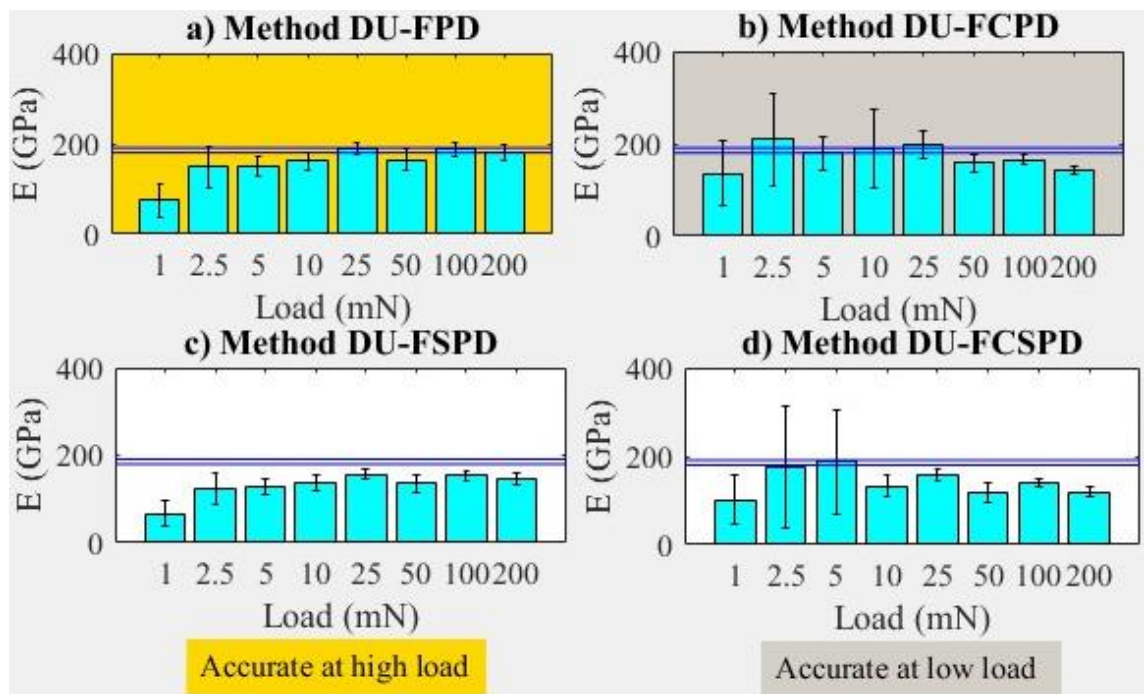
7.4.10 Mild steel elastic moduli (O methods) against load plots



7.4.11 Mild steel elastic moduli (DU methods without datum) against load plots

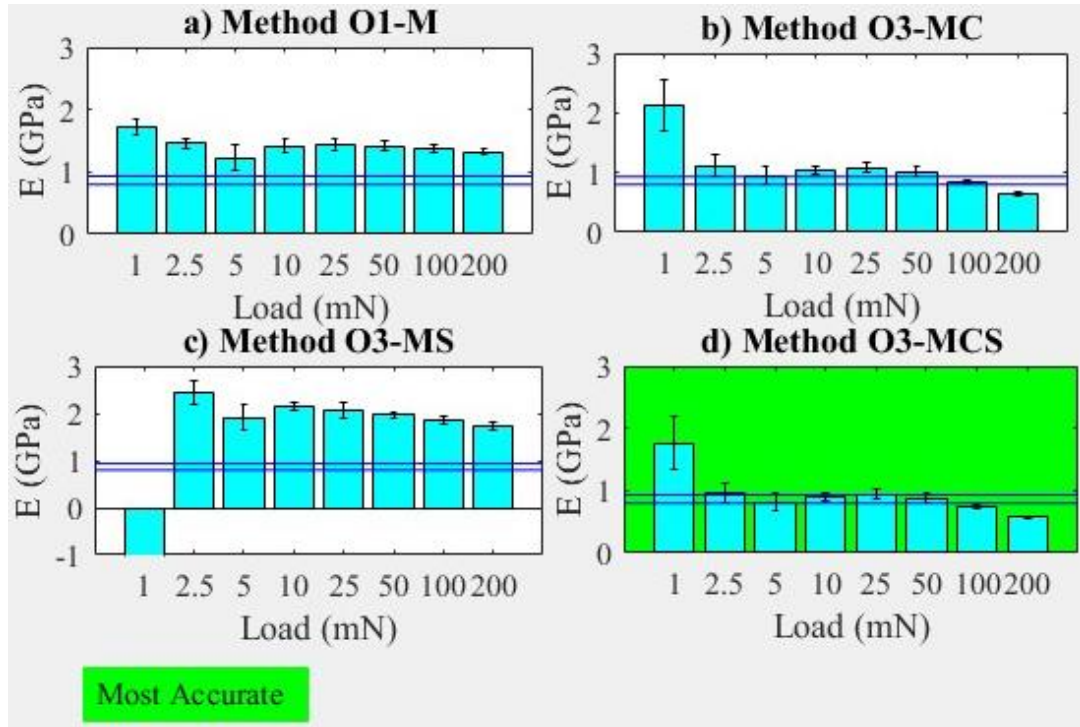


7.4.12 Mild steel elastic moduli (DU methods with datum) against load plots

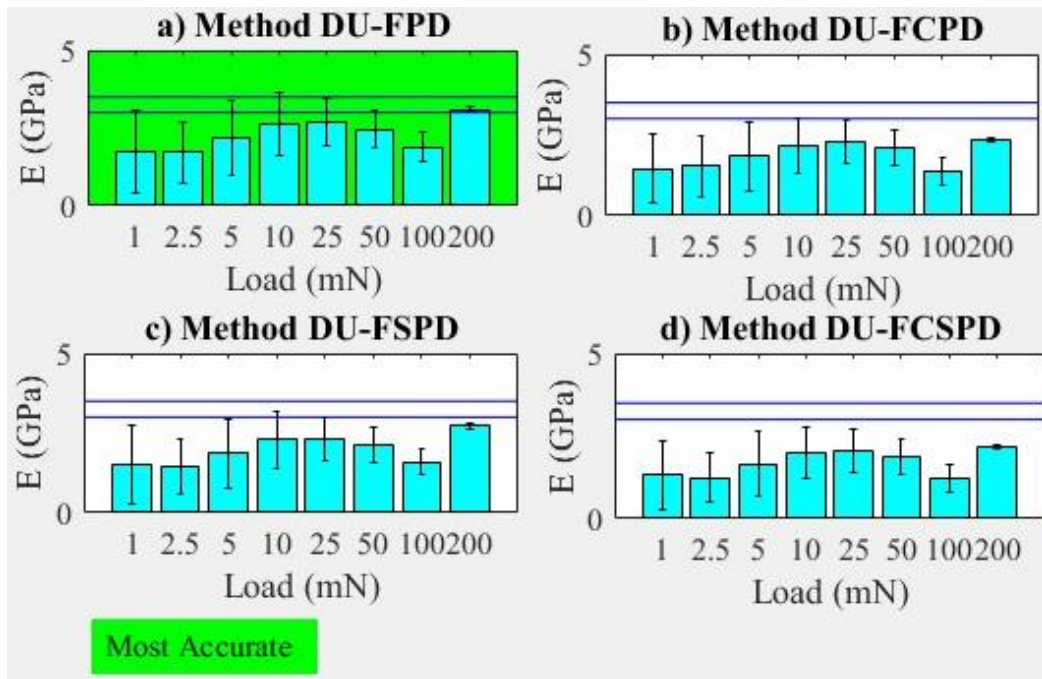


7.5 Elastic moduli against load plots for polymeric materials

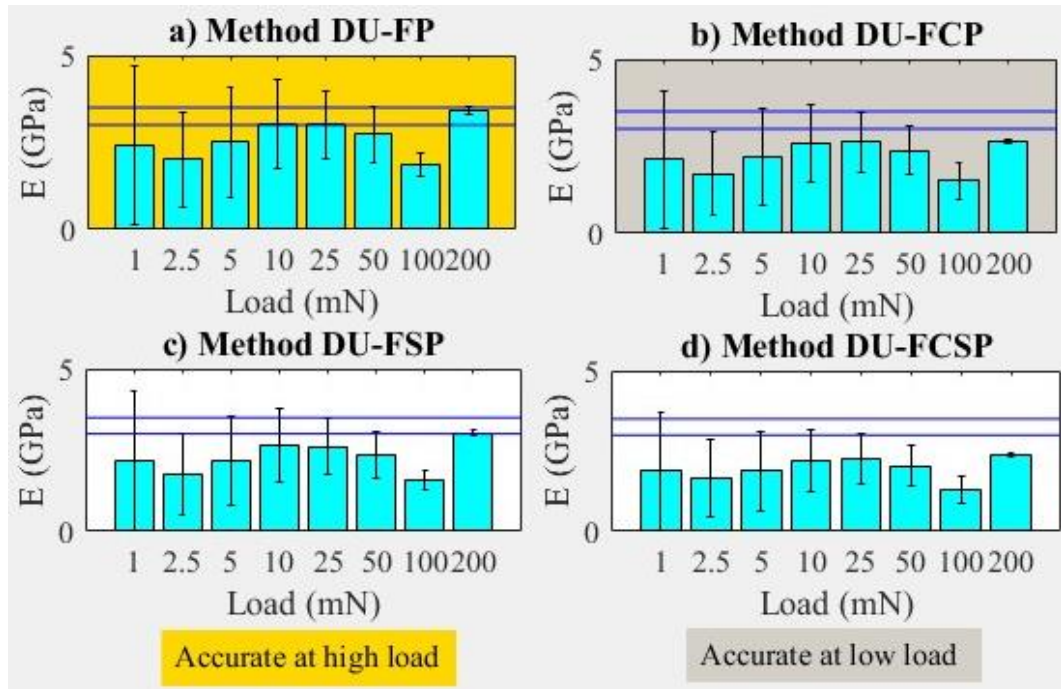
7.5.1 Nylon elastic moduli (O methods) against load plots



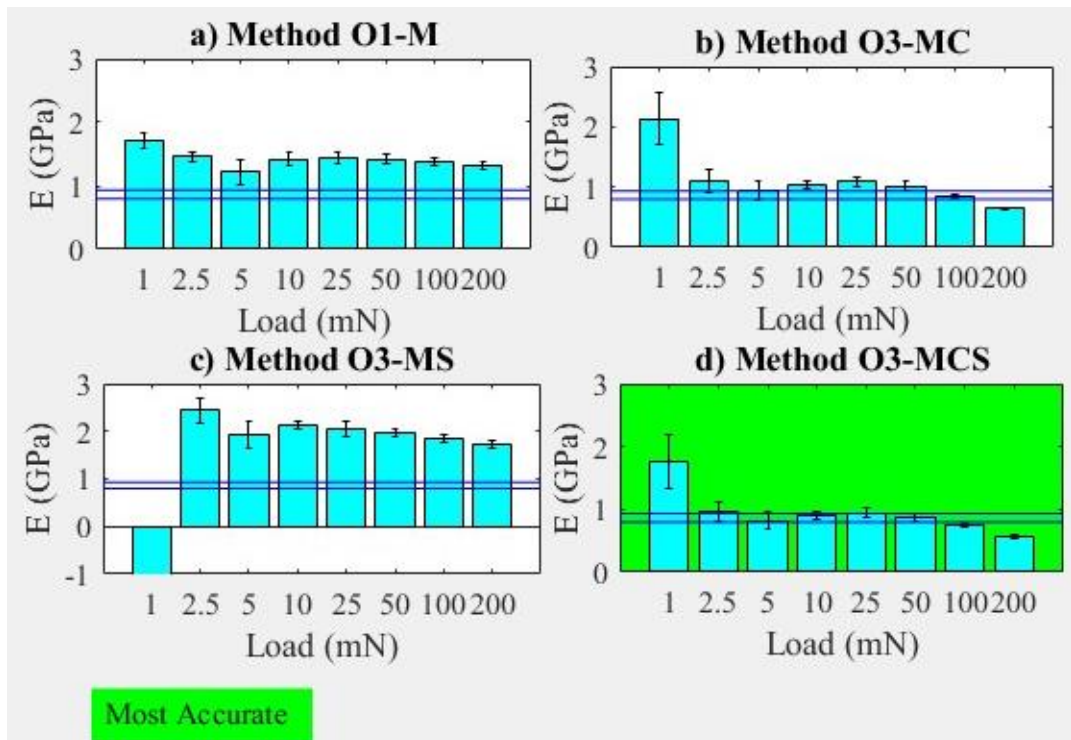
7.5.2 Nylon elastic moduli (DU methods with datum) against load plots



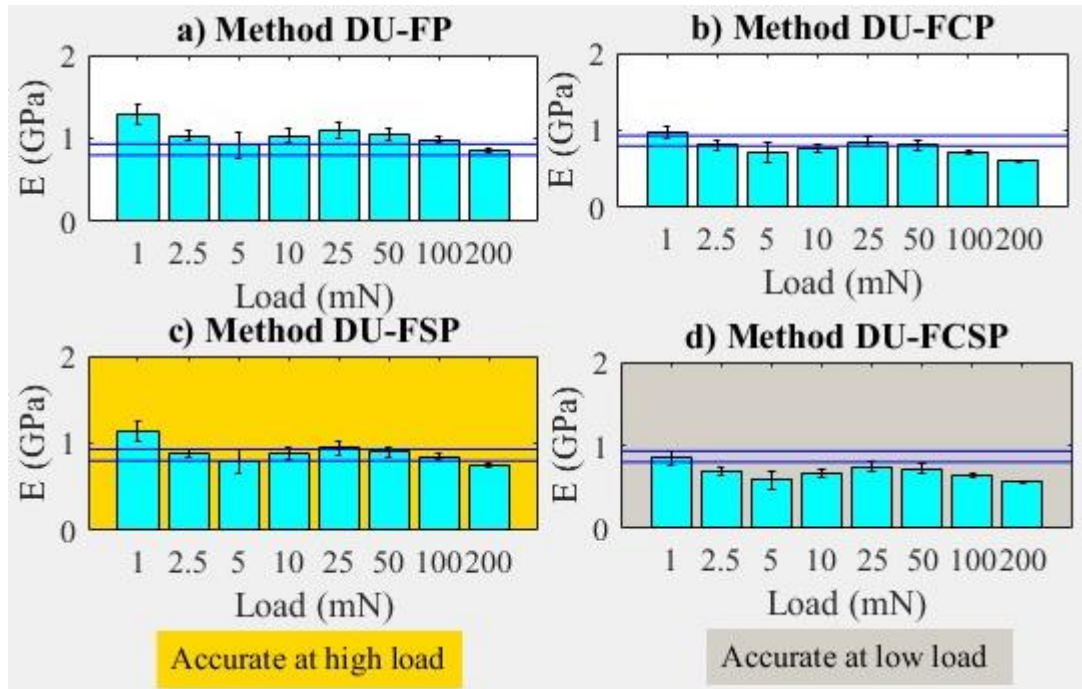
7.5.3 Nylon elastic moduli (DU methods without datum) against load



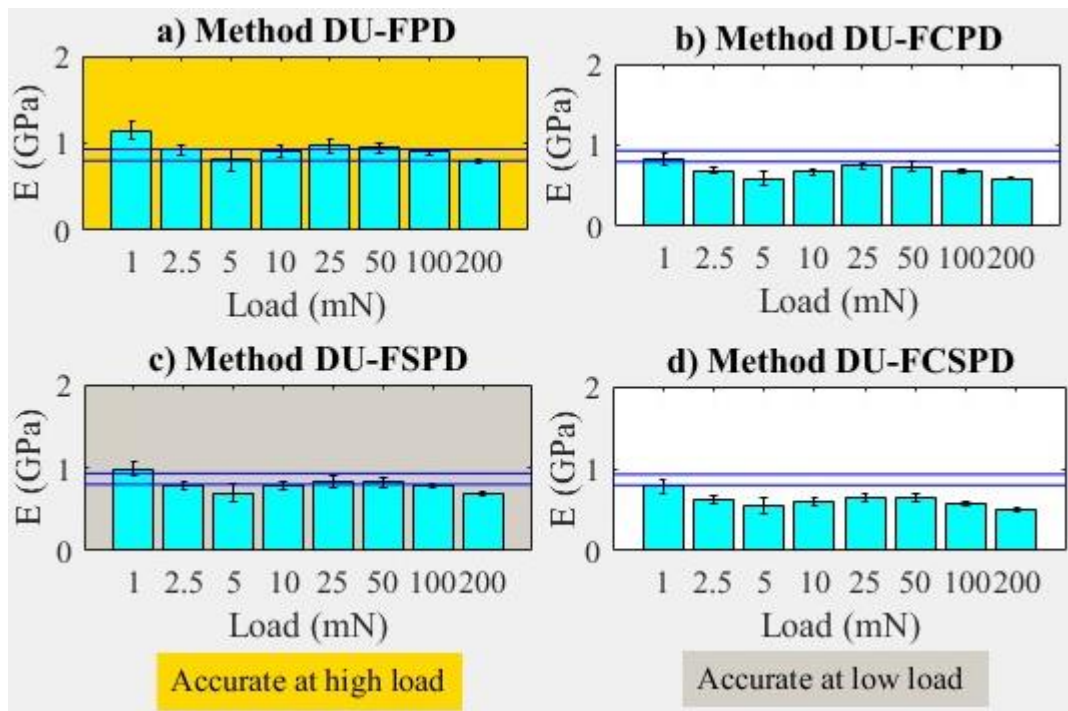
7.5.4 Polyethylene HD elastic moduli (O methods) against load plots



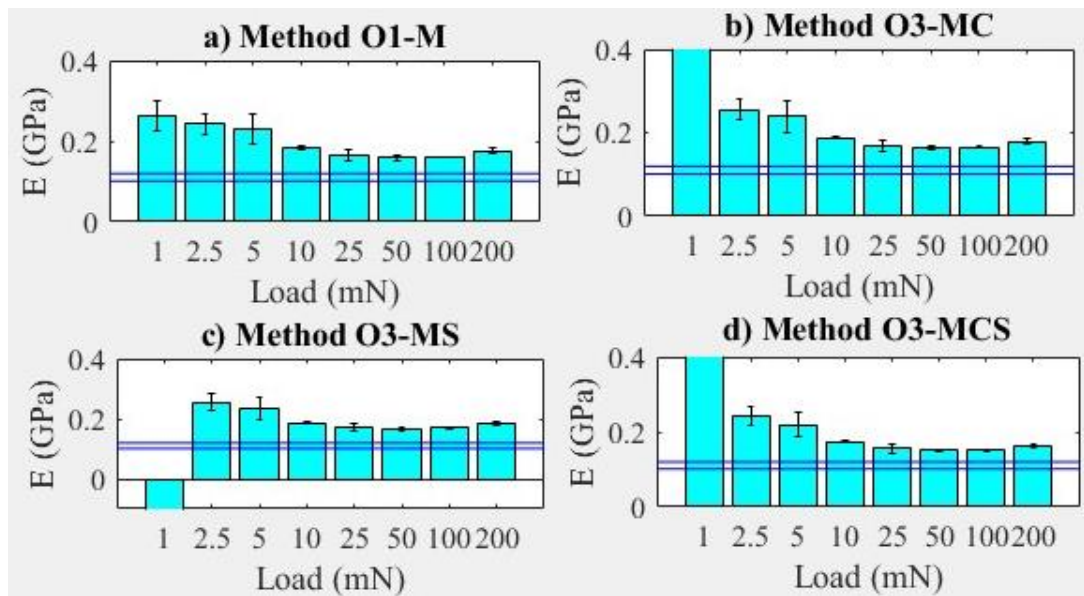
7.5.5 Polyethylene HD elastic moduli (DU methods without datum) against load plots



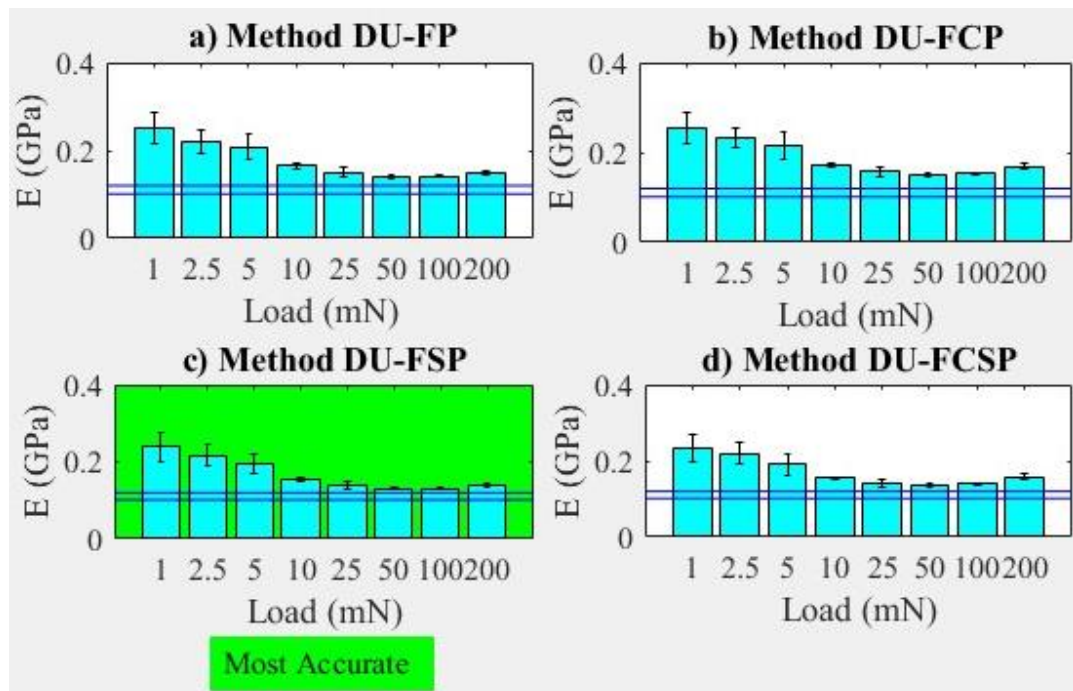
7.5.6 Polyethylene HD elastic moduli (DU methods with datum) against load plots



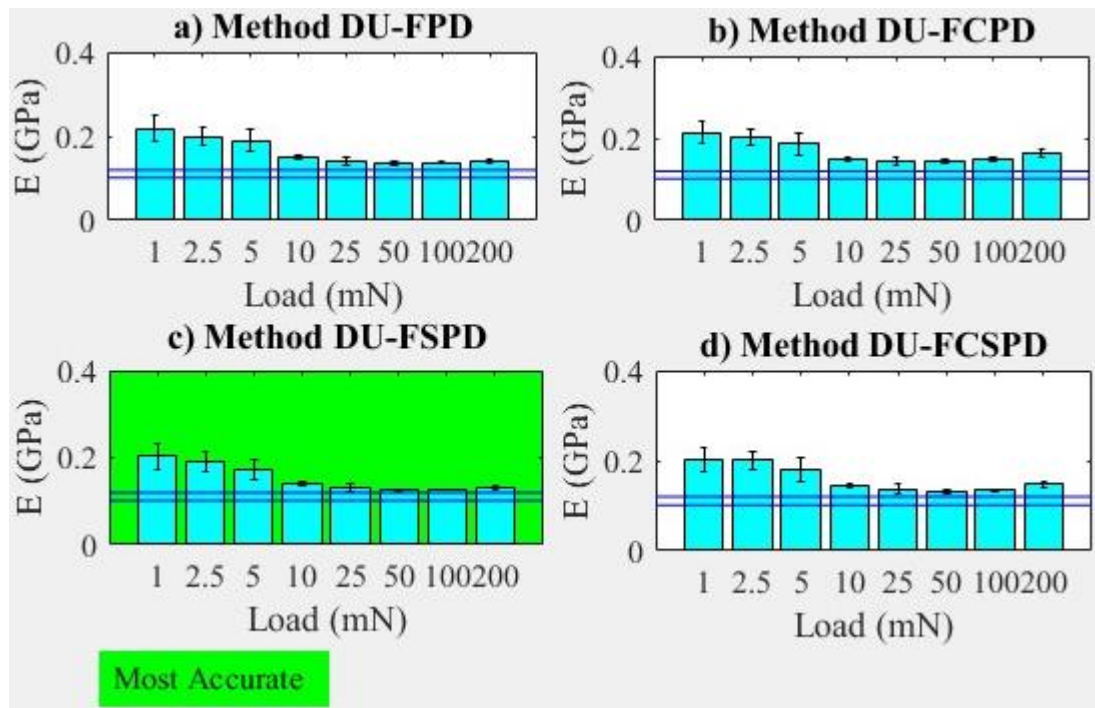
7.5.7 Polyethylene LD elastic moduli (O methods) against load plots



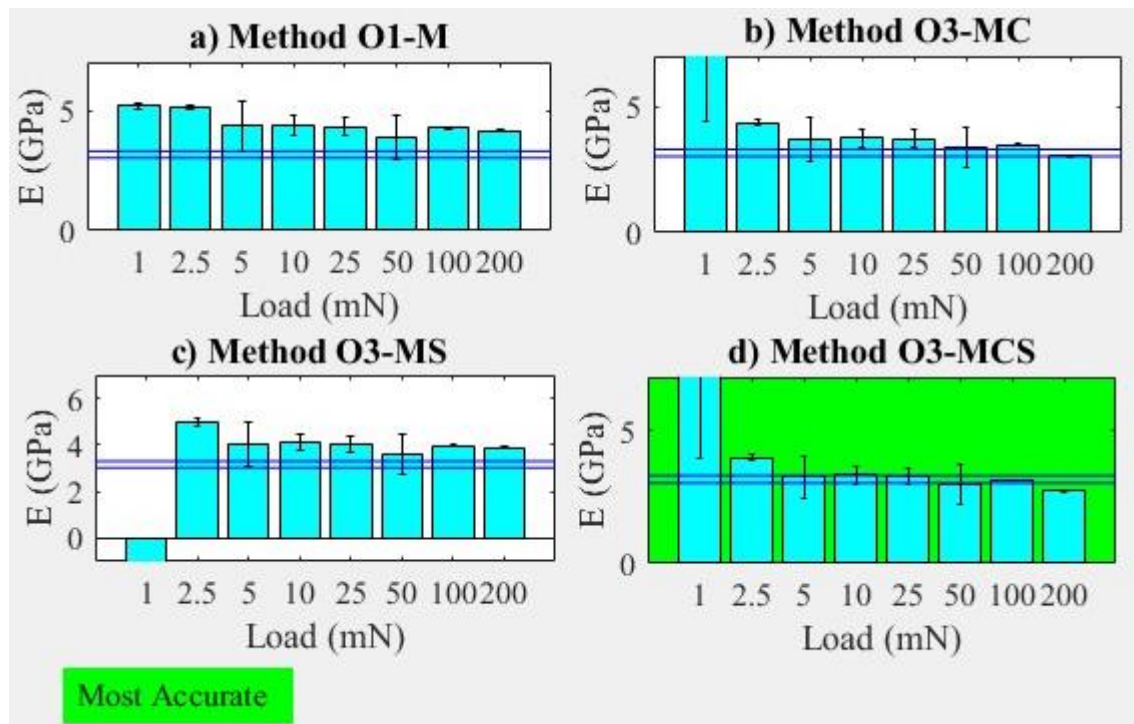
7.5.8 Polyethylene LD elastic moduli (DU methods without datum) against load plots



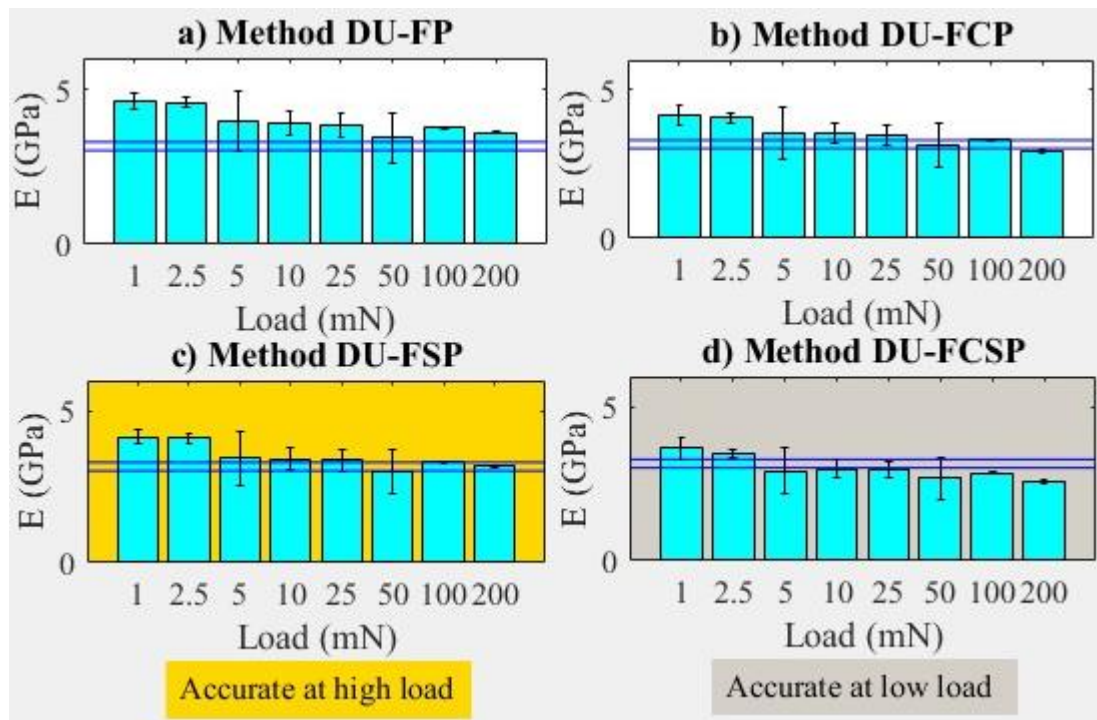
7.5.9 Polyethylene LD elastic moduli (DU methods with datum) against load plots



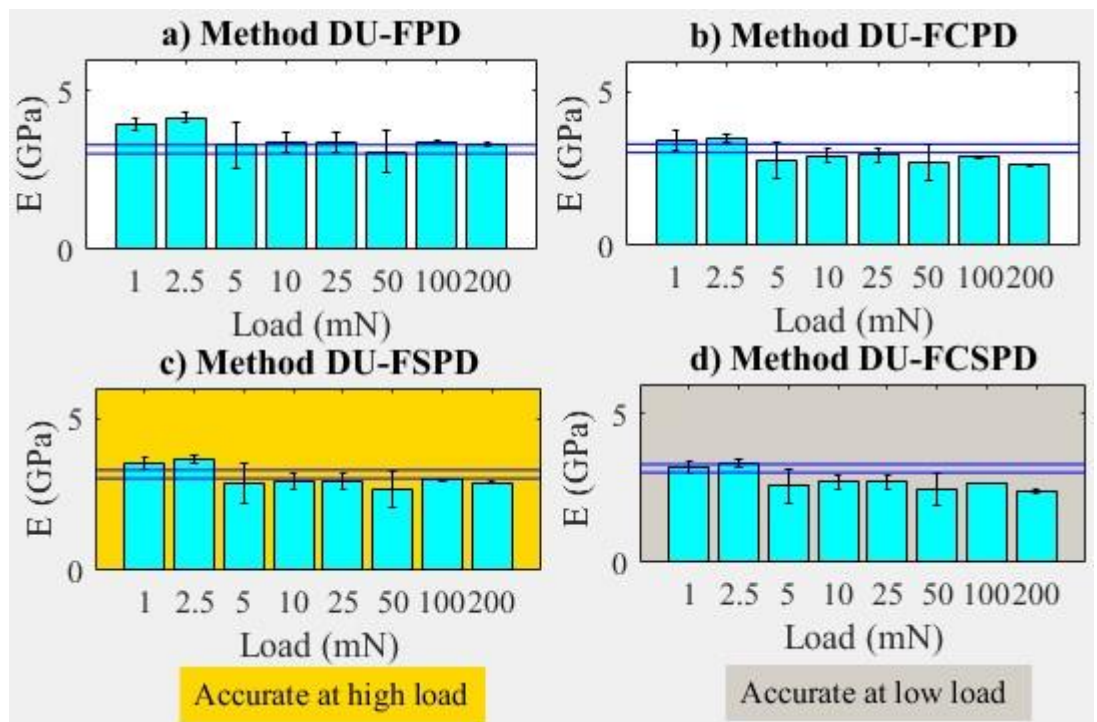
7.5.10 Polystyrene elastic moduli (O methods) against load plots



7.5.11 Polystyrene elastic moduli (DU methods without datum) against load plots



7.5.12 Polystyrene elastic moduli (DU methods with datum) against load plots



Appendix 8.

8.1 Coating characterisation Experiment 8.1

- a) Full factorial DOE, depth-controlled indentation tests, for three different coatings, TiN with 155 nm thickness, TiO₂ with 199 nm thickness and AZO with 123 nm thickness, all deposited on a PET substrate. 100-20% of the raw unloading data was used with post thermal drift. For details on number of indents, maximum depths, hold time, and corresponding loading and unloading rate see Table- 9 1.
- b) Full factorial DOE, depth-controlled indentation tests, for three different coatings, TiN with 155 nm thickness, TiO₂ with 199 nm thickness and AZO with 123 nm thickness, all deposited on a steel substrate. 100-20% of the raw unloading data was used with post thermal drift. For details on number of indents, maximum depths, hold time, and corresponding loading and unloading rate see Table- 9 1.
- c) Full factorial DOE, depth-controlled indentation tests, for TiN 1.2 µm thick sample deposited on a 3 mm thick silicon wafer. Using 100-20% of the raw unloading data. For details of loads, hold time, and corresponding loading and unloading rate see Table- 9-1.
- d) Full factorial DOE, depth-controlled indentation tests, for TiO₂ 0.8 µm thick sample deposited on a 3 mm thick silicon wafer. Using 100-20% of the raw unloading data. For details of loads, hold time, and corresponding loading and unloading rate see Table- 9 1.

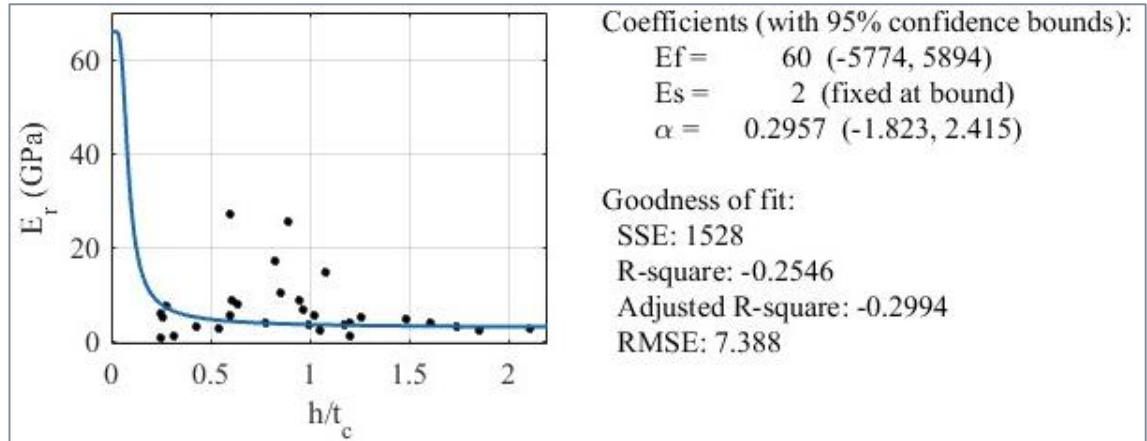
Table- 9-1 Details of load and corresponding loading and unloading rate

Experiment	N.O. Indents	Maximum Depth (nm)	Loading and unloading rates (mNs ⁻¹)	Dwell time (s)
a	5	30	0.001	5
	5	70	0.001	5
	5	100	0.001	5
	5	130	0.001	5
	5	170	0.001	5
	5	200	0.001	5
b	5	10	0.05	5
	5	40	0.05	5
	5	70	0.05	5
	5	100	0.05	5
	5	130	0.05	5
	5	170	0.05	5
	5	200	0.05	5
c & d	5	50	0.05	5
	5	100	0.05	5
	5	300	0.05	5
	5	500	0.05	5
	5	800	0.05	5
	5	1500	0.05	5

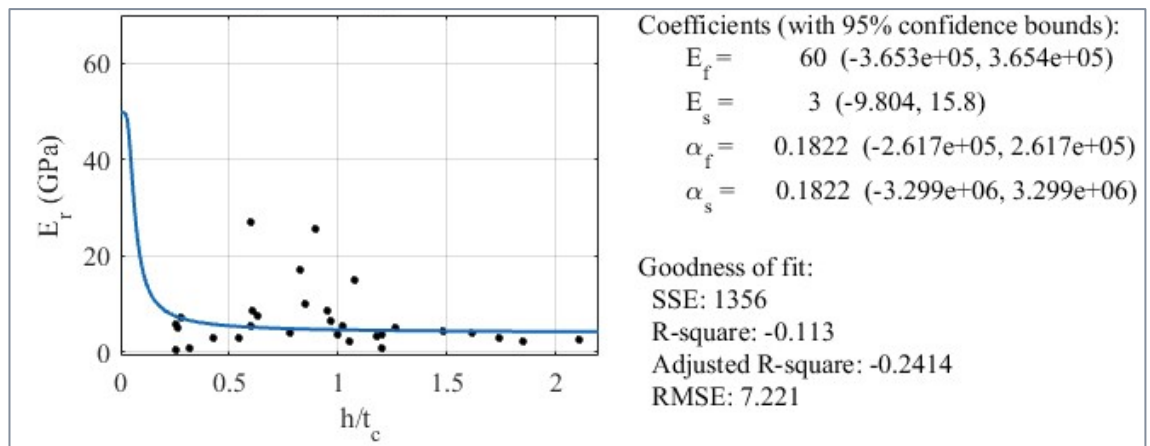
8.2 Coating characterisation fits

8.2.1 TiN on PET

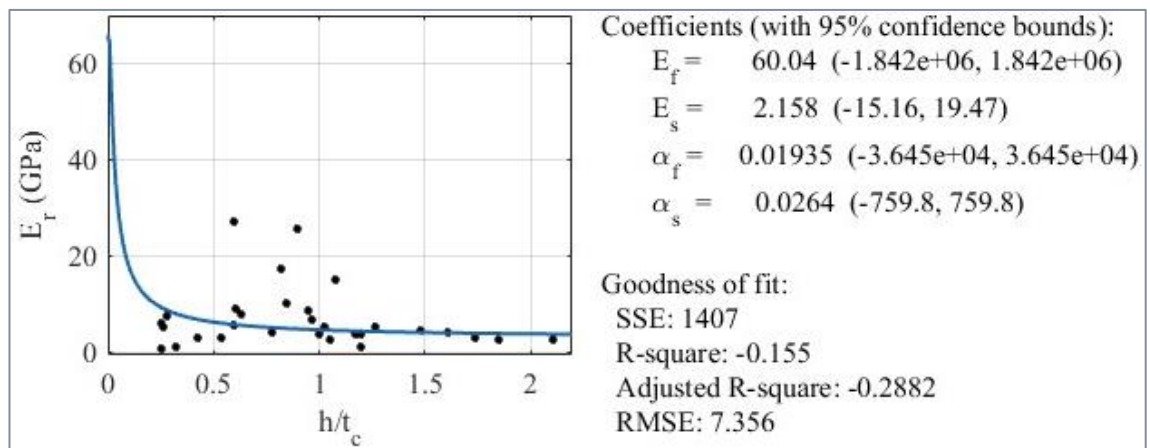
a) TiN on PET, DN model



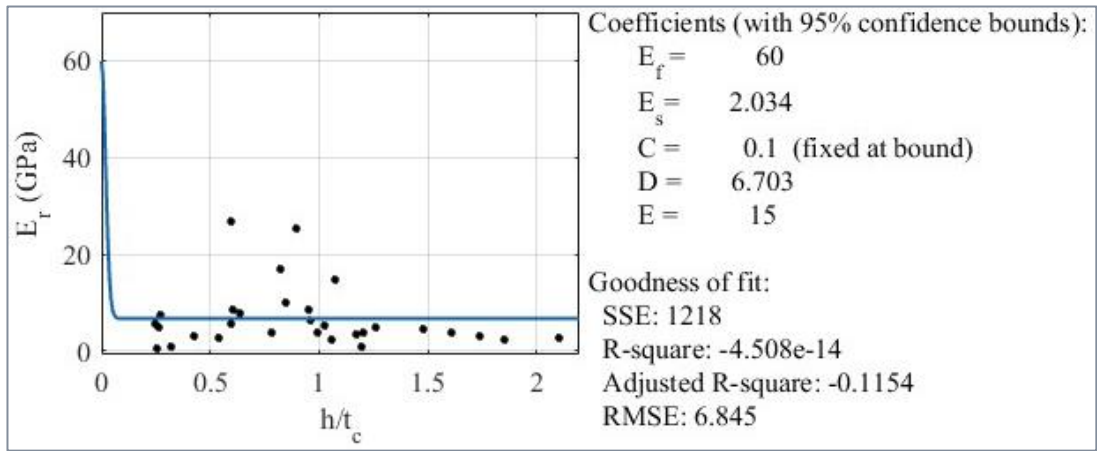
b) TiN on PET, DEITM model



c) TiN on PET, ADEITM model

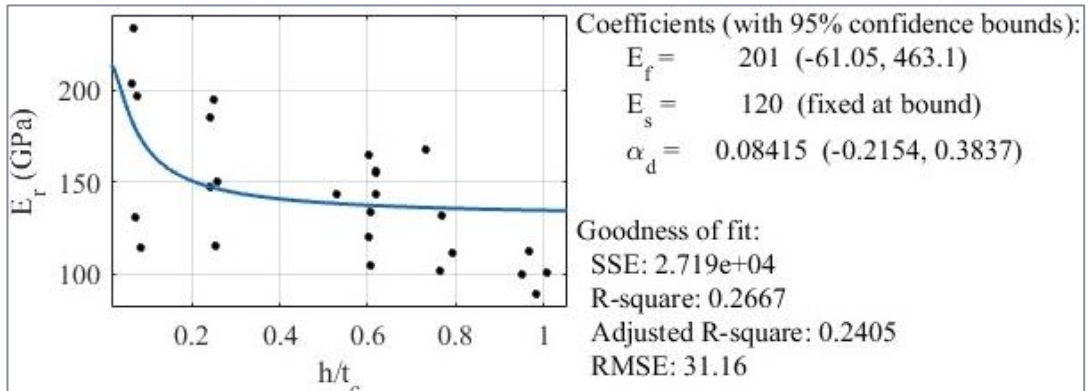


d) TiN on PET, 5PL model

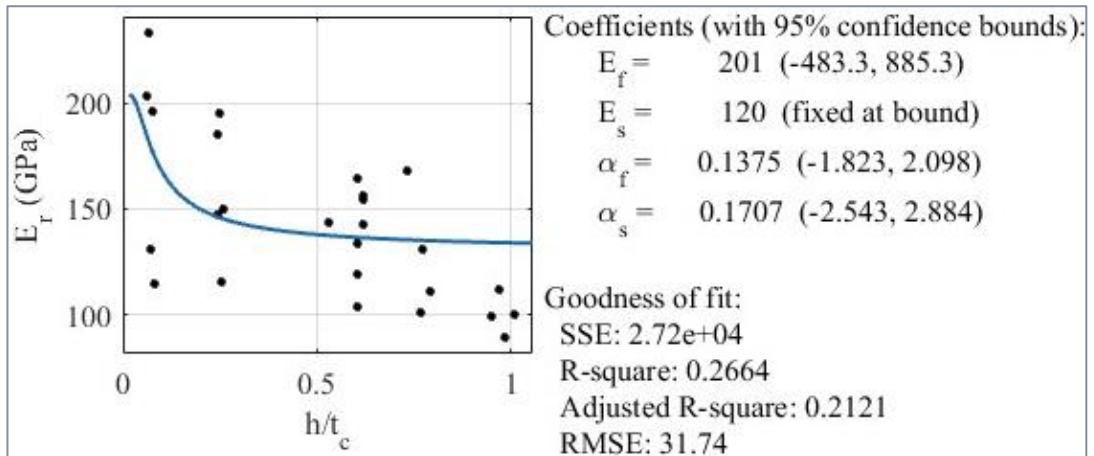


8.2.2 TiN on Steel

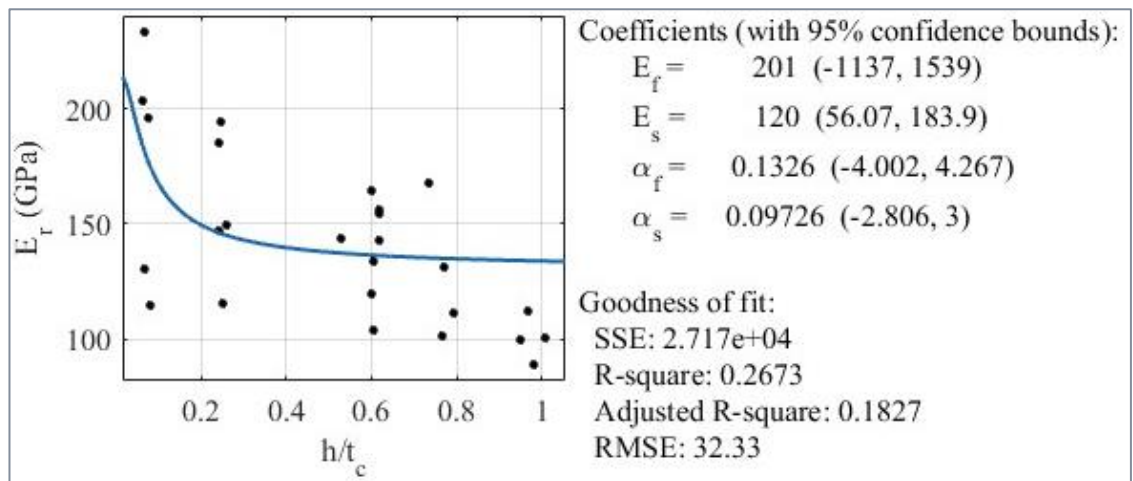
a) TiN on Steel, DN model



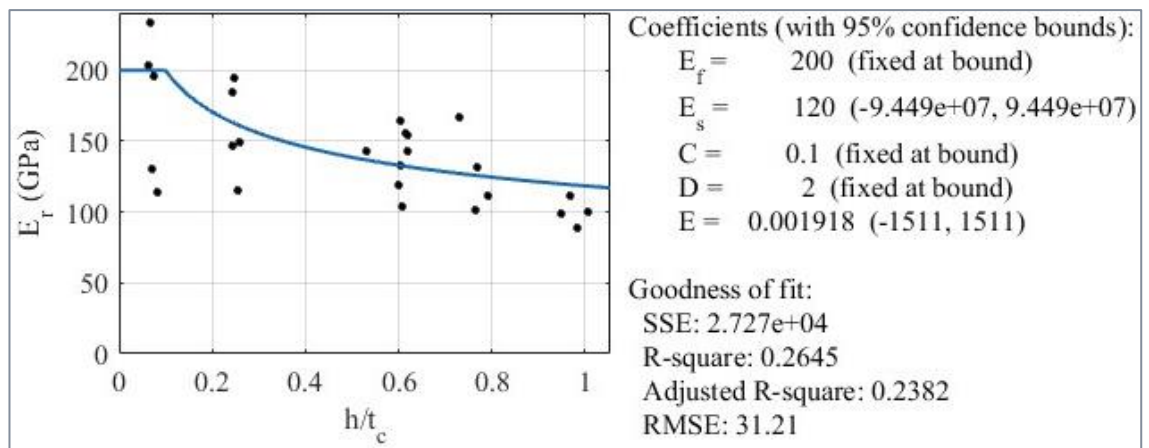
b) TiN on Steel, DEITM model



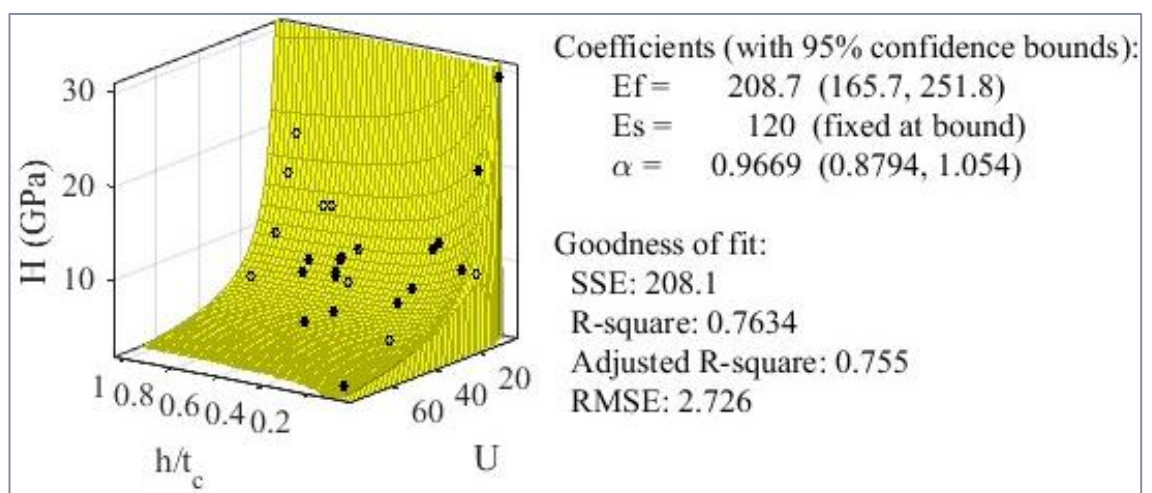
c) TiN on Steel, ADEITM model



e) TiN on Steel, 5PL model

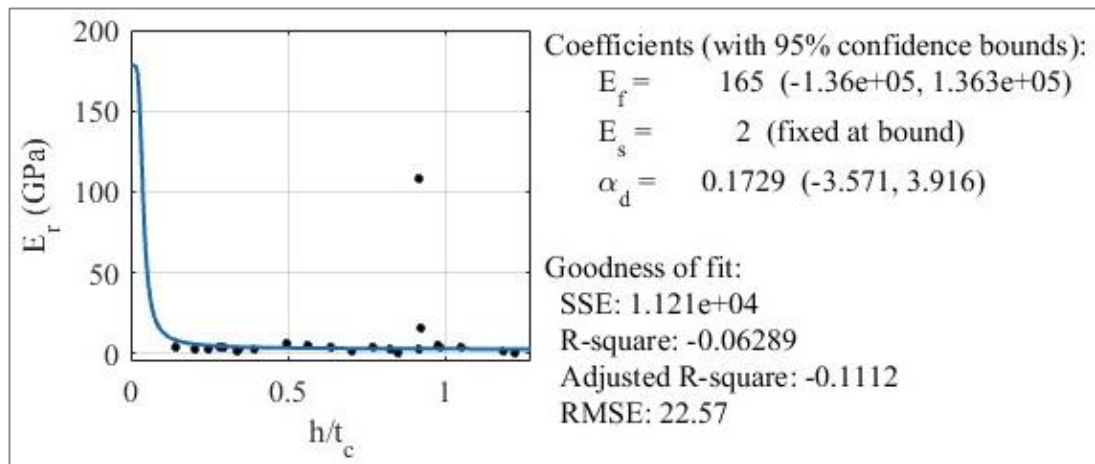


f) TiN on Steel, EM model

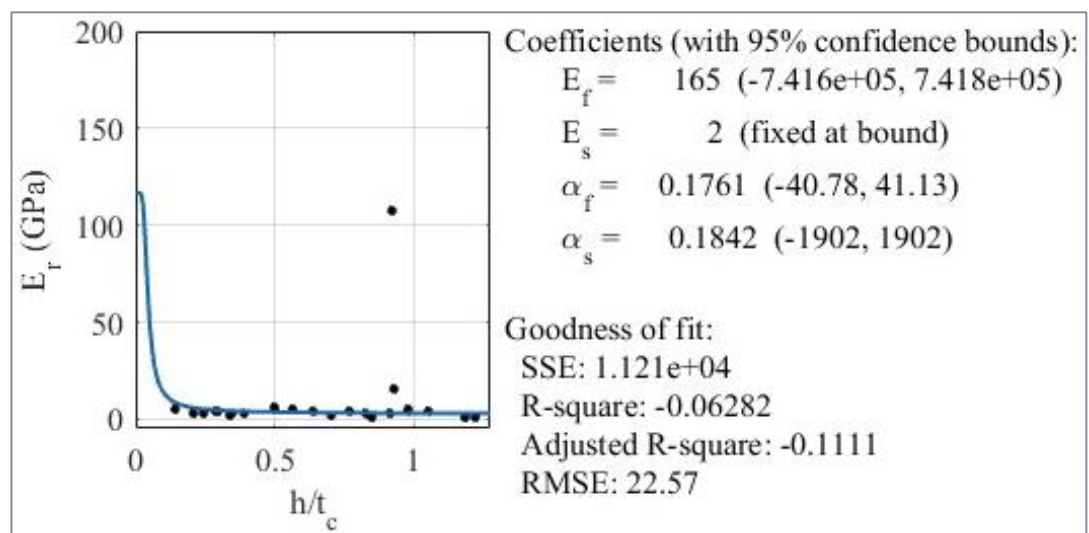


8.2.3 TiO₂ on PET

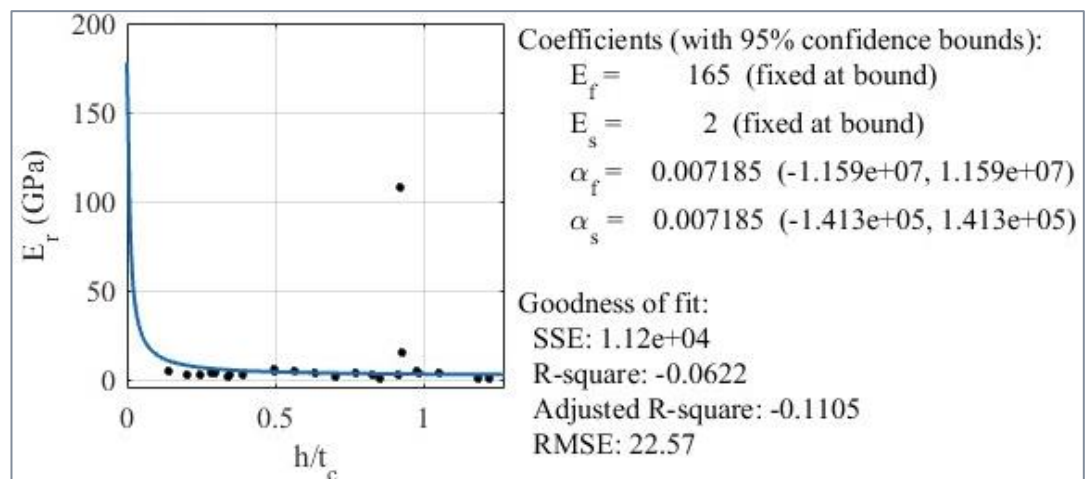
a) TiO₂ on PET, DN model



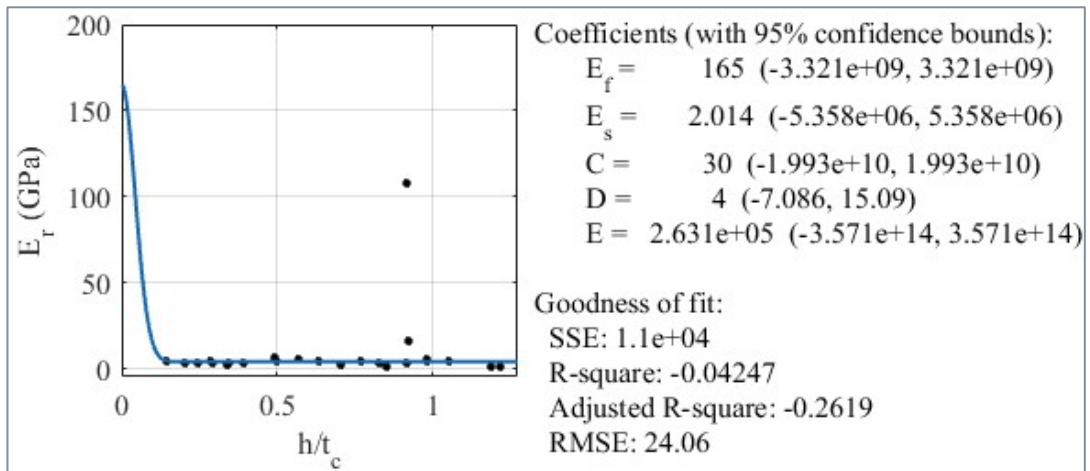
b) TiO₂ on PET, DEITM model



c) TiO₂ on PET, ADEITM model

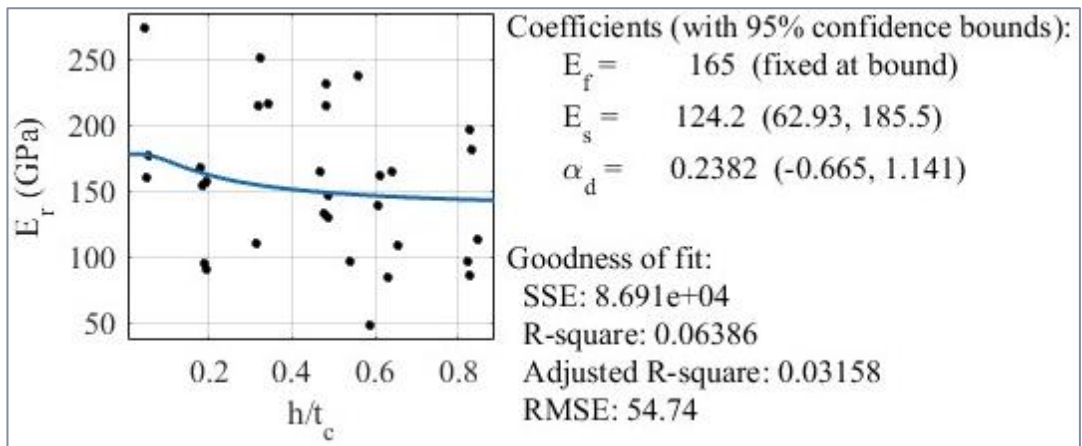


d) TiO₂ on PET, SPL model

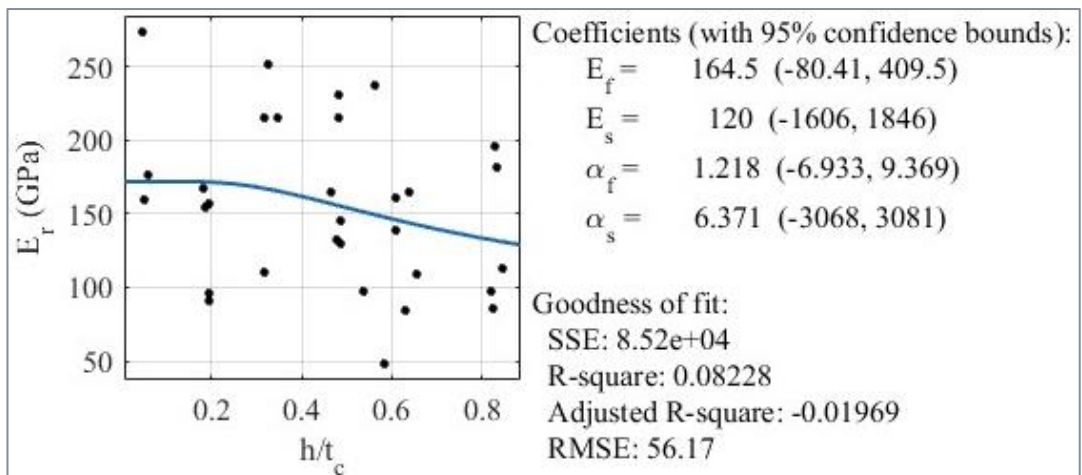


8.2.4 TiO₂ on Steel

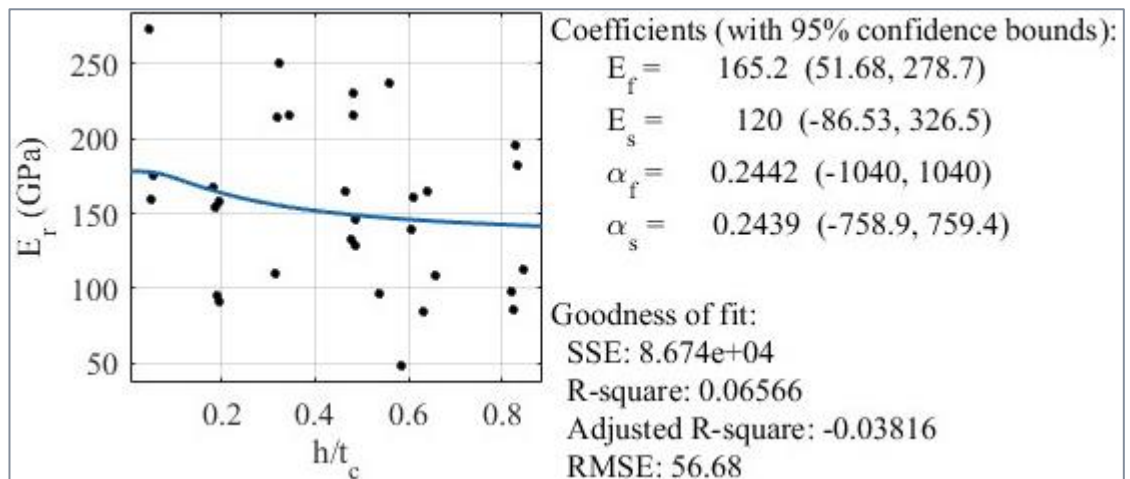
a) TiO₂ on Steel, DN model



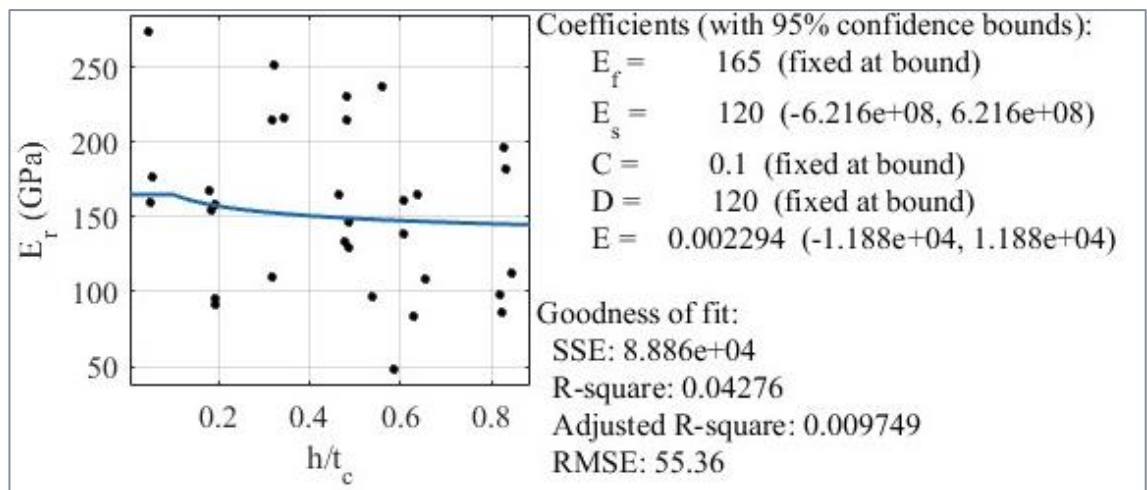
b) TiO₂ on Steel, DEITM model



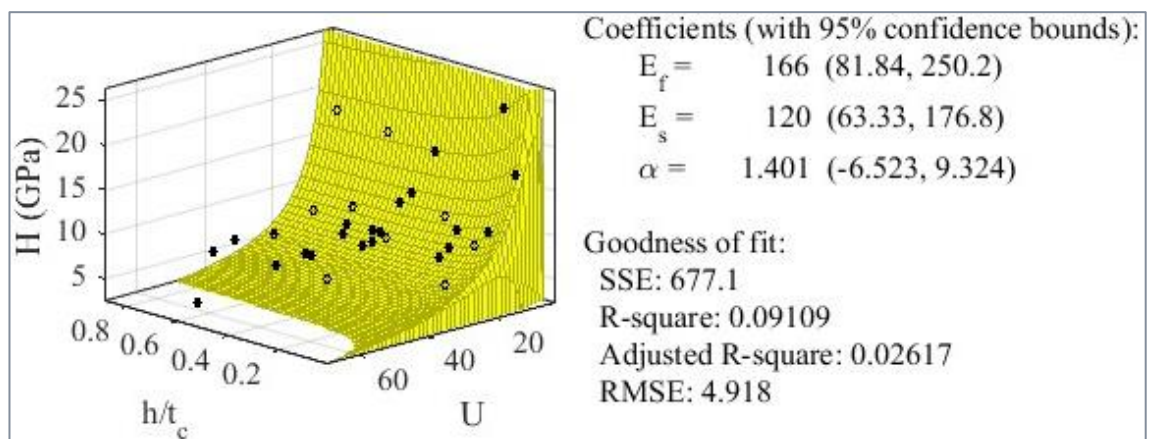
c) TiO₂ on Steel, ADEITM model



d) TiO₂ on Steel, 5PL model

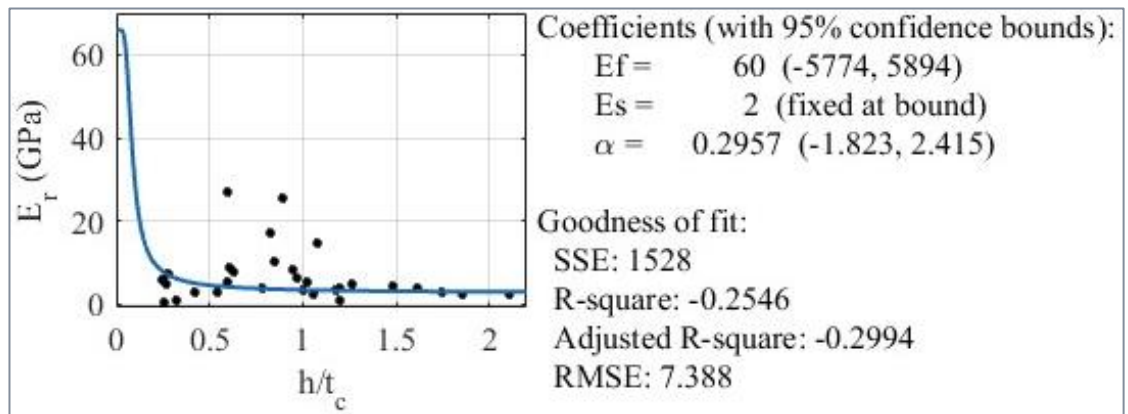


e) TiO₂ on Steel, EM model

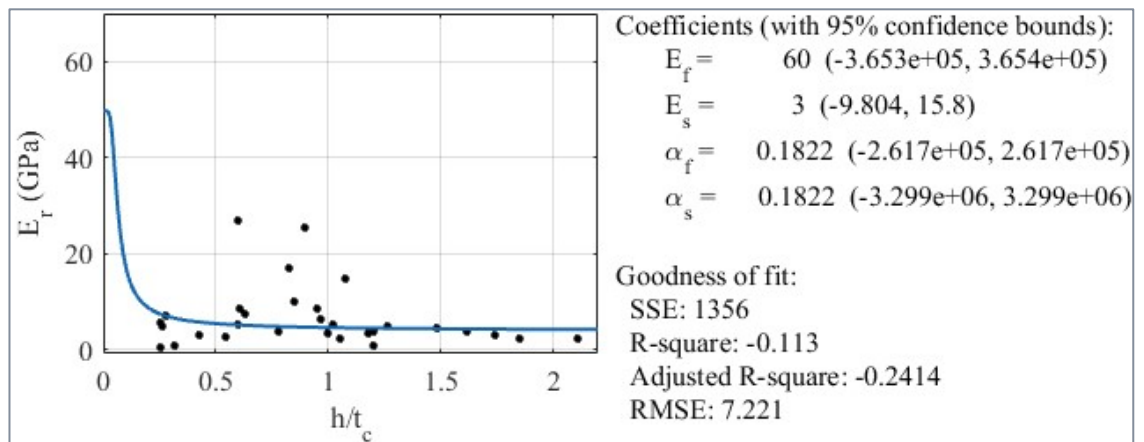


8.2.5 AZO on PET

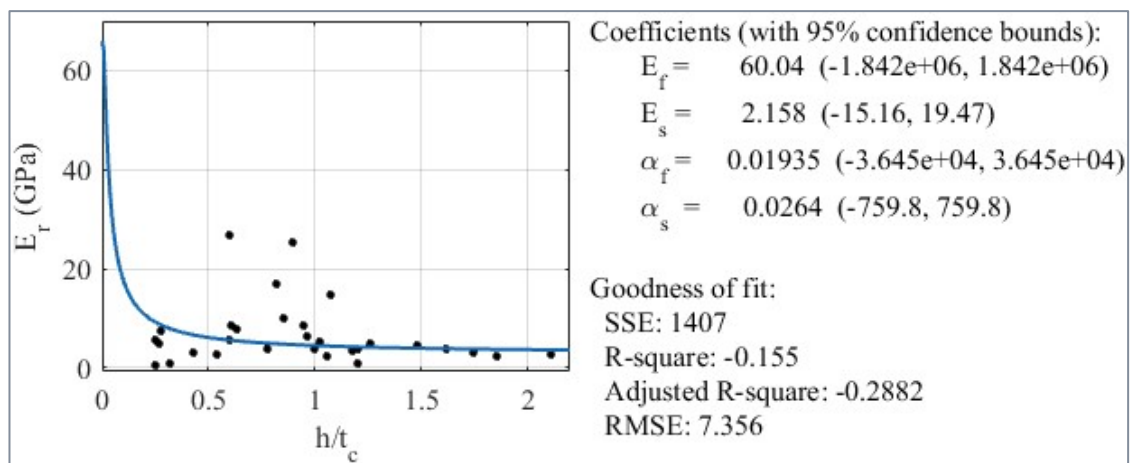
a) AZO on PET, DN model



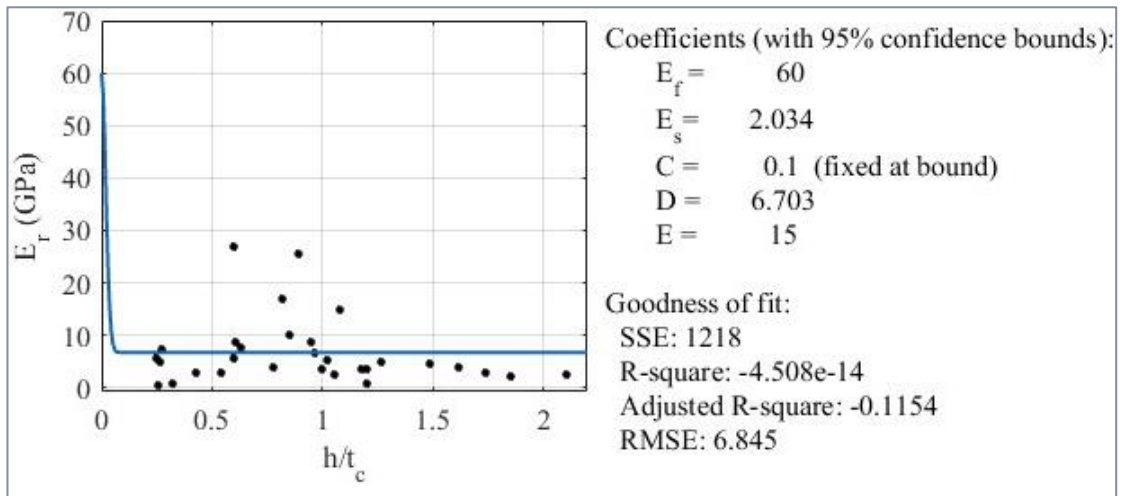
b) AZO on PET, DEITM model



c) AZO on PET, ADEITM model

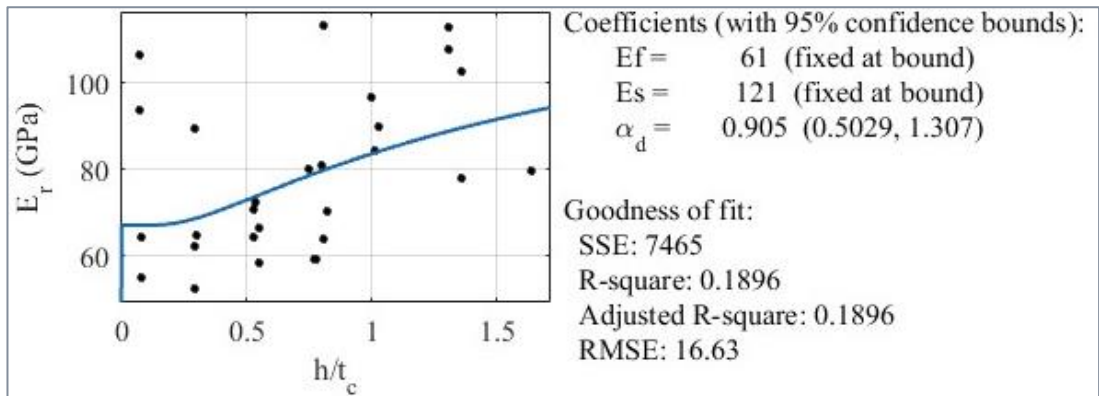


d) AZO on PET, 5PL model

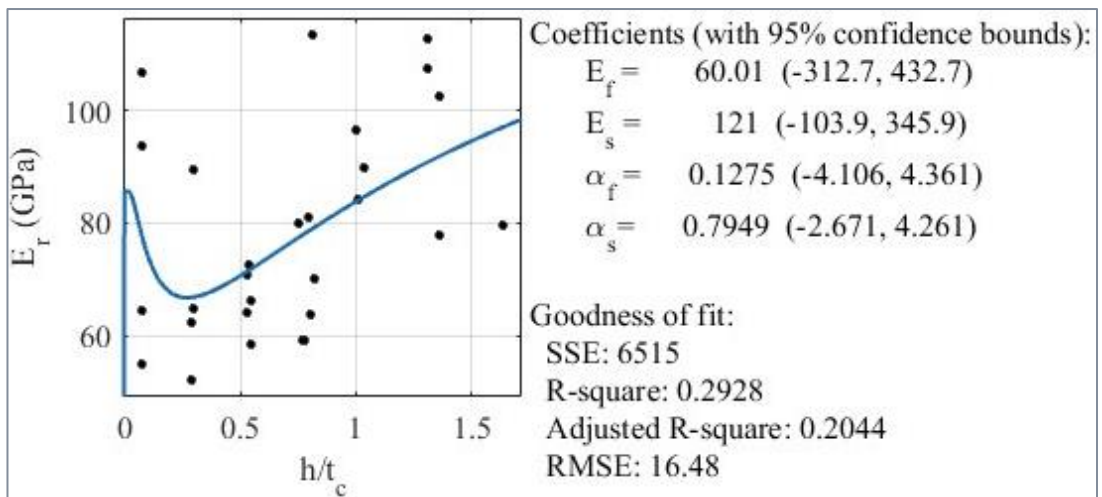


8.2.6 AZO on Steel

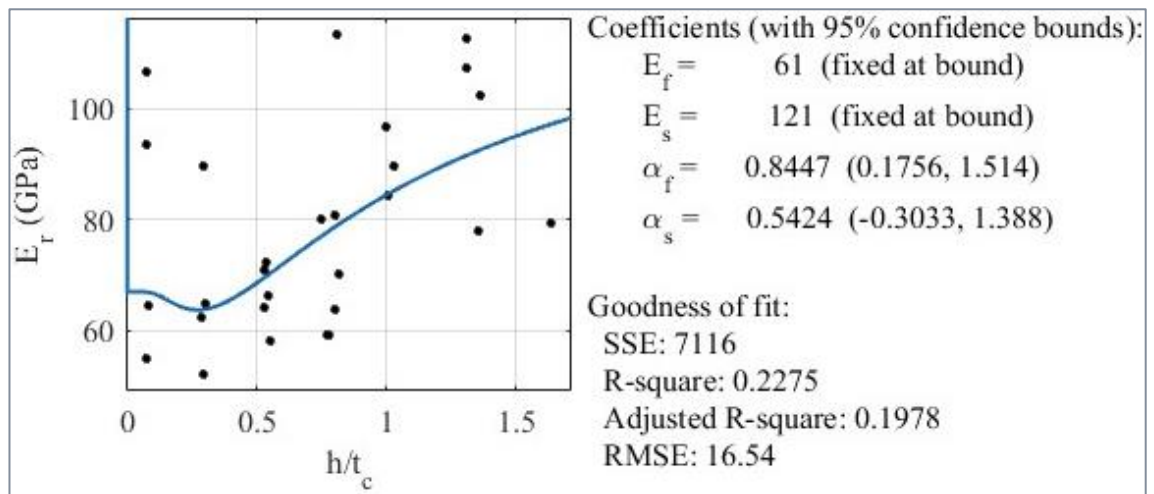
a) AZO on Steel, DN model



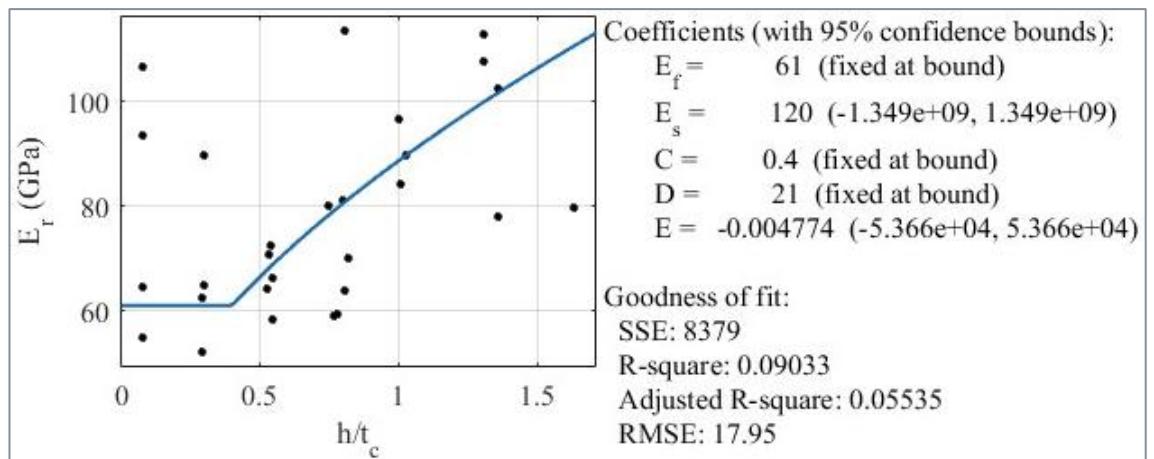
b) AZO on Steel, DEITM model



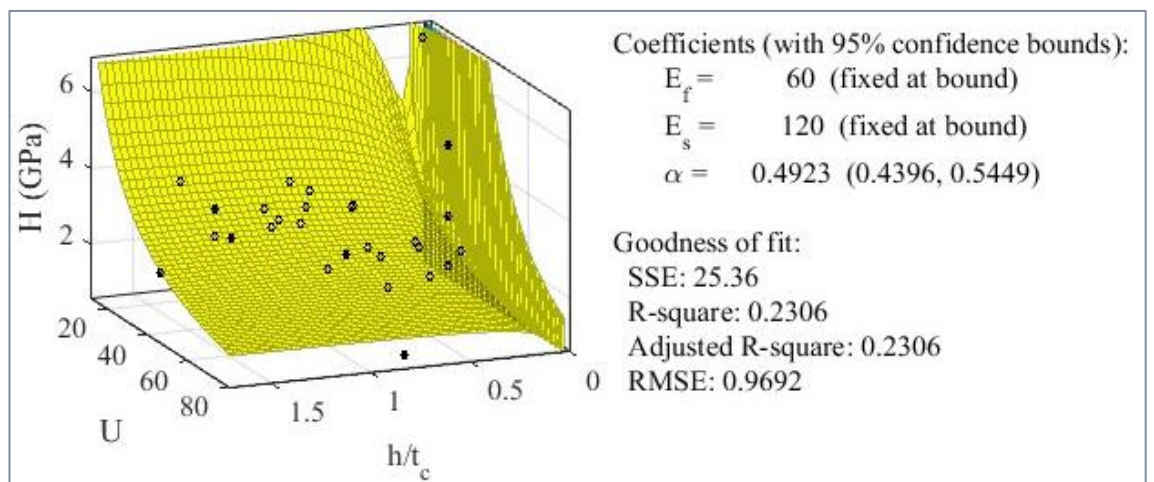
c) AZO on Steel, ADEITM model



d) AZO on Steel, 5PL model



f) AZO on Steel, EM model



© Copyright by

Abdul Shah

2019